frontiers | Research Topics

Quantitative characterization and engineering application of pores and fractures of different scales in unconventional reservoirs, volume III

Edited by
Hu Li, Shuai Yin and Wenlong Ding

Published in
Frontiers in Earth Science

ISSN 1664-8714
ISBN 978-2-8325-3671-1
DOI 10.3389/978-2-8325-3671-1

About Frontiers

Frontiers is more than just an open access publisher of scholarly articles: it is a pioneering approach to the world of academia, radically improving the way scholarly research is managed. The grand vision of Frontiers is a world where all people have an equal opportunity to seek, share and generate knowledge. Frontiers provides immediate and permanent online open access to all its publications, but this alone is not enough to realize our grand goals.

Frontiers journal series

The Frontiers journal series is a multi-tier and interdisciplinary set of open-access, online journals, promising a paradigm shift from the current review, selection and dissemination processes in academic publishing. All Frontiers journals are driven by researchers for researchers; therefore, they constitute a service to the scholarly community. At the same time, the *Frontiers journal series* operates on a revolutionary invention, the tiered publishing system, initially addressing specific communities of scholars, and gradually climbing up to broader public understanding, thus serving the interests of the lay society, too.

Dedication to quality

Each Frontiers article is a landmark of the highest quality, thanks to genuinely collaborative interactions between authors and review editors, who include some of the world's best academicians. Research must be certified by peers before entering a stream of knowledge that may eventually reach the public - and shape society; therefore, Frontiers only applies the most rigorous and unbiased reviews. Frontiers revolutionizes research publishing by freely delivering the most outstanding research, evaluated with no bias from both the academic and social point of view. By applying the most advanced information technologies, Frontiers is catapulting scholarly publishing into a new generation.

What are Frontiers Research Topics?

Frontiers Research Topics are very popular trademarks of the *Frontiers journals series*: they are collections of at least ten articles, all centered on a particular subject. With their unique mix of varied contributions from Original Research to Review Articles, Frontiers Research Topics unify the most influential researchers, the latest key findings and historical advances in a hot research area.

Find out more on how to host your own Frontiers Research Topic or contribute to one as an author by contacting the Frontiers editorial office: frontiersin.org/about/contact

Quantitative characterization and engineering application of pores and fractures of different scales in unconventional reservoirs, volume III

Topic editors

Hu Li — Southwest Petroleum University, China

Shuai Yin — Xi'an Shiyou University, China

Wenlong Ding — China University of Geosciences, China

Citation

Li, H., Yin, S., Ding, W., eds. (2023). *Quantitative characterization and engineering application of pores and fractures of different scales in unconventional reservoirs, volume III*. Lausanne: Frontiers Media SA. doi: 10.3389/978-2-8325-3671-1

Table of contents

frontiers | Frontiers in Earth Science

TYPE Editorial
PUBLISHED 25 September 2023
DOI 10.3389/feart.2023.1294427

OPEN ACCESS

EDITED AND REVIEWED BY
Derek Keir,
University of Southampton,
United Kingdom

*CORRESPONDENCE
Hu Li,
lihu860628@126.com

RECEIVED 14 September 2023
ACCEPTED 18 September 2023
PUBLISHED 25 September 2023

CITATION
Li H, Yin S and Ding W (2023), Editorial: Quantitative characterization and engineering application of pores and fractures of different scales in unconventional reservoirs, volume III. *Front. Earth Sci.* 11:1294427. doi: 10.3389/feart.2023.1294427

Editorial: Quantitative characterization and engineering application of pores and fractures of different scales in unconventional reservoirs, volume III

Hu Li[1,2]*, Shuai Yin[3] and Wenlong Ding[4]

[1]Shale Gas Evaluation and Exploitation Key Laboratory of Sichuan Province, Chengdu, China, [2]School of Geoscience and Technology, Southwest Petroleum University, Chengdu, China, [3]School of Earth Science and Engineering, Xi'an Shiyou University, Xi'an, China, [4]School of Energy Resources, China University of Geosciences, Beijing, China

KEYWORDS

tight sandstone, shale gas, volcanic reservoir, multi-scale fracture systems, pore structure, reservoir characteristics

Editorial on the Research Topic
Quantitative characterization and engineering application of pores and fractures of different scales in unconventional reservoirs, volume III

1 Introduction

Unconventional oil and gas resources have emerged as a pivotal area in the global petroleum industry, representing a significant shift from conventional hydrocarbon exploration and production. These unconventional resources, which encompass reservoirs like shale, tight sandstones, tight carbonates, and volcanic rocks, pose distinct challenges due to their intricate pore-fracture systems and the unconventional mechanisms governing fluid flow and accumulation (Gao and Li, 2016; Li et al., 2019; Li et al., 2020; Radwan et al., 2021; Li, 2023). Notably, each type of unconventional reservoir exhibits unique characteristics, necessitating a comprehensive and precise quantification of their pore and fracture attributes. This quantification is pivotal to advancing the exploration and production strategies for unconventional oil and gas reservoirs.

In recent years, there has been a remarkable surge in technological advancements and their practical application in reservoir characterization. These innovations span various disciplines, including high-resolution CT scanning, nuclear magnetic resonance (NMR), field-emission scanning electron microscopy (FE-SEM), atomic force microscopy (AFM), and gas adsorption techniques (Fan et al., 2020a; Li et al., 2022a; Li, 2022; Zhu et al., 2023). These cutting-edge technologies have collectively enabled researchers and industry professionals to undertake quantitative assessments of the intricate three-dimensional pore structures and the behavior of mobile fluids within tight reservoirs.

The significance of this Research Topic, volume III within the series '*Quantitative characterization and engineering application of pores and fractures of different scales in unconventional reservoirs*' is underscored by its compilation of 36 exceptional contributions from esteemed scholars worldwide. Among these submissions, 14 have been selected for publication, reflecting the rigorous standards upheld. Notably, including these research papers marks a pivotal milestone in further advancing the field, providing fresh and innovative perspectives for the quantitative characterization of multiscale pore-fracture systems, focusing on tight carbonate and shale reservoirs. This Research Topic serves as a valuable resource for researchers, professionals, and organizations engaged in exploring and producing unconventional oil and gas resources, facilitating more effective decision-making and enhancing the industry's sustainability.

2 Quantitative characterization of multi-scale pores and fractures in unconventional reservoirs

2.1 Tight carbonate reservoir

Compared to the previous two research topics, this focuses on the recent advancements in the characterization of tight carbonate reservoirs. Carbonate reservoirs account for over half of the total oil and gas reserves, making them paramount in the world's hydrocarbon resources. Among carbonate reservoirs, tight carbonate reservoirs are a significant subset. However, these reservoirs often exhibit poor petrophysical properties high heterogeneity, and pose challenges in development (Li et al., 2021; Shan et al., 2021). The quantitative characterization of the pore-fracture system within such reservoirs is crucial for effectively exploring and producing oil and gas resources.

In recent years, with the fine exploration of carbonate reservoirs in the Qixia Formation of the central Sichuan Basin, researchers have made important oil and gas discoveries in the dolomite reservoirs. The petrology, pore structures, physical properties, and geochemical characteristics of the dolomite reservoirs have been systematically studied based on a large number of cores, thin sections, physical properties, and geochemical tests, and the genesis and main controlling factors of dolomite reservoirs are clarified Tan et al. Liu et al. also take the Qixia Formation of the Gaomo block as an example, and they have studied distribution characteristics of sedimentary microfacies of a system tract under a high-resolution sequence framework. In this study, the vertical fourth-order sequence is divided using the high vertical resolutions of gamma-ray (GR), uranium (U), thorium (Th), and potassium (K) curves in the logging curves, and the sequence is divided in the depth system is then accurately superimposed on the seismic profile through one-dimensional forward modeling. Different lithofacies' origin and pore-throat structure are key issues in the exploration and development of tight oolitic reservoirs. Ren et al. first classify the lithofacies of oolitic reservoirs according to the macro–micro petrological characteristics. Then, different lithofacies' pore type, throat type, and petrophysical properties are discussed using 3D CT scanning, low-field nuclear magnetic resonance (NMR), MICP, and scanning electron microscopy (SEM). Finally, based on cathodoluminescence (CL), stable isotope, and rare Earth element (REE) data, factors controlling the origin of different lithofacies are studied, and a sedimentary-diagenetic evolution model is established. The heterogeneity of deep carbonate reservoirs is strong, it is significant for exploration and development to clarify the key stages of oil and gas accumulation. Zhang et al. have systematically investigated the key stage and model of hydrocarbon accumulation using the data of the cores, thin sections, cathode luminescence tests, laser ablation U-Pb isotope geochronometry, bitumen reflectance, and fluid inclusion tests, and seismic interpretation in the Gucheng area of Tarim Basin. Then, the favorable zones for hydrocarbon exploration in the Gucheng area were determined.

2.2 Shale reservoirs

The characteristics of source-rock gas reservoirs, which combine gas source and storage in one, have made reservoir characterization and evaluation essential for area assessment, sweet spot prediction, and development plan design and implementation (Abolghasemi and Andersen, 2021; Li et al., 2022b; Fan et al., 2022; Wood, 2022; Li et al., 2023a). This Research Topic continues to report on various aspects related to the characterization of pores and fractures in shale reservoirs. The Jurassic Lianggaoshan Formation lacustrine shale oil is Southwest China's most potential exploration target for unconventional hydrocarbon resources. To accurately characterize the pore structure characteristics of shale reservoir, Lai et al. use Nuclear magnetic resonance (NMR), scanning electron microscopy (SEM), low-temperature N_2 adsorption (LTNA), and high-pressure mercury intrusion mercury injection capillary pressure to reveal pore structure and its controlling factors of Lianggaoshan Formation lacustrine shale reservoir. The enrichment of organic matter has little effect on the development of micropores and does not affect the mesopore and macropore development. Quartz particles in Lianggaoshan lacustrine shale do not facilitate the development of micropore and mesopore-macropore. Intraparticle pore in feldspar clast is an important component of mesopore and macropore. Clay minerals have no positive effect on the formation of micropores and mesopore-macropores. Hu et al. have analyzed high-quality shale logging response characteristics and drilling logging, seismic, and analytical test data in the WY area to establish a rock physical model of seismic attribute parameters and shale reservoir quality parameters. Seismic elastic parameters are converted into indicators that directly reflect shale reservoir quality and predict the quality parameters. Taking the typical block of the Longmaxi shale reservoir in southern Sichuan as the engineering background, Feng et al. use the finite element method to develop a numerical model of a two-dimensional fracture closure variation subjected to the non-hydrostatic stress field. It explores the influence of different fracture occurrences and rock mechanical parameters on stress sensitivity. The theoretical model verifies the numerical simulation results to reveal the stress sensitivity mechanism of the fractured reservoir. In addition, Yu et al. studied the main controlling factors of natural fractures in tight reservoirs of the Lucaogou Formation in the Jimsar Sag of Xinjiang. There are mainly

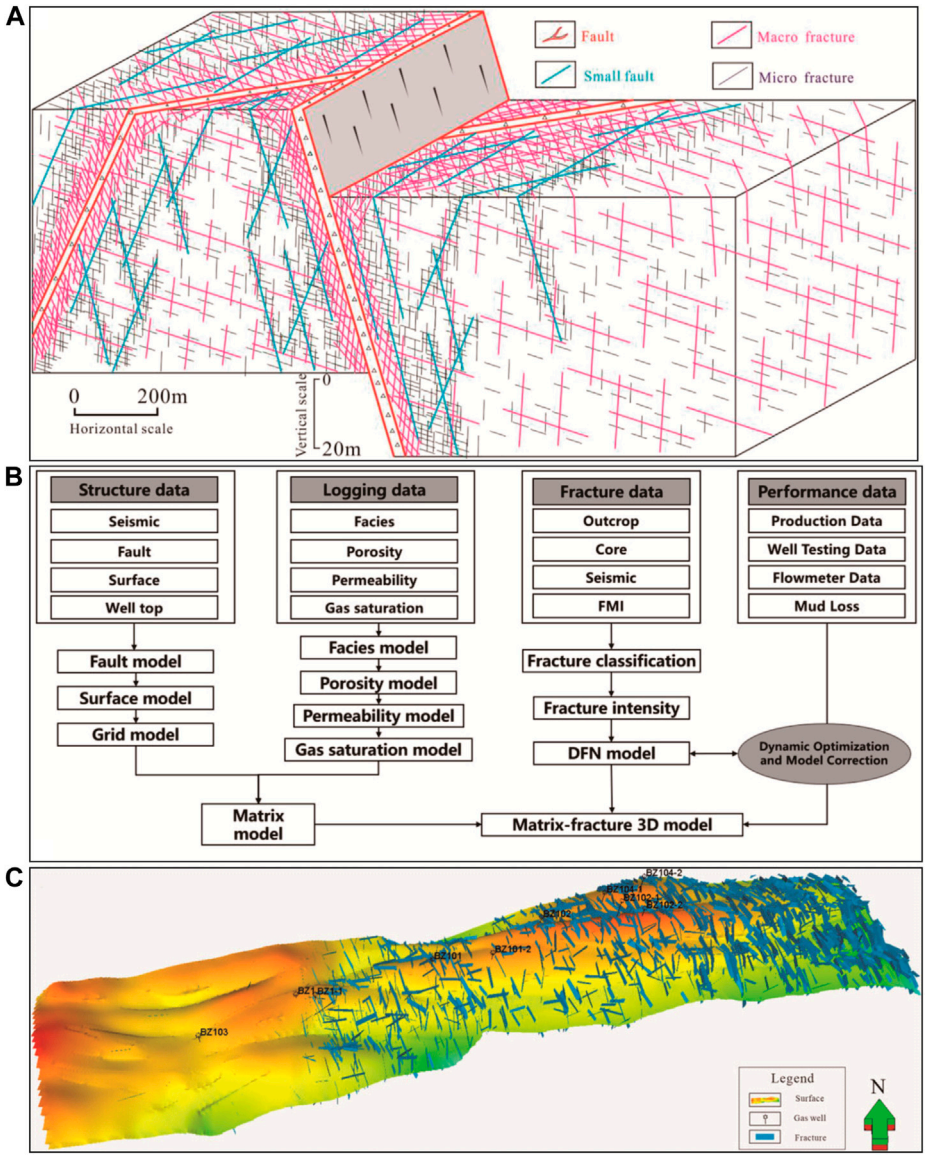

FIGURE 1
The main fracture modeling techniques in the Research Topic. **(A)**. The typical structure model of fracture networks under various configurations (Mi et al.); **(B, C)**. A generalizable of the flow chart of multi-scale fracture-matrix-performance 3D geological modeling and the modeling results (Liu et al.).

three types of natural fractures: tectonic, diagenetic, and abnormal overpressure-induced fractures. Large tectonic stress, smaller bed thickness, and higher total organic carbon are favorable for developing tectonic fractures and bedding seams.

2.3 Volcanic reservoirs

Volcanic rock oil and gas reservoirs are widely distributed in more than 40 basins across 13 countries worldwide, constituting a significant oil and gas exploration domain. Research on volcanic rock oil and gas reservoirs includes reservoir characteristics, distribution patterns, formation mechanisms, and controlling factors (Fan et al., 2020b; Tang et al., 2020; Wang and Wang, 2021). These reservoirs possess distinct features, such as the development of primary pores and fractures, high soluble component content under acidic conditions conducive to secondary porosity formation, modification due to pre-burial weathering and leaching processes, and even the presence of volcanic material components in sedimentary rocks, which help prevent intergranular pores from being filled with silica and promote pore preservation.

Identifying the characteristics and main factors controlling high-quality volcanic reservoirs is the key to increasing oil and gas reserves and production in the Shixi area of the Junggar Basin. Through core observations, thin section identification, physical property, and pore structure analyses, combined with production data, the main controlling factors and development modes of high-quality reservoirs are analyzed by Yiming et al. Lithology and lithofacies, weathering and corrosion, and fractures are the main

factors controlling the development of high-quality volcanic reservoirs. Intermediate mafic lava is a special oil and gas reservoir. Yue et al. have evaluated the intermediate mafic lava flows of the Yingcheng Formation in the Dongling area of Songliao Basin by analyzing drilling cores, corresponding thin sections, and scanning electron microscope (SEM) images, as well as well-logging and seismic attributes. We also performed helium gas experiments and high-pressure mercury intrusion (HPMI) analysis to assess the reservoir's physical properties and pore structure, respectively. The reservoir quality is best in the Crater-proximal facies (CF-PF). Metamorphic rocks are often associated with volcanic activity, Mi et al. take the Bozhong 19–6 metamorphic buried hill as an example, and they use image logs, core samples, thin sections, scanning electron microscope, *etc.*, to characterize genesis and distribution of multi-scale fractures, clarify fracture distribution modes and their contributions to storage capacity, establish structure model of fracture networks under various configurations, and discuss development characteristics and their impact on productivity (Figure 1A). In addition, Liu et al. have established the 3D geological modeling of a deep fractured low porosity sandstone gas reservoir in the Kuqa Depression of Tarim Basin. This method includes four key techniques: 1) Structural modeling using well-to-seismic ties, 2) facies modeling utilizing stochastic objects, 3) reservoir petrophysical modeling under facies constraints, and 4) fracture modeling under multiple-condition constraints and static-performance data combination (Figures 1B,C).

3 Summary

In summary, the 14 high-quality papers featured in this Research Topic significantly advance our understanding of the quantitative characterization and engineering application of pores and fractures in unconventional reservoirs. As we alluded to in the previous Research Topic, the current edition emphasizes the quantitative characterization and predictive research progress of fractures within tight reservoirs (Wang et al., 2022; Li et al., 2023b). This Research Topic provides a valuable platform for scholars and experts to delve into the intricacies of these critical reservoir features.

We are genuinely grateful for the opportunity to present this dynamic Research Topic, and we trust that our readers will find immense value in the breadth and depth of the research contributions. Moreover, we are excited to announce the involvement of Professor Ahmed E. Radwan in another Research Topic titled "Differences in Shale Oil and Gas Reservoirs across Various Sedimentary Environments: Theories and Applications." We eagerly anticipate the active participation of more scholars in this research theme, as it promises to foster insightful discussions about the distinctions inherent in shale oil and gas reservoirs. Through collaborative efforts, we aspire to unravel further complexities and drive innovation in unconventional reservoir studies.

Author contributions

HL: Conceptualization, Data curation, Formal Analysis, Funding acquisition, Investigation, Project administration, Supervision, Validation, Writing–original draft, Writing–review and editing. SY: Investigation, Methodology, Resources, Software, Writing–original draft, Writing–review and editing. WD: Investigation, Validation, Visualization, Writing–original draft, Writing–review and editing.

Funding

This work was supported by the Open funds of Shale Gas Evaluation and Exploitation Key Laboratory of Sichuan Province (Nos. YSK2023001 and YSK2022002), and the key R & D projects of the Deyang Science and Technology Plan (No. 2022SZ049).

Conflict of interest

The authors declare that the research was conducted in the absence of any commercial or financial relationships that could be construed as a potential conflict of interest.

The author(s) declared that they were an editorial board member of Frontiers, at the time of submission. This had no impact on the peer review process and the final decision

Publisher's note

References

Abolghasemi, E., and Andersen, P. Ø. (2021). The influence of adsorption layer thickness and pore geometry on gas production from tight compressible shales. *Adv. Geo-Energy Res.* 6 (1), 4–22. doi:10.46690/ager.2022.01.02

Fan, C. H., Li, H., Qin, Q. R., He, S., and Zhong, C. (2020a). Geological conditions and exploration potential of shale gas reservoir in Wufeng and Longmaxi Formation of southeastern Sichuan Basin, China. *J. Petrol. Sci. Eng.* 191, 107138. doi:10.1016/j.petrol.2020.107138

Fan, C. H., Li, H., Qin, Q. R., Shang, L., Yuan, Y. F., and Li, Z. (2020b). Formation mechanisms and distribution of weathered volcanic reservoirs: A case study of the carboniferous volcanic rocks in northwest junggar basin, China. *Energy Sci. Eng.* 8 (8), 2841–2858. doi:10.1002/ese3.702

Fan, C. H., Xie, H. B., Li, H., Zhao, S. X., Shi, X. C., Liu, J. F., et al. (2022). Complicated fault characterization and its influence on shale gas preservation in the southern margin of the Sichuan basin, China. *Lithosphere* 2022, 8035106. doi:10.2113/2022/8035106

Gao, H., and Li, H. A. (2016). Pore structure characterization, permeability evaluation and enhanced gas recovery techniques of tight gas sandstones. *J. Nat. Gas. Sci. Eng.* 28, 536–547. doi:10.1016/j.jngse.2015.12.018

Li, H., Ding, W. L., and Yin, S. (2023b). Quantitative characterization and engineering application of pores and fractures of different scales in unconventional reservoirs-Volume II. *Front. Earth Sci.* 10, 1133707. doi:10.3389/feart.2022.1133707

Li, H. (2023). Coordinated development of shale gas benefit exploitation and ecological environmental conservation in China: A mini review. *Front. Ecol. Evol.* 11, 1232395. doi:10.3389/fevo.2023.1232395

Li, J., Li, H., Yang, C., Ren, X. H., and Li, Y. D. (2023a). Geological characteristics of deep shale gas and their effects on shale fracability in the Wufeng–Longmaxi Formations of the southern Sichuan Basin, China. *Lithosphere* 2023 (1), 4936993. doi:10.2113/2023/4936993

Li, J., Li, H., Yang, C., Wu, Y. J., Gao, Z., and Jiang, S. L. (2022b). Geological characteristics and controlling factors of deep shale gas enrichment of the Wufeng-Longmaxi Formation in the southern Sichuan basin, China. *Lithosphere* 2022, 4737801. doi:10.2113/2022/4737801

Li, H., Qin, Q. R., Zhang, B. J., Ge, X. Y., Hu, X., Fan, C. H., et al. (2020). Tectonic fracture formation and distribution in ultradeep marine carbonate gas reservoirs: A case study of the maokou formation in the jiulongshan gas field, Sichuan basin, southwest China. *Energy Fuel* 34 (11), 14132–14146. doi:10.1021/acs.energyfuels.0c03327

Li, H. (2022). Research progress on evaluation methods and factors influencing shale brittleness: a review. *Energy Rep.* 8, 4344–4358. doi:10.1016/j.egyr.2022.03.120

Li, H., Tang, H. M., Qin, Q. R., Zhou, J. L., Qin, Z. J., Fan, C. H., et al. (2019). Characteristics, formation periods and genetic mechanisms of tectonic fractures in the tight gas sandstones reservoir: A case study of xujiahe formation in YB area, Sichuan basin, China. *J. Petrol. Sci. Eng.* 178, 723–735. doi:10.1016/j.petrol.2019.04.007

Li, H., Wang, Q., Qin, Q. R., and Ge, X. Y. (2021). Characteristics of natural fractures in an ultra deep marine carbonate gas reservoir and their impact on the reservoir: A case study of the maokou formation of the JLS structure in the Sichuan basin, China. *Energy Fuel* 35 (16), 13098–13108. doi:10.1021/acs.energyfuels.1c01581

Li, H., Zhou, J. L., Mou, X. Y., Guo, H. X., Wang, X. X., An, H. Y., et al. (2022a). Pore structure and fractal characteristics of the marine shale of the Longmaxi Formation in the Changning area, southern Sichuan basin, China. *Front. Earth Sci.* 10, 1018274. doi:10.3389/feart.2022.1018274

Radwan, A. E., Trippetta, F., Kassem, A. A., and Kania, M. (2021). Multi-scale characterization of unconventional tight carbonate reservoir: insights from october oil filed, gulf of suez rift basin, Egypt. *J. Petrol. Sci. Eng.* 197, 107968. doi:10.1016/j.petrol.2020.107968

Shan, S. C., Wu, Y. Z., Fu, Y. K., and Zhou, P. H. (2021). Shear mechanical properties of anchored rock mass under impact load. *J. Min. Strata Control Eng.* 3 (4), 043034. doi:10.13532/j.jmsce.cn10-1638/td.20211014.001

Tang, H. F., Wang, P. J., Bian, W. H., Huang, Y. L., Gao, Y. F., and Dai, X. J. (2020). Review of volcanic reservoir geology. *Acta Petrol. Sin.* 41 (12), 1744–1773. doi:10.7623/syxb202012026

Wang, J., and Wang, X. L. (2021). Seepage characteristic and fracture development of protected seam caused by mining protecting strata. *J. Min. Strata Control Eng.* 3 (3), 033511. doi:10.13532/j.jmsce.cn10-1638/td.20201215.001

Wang, X., Li, J., Jiang, W., Zhang, H., Feng, Y., and Yang, Z. (2022). Characteristics, current exploration practices, and prospects of continental shale oil in China. *Adv. Geo-Energy Res.* 6 (6), 454–459. doi:10.46690/ager.2022.06.02

Wood, D. A. (2022). Predicting brittleness indices of prospective shale formations from sparse well-log suites assisted by derivative and volatility attributes. *Adv. Geo-Energy Res.* 6 (4), 334–346. doi:10.46690/ager.2022.04.08

Zhu, B. Y., Meng, J. H., Pan, R. F., Hu, H. Y., Song, C., Zhu, Z. P., et al. (2023). New insights into the evaluation criteria for high-quality deep marine shale gas reservoirs in the Longmaxi formation: evidence from organic matter pore development characteristics. *Front. Ecol. Evol.* 11, 1138991. doi:10.3389/fevo.2023.1138991

frontiers | Frontiers in Earth Science

TYPE Original Research
PUBLISHED 04 January 2023
DOI 10.3389/feart.2022.1108032

OPEN ACCESS

EDITED BY
Hu Li,
Southwest Petroleum University, China

REVIEWED BY
Xiaodong Lan,
China University of Geosciences, China
Jinxiong Shi,
Yangtze University, China

*CORRESPONDENCE
Lei Gong,
kcgonglei@foxmail.com

SPECIALTY SECTION
This article was submitted to Structural Geology and Tectonics, a section of the journal Frontiers in Earth Science

RECEIVED 25 November 2022
ACCEPTED 09 December 2022
PUBLISHED 04 January 2023

CITATION
Mi L, Fan H, Fan T, Gong L, Niu T, Su X, Luo J and Sun Y (2023), Development characteristics of multi-scale fracture network systems in metamorphic buried hills.
Front. Earth Sci. 10:1108032.
doi: 10.3389/feart.2022.1108032

Development characteristics of multi-scale fracture network systems in metamorphic buried hills

Lijun Mi[1], Hongjun Fan[1], Tingen Fan[1], Lei Gong[2]*, Tao Niu[1], Xiaocen Su[2], Jianghua Luo[1] and Yonghe Sun[2,3]

[1]CNOOC Research Institute Ltd, Beijing, China, [2]Bohai-Rim Energy Research Institute, Northeast Petroleum University, Qinhuangdao, China, [3]Institute of Chongqing Unconventional Oil and Gas Development, Chongqing University of Science and Technology, Chongqing, China

Natural fractures are regarded as important reservoir spaces and effective seepage channels at metamorphic buried hills. Continuous networks associated with multi-scale fractures with good connectivity is critical for high-quality reservoirs as well as high and stable production in the tight metamorphic rocks. The multi-scale fractures in Bozhong 19–6 metamorphic buried hills were well characterized through integrating image logs, cores, thin-sections, and scanning electron microscope, *etc.* After that, power-law distribution of multi-scale fractures was established to understand contribution of fractures to reservoir quality and figure out structure models of fracture networks as well as their impact on production. Results show that parameters of fracture systems vary regularly with fracture scales. Fracture development degree, e.g., cumulative areal density, increases as a power law function with decreasing fracture size from macro to micro (e.g., aperture and/or length), where storage space associated with micro fractures is also increased. Reversely, fracture connectivity and permeability follow a significant decreasing trend. Five structure models of fracture network were established based on combination pattern of multi-scale fractures: multi-scale fracture network with high-density and multi-sets, large-scale fracture network with medium-density and multi-sets, small-scale fracture network with high-density and multi-sets, large-scale fracture network with low-density and multi-sets, and small-scale fracture network with low-density and single-set. The former two fracture networks can be widely developed into high-quality reservoirs, contributing greatly to high and stable yields. Fracturing is required for the third and the fourth fracture networks to obtain stable production, while it is difficult for the fifth fracture network to obtain industrial oil and gas flow.

KEYWORDS

metamorphic buried hills, multi-scale fractures, structure models of fracture networks, contribution, power-law distribution

Introduction

Buried hills have been regarded as important oil and gas exploration targets for a long time. Currently a large number of theories have been developed to understand buried hill oil-gas accumulations (Ye et al., 2021; Zhou et al., 2022). Exploration practice has confirmed that diverse lithology were developed at buried hill reservoirs, e.g., volcanic rocks, carbonate rocks, clastic rocks and metamorphic rocks, where metamorphic reservoirs have the largest exploration potential (Hou et al., 2013; Wang et al., 2015; Zhou et al., 2022). Major breakthroughs have been recently made in Archaean metamorphic buried hills in the Bohai Bay Basin, China, e.g., Bozhong 19–6 metamorphic buried hill, Xinglongtai buried hills and Jinzhou 25–1 metamorphic buried hills at Liaohe Basin, which have obtained hundred million tons of reserves (Hu et al., 2017; Wang et al., 2019; Xu et al., 2020; Ye et al., 2021). Long-period weathering, diverse lithology, and multiple tectonic stress brought complex reservoir structure to Archaean metamorphic buried hills. Hence, how to effectively evaluate buried hills has always been a challenge for researchers (Xu et al., 2020). Previous researchers on metamorphic reservoirs mainly focused on characterization of fractured reservoirs at buried hills, fracture genesis and its impact on reservoir quality (Wang et al., 2022). Multiple reservoirs have been found at metamorphic buried hills, e.g., weathering crust reservoirs on top and fractured reservoirs within buried hills. Scholars have described fracture development phases and filling behaviors, and reported that fracture development in buried hills were closely related to multiple tectonic activities. Researchers show that natural fractures are not only storage space for metamorphic buried hills, but also effective seepage channels (Gao et al., 2015; Gong et al., 2016; Fan et al., 2021; Zeng et al., 2022a). Natural fractures not only connect various pores and enhance seepage capacity, but also are key factors governing high yield of metamorphic buried hills (Huang et al., 2016; Hu et al., 2017; Xue et al., 2020). However, increasing exploration and development activities at buried hill reservoirs gradually expose our poor understanding of multi-scale fracture development and its spatial configuration at buried hills (Cao et al., 2021; Li et al., 2022a), that is, fracture development degree may not be the only factor determining high and stable production of single wells. Fractures of multiple scales are varied in lengths and apertures, resulting in different connectivity and storage capacity. Therefore, understanding configuration mode and spatial distribution of multi-scale fractures is important to guide drilling and development scheme of buried hill reservoirs (Gong et al., 2017). Taking Bozhong 19–6 metamorphic buried hill as an example, this paper uses image logs, core samples, thin sections, scanning electron microscope, *etc.*, to characterize genesis and distribution of multi-scale fractures, clarify fracture distribution modes and

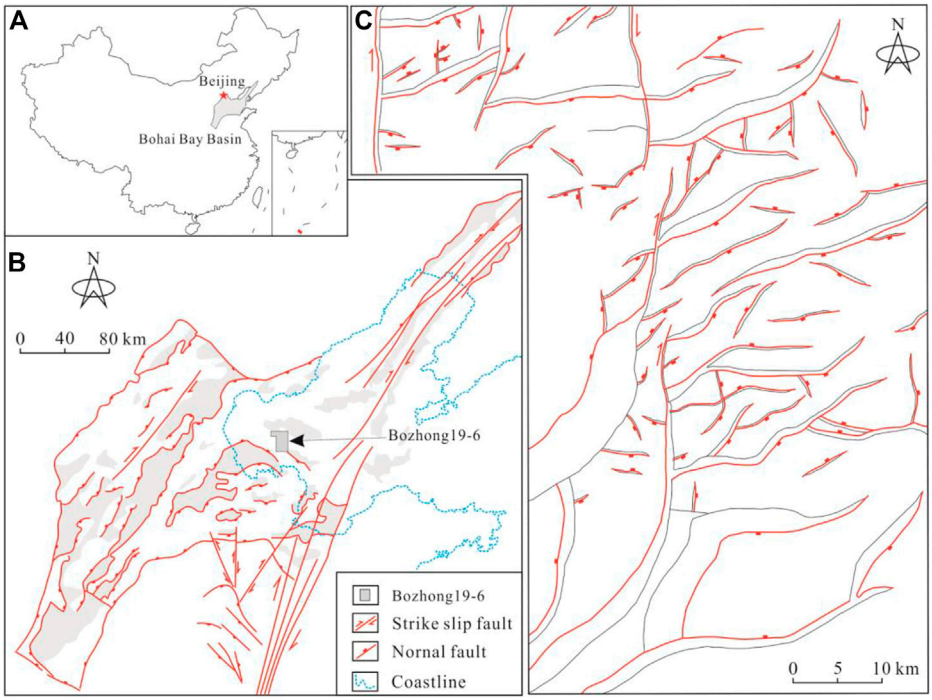

FIGURE 1
Location and structure outline of Bozhong 19–6 metamorphic buried hill. **(A)** Location of the Bohai Bay Basin. **(B)** Location of the Bozhong 19–6. **(C)** structure outline of Bozhong 19–6

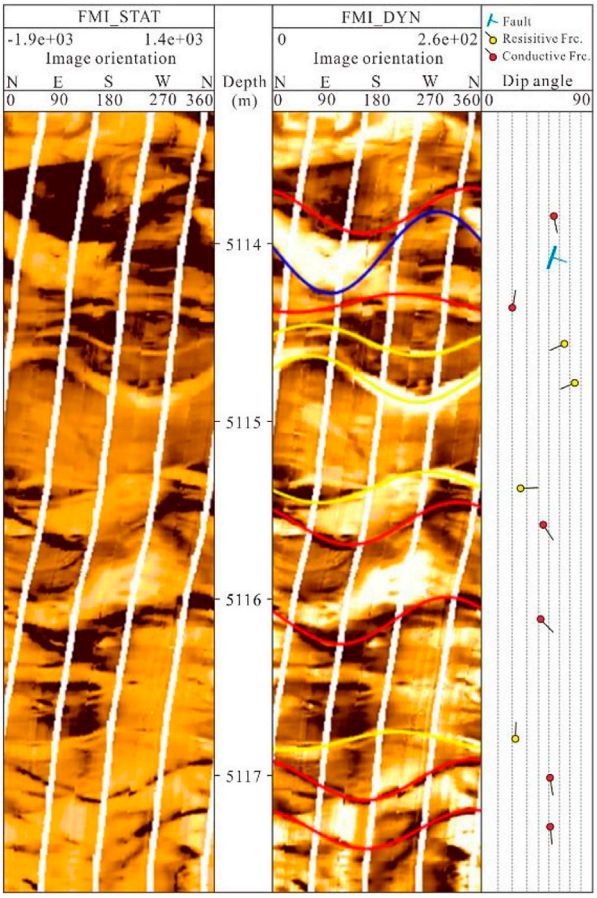

FIGURE 2
Fracture types and development characteristics on image logs in the study area.

their contributions to storage capacity, establish structure model of fracture networks under various configurations, and discuss development characteristics and their impact on productivity.

Geological setting

Bozhong 19–6 buried hill is located in the southwest of Bozhong Sag, Bohai Bay Basin, China (Figures 1A,B). It is a nearly NS extending structural ridge bounded by the Southwest Sag, the central Sag, the South Sag and the Huanghekou Sag. It is a faulted anticline complicated by three strike-slip faults and their derivatives (Figure 1C) (Gong et al., 2019a; Xu et al., 2020; Xue et al., 2020). Four sets of faults, i.e., N-S trending, NNE-SSW trending, NEE-SWW trending and E-W trending, were developed at the top of Bozhong 19–6 buried hills. It is dominated by Archean metamorphic rocks, which is overlaid by Paleogene Kongdian Formation, Shahejie Formation, Dongying Formation, Neogene Guantao Formation, Minghuazhen Formation and Quaternary Pingyuan Formation (Li et al., 2019). Dark mudstone at the third Member and the first Member of Shahejie Formation, and the third Member of Dongying Formation are the primary source rocks in the study area. It is a typical tight reservoirs, with weak overpressure and normal pressure. The Archean metamorphic rocks are mainly granite-gneiss and plagioclase gneiss, while postintrusive dykes, e.g., diorite-porphyrite, *etc.*, are also developed (Zeng et al., 2016; Hou et al., 2019; Xu et al., 2019; Ye et al., 2021). Metamorphic rocks are minerally dominated by light minerals, e.g., quartz, plagioclase and K-feldspar, and dark minerals, e.g., biotite and amphibole, with proportion of light minerals >90%. Controlled by structure, weathering and

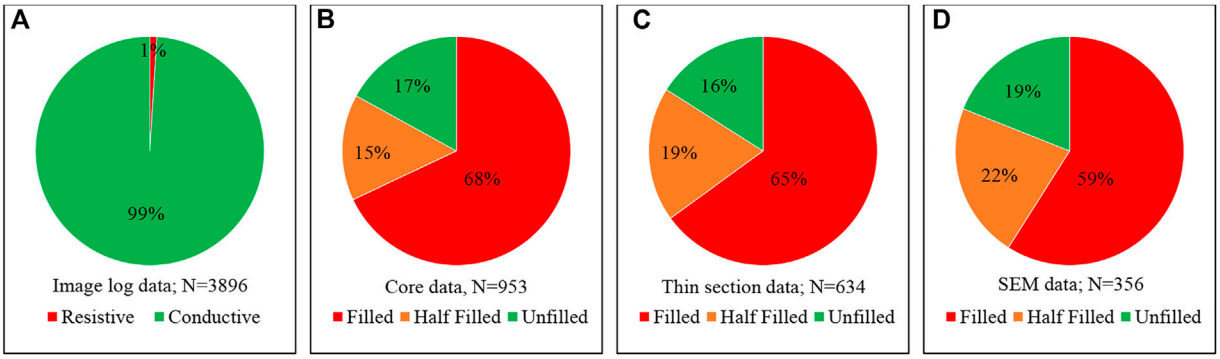

FIGURE 3
Effectiveness of fractures with multiple scales. **(A)** Effectiveness of fractures from image log data; **(B)** effectiveness of fractures from core data; **(C)** effectiveness of fractures from thin section data; **(D)** effectiveness of fractures from SEM data.

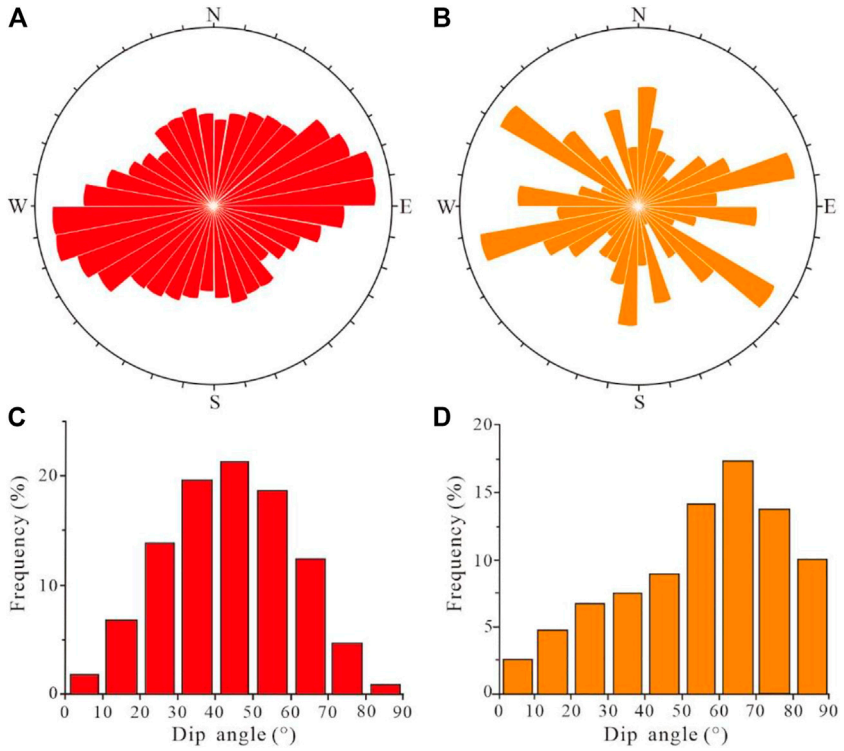

FIGURE 4
Fracture occurrence at weathering zone and inner zone. Rose diagrams showing fracture strikes at weathering zone **(A)** and at inner zone **(B)**. Fracture dip angle at weathering zone **(C)** and at inner zone **(D)**.

lithology, Bozhong 19–6 buried hill can be vertically divided into weathering zone and inner zone (Luo et al., 2013; Luo et al., 2015; Luo et al., 2016). Reservoirs at weathering zone are composed of structural fractures, weathering fractures, dissolved pores, *etc.*, where well-developed fractures result in continuous bed-like reservoirs. Reservoirs at inner zone is dominated by structural fractures, which is distributed in belt pattern controlled by high-angle faults.

Multi-scale fracture development

Fracture development evidenced by image logs

Conductive fractures, resistive fractures, small faults, induced fractures, *etc.*, have been identified from image logs of 18 wells (Figure 2A), while induced fractures as artificial fractures are not in our research category. Conductive fractures are the most popular ones among these three natural fracture types, accounting for 99% of the total fractures number (Figure 3A). It is a good indicator of effective fracture networks in the study area. However, fillings identified from cores and thin-sections confirm (Figures 3B,C) that 59 %–68% of natural fractures are completely filled by minerals, e.g., quartz or calcite. Such a low resistive fracture number can be explained by that filling minerals are similar with that of parent rocks, making it difficult to distinguish them on image logs. In other words, image logs can only identify effective fractures.

The metamorphic rock reservoirs in the study area have complex fracture orientations, especially at the weathering zone on the upper part of the buried hill, where fractures are developed in almost all directions (Figure 4A). It can be attributed to a large number of unsystematic weathering fractures. Fractures at the inner zone commonly follow four orientations, e.g., NEE-SWW trending, near E-W trending, near N-S trending and NW-SE trending (Figure 4B). The fracture dip angles at weathering zone are mainly distributed at 30°–60°, which is dominated by oblique fractures, with low-angle fractures and nearly vertical fractures of secondary importance (Figure 4C). Medium to high dip angle at the inner zone suggests that it is dominated by structural fractures (Figure 4D). The conductive fractures identified on image logs have large size, with fracture aperture of 50–250 μm (average value: 120.7 μm) (Figure 5A). The fracture areal density is about 1–5 m/m^2, with an average of 2.4 m/m^2 (Figure 5B). The density in the weathering zone is higher than that in the inner zone. Fracture porosity detected by image logs is relatively low, about 0.02%–0.2%, with an average of 0.10% (Figure 5C).

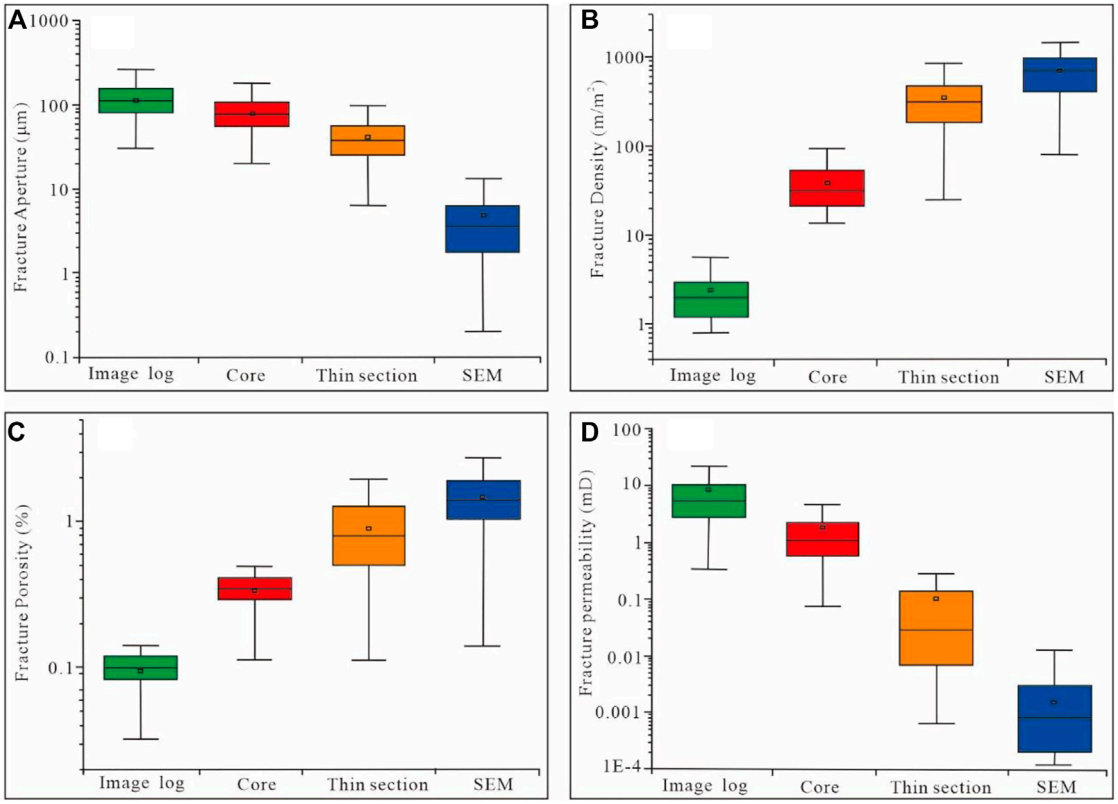

FIGURE 5
Parameters distribution of fractures at multiple scales. **(A)** Fracture aperture. **(B)** Fracture areal density. **(C)** Fracture porosity. **(D)** Fracture permeability.

Fracture permeability detected by image logs is about 3–10 mD, with an average of 8.35 mD (Figure 5D), effectively improving reservoir seepage capacity.

Fracture development on cores

Fractures on cores can be genetically divided into structural fractures and weathering fractures based on geological origin. Structural fractures are the most popular type in metamorphic reservoirs in the study area, with multi-stages, multi-directions (multi-sets), uneven development, difference in filling behaviors (Figures 6A,B). Structural fractures have medium to high dip angles, ranging from 60° to 90°. They have large length on cores (diameter of 3 inches), generally larger than 10 cm (mainly 12–20 cm), with an average of 17.09 cm. Their areal density is mainly 10–30 m/m^2, with an average of 20.1 m/m^2. Calcite and quartz filling can be widely observed, with full-filled fractures of 72%, half-filled fractures of 13% and unfilled fractures of 15%, 28% of them are effective fractures.

Weathering fractures are mainly developed at weathering zone in honeycomb pattern or network pattern (Figure 6C). They are poorly oriented, with curved or arc-shaped surface and unstable occurrence. They are developed in all directions, with dip angles from 0° to 90°. They are short in length, in a range of 4–7 cm, with an average of 5.81 cm, while some can be decimeter-scale. Weathering fractures are well developed, with areal density of 30–70 m/m^2 (average value: 53.0 m/m^2, and up to 93 m/m^2 locally). They are often filled with argillaceous or clay minerals, or are disseminated with iron (oxidized to red) (Figure 3C). They are slightly filled compared with structural fractures, with full-filled ones of 68%, half-filled ones of 15% and unfilled ones of 17%, 32% of them are effective fractures.

Fracture development on thin-sections

Fractures can be divided into intergranular ones, intragranular ones and grain-edge ones based on relationship between micro fractures and mineral grains (Zeng et al., 2013; Gong et al., 2019b). Fractures observation on 265 thin-sections shows that intergranular fractures are popular in the study area (Figures 7A,B). These fractures cut through multiple mineral grains, and even develop throughout the whole thin section. These microfractures are also

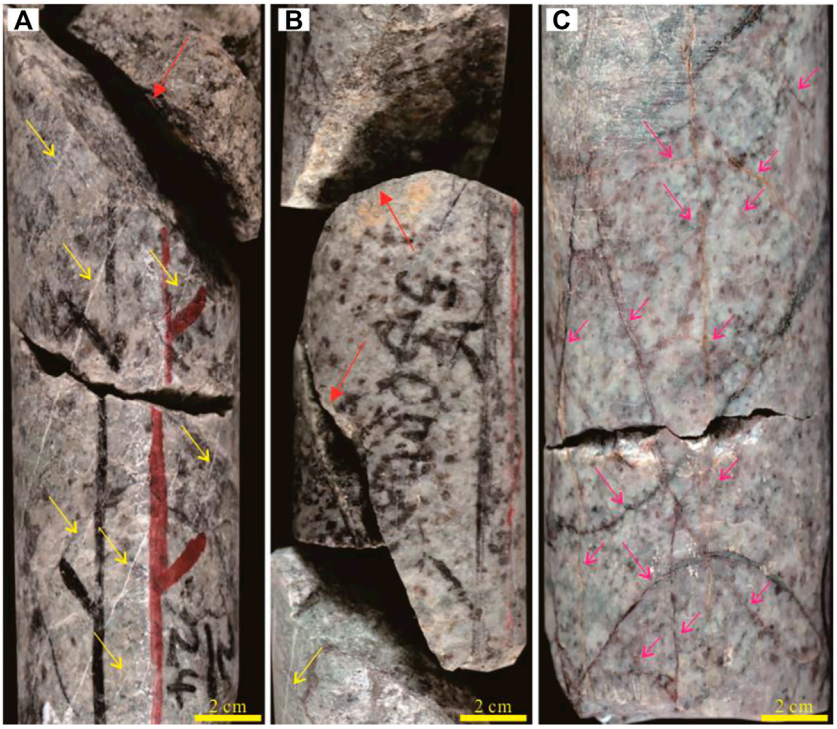

FIGURE 6
Fracture types and development characteristics on cores. Red arrows represent unfilled structural fractures, yellow arrows are calcite-filled structural fractures, purple arrows in Figure 6. **(A)** Calcite-filled and unfilled structural fractures. **(B)** Unfilled and calcite-filled structural fractures. **(C)** Weathering fractures.

highly filled, with full filling accounting for 70%, semi-filling accounting for 14% and unfilled ones accounting for 16%, while filling at weathering zone is slightly lower than that at inner zone. 14 filling mineral types can be identified, e.g., carbonate minerals (dolomite, calcite, ankerite and ferroan calcite), felsic matrix, quartz, argillaceous (ferrous), authigenic clay minerals (chlorite, kaolinite) and pyrite and siderite, *etc.* Fracture aperture is mainly distributed in 10–150 um, with peak value at 20–50 um (Figure 5A). Filled fractures are 40–150 um in aperture (peak value at 50–80 um), while unfilled fractures are 10–60 um in aperture (peak value at 20–40 um).

The intergranular fractures are well developed, with areal density of 200–600 m/m^2 (an average value of 345.4 m/m^2) (Figure 5B). The porosity of micro fractures on thin-sections is mainly 0.5%–1.2%, with an average of 0.88% (Figure 5C), while permeability is between 0.01 mD and 1 mD, with an average of 0.13 mD (Figure 5D).

Fracture development on SEM

Micro fractures under scanning electron microscope are mainly developed within mineral grains as intragranular fractures (e.g., cleavage cracks in feldspar, mica, calcite and quartz cracks) and grain-edge fractures. They have small apertures, ranging from 2 μm to 8 μm, with an average value of 5.8 μm (Figure 5A). The aperture of full-filled fractures is mainly distributed between 10 μm and 30 μm, averaging of 21.8 μm. Although aperture is small, intragranular fractures are developed in almost all mineral grains, while multi-phase fractures can be observed at some grains. The areal density of intragranular fractures is mainly 400–1000 m/m^2, with peak at 600–800 m/m^2 and average value of 700.5 m/m^2 (Figure 5B). Porosity of intragranular fractures is about 1.0%–2.5%, with an average of 1.47% (Figure 5C), while permeability is about 0.0001–0.01 mD, with an average of 0.0087 mD (Figure 5D).

Discussions

Multi-scale fracture classification and its contribution to reservoir

Multi-scale fracture development description shows that fracture size is negatively correlated with fracture development degree (Figure 5B). Investigations on multi-scale fractures from

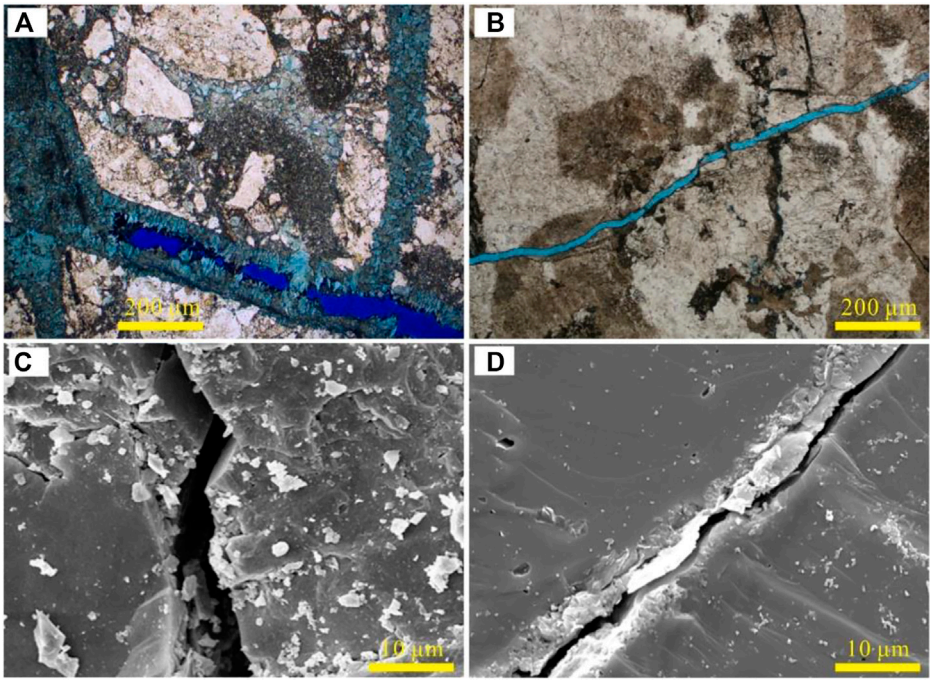

FIGURE 7
Development characteristics of micro fractures. **(A)** Intergranular fracture, full to half filled; **(B)** intergranular fracture, unfilled; **(C)** intragranular fracture, unfilled; **(D)** intragranular fracture, half filled.

outcrops, cores, thin-sections, *etc.*, show that length and aperture are generally distributed at power-law pattern (Fu et al., 2007; Gong et al., 2012), while specific parameters of power law distribution vary with fracture size and development degree (Bonnet et al., 2001; Maerten et al., 2006; Ortega et al., 2006; Li et al., 2012; Strijker et al., 2012; Johri et al., 2014; Gong et al., 2018; Pan et al., 2019; Gong et al., 2021; Zhu et al., 2021; Li et al., 2022b; Zhu et al., 2022). 3D geological modeling of multi-scale fractures can be performed based on the power law pattern of multi-scale fractures (Zeng et al., 2020; Lyu et al., 2021; Zeng et al., 2022b). The power law distribution of fractures with different scales (apertures) was studied in this study, based on which, structure models of fracture networks were established to classify fracture scales and analyze contribution of multi-scale fractures to storage capacity and their roles in oil field development.

Power-law distribution of (Figure 8B) multi-scale fractures in weathering zone is established based on their areal density distribution (Figure 8A), which can be used to determine certain fracture development intensity (the lateral axis represents fracture scale (aperture), and the vertical axis represents development intensity of fractures with size larger than certain value). Meanwhile, porosity and permeability distribution models were established for fractures with various scales (Figures 9, 10). Figures 9, 10 show that storage capacity of fractures varies greatly with their scales. Consequently, natural fracture system in the study area can be divided into two types and four sub-types based on identify methods, fracture scales and their contributions to reservoirs. Specifically, the two types are macro fractures and micro fractures, and the four sub-types are fractures of image log scale, fractures of core scale, fractures of thin-section scale, and fractures of SEM scale (Figure 8C and Table 1).

Fractures of image log scale are defined as those can be identified on image logs with aperture >100 μm. Their density at the weathering zone is mainly 1–10 m/m^2, contributing 0.1%–0.2% to porosity and 2–20 mD to permeability. They are well connected as primary seepage channels, which contributes greatly to high production at early development stage.

Fractures of core-scale can be directly observed with eye from cores, with apertures of 40–100 μm. Their density at the weathering zone of the study area is mainly 10–50 m/m^2, which can increase porosity by 0.2%–0.5% and increase permeability by 0.2–2 mD. They are not only well connected, but also can provide storage space. Therefore, they are both important seepage channels and storage spaces, which is important for stable production at early development.

Fractures of thin-section scale are those can only be observed under optical microscope, commonly intergranular fracture with an aperture of 10–40 μm. Their density is mainly 50–300 m/m^2,

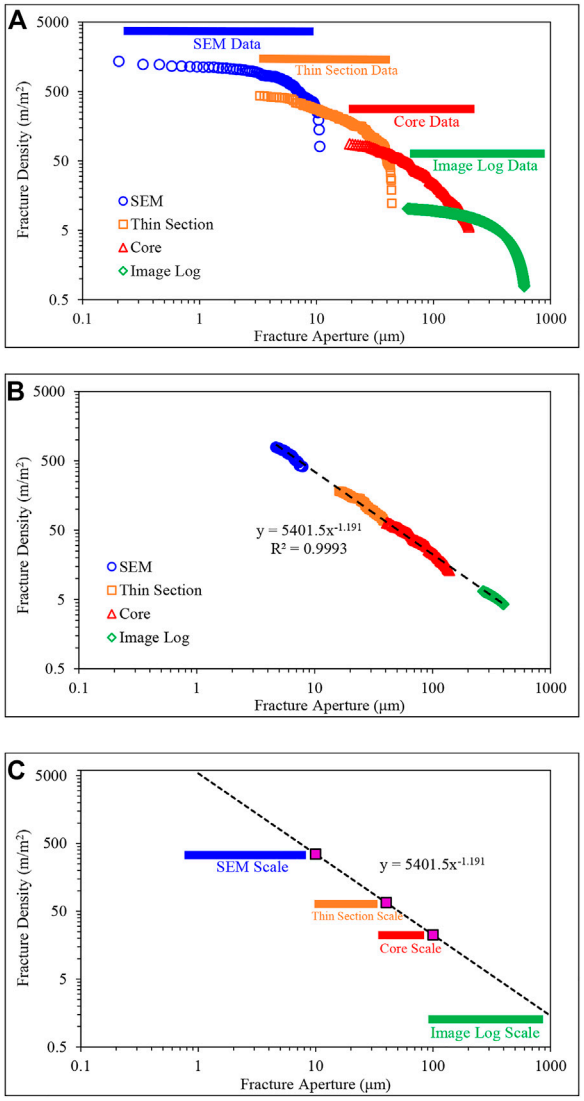

FIGURE 8
Density distribution of multi-scale fractures. **(A)** Density distribution of multi-scale fractures from statistical data. Density of certain fracture follows lognormal distribution. **(B)** Power-law distribution of fracture density based on multi-scale fractures. **(C)** Power-law distribution model of fractures and fracture classification in the study area.

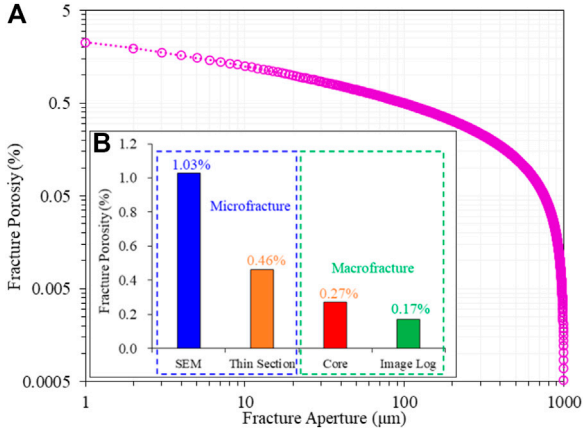

FIGURE 9
Porosity of fractures with multiple scales at BZ 19–6 metamorphic rock reservoir. **(A)** Contribution of fractures with different apertures to porosity. **(B)** Contribution of fractures of different scales to porosity.

which can provide porosity of 0.5%–1.0% and permeability of 0.02–0.2 mD. These fractures can both increase porosity and connect matrix pores and micro fractures, which plays an important role in stable production at middle development period.

Fractures of SEM scale are those can only be observed under scanning electron microscope, which are typical intergranular fractures and grain-edge fractures with aperture of 1–10 μm. They are mainly developed within mineral grains. Their density at the weathering zone is about 300–5,000 m/m^2, whose porosity is about 1.0%–2.0% with permeability <0.02 mD. Although they are small in scale and aperture, high density can increase porosity greatly, enabling them to be reservoirs. They can provide recoverable reserves at later development stage, depending greatly on their connectivity with fractures of thin-section scale.

Structure models of multi-scale fracture network

Exploration activities show that well productivity or reserves is not only related to reservoir quality and fracture density, but also comprehensively controlled by factors, e.g., fracture sets, fracture scale (length), fracture connectivity, and multi-scale fracture configuration, *etc.*, since sometimes high and stable production cannot be obtained from reservoirs with high porosity. Therefore, five fracture configurations and network structures were constructed based on fracture density, fracture sets, fracture scale as well as fault distribution: multi-scale fracture network with high-density and multi-sets, large-scale fracture network with medium-density and multi-sets, small-scale fracture network with high-density and multi-sets, large-scale fracture network with low-density and multi-sets, and small-scale fracture network with low-density and single-set.

The multi-scale fracture networks with high-density and multi-sets are mainly developed at structures with multi-stage active faults and long-term active faults (in parallel or intersected pattern) (Figure 11). This fracture network pattern can develop multi-scale fractures (i.e., large faults, small faults, marco-fractures and micro-fractures) with high fracture density and

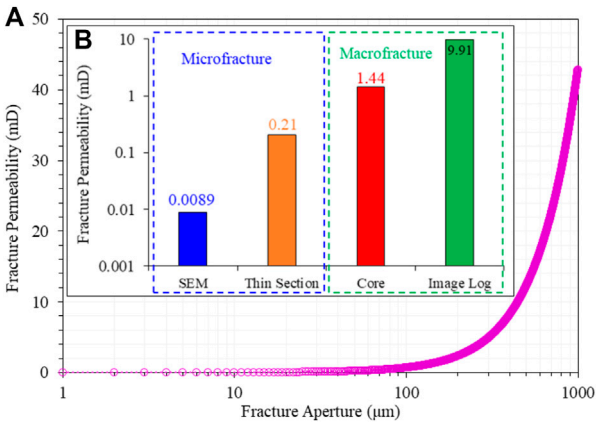

FIGURE 10
Permeability of fractures with multiple scales at BZ 19–6 metamorphic rock reservoir. **(A)** Contribution of fractures with different apertures to permeability. **(B)** Contribution of fractures of different scales to permeability.

good connectivity. The small faults with large apertures and length of hundreds meters to kilometers of meters can effectively communicate multi-scale fracture systems and further connect with matrix pore system, thus forming large-scale and well-connected reservoirs. High and stable oil and gas production can be obtained from this kind of fracture systems.

The large-scale fracture networks with medium-density and multi-sets are mainly developed at the middle and lower part of weathering zone, where many faults are developed at single stage (in parallel or intersected pattern) (Figure 12). They are dominated by large-scale structural fractures, followed by a small group of weathering fractures. However, they are well-connected to form continuous and well-connected reservoirs.

The small-scale fracture networks with high-density and multi-sets are commonly have high fracture density. However, small aperture and length as well as poor connectivity make it difficult to form widely-connected reservoirs (Figure 13). They are mainly developed at the upper part of weathering zone and strata with altered brittleness and ductility. High oil and gas production can be obtained

TABLE 1 Fracture types at BZ 19–6 metamorphic rock reservoir and its contribution to reservoir property.

Fracture types		Density (m/m^2)	Aperture (μm)	Connectivity	Porosity (%)	Permeability (mD)	Contribution
Macrofracture	Image log	1–10	>100	Well	0.1–0.2	2–20	seepage channel
	Core	10–50	40–100	Well	0.2–0.5	0.2–2	seepage channel and storage space
Microfracture	Thin section	50–300	10–40	Moderate-well	0.5–1	0.02–0.2	storage space and connect pores
	SEM	300–5,000	1–10	Poor-moderate	1–2	<0.02	storage space

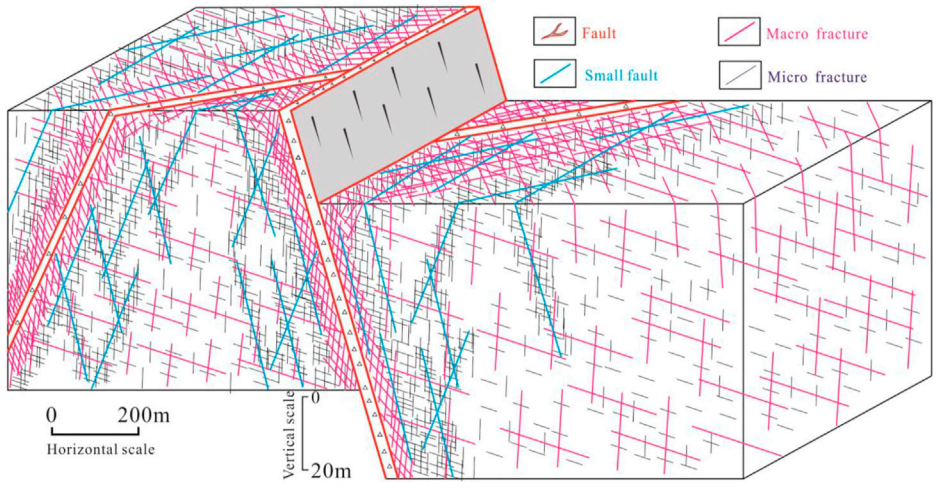

FIGURE 11
Schematic diagram of multi-scale fracture network with high-density and multi-sets.

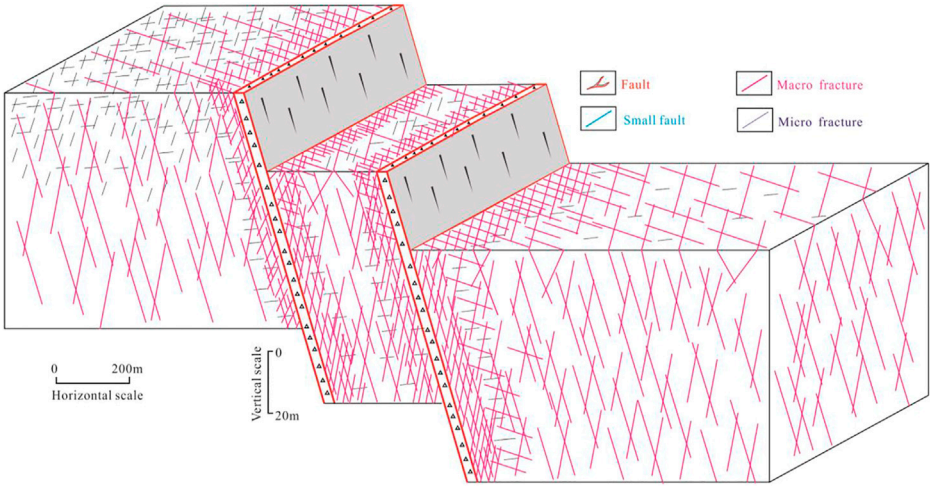

FIGURE 12
Schematic diagram of large-scale fracture network with medium-density and multi-sets.

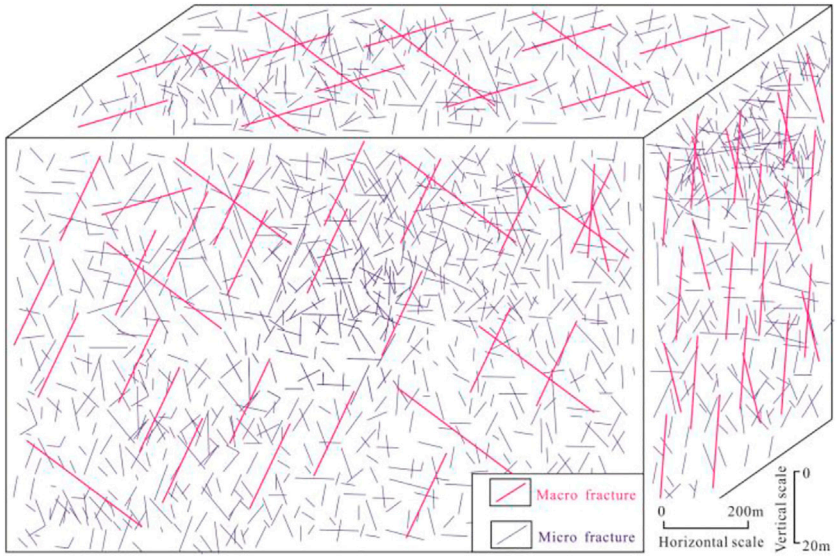

FIGURE 13
Schematic diagram of small-scale fracture network with high-density and multi-sets.

from it at initial stage, where fracturing is required to improve and stable long-term oil and gas production.

The large-scale fracture networks with low-density and multi-sets are mainly developed in the inner zone, with large structural fractures, low fracture density and fair connectivity. Fractures are commonly well developed at the edge of the faults and brittle strata, where industrial oil and gas flow can also be obtained. Small-scale fracture network with low-density and single-set is mainly developed at basements with poor connectivity, which is generally not regarded as reservoir.

Conclusion

Multi-scale fracture systems were developed at the Bozhong 19–6 metamorphic rock reservoir, where system parameters vary regularly with fracture scales. Macro fractures with large length and

aperture can contribute greatly to reservoir permeability (2-20 mD), however, their low density can only provide limited porosity (0.1%–0.2%) to reservoirs. The micro fractures with high density are important reservoirs with porosity of 1%–2%. However, small aperture and length can only communicate matrix pores, contributing minor to reservoir permeability (<0.02 mD). Density of single-scale fractures follows lognormal distribution pattern, while multi-scale fractures follow power-law distribution pattern. Hence, fracture density of certain scale can be accurately predicted with the power-law distribution.

Five structure models of fracture networks are established based on fracture development at different structures of the buried hills. The multi-scale fracture networks with high-density and multi-sets are mainly developed at structures with multi-stage faults and long-term faults. They can form widely-distributed reservoirs with good connectivity, contributing to high and stable oil and gas production. The small-scale fracture networks with high-density and multi-sets are developed at the upper part of weathering zone. However, small aperture and length as well as poor connectivity limits the development of widely-connected reservoirs, where fracturing is required to stable long-term oil and gas production. The large-scale fracture networks with medium-density and multi-sets are mainly developed at the inner zone, mainly composed of large-scale structural fractures, with low density and fair connectivity. Industrial oil and gas flow can also be obtained from this network *via* fracturing. The small-scale fracture networks with low-density and single-set are mainly developed at basements with poor connectivity, which is generally not regarded as reservoir.

Data availability statement

The original contributions presented in the study are included in the article/Supplementary Material, further inquiries can be directed to the corresponding author.

Author contributions

Conceptualization, HF and TN; Data curation, LM and XS; Formal analysis, JL; Investigation, TF; Methodology, LG; Writing—review & editing, LG, YS, and XS.

Funding

This study is financially supported by National Natural Science Foundation of China (Grant No. 42072155), Natural Science Foundation of Heilongjiang Province (Grant No. YQ 2022D006), Young Innovative Talents Training Program for Universities in Heilongjiang Province (grant no. UNPYSCT-2020147) and Postdoctoral Research Foundation of Heilongjiang Province (Grant No. LBH-Q21001).

Conflict of interest

The authors LM, HF, TF, TN, and JL were employed by CNOOC Research Institute Ltd, China.

The remaining authors declare that the research was conducted in the absence of any commercial or financial relationships that could be construed as a potential conflict of interest.

Publisher's note

References

Bonnet, E., Bour, O., Odling, N. E., Davy, P., Main, I., Cowie, P., et al. (2001). Scaling of fracture systems in geological media. *Rev. Geophys.* 39 (3), 347–383. doi:10.1029/1999RG000074

Cao, D. S., Zeng, L. B., Lvy, W. Y., Xu, X., and Tian, H. (2021). Progress in brittleness evaluation and prediction methods in unconventional reservoirs. *Petroleum Sci. Bull.* 01, 31–45. doi:10.3969/j.issn.2096-1693.2021.01.003

Fan, T. E., Niu, T., Fan, H. J., Wang, S., Xiao, K., and Luo, J. H. (2021). Geological model and development strategy of Archean buried hill reservoirin BZ19-6 condensate field. *China Offshore Oil Gas* 33 (03), 85–92. doi:10.11935/j.issn.1673-1506.2021.03.009

Fu, X. F., Su, Y. P., Lv, Y. F., Zhang, Y. F., and Fu, G. (2007). Fractal characteristic and geological meaning of fault and fracture. *Earth Science-Journal China Univ. Geosciences* 32 (2), 227–234. doi:10.3321/j.issn:1000-2383.2007.02.011

Gao, S., Zeng, L. B., Ma, S. Z., He, Y. H., Gong, L., Zhao, X. Y., et al. (2015). Quantitative prediction of fractures with different directions in tight sandstone reservoirs. *Nat. Gas. Geosci.* 26 (03), 427–434. doi:10.11764/j.issn.1672-1926.2015.03.0427

Gong, L., Fu, X. F., Gao, S., Zhao, P. Q., Luo, Q. Y., Zeng, L. B., et al. (2018). Characterization and prediction of complex natural fractures in the tight conglomerate reservoirs: A fractal method. *Energies* 11 (9), 2311. doi:10.3390/en11092311

Gong, L., Gao, M. Z., Zeng, L. B., Fu, X. F., Gao, Z. Y., Gao, A., et al. (2017). Controlling factors on fracture development in the tight sandstone reservoirs: A case study of jurassic-neogene in the kuqa foreland basin. *Nat. Gas. Geosci.* 28 (2), 199–208. doi:10.11764/j.issn.1672-1926.2016.12.003

Gong, L., Gao, S., Liu, B., Yang, J. G., Fu, X. F., Xiao, F., et al. (2021). Quantitative prediction of natural fractures in shale oil reservoirs. *Geofluids* 2021, 1–15. doi:10.1155/2021/5571855

Gong, L., Liu, B., Fu, X. F., Jabbari, H., Gao, S., Yue, W. T., et al. (2019). Quantitative prediction of sub-seismic faults and their impact on waterflood performance: Bozhong 34 oilfield case study. *J. Petroleum Sci. Eng.* 172, 60–69. doi:10.1016/j.petrol.2018.09.049

Gong, L., Su, X. C., Gao, S., Fu, X. F., Jabbari, H., Wang, X. X., et al. (2019). Characteristics and formation mechanism of natural fractures in the tight gas sandstones of Jiulongshan gas field, China. *J. Petroleum Sci. Eng.* 175, 1112–1121. doi:10.1016/j.petrol.2019.01.021

Gong, L., Zeng, L. B., Chen, S. M., Gao, S., Zhang, B. J., Zu, K. W., et al. (2016). Characteristics of micro-fractures and contribution to the compact conglomerate

reservoirs. *Geotect. Metallogenia* 40 (1), 38–46. doi:10.16539/j.ddgzyckx.2016.01.004

Gong, L., Zeng, L. B., Miao, F. B., Wang, Y. S., Wei, Y., Li, J., et al. (2012). Application of fractal geometry on the description of complex fracture systems. *J. Hunan Univ. Sci. Technol. Nat. Sci. Ed.* 27 (4), 6–10. doi:10.3969/j.issn.0563-5020.2013.01.014

Hou, L. H., Luo, X., Wang, J. H., Yang, F., Zhao, X., and Mao, Z. G. (2013). Weathered volcanic crust and its petroleum geologic significance: A case study of the carboniferous volcanic crust in northern xinjiang. *Petroleum Explor. Dev.* 40 (3), 257–265. doi:10.11698/PED.2013.03.01

Hou, M. C., Cao, H. Y., Li, H. Y., Chen, A. Q., Wei, A. J., Chen, Y., et al. (2019). Characteristics and controlling factors of deep buried-hill reservoirs in the BZ19-6 structural belt, Bohai Sea area. *Geol. Explor.* 39 (01), 33–44. doi:10.3787/j.issn.1000-0976.2019.01.004

Hu, Z. W., Xu, C. G., Yang, B., Huang, Z., and Su, W. (2017). Reservoir forming mechanism of Penglai 9-1 granite buried-hills and its oil geology significance in Bohai Sea. *Acta Pet. Sin.* 38 (03), 274–285. doi:10.7623/syxb201703004

Huang, J. H., Tan, X. F., Cheng, Y. J., Li, Z. M., Ma, L. J., Zhang, H. L., et al. (2016). Structural features of weathering crust of granitic basement rock and its petroleum geological significance a case study of basement weathering crust of Dongping Area in Qaidam Basin. *Earth Sci.* 41 (12), 2041–2060. doi:10.3799/dqkx.2016.528

Johri, M., Zoback, M. D., and Hennings, P. (2014). A scaling law to characterize fault-damage zones at reservoir depths. *AAPG Bull.* 98 (10), 2057–2079. doi:10.1306/05061413173

Li, H., Tang, H. M., Qin, Q. R., Zhou, J. L., Qin, Z. J., Fan, C. H., et al. (2019). Characteristics, formation periods and genetic mechanisms of tectonic fractures in the tight gas sandstones reservoir: A case study of xujiahe formation in YB area, sichuan basin, China. *J. Petrol. Sci. Eng.* 178, 723–735. doi:10.1016/j.petrol.2019.04.007

Li, H., Zhou, J. L., Mou, X. Y., Guo, H. X., Wang, X. X., An, H. Y., et al. (2022). Pore structure and fractal characteristics of the marine shale of the longmaxi formation in the changning area, southern sichuan basin, China. *Front. Earth Sci.* 10, 1018274. doi:10.3389/feart.2022.1018274

Li, J., Li, H., Yang, C., Wu, Y. J., Gao, Z., and Jiang, S. L. (2022). Geological characteristics and controlling factors of deep shale gas enrichment of the wufeng-longmaxi formation in the southern sichuan basin, China. *Lithosphere*, 2022, 4737801. doi:10.2113/2022/4737801

Li, Y. G., Gong, L., Zeng, L. B., Ma, H. L., Yang, H., Zhang, B. J., et al. (2012). Characteristics of fractures and their contribution to the deliverability of tight conglomerate reservoirs in the Jiulongshan Structure, Sichuan Basin. *Nat. Gas. Ind.* 32 (1), 22–26. doi:10.3787/j.issn.1000-0976.2012.01.004

Luo, Q., George, S., Xu, Y., and Zhong, N. (2016). Organic geochemical characteristics of the mesoproterozoic hongshuizhuang formation from northern China: Implications for thermal maturity and biological sources. *Org. Geochem.* 99, 23–37. doi:10.1016/j.orggeochem.2016.05.004

Luo, Q., Zhong, N., Wang, Y., Ma, L., and Li, M. (2015). Provenance and paleoweathering reconstruction of the mesoproterozoic hongshuizhuang formation (1.4 Ga), northern north China. *Int. J. Earth Sci.* 104 (7), 1701–1720. doi:10.1007/s00531-015-1163-5

Luo, Q., Zhong, N., Zhu, L., Wang, Y., Qin, J., Qi, L., et al. (2013). Correlation of burial organic carbon and paleoproductivity in the Mesoproterozoic Hongshuizhuang Formation, northern North China. *Chin. Sci. Bull.* 58, 1299–1309. doi:10.1007/s11434-012-5534-z

Lyu, W. Y., Zeng, L. B., Chen, S. Q., Lyu, P., Dong, S. Q., Hui, C., et al. (2021). Characterization methods of multi-scale natural fractures in tight and low-permeability sandstone reservoirs. *Geol. Rev.* 67 (02), 543–556. doi:10.16509/j.georeview.2021.02.020

Maerten, L., Gillespie, P., and Daniel, J. (2006). Three-dimensional geomechanical modeling for constraint of subseismic fault simulation. *AAPG Bull.* 90 (9), 1337–1358. doi:10.1306/03130605148

Ortega, O. J., Marrett, R. A., and Loubach, S. E. (2006). A scale-independent approach to fracture intensity and average spacing measurement. *AAPG Bull.* 90 (2), 193–208. doi:10.1306/08250505059

Pan, Z. K., Liu, D. D., Huang, Z. X., Jiang, Z. X., Song, Y., Guo, J., et al. (2019). Paleotemperature and paleopressure of methane inclusions in fracture cements from the Wufeng-Longmaxi shales in the Luzhou area, southern Sichuan Basin. *Petroleum Sci. Bull.* 03, 242–253. doi:10.3969/j.issn.2096-1693.2019.03.022

Strijker, G., Bertotti, G., and Luthi, S. M. (2012). Multi-scale fracture network analysis from an outcrop analogue: A case study from the cambro-ordovician clastic succession in petra, Jordan. *Mar. Petroleum Geol.* 38 (1), 104–116. doi:10.1016/j.marpetgeo.2012.07.003

Wang, D. Y., Wang, Q. B., Liu, X. J., Zhao, M., Hao, Y. W., and YiWei, H. (2019). Characteristics and developing patterns of gneiss buried hill weathering crust reservoir in the sea area of the Bohai Bay basin. *Acta Petrol. Sin.* 35 (4), 1181–1193. doi:10.18654/1000-0569/2019.04.13

Wang, J., Hu, C. G., Pan, Y. L., Huang, Q. J., Yuan, H. Q., Gong, L., et al. (2022). Fracture development characteristics and comprehensive evaluation of buried hill metamorphic reservoir in Jihua 1 area. *Chin. J. Geol.* 57 (2), 463–477. doi:10.12017/dzkx.2022.027

Wang, X., Zhou, X. H., Xu, G. S., Liu, P. B., Gao, K. S., and Guan, D. Y. (2015). Characteristics and controlling factors of reservoirs in Penglai 9-1 large – scale oilfield in buried granite hills, Bohai Sea. *Oil & Gas Geol.* 36 (02), 262–270. doi:10.11743/ogg20150211

Xu, C. G., Du, X. F., Liu, X. J., Xu, W., and Hao, Y. W. (2020). Formation mechanism of high-quality deep buried-hill reservoir of Archaean metamorphic rocks and its significance in petroleum exploration in Bohai Sea area. *Oil & Gas Geol.* 41 (02), 235–247. doi:10.11743/ogg20200201

Xu, C. G., Yu, H. B., Wang, J., and Liu, X. J. (2019). Formation conditions and accumulation characteristics of Bozhong 19-6 large condensate gas field in offshore Bohai Bay Basin. *Petroleum Explor. Dev.* 46 (01), 27–40. doi:10.1016/s1876-3804(19)30003-5

Xue, Y. A., Wang, Q., Niu, C. M., Miao, Q. Y., Liu, M. X., and Yin, J. (2020). Hydrocarbon charging and accumulation of BZ 19-6 gas condensate field in deep buried hills of Bozhong Depression, Bohai Sea. *Oil & Gas Geol.* 41 (05), 891–902. doi:10.11743/ogg20200501

Ye, T., Niu, C. M., Wang, Q. B., Dai, L. M., and Li, F. (2021). Characteristics and controlling factors of large bedrock buried-hill reservoirs in the Bohai Bay Basin—A case study of the BZ19-6 condensate field. *Acta Geol. Sin.* 95 (06), 1889–1902. doi:10.19762/j.cnki.dizhixuebao.2021132

Zeng, L. B., Gong, L., Guan, C., Zhang, B. J., Wang, Q. Q., Zeng, Q., et al. (2022). Natural fractures and their contribution to tight gas conglomerate reservoirs: A case study in the northwestern sichuan basin, China. *J. Petroleum Sci. Eng.* 210, 110028. doi:10.1016/j.petrol.2021.110028

Zeng, L. B., Lyu, P., Qu, X. F., and Fan, J. M. (2020). Multi-scale fractures in tight sandstone reservoirs with low permeability and geological conditions of their development. *Oil & Gas Geol.* 41 (3), 449–453. doi:10.11743/ogg20200301

Zeng, L. B., Lyu, W. Y., Xu, X., Tian, H., Lu, S. L., and Zhang, M. Q. (2022). Development characteristics, formation mechanism and hydrocarbon significance of bedding fractures in typical tight sandstone and shale. *Acta Pet. Sin.* 43 (02), 180–191. doi:10.7623/syxb202202002

Zeng, L. B., Su, H., Tang, X. M., Peng, Y. M., and Gong, L. (2013). Fractured tight sandstone oil and gas reservoirs: A new play type in the dongpu depression, Bohai Bay Basin, China. *AAPG Bull.* 97 (3), 363–377. doi:10.1306/09121212057

Zeng, L. B., Zhu, R. K., Gao, Z. Y., Gong, L., and Liu, G. P. (2016). Structural diagenesis and its petroleum geological significance. *Petroleum Sci. Bull.* 02, 191–197. doi:10.3969/j.issn.2096-1693.2016.02.015

Zhou, X. H., Wang, Q. B., Feng, C., Ye, T., Liu, X. J., Hao, Y. W., et al. (2022). Formation conditions and geological significance of large archean buried hill reservoirs in Bohai sea. *Earth Sci.* 47 (05), 1534–1548. doi:10.3799/dqkx.2021.249

Zhu, H. Y., Song, Y. J., and Tang, X. H. (2021). Research progress on 4-dimensional stress evolution and complex fracture propagation of infill wells in shale gas reservoirs. *Petroleum Sci. Bull.* 03, 396–416. doi:10.3969/j.issn.2096-1693.2021.03.032

Zhu, W. W., Lei, G., He, X. P., Patzek, T., and Wang, M. (2022). Fractal and multifractal characterization of stochastic fracture networks and real outcrops. *J. Struct. Geol.* 155, 104508. doi:10.1016/J.JSG.2021.104508

frontiers | Frontiers in Earth Science

TYPE Original Research
PUBLISHED 12 January 2023
DOI 10.3389/feart.2022.1112190

OPEN ACCESS

EDITED BY
Wenlong Ding,
China University of Geosciences, China

REVIEWED BY
Zhu Baiyu,
Yangtze University, China
Guorong Li,
Chengdu University of Technology, China
Binfeng Cao,
Key Laboratory of Oil and Gas Resources Research, Institute of Geology and Geophysics (CAS), China

*CORRESPONDENCE
Guanxiong Ren,
rgxxly1991@163.com

SPECIALTY SECTION
This article was submitted to Economic Geology, a section of the journal Frontiers in Earth Science

RECEIVED 30 November 2022
ACCEPTED 28 December 2022
PUBLISHED 12 January 2023

CITATION
Ren G, Qin Q, Zhang Q, Guo Y and Ye Z (2023), Study on reservoir characteristics, pore-throat structure, and origin of tight oolitic reservoirs: A case study of Triassic Feixianguan Formation, NE Sichuan Basin, SW China.
Front. Earth Sci. 10:1112190.
doi: 10.3389/feart.2022.1112190

Study on reservoir characteristics, pore-throat structure, and origin of tight oolitic reservoirs: A case study of Triassic Feixianguan Formation, NE Sichuan Basin, SW China

Guanxiong Ren[1,2]*, Qirong Qin[1,2], Qiang Zhang[3], Yanbo Guo[4] and Zhaoyang Ye[4]

[1]School of Geosciences and Technology, Southwest Petroleum University, Chengdu, China, [2]State Key Laboratory of Oil and Gas Reservoirs Geology and Development Engineering, Chengdu, China, [3]PetroChina Southwest Oil and Gas Field CDB Operating Company, Dazhou, China, [4]Chongqing Gas Mine, PetroChina Southwest Oil and Gas Field Company, Chongqing, China

The origin and pore-throat structure of different lithofacies are key issues in exploration and development of tight oolitic reservoirs. Based on core and thin section observation, four types of lithofacies can be recognized in the Feixianguan Formation oolitic reservoir: 1) oolitic limestone with intergranular pores (Lithofacies A), 2) oolitic limestone with mold pores (Lithofacies B), 3) oolitic dolostone (Lithofacies C), and 4) silty crystalline dolomite and fine crystalline dolostone (Lithofacies D). The subsurface core samples from the different lithofacies were studied using mercury injection, 3D CT scanning, and nuclear magnetic resonance, indicating that Lithofacies D possesses the best pore-throat structure and reservoir connectivity. The pore-throat structure of Lithofacies C is very similar to that of D, but the heterogeneity is much stronger. By comparison, the pore-throat structure of Lithofacies A and B is relatively poor. Although the pore heterogeneity of Lithofacies B is weaker than that of Lithofacies A, there is no effective throat connection in Lithofacies B. On the basis of oolitic shoal deposition, the factors controlling the origin of different lithofacies are meteoric freshwater leaching and then dolomitization. Meteoric freshwater leaching dominates the origin of Lithofacies B but does not affect the origin of Lithofacies C. Lithofacies C is jointly controlled by seepage-reflux and hydrothermal dolomitization fluids. The origin of Lithofacies D is only controlled by seepage-reflux dolomitization. Some other diagenesis effects may also have an impact on petrophysical properties of different lithofacies, but they do not play a decisive role in the origin of different lithofacies.

KEYWORDS

tight oolitic reservoir, dolomitization, formation mechanism, controlling factors, lithofacies, Feixianguan Formation

1 Introduction

Oolitic shoal commonly possesses high primary interparticle porosity, as well as large cumulative thickness, and wide distribution range (Enos and Sawatsky, 1981; Schmoker and Hester, 1986). Therefore, oolitic shoal has always been the ideal target of oil and gas exploration since 1960s (Akin and Graves, 1969). At present, successful exploration cases have been obtained in the oolitic reservoir of the Carboniferous, Permian, Triassic, and Jurassic periods throughout the world, such as Walker Creek Oilfield in Arkansas (Swirydczuk, 1988; Bliefnick

and Kaldi, 1996), Big Bow and Sand Arroyo Creek Oilfield in southwest Kansas (Qi et al., 2007), De Wijk and Wanneperveen Oilfield in the Netherlands (Palermo et al., 2008), South Pars Gas field and Balal Oilfield in Iran (Esrafili-Dizaji and Rahimpour-Bonab, 2014; Ebrahim et al., 2018), Villeperdue Oilfield in Paris Basin of France (Granier, 1995), and Puguang Gas field in Sichuan Basin of China (Li H et al., 2020; Li Y et al., 2020).

However, an oolitic reservoir shows strong heterogeneity in pore type, porosity, permeability, and pore-throat structure, which has great influence on exploration and development deployment. Swirydczuk (1988) first proposed that original mineralogy and diagenesis jointly control permeability and pore type in the oolitic reservoir. Bliefnick and Kaldi (1996) used high-pressure mercury injection (MICP) to compare the differences in pore structure of different lithofacies in oolitic limestone reservoirs. It is considered that mechanical compaction and calcite cementation are the negative factors of pore-throat structure, and the higher the degree of sorting, the better the pore structure. However, Makhloufi et al. (2013) argued that early compaction, with the development of grain interpenetration, permits better connectivity in the pore-throat structure, leading to better reservoir properties. Other researchers also noticed the differences in reservoir characteristics of different lithofacies in oolitic reservoirs (Palermo et al., 2008; Esrafili-Dizaji and Rahimpour-Bonab, 2014), but the research objects focus on geometry and distribution of oolitic shoal deposits (Qi et al., 2007; Qiao et al., 2016) and diagenetic evolution of porosity in different lithofacies (Esrafili-Dizaji and Rahimpour-Bonab, 2014; Li et al., 2017; Morad et al., 2019). At present, previous studies on pore-throat structure of oolitic reservoirs are rare, and only a few studies have discussed pore structure using MICP without lithofacies classification (Wang et al., 2018; Zhou et al., 2019). Lack of detailed comparison of pore-throat structure differences between different lithofacies leads to insufficient discussion on controlling factors.

The proven reserves of oolitic gas reservoirs in the Triassic Feixianguan Formation around the Kaijiang–Liangping Trough in the northeastern Sichuan Basin have exceeded 5,000 × 10^8 m^3 (Zou et al., 2011). With the deepening of exploration and development, previous studies have illustrated that the oolitic reservoirs of different wells are composed of one lithofacies or multiple lithofacies combinations (Wang et al., 2018; Gu et al., 2021), and the gas production of each well varies greatly. The unclear understanding of reservoir characteristics, pore-throat structure, and controlling factors has become the decisive factor restricting the next exploration and development.

In this study, we first classify the lithofacies of oolitic reservoirs according to the macro–micro petrological characteristics. Then, pore type, throat type, and petrophysical property of different lithofacies are discussed using 3D CT scanning, low-field nuclear magnetic resonance (NMR), MICP, and scanning electron microscopy (SEM) (Fan et al., 2020). Finally, based on cathodoluminescence (CL), stable isotope, and rare Earth element (REE) data, factors controlling the origin of different lithofacies are studied, and a sedimentary-diagenetic evolution model is established. This study helps guide the further exploration and development of oolitic reservoirs.

2 Geological background

The Sichuan Basin lies on the relatively northwestern side of the Yangtze platform and is surrounded by the Daba and Micang mountains in the north, the Longmen Mountains in the west, Lou Mountain and the Daliang Mountains in the south, and Qiyue Mountain in the east (Wei et al., 2018; Jin et al., 2020; Ren et al., 2022).The basin in its geological history has experienced both tectonic evolution stages featuring tensile stress from the Sinian to Middle Triassic and horizontal compressive stress from the Late Triassic to Quaternary (Wang and Jin, 2002; Liu et al., 2011; Li et al., 2019a). Furthermore, it is divided into six tectonic cycles of Yangtze, Caledonian, Hercynian, Indosinian, Yanshan, and Himalayan (Deng, 1992; He et al., 2011). Based on the regional structural characteristics, the present structural features, and the previous research results, the basin is divided into three structural zones by the Huayingshan and Longquanshan faults, and subdivided into six secondary structural zones, namely, fault–fold belts of high steep in eastern Sichuan, low steep in southern Sichuan, low gentle in southwestern Sichuan, gentle in central Sichuan, gentle in northern Sichuan, and low gentle in western Sichuan (Zhou et al., 2016; Li et al., 2019a).

The study area is located in eastern Sichuan Basin (Figure 1A). Due to the combined effects of the "Emei" taphrogenesis and the formation and evolution of the Micangshan Fault Zone and the Guangwang Basin in the north, the study area is in the extensional tectonic setting during the Late Permian–Early Triassic, forming the Kaijiang–Liangping Trough (Xing et al., 2017). The trough is formed during the early Changxingian (Late Permian) due to rapid basement subsidence associated with the "Emei" taphrogenesis (Tan et al., 2012). As a result, a trough-platform sedimentary pattern comprising open platform facies, platform-margin facies, slope facies, ocean trough (basin) facies, and so on existed in both east and west sides of the trough (Zou et al., 2011). With the filling of sediments into the trough, the platform-margin facies gradually migrated to the center of the trough (Gu et al., 2021). Until the third member of Feixianguan Formation, the study area evolved into an open platform facies, which mainly consists of intra-platform oolitic shoal and inter-shoal sediments (Gu et al., 2020). At the end of the Feixianguan deposition (sedimentary period of the fourth member), the evaporation platform facies dominates the study area, which is comprised of gypsum rocks, gypsum-bearing dolomicrite, and mudstone (Figure 1B). Based on the evolution of sedimentary facies and lithology, the Feixianguan Formation can be divided into four members, namely, the first member (T_1f^1), the second member (T_1f^2), the third member (T_1f^3), and the fourth member (T_1f^4) (Figure 2).

3 Samples and methods

The results obtained by the comprehensive study on Feixianguan Formation tight oolitic reservoir were based on core analysis data from 12 cored wells, including TS5, TS11, TS14, TD110, TD102, and TD100 (Figure 1A). To ensure the reliability of this study, samples should be collected and selected in accordance with the following principles: 1) samples shall not be collected from the development parts such as structurally crushed and weathered zones; 2) the structure and state of the sample should be collected as undamaged as possible. The thin sections of drilling cuttings were prepared from the non-cored wells, in order to establish a complete lithology column. First, all core samples involved in the experiments were used for thin sections and SEM analysis individually. The polarized light microscope, CL, and SEM

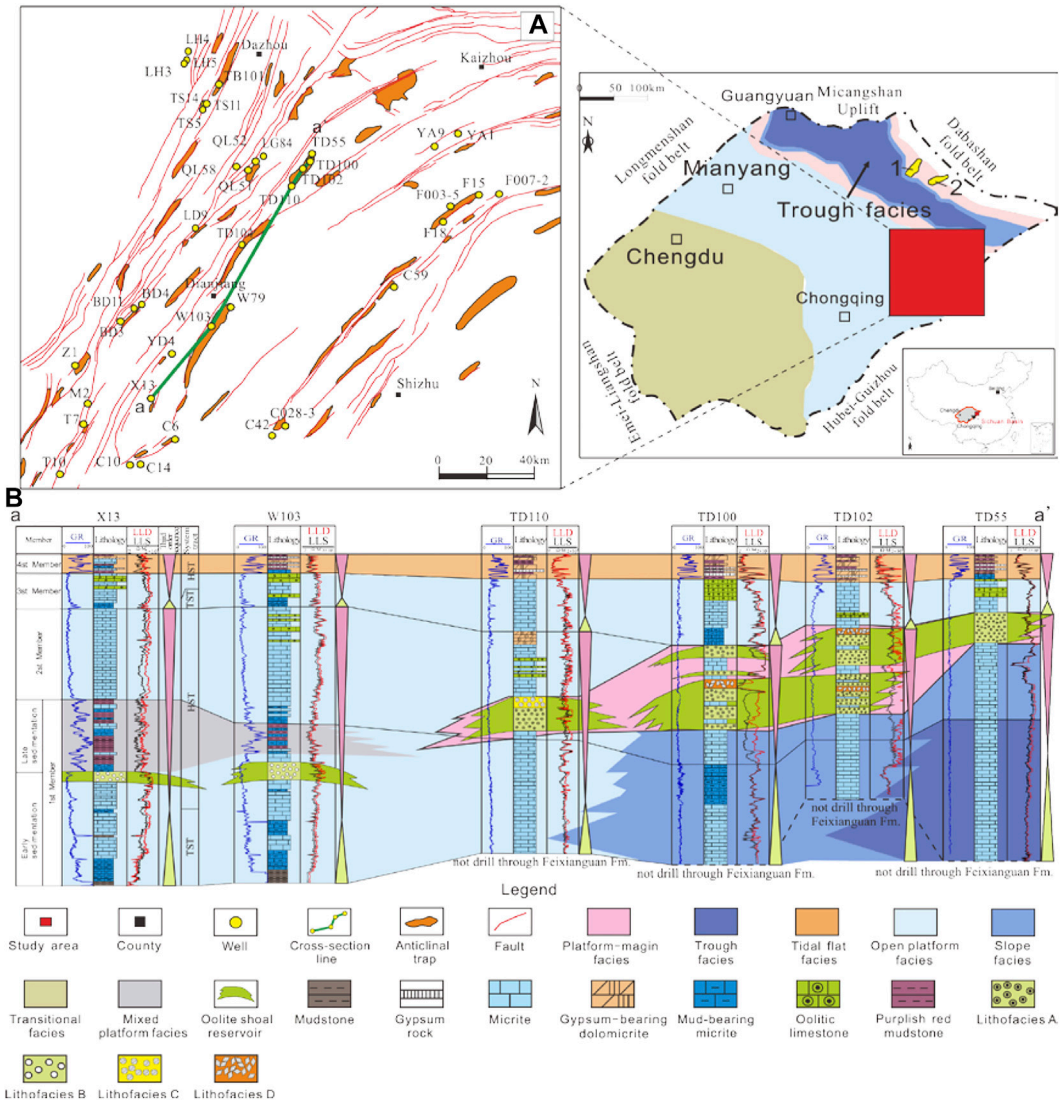

FIGURE 1
Geological setting of Feixianguan Formation in the study area. **(A)** Location of the study area in China and locations of the representative wells; the numbers 1–2 represent Puguang and Luojiazhai–Gunziping gas fields, respectively. **(B)** Cross-well section of sedimentary facies and the stratigraphic framework.

were used to classify lithofacies. In addition to these studies, two core plugs and one full-diameter core sample were drilled from different lithofacies. Under the test conditions of an injection pressure of 50 MPa and confining pressure range of 0–100 MPa, the porosimeter–permeameter HKGP-3 was used to determine porosity and permeability of core plug samples. Then, the core plug samples were fully saturated with brine. The NMR T_2 spectrum of the core plug samples was acquired by using NUMAG's C12–010V low-field NMR spectrometer under 100% water saturation (Shen et al., 2019; Li 2022). A 3D CT scanning of core samples was then performed using a nanoVoxel-4000 3D X-ray microscope (XRM). Finally, the core plug samples were tested using MICP. The capillary pressure curves and the histogram graphs of the pore-throat radius were obtained (He et al., 2021; Kang 2021; Li H et al., 2022; Li J et al., 2022). Meanwhile, the critical parameters are the following: threshold pressure (P_{cd}), median radius (r_{50}), maximum throat radius (r_{max}), maximum mercury saturation (S_{max}), and mercury extrusion efficiency (E_w).

The remaining samples were used to select fresh sections by avoiding calcite veins and organic matter and grounded to 200 mesh size for rare Earth element (REE) and carbon–oxygen isotope analysis. REE (n = 25 samples) measurements were carried out by inductively coupled plasma-mass spectrometry (ICP-MS). Considering the relationship between carbonate diagenetic fluids and normal seawater, this study selected REE content of seawater published by Kawabe et al. (1998) as the standard. Because REE content of seawater is very low, the REE content of seawater is magnified by 10^4 times before standardization. Eu, Ce, and Pr anomaly values were calculated as follows: $\delta Ce=2Ce_N/(La_N+Pr_N)$; $\delta Eu=2Eu_N/(Sm_N+Gd_N)$; $\delta Pr=2Pr_N/(Ce_N+Nd_N)$ (Shields and Stile, 2001).

The samples for isotopic analysis were microdrilled from the cores. Stable isotopes ($\delta^{18}O$ and $\delta^{13}C$) (n = 48 samples) of different rock fabrics were carried out by using the carbonate reaction method. These test samples reacted in the phosphoric acid bath method at 90°C, and

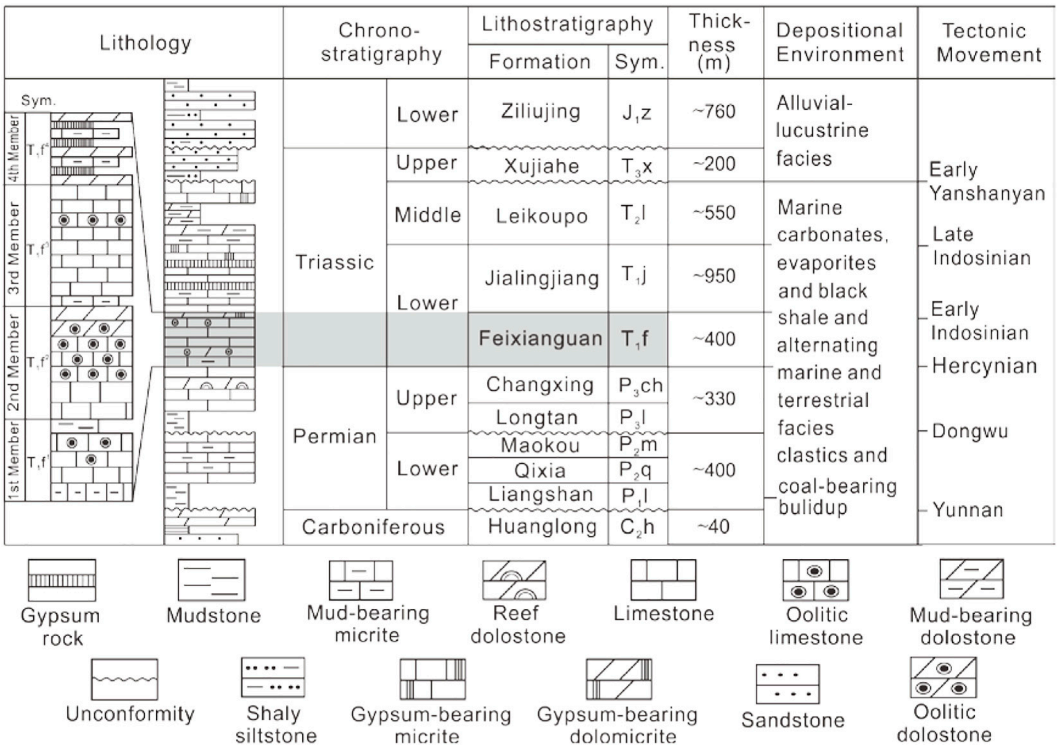

FIGURE 2
Generalized stratigraphy and tectonic history of the study area (modified from Hao et al., 2008). Sym, symbol.

the CO_2 generated was examined using Elementar IsoPrime GC5. Standard isobaric corrections were adopted, while strontium was separated using the Eichrom Sr-Spec resin and measured on a Triton Plus thermal ionization mass spectrometer. All stable isotope data are converted to permille (‰) relative to Vienna Pee Dee Belemnite (VPDB) and corrected by fractionation factors supplied by Fairchild and Spiro (1987). Precision of the $\delta^{18}O$ and $\delta^{13}C$ ratio data is greater than ±.1‰.

4 Results and discussion

4.1 Reservoir characterization of tight oolitic reservoirs

4.1.1 Lithofacies, pore, and throat types

The rock fabrics, depositional structure, and diagenesis of carbonate reservoirs are extremely complex, which lead to complexity in the reservoir space (Guo et al., 2016; Kiani et al., 2021; Abraham-A et al., 2022; Forstner and Laubach, 2022). Typically, the primary pore types are hard to preserve through the late-stage diagenetic environment. Therefore, carbonate reservoirs often possess the characteristics, such as abrupt changes in lithology, various pore types, and unpredictable petrophysical properties. Based on observation of cores and thin sections, the lithofacies of the oolitic reservoir in Feixianguan Formation were classified into four types, namely, Lithofacies A, Lithofacies B, Lithofacies C, and Lithofacies D.

Lithofacies A is oolitic limestone featured by gray colors in the core (Figure 3A). Microscopically, Lithofacies A is composed of ooids and sparry calcite cement (Figure 3B), and the size of each ooid ranged from 500 μm–900 μm and was fabric-selectively replaced by very fine crystalline dolomite (Figure 3C). The main pore type of Lithofacies A is intergranular pores (100–240 μm in diameter) developing between ooids (Figure 3C). The intergranular pores are mainly connected by the tube-shaped throat (50 μm–80 μm in diameter) (Figure 3D).

Lithofacies B is oolitic limestone featured by greyish white color in the core (Figure 3E). Microscopically, most of the ooids in Lithofacies B are fabric-selectively dissolved (Figure 3F), but outermost concentric laminations are well-preserved (Figures 3G, H). The only pore type of Lithofacies B is mold pore (250–500 μm in diameter), and the throat is not developed (Figure 3H).

Lithofacies C is oolitic dolostone featured by white color in the core (Figure 3I). Microscopically, Lithofacies C is composed by subhedral silty crystalline dolomite (Figure 3J) and is characterized by signs of shadowy ooid outlines due to intense dolomitization (Figure 3K). The major pore type of Lithofacies C is intergranular dissolution pore (250 μm–500 μm in diameter) connected by a necking throat (Figure 3L). Very often, the difference between the pores and throats does not become obvious, and this necking throat mainly appears in the intergranular dissolution pores (Figure 3L).

Lithofacies D is oolitic dolostone composed of euhedral silty crystalline dolomite and fine crystalline dolomite (Figures 3M, N). The pore type of Lithofacies D is the intercrystalline pore (100 μm–150 μm in diameter) connected by a flaky throat (15 μm–40 μm in diameter) (Figures 3O, P).

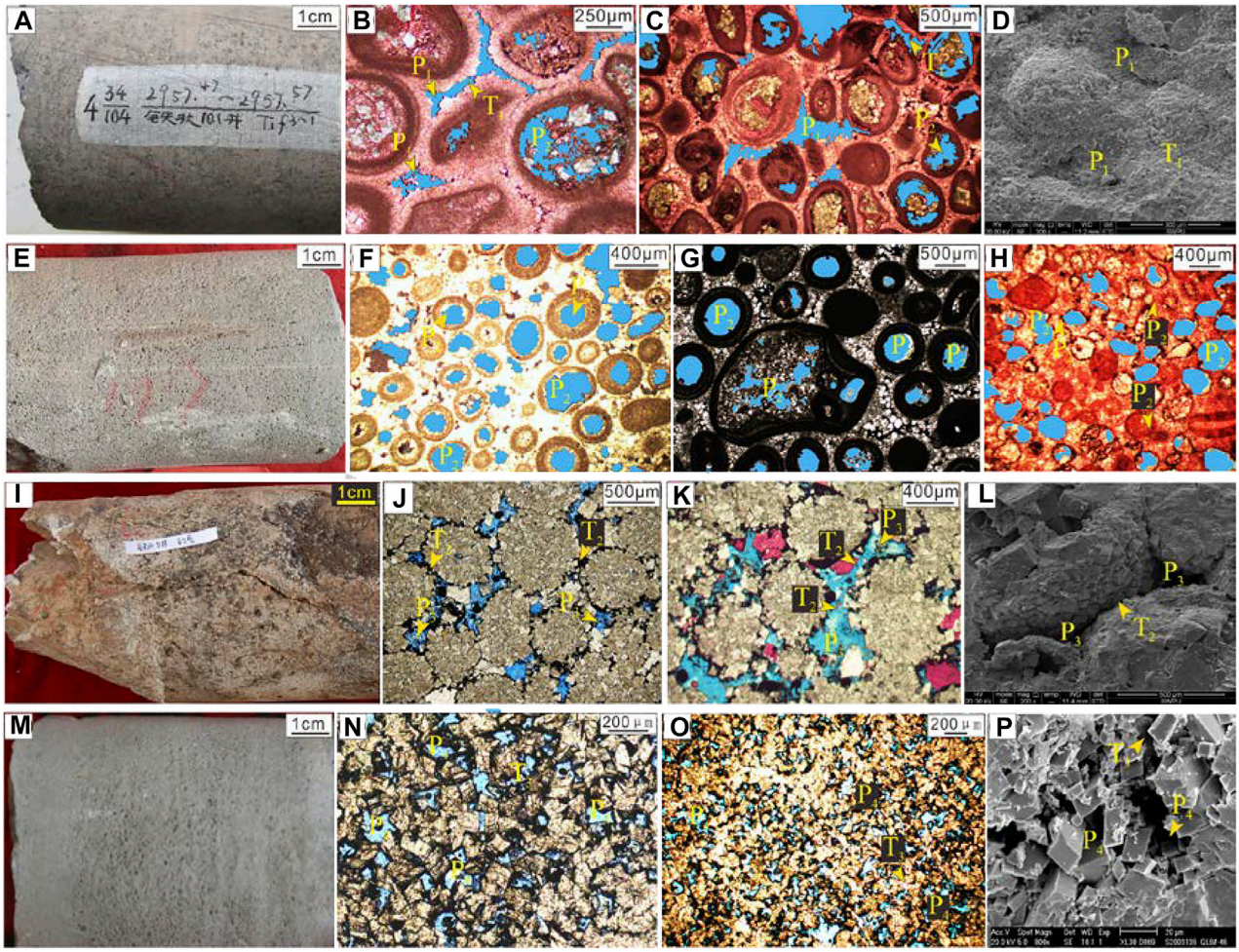

FIGURE 3
Petrological characteristics of different lithofacies in Feixianguan Formation tight oolitic reservoir. **(A)** Intergranular pores (P_1) present as clearly visible pinholes in the drill core, Lithofacies A, Well TB101, 2957.47 m–2957.57 m; **(B)** several intergranular pores (P_1) are connected through tube-shaped throats (T_1), Lithofacies A, Well TB101, 2,956.84 m (PPL); **(C)** intergranular pores (P_1) are connected through tube-shaped throats (T_1), Lithofacies A, Well TD110, 3,457.3 m (PPL); **(D)** intergranular pores (P_1), Lithofacies A, Well TD110, 3,457.3 m (SEM); **(E)** mold pores (P_2) without throats, Lithofacies B, Well C10; **(F)** mold pores (P_2), Lithofacies B, Well C14, 1,678.33 m (PPL); **(G)** mold pores (P_2), Lithofacies B, Well C10 (PPL); **(H)** mold pores (P_2), Lithofacies B, Well X13, 3,297.94 m (PPL); **(I)** intergranular dissolution pores (P_3) present as clearly visible pinholes in drill cores, Lithofacies C, Well TS5, 2,863.32 m; **(J)** intergranular dissolution pores (P_3) are connected by the necking throat (T_2), Lithofacies C, Well TS5, 2,853.36 m (PPL) (Wang et al., 2018); **(K)** intergranular dissolution pores (P_3) are connected by the necking throat (T_2), Lithofacies C, Well TS5, 2,867.34 m (PPL); **(L)** intergranular dissolution pores (P_3) are connected by necking throat (T_2), Lithofacies C, Well TS5, 2,867.34 m (SEM); **(M)** intercrystalline pores (P_4) in the drill core, Lithofacies D, Well TD100, 3,823.41 m; **(N)** intercrystalline pores (P_4) are connected by the flaky throat (T_3), Lithofacies D, Well TD100, 3,823.41 m (PPL); **(O)** intercrystalline pores (P_4), Lithofacies D, Well TD110, 3,448.85 m (PPL); **(P)** intercrystalline pores (P_4) and flaky throat (T_3), Lithofacies D, Well TD110, 3,448.85 m (SEM).

4.1.2 Petrophysical property

Porosity and permeability are measured on 744 core plugs collected from 1) Lithofacies A (n = 480), 2) Lithofacies B (n = 26), 3) Lithofacies C (n = 85), and 4) Lithofacies D (n = 153). The average porosity of these four lithofacies is 2.7%, 2.6%, 7.0%, and 7.5%, respectively (Figure 4).

According to the Oil and Gas Industry Standard of the People's Republic of China (No. SY/T 6285-2011), Lithofacies A is characterized by ultra-low porosity and ultra-low permeability (Kralikova et al., 2016; Gao, 2019; Liu et al., 2022). The porosity distribution of Lithofacies A ranges from 2.00% to 8.90%, with an average value of 2.72%, mainly concentrated in 2.00%–4.00% (accounting for 93.21%) (Figure 4C). The permeability distribution of Lithofacies A ranges from less than .001 mD to 19.80 mD, with an average value of .20 mD, mainly concentrated in the two intervals of less than .001 mD (account for 52.43%) and .001 mD–.01 mD (accounting for 33.48%) (Figure 4D). Lithofacies B is characterized by ultra-low porosity and ultra-low permeability. The porosity distribution of Lithofacies B ranges from 2.05% to 4.08%, with an average value of 2.59%, mainly concentrated in 2.00%–4.00% (account for 96.15%) (Figure 4C). The permeability of Lithofacies B is less than .0100 mD with an average of .0076 mD (Figure 4D).

Lithofacies C is characterized by low porosity and medium permeability, with porosity distribution ranging from 2.00% to 23.85%, with an average of 7.03% (Figure 4E). The permeability distribution of Lithofacies C ranges from less than .001 mD to 423.000 mD, with an average value of 29.260 mD, and it is distributed among various permeability intervals (Figure 4F). Lithofacies D is characterized by

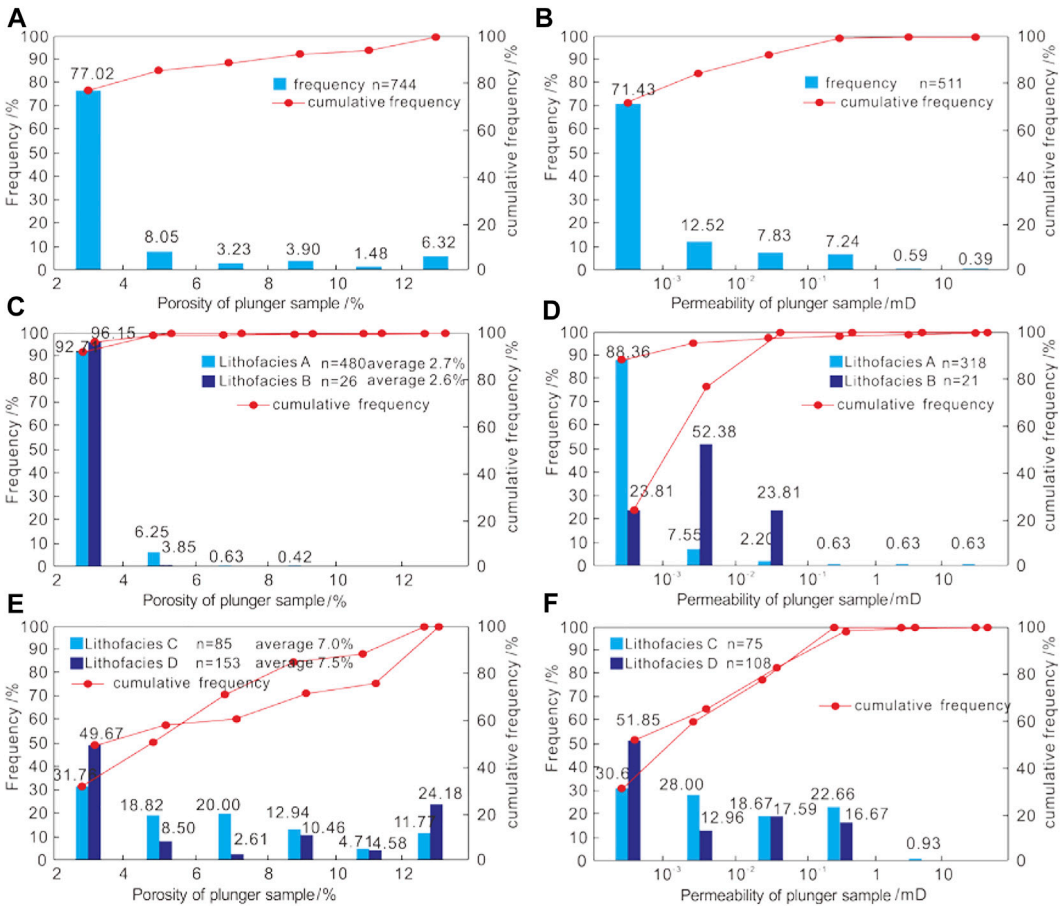

FIGURE 4
Petrophysical property of Feixianguan Formation tight oolitic reservoir.

low porosity and ultra-low permeability. The porosity of Lithofacies D ranges from 2.02% to 12.23%, with an average of 5.26%. They are distributed in all porosity intervals but mainly concentrated in the interval less than 8.00% (accounting for 88.46%) (Figure 4E). The permeability of Lithofacies D ranges from .0009 mD to 1.0200 mD, with an average value of .1700 mD, mainly concentrated in .0010 mD–1.0000 mD (accounting for 90.91%) (Figure 4F).

4.2 Pore-throat structure of different lithofacies

The pore-throat structure of a reservoir refers to the geometry, size, distribution, and connectivity of the pore body and throat. The pore-throat structure is the main controlling factor of the flow capability in a reservoir (Li et al., 2019b; Gu et al., 2020; Fan et al., 2022; Tang et al., 2022). In addition to the results discussed previously, we also carried out the pore-throat structure study using NMR, 3D-CT, and MICP data (Figure 5).

4.2.1 Lithofacies A

Lithofacies A is dominated by micropores, which are residual intergranular pores after cementation (Figure 5). The NMR T_2 spectrum reflects a bimodal pore-throat range of these samples. NMR signals with the relaxation time between 0.1 ms and 1 ms represent smaller pore-throat size, and the corresponding porosity component is generally less than .015%. NMR signals with the relaxation time between 10 ms and 100 ms represent slightly larger pore-throat size, and the corresponding porosity component is generally less than .06%, indicating that the heterogeneity of pore-throat in Lithofacies A is strong and the contribution of slightly larger pore-throat to porosity is obviously greater than that of small pore-throat. Curves for Lithofacies A samples (n = 3) show high displacement pressures and low mercury saturation at any given pressure, indicating pore-throats are smaller and pores are less well connected.

4.2.2 Lithofacies B

Lithofacies B is dominated by mold pores ranging from 200 μm to 600 μm (Figure 5). The NMR T_2 spectrum reflects a bimodal pore-throat range of these samples. NMR signals with the relaxation time between 0.1 ms and 1 ms represent smaller mold pores, and the corresponding porosity component is generally less than .010%. NMR signals with the relaxation time between 10 ms and 500 ms represent larger mold pore, and the corresponding porosity component is generally greater than .05%, indicating that the heterogeneity of Lithofacies B is relatively weak and the contribution of larger mold pores to porosity is obviously greater

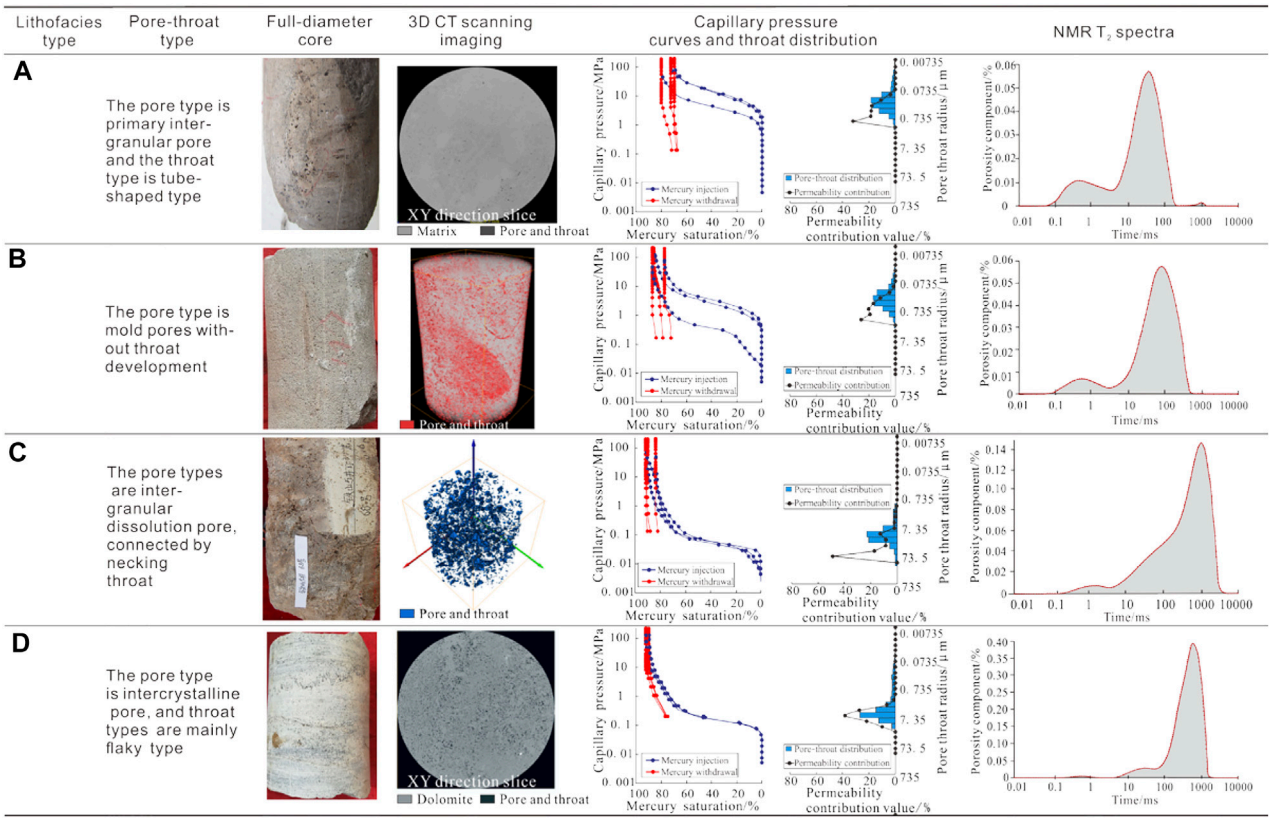

FIGURE 5
Pore-throat structure characteristics of different lithofacies in Feixianguan Formation tight oolitic reservoir.

than that of small mold pores. Curves for Lithofacies B samples (n = 3) show high displacement pressure and low mercury saturation at any given pressure, indicating mold pores are smaller and pores are less well connected.

4.2.3 Lithofacies C

Lithofacies C is dominated by macropores and small vugs, which are identified as intergranular dissolution pores and enlarged vugs by further dissolution (Figure 5). The NMR T_2 spectrum reflects a unimodal pore-throat range, indicating that the difference between the pore diameter and throat diameter is very small. NMR signals with the relaxation time greater than 100 ms represent larger pore-throat size, and the porosity component corresponding to these pore-throats is generally greater than .06%, indicating that the heterogeneity of pore-throats is weak. Also, the range of pore-throat radius also shows that the heterogeneity is weak. The large, well-connected pores and throats of Lithofacies C samples (n = 3) are indicated by low displacement pressures and the high mercury saturation at low injection pressures (.05 MPa–0.1 MPa). The broad, relatively flat plateaus between 0% and 70% mercury saturation suggest that about 70% of the pore volume is accessed by throats with an effective radius between 6 μm and 165 μm. The contribution of permeability mainly comes from the pore-throat with the radius greater than 15 μm.

4.2.4 Lithofacies D

Lithofacies D is dominated by micropores, which are intercrystalline pores formed by intense dolomitization (Figure 5). The NMR T_2 spectrum reflects a unimodal pore-throat range, indicating that the difference between the pore diameter and throat diameter is very small (Wang et al., 2019). NMR signals with the relaxation time between 100 ms and 1,000 ms represent a large pore-throat range, and the corresponding porosity component is generally greater than .10%, indicating that the heterogeneity of Lithofacies D is weak. Also, the range of pore-throat radius shows that the heterogeneity is weak. The large, well-connected pores and throats of Lithofacies D samples (n = 3) are indicated by low displacement pressure and high mercury saturation at relatively low injection pressures (.1M Pa–.5 MPa). The broad, relatively flat plateaus between 0% and 70% mercury saturation suggest that about 70% of the pore volume is accessed by throats with an effective radius between 1 μm and 147 μm. The contribution of permeability mainly comes from the pore-throat with the radius between 3 μm and 40 μm.

4.3 Origin of different lithofacies

4.3.1 Controlling factor of sedimentation

Whether the facies are deposited with platform-margin oolitic shoal or the open platform oolitic shoal, the porous sediments formed in the relatively high-energy environment are the most original material basis for reservoir rock (Tan et al., 2012; Mahmud et al., 2020). Early Triassic transgression led to a rapid sea-level rise in the study area during the early stage of T_1f^1 deposition. Because the landform is high in southwest and low in northeast (Xing et al.,

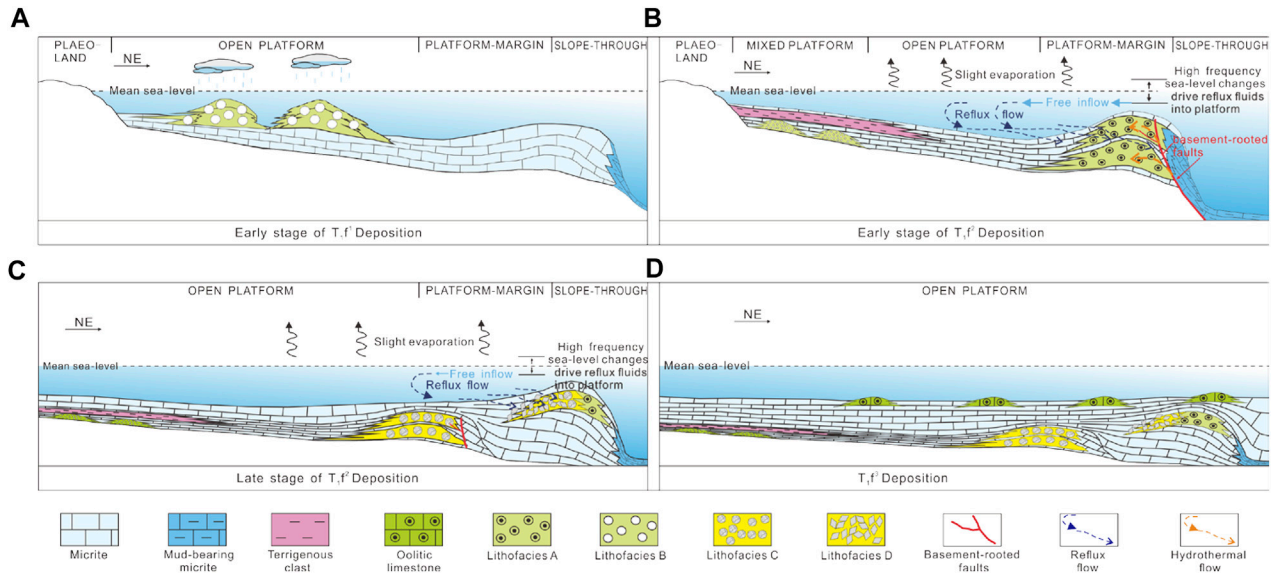

FIGURE 6
Sedimentary-diagenetic evolution model of different lithofacies in Feixianguan Formation tight oolitic reservoir.

2017; Ngene et al., 2022; Xia et al., 2022), at this time, the open platform landform highland is in the advantageous position of sedimentary oolitic shoals. Since the top of the oolitic shoals are close to the sea level, the oolitic shoals are susceptible to meteoric freshwater (Figure 6A). With the gradual decline in sea level and the increase in terrigenous debris input, the sedimentary process of oolitic shoals in the open platform stopped (Figure 6B). At this time, the platform-margin is near the wave base level, forming thick oolitic shoals due to high energy. After the formation of oolitic shoals on the platform margin, it is beneficial to forming a barrier environment behind the shoals (Figure 6C). As the sediments continuously filled the trough during T_1f^1–T_1f^2 deposition, the platform margin gradually moves to the trough. The barrier environment behind the shoals can be formed multiple times during this period. The whole study area evolved into an open platform, and the difference in sedimentary geomorphology disappeared, which is not conducive to inducing constructive diagenesis (Figure 6D).

4.3.2 Controlling factor of diagenesis

4.3.2.1 Fabric-selective dissolution

The exploration experience of oolitic reservoirs around the world indicates that fabric-selective dissolution is involved in the reservoir-forming process, such as Kangan Formation (Tavakoli et al., 2011; Enayati-Bidgoli et al., 2014; Rahimpour-Bonab et al., 2014) in South Pars gas field of the Persian Gulf Basin, Iran, Dalan Formation (Esrafili-Dizaji and Rahimpour-Bonab, 2013) in Zagros area, Messinian stage of the Neogene Miocene in Southeast Spain (Goldstein et al., 2013), and Arab Formation of the Jurassic in Balal Oilfield, Iran (Ebrahim et al., 2018). Lithofacies B is developed in the southwest of the study area, which is characterized by mold pores and multi-stage calcite cement. This phenomenon is strong evidence for the fabric-selective dissolution of the aragonite grains (Moore, 2001; Qie et al., 2021). The southwest part of the study area is close to the paleo-land. Under this background, the depth of seawater in the southwest of the study area is less than that of other parts of the study area. The sedimentary environment of this area is relatively open, and the microscopic characteristics show that it is not affected by dolomitization. The ooids are formed continuously in the turbulent seawater of the submarine paleogeomorphic highland and then deposited, and the ooids are cemented by two-stage sparry calcite. When this area is located in the highstand system tract, the relative decline in the sea level and the vertical accretion of oolitic shoal in the open platform lead to be exposed beyond the sea level. Because of the unstable chemical properties and large specific surface area of aragonite ooids, fabric-selective dissolution is triggered by meteoric freshwater leaching during the syngenetic stage, while calcite cement is preserved because of its stable chemical properties and small specific surface area (Figure 6).

4.3.2.2 Dolomitization

The mechanism interpreted for dolomitization of Feixianguan oolitic dolostone mainly focuses on Eastern Kaijiang–Liangping Trough, including marine-meteoric mixing-zone (Yang et al., 2006), reflux (Jiang et al., 2013; Gu et al., 2020), thermal convection (Huang et al., 2011), or buried (Zheng et al., 2008) model. However, the marine-meteoric mixing-zone model has been questioned for its validity by academia (Hardie, 1987; Machel and Burton, 1994; Luczaj, 2006; Li et al., 2020), and the thermal-convection model seems relatively idealized. In terms of significant difference in the sedimentary environment between Eastern and Western Kaijiang–Liangping Trough, few studies suggest that hydrothermal brine and seepage-reflux brine are responsible for dolomitization in the platform margin of Western Kaijiang–Liangping Trough (Wang et al., 2018; Li et al., 2021a; Li et al., 2021b; Gu et al., 2021). For a long time, the contribution of dolomitization to carbonate reservoir formation has been controversial, and three main viewpoints have been proposed. First, dolomitization has limited contribution to the reservoir space; second, dolomitization only forms the dolomite framework to preserve primary pores; third, saddle dolomite

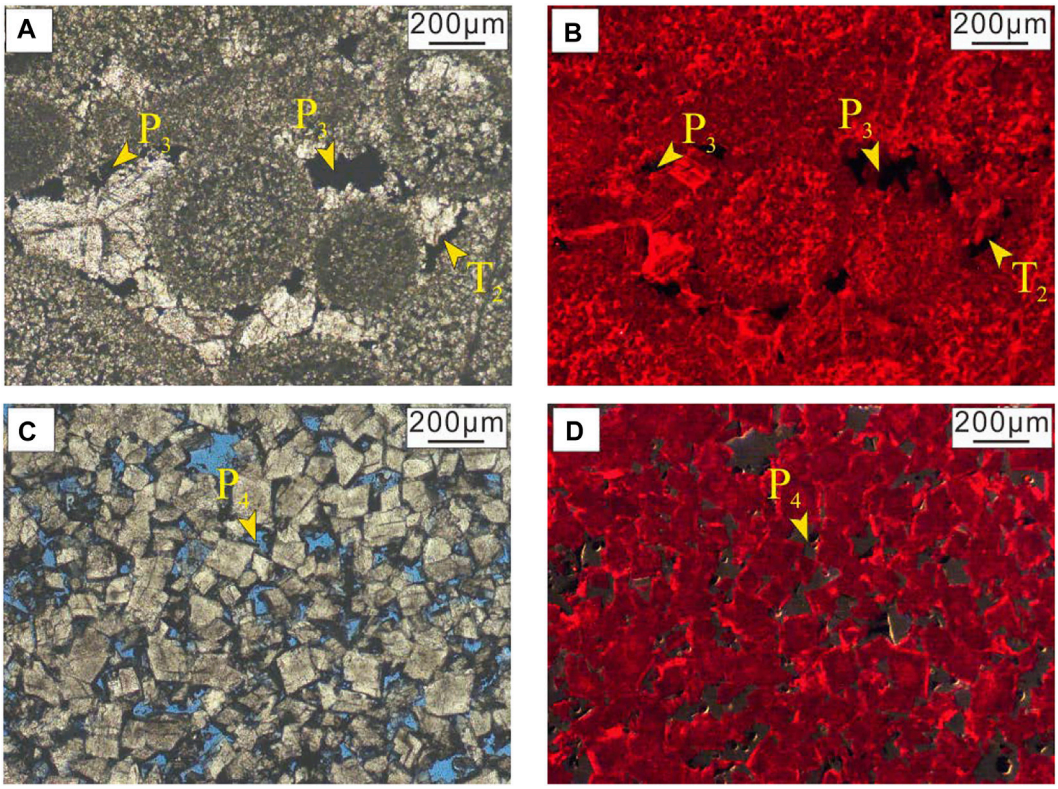

FIGURE 7
CL characteristics of Lithofacies C and D in Feixianguan Formation tight oolitic reservoir.

directly precipitated from dolomitization fluid blocks the reservoir space formed by other diagenesis processes (Shen et al., 2016; Zhao et al., 2018; Zhou et al., 2021). There is no saddle dolomite and other minerals precipitated by dolomitization fluid in the oolitic reservoir. According to the proportion of dolomite in the oolitic reservoir, it can be considered that dolomitization is the key to the formation or preservation of the reservoir space in the study area from either the first or the second point of view. Therefore, it is necessary to re-evaluate the dolomitization model in the study area.

Based on petrological characteristics, no compaction deformation of ooid is observed in Lithofacies C and D in the study area. A shadowy outline of ooids and dolomite crystalline are observed to be relatively loose, and stylolite is not observed. In Lithofacies C, dolomitization is fabric-selective, and usually ooids and first-stage cements are preferentially dolomitized (Figure 3). Under CL (Figure 7), Lithofacies C and D are non-luminescent. The $\delta^{18}O$ values of Lithofacies C and D samples are lower than those of normal Triassic seawater (Allan and Wiggins, 1993; Yoshida and Santosh, 2020), which indicates that the aging effect causes negative oxygen isotope migration in all samples (Figure 8). The unique geochemical characteristics of REE make it record the information of diagenetic fluids and diagenetic environment. It is an important method to understand diagenetic fluids and their origin. The ΣREE in all samples is lower than 12×10^{-6}, which generally shows the characteristics of low REE content in marine carbonate rocks (Hu et al., 2010). All Lithofacies D samples are similar to marine limestone including Lithofacies A, showing high LREE content, low HREE content, large positive Ce anomaly, and large positive Y anomaly.

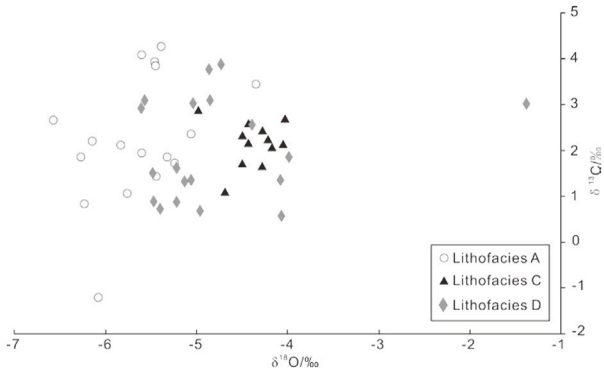

FIGURE 8
$\delta^{13}C$ vs.$\delta^{18}O$ of different lithofacies in Feixianguan Formation tight oolitic reservoir.

The first half of the segments show similar features of marine fluids; the second half of the segments for Lithofacies C samples show large fluctuation and are similar to saddle dolomite curves with remarkable positive Eu anomalies, which are related to hydrothermal activities (Hu et al., 2010; Jiang et al., 2016; Gu et al., 2019).

The petrological characteristics indicate that dolomitization occurred before large-scale compaction (Figure 3). Fabric-selective dolomitization and CL characteristics indicate that dolomitization of Lithofacies C and D occurs mostly before mineral stabilization, and the corresponding diagenetic environment is a submarine-shallow

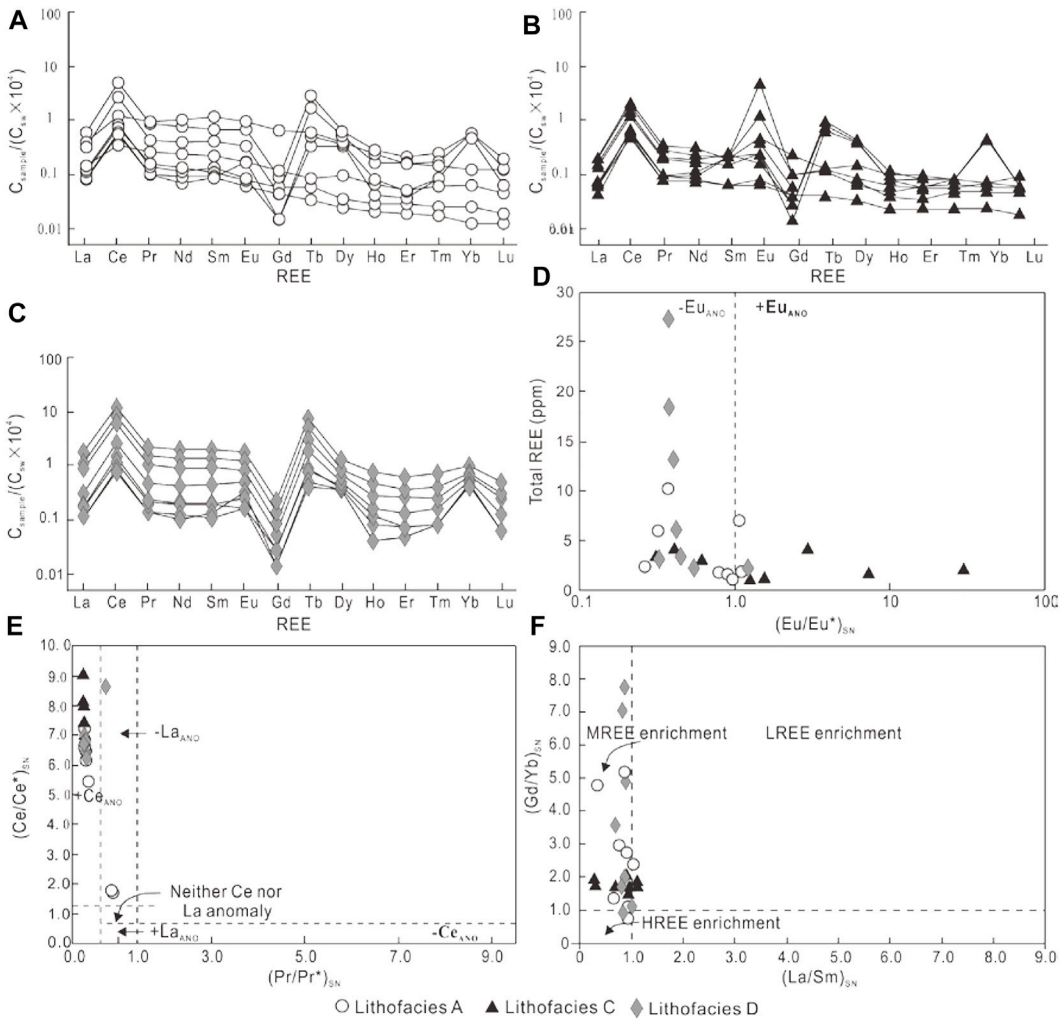

FIGURE 9
Seawater-normalized REE patterns and binary diagram of different lithofacies in Feixianguan Formation tight oolitic reservoir.

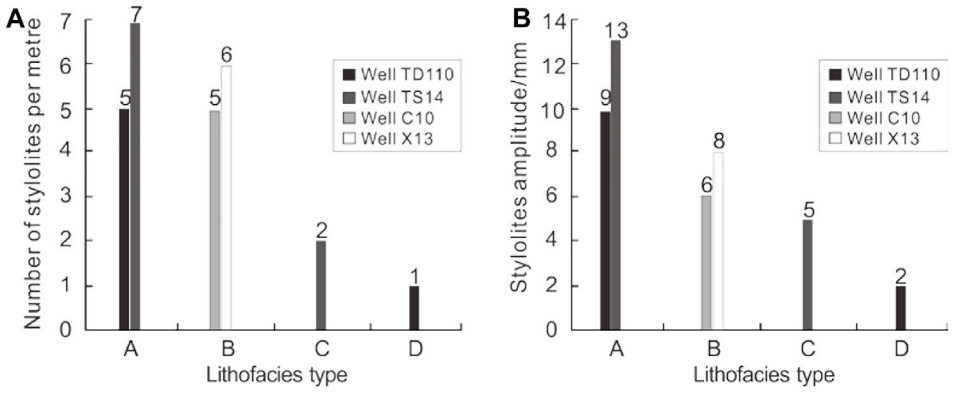

FIGURE 10
Histograms showing frequency **(A)** and amplitude **(B)** of the stylolites in different lithofacies of Feixianguan Formation tight oolitic reservoir.

burial environment which is low in Fe or rich in Mn. Compared with Lithofacies A which has not undergone obvious dolomitization, the $\delta^{18}O$ of Lithofacies C and D shows a positive migration. It shows that the enrichment of ^{18}O in reflux brine is caused by slight evaporation (Figure 8). Due to the barrier effect of platform-margin oolitic shoal during the deposition of T_1f^1–T_1f^2, penesaline seawater is formed by

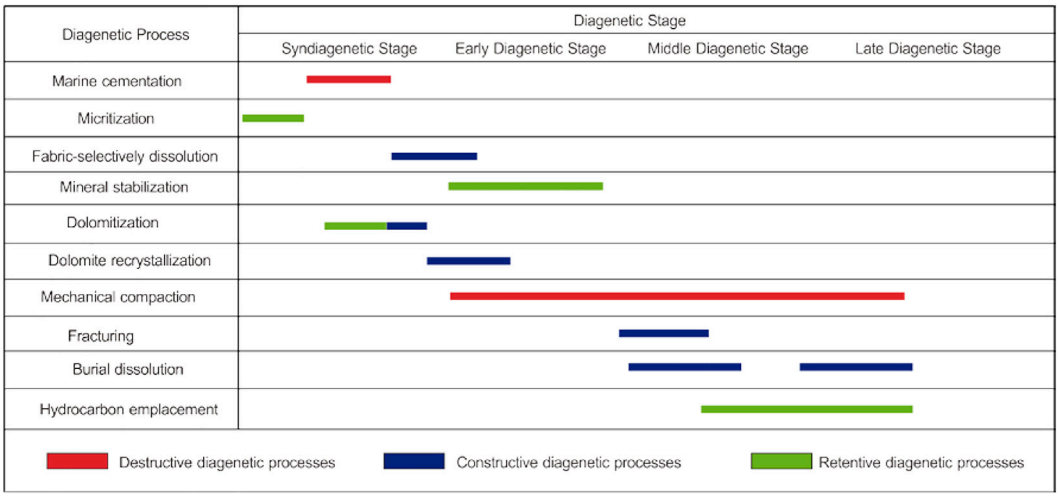

FIGURE 11
Paragenetic sequence of the diagenetic processes in Feixianguan Formation tight oolitic reservoir.

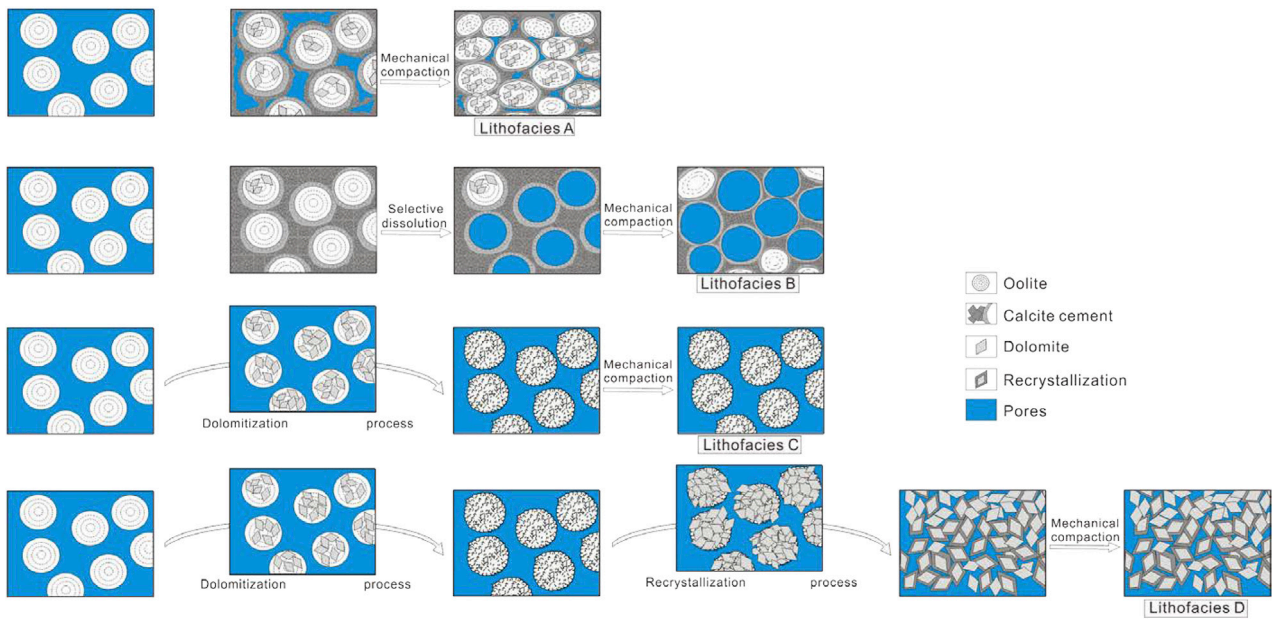

FIGURE 12
Diagenetic evolution of different lithofacies in Feixianguan Formation tight oolitic reservoir.

slight evaporation behind platform-margin oolitic shoals (Figures 6B, C). In the water–rock reaction process between hydrothermal fluids and oolitic limestone, Ca^{2+} in limestone is replaced by Eu^{2+} due to their equal valence and similar ionic radius; this leads to a positive Eu anomaly of Lithofacies C (Figure 9). The NW-trending basement faults of the Late Permian–Early Triassic provide migration channels for the upward migration of hydrothermal fluids (Wang et al., 2018). This study demonstrates that hydrothermal fluids also participate in the dolomitization of Lithofacies C (Figures 6A, B). Although the dolomitization mechanism of Lithofacies D is the same as that of C, the shadowy ooid outlines almost completely disappear and the crystal rim exhibits bright red (Figures 6C, D), indicating that the strong recrystallization of dolomite occurs during the dolomitization process, which further improves the pore-throat structure of Lithofacies D.

4.3.2.3 Other diagenesis effects

Some other diagenesis effects may also have an impact on petrophysical properties of different lithofacies, but they do not play a decisive role in the origin of different lithofacies (Shan et al., 2021; Sun, 2023). The microscopic characteristics of different lithofacies and the development degree of stylolites show that the mechanical compaction has a destructive effect on the petrophysical properties of Lithofacies A and B but has little effect on Lithofacies C and D, indicating that dolomitization has

remarkable effect on improving the anti-compaction of reservoir lithofacies (Figure 10). During the syndiagenetic stage, micritization can be observed in many ooids, but the effect on rock fabric is extremely slight, which does not affect the differential evolution of lithofacies. During the middle-late diagenetic stage (Figure 11), accompanied by hydrocarbon charge and subsequent oxidative cracking of hydrocarbons, the organic acid or thermogenic sulfate reduction (TSR)-induced burial dissolution occurs in the oolitic reservoirs of the study area (Cai et al., 2014). The identified diagenetic processes that took place in different diagenetic stages are presented in Figure 12.

5 Conclusion

1) Four types of lithofacies exist in Feixianguan oolitic reservoirs of NE Sichuan Basin, namely, Lithofacies A, Lithofacies B, Lithofacies C, and Lithofacies D. The pore type of Lithofacies A is intergranular pores connected by the tube-shaped throat. Lithofacies B is characterized by mold pores, with the poorly developed throat. The pore type of Lithofacies C and D is intergranular dissolution pores connected by the necking throat and intercrystalline pore connected by the flaky throat, respectively.
2) Lithofacies A possesses small intergranular pores (100 μm–240 μm) that are connected by few tube-shaped throats with a bimodal pore-throat range. The heterogeneity of pore-throat in Lithofacies A is strong, and the contribution of slightly larger pore-throats to porosity is obviously greater than that of small pore-throats. Lithofacies B dominated by mold pores (200 μm–600 μm) also reflects a bimodal pore-throat range. Although the pore heterogeneity of Lithofacies B is weaker than that of Lithofacies A, there is no effective throat connection between the mold pores in Lithofacies B. Lithofacies C dominated by intergranular dissolution pores and vugs possess fairly larger pores (and vugs) that are well connected by large throats with a fairly narrow pore-throat size range. The heterogeneity of pore-throat in Lithofacies C is weak. The pore-throat structure of Lithofacies D is very similar to that of Lithofacies C, but the heterogeneity is obviously much weaker.
3) On the basis of oolitic shoal deposition, the main factors of diagenesis controlling the origin of different lithofacies are fabric-selective dissolution triggered by meteoric freshwater and dolomitization triggered by dolomitization fluids. The origin of Lithofacies B is dominated by meteoric freshwater leaching. The origin of Lithofacies C is not influenced by meteoric freshwater leaching but formed by the effect of seepage reflux and hydrothermal dolomitization fluids. The origin of Lithofacies D is only controlled by seepage-reflux dolomitization. Some other diagenesis effects may also have an impact on petrophysical properties of different lithofacies, but they do not play a decisive role in the origin of different lithofacies.

Data availability statement

The original contributions presented in the study are included in the article/Supplementary Material; further inquiries can be directed to the corresponding author.

Author contributions

GR: experiments, data analysis, visualization, and writing—original draft. QQ: conceptualization, methodology, and supervision. QZ: project administration and supervision. YG: supervision and revising the manuscript. ZY: data analysis and revising the manuscript.

Funding

This study was financially supported by Comprehensive Exploration Research Project of PetroChina Southwest Oil and Gas Field Company in 2019 (No. XNS05JS2019-19) and the National Natural Science Foundation (No. 41402126).

Conflict of interest

Author QZ was employed by PetroChina Southwest Oil and Gas Field CDB Operating Company. Authors YG and ZY were employed by PetroChina Southwest Oil and Gas Field Company.

The remaining authors declare that the research was conducted in the absence of any commercial or financial relationships that could be construed as a potential conflict of interest.

Publisher's note

All claims expressed in this article are solely those of the authors and do not necessarily represent those of their affiliated organizations, or those of the publisher, the editors, and the reviewers. Any product that may be evaluated in this article, or claim that may be made by its manufacturer, is not guaranteed or endorsed by the publisher.

References

Abraham-A, R. M., Taioli, F., and Nzekwu, A. I. (2022). Physical properties of sandstone reservoirs: Implication for fluid mobility. *Energy Geosci.* 3 (4), 349–359. doi:10.1016/j.engeos.2022.06.001

Akin, R. H., and Graves, R. W. (1969). Reynolds oolite of southern Arkansas. *AAPG Bull.* 53 (9), 1909–1922.

Allan, J. R., and Wiggins, W. D. (1993). Dolomite reservoirs: Geochemical techniques for evaluating origin and distribution. *AAPG Contin. Educ. Course Note Ser.* 36, 129. doi:10.1016/0920-4105(95)00034-8

Bliefnick, D. M., and Kaldi, J. G. (1996). Pore geometry: Control on reservoir properties, walker Creek field, columbia and lafayette counties, Arkansas. *AAPG Bull.* 80 (7), 1027–1044. doi:10.1306/64ED8C82-1724-11D7-8645000102C1865D

Cai, C. F., He, W. X., Jiang, L., Li, K. K., Xiang, L., and Jia, L. Q. (2014). Petrological and geochemical constraints on porosity difference between Lower Triassic sour- and sweet-gas carbonate reservoirs in the Sichuan Basin. *Mar. Pet. Geol.* 56, 34–50. doi:10.1016/j.marpetgeo.2014.04.003

Deng, K. (1992). Formation and evolution of Sichuan Basin and domains oil and gas exploration. *Nat. Gas. Ind.* 12 (5), 7–13.

Ebrahim, S., Abdolhossien, A., Ali, K., Mohsen, S., and Seyed Mohammad, Z. (2018). Diagenetic and depositional impacts on the reservoir quality of the upper jurassic Arab Formation in the balal oilfield, offshore Iran. *Acta Geol. Sin. Engl. Ed.* 92 (4), 1523–1543. doi:10.1111/1755-6724.13641

Enayati-Bidgoli, A. H., Rahimpour-Bonab, H., and Mehrabi, H. (2014). Flow unit characterisation in the Permian-Triassic carbonate reservoir succession at South Pars Gasfield, offshore Iran. *J. Petroleum Geol.* 37 (3), 205–230. doi:10.1111/jpg.12580

Enos, P., and Sawatsky, L. H. (1981). Pore networks in Holocene carbonate sediments. *J. Sediment. Petrology* 51 (3), 961–985. doi:10.1306/212F7DF1-2B24-11D7-8648000102C1865D

Esrafili-Dizaji, B., and Rahimpour-Bonab, H. (2013). A review of permo-triassic reservoir rocks in the Zagros area, SW Iran: Influence of the Qatar-fars arch. *J. Petroleum Geol.* 36 (3), 257–279. doi:10.1111/jpg.12555

Esrafili-Dizaji, B., and Rahimpour-Bonab, H. (2014). Generation and evolution of oolitic shoal reservoirs in the Permo-Triassic carbonates, the South Pars Field, Iran. *Facies* 60 (4), 921–940. doi:10.1007/s10347-014-0414-4

Fairchild, J. J., and Spiro, B. (1987). Petrological and isotopic implications of some contrasting Late Precambrian carbonates, NE Spitsbergen. *Sedimentology* 34 (6), 973–989. doi:10.1111/j.1365-3091.1987.tb00587.x

Fan, C. H., Li, H., Qin, Q. R., He, S., and Zhong, C. (2020). Geological conditions and exploration potential of shale gas reservoir in Wufeng and Longmaxi Formation of southeastern Sichuan Basin, China. *J. Petrol. Sci. Eng.* 191, 107138. doi:10.1016/j.petrol.2020.107138

Fan, C., Xie, H. B., Li, H., Zhao, S., Shi, X., Liu, J., et al. (2022). Complicated Fault characterization and its influence on shale gas preservation in the southern margin of the Sichuan Basin, China. *Lithosphere* 2022, 8035106. doi:10.2113/2022/8035106

Forstner, S. R., and Laubach, S. E. (2022). Scale-dependent fracture networks. *J. Struct. Geol.* 165, 104748. doi:10.1016/j.jsg.2022.104748

Gao, F. Q. (2019). Use of numerical modeling for analyzing rock mechanic problems in underground coal mine practices. *J. Min. Strata Control Eng.* 1 (1), 013004. doi:10.13532/j.jmsce.cn10-1638/td.2019.02.009

Goldstein, R. H., Franseen, E. K., and Lipinski, C. J. (2013). Topographic and sea level controls on oolite-microbialite-coralgal reef sequences: The terminal carbonate complex of southeast Spain. *AAPG Bull.* 97 (11), 1997–2034. doi:10.1306/06191312170

Granier, B. A. (1995). A sedimentological model of the Callovian oolite reservoir of the Villeperdue oil field, Paris Basin (France). *Pet. Geosci.* 1 (2), 145–150. doi:10.1144/petgeo.1.2.145

Gu, Y., Zhou, L., Jiang, Y., Jiang, C., Luo, M., and Zhu, X. (2019). A model of hydrothermal dolomite reservoir facies in Precambrian dolomite, Central Sichuan Basin, SW China and its geochemical characteristics. *Acta Geol. Sin. Engl. Ed.* 93 (1), 130–145. doi:10.1111/1755-6724.13770

Gu, Y., Jiang, Y., Qing, H., Feng, L., Feng, L., Fu, Y., et al. (2020). Reservoir characteristics, pore structure, and main controlling factors of oolitic shoal reservoir in Feixianguan Formation: A case study from eastern Kaijiang-Liangping Trough. *Arabian J. Geosciences* 13, 309. doi:10.1007/s12517-020-05286-x

Gu, Y., Jiang, Y., Lei, X., Chen, Z., Zhou, L., Fu, Y., et al. (2021). The major controlling factors and different oolitic shoal reservoir characteristics of the Triassic Feixianguan Formation, Eastern Longgang area, NE Sichuan Basin, SW China. *Acta Geol. Sin. Engl. Ed.* 95 (3), 895–908. doi:10.1111/1755-6724.14672

Guo, P., Yao, L. H., and Ren, D. S. (2016). Simulation of three-dimensional tectonic stress fields and quantitative prediction of tectonic fracture within the Damintun Depression, Liaohe Basin, northeast China. *J. Struct. Geol.* 86, 211–223. doi:10.1016/j.jsg.2016.03.007

Hao, F., Guo, T., Zhu, Y., Cai, X., Zou, H., and Li, P. (2008). Evidence for multiple stages of oil cracking and thermochemical sulfate reduction in the Puguang gas field, Sichuan Basin, China. *AAPG Bull.* 92, 611–637. doi:10.1306/01210807090

Hardie, L. A. (1987). Dolomitization: A critical view of some current views. *J. Sediment. Res.* 57 (1), 166–183. doi:10.1306/212F8AD5-2B24-11D7-8648000102C1865D

He, D. F., Li, D. S., Zhang, G. W., Zhao, L. Z., Fang, C., Lu, R. Q., et al. (2011). Formation and evolution of multi-cycle superposed Sichuan Basin, China. *Chin. J. Geol.* 46 (3), 589–606.

He, S., Qin, Q., Li, H., and Long, S. (2021). Influence of mineral compositions on shale pore development of Longmaxi Formation in the Dingshan area, southeastern Sichuan Basin, China. *Energy Fuels* 35 (13), 10551–10561. doi:10.1021/acs.energyfuels.1c01026

Hu, W., Chen, Q., Wang, X., and Cao, J. (2010). REE models for the discrimination of fluids in the formation and evolution of dolomite reservoirs. *Oil Gas Geol.* 31 (6), 810–818. doi:10.1016/S1876-3804(11)60008-6

Huang, S., Huang, Y., Lan, Y., and Huang, K. (2011). A comparative study on strontium isotope composition of dolomites and their coeval seawater in the Late Permian-Early Triassic, NE Sichuan Basin. *Acta Petrol. Sin.* 27 (12), 3831–3842.

Jiang, L., Cai, C. F., Worden, R. H., Li, K. K., and Xiang, L. (2013). Reflux dolomitization of the upper permian changxing formation and the lower triassic Feixianguan Formation, NE Sichuan Basin, China. *Geofluids* 13 (2), 232–245. doi:10.1111/gfl.12034

Jiang, Y., Tao, Y., Gu, Y., Wang, J., Qiang, Z., Jiang, N., et al. (2016). Hydrothermal dolomitization in dengying formation, gaoshiti-moxi area, Sichuan Basin, SW China. *Petroleum Explor. Dev.* 43 (1), 54–64. doi:10.1016/S1876-3804(16)30006-4

Jin, M. D., Li, B. S., Zhu, X., Dai, L. C., Jiang, Z. L., Wu, H., et al. (2020). Characteristics and main controlling factors of reservoirs in the fourth member of Sinian Dengying Formation in Yuanba and its peripheral area, northeastern Sichuan Basin, SW China. *Petroleum Explor. Dev.* 47 (6), 1172–1182. doi:10.1016/S1876-3804(20)60127-1

Kang, H, P. (2021). Temporal scale analysis on coal mining and strata control technologies. *J. Min. Strata Control Eng.* 3 (1), 013538. doi:10.13532/j.jmsce.cn10-1638/td.20200814.001

Kawabe, I., Toriumi, T., Ohta, A., and Miura, N. (1998). Monoisotopic REE abundances in seawater and the origin of seawater tetrad effect. *Geochem J.* 32 (4), 213–229. doi:10.2343/geochemj.32.213

Kiani, S., Jafari, S., Apourvari, S. N., and Mehrjoo, H. (2021). Simulation study of wormhole formation and propagation during matrix acidizing of carbonate reservoirs using a novel *in-situ* generated hydrochloric acid. *Adv. Geo-Energy Res.* 5 (1), 64–74. doi:10.46690/ager.2021.01.07

Kralikova, S., Vojtko, R., Hok, J., Fugenschuh, B., and Kovac, M. (2016). Low-temperature constraints on the Alpine thermal evolution of the Western Carpathian basement rock complexes. *J. Struct. Geol.* 91, 144–160. doi:10.1016/j.jsg.2016.09.006

Li, W. P., Liu, S. F., Wang, Y., Qian, T., and Gao, T. J. (2017). Duplex thrusting in the South Dabashan arcuate belt, central China. *J. Struct. Geol.* 103, 120–136. doi:10.1016/j.jsg.2017.09.007

Li, H., Li, Z. Q., Long, W., Wan, S. S., Ding, S., Wang, S. Z., et al. (2019a). Vertical configuration of Sichuan Basin and its superimposed characteristics of the prototype basin. *J. Chengdu Unniversity Technol. Sci. Technol. Ed.* 46 (3), 257–267. doi:10.3969/j.issn.1671-9727.2019.03.01

Li, H., Tang, H. M., Qin, Q. R., Zhou, J. L., Qin, Z. J., Fan, C. H., et al. (2019b). Characteristics, formation periods and genetic mechanisms of tectonic fractures in the tight gas sandstones reservoir: A case study of xujiahe Formation in YB area, Sichuan Basin, China. *J. Petrol. Sci. Eng.* 178, 723–735. doi:10.1016/j.petrol.2019.04.007

Li, H., Wang, Q., Qin, Q. R., and Ge, X. Y. (2021a). Characteristics of natural fractures in an ultradeep marine carbonate gas reservoir and their impact on the reservoir: A case study of the maokou Formation of the jls structure in the Sichuan Basin, China. *Energy & Fuels* 35 (16), 13098–13108. doi:10.1021/acs.energyfuels.1c01581

Li, H., Peng, R., Du, W. S., Li, X. P., and Zhang, N. B. (2021b). Experimental study on structural sensitivity and intervention mechanism of mechanical behavior of coal samples. *J. Min. Strata Control Eng.* 3 (4), 043012. doi:10.13532/j.jmsce.cn10-1638/td.20210820.001

Li, H., Qin, Q. R., Zhang, B. J., Ge, X. Y., Hu, X., Fan, C. H., et al. (2020). Tectonic fracture formation and distribution in ultradeep marine carbonate gas reservoirs: A case study of the maokou Formation in the jiulongshan gas field, Sichuan Basin, southwest China. *Energy & Fuels* 34 (11), 14132–14146. doi:10.1021/acs.energyfuels.0c03327

Li, H., Zhou, J. L., Mou, X. Y., Guo, H. X., Wang, X. X., An, H. Y., et al. (2022). Pore structure and fractal characteristics of the marine shale of the longmaxi Formation in the changning area, southern Sichuan Basin, China. *Front. Earth Sci.* 10, 1018274. doi:10.3389/feart.2022.1018274

Li, J., Li, H., Yang, C., Wu, Y. J., Gao, Z., and Jiang, S. L. (2022). Geological characteristics and controlling factors of deep shale gas enrichment of the wufeng-longmaxi Formation in the southern Sichuan Basin, China. *Lithosphere* 2022, 4737801. doi:10.2113/2022/4737801

Li, K., George, S. C., Cai, C. F., Zhang, X., and Tan, X. (2020). Comparison of differential diagenesis of two oolites on the Lower Triassic platform margin, NE Sichuan Basin: Implications for the co-evolution of rock structure and porosity. *Mar. Petroleum Geol.* 119, 104485. doi:10.1016/j.marpetgeo.2020.104485

Li, Y., Zhou, D., Wang, W., Jiang, T., and Xue, Z. (2020). Development of unconventional gas and technologies adopted in China. *Energy Geosci.* 1 (1-2), 55–68. doi:10.1016/j.engeos.2020.04.004

Li, H. (2022). Research progress on evaluation methods and factors influencing shale brittleness: A review. *Energy Rep.* 8, 4344–4358. doi:10.1016/j.egyr.2022.03.120

Liu, S., Li, Z., Sun, W., Deng, B., Luo, Z., Wang, G., et al. (2011). Basin geological features of superimposed basin and hydrocarbon accumulation in Sichuan Basin, China. *Chin. J. Geol.* 46 (1), 233–257. doi:10.3969/j.issn.0563-5020.2011.01.019

Liu, C., Zhang, L., Li, Y., Liu, F., Martyushev, D. A., and Yang, Y. (2022). Effects of microfractures on permeability in carbonate rocks based on digital core technology. *Adv. Geo-Energy Res.* 6 (1), 86–90. doi:10.46690/ager.2022.01.07

Luczaj, J. A. (2006). Evidence against the dorag (mixing-zone) model for dolomitization along the Wisconsin arch? A case for hydrothermal diagenesis. *AAPG Bull.* 90 (11), 1719–1738. doi:10.1306/01130605077

Machel, H. G., and Burton, E. A. (1994). Golden grove dolomite, Barbados: Origin from modified seawater. *J. Sediment. Res.* 64 (4), 741–751. doi:10.1306/D4267EAB-2B26-11D7-8648000102C1865D

Mahmud, H., Hisham, M., Mahmud, M., Leong, V., and Shafiq, M. (2020). Petrophysical interpretations of subsurface stratigraphic correlations, Baram Delta, Sarawak, Malaysia. *Energy Geosci.* 1 (3-4), 100–114. doi:10.1016/j.engeos.2020.04.005

Makhloufi, Y., Collin, P., Bergerat, F., Casteleyn, L., Claes, S., David, C., et al. (2013). Impact of sedimentology and diagenesis on the petrophysical properties of a tight oolitic carbonate reservoir: The case of the Oolithe Blanche Formation (Bathonian, Paris Basin, France). *Mar. Petroleum Geol.* 48, 323–340. doi:10.1016/j.marpetgeo.2013.08.021

Moore, C. H. (2001). *Carbonate reservoirs: Porosity evolution and diagenesis in a sequence stratigraphic framework*. Amsterdam: Elsevier, 444.

Morad, S., Al Suwaidi, M., Mansurbeg, H., Morad, D., Ceriani, A., Paganoni, M., et al. (2019). Diagenesis of a limestone reservoir (lower cretaceous), abu dhabi, united Arab emirates: Comparison between the anticline crest and flanks. *Sediment. Geol.* 380, 127–142. doi:10.1016/j.sedgeo.2018.12.004

Ngene, T., Mukhopadhyay, M., and Ampana, S. (2022). Reconnaissance investigation of geothermal resources in parts of the Middle Benue Trough, Nigeria using remote sensing and geophysical methods. *Energy Geosci.* 3 (4), 360–371. doi:10.1016/j.engeos.2022.06.002

Palermo, D., Aigner, T., Geluk, M., Poeppelreiter, M., and Pipping, K. (2008). Reservoir potential of a lacustrine mixed carbonate/siliciclastic gas reservoir: The lower triassic rogenstein in The Netherlands. *J. Petroleum Geol.* 31 (1), 61–96. doi:10.1111/j.1747-5457.2008.00407.x

Qi, L., Carr, T. R., and Goldstein, R. H. (2007). Geostatistical three-dimensional modeling of oolite shoals, St. Louis Limestone, southwest Kansas. *AAPG Bull.* 91 (1), 69–96. doi:10.1306/08090605167

Qiao, Z., Janson, X., Shen, A., Zheng, J., Zeng, H., and Wang, X. (2016). Lithofacies, architecture, and reservoir heterogeneity of tidal-dominated platform marginal oolitic shoal: An analogue of oolitic reservoirs of lower triassic Feixianguan Formation, Sichuan Basin, SW China. *Mar. Petroleum Geol.* 76, 290–309. doi:10.1016/j.marpetgeo.2016.05.030

Qie, L., Shi, Y. N., and Liu, J. G. (2021). Experimental study on grouting diffusion of gangue solid filling bulk materials. *J. Min. Strata Control Eng.* 3 (2), 023011. doi:10.13532/j.jmsce.cn10-1638/td.20201111.001

Rahimpour-Bonab, H., Enayati-Bidgoli, A. H., and Navidtalab, A. (2014). Appraisal of intra reservoir barriers in the permo-triassic successions of the central Persian Gulf, offshore Iran. *Geol. Acta* 12 (1), 87–107. doi:10.1344/105.000002076

Ren, G., Qin, Q., Qin, Z., Guo, Y., and Ye, Z. (2022). Effects of diagenesis on quality of deep dolomite reservoirs:A case study of the Upper Cambrian Xixiangchi Formation in the eastern Sichuan Basin, China. *Front. Earth Sci.* 10, 984463. doi:10.3389/feart.2022.984463

Schmoker, J., and Hester, T. (1986). Porosity of the miami limestone (late pleistocene), lower Florida keys. *J. Sediment. Petrology* 56 (5), 629–634. doi:10.1306/212F89F4-2B24-11D7-8648000102C1865D

Shan, S. C., Wu, Y. Z., Fu, Y. K., and Zhou, P. H. (2021). Shear mechanical properties of anchored rock mass under impact load. *J. Min. Strata Control Eng.* 3 (4), 043034. doi:10.13532/j.jmsce.cn10-1638/td.20211014.001

Shen, A., Zheng, J., Chen, Y., Ni, X., and Huang, L. (2016). Characteristics, origin and distribution of dolomite reservoirs in lower-middle cambrian, tarim basin, NW China. *Petroleum Explor. Dev.* 43 (3), 375–385. doi:10.1016/S1876-3804(16)30044-1

Shen, W., Li, X., Cihan, A., Lu, X., and Liu, X. (2019). Experimental and numerical simulation of water adsorption and diffusion in shale gas reservoir rocks. *Adv. Geo-Energy Res.* 3 (2), 165–174. doi:10.26804/ager.2019.02.06

Shields, G., and Stile, P. (2001). Diagenetic constraints on the use of cerium anomalies as palaeoseawater redox proxies: An isotopic and REE study of Cambrian phosphorites. *Chem. Geol.* 175 (1-2), 29–48. doi:10.1016/S0009-2541(00)00362-4

Sun, Z. M. (2023). Superimposed hydrocarbon accumulation through multi-source and multi-stage evolution in the cambrian xixiangchi group of eastern Sichuan Basin: A case study of the pingqiao gas-bearing anticline. *Energy Geosci.* 4 (1), 131–142. doi:10.1016/j.engeos.2022.09.001

Swirydczuk, K. (1988). Mineralogical controlon porosity type in upper jurassic smackover ooid grainstones, southern Arkansas and northern Louisiana. *J. Sediment. petrology* 58 (2), 339–347. doi:10.1306/212F8D8C-2B24-11D7-8648000102C1865D

Tan, X., Zhao, L., Luo, B., Jiang, X., Cao, J., Liu, H., et al. (2012). Comparison of basic features and origins of oolitic shoal reservoirs between carbonate platform interior and platform margin locations in the Lower Triassic Feixianguan Formation of the Sichuan Basin, southwest China. *Petroleum Sci.* 9, 417–428. doi:10.1007/s12182-012-0229-2

Tang, Y., Tan, S. H., Wang, R. F., Wang, H., Xia, C. M., and Chen, K. Y. (2022). Analysis of tight oil accumulation conditions and prediction of sweet spots in ordos basin: A case study. *Energy Energy Geosci.* 3 (4), 417–426. doi:10.1016/j.engeos.2021.09.002

Tavakoli, V., Rahimpour-Bonab, H., and Esrafili-Dizaji, B. (2011). Diagenetic controlled reservoir quality of South Pars gas field, an integrated approach. *Comptes rendus - Géoscience* 343 (1), 55–71. doi:10.1016/j.crte.2010.10.004

Wang, Q., and Jin, Z. (2002). Superimposed basin and oil-gas formation and accumulation. *Chin. Basic Sci.* 6, 4–7. doi:10.3969/j.issn.1009-2412.2002.06.001

Wang, Z., Jiang, C., Jiang, Y., Zhang, J., and Gu, Y. (2018). Distribution patterns and controlling factors for reservoir characteristic difference of oolitic shoals, Feixian'guan Formation, eastern Longgang area, SW China. *Arabian J. Geosciences* 11, 751. doi:10.1007/s12517-018-4082-5

Wang, X., Yin, H., Zhao, X., Li, B., and Yang, Y. (2019). Microscopic remaining oil distribution and quantitative analysis of polymer flooding based on CT scanning. *Adv. Geo-Energy Res.* 3 (4), 448–456. doi:10.26804/ager.2019.04.10

Wei, G., Yang, W., Xie, W., Jin, H., Su, N., Sun, A., et al. (2018). Accumulation modes and exploration domains of Sinian-Cambrian natural gas in Sichuan Basin. *Acta Pet. Sin.* 39 (12), 1317–1327. doi:10.7623/syxb201812001

Xia, D. L., Wu, Y., Zou, M., Xia, D. D., and Pang, W. (2022). Quality characterization of tight sandstone reservoirs in the yanchang Formation of the honghe oilfield, ordos basin, central China. *Energy Geosci.* 3 (4), 444–452. doi:10.1016/j.engeos.2021.07.001

Xing, F., Lu, Y., Guo, T., Li, S., Hou, M., Hu, H., et al. (2017). Sedimentary texture diversity of different carbonate platform margins and it its significance for petroleum exploration: A case study of carbonate platform margins in feixianguan period of the early triassic, NE Sichuan Basin, China. *Acta Petrol. Sin.* 33 (4), 1305–1316.

Yang, X., Zhao, W., Cao, H., Yang, Y., Zhang, B., and Tao, S. (2006). Fomation and distribution of Triassic Feixianguan oolitic bank favorable reservoir in the NE Sichuan Basin. *Petroleum Explor. Dev.* 33 (1), 17–21. doi:10.3321/j.issn:1000-0747.2006.01.004

Yoshida, M., and Santosh, M. (2020). Energetics of the solid earth: An integrated perspective. *Energy Geosci.* 1 (1-2), 28–35. doi:10.1016/j.engeos.2020.04.001

Zhao, W., Shen, A., Qiao, Z., Pan, L., Hu, A., and Zhang, J. (2018). Genetic types and distinguished characteristics of dolomite and the origin of dolomite reservoirs. *Petroleum Explor. Dev.* 45 (6), 983–997. doi:10.1016/s1876-3804(18)30103-4

Zheng, R., Geng, W., Zheng, C., Li, S., Li, G., Luo, P., et al. (2008). Genesis of dolostone reseryoir of Feixianguan Formation in lower triassic of northeast Sichuan Basin. *Acta Pet. Sin.* 29 (6), 815–821. doi:10.3321/j.issn:0253-2697.2008.06.005

Zhou, Z., Wang, X., Yin, G., Yuan, S., and Zeng, S. (2016). Characteristics and Genesis of the (sinian) dengying formation reservoir in central sichuan, China. *J. Nat. Gas Sci. Eng.* 29, 311–321. doi:10.1016/j.jngse.2015.12.005

Zhou, J., Deng, H., Yu, Z., Guo, Q., Zhang, R., Zhang, J., et al. (2019). The Genesis and prediction of dolomite reservoir in reef-shoal of changxing formation-feixianguan Formation in Sichuan Basin. *J. Petroleum Sci. Eng.* 178, 324–335. doi:10.1016/j.petrol.2019.03.020

Zhou, Y., Jiang, Y., Liang, J., Gu, Y., Fu, Y., and Xiao, Y. (2021). Reservoir characteristics and major controlling factors of the cambrian xixiangchi formation, central Sichuan Basin, southwest China. *J. Energy Eng.* 147 (6), 04021051. doi:10.1061/(ASCE)EY.1943-7897.0000803

Zou, C., Xu, C., Wang, Z., Hu, S., Yang, G., Li, J., et al. (2011). Geological characteristics and forming conditions of the platform margin large reef-shoal gas province in the Sichuan Basin. *Petroleum Explor. Dev.* 38 (6), 641–651. doi:10.1016/s1876-3804(12)60001-9

frontiers | Frontiers in Earth Science

TYPE Original Research
PUBLISHED 12 January 2023
DOI 10.3389/feart.2022.1108734

OPEN ACCESS

EDITED BY
Hu Li,
Southwest Petroleum University, China

REVIEWED BY
Xixin Wang,
Yangtze University, China
Yunfeng Zhang,
Southwest Petroleum University, China
Xiujian Ding,
China University of Petroleum, China

*CORRESPONDENCE
You Zhang,
zhangshiyouda@126.com

SPECIALTY SECTION
This article was submitted to Structural Geology and Tectonics, a section of the journal Frontiers in Earth Science

RECEIVED 26 November 2022
ACCEPTED 28 December 2022
PUBLISHED 12 January 2023

CITATION
Zhang Y, Li Q, Niu Y, Li B, Shi Y and Pang Y (2023), Key stage and model of hydrocarbon accumulation of Ordovician reservoir in Gucheng area, Tarim Basin, China.
Front. Earth Sci. 10:1108734.
doi: 10.3389/feart.2022.1108734

Key stage and model of hydrocarbon accumulation of Ordovician reservoir in Gucheng area, Tarim Basin, China

You Zhang[1]*, Qiang Li[2], Yongbin Niu[3], Bin Li[4], Yanqing Shi[4] and Yumao Pang[5]

[1]PetroChina Hangzhou Research Institute of Petroleum Geology, Hangzhou, China, [2]Exploration and Development Research Institute, PetroChina Daqing Oilfield Company, Daqing, China, [3]College of Resource and Environment, Henan Polytechnic University, Jiaozuo, China, [4]College of Geosciences, China University of Petroleum (Beijing), Beijing, China, [5]College of Earth Science and Engineering, Shandong University of Science and Technology, Qingdao, China

The heterogeneity of deep carbonate reservoirs is strong, it is significant for exploration and development to clarify the key stages of oil and gas accumulation. Taking the Ordovician in the Gucheng area of Tarim Basin as an example, this paper systematically investigated the key stage and model of hydrocarbon accumulation using the data of the cores, thin sections, cathode luminescence tests, laser ablation U-Pb isotope geochronometry, bitumen reflectance, and fluid inclusion tests, and seismic interpretation. (1) The Tarim Basin mainly develops three sets of effective source rocks, namely the Cambrian Yuertusi Formation, Cambrian Moheershan Formation, and Mid-Lower Ordovician Heituwa Formation, which are concentrated in the slope-basin facies of eastern Tarim Basin. (2) The Gucheng area is located in a favorable paleo-structural position. The pathway system composed of vertical faults and lateral unconformities occurs in the paleo-uplift, which is critical for hydrocarbon migration and accumulation. (3) The laser in-situ U-Pb dating, distribution and genesis of reservoir bitumen, burial-thermal maturation history, and the homogenization temperature of fluid inclusions suggest that the multi-stage tectonic thermal events of the Caledonian and Hercynian stages result in key adjustment and modification to deep hydrocarbon accumulation. Due to magmatic hydrothermal activities, the Caledonian primary oil reservoir massively evolved into oil-cracking gas reservoirs and residual paleo-oil reservoirs. (4) The paleo tectonic-fluid effect plays an important factor controlling the development of the Ordovician reservoirs. The evolution of the hydrocarbon accumulation in Gucheng area can be divided into three stages, namely formation of primary oil and gas reservoirs, oil-cracking gas reservoirs, and adjustment, destruction and reforming of gas reservoirs. To sum up, the western and northern parts of the paleo-uplift with favorable source-reservoir-cap rock assemblage and less effects of hydrothermal activities are the favorable zones for hydrocarbon exploration in the Gucheng area, the Tarim Basin.

KEYWORDS

key accumulation stage, laser *in situ* U–Pb dating, hydrocarbon accumulation, Ordovician, Gucheng area

1 Introduction

Over the recent years, significant breakthroughs have been continuously made in carbonate rocks of the marine facies, which has become the major strategic field for sustainable development of deep hydrocarbon exploration in China (Jia and Pang 2013; Sun et al., 2013; Dong et al., 2020; Li H et al., 2022). The Ordovician of the Gucheng area, Tarim Basin, is deposited in the slope belt of the carbonate platform-basin transition. Compared with that of the carbonate platform facies in the basin, it presents more diverse reservoir types and is closer to the Cambrian–Lower Ordovician source rock. Therefore, the Gucheng area is considered to be one of the areas in the Tarim Basin with the best conditions for hydrocarbon generation and storage (Shen et al., 2018; Zhang et al., 2018; Hong et al., 2020; Zhang et al., 2021). By the end of 2021, PetroChina had made massive physical efforts of two-(2D) and three-(3D) dimensional seismic prospecting and drilling across its 1.9×10^4 km^2 lease area in the Gucheng area, and 18 prospecting wells have been drilled during the past 10 years. The exploration suffers from low success rates of prospecting wells, complex reservoirs, complicated conditions for hydrocarbon accumulation, the occurrence of pyrobitumen, and poor oil testing results due to poor reservoir porosity. A review of the whole exploration practice in eastern Tarim Basin reveals that hydrocarbon was discovered only in relatively limited areas, and no proven reserves have been submitted yet. Accordingly, doubts are raised regarding the exploration potential of the Lower Paleozoic carbonate rock of the Gucheng area of the eastern Tarim Basin.

Extensive work has been performed from numerous points of views, in terms of the stratigraphic sequence (Fan et al., 2007; Zhao et al., 2010; Lin et al., 2013; Zhao, 2015), lithofacies paleogeography (Feng et al., 2006; Feng et al., 2007; Liu et al., 2011; Zhang et al., 2015), structural–sedimentary evolution (Zhang et al., 2007; Han et al., 2009; Li Q et al., 2014; Wang G et al., 2014), characteristics and formation mechanisms of reservoir rocks (Zheng et al., 2016; Shao et al., 2019), and control factors of hydrocarbon accumulation and exploration fields (Cao et al., 2019; Lv et al., 2022; Tochukwu et al., 2022), and some commonly accepted basic understandings have been obtained. For instance, the hydrocarbon exploration in the Tarim Basin shall highlight the Gucheng area with a good source–reservoir rock configuration. However, the specific hydrocarbon accumulation conditions of the key blocks and key risk exploration fields remain controversial, and the previous understanding can no longer meet the requirement of risk exploration (Hou et al., 2020). The deep carbonate rocks have undergone multi-stage transformation, and it is difficult to accurately determine the reservoir formation process by relying on the traditional oil and gas reservoir formation research methods and technologies. Previous research shows that the effective combination of various elements, such as the source rock, reservoir rock, cap rock, migration pathway, and trap, is the key factor to hydrocarbon accumulation (Zhao et al., 2006; Zhang et al., 2011a; Li J et al., 2022; Richardson et al., 2022). In this paper, the formation period of carbonate reservoirs in the study area is precisely determined by laser *in situ* U–Pb isotope dating technology. This research discusses the key stage and model of hydrocarbon accumulation of the Ordovician reservoir in the Gucheng area, from perspectives of source rock conditions, hydrocarbon migration pathways, formation mechanisms of reservoir rocks, and modification of tectonic thermal events. Also, the favorable exploration zones are evaluated according to lessons learned from failure wells and exploration practice. The aforementioned research results are expected to provide more reliable references for ultra-deep hydrocarbon exploration in the Tarim Basin and similar areas.

2 Geological setting

The Gucheng area is located in the east of the Tazhong uplift and southwestward of the Shunnan slope and northward of the Lunnan area. It connects with the Manjiaer sag and Tadong uplift. It is cut by the Cheerchen fault belt in the south (Figure 1A). In terms of geotectonics, the Gucheng lower uplift lies in the transition between the Tazhong and Tadong uplifts. It was formed during the middle Caledonian orogeny and finalized during the late Caledonian orogeny. Subsequently, it was further uplifted due to the Hercynian Northward compression and yet remained tectonically stable during the Indosinian–Himalayan movement (Dai et al., 1996; He et al., 2005; Gao, 2019).

A relatively complete stratigraphic association of the Sinian–Ordovician carbonate rocks develops in the Gucheng area, which is most of the carbonate platform and slope-basin deposition (Cai et al., 2013; Huang et al., 2013). The Cambrian–Ordovician in the study area presents an overall paleo-geographic framework characterized by a "platform in west and basin in east." In other words, the western part is the carbonate platform deposition, while the eastern part is the deposition of the platform margin and basin environments. The platform deposition is associated with a shallow water depth and development of the mound and shoal of the platform margin and the intra-platform grain shoal, of which the scales are controlled by the type and evolution of the platform. Moreover, the slope–basin deposition is found with a predominance of muddy sediments and considered favorable for development of high-quality source rocks (Figure 1B).

3 Samples and methods

The samples of this research are all collected from the 18 prospecting wells penetrating the Ordovician carbonate rock in the Gucheng area, Tarim Basin (Figure 1A). The conventional way to determine the relative sequence of diagenetic processes in research is mainly based on the contact relationships of minerals of varying stages revealed by the features observed in core observation and thin-section microscopy. The absolute age of minerals of a given stage can also be measured using the solution-based U–Pb isotope geochronometry (Woodhead et al., 2006; Woodhead and Pickering, 2012; Yuan et al., 2022). Nonetheless, these methods have the following disadvantages: first, the method based on the contact relationship among minerals of varying stages can only determine the relative sequence of diagenetic processes of a given sample, and in other words, it cannot directly determine the formation sequence of the same mineral component in different samples. Second, the solution-based U–Pb dating demands that samples to be tested have a sufficient content of U and Pb and consumes a large quantity of samples. However, the ancient marine carbonate rock is commonly associated with low content of U and Pb (Pickering et al., 2010) and small diameters of diagenetic components, resulting in failure to provide enough samples for

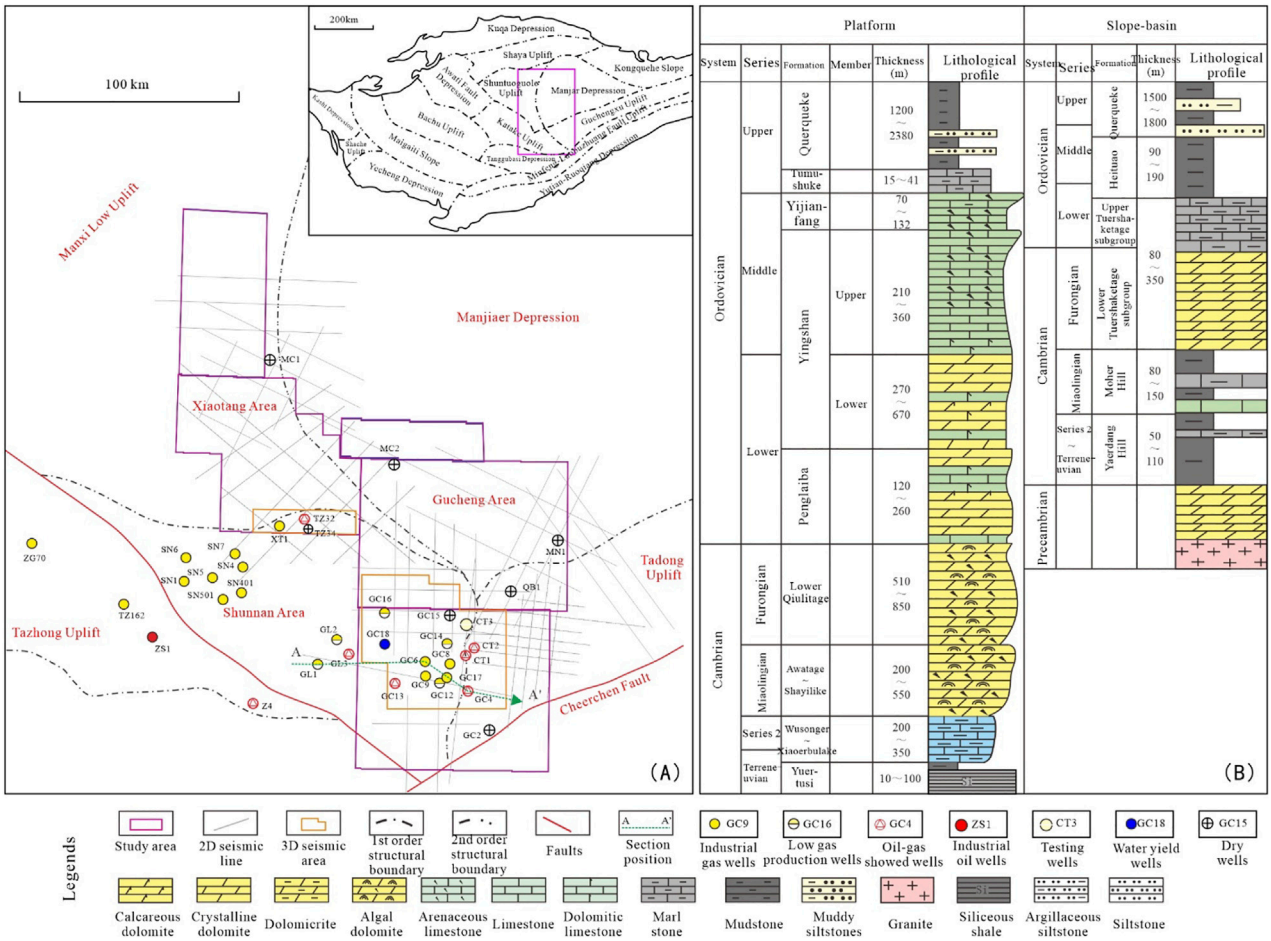

FIGURE 1
Geological setting of the Gucheng area. **(A)**. Structural location of the Gucheng area in Tarim Basin; **(B)**. Comprehensive stratigraphic column of the Ordovician.

tests (Hu et al., 2020; Li 2022), which restrains the application of the method. Over the past few years, these problems are all solved by the extensive application of laser ablation (LA)-based *in situ* U–Pb dating (Li Y. L et al., 2014; Coogan et al., 2016; Roberts et al., 2017; Roberts et al., 2020). After importing and digesting the foreign advanced technology, the CNPC Key Laboratory of Carbonate Reservoirs develops the LA-based *in situ* U–Pb dating specific to low U-content carbonate minerals. The test instrument is the LA-ICP-MS (Element XR), the reference materials are WC-1 (Roberts et al., 2017) and AHX-1 (Shen et al., 2019), and the isotope correction reference material is NIST 614 (Norman et al., 1996). The laser beam diameter is 100 μm, and the ablation frequency is 10 Hz. The main test procedure is presented below: (1) Prepare the sample target. (2) Determine the test zone according to the status of the target component (the LA target is marked in red. (3) Perform the LA and mass spectrometry across the test zone point by point. (4) Process the acquired test data and develop the Concordia diagram. This research targets the Ordovician of the Gucheng area in eastern Tarim and clarifies the key diagenetic stages *via* the comprehensive analysis based on the LA *in situ* U–Pb geochronometry assisted by the thin-section petrographic analysis and laser elemental surface scanning to provide references for studying the heterogeneity of the Ordovician reservoirs in the Tarim Basin.

To illustrate the 3D distribution of pore-throats of the reservoir, the micro-nano-scale refined description is performed to produce the 3D pore-throat distribution model, using the high-precision micro-nano CT 3D imaging technology and e-core software for digital cores. The statistics of the parameters such as the pore-throat radius, shape factor, and spatial connectivity are obtained for pore-throat characterization.

The thin-section, cathode luminescence, and inclusion tests are finished in the CNPC Key Laboratory of Carbonate Reservoirs, and for the test methods, please refer to Pan et al. (2016).

4 Results and discussion

4.1 Source rocks

The facies of the slope-basin in eastern Tarim is the main distribution area of sources rocks in the Tarim Basin. In particular, it is claimed that the Gucheng area of eastern Tarim mainly develops the Cambrian Yuertusi Formation, Cambrian

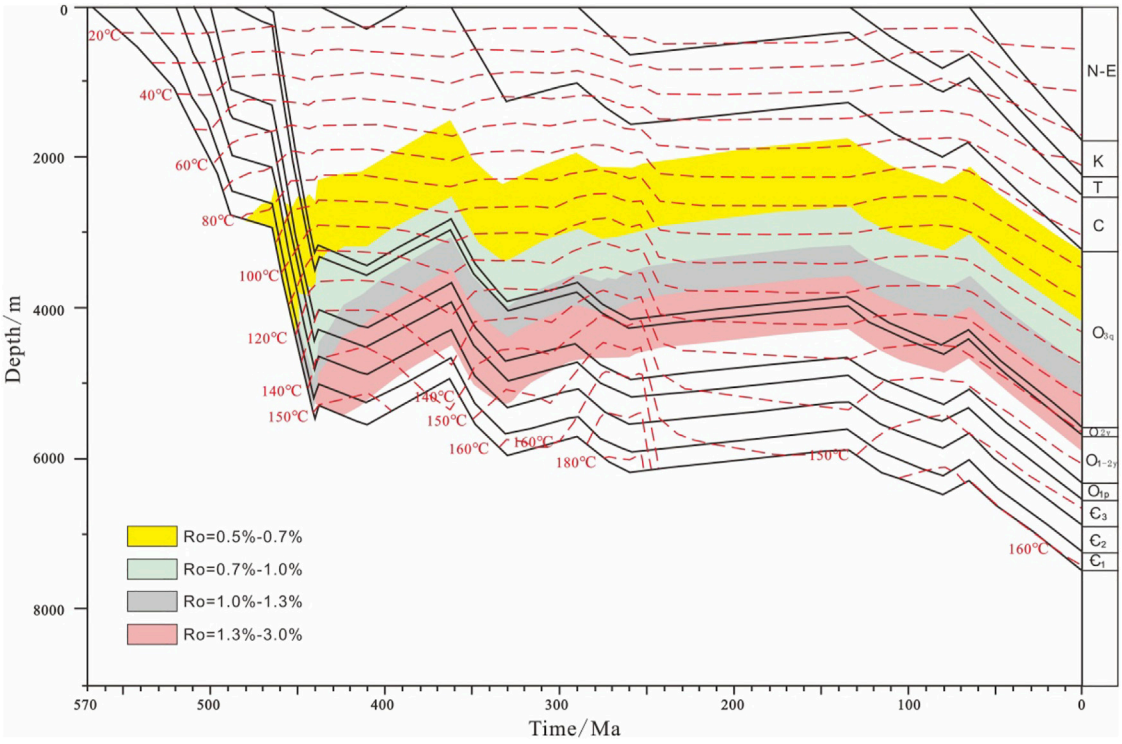

FIGURE 2
History of burial–thermal maturation of a typical well in Gucheng area.

Moheershan Formation, and Mid-Lower Ordovician Heituwa Formation, three sets of effective source rocks, which mostly spread over the slope–basin facies belt of the eastern Gucheng uplift, eastern Tarim, after numerous studies reviewed the development of sources on the periphery of the Gucheng area in accordance with the field outcrops and newly acquired drilling and seismic data (Zhu et al., 2016; Guan et al., 2019).

The Terreneuvian source rock of the Cambrian mainly occurs in the Yuertusi Formation of the platform facies belt in the west and the Xidashan–Xishanbulake Formations of the basin facies belt in the east. Zhu et al. (2016); Li et al. (2020) performed geochemical analysis of over 10 outcrops of the Cambrian Yuertusi Formation in the Aksu area, and the black shale of the Yuertusi Formation presents TOC height up to 4%–16%, the highest among the discovered marine source rocks in China. Well Luntan-1 reveals that the black mudstone of the Cambrian Yuertusi Formation is 18 m thick, with TOC of 2.43%–18.48% (averaging 10.1%) and Ro of 1.5%–1.8%, and is considered a high-quality source rock (Yang et al., 2020). Wells TD1 and TD2 in the basin facies belt in the east also reveal this highly over-mature source rock, similar to that in the platform facies belt. The Miaolingian source rock of Cambrian mainly develops in the Moheershan Formation of the platform margin slope–basin facies belt in eastern Tarim, which is encountered in Wells TD2 and TD1 in the basin facies belt. It presents TOC of .51%–2.58% (averaging 1.60%) and Ro of 2.54% and is considered a medium–relatively high-quality source rock. The Mid-Lower Ordovician source rock is concentrated in the Heituwa Formation of eastern Tarim. It is the black shale of the basin facies deposition, with TOC of .50%–1.64% and Ro of 1.16%–2.10%, and represents a medium–highly mature medium–high-quality source rock (Cao et al., 2019).

The analysis of the burial-thermal maturation history (Figure 2) shows that this source rock reaches the peak hydrocarbon generation and expulsion during the middle Caledonian stage. Massive gas generation *via* oil cracking of paleo-oil reservoirs occurs in the late Caledonian and late Hercynian stages. A large quantity of over-mature gas is generated during the Indosinian–Himalayan stage (Zhang et al., 2011a; Zhang et al., 2011b), which results in sufficient hydrocarbon supply of the Ordovician in the Gucheng area, Tarim Basin. The statistical overview of the source rock parameters is shown in Table 1.

4.2 Effective migration pathways

As for pathways for hydrocarbon migration, the network pathway system composed of vertical fault systems and lateral unconformities is found with extensive development across the paleo-uplift area, which serves as a good migration channel and effective pathway system of hydrocarbon migration and accumulation (Figure 3) (Mahmud et al., 2020; Shan et al., 2021). On one hand, multiple regional karst unconformities occur at the tops of the Yijianfang, Yingshan, and Penglaiba Formations and Furongian of Cambrian. Moreover, the effective reservoir thickness is large, and the lateral spreading of the reservoir rock is broadened and continuous. These are all in favor of hydrocarbons migrating along unconformities toward the higher position of the flank and accumulating in place. On the other hand, the Gucheng area is found with the development of multiple high-angle tensile normal faults penetrating downward the

TABLE 1 Source rock parameters.

System	Series	Formation	TOC	Ro
Cambrian	Terreneuvian	Yuertusi Formation	2.43%–18.48%	1.5%–1.8%
	Miaolingian	Moheershan Formation	.51%–2.58%	2.54%
Ordovician	Mid-Lower	Heituwa Formation	.50%–1.64%	1.16%–2.10%

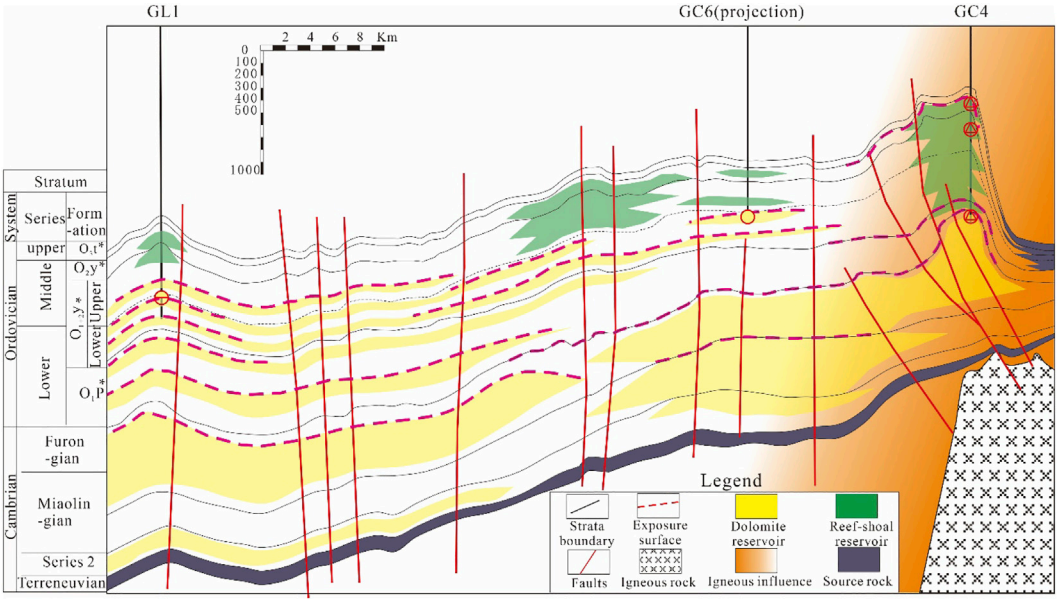

FIGURE 3
Pathway system composed of vertical faults and lateral unconformities in the Gucheng area. (Section location, AA′, is shown in Figure 1A).

Cambrian source rock and yet not cutting the overlying regional cap rocks (the Tumuxiuke Formation marlstone and the Queerqueke Formation mudstone). They provide effective vertical channels for hydrocarbon migration from the Cambrian source rock, while maintaining the integrity of the lithological–structural composite trap. Such faults are key factors for hydrocarbon accumulation in the Ordovician in the Gucheng area. In addition, due to invasion of igneous rocks, the paleo-oil reservoirs are baked and destructed, and yet such effects are lower down as further away from the invaded igneous rock (Figure 3). Tumuxiuke Fm is abbreviated as O_3t, Yijianfang Fm is abbreviated as O_2y, Yingshan Fm is abbreviated as $O_{1+2}y$, and Penglaiba Fm is abbreviated as O_1P. They all belong to the Ordovician.

4.3 Adjustment and modification of hydrocarbon accumulation by tectonic thermal events

The slope of the Gucheng area, Tarim Basin, lies at the east end of the Tazhong paleo-uplift, and the paleo-uplift background was established in the early Caledonian period. The southern part of this structural belt is relatively close to the Cheerchen fault, which is highly active during the late Caledonian stage and the late Permian, associated with massive invasion of igneous rocks (Ran et al., 2008; Liu et al., 2010; Zhang et al., 2014). Such Permian massive magmatic invasion alters the geothermal field at that time (raised geothermal thermal gradients), and accordingly, the immature source rock on the periphery of the depression reaches the oil generation threshold, which promotes the hydrocarbon generation rate and quantity and accelerates the evolution of the source rock of the basin. As for the mature source rock in the basin, it is converted into over-mature source rock and enters the depletion stage of hydrocarbon generation (Ran et al., 2008; Liu et al., 2010; Zhang et al., 2014). The adjustment and modification of oil and gas reservoirs attributed to tectonic thermal events have critical influences on the formation and evolution of oil and gas reservoirs in terms of both materials and energy and complicate the hydrocarbon accumulation in the Ordovician of the Gucheng area.

4.3.1 Evidence from the laser *in situ* U–Pb dating

The Ordovician dolomite reservoir in the Gucheng area, Tarim Basin, has gone through superimposed modification of diagenetic fluids of multiple stages during its formation, which results in the high heterogeneity of the reservoir. To clarify the relative sequence of diagenetic processes of varying stages during the pore evolution of the Ordovician dolomite reservoir and their coupling relationships with pores of the reservoir, precisely determining the stages of the

TABLE 2 Components of tested samples and results of the laser *in situ* U–Pb dating.

Sample no.	Depth/m	Lithology	Tested component		U–Pb dating
			No.	Occurrence	
DQ17	6,058.22	Gray fine dolomite, with part of pore-vugs filled with calcite	①	Intergrowth-crystalline calcite	469 ± 22 Ma
			②	Surrounding rock fine dolomite	474.7 ± 7.5 Ma
DQ11	6,345.19	Dark gray fine–medium dolomite, with pore-vugs filled with coarse dolomite	③	Coarse dolomite	/*
			④	Surrounding rock fine–medium dolomite	346 ± 38 Ma

Remarks: "/" represents failure of the laser *in situ* U–Pb dating.

key diagenetic processes is critical. This research, based on the laser *in situ* U–Pb dating and laser *in situ* elemental surface scanning and imaging, performs a systematic isotope dating analysis for the three major textural constituents, the surrounding rock matrix, medium–coarse dolomite on the wall of the pore-vug, and calcite cement inside the pore-vug. The test results are shown in Table 2; Figure 4.

The fine dolomite of the surrounding rock and intergrowth-crystalline calcite in Sample DQ17 are tested (Figures 4A, B). The fine dolomite of the surrounding rock is dated to be 474.7 ± 7.5 Ma (Figure 4C), corresponding to the age of the Ordovician Yingshan Formation in the study area. The intergrowth-crystalline calcite is dated back to 469 ± 22 Ma (Figure 4D), which suggests that the Ordovician is subjected to the stage of calcium-rich hydrothermal fluids during the Caledonian orogeny and pore-vugs are filled with calcite. The fine–medium dolomite of the surrounding rock and the coarse dolomite in the pore-vug in Sample DQ11 are tested (Figure 4E). Owing to the extremely low content of uranium in the coarse dolomite of the fracture-vug, the laser *in situ* U-Pb dating fails. The fine–medium dolomite of the dark gray surrounding rock formed 346 ± 38 Ma (Figure 4F), indicating a stage of magnesium-rich hydrothermal fluids during the early Hercynian stage, with fractures and vugs filled by coarse calcite (Figures 5A–D), with high positive anomalies of the elements Y and Ce (Figures 5E, F). The filling of the coarse dolomite occurs after the formation of the fine–medium dolomite of the dark gray surrounding rock, which implies that the invasion of hydrothermal fluids migrates along the early Hercynian fault and the filling of coarse dolomite shall be slightly later than 346 Ma. The laser *in situ* U–Pb dating and the *in situ* elemental surface scanning and imaging show that the multi-stage tectonic thermal events during the Caledonian and Hercynian movement have essential adjustment and modification effects on deep hydrocarbon accumulation, accompanied by filling with saddle dolomite and calcite.

4.3.2 Evidence from the reservoir bitumen distribution and genesis

The drilling and core of wells in the study area reveal that from the Yijianfang Formation to the Upper Yingshan Formation and in the Penglaiba Formation occurs the over 1,000-m-thick bitumen paleo-oil reservoir. The reservoir bitumen extensively develops in the dissolution pore-vug (Figure 6A), stylolite and structural fracture (Figure 6B), inter-crystalline (dissolution) pore (Figure 6C), and mold (visceral foramen) pore (Figure 6D) of the Ordovician carbonate reservoir of the paleo-uplift, and presents itself in filling forms of strips, grains, veins, and blocks (Li et al., 2019; Li et al., 2021a; Hou et al., 2020; Qie et al., 2021).

There have been many important understandings provided by previous studies on reservoir bitumen genesis. From the perspective of the genesis, the reservoir bitumen can be divided into three categories: pyrobitumen, biodegraded bitumen, and precipitated asphalt (Zhao et al., 2007). There are significant differences in morphology and maturity of bitumen of different geneses. Due to the high temperature and high pressure, the edge of the pyrobitumen is clearer, while the biodegraded bitumen and precipitated asphalt are often dispersed with blur edges and irregular shapes (Jacob, 1989). In addition, the reflectance of the pyrobitumen derived from crude oil cracking is much higher than those of precipitated asphalt and biodegraded bitumen (Hwang et al., 1998; Gao and Hu, 2002). The reflectance of pyrobitumen is generally above 4.0%–6.0%, and that of precipitated bitumen is usually .5%–1.5% (Ran et al., 2008).

The occurrence and reflectance of the reservoir's solid bitumen in the Gucheng area show that the solid bitumen is the pyrobitumen produced *via* the large-scale oil cracking of the original reservoirs affected by magmatic hydrothermal activities. Regardless of dolomite or limestone, the contained bitumen presents clear and straight edges, shapes of regular polygons, and vesicles developed on bitumen surfaces, which are typical features of pyrobitumen and indicate that the paleo-oil reservoir has experienced high-temperature baking. The solid bitumen reflectance is high, from 3.94%–7.75%. The measured reflectance of the same sample is highly variable and the bitumen is highly anisotropic, which implies intensive high thermal maturation. During the process of hydrothermal fluids flowing along faults and fractures, some special minerals, such as quartz, pyrite, fluorite, and bitumen (mainly pyrobitumen), precipitated, due to variation of pressure and temperature and interaction with surrounding rocks (Jin et al., 2006; Chen, 2008). In addition, the development of the siliceous hydrothermal filling also reflects the intensity of hydrothermal alteration (Figures 6E, F).

4.3.3 Evidence from homogenization temperatures of fluid inclusions

Fluid inclusions of the Ordovician reservoir rock in the Gucheng area mainly occur in the calcite vein, granular calcite, and crystalline quartz overgrowth and formed in the middle and late diagenesis. Observation identifies five types of fluid inclusions, namely, solid bitumen inclusion, hydrocarbon-containing brine

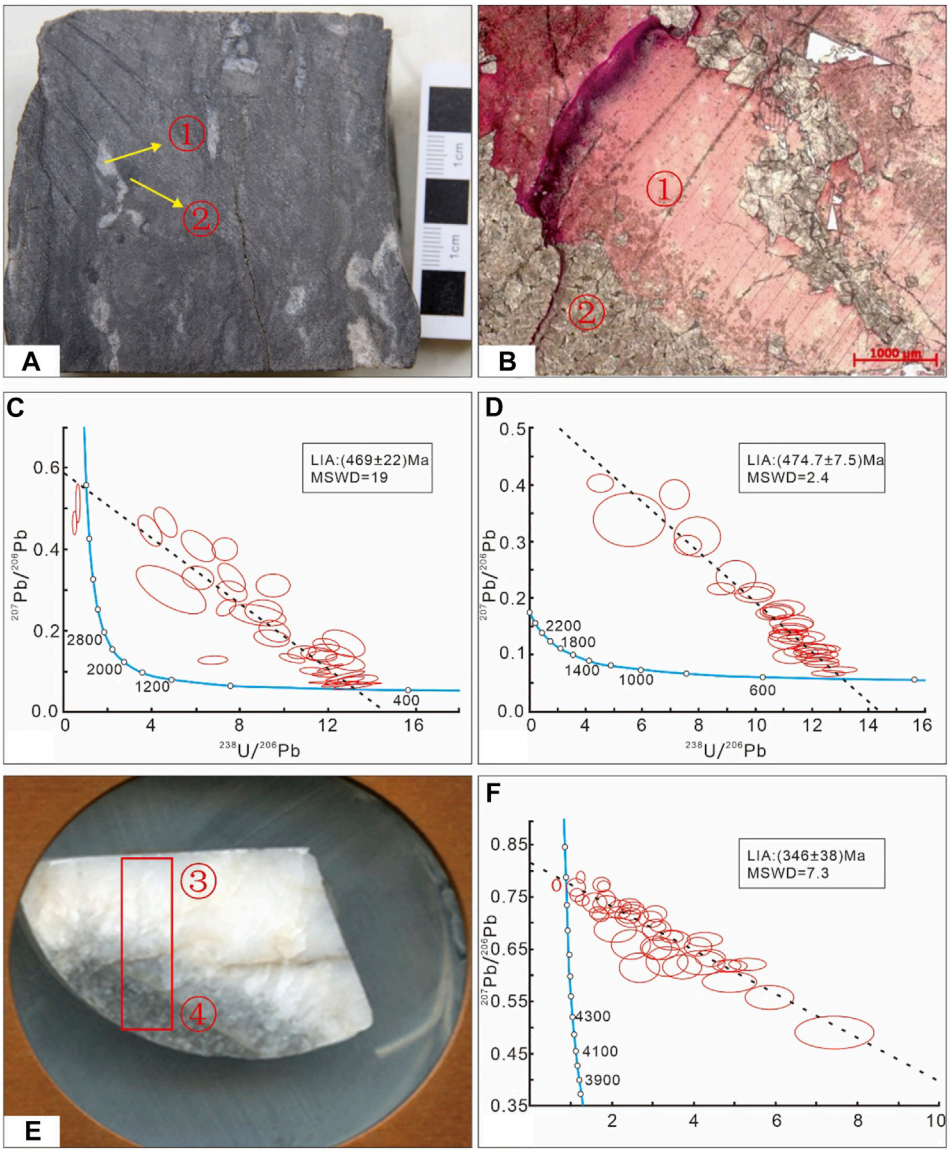

FIGURE 4
Characteristics of the Ordovician carbonate rock samples of the Tarim Basin (with marked sampling positions), and the U–Pb Concordia diagram. **(A)**. Two textural constituents of the ample tested in DQ17: ① the intergrowth-crystalline calcite in the pore-vug and ② the fine dolomite of the surrounding rock; **(B)**. Sampling positions for the thin section of sample DQ17: ① the intergrowth-crystalline calcite in the pore-vug and ② the fine dolomite of the surrounding rock; **(C)**. U–Pb isotope dating of the intergrowth-crystalline calcite in Sample DQ17; **(D)**. U–Pb isotope dating of the surrounding rock fine dolomite in Sample DQ17; **(E)**. Two tested textural constituents of Sample DQ11: ③ the coarse dolomite in the pore-vug and ④ the fine–medium dolomite in the surrounding rock; **(F)**. U–Pb isotope dating of the surrounding rock fine dolomite in Sample DQ11.

inclusion, two-phase brine inclusion, gas–liquid two-phase inclusion, and gaseous hydrocarbon inclusion. The bitumen inclusion is derived from the oil inclusion. Heavy hydrocarbons crack due to higher temperatures, and the inside pressure is raised to trigger bursting. Light hydrocarbons escape from the inclusion, and bitumen is left to form the bitumen inclusion, which is a direct evidence of oil emplacement. Gaseous hydrocarbon inclusions and gas–liquid two-phase inclusions may be derived from trapped cracking gas *via* oil cracking and also later charging of natural gas.

Identification and microthermometry have been performed for the hydrocarbon inclusions and associated brine inclusions in the Gucheng area (Table 3). The homogenization temperature of the organic fluid inclusion typically stands for the lowest temperature at the time the inclusion is captured. In other words, the temperature of the hydrocarbons migrates into the reservoir. Therefore, the peak temperature is indicative of the peak hydrocarbon migration. The analysis of oil stability of the marine facies reservoir in the platform-basin area of the Tarim Basin shows that 150°C is the threshold of crude oil cracking, and massive cracking is anticipated with a temperature over 200°C (Zhao et al., 2001), far higher than the formation temperature in cases of normal geothermal gradients. This suggests that the fluid temperature of the precipitated calcite vein is higher than the temperature of the surrounding rock, and thus such fluids are

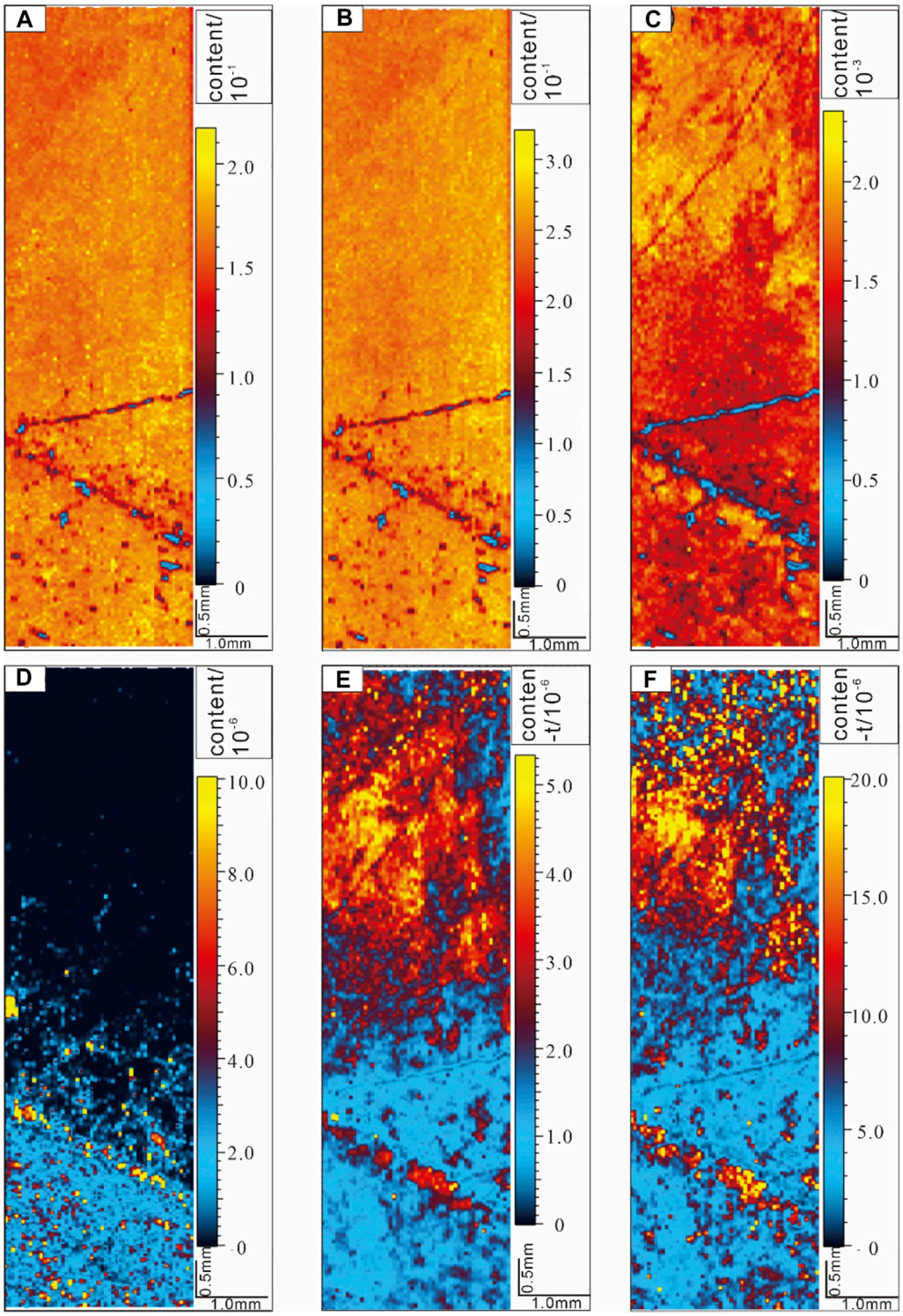

FIGURE 5
Element surface scanning images of Sample DQ11 in the Tarim Basin. **(A)**. Concentration of ^{25}Mg in horizontal distribution; **(B)** concentration of ^{43}Ca in horizontal distribution; **(C)** concentration of ^{55}Mn in horizontal distribution; **(D)** concentration of ^{238}U in horizontal distribution; **(E)** concentration of ^{89}Y in horizontal distribution; **(F)** concentration of ^{140}Ce in horizontal distribution.

typical deep hydrothermal fluids. Some geologists (Cai et al., 2008; Li K. K et al., 2010; Zhu et al., 2013) also validate the presence of hydrothermal fluids in the Lower Paleozoic of the Tarim Basin, according to the fact that the formation temperature of calcite is higher than the burial temperature.

4.3.4 Effective of paleo tectonic-fluid is a critical factor controlling the formation of hydrocarbon accumulation

The deep carbonate rock has gone through multi-stage variation of fluid-diagenetic environments of the tectonic, thermal, pressure,

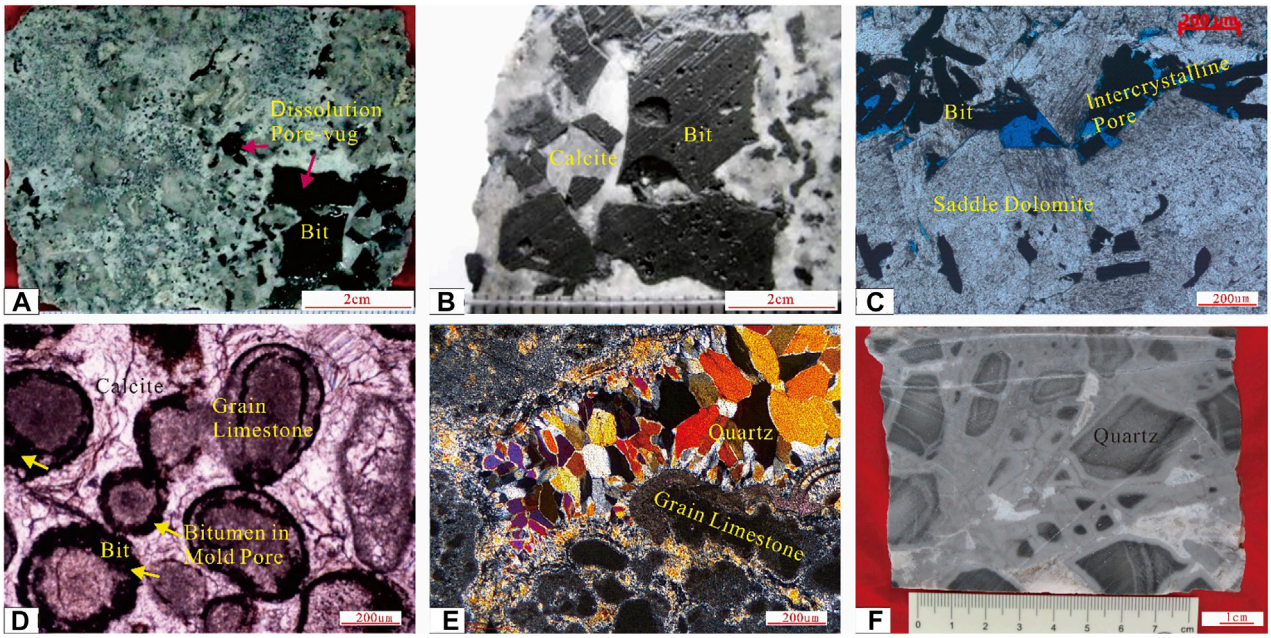

FIGURE 6
Occurrence of bitumen and siliceous hydrothermal metasomatism in the Ordovician carbonate reservoir in the Gucheng area. **(A)**. Bitumen in the dissolution pore-vug, Well GC4, Penglaiba Formation, 6,509 m; **(B)**. bitumen in the stylolite and structural fracture, with vesicles occurring on the bitumen surface, Well GC4, Yijianfang Formation, 5,597–5,600 m; **(C)** bitumen in the intercrystalline pore of dolomite, Well GC9, Yingshan Formation, 6,097.8 m; **(D)** bitumen in the mold pore, Well GC7, Yijianfang Formation, 5,662 m; **(E)** siliceous hydrothermal filling, Well GC15, Yingshan Formation, 6,356.7 m; **(F)** siliceous hydrothermal filling, Well GC14, Yingshan Formation, 6652 m.

and fluid regimes and time. The diagenesis is complicated, the diagenetic modification of multiple stages is superimposed, and the reservoir presents high heterogeneity (Chen et al., 2007; Zhao et al., 2012; Wang T. G et al., 2014; Li J et al., 2022). The temperature–pressure fields and fluid types are varied in different tectonic–burial–thermal maturation stages (Huang and Hou, 2001; Li Z et al., 2010; Fan et al., 2020; Li et al., 2021b). The Ordovician reservoir rock in the Gucheng area can be divided into two types, the Ordovician karst-dolomitization reservoir and the karst reef flat reservoir. In this research, the Ordovician karst-dolomitization reservoir is taken as an example to investigate the formation mechanisms of the complicated reservoir, such as the paleo-uplift setting, sedimentary facies, penecontemporaneous dissolution, and tectonic thermal events.

The Lower Ordovician karst-dolomitization reservoir in the Gucheng area, Tarim Basin, mainly occurs in the inner dolomitized shoal of the shallow-water ramp platform of the Lower Yingshan Formation and Penglaiba Formation. The reservoir space is dominated by residual pores, dissolution pore-vugs (Figure 7A), inter-crystalline or inter-granular (dissolution) pores (Figures 7B, C), and fractures. The reservoir samples mostly present medium–low porosity with medium–narrow throats, with high connectivity in local areas. The reservoir rocks are divided into the pore-vug type and fracture-vug type.

The CT comprehensive characterization of the Ordovician dolomite reservoir is shown in Figure 7D. CT scans of the reservoir pores show that the reservoir of the dolomitized shoal has higher micro-heterogeneity, manifested as the skewed distribution of pore-throats (uneven pore-vug diameter distribution from .2 mm–10 mm), medium-narrow throats, a lower quantity of throats with uneven distribution of radii, and higher connectivity in local areas.

The development of the karst-dolomitization reservoir of the Lower Yingshan Formation and Penglaiba Formation is controlled by the paleo-uplift and sedimentary facies settings in the early stage. Moreover, the reservoir is subjected to the superimposed modification of the penecontemporaneous karstification, shallow burial dolomitization, and late faulting–hydrothermal activity. After a comprehensive analysis, it is claimed that the inner grain shoal of the shallow-water ramp serves as the basis for development of the dolomite reservoir, while the penecontemporaneous exposure dissolution is key to the formation of the reservoir. Pores are mostly inherited from the previous dolomitized shoal, while the faulting–hydrothermal modification creates important extra pores. (1) The shoal facies is the basis of the development of the dolomitized shoal reservoir, and the distribution of high-quality reservoirs is closely related to the inner dolomitized shoal of the shallow-water ramp. The reservoir dominated by the matrix pore-vug is mostly found in the fine–medium dolomite, which presents the phantom granular texture and along-bedding development of pores. This suggests that the dolomitized shoal is the basis for large-scale development of the reservoir, and the reservoir is a typical shoal-controlled reservoir. In addition, according to the analysis of the residual or restored original rock texture, the original rock of the crystalline dolomite is mostly grainstone of the shoal facies. The inter-granular (crystalline) pores of the dolomitized shoal deposition are the main reservoir space, and the sparry grainstone and wackestone are tight with fewer pores. (2) The

TABLE 3 Homogenization temperatures of brine inclusions in minerals filling the fracture-vug of the Ordovician of the Gucheng area, Tarim Basin. Liquid hydrocarbon inclusion is abbreviated as LHI. Solid bitumen inclusion is abbreviated as SBI. Gas–liquid two-phase inclusion is abbreviated as GLI. Gaseous hydrocarbon inclusion is abbreviated as GHI. Brine inclusion is abbreviated as BI.

Sample no.	Host mineral	Inclusion type	Color and shape	Test spots	Homogenization Temperature/oC		
					Max	Min	Average
Sygc001	Early fracture-vug calcite	LHI or SBI	Light blue fluorescence, irregular	11	116	123	118
Sygc002	Calcite vein	LHI or SBI	Light blue fluorescence, irregular	6			
Sygc003	Late calcite filling of pore-vugs and calcite vein	GLI	Oval and round	13	140	163	152
Sygc004	Quartz in karst vugs	GLI	Oval and round	9			
Sygc005	Recrystallization quartz overgrowth	GHI and GLI	Rectangular, oval, round, and irregular	7	167	185	171
Sygc006	Calcite vein	GHI and GLI	Rectangular, oval, round, and irregular	10			
Sygc007	Calcite vein	GHI and BI	Oval and irregular	11	150	210	203
Sygc008	Late calcite filling of fracture-vugs	GHI and BI	Oval, rectangular, and irregular	9	153	210	207

penecontemporaneous exposure dissolution is key to the formation of pores. The systematic coring over 100 m in Well GC601 reveals that the cored interval has over 30 exposure karst surfaces associated with extensive geopetal textures and vadose silt zones. The pore-vug interval mainly occurs in the dolomitized shoal below the top exposure surface of the high-frequency cycle, representing a typical penecontemporaneous fabric-selective dissolution and providing flow channels for dolomitization fluids in the later shallow-burial stage. (3) The dolomite reservoir mainly presents itself along the permeable shoal, fault, and unconformity surface. Pores are mostly the previous pores that are inherited and preserved. The samples are generally seen with brown luminescence under the cathode ray, and some crystals present bright red rims (Figure 7E), which indicates that the dolomite of the study area is mainly the burial metasomatism genesis, with late hydrothermal modification in local areas. The hydrothermal fluids derived from deeper layers serve as the diagenetic media for the saddle dolomite. From the perspective of the dissolution–precipitation of minerals with material balance and varying temperature and pressure conditions, the dissolution and cementation are in unity of opposites. The end of the tectonic hydrothermal activity is often associated with fillings of siliceous hydrothermal fluids, saddle dolomite, and calcite (Figure 7F) (Jiao et al., 2011; Chen et al., 2012).

4.4 Hydrocarbon accumulation model and predicted favorable zones of the Ordovician in the Gucheng area, Tarim Basin

4.4.1 Hydrocarbon accumulation model

The overall paleo-geographic framework of the Ordovician in the Gucheng area, Tarim Basin, features the transition from the platform environment to the basin environment. The Ordovician is close to the main source rock, and the hydrocarbon generation and accumulation are characterized by the generation in the basin and storage in the platform. According to the staged basin structural evolution, burial–thermal maturation simulation, and analysis of the main control factors of hydrocarbon accumulation, the hydrocarbon accumulation of the ancient deep carbonate reservoir can be divided into three stages (Figure 8).

4.4.2 Prediction of favorable zones

Crude oil cracking of paleo-oil reservoirs to generate gas is an important way to form deep natural gas, and such cracking gas is the main target for natural gas exploration of highly over-mature marine carbonate reservoirs in China (Zhao et al., 2007; Wang et al., 2008; Song et al., 2021; Wang and Wang, 2021). The analysis of the main controlling factors of the hydrocarbon accumulation in the Gucheng area, Tarim Basin, and the corresponding hydrocarbon accumulation evolution model suggest that the crude oil of the paleo-oil reservoir is massively converted into pyrobitumen and natural gas. The phase transition of deep fluids results in more rigorous requirements of hydrocarbon accumulation. With respect to the hydrocarbon exploration of the Ordovician in the Gucheng area, Tarim Basin, the following principle is recommended. The Caledonian–Early Hercynian primary oil reservoir shall be searched in the upper Ordovician karst reef flat reservoir on the periphery of the depression, far away from igneous rock invasion. The Late Hercynian cracking gas reservoir shall mostly occur in the Lower

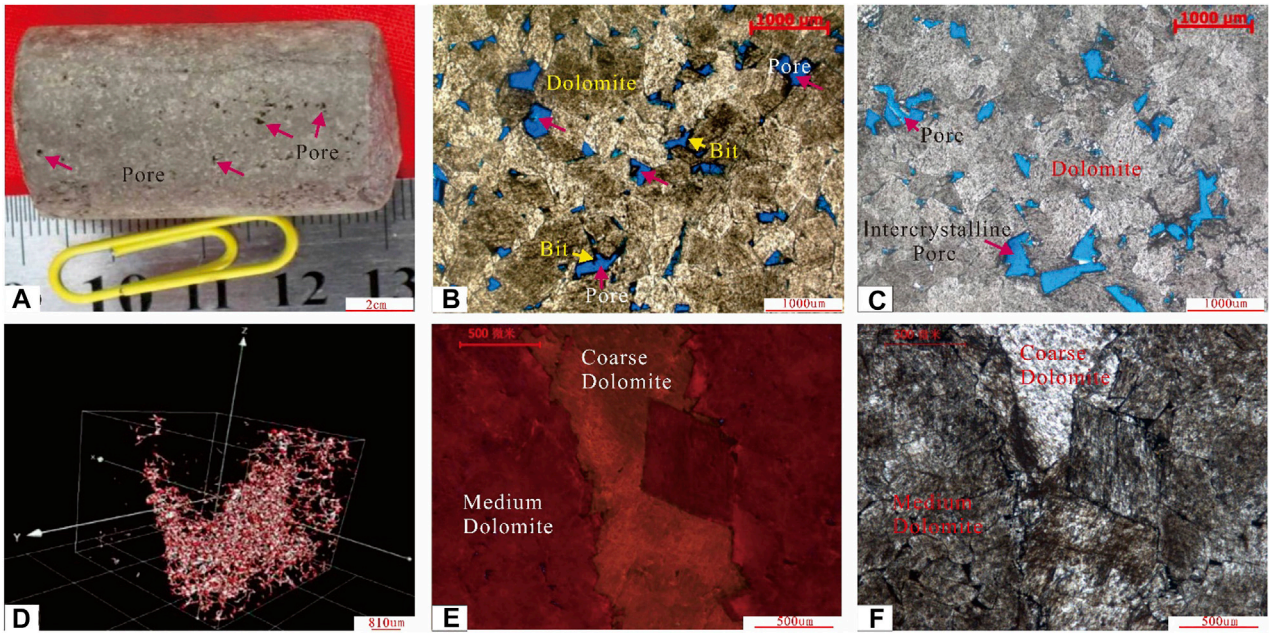

FIGURE 7
Reservoir space types and characteristics of the Ordovician karst-dolomitization reservoir in the Gucheng area, Tarim Basin. **(A)** Gray medium–coarse dolomite with dissolution pore-vugs (intergranular pore), Well GC13, the Yingshan Formation, 6,268 m; **(B)** medium–coarse dolomite with intercrystalline pores filled with bitumen, Well GC13, the Yingshan Formation, 6,268 m; **(C)** coarse dolomite with intercrystalline dissolution pores, Well GC9, the Yingshan Formation, 6,095.50 m; **(D)** pore-throat network model (with resolution of .9 um) with red representing pores and white representing throats, Well GC8, the Lower Yingshan Formation, 6,074.0 m; **(E)** medium–coarse dolomite with brown luminescence under the cathode ray and some crystals with red rims, Well GC14, the Yingshan Formation, 6,237.2 m; **(F)** medium–coarse dolomite with calcite hydrothermal filling, Well GC14, the Yingshan Formation, 6,237.2 m.

Ordovician karst-dolomitization reservoir along the paleo-oil reservoir and depression periphery. The exploration of the Himalayan gas reservoir shall focus on the large-scale gas generation of the liquid hydrocarbon scattered within the source rock during the highly over-mature stage. In summary, the western and northern parts of the paleo-uplift, with the premium source–reservoir–cap rock assemblage and fewer effects of faulting and tectonic hydrothermal activities, are the favorable exploration zones of hydrocarbon migration and accumulation.

5 Conclusion

1) The Ordovician oil and gas reservoir in the study area is attributed to the oil-cracking gas and late natural gas charging. The main controlling factors of the hydrocarbon accumulation in the Ordovician of the Gucheng area are the favorable paleo-structural setting, effective development of source rock, effective pathway system, modification of tectonic thermal events to hydrocarbon accumulation, and development conditions for high-quality reservoir rocks.
2) The paleo-tectonic-fluid effect is an important factor controlling the development of the reservoir rock and natural gas accumulation. The Ordovician karst-dolomitization reservoir is taken as an example to investigate the superimposed modification of various mechanisms, such as the paleo-uplift setting, sedimentary facies belt, penecontemporaneous dissolution, and tectonic thermal event. The grain shoal is the basis for the development of the dolomite reservoir, while the penecontemporaneous exposure dissolution is the key factor for reservoir formation. Pores are mostly inherited from the previous dolomitized shoal deposit, and faulting–hydrothermal modification creates important extra pores.
3) The formation and evolution of the Ordovician oil and gas reservoir in the Gucheng area, Tarim Basin, can be divided into three stages: the formation of primary oil and gas reservoirs, oil-cracking gas reservoirs, and adjustment, destruction, and reforming of gas reservoirs. The hydrocarbon accumulation model has the characteristics of multi-stage evolution.
4) Deep hydrothermal fluids migrate upward *via* faults, which is manifested as both destruction of the fault and vug-fracture reservoir system and constructive dissolution in different areas. The distribution mechanism for dissolution expansion and cementation still needs further investigation. Given the major challenge of poor continuity of high-quality reservoir and reservoir heterogeneity, it is recommended to quantitatively analyze the mechanisms of formation and preservation (dissolution and precipitation) of pores in the reservoir during the paleo–tectonic–hydrothermal process so as to reveal the distribution pattern and scale of high-quality reservoir rocks. In addition, given the small impedance difference between the low-porosity, low-permeability dolomite reservoir and tight limestone, it is suggested to enhance the seismic prediction technology for high-quality reservoirs, with the geological background of the study area taken into consideration. The future exploration practice shall target the northern and western parts of the

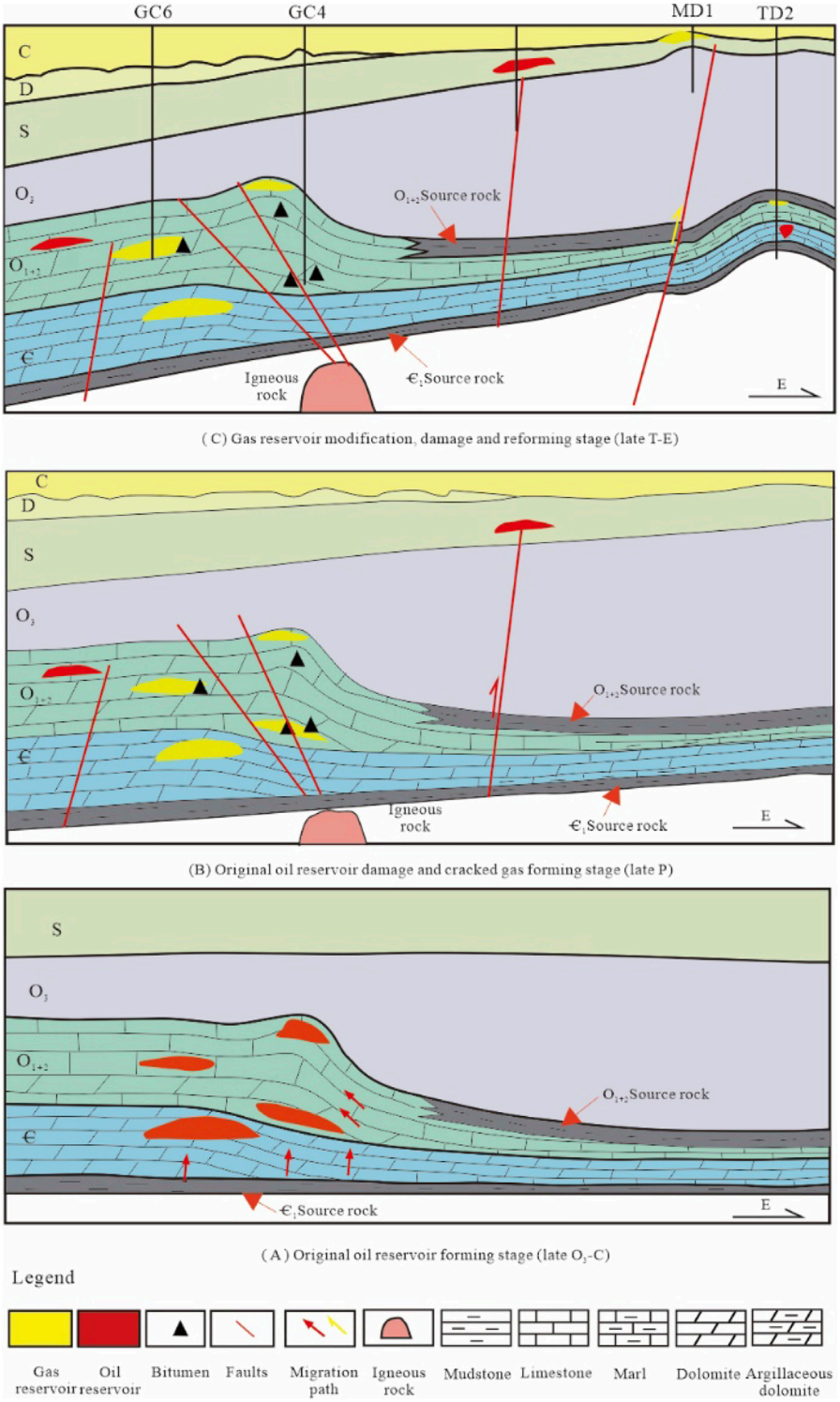

FIGURE 8
Hydrocarbon accumulation and evolution model in Gucheng area, Tarim Basin. **(A)** Formation of the primary oil and gas reservoir. The hydrocarbon generation of the three source rocks in the Cambrian–Ordovician of the Tarim Basin lasts until the late Hercynian stage, during which the primary oil reservoirs are formed, mostly in carbonate rock traps with some in the Silurian clastic rock. **(B)** Destruction and cracking of the primary oil reservoir. Due to the magmatic hydrothermal activities of multi-stage tectonic thermal events during the Caledonian and Hercynian stages, the primary oil reservoirs are subjected to oil cracking and the cracking gas reservoirs and residual paleo-oil reservoirs (or bitumen) are formed. **(C)** Adjustment, destruction, and reforming of gas reservoirs. The study area is tectonically stable after the Triassic. The trap integrity is maintained, and the preservation condition is good. The Cambrian–Ordovician source rock in the Manjiaer depression enters the hydrocarbon generation depletion stage, and part of crude oil is converted into natural gas *via* cracking, which forms condensate reservoirs. The dispersed residual organic matter in the source starts to generate gas at a large scale and forms the Himalayan gas reservoir, mostly occurring in traps related to the Himalayan movement.

Gucheng uplift that has a good source–reservoir–cap rock assemblage and is less affected by faulting and magmatic invasion.

Data availability statement

The original contributions presented in the study are included in the article/Supplementary Material, further inquiries can be directed to the corresponding author.

Author contributions

YZ, YN, and QL contributed in writing, reviewing, and editing; data curation; and writing—original draft preparation; BL, YS, and YP contributed in formal analysis, validation, and reviewing.

Funding

This study was supported by the National Science and Technology Major Project (No. 2016ZX05004-002).

Acknowledgments

We thank all editors and reviewers for their helpful comments and suggestions.

Conflict of interest

Author YN was employed by PetroChina Daqing Oilfield Company.

The remaining authors declare that the research was conducted in the absence of any commercial or financial relationships that could be construed as a potential conflict of interest.

Publisher's note

References

Cai, C. F., Li, K. K., Li, H. T., and Zhang, B. S. (2008). Evidence for cross formational hot brine flow from integrated 87Sr/86Sr, REE and fluid inclusions of the Ordovician veins in Central Tarim, China. *Appl. Geochem.* 23, 2226–2235. doi:10.1016/j.apgeochem.2008.03.009

Cai, X. Y., Dou, L. W., Jiang, H. S., Yu, T. X., and Cao, Z. C. (2013). Cambrian stratigraphic division and correlation in the eastern Tarim Basin. *J. Stratigr.* 37, 619. doi:10.19839/j.cnki.dcxzz.2013.04.081

Cao, Y. H., Wang, S., Zhang, Y. J., Yang, M., Yan, L., Zhao, Y. M., et al. (2019). Petroleum geological conditions and exploration potential of lower paleozoic carbonate rocks in Gucheng area, Tarim Basin, China. *Pet. Explor. Dev.* 46, 1165–1181. doi:10.1016/s1876-3804(19)60271-5

Chen, J. S., Li, Z., Wang, Z. Y., Tan, X. C., Li, L., and Ma, Q. (2007). Paleokarstification and reservoir distribution of ordovician carbonates in Tarim Basin. *Acta Sedimentol. Sin.* 25, 858–868. doi:10.14027/j.cnki.cjxb.2007.06.00

Chen, X., Zhao, W. Z., Zhang, L. P., Zhao, Z. J., Liu, Y. H., Zhang, B. M., et al. (2012). Discovery and exploration significance of structure-controlled hydrothermal dolomites in the Middle Permian of the central Sichuan Basin. *Acta Pet. Sin.* 33, 562–569. doi:10.7623/syxb201204004

Chen, D. Z. (2008). Structure-controlled hydrothermal dolomitization and hydrothermal dolomite reservoirs. *Oil Gas. Geol.* 29, 614–622. doi:10.11743/ogg20080510

Coogan, L. A., Parrish, R. R., and Roberts, N. M. (2016). Early hydrothermal carbon uptake by the upper oceanic crust: Insight from *in situ* U-Pb dating. *Geol.* 44, 147–150. doi:10.1130/G37212.1

Dai, J. X., Song, Y., and Zhang, H. F. (1996). Main factors controlling the foundation of medium-giant gas fields in China. *Sci. China (Series D).* 26 (6), 481–510. doi:10.1007/bf02878575

Dong, S., Zeng, L., Lyu, W., Xia, D., Liu, G., Wu, Y., et al. (2020). Fracture identification and evaluation using conventional logs in tight sandstones: A case study in the ordos basin, China. *Energy Geosci.* 1 (3-4), 115–123. doi:10.1016/j.engeos.2020.06.003

Fan, T. L., Yu, B. S., and Gao, Z. Q. (2007). Characteristics of carbonate sequence stratigraphy and its control on oil-gas in Tarim Basin. *Geosci.* 21, 57–65. doi:10.3969/j.issn.1000-8527.2007.01.006

Fan, C. H., Li, H., Qin, Q. R., He, S., and Zhong, C. (2020). Geological conditions and exploration potential of shale gas reservoir in Wufeng and Longmaxi Formation of southeastern Sichuan Basin, China. *J. Petrol. Sci. Eng.* 191, 107138. doi:10.1016/j.petrol.2020.107138

Feng, Z. Z., Bao, Z. D., Wu, B. M., Jin, Z. K., and Shi, X. Z. (2006). Lithofacies palaeogeography of the cambrian in Tarim area. *J. Palaeog.* 8, 427–439. doi:10.3969/j.issn.1671-1505.2006.04.001

Feng, Z. Z., Bao, Z. D., Wu, B. M., Jin, Z. K., Shi, X. Z., and Luo, A. R. (2007). Lithofacies palaeogeography of the ordovician in Tarim area. *J. Palaeog.* 9, 447–460. doi:10.7605/gdlxb.2007.05.001

Gao, Z. N., and Hu, H. Z. (2002). High pressure to the impact on the evolution of texture and compositon of natural bitumen. *Acta Sedimentol. Sin.* 20, 499–503. doi:10.14027/j.cnki.cjxb.2002.03.023

Gao, F. Q. (2019). Use of numerical modeling for analyzing rock mechanic problems in underground coal mine practices. *J. Min. Strata Control Eng.* 1 (1), 013004. doi:10.13532/j.jmsce.cn10-1638/td.2019.02.009

Guan, S. W., Zhang, C. Y., Ren, R., Zhang, S. C., Wu, L., Wang, L., et al. (2019). Early Cambrian syndepositional structure of the northern Tarim Basin and a discussion of Cambrian subsalt and deep exploration. *Petr. Explor. Dev.* 46, 1141–1152. doi:10.1016/s1876-3804(19)60269-7

Han, C. W., Ma, P. L., Zhu, D. X., Du, D. W., Xiao, J., and Liu, X. M. (2009). The tectonic characteristics and its evolution in the eastern Tarim Basin. *Xinjiang. Geotect. Metall.* 33, 131–135. doi:10.16539/j.ddgzyckx.2009.01.001

He, D. F., Jia, C. Z., Li, D. S., Zhang, C. J., Meng, Q. R., and Shi, X. (2005). Formation and evolution of polycyclic superimposed Tarim Basin. *Oil Gas. Geol.* 26, 64–77. doi:10.3321/j.issn:0253-9985.2005.01.010

Hong, D., Cao, J., Wu, T., Dang, S., Hu, W., and Yao, S. (2020). Authigenic clay minerals and calcite dissolution influence reservoir quality in tight sandstones: Insights from the central Junggar Basin, NW China. *Energy Geosci.* 1 (1-2), 8–19. doi:10.1016/j.engeos.2020.03.001

Hu, A. P., Shen, A. J., Liang, F., Zhao, J. X., Luo, X. Y., Feng, Y. X., et al. (2020). Application of laser *in-situ* U-Pb dating to reconstruct the reservoir porosity evolution in the Cambrian Xiaoerbulake Formation, Tarim Basin. *Oil Gas. Geol.* 41, 37–49. doi:10.11743/ogg20200104

Huang, S. J., and Hou, Z. J. (2001). Spatio-temporal variation of subsurface porosity and permeability and its influential factors. *Acta Sedimentol. Sin.* 19, 224–232. doi:10.14027/j.cnki.cjxb.2001.02.010

Huang, S. W., Zhang, Y., Zheng, X. P., Zhu, Q. F., Shao, G. M., Cao, Y. Q., et al. (2013). Types and characteristics of carbonate reservoirs and their implication on hydrocarbon exploration: A case study from the eastern Tarim Basin, NW China. *J. Nat. Gas Geoscience* 2, 73–79. doi:10.1016/j.jnggs.2017.02.001

Hwang, R. S., Teerman, S., and Carlson, R. (1998). Geochemical comparison of reservoir solid bitumens with diverse origins. *Org. Geochem.* 29, 505–517. doi:10.1016/S0146-6380(98)00078-3

Jacob, H. (1989). Classification, structure, Genesis and practical importance of natural solid oil bitumen ("migrabitumen"). *Int. J. Coal Geol.* 11, 65–79. doi:10.1016/0166-5162(89)90113-4

Jia, C. Z., and Pang, X. Q. (2013). Research processes and main development directions of deep hydrocarbon geological theories. *Acta Pet. Sin.* 36, 1457–1469. doi:10.7623/syxb201512001

Jiao, C. L., He, Z. L., Xing, X. J., Qin, H. R., He, B. Z., and Li, C. C. (2011). Tectonic hydrothermal dolomite and its significance of reservoirs in Tarim Basin. *Acta Petrol. Sin.* 27, 277–284. doi:10.1000-0569/2011/027(01)-0277-84

Jin, Z. J., Zhu, D. Y., and Hu, W. X. (2006). Geological and geochemical signatures of hydrothermal activity and their influence on carbonate reservoir beds in the Tarim Basin. *Acta Geol. Sin.* 80, 245–253. doi:10.3321/j.issn:0001-5717.2006.02.009

Li, H., Tang, H. M., Qin, Q. R., Zhou, J. L., Qin, Z. J., Fan, C. H., et al. (2019). Characteristics, formation periods and genetic mechanisms of tectonic fractures in the tight gas sandstones reservoir: A case study of xujiahe Formation in YB area, sichuan basin, China. *J. Petroleum Sci. Eng.* 178, 723–735. doi:10.1016/j.petrol.2019.04.007

Li, Y., Zhou, D., Wang, W., Jiang, T., and Xue, Z. (2020). Development of unconventional gas and technologies adopted in China. *Energy Geosci.* 1 (1-2), 55–68. doi:10.1016/j.engeos.2020.04.004

Li, H., Wang, Q., Qin, Q. R., and Ge, X. Y. (2021a). Characteristics of natural fractures in an ultradeep marine carbonate gas reservoir and their impact on the reservoir: A case study of the maokou Formation of the JLS structure in the sichuan basin, China. *Energy & Fuels* 35 (16), 13098–13108. doi:10.1021/acs.energyfuels.1c01581

Li, H., Peng, R., Du, W. S., Li, X. P., and Zhang, N. B. (2021b). Experimental study on structural sensitivity and intervention mechanism of mechanical behavior of coal samples. *J. Min. Strata Control Eng.* 3 (4), 043012. doi:10.13532/j.jmsce.cn10-1638/td.20210820.001

Li, H., Zhou, J. L., Mou, X. Y., Guo, H. X., Wang, X. X., An, H. Y., et al. (2022). Pore structure and fractal characteristics of the marine shale of the longmaxi Formation in the changning area, southern sichuan basin, China. *Front. Earth Sci.* 10, 1018274. doi:10.3389/feart.2022.1018274

Li, J., Li, H., Yang, C., Wu, Y. J., Gao, Z., and Jiang, S. L. (2022). Geological characteristics and controlling factors of deep shale gas enrichment of the Wufeng-Longmaxi Formation in the southern Sichuan Basin, China. *Lithosphere* 2022, 4737801. doi:10.2113/2022/4737801

Li, K. K., Cai, C. F., He, H., Jiang, L., Cai, L. L., Xiang, L., et al. (2010). Origin of palaeo-waters in the Ordovician carbonates in Tahe oilfield, Tarim Basin: Constraints from fluid inclusions and Sr, C and O isotopes. *Geofl.* 11, 71–86. doi:10.1111/j.1468-8123.2010.00312.x

Li, Q., Parrish, R. R., Horstwood, M. S. A., and McArthur, J. M. (2014). U-Pb dating of cements in Mesozoic ammonites. *Chem. Geol.* 376, 76–83. doi:10.1016/j.chemgeo.2014.03.020

Li, Y. L., Wang, X. D., Sun, X. D., Tian, X. B., Jin, Z. L., and Yan, B. (2014). Structural evolution and favorable exploration direction for Gucheng low uplift. *Pet. Geol. Oilf. Dev. Daqing.* 33, 97–102. doi:10.3960/J.ISSN.1000-3754.2014.05.016

Li, Z., Huang, S. J., Liu, J. Q., Cai, C. F., Li, Y. J., Li, K. K., et al. (2010). Buried diagenesis, structurally controlled thermal fluid process and their effect on ordovician carbonate reservoirs in tahe, Tarim Basin. *Acta Sedimentol. Sin.* 28, 969–979. doi:10.14027/j.cnki.cjxb.2010.05.02

Li, H. (2022). Research progress on evaluation methods and factors influencing shale brittleness: A review. *Energy Rep.* 8, 4344–4358. doi:10.1016/j.egyr.2022.03.120

Lin, C. S., Yang, H. J., Cai, Z. Z., Yu, B. S., Chen, J. Q., Li, H., et al. (2013). Evolution of depositional architecture of the ordovician carbonate platform in the Tarim Basin and its response to basin processes. *Acta Sedimentol. Sin.* 31, 907–919. doi:10.14027/j.cnki.cjxb.2013.05.017

Liu, C. X., Li, T. G., and Liu, C. X. (2010). Deep fluid activity in Central Tarim Basin and its heating effects on hydrocarbon generation and accumulation. *J. Jilin Univ. Earth Sci. Ed.* 40, 279–285. doi:10.13278/j.cnki.jjuese.2010.02.019

Liu, W., Zhang, G. Y., Pan, W. Q., Deng, S. H., and Li, H. H. (2011). Lithofacies palaeogeography and sedimentary evolution of the Cambrian in Tarim area. *J. Palaeog.* 13, 529–538. doi:10.7605/gdlxb.2011.05.007

Lv, J., Yin, S., Sun, Y. H., Liu, L. J., Li, W. Z., Tao, D. S., et al. (2022). A new method for predicting injection multiples of extreme displacement in waterflood reservoirs. *Energy Geosci.* 4 (3), 465–472. doi:10.1016/j.engeos.2022.01.002

Mahmud, H., Hisham, M., Mahmud, M., Leong, V., and Shafiq, M. (2020). Petrophysical interpretations of subsurface stratigraphic correlations, Baram Delta, Sarawak, Malaysia. *Energy Geosci.* 1 (3-4), 100–114. doi:10.1016/j.engeos.2020.04.005

Norman, M. D., Pearson, N. J., Sharma, A., and Griffin, W. L. (1996). Quantitative analysis of trace elements in geological materials by laser ablation ICPMS: Instrumental operating conditions and calibration values of NIST glasses. *Geost. Newsl.* 20, 247–261. doi:10.1111/j.1751-908X.1996.tb00186.x

Pan, L. Y., Shen, A. J., Shou, J. F., Hu, A. P., and Wei, D. X. (2016). Fluid inclusion and geochemical evidence for the origin of sparry calcite cements in Upper Permian Changxing reefal limestones, eastern Sichuan Basin (SW China). *J. Geochem. Explor.* 171, 124–132. doi:10.1016/j.gexplo.2016.01.006

Pickering, R., Kramers, J. D., Partridge, T., Kodolayi, J., and Pettke, T. (2010). U-Pb dating of calcite–aragonite layers in speleothems from hominin sites in South Africa by MC-ICP-MS. *Quat. Geochronol.* 5, 544–558. doi:10.1016/j.quageo.2009.12.004

Qie, L., Shi, Y. N., and Liu, J. G. (2021). Experimental study on grouting diffusion of gangue solid filling bulk materials. *J. Min. Strata Control Eng.* 3 (2), 023011. doi:10.13532/j.jmsce.cn10-1638/td.20201111.001

Ran, Q. G., Cheng, H. G., Xiao, Z. Y., Ye, X. L., Wu, D. M., and Sang, H. (2008). Tectonic thermal event and its influence on cracking of crude oil in Eastern Tarim Basin. *Geosci.* 22, 541–548. doi:10.3969/j.issn.1000-8527.2008.04.008

Richardson, M., Abraham, A., Fabio, T., and Anthony, I. N. (2022). Physical properties of sandstone reservoirs: Implication for fluid mobility. *Energy Geosci.* 4 (3), 349–359. doi:10.1016/j.engeos.2022.06.001

Roberts, N. M., Rasbury, E. T., Parrish, R. R., Smith, C. J., Horstwood, M. S. A., and Condon, D. J. (2017). A calcite reference material for LA-ICP-MS U-Pb geochronology. *Geochem. Geophy. Geosy.* 18, 2807–2814. doi:10.1002/2016GC006784

Roberts, N. M. W., Drost, K., Horstood, M. S. A., Condon, D. J., Chew, D., Drake, H., et al. (2020). Laser ablation inductively coupled plasma mass spectrometry (LA-ICP-MS) U-Pb carbonate geochronology: Strategies, progress, and limitations. *Geochronol.* 2, 33–61. doi:10.5194/gchron-2-33-2020

Shan, S. C., Wu, Y. Z., Fu, Y. K., and Zhou, P. H. (2021). Shear mechanical properties of anchored rock mass under impact load. *J. Min. Strata Control Eng.* 3 (4), 043034. doi:10.13532/j.jmsce.cn10-1638/td.20211014.001

Shao, H. M., Lu, X., Gao, B., Hong, S. X., Pan, H. F., Xu, Z. Y., et al. (2019). Geochemical analyzing technique of the microzone's normal position and its application: A case study on the diagenetic evolution of the carbonate reservoir in Gucheng area. *Pet. Geo. Oilf. Dev. Daqing.* 38, 160–168. doi:10.19597/J.ISSN.1000-3754.201907005

Shen, A. J., Fu, X. D., Zhang, Y., Zheng, X. O., Liu, W., Shao, G. M., et al. (2018). A study of source rocks & carbonate reservoirs and its implication on exploration plays from Sinian to Lower Paleozoic in the east of Tarim Basin, northwest China. *Nat. Gas. Geosci.* 29, 1–16. doi:10.11764/j.issn.1672-1926.2017.08.019

Shen, A. J., Hu, A. P., Cheng, T., Liang, F., Pan, W. Q., Feng, X. Y., et al. (2019). Laser ablation *in situ* U-Pb dating and its application to diagenesis-porosity evolution of carbonate reservoirs. *Petr. Explor. Dev.* 46, 1127–1140. doi:10.1016/s1876-3804(19)60268-5

Song, J. F., Lu, C. P., Li, Z. W., Ou, Y. G. C., Cao, X. M., and Zhou, F. L. (2021). Characteristics of stress distribution and microseismic activity in rock parting occurrence area. *J. Min. Strata Control Eng.* 3 (4), 043518. doi:10.13532/j.jmsce.cn10-1638/td.20210607.002

Sun, L. D., Zou, C. N., Zhu, R. K., Zhang, Y. H., Zhang, S. C., Zhang, B. M., et al. (2013). Formation, distribution and potential of deep hydrocarbon resources in China. *Pet. Explor. Dev.* 40, 687–695. doi:10.1016/s1876-3804(13)60093-2

Tochukwu, N., Manoj, M., and Suame, A. (2022). Reconnaissance investigation of geothermal resources in parts of the Middle Benue Trough, Nigeria using remote sensing and geophysical methods. *Energy Geosci.* 4 (3), 360–371. doi:10.1016/j.engeos.2022.06.002

Wang, J., and Wang, X. L. (2021). Seepage characteristic and fracture development of protected seam caused by mining protecting strata. *J. Min. Strata Control Eng.* 3 (3), 033511. doi:10.13532/j.jmsce.cn10-1638/td.20201215.001

Wang, T. S., Geng, A. S., Xiong, Y. Q., Liao, Z. W., and Li, X. (2008). Kinetic simulation study on generation of gasous hydrocarbons from the pyrolysis of marine crude oil and its asphaltene in Tarim Basin. *Acta Pet. Sin.* 29, 167–172. doi:10.3321/j.issn:0253-2697.2008.02.002

Wang, G., Fan, T. L., and Liu, H. L. (2014). Characteristics and evolution of ordovician carbonate platform marginal facies in tazhong-gucheng area. *Tarim. Basin. Geosci.* 28, 995–1007. doi:10.3969/j.issn.1000-8527.2014.05.015

Wang, T. G., Song, D. F., Li, M. J., Yang, C. Y., Ni, Z. Y., Li, H. L., et al. (2014). Natural gas source and deep gas exploration potential of the Ordovician Yingshan Formation in the Shunnan-Gucheng region, Tarim Basin. *Oil Gas. Geol.* 35, 753–762. doi:10.11743/ogg20140602

Woodhead, J., and Pickering, R. (2012). Beyond 500 ka: Progress and prospects in the U-Pb chronology of speleothems. *Quat. Int.* 540, 540. doi:10.1016/j.quaint.2012.08.1895

Woodhead, J., Hellstrom, J., Maas, R., Drysdale, R., Zanchetta, G., Devine, P., et al. (2006). U-Pb geochronology of speleothems by MC-ICPMS. *Quat. Geochronol.* 1, 208–221. doi:10.1016/j.quageo.2006.08.002

Yang, H. J., Chen, Y. Q., Tian, J., Du, J. H., Zhu, Y. F., Li, H. H., et al. (2020). Great discovery and its significance of ultra-deep oil and gas exploration in well Luntan-1 of the Tarim Basin. *China Pet. Explor.* 25, 62–72. doi:10.3969/j.issn.1672-7703.2020.02.007

Yuan, H., Yin, S., Dong, L., and Tan, C. Q. (2022). Restoration of the pre-Jurassic paleogeomorphology and its control on hydrocarbon distribution in Western Ordos Basin. *Energy Geosci.* 4 (3), 485–494. doi:10.1016/j.engeos.2021.06.007

Zhang, Y. Q., Jia, J. D., Jin, J. Q., and Liu, Q. Y. (2007). Characteristics of cambrian-ordovician sedimentary facies in Tadong region and its sedimentary model. *Nat. Gas. Geosci.* 18, 229–234. doi:10.3969/j.issn.1672-1926.2007.02.014

Zhang, S. C., Zhang, B. M., Li, B. L., Zhu, G. Y., Su, J., and Wang, X. M. (2011a). History of hydrocarbon accumulations spanning important tectonic phases in marine sedimentary basins of China: Taking the Tarim Basin as an example. *Pet. Explor. Dev.* 38, 1–15. doi:10.1016/s1876-3804(11)60010-4

Zhang, S. C., Zhu, G. Y., Yang, H. J., Su, J., Yang, D. B., Zhu, Y. F., et al. (2011b). The phases of Ordovician hydrocarbon and their origin in the Tabei uplift, Tarim Basin. *Acta Petrol. Sin.* 27, 2447–2460.

Zhang, W., Guan, P., and Jian, X. (2014). Effects of Permian volcanic-magmatic activity on the Paleozoic oil and gas generating and storing conditions in the Tarim Basin. *Acta Sedimentol. Sin.* 32, 148–158. doi:10.14027/j.cnki.cjxb.2014.01.017

Zhang, G. Y., Liu, W., Zhang, L., Yu, B. S., Li, H. H., Zhang, B. M., et al. (2015). Cambrian-Ordovician prototypic basin, paleogeography and petroleum of Tarim Craton. *Earth Sci. Front.* 22, 269–276. doi:10.13745/j.esf.2015.03.023

Zhang, J. L., Feng, Z. H., Li, Q., and Zhang, B. (2018). Evolution of Cambrian mound-beach gas reservoirs in Gucheng platform margin zone. *Tarim. Basin. Pet. Geol. Exper.* 40, 655–661. doi:10.11781/sysydz201805655

Zhang, Y., Li, Q., Zheng, X. P., Li, Y. L., Shen, A. J., Zhu, M., et al. (2021). Cambrian-Ordovician platform type, evolution process and exploration potential in the Gucheng-Xiaotang area of eastern Tarim Basin. *Acta Pet. Sin.* 42, 447–465. doi:10.7623/syxb202104003

Zhao, M. J., Zhang, S. C., and Liao, Z. Q. (2001). The cracking gas from crude oil and its significance in gas exploration. *Petr. Explor. Dev.* 28, 47–56. doi:10.3321/j.issn:1000-0747.2001.04.014

Zhao, Z. J., Jia, C. Z., Zhou, X. Y., and Wang, Z. M. (2006). Key factors of oil-gas reservoir-forming and exploration targets in Ordovician in Tazhong area. *TarimBasin. China Pet. Explor.* 11, 6–16. doi:10.3969/j.issn.1672-7703.2006.04.002

Zhao, M. J., Zhang, S. C., Zhao, L., Liu, P. C., and Da, J. (2007). Geochemistry characteristics and Genesis of the paleoreservoir bitumen and natural gas in Nanpanjiang Basin. *Sci. China Ser. D. Earth Sci.* 37, 167–177. doi:10.3321/j.issn:1006-9267.2007.02.004

Zhao, Z. J., Zhang, Y. B., Pan, M., Wu, X. N., and Pan, W. Q. (2010). Cambrian sequence stratigraphic framework in Tarim Basin. *Geol. Rev.* 56, 609–620. doi:10.16509/j.georeview.2010.05.001

Zhao, W. Z., Shen, A. J., Hu, S. Y., Zhang, B. M., Pan, W. Q., Zhou, J. G., et al. (2012). Geological conditions and distributional features of large-scale carbonate reservoirs onshore China. *Petr. Explor. Dev.* 39, 1–14. doi:10.1016/s1876-3804(12)60010-x

Zhao, Z. J. (2015). Indicators of global sea-level change and research methods of marine tectonic sequences: Take ordovician of Tarim Basin as an example. *Acta Pet. Sin.* 36, 262–273. doi:10.7623/syxb201503002

Zheng, X. P., Zhang, Y., Chen, X. G., Yang, Z., Shao, G. M., and Bai, X. (2016). Natural gas exploration domains and analysis of carbonate reservoir characteristics in the east of Tarim Basin, NW China. *Nat. Gas. Geosci.* 27, 765–771. doi:10.11764/j.issn.1672-1926.2016.05.0765

Zhu, D. Y., Meng, Q. Q., Hu, W. X., and Jin, Z. Z. (2013). Differences between fluid activities in the central and north Tarim Basin. *Geochem.* 42, 82–94. doi:10.19700/j.0379-1726.2013.01.008

Zhu, G. Y., Chen, F. R., Chen, Z. Y., Zhang, Y., Xing, X., Tao, X. W., et al. (2016). Discovery and basic characteristics of the high-quality source rocks of the cambrian Yuertusi Formation in Tarim Basin. *Nat. Gas. Geosci.* 27, 8–21. doi:10.11764/j.issn.1672-1926.2016.01.0008

frontiers | Frontiers in Earth Science

TYPE Original Research
PUBLISHED 01 February 2023
DOI 10.3389/feart.2023.1101242

OPEN ACCESS

EDITED BY
Wenlong Ding,
China University of Geosciences, China

REVIEWED BY
Shuncun Zhang,
Northwest Institute of Eco-Environment and Resources (CAS), China
Jianguo Yan,
Chengdu University of Technology, China

*CORRESPONDENCE
Shimin Liu,
1409064189@qq.com

SPECIALTY SECTION
This article was submitted to Economic Geology, a section of the journal Frontiers in Earth Science

RECEIVED 17 November 2022
ACCEPTED 19 January 2023
PUBLISHED 01 February 2023

CITATION
Liu S, Zhou L, Guan X, Chen X, Wu Y, Tan L, Qiu Z, Qian Y and Zhou J (2023), Research on distribution characteristics of sedimentary microfacies of a system tract under a high resolution sequence framework: A case study of Qixia Formation in Gaomo block, central Sichuan.
Front. Earth Sci. 11:1101242.
doi: 10.3389/feart.2023.1101242

Research on distribution characteristics of sedimentary microfacies of a system tract under a high resolution sequence framework: A case study of Qixia Formation in Gaomo block, central Sichuan

Shimin Liu[1]*, Lu Zhou[1,2], Xu Guan[3], Xiao Chen[3], Yong Wu[1], Lufan Tan[4], Zehua Qiu[1], Yujie Qian[1] and Jianghui Zhou[1]

[1]Southwest Petroleum University a. School of Geoscience and Technology; b Sichuan Province Key Laboratory of Natural Gas Geology, Southwest Petroleum University, Chengdu, Sichuan, China, [2]State Key Laboratory of Oil and Gas Reservoir Geology and Exploration, Southwest Petroleum University, Chengdu, China, [3]Research Institute of Exploration and Development, Petro China Southwest Oil and Gas Field Company, Chengdu, China, [4]BGP Southwest Geophysical Company, Chengdu, China

In conventional sequence stratigraphy research, owing to the limitation of the resolution of seismic data, strata can only be divided into third order sequences at most on the seismic profile. In this study, the vertical fourth order sequence is divided using the high vertical resolutions of gamma ray (GR), uranium (U), thorium (Th), and potassium (K) curves in the logging curves, and the sequence divided in the depth system is then accurately superimposed on the seismic profile through one dimensional forward modelling. Subsequently, through three dimensional Fourier transform technology, the dip angle and azimuth information of the seismic data in the entire region are scanned to obtain the horizons. Through the progradation and retrogradation characteristics of sediments in the Wheeler system, guided by the sequence framework, the horizontal interpretation of the fourth order sequence system tract is conducted in the entire region. Finally, through attribute optimisation, the root mean square amplitude attribute, with the highest degree of coincidence with well data, is selected to study the evolution characteristics of sedimentary microfacies in different periods in the four system tracts. Notably, the strata of Qixia Formation in the study area can be divided into two-fourth order sequences, wherein SQ1 comprised transgressive systems tract 1 (TST1) and high stand systems tract 1 (HST1), and SQ2 comprised TST2 and HST2. With the change in the relative sea level cycle, the strata of Qixia Formation in the study area are developed by overlapping the sedimentary microfacies of the interbank depression, interbank sea, and intraplatform shoal from bottom to top.

KEYWORDS

sichuan basin, qixia formation, fourth order sequence, system, sedimentary microfacies, tainei beach

1 Introduction

In recent years, many studies have been conducted on the sedimentary facies and reservoir prediction of Qixia Formation in the Sichuan Basin. For example, DAI Danshen suggested that the gas producing beds of the Permian system were concentrated in areas with dense fractures. With in-depth study, gas reservoirs with huge geological reserves were also found in the dolomite reservoirs of the shoal area. Since then, the study on the sedimentation and sequence of the Sichuan Basin has begun. For example, FengZengzhao stated that the Sichuan Basin, as a whole, belongs to the carbonate platform facies (Feng et al., 1996). On this basis, Huangxianping et al. further identified the marginal shoals, and considered that the marginal shoals were closely distributed in an arc along the basin margin from West Sichuan to South Sichuan (Huang et al., 2004). On this basis, Chenzongqing further identified the inner shoal and the gentle slope of the inner platform in the basin (Chen, 2007). Thus far, the beach facies gas reservoir of Qixia Formation in the Sichuan Basin has been well established, which is mainly located in the platform margin beach and intraplatform shoal facies zone.

However, most of the previous studies described the overall phenomenon and did not conduct a detailed investigation of sedimentary microfacies in local specific areas under the high-precision sequence framework (Huang, et al., 2014; Jiang et al., 2014; Dai et al., 2017; Xiao et al., 2020; Li et al., 2021; Zhang, et al., 2022c). Among the controlling factors of the gas bearing reservoir of Qixia Formation, beach facies sedimentation is the material basis for reservoir development, the carrier of primary pores and soluble minerals, and will affect all diagenetic transformation after sedimentation (Hu et al., 2018). Therefore, the detailed description of sedimentary microfacies in the study area is of great significance for oil and gas reservoir prediction, exploration, and development.

Based on previous studies (Jorgson, 1981; Sheu and Burke, 1982; Sheu, 1990; Mei et al., 2007; Elisa et al., 2011; Zhang, et al., 2014; Zhang, et al., 2019) and the newly obtained drilling cores and logging and seismic data, combined with new mining achievements in the Permian strata in recent years, we conduct a detailed sequence and sedimentary analysis of the Gaomo block in the middle of Sichuan Basin. We aim to reveal the relationship between the distribution of sedimentary facies and relative sea level change cycles of Qixia Formation in the study area, and study the distribution law of beach facies in Qixia Formation.

2 Geological setting

2.1 Geological background of the study area

The lower Permian in the Sichuan Basin comprises the Liangshan Formation, whereas the Middle Permian comprises the Qixia and Maokou formations (Li H et al., 2019; Fan et al., 2020; Li, 2022). Before the Permian sedimentation, the late Caledonian structure in the Sichuan Basin mainly comprised vertical uplift, forming a pattern of great uplift and depression. The overall sedimentation is high in the southwest and low in the north and east. In the early Hercynian period, namely, the early Soochow movement, the largescale uplift and palaeouplift of the Sichuan Basin were 'flattened', resulting in "peneplanarisation" (Li R et al., 2019). After these two periods of uplift, denudation, and planation, the Permian sedimentary environment gradually developed with high and low sedimentation in southwest and northeast Sichuan Basin, respectively. In the early Permian, the Sichuan Basin sank completely due to the Yunnan movement, and the ancient land was completely submerged. The large-area transgressive systems tract ensured that the middle and lower Permian covered the upper part of the Carboniferous, Silurian, and Ordovician. In the early stage (Liangshan formation period), the sediments are thin coal bearing terrigenous clastic rock, shale, and aluminous mudstone deposited on the upper part of the weathering crust. Subsequently (during the Qixia Formation), the large-scale transgressive systems tract occurred, mainly developing stable shallow water carbonate basin sediments (Li, 2018), namely, the marine carbonate platform. Finally, the platform margin beach high zone and the high band in the platform shown in Figure 1A are formed in the high sedimentary parts of the basin (western and eastern Sichuan).

2.2 Lithological characteristics

The Qixia Formation in the study area is generally characterised by marine carbonate basin sedimentation (Wu et al., 2010). The lithology mainly comprises limestone and dolomite. The dolomite layer is thin and shows superimposed distribution. It is composed of P_1q^1b, P_1q^1a and P_1q^2 members from bottom to top. The sequence boundary marks are the physical manifestation of the rise and fall of relative sea level during sedimentation (Wu et al., 2013). The lithology and lithofacies transition surface indicate the absence and mutation of lithology and lithofacies in the vertical sequence, and obvious abrupt signs of the lithology and sedimentary environment are observed above and below the boundary (Wen et al., 2020). As the lithology and lithofacies near the top and bottom of Qixia Formation are obviously different from those of the overlying Maokou Formation and the underlying Liangshan Formation (as shown in Figure 2), the top and bottom interfaces of Qixia Formation are considered to be the lithology and lithofacies conversion surfaces. Additionally, the bottom of Qixia Formation acts as an unconformity interface, eroding the strata of Liangshan and Meitan formations in some areas; thus, the top and bottom interfaces of Qixia Formation are considered as sequence boundaries.

Figure 2 shows the statistical lithologic distribution map at the top and bottom interfaces of Qixia Formation according to the logging data (Zhang, et al., 2022a; Li H et al., 2022). The first transgressive systems tract occurred during the q_1b sub member period. Its lithology mainly comprises argillaceous limestone, siliceous limestone, and dark grey limestone. Chert blocks are also observed in some areas, and this lithology is characteristic of deep-water open platform subfacies. The underlying Liangshan formation and other strata mainly include shale (Li J et al., 2022; Wu et al., 2022), sandstone (Abraham-A et al., 2022; Xia et al., 2022), and other lithology, showing the lithological characteristics of coastal swamp subfacies.

The second member of the Qixia Formation is basically in the late stage of high stand systems tract, and the lithology mainly comprises light grey and greyish brown limestone, belonging to shallow open platform (Zhang et al., 2020). A new transgressive systems tract started during the Maokou Formation, subsequently followed by sea level rise. The lithology mainly comprises dark grey and black grey limestone,

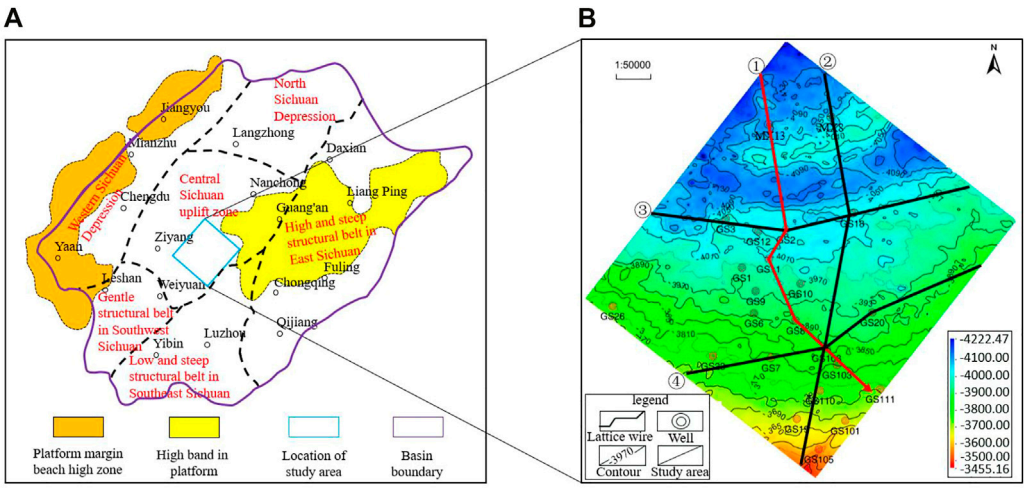

FIGURE 1
Geological background of Qixia Formation and location map of the study area in the **(A)** Sichuan Basin and **(B)** Qixia structure map.

argillaceous limestone, and others, which is characteristic of a deep-water reduction environment. Thus, it belongs to the deep-water open platform subfacies.

3 Materials and methods

3.1 Data

The study area is located in the Moxi Gaoshiti area (Figure 1A). The terrain of the entire area is high in the south and low in the north. It is located in the central Sichuan uplift zone, adjacent to the high band in the platform. The study area is approximately 2844.65 km^2.

3.2 Methods

The three dimensional seismic data volume not only contains the waveform, frequency, amplitude, and other information, but also contains the dip and azimuth information, which is of great significance for studying the sequence geology. Through the three dimensional Fourier transform technology, the seismic data of the target layer in the whole area are scanned, and the dip guide body under different parameters is compared. We then calculated the horizon body, and selected the horizon body that can best reflect the logging sequence interpretation scheme according to its coincidence with the event axis and the previously divided sequence and system tract boundaries; this was followed by the levelling in the Wheeler system. The levelled horizon body is then converted from the traditional time system to the relative geological age. This can satisfactorily show the progradation and retrogradation characteristics of sediments in the same geological age, and can explain the cyclic changes in the relative sea level.

In this study, firstly, by establishing the sequence stratigraphic framework, four well connection frame lines covering the whole area are established through the existing well locations in the study area. Through the calculation of the steering cube, horizon cube, and Wheeler system conversion, and combined with the well logging sequence division scheme, the system tracts of well connection frame lines are divided and mutually verified. Subsequently, as a guide, the main survey lines and liaison lines are interpreted to realise the fourth order sequence division on the seismic profile. Thereafter, we studied the evolution of sedimentary microfacies in each system tract.

3.2.1 Establishment of the sequence stratigraphic framework

3.2.1.1 Single well division sequence boundary

Owing to its high vertical resolution (Liu et al., 2020), the logging curve can sensitively reflect the stratification and cyclicity of the strata (Serra, 1984; Li, J et al., 2022; Zhang, et al., 2022b), and plays an important role in sequence division. According to previous research, the maximum flooding surface is characterised by high gamma ray (GR) values (Ji et al., 2012), namely, high GR values in transgressive systems tract and low GR values in high stand systems tract. As the GR logging curve can approximately reflect the vertical change of shale content, the higher the shale content, the stronger the is radioactivity, and the higher is the GR value. During the transgressive systems tract, owing to the deepening of the water body, the hydrodynamic force became weaker, which was more conducive to the formation of argillaceous sediments. During the high stand systems tract, the sea level dropped, the hydrodynamic force was strengthened, and the shallow and warm environment was more conducive to the deposition of carbonate rocks, and was not conducive to the deposition of mudstone.

Simultaneously, uranium (U), thorium (Th), and potassium (K) of natural GR spectrometry logging also play an important role in sequence boundary identification and system tract division because of their high sensitivity to formation lithology; namely, they have high K values, low U values, and high Th values at the maximum flooding surface. According to previous research results, a corresponding relationship was observed between the U content

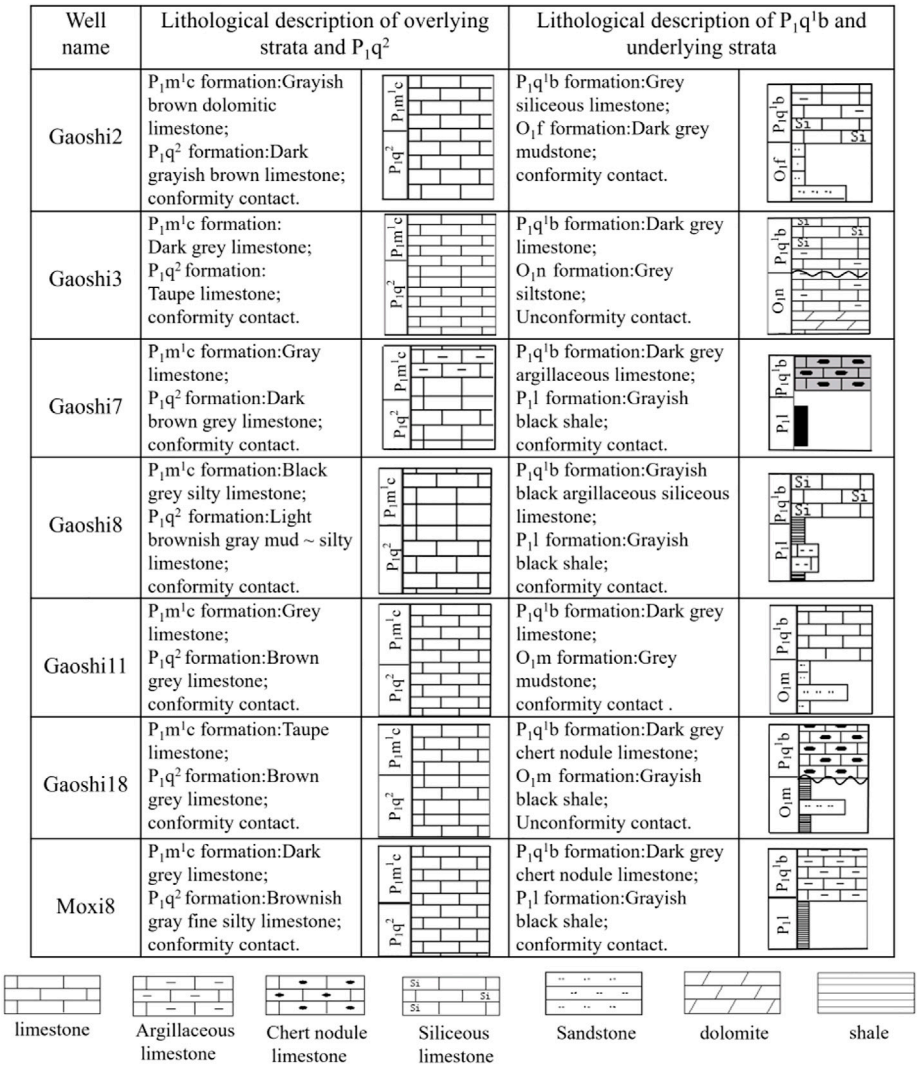

FIGURE 2
Lithological characteristics of underground Qixia Formation and surrounding rock in the study area.

and organic carbon content. The organic carbon content is controlled by the depth of the water body. Generally, U can be used as a characterisation parameter of the palaeo sedimentary environment (Chao et al., 2021). The organic carbon content is denoted by $\delta^{13}C$ because it can effectively indicate the changes in the ancient sea level and is not easily affected by late diagenesis; $\delta^{13}C$ data is commonly used to verify the accuracy of sequence division. Simultaneously, K in sedimentary rocks is mainly positively correlated with the mass fraction of clay and potassium salt. A high K value is observed during the transgressive systems tract, especially at the maximum flooding surface; thus, the K value can be used to reflect the change in the relative sea level.

Th/U and Th/K ratio curves can also reflect the changes in the relative sea level. The Th/U ratio can indicate the oxidation or reduction degree of the palaeoenvironment. High Th/U values indicate the presence of oxidation conditions in the stratum. With the decrease in the relative sea level, the U content decreases, corresponding to a high-level system. Similarly, low Th/U values can reflect the increase in the relative sea level, and the stratum is deposited in a reduction environment, corresponding to the transgressive systems tract. Th/K can also reflect the change of water depth. High Th/K values indicate that this period has experienced weathering, corresponding to the high-level system period, and that the relative sea level decreased. Low Th/K values indicate that this period was dominated by a reducing environment, the base level decreased, and was in a transgressive systems tract period.

According to the afore mentioned carbonate sequence division principles, and combined with the classic sequence stratigraphy theory of Vail (Vail and Mithum, 1979), the strata of Qixia Formation in the study area are divided into two-fourth order sequences (SQ1 and SQ2) by considering the example of the Gaoshi 2 well. This division was mainly based on GR curves, combined with U, Th, and K values, and Th/U and Th/K ratio curves. SQ1 comprises transgressive systems tract 1 (TST1) and high stand systems tract 1 (HST1), and SQ2 comprises transgressive systems tract 2 (TST2) and high stand systems tract 2 (HST2).

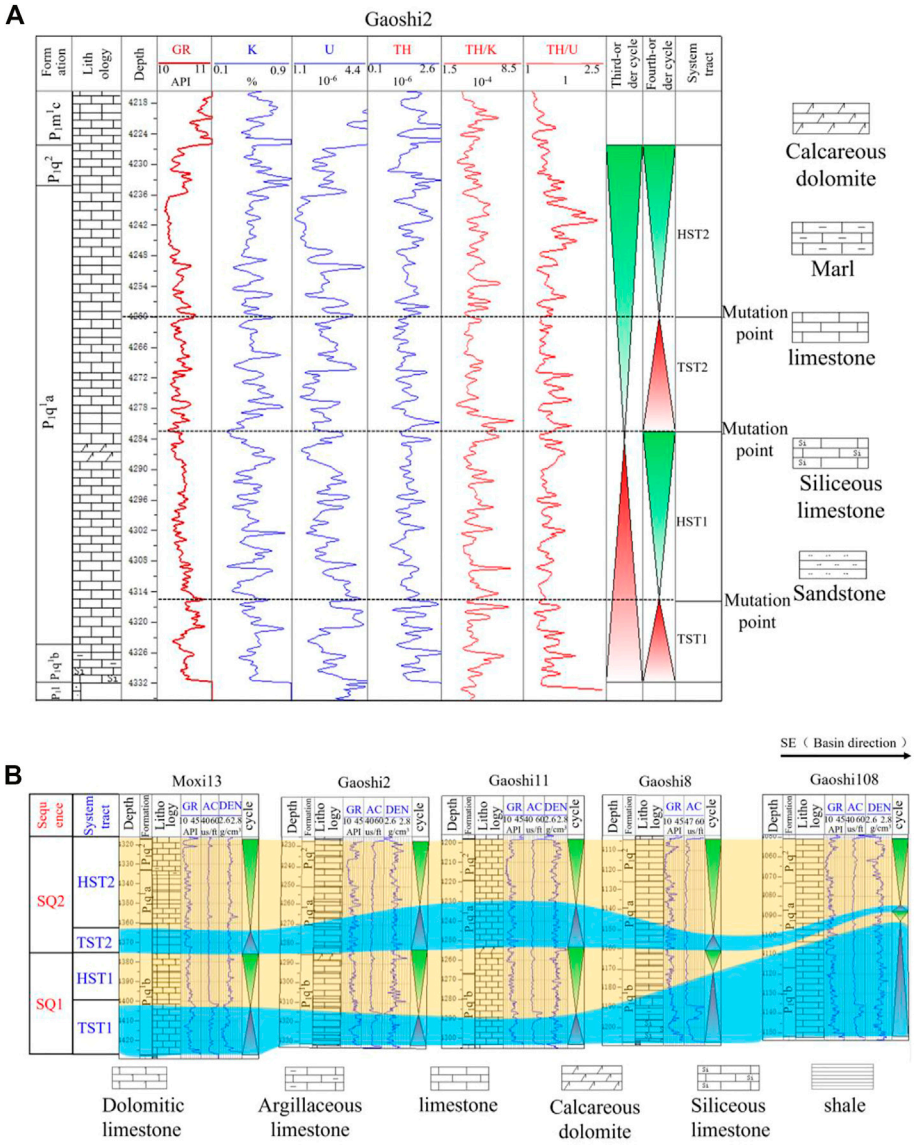

FIGURE 3
(A) Well logging sequence division of well Gaoshi2; **(B)** Correlation diagram of Qixia Formation systems tract of Moxi13-Gaoshi2-Gaoshi11-Gaoshi8-Gaoshi108 (①) well connection profile. See Figure 1B for the plane position of the well connection correlation diagram.

Figure 3A shows that during the TST1 period, the relative sea level rose, the water body deepened, and the shale content increased. The logging curve showed high GR values, increased clay and potassium salt content, high K values, high Th values, and decreased organic carbon and U content. The logging curve showed the characteristics of low U, low Th/U, and low Th/K values, and obvious mutation points were observed on the maximum flooding surface.

During the HST1 period, the relative sea level decreased, the water body became shallower, the content of argillaceous matter decreased, the content of clay and potassium salt decreased, the content of organic carbon and uranium increased, and some areas were even exposed to the water surface. This period showed the characteristics of low GR, low K, low Th, high U, high Th/U, and high Th/K values on the logging curve. Similarly, the characteristics of TST2 and HST2 were similar to those of TST1 and HST1; thus, they have not been described further.

3.2.1.2 Division of the well connection sequence

According to the aforementioned sequence division principles, the 12 wells in the entire area are divided into system tracts. Subsequently, by selecting representative well locations, combined with the understanding of the stratigraphy of the whole region, four well connection frame lines were established in the study area; namely, Gaoshi3-Gaoshi2-Gaoshi18 (③),Gaoshi7-Gaoshi108-Gaoshi 20 (④) well connection lines in the east-west direction, and Moxi13-Gaoshi2-Gaoshi11-Gaoshi8-Gaoshi108 (①) and Moxi 8- Gaoshi18-Gaoshi108- Gaoshi110 (②) well connection lines in the north-south direction. Thus, they can be used to guide the sequence interpretation in the entire region as well as the mutual verification. The Moxi13-Gaoshi2-Gaoshi11-Gaoshi8-Gaoshi108 (①) well connection line is shown below as an example.

As shown in Figure 3B, vertically, all wells generally show the following characteristics: the well section of the high stand systems

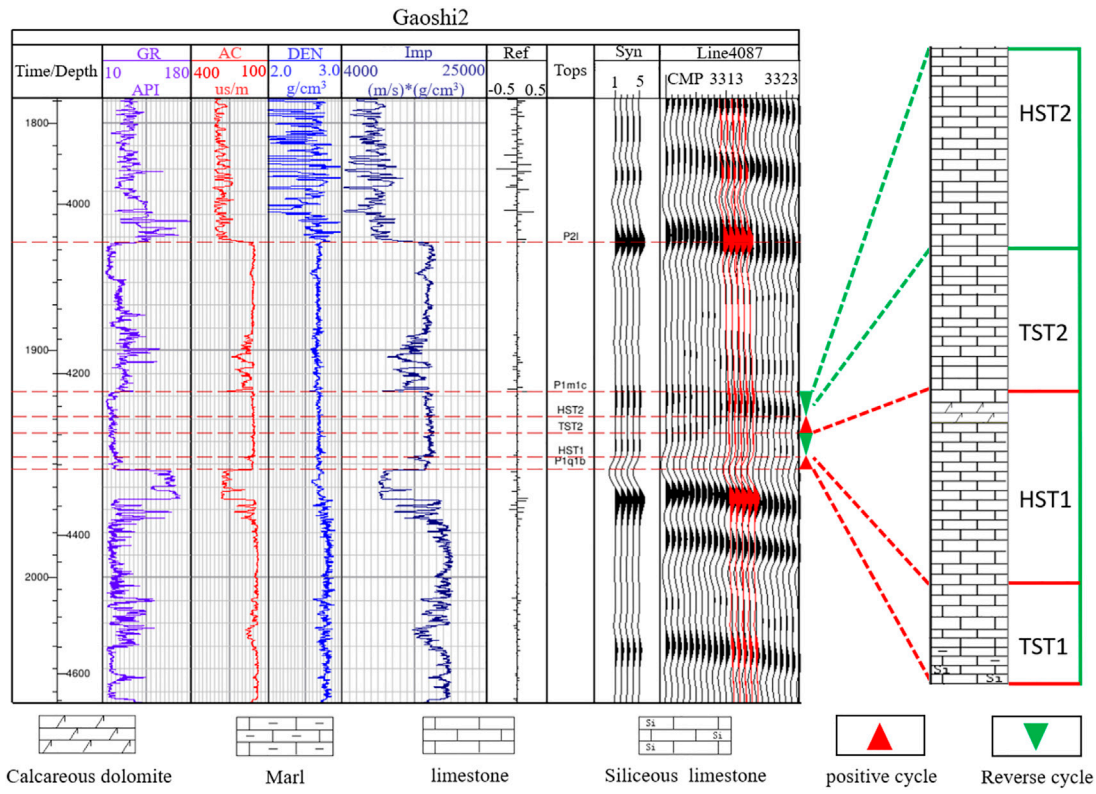

FIGURE 4
Seismic calibration profile of the Gaoshi 2 well of the Qixia Formation.

tract is thicker than that of the low stand system (except for wells Gaoshi 108 and Gaoshi 8 near the seaward side), indicating that the sea level changes experienced twice by the study area are a result of rapid transgressive systems tract and slow regression. The reason for the absence of a low stand system in the Vail classic sequence stratigraphy is that this period is considered to be dominated by a rapid transgressive systems tract (Mei, 2010), and the sea level increased rapidly. The deep water environment hindered the deposition of carbonate rocks in the low stand system and formed sedimentary discontinuities. However, wells Gaoshi 108 and Gaoshi 8 are located near the seaward side, resulting in thick sediments in the TST1 period.

Laterally, during TST1, the sediments in study area were thick in the southeast and thin in the northwest, indicating that the main sedimentary position during TST1 was southeast of the study area, and the lithology mainly comprised dark grey limestone, argillaceous limestone, and siliceous limestone. In HST1, the sedimentary thickness in the northwest is much greater than that in the southeast. In particular, the sedimentary thickness was the largest at well Gaoshi11, namely, the northwest region was the main sedimentary part in HST1, and the lithology mainly comprised dolomitic limestone and light limestone. Similarly, in the TST2 period, the sediments were thick in the northwest and thin in the southeast. The sedimentary parts were more concentrated in the north of the study area, and the lithology was mainly brown limestone and dark grey limestone. During high stand systems tract 2, the sediments were still mainly thick in the northwest and thin in the southeast. The main sedimentary area was in the west. The lithology mainly comprises grey limestone and dolomitic limestone.

3.2.1.3 Well seismic joint calibration

Through the one dimensional forward modelling method, the density and acoustic curves are used to obtain synthetic seismic records. This provided time significance to the depth data of the logging curve (Li, 2017) to study the distribution and waveform characteristics of the divided sequence on the seismic profile, and then conduct the horizontal prediction of the sequence in the whole region.

As shown in Figure 4, considering well Gaoshi 2 as an example, through the comparison between synthetic seismic records and seismic traces near the well, Longtan Formation, as the marker coal seam, is characterized by strong amplitude, low frequency, and strong continuous wave peak reflection, which is continuously reflected in the whole area. The bottom of Maokou Formation (Qixiading) shows moderately strong amplitude wave peak reflection, and a bifurcation phenomenon is observed near the Gaoshi 2 well. The two reflection events with medium amplitudes on the left begin to merge into a medium strong reflection axis with greater amplitude. We considered that this mainly occurs because the Maokou Formation (Qixiading) is the sequence boundary, and the existence of a local unconformity leads to such seismic reflection characteristics. The bottom of Qixia Formation is characterised by low frequency trough reflection. As the bottom boundary of the sequence, it shows continuous reflection characteristics in the whole region.

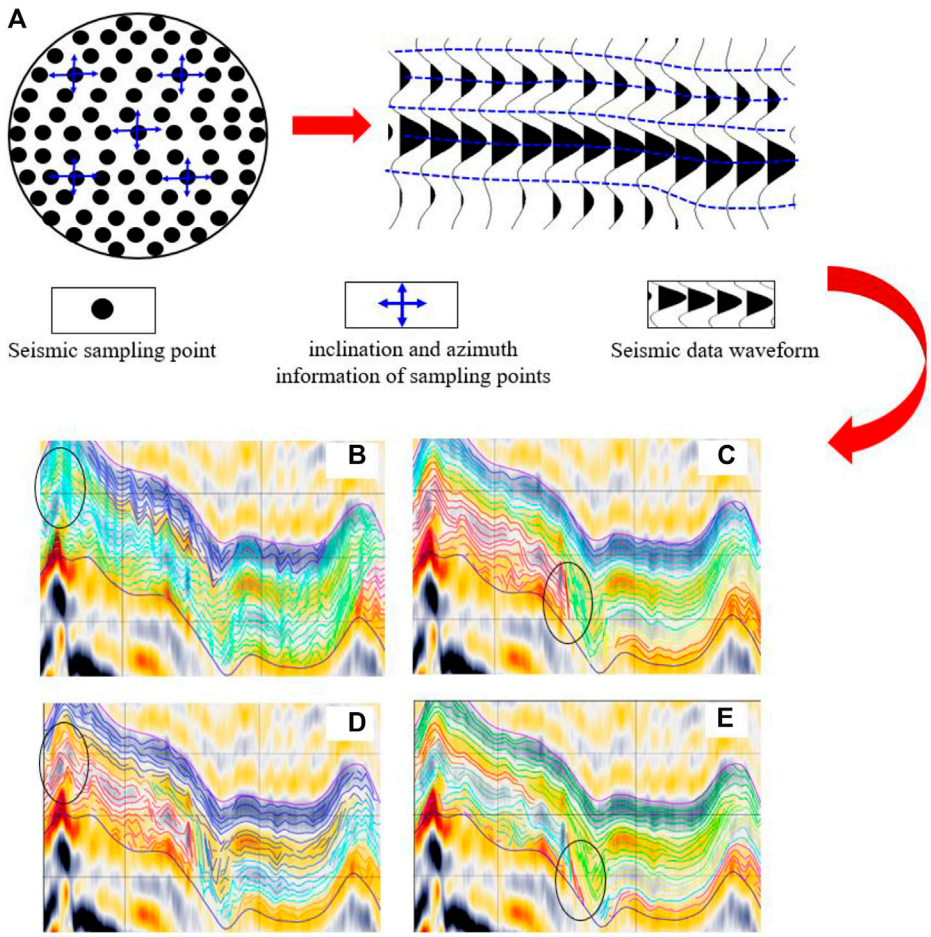

FIGURE 5
(A) Calculation and tracking model of the horizon; and Comparison of lower levels with different parameters; **(B)** FFF111_: the horizon volume calculated by 333 algorithms (the horizon volume passes through the layer); **(C)** PCA111_: the horizon volume calculated by 333 algorithms (the degree of coincidence with the event axis is inadequate); **(D)** PCA111_ 11: horizons calculated by the algorithm (poor continuity of horizons); and **(E)** PCA111_: horizon volume calculated by 662 algorithms (the best coincidence effect).

The thickness of the target layer of Qixia Formation in the whole area is small. In conventional sequence stratigraphy research, owing to the limitation of resolution, the strata can only be divided into third order sequences on the seismic profile. However, with the help of the high vertical resolution of the logging curve, the strata can be divided into fourth order sequences. Although their waveform characteristics are not obvious, the distribution range and overall waveform characteristics of the fourth order sequences can be roughly divided according to the logging curve. As shown in the Figure 4, the reflection amplitudes of TST1 and HST1 are weak, but their continuity is good. The reflection amplitudes of TST2 and HST2 are strong, but their continuity is poor.

3.2.2 The principle of predicting the planar distribution of the system tract

3.2.2.1 Steering cube

Every seismic sampling point contains dip and azimuth information in the direction of the main survey line and connecting survey line. As shown in Figure 5A, the role of the dip angle guider is to scan the information in the line and trace directions of each sampling point in the three dimensional range using the three dimensional Fourier transform technology. This is done to generate a guider containing the dip angle and azimuth angle, automatically track the pre-calculated dip field from the starting position, and integrate the sampling points with similar dip angle information to track the seismic reflection.

3.2.2.2 Horizon cube

According to the previously calculated steering cube, the Qixia Formation interval is calculated with various parameters. The horizon cube of different interpretation schemes (as shown in Figure 5 b、c、d、e) are compared with the coincidence degree between the horizon body and the event axis. We found that the PCA111_662 parameter is the best. Here, PCA is the main component analysis algorithm; FFT represents the fast Fourier algorithm; 111 represents the calculation step size, namely, every other sampling point is scanned in the direction of the line, trace, and time; 662 is the median filtering parameter, namely, every six sampling points are filtered in the direction of the line and trace, and every two sampling points are filtered in the direction of time to ensure the best coincidence effect of the horizon. Thus,

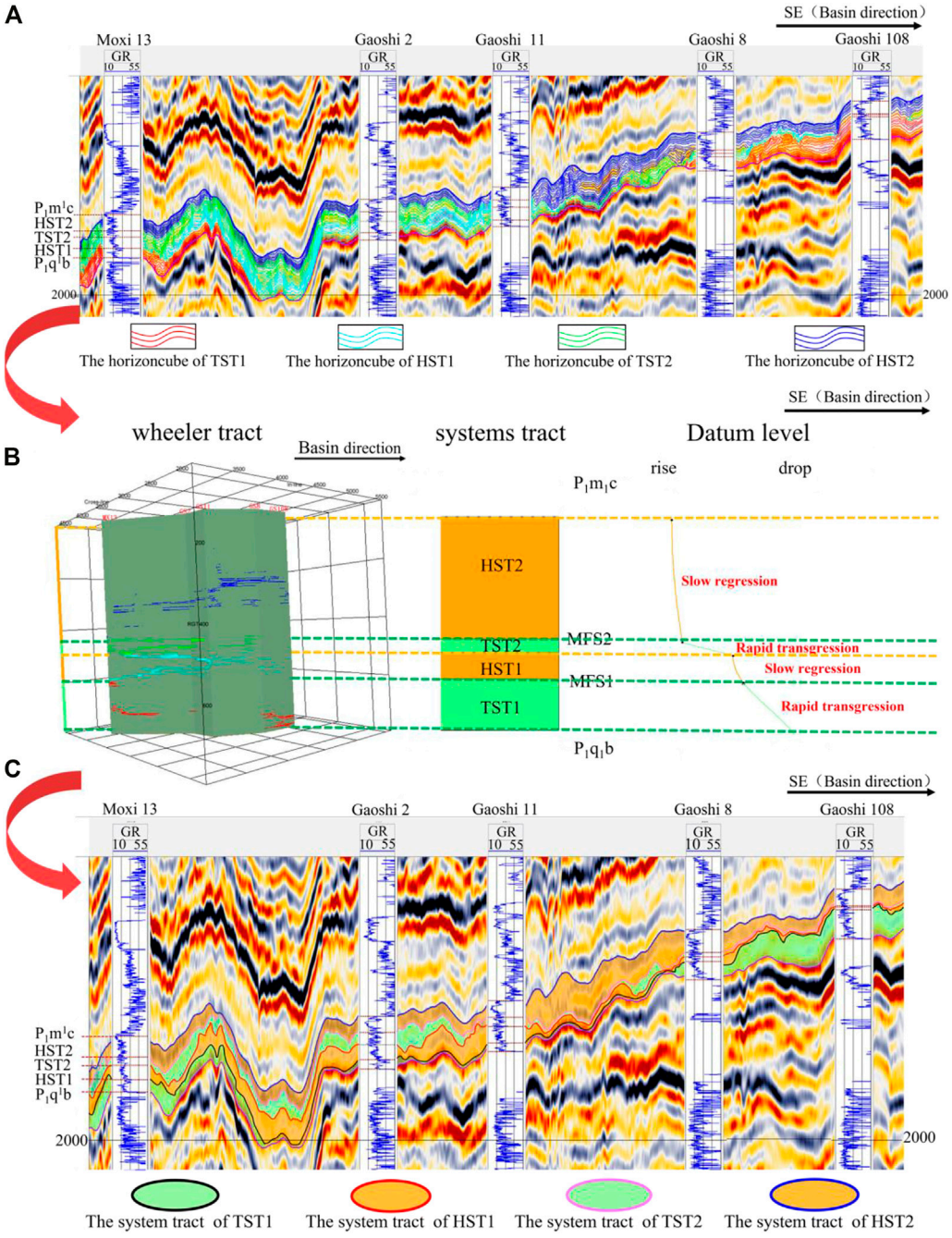

FIGURE 6
(A) Comparison of Moxi13-Gaoshi2-Gaoshi11-Gaoshi8-Gaoshi108 (①) well connection seismic profile of the Qixia Formation horizon. See Figure 1B for the plane position of the profile shown in the figure; **(B)**Diagram explaining the Moxi13-Gaoshi2-Gaoshi11-Gaoshi8-Gaoshi108 (①) well frame system; **(C)** System comparison of the Moxi13-Gaoshi2-Gaoshi11-Gaoshi8-Gaoshi108 (①) well frame seismic profile. See Figure 1B for the plane position of the profile shown in the figure.

PCA111 is finally selected and _662 is used as the calculation parameter of the horizon body.

3.2.3 Establishing the sequence framework of the whole region

Through the calculation of the four well connection frame line horizons covering the whole region, the subsequent Wheeler conversion-interpretation system can be employed. This system can be considered as a guide to conduct the system interpretation of the main survey line and connecting survey line in the whole region. We then calculated the Gaoshi3-Gaoshi2-Gaoshi18 (③),Gaoshi7-Gaoshi108-Gaoshi 20 (④), Moxi13-Gaoshi2-Gaoshi11-Gaoshi8-Gaoshi108 (①), and Moxi 8- Gaoshi18-Gaoshi108- Gaoshi110 (②) well frames, respectively. Subsequently, we considered the Moxi13-Gaoshi2-Gaoshi11-Gaoshi8-Gaoshi108 (①) well frame as an example, As shown in

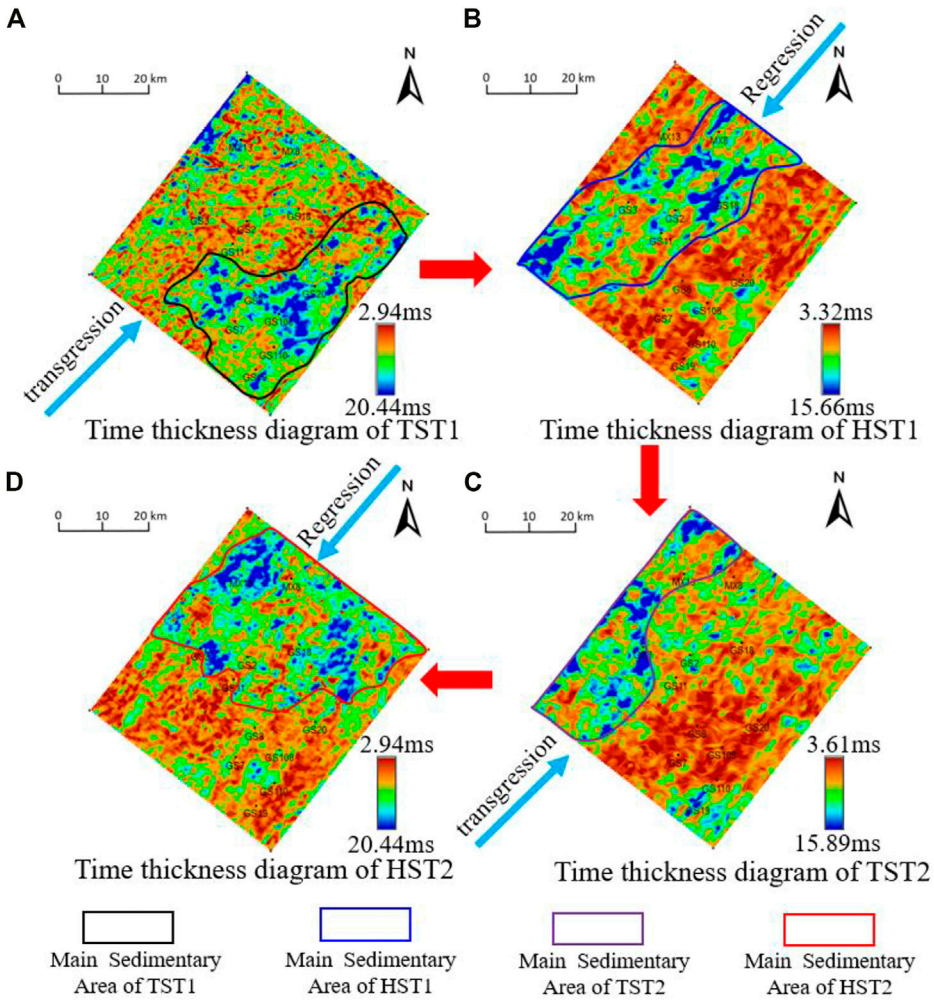

FIGURE 7
Time thickness diagram of each system tract **(A)** Time thickness diagram of TST1; **(B)** Time thickness diagram of HST1; **(C)** Time thickness diagram of TST2; **(D)** Time thickness diagram of HST2.

Figure 6A, and calculated its horizons for subsequent sequence stratigraphic analysis, as shown below.

3.2.4 Frame wheeler tract interpretation

Wheeler domain transformation is conducted for each horizon, and the time series is transformed into a relative geological time series, namely, the Wheeler domain. According to the levelled horizon cube converted by the Wheeler system, the distribution form of sediments can be clearly displayed. With the help of its progradation and retrogradation characteristics, the system interpretation and relative sea level change analysis can be conducted (Yan, 2019).

Obvious progradation and retrogradation features can be found in the Wheeler system layout of the Moxi13-Gaoshi2-Gaoshi11-Gaoshi8-Gaoshi108 (①) well connection line. As shown in Figure 6B, during the TST1 period, the relative sea level rose rapidly, and the sediments were retrograded and migrated from the sea to the shore. During the HST1 period, the relative sea level decreased slowly, and the sediments migrated to the sea, showing the characteristics of progradation at the maximum flooding surface. During the TST2 period, the sea water subsequently rose rapidly, the sediments retrograded to the shore and were mainly deposited in the shore direction, and the transgressive systems tract stopped at the maximum flooding surface. During the HST2 period, the sea level subsequently decreased slowly, and the sediments migrated to the sea.

3.2.5 Well seismic joint correlation interpretation system tract boundary

The interpreted system tracts are projected onto the seismic profile (as shown in Figure 6C), and the boundaries of each system tract are traced according to the interpretation scope of the system tracts, which are TST1, HST1, TST2, and HST2 from bottom to top. According to the logging curve, lithology interpretation data, and other information, combined with author's understanding of the study area, the fourth order sequence division of a single well is conducted for 12 wells in the study area (as shown in Figure 6A), and the sequence framework of connected wells is then established on this basis. Finally, the system tract interpretation results from the seismic profile are used for the joint comparison of the well seismic data with the system tract of logging interpretation. We found that the result of the Wheeler system

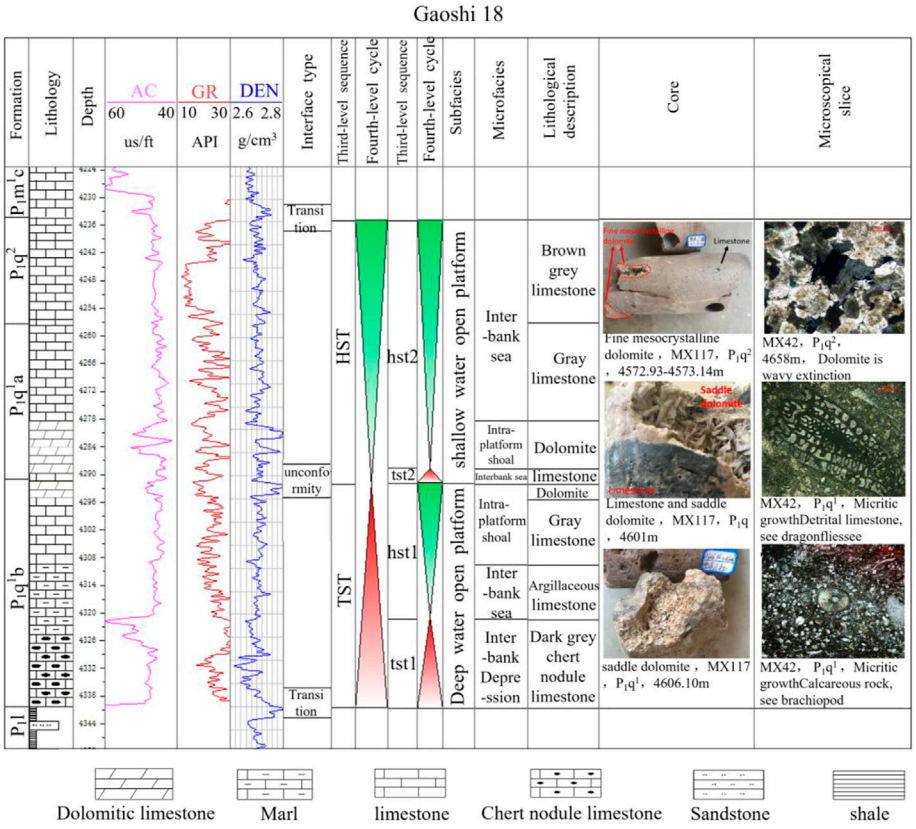

FIGURE 8
Comprehensive histogram of well Gaoshi 18 in Gaomo block of the Qixia Formation, Sichuan Basin.

interpretation (Figure 3B) is basically consistent with that of the logging interpretation (Figure 6C).

3.2.6 Planar distribution characteristics of system tracts

According to the sequence boundary traced by the frame line, the system tracts of the main survey line and the connecting survey line are interpreted for the whole region. Thereafter, the thickness map of the whole region is drawn for the sequence top boundary interpreted by TST1, HST1, TST2, and HST2 to study the main distribution range and palaeogeomorphology of each system tract. In the Figure 7, the cold colour indicates that the system tract is a major sedimentary area with a large sedimentary thickness, and that it was in the low part of the palaeogeomorphology before deposition. In contrast, the warm colour indicates that the sedimentary thickness is small and the pre-sedimentary palaeogeomorphology is high. In the next period of relative sea level change, the intraplatform shoal reservoir could easily be developed in the high part of the palaeogeomorphology.

Owing to the limitation of various factors, when the relative sea level changes, the production rates of carbonate rocks differ in different parts, which also results in different main depositional areas of each system tract. During the TST1 period, seawater influx from the southwest direction occurred to result in the transgressive systems tract. At this stage, the main sedimentary area is southeast of the study area (as shown in Figure 7A); During HST1, the relative sea level began to decline after a short rise, mainly in the middle part of the study area (see Figure 7B). During the TST2 period, when the relative sea level rose, seawater subsequently flowed in from the southwest to result in the transgressive systems tract. At this stage, the main sedimentary area was northwest of the study area (as shown in Figure 7C). During HST2, the relative sea level rose briefly and then fell thereafter. The main sedimentary area is northern of the study area (as shown in Figure 7D).

4 Results and discussion

4.1 Sedimentary facies analysis of a single well

System tracts are the aggregation of a series of contemporaneous sedimentary systems. With the change in the relative sea level, the sedimentary microfacies of different system tracts and even the same system tract are different. Owing to the high vertical resolution of logging data and complete data, the sedimentary microfacies of each well in the study area are divided according to the interpreted lithology and sedimentary environment in combination with logging, drilling, core and other data. This facilitates the subsequent study of the evolution process of sedimentary facies in the same geological age (Li, H et al., 2019).

As the lithology and lithofacies of well Gaoshi 18 change more obviously, the sedimentary microfacies of a single well are divided by considering the example of well Gaoshi 18. As shown in Figure 8, from bottom to top, the sedimentary mode of well Gaoshi 18 is as

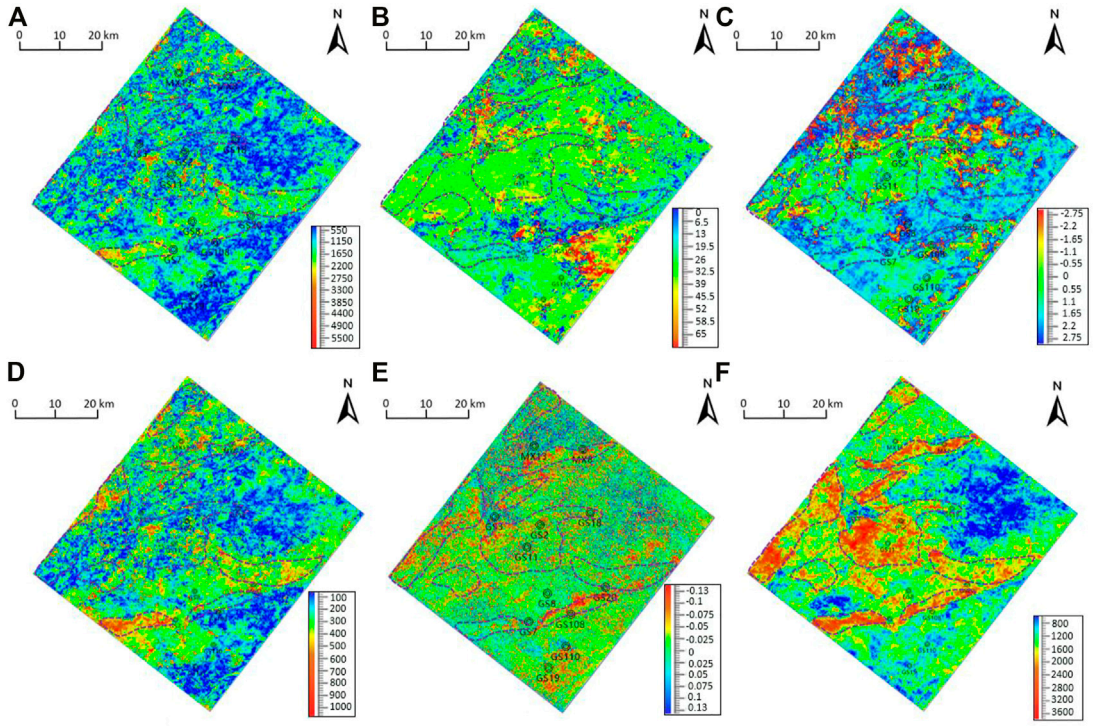

FIGURE 9
Comparison chart of attribute optimisation slices during HST1 in the study area: **(A)** instantaneous amplitude attribute; **(B)** instantaneous frequency attribute; **(C)** instantaneous phase attribute; **(D)** dessert attribute; **(E)** curvature attribute; and **(F)** root mean square amplitude attribute.

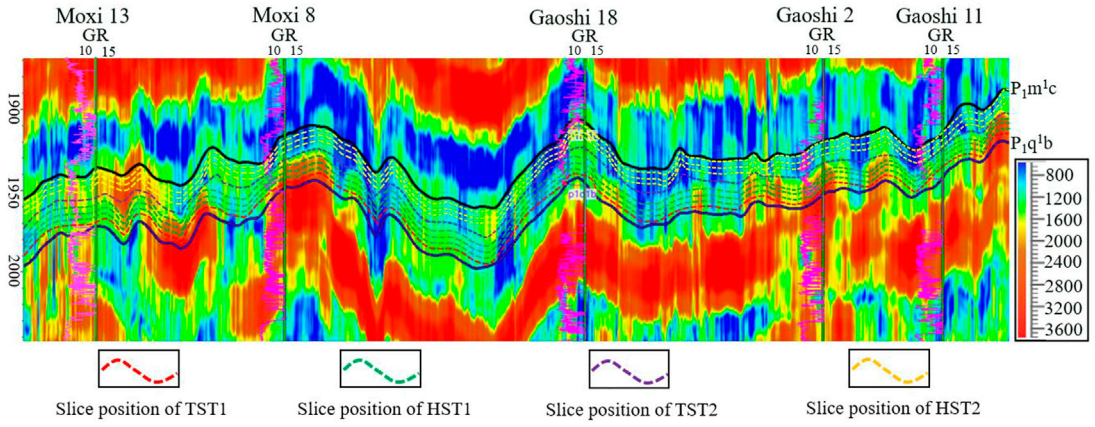

FIGURE 10
Root mean square amplitude attribute profile and slice location.

follows: the sedimentary microfacies of deep-water interbank depression, interbank sea, and intraplatform shoal overlap each other. Among them, the deep-water interbank depression is marked by the discovery of brachiopods and dragonfly mud crystal bioclastic sediments. The lithology mainly comprises dark grey chert nodule limestone. The logging curve shows low density, low acoustic wave time difference, and high GR; thus, it belongs to the poor reservoir facies zone. The dark grey chert nodule limestone indicates that the sedimentary environment was the deep water reduction environment. The relatively high interbank sea mainly comprises argillaceous limestone. At this time, the sea water depth was still deep and the hydrodynamic force was weak. There are more argillaceous sediments when the limestone was produced. With the gradual decrease of the relative sea level and the gradual enhancement of hydrodynamic force, the shallow environment was conducive to the survival of reef building organisms and the

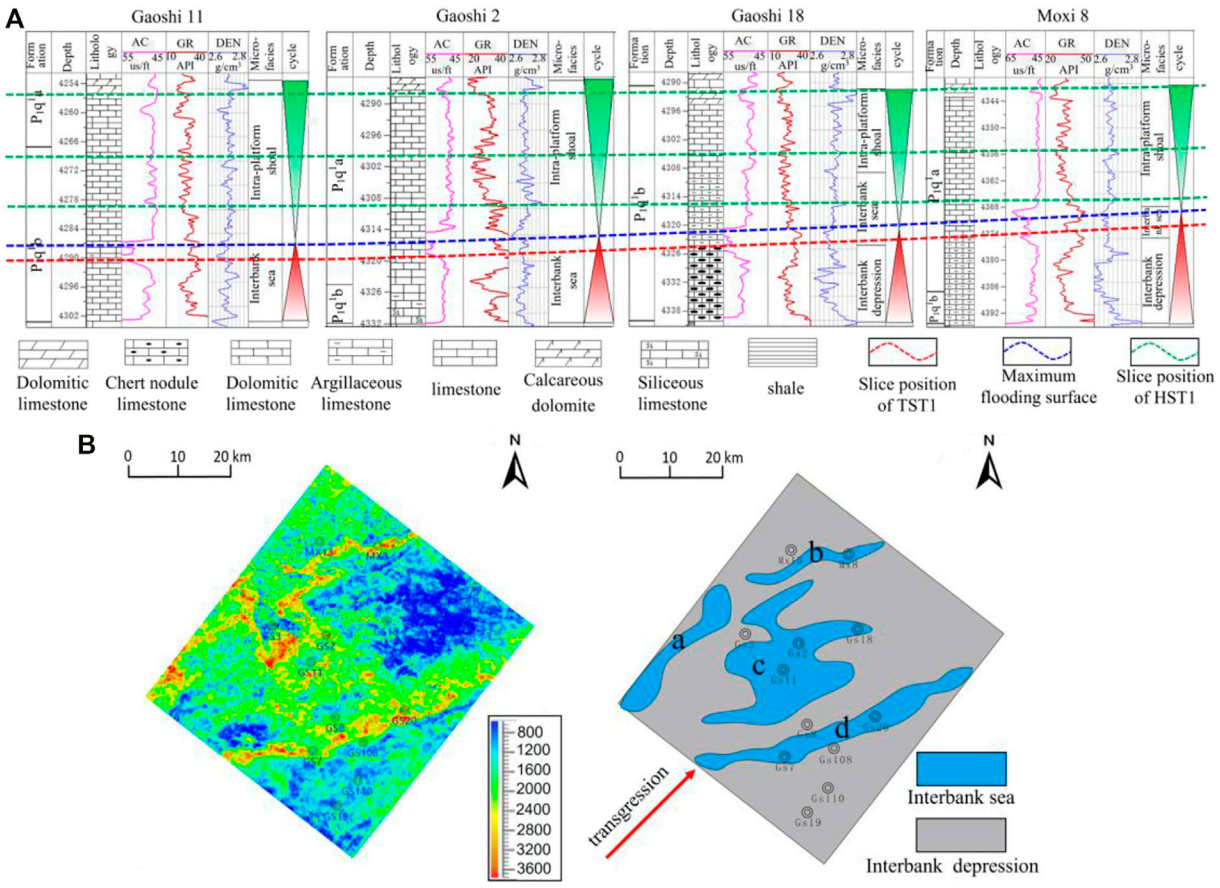

FIGURE 11
(A) log curve and sedimentary microfacies interpretation diagram of representative well location in SQ1 period; **(B)** Typical root mean square amplitude attribute slice and corresponding sedimentary microfacies interpretation during TST1.

formation of carbonate rocks. The microfacies of the inner platform beach mainly comprise meso-crystalline dolomite, saddle dolomite, greyish brown limestone, grey limestone, and other light coloured limestone. The logging curve of dolomite shows the characteristics of high density, high acoustic time difference, and low GR. It is a good oil and gas reservoir facies zone (Hu et al., 2010). The light colour indicates that it was deposited in a shallow water oxidation environment. With the cyclic change of relative sea level, the sedimentary microfacies of the interbank depression, interbank sea, and intraplatform shoal also overlap with each other.

4.2 Optimisation of seismic attributes and division of sedimentary facies

Different seismic attributes have different sensitivities to sedimentary facies, and seismic attributes do not have clear geological significance (Chen and Sidney, 1997; Liu et al., 2009; Deng and Chen, 2021). Therefore, the identification and optimisation of different attributes are of great significance for the detailed interpretation of sedimentary microfacies in the study area. By calculating various seismic attributes (Ngene et al., 2022), combined with thin section, core, drilling, and other data and results of previous studies, the seismic attributes that can best reflect the sedimentary microfacies in the study area are optimised. Considering the example of the HST1 period, six conventional seismic attributes are calculated.

According to the interpretation and core drilling, a dolomite reservoir was encountered in wells Moxi 8, Moxi13, Gaoshi 2, Gaoshi 11, and Gaoshi 18 during the HST1 period (as shown in Figure 11A. The single well sedimentary facies was interpreted as the sedimentary microfacies of the inner platform beach. As shown in Figure 9, the prediction results of instantaneous amplitude, instantaneous frequency, instantaneous phase, and dessert attributes were poor, and the curvature attributes were in good agreement. The root mean square amplitude attribute has the best prediction effect. Among them, the sedimentary microfacies of the intraplatform beach have high root mean square amplitude, which is in the warm region, and the sedimentary microfacies of the inter beach sea have low root mean square amplitude, which is in the cold region.

4.3 Qualitative and optimal division of sedimentary microfacies using attribute slice

Through qualitative analysis and optimisation of seismic attributes, reasonable seismic attributes are determined. 22 attribute slices are cut from each of the four system tracts. Combined with logging data, the slices with the highest degree of

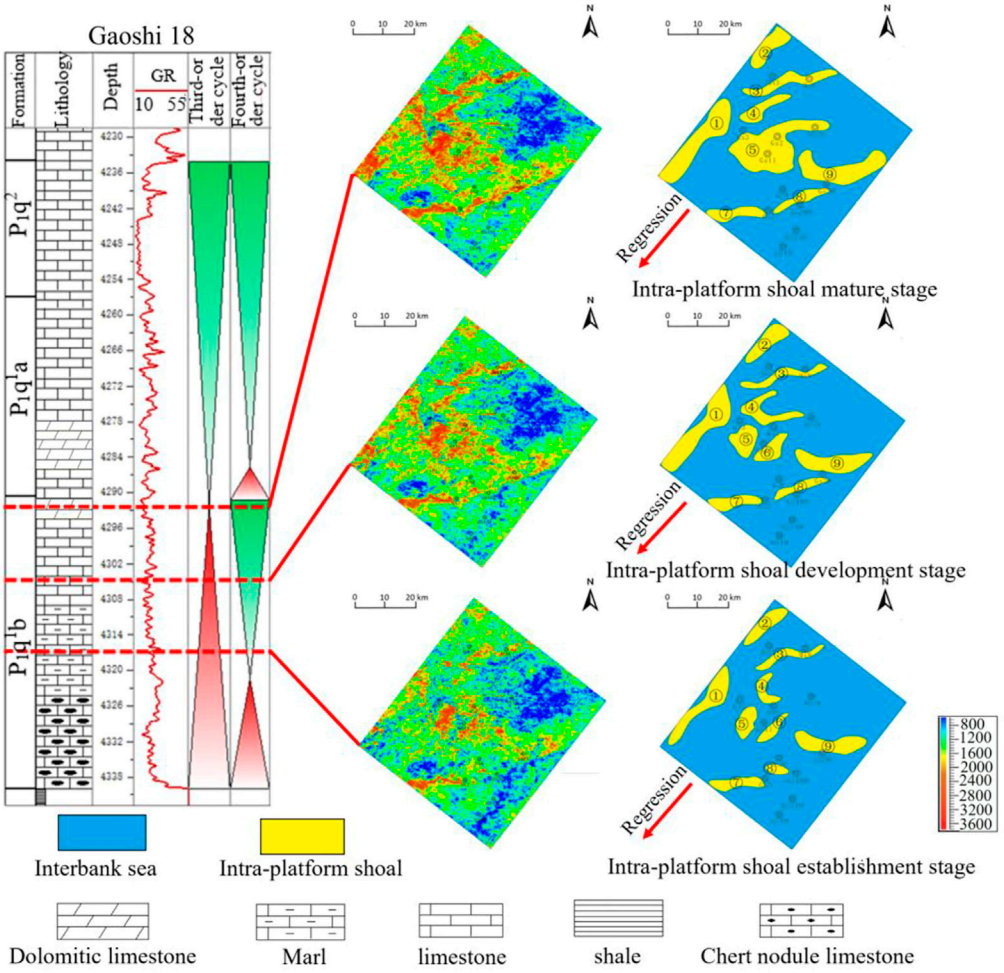

FIGURE 12
Typical root mean square amplitude attribute slice and corresponding sedimentary microfacies interpretation in HST1.

coincidence with the well divided sedimentary facies are selected to study the distribution rules of the sedimentary microfacies in different periods. The well locations of dolomite reservoirs drilled in the study area mainly include Moxi 13, Moxi 8, Gaoshi 18, Gaoshi 2, and Gaoshi 11. As the root mean square attribute is one that can reflect the continuity of the stratum, the more stable the local layer, the more uniform is the lithology, the greater the is root mean square amplitude, and the smaller is the reverse. Additionally, the sedimentary microfacies divided in combination with the root mean square amplitude attribute slice have a high degree of coincidence with the lithology and sedimentary facies divided by the well data. Therefore, the sedimentary evolution process of each system tract is studied along with the logging data (Figure 10).

4.3.1 Study on the sedimentary microfacies of TST1

According to the lithology statistics of 12 wells in the study area, during TST1, dark grey chert nodule limestone (such as in Gaoshi 18), siliceous limestone (such as in Gaoshi 19), argillaceous limestone (such as in Moxi 8), and grey limestone (Moxi 13) are mainly used. Among them, the first three lithologies are dark in colour and high in density, as they are the product of deep water sedimentation, and are classified as the sedimentary microfacies of interbank depressions. Alternatively, the grey limestone area, which is light in colour and was deposited in relatively shallow water, is classified as the sedimentary microfacies of interbank seas. As the sedimentary microfacies in the interbank depression are located below the wave base (with weak hydrodynamic force and high shale content), together with chert and siliceous sediments, the overall sedimentary lithology of the facies zone is complex. Thus, the root mean square amplitude attribute is low. However, the intertidal marine microfacies dominated by grey limestone have high root mean square amplitude owing to their single lithology and stable sedimentation. Subsequently, we selected the appropriate threshold value, combined the distribution characteristics of sedimentary facies determined by well data, and divided the sedimentary microfacies on the plane attribute slice.

As shown in Figure 11B, the interbank depression microfacies are mainly developed during TST1. When seawater flows in from the southwest, the interbank depression was formed in relatively low places with the deepening of the water body. As it is located below the wave base, the hydrodynamic force is weak, which is conducive to the deposition of fine grained argillaceous sediments. Therefore, the lithology mainly comprises argillaceous limestone, and the logging curve shows low density, low acoustic wave time difference, and high

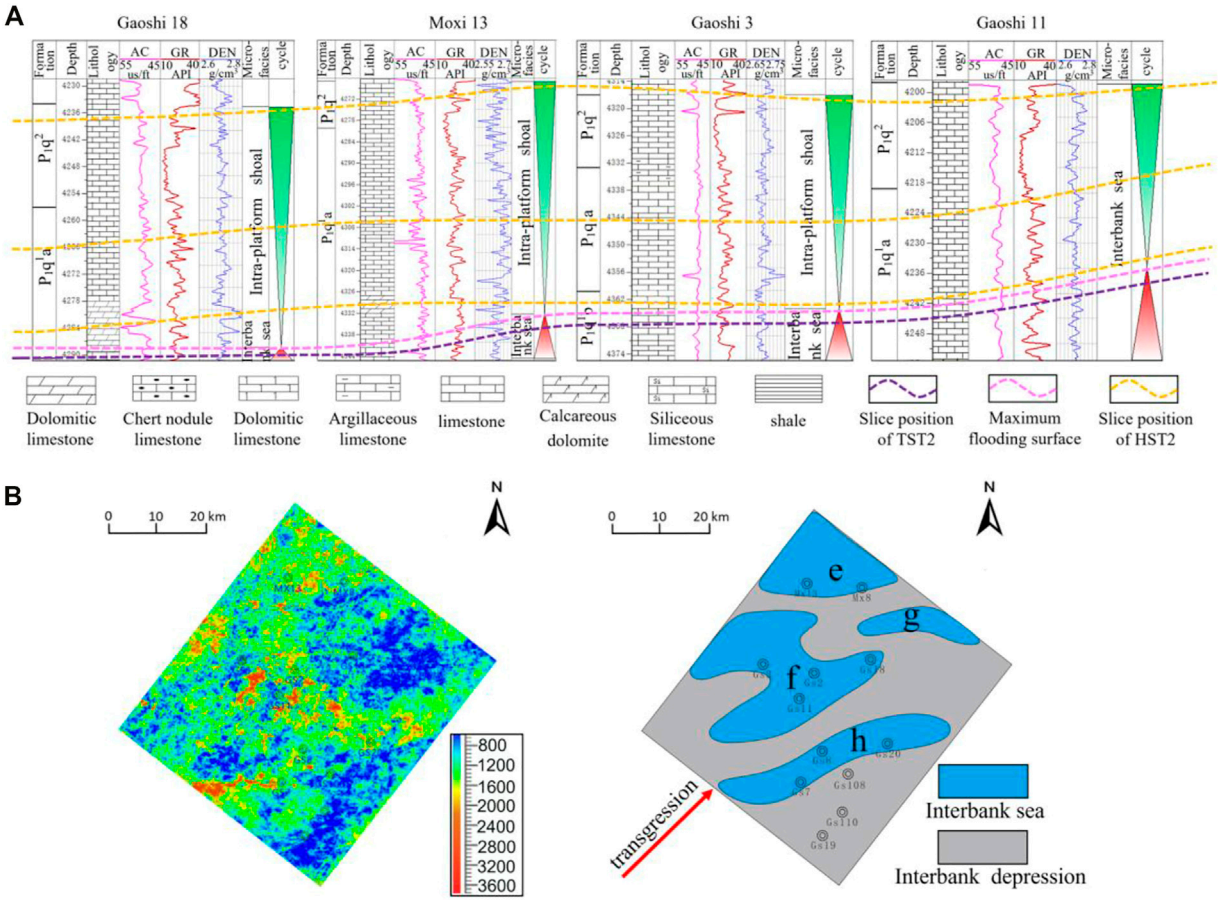

FIGURE 13
(A) Log curve and sedimentary microfacies interpretation diagram of representative well location in SQ2 period;; **(B)**log curve of surface well location and sedimentary microfacies interpretation diagram in SQ2 period.

GR, indicating that the sediments belong to poor reservoir facies zone, as shown in Figure 11A. Conversely, the inter beach marine sedimentary microfacies granular shoals are formed at relatively high positions, forming grey limestone bands distributed in the southwest-northeast direction, as shown in Figures 11A–D. The direction of extension is consistent with that of the transgressive systems tract, and the sediments are more concentrated in area C of the central region, thereby laying a foundation for the formation of intraplatform shoals during HST1.

4.3.2 Study on the sedimentary microfacies of HST1

During the HST1 period, the lithology mainly comprised argillaceous limestone, grey limestone, calcareous dolomite, and dolomite. The area containing the distribution of calcareous dolomite and dolomite is classified as intraplatform shoal sedimentary microfacies, and that containing argillaceous limestone and limestone is classified as interbank sea microfacies. Similarly, the lithology of the inner platform beach area containing dolomite is more uniform and has high root mean square amplitude. The sedimentary facies of the interbank sea were deposited in a deeper water body and have more complex lithology, and belong to the area of low root mean square amplitude. Based on the sedimentary facies preliminarily divided by well data, the following divisions are made on attribute slices, as shown below.

As shown in Figure 12, during the HST1 period, the relative sea level began to decline after a short rise. In the TST1 period, the interbank depression began to gradually evolve into interbank sea microfacies. The original interbank sea zones, with higher structures, gradually evolved into intraplatform shoals. Their root mean square amplitudes are high. The logging curves indicate that they have the characteristics of high density, high acoustic time difference, and low GR. They are good oil and gas reservoir facies zones, which are mainly distributed in the central and western regions of the study area. For example, the interbank sea zone a evolved into two intraplatform shoal facies zones ① and ②, and the zone B is preserved well and perfectly transited to the intraplatform shoal ③. The differentiation of the C band is the most obvious. Along the regression direction, intraplatform shoal bands ④, ⑤, and ⑥ were formed with thick middle and slender sides, and band D evolved into intraplatform shoals ⑦, ⑧, and ⑨. Among them, well Moxi 18 has been drilled in beach ③, and wells Gaoshi 18, Gaoshi 11 and Gaoshi 2 have been drilled in beach ⑤. The well data show that the dolomite reservoir, and the remaining areas ①, ②, ④, ⑥, ⑦, ⑧, and ⑨ are the development facies zones of the predicted intraplatform beach.

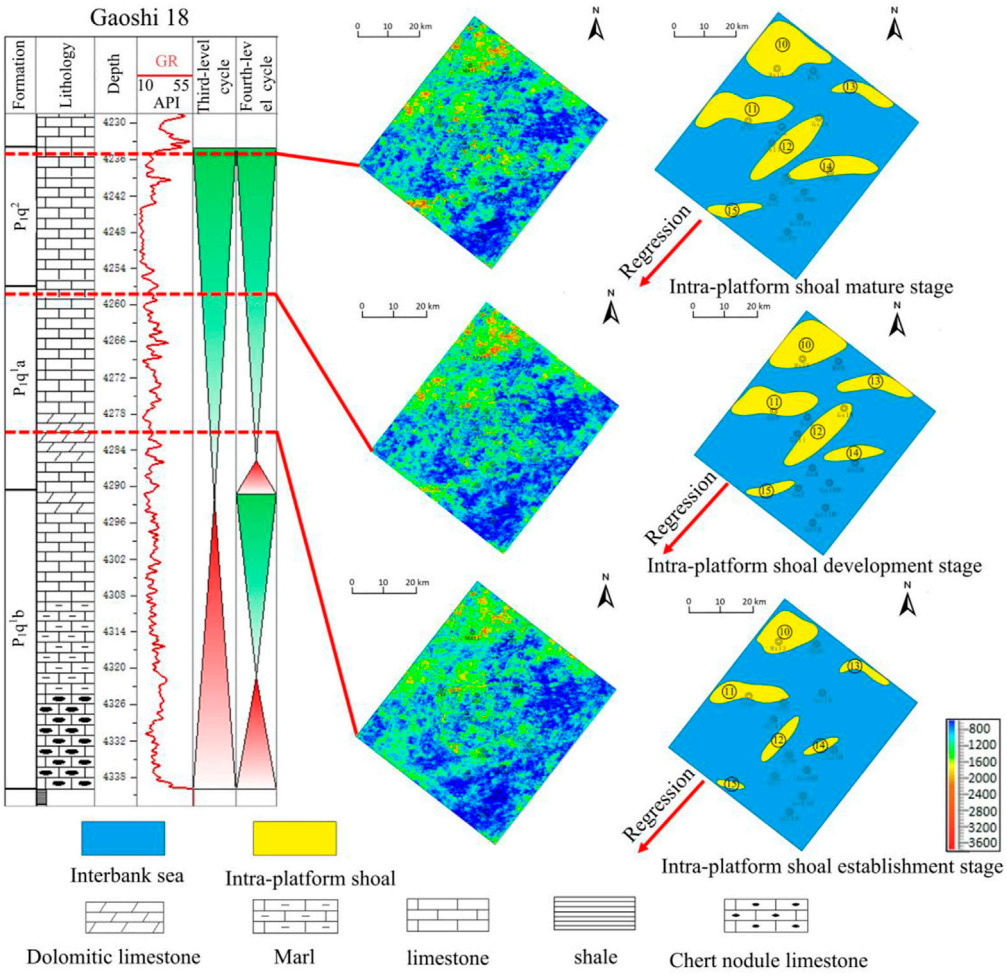

FIGURE 14
Typical root mean square amplitude attribute slice and corresponding sedimentary microfacies interpretation in HST2.

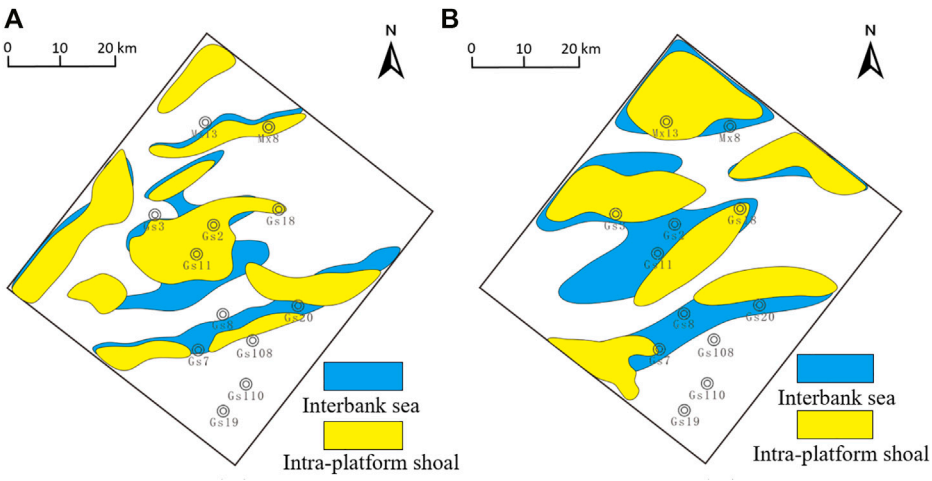

FIGURE 15
Evolution diagram of sedimentary microfacies in each fourth order sequence: **(A)** evolution diagram of the sedimentary microfacies in the SQ1 period (interbank sea microfacies in TST1 period gradually evolved into intraplatform shoal microfacies in the HST1 period); **(B)** evolution map of the interbank sea to intraplatform beach in the SQ2 period (interbank sea microfacies in the TST2 period gradually evolved into intraplatform beach microfacies in the HST2 period).

4.3.3 Study on the sedimentary microfacies of TST2

As shown in Figure 13A, during TST2, the sea level rose again, forming a depositional system dominated by interbank depressions and interbank seas. As TST1 and HST1 belong to deep-water open platform subfacies, and TST2 and HST2 belong to shallow-water open platform subfacies, compared to the interbank sea strip formed in the TST1 period, because the water body is shallower, the interbank sea microfacies can form more easily. Thus, the interbank sea distribution area at this stage progressively became wider. The distribution characteristics in the southwest-northeast direction are consistent with the direction of the transgressive systems tract, mainly forming four interbank sea strips e, f, g, and h, As shown in Figure 13B.

4.3.4 Study on the sedimentary microfacies of HST2

As shown in Figure 14, during the HST2 period, the relative sea level began to decline, forming the inter beach sea and intra platform beach depositional systems. The interbank sea zone at the high part of the structure in the TST2 period subsequently evolved into the intraplatform shoal microfacies, and still extended in the southwest-northeast direction e. Strip G is basically transformed into inner Taiwan shoals ⑩ and ⑪; a portion of the high part of the sea strip between beach f is transformed into inner Taiwan shoals ⑪ and ⑫; and strip h is evolved into inner Taiwan shoals ⑭ and ⑮. Among them, the well location of MX 13 has been drilled for intraplatform shoal system ⑩, that of Gaoshi 3 has been drilled for beach body ⑪, and that of Gaoshi 18 well location has been drilled for beach body ⑫. The interpretation results indicate the presence of a dolomite reservoir, and the remaining areas ⑬, ⑭, and ⑮ are the predicted intraplatform shoal development facies zones.

4.4 Evolution analysis of sedimentary microfacies

To study the sedimentary evolution process between and within the fourth order sequences, the interbank sea microfacies at the top of TST1 and the intraplatform shoal microfacies at the top of HST1, TST2, and HST2 are superimposed (as shown in Figure 15) Through comparison, we found that the interbank sea microfacies and intraplatform shoal microfacies are highly consistent.

During the Qixia Formation, with the rise of sea level, a large number of marine organisms began to multiply, and the study area changed from a terrigenous clastic sedimentary environment to carbonate open platform sedimentary environment. In the SQ1 period, the water body was relatively deep, and the whole area was a relatively deep-water open platform, which can be divided into TST1 and HST1. During the TST1 period, the interbank depressions are mainly developed, and the interbank sea microfacies are locally high, as shown in Figure 15A. With the decrease in sea level, the interbank sea microfacies with high terrain during the TST1 period gradually evolved into intraplatform shoal microfacies. During SQ2, the water level decreased on the whole, and resulted in the formation of a shallow water open platform subfacies, which can be divided into TST2 and HST2. The sea level in TST2 began to rise again and developed interbank depressions and interbank sea microfacies, as shown in Figure 15B. As the entirety of the water body was shallow, the interbank sea microfacies during TST2 were more widely distributed. With the decrease in the relative sea level, some interbank sea microfacies began to evolve into intraplatform shoal microfacies. Its distribution is also wider than that of the HST1 period.

5 Conclusion

(1) According to the carbonate sequence division principle, the Qixia Formation in the study area is divided into one-third order sequence and two-fourth order sequences: SQ1 and SQ2. SQ1 comprises TST1 and HST1, and SQ2 comprises TST2 and HST2. Owing to the two rapid transgressive systems tracts, the relative sea level rose rapidly, and the deep water environment hindered the deposition of carbonate rocks during the low stand system, forming sedimentary discontinuities; thus, the low stand system was missing.

(2) The Qixia Formation in the study area generally comprises the open platform sedimentary facies, which can be further divided into deep water open platform subfacies and shallow water open platform subfacies according to the water depth. From bottom to top, it is composed of inter beach depression microfacies, inter beach sea microfacies, and intraplatform beach microfacies. The dolomite reservoir with good porosity and permeability is located in the beach facies zone within the platform.

(3) The change in the sedimentary microfacies in the study area corresponds to the change in the relative sea level, and the favourable reservoir facies will also migrate accordingly. In the low stand system, the interbank depressions in the lower part of the structure will evolve into interbank seas in the high stand systems tract with the decrease in sea level, whereas the interbank seas in the higher part of the structure will also partially evolve into intraplatform shoal microfacies. With the changes in multi-stage relative sea level, the spatial distribution of the intraplatform beach facies zone will also migrate.

Data availability statement

Raw data supporting the conclusions of this paper will be provided by the author without any improper reservation.

Author contributions

SL, LZ contributed to the conception and design of the design and modification of experimental ideas. SL wrote the first draft of the manuscript. XG, XC, and YW Provide initial data and make suggestions on research progress, LT, ZQ, YQ, and JZ conducted some statistical analysis and data collation.

Funding

This research was supported by the national major science and technology project “Establishment of deep oil and gas transport framework and analysis of oil and gas accumulation in typical basins” (No: 2017ZX05008-004-008).

Conflict of interest

Authors XG and XC were employed by Petro China Southwest Oil and Gas Field Company. LF was employed by the company BGP Southwest Geophysical Company.

The remaining authors declare that the research was conducted in the absence of any commercial or financial relationships that could be construed as a potential conflict of interest.

Publisher's note

All claims expressed in this article are solely those of the authors and do not necessarily represent those of their affiliated organizations, or those of the publisher, the editors and the reviewers. Any product that may be evaluated in this article, or claim that may be made by its manufacturer, is not guaranteed or endorsed by the publisher.

References

Abraham-A, , R. M., Taioli, F., and Nzekwu, A. I. (2022). Physical properties of sandstone reservoirs: Implication for fluid mobility. *Energy Geosci.* 3 (4), 349–359. doi:10.1016/j.engeos.2022.06.001

Chao, Q. C., Bai, Z. Z., Li, H. W., and Zhang, L. L. (2021). Application of wavelet transform of logging data in sequence stratigraphic division of Cambrian xixiangchi group in Central Sichuan. *Bull. Geol. Sci. Technol.* 40 (04), 242–251. doi:10.19509/j.cnki.dzkq.2021.0418

Chen, Q., and Sidney, S. (1997). Seismic attribute technology for reservoir forecasting and monitoring. *Lead. Edge* 16 (5), 445–448. doi:10.1190/1.1437657

Chen, Z. Q. (2007). Exploration for natural gas in middle permian Maokou Formation of Sichuan Basin. *China Pet. Explor.* 12 (5), 1–11. doi:10.3969/j.issn.1672-7703.2007.05.001

Dai, X. F., Zhang, M., Jiang, Q. C., and Feng, Z. (2017). Karst reservoirs seismic prediction of lower permian Maokou Formation in central Sichuan Basin, SW China. *Petroleum Explor. Dev.* 44 (1), 79–88. doi:10.1016/s1876-3804(17)30010-1

Deng, R. B., and Chen, Q. (2021). Forward modeling of fracture prediction based on seismic attribute modeling. *Earthq. Res. Adv.* 2021, 57–58. doi:10.1017/cbo9780511843655.003

Elisa, F. D., Peter, H., Luc, S., David, K., Antoni, C., Gustavo, T., et al. (2011). Insights into fluid flow and water-rock interaction during deformation of carbonate sequences in the Mexican fold-thrust belt. *J. Struct. Geol.* 33 (8), 1237–1253. doi:10.1016/j.jsg.2011.05.009

Fan, C. H., Li, H., Qin, Q. R., He, S., and Zhong, C. (2020). Geological conditions and exploration potential of shale gas reservoir in Wufeng and Longmaxi Formation of southeastern Sichuan. Basin, China. *J. Petrol. Sci. Eng.* 191, 107138. doi:10.1016/j.petrol.2020.107138

Feng, Z. Z., Yang, Y. Q., Jin, Z. K., and Zhidong, B. (1996). Lithofacies paleogeography of the permian of south China. *Acta Sedimentol. Sin.* 14 (2), 3–12. CNKI:SUN:CJXB.0.1996-02-000.

Hu, A. P., Pan, L. Y., and Hao, Y. (2018). Origin,character isticsand distribution of dolostone reservoir in Qixia Formation and Maokou Formation,Sichuan Basin,China. *Mar. Orig. Pet. Geol.* 23 (02), 39–52. CNKI:SUN:HXYQ.0.2018-02-006.

Hu, M. Y., Wei, G. Q., and Hu, Z. G. (2010). Sequence lithofacies palaeogeography of the middle Permian Qixia formation in Sichuan basin. *J. Palaeogeogr.* 12 (5), 515–526. doi:10.1017/S0004972710001772

Huang, S. J., Huang, K. K., Lu, J., and Lan, Y. F. (2014). The relationship between dolomite textures and their formation temperature: A case study from the permian-triassic of the Sichuan Basin and the lower paleozoic of the tarim basin. *Petroleum Sci.* 11 (01), 39–51. doi:10.1007/s12182-014-0316-7

Huang, X. P., Yang, T. Q., and Zhang, H. M. (2004). Research on the sedimentary facies and exploration potential areas of Lower Permian in Sichuan Basin. *Nat. Gas. Ind.* 24 (1), 10–12. doi:10.3321/j.issn:1000-0976.2004.01.004

Ji, X., Zhang, Y., Zang, D., and Shen, P. (2012). Carbonate reef-shoal reservoir identification in Western longgang, Sichuan Basin. *Oil Geophys. Prospect.* 47 (2), 309–314. CNKI:SUN:SYDQ.0.2012-02-022.

Jiang, L., Richard, H. W., Cai, C. F., Li, K. K., Xiang, L., Cai, L. L., et al. (2014). Dolomitization of gas reservoirs: The upper permian changxing and lower triassic feixianguan formations, northeast Sichuan basin, China. *J. Sediment. Res.* 84 (10), 792–815. doi:10.2110/jsr.2014.65

Jorgnson, N. O. (1981). Mg and Sr distribution in carbonate rocks from the Maastrichtian/Danian boundary of the Danish subbasin and the North Sea Central Graben. *Sediment. Geol.* 30 (4), 311–325. doi:10.1016/0037-0738(81)90027-0

Li, H. (2022). Research progress on evaluation methods and factors influencing shale brittleness: A review. *Energy Rep.* 8, 4344–4358. doi:10.1016/j.egyr.2022.03.120

Li, H., Tang, H. M., Qin, Q. R., Zhou, J. L., Qin, Z. J., Fan, C. H., et al. (2019). Characteristics, formation periods and genetic mechanisms of tectonic fractures in the tight gas sandstones reservoir: A case study of xujiahe Formation in YB area, Sichuan Basin, China. *J. Petrol. Sci. Eng.* 178, 723–735. doi:10.1016/j.petrol.2019.04.007

Li, H., Zhou, J. L., Mou, X. Y., Guo, H. X., Wang, X. X., An, H. Y., et al. (2022). Pore structure and fractal characteristics of the marine shale of the Longmaxi Formation in the changning area, southern Sichuan Basin, China. *Front. Earth Sci.* 10, 1018274. doi:10.3389/feart.2022.1018274

Li, J., Chen, L. W., Hao, C. M., Zhang, J., Chen, S., and Gui, H. R. (2021). Geochemical characteristics and geological significance of chert nodules in Qixia formation, Pingding Mountain, lower Yangtze Plate. *J. Mt. Sci.* 18 (01), 88–100. doi:10.1007/s11629-020-5982-x

Li, J., Li, H., Yang, C., Wu, Y. J., Gao, Z., and Jiang, S. L. (2022). Geological characteristics and controlling factors of deep shale gas enrichment of the Wufeng-Longmaxi Formation in the southern Sichuan Basin, China. *Lithosphere* 2022, 4737801. doi:10.2113/2022/4737801

Li, Q. (2018). *Characteristics of sedimentary system of Maokou Formation of middle permian in northwest sichuan*. Chengdu, China: Chengdu University of Technology. CNKI: CDMD: 2.1018.258776.

Li, X. F. (2017). *Research and application of forward modeling response characteristics of carbonate gas reservoirs*. Jingzhou, China: Yangtze University, 170970. CNKI:CDMD:2.1017.

Li, R, R., Hu, M. Y., Yang, W., and Mankong, L. (2019). Sedimenta-ryfacies model and favorable reservoir distribution of the Middle Permianin Sichuan Basin. *Oil&Gas Geol.* 40 (2), 369–379. doi:10.11743/ogg20190215

Liu, L. f., Sun, Z. D., and Yang, H. J. (2009). Seismic attribute optimization method and its application for fractured-vuggy carbonate reservoir. *Oil Geophys. Prospect.* 44 (6), 747–754. doi:10.1287/mksc.1080.0385

Liu, X. C., Lu, Y. C., Du, X. B., Xiangquan, L., Weibing, L., Jingyu, Z., et al. (2020). Application of geostatistical in-version constrained by sequence framework in thin bedded sandbody prediction. *Bull. Geol. Sci. Technol-ogy* 39 (3), 99–109. CNKI:SUN:DZKQ.0.2020-03-014.

Mei, M. X. (2010). Correlation of sequence boundaries according to discerning between normal and forced regressions: The first advance in sequence stratigraphy. *J. Palaeogeogr.* 12 (5), 549–564. doi:10.7605/gdlxb.2010.05.005

Mei, M. X., Ma, Y. S., Zhang, H., Xiaoqing, M., and Yonghong, C. (2007). From Basin black shales to platform carbonate rocks:A study on sequence stratigraphy for the lower cambrian of the upper-yangtze region in south China. *Acta Geol. Sin. Ed.* 81 (05), 739–755. doi:10.1111/j.1755-6724.2007.tb00999.x

Ngene, T., Mukhopadhyay, M., and Ampana, S. (2022). Reconnaissance investigation of geothermal resources in parts of the Middle Benue Trough, Nigeria using remote sensing and geophysical methods. *Energy Geosci.* 3 (4), 360–371. doi:10.1016/j.engeos.2022.06.002

Serra, O. (1984). "Foundamentals of well-log interpretation:The acquisition of logging data," in *Development in petroleum science* (Amsterdam, Netherlands: Elsevier). doi:10.1016/s0376-7361(08)x7023-2

Sheu, D.-D. (1990). 13C and 18O compositions of carbonates from a cyclic carbonate-evaporite rock sequence: Evidences for meteoric water input. *Chem. Geol.* 81 (1–2), 157–162. doi:10.1016/0009-2541(90)90045-9

Sheu, D.-D., and Burke, B. (1982). Inferred paleosalinity and phosphate content of carbonate rocks from a cyclic evaporite-carbonate rock sequence. *J. Sediment. Res.* 52 (3), 897–903. doi:10.1130/0091-7613(1982)10<666

Vail, P. R., and Mitchum, R. M. (1979). Global cycles of relative change of sea level. *AAPG Bull.* l977, 83–98. doi:10.1306/M29405C32

Wen, J., Peng, J., and Chen, Y. L. (2020). Study on sequence stratigraphy of canglangpu Formation in the central-northern Sichuan Basin. *Fault-Block Oil Gas Field* 27 (4), 424–431. doi:10.3969/j.issn.1671-1815.2013.19.029

Wu, J., Wang, Y,Z., and Gao, Z. Q. (2013). Using carbon and oxygen isotopes to identify carbonatestrata sequence interface. *Sci. Technol. Eng.* 13 (19), 5579–5585. doi:10.1155/2011/410621

Wu, L. Q., Hu, M. Y., and Hu, Z. G. (2010). Study on the middle permian sequence stratigraphy of Sichuan Basin. *Petroleum Geol. Eng.* 24 (6), 10–13. doi:10.3969/j.issn.1673-8217.2010.06.003

Wu, Z. H., Tang, M. T., Zuo, Y. J., Lou, Y. L., Wang, W. T., Liu, H., et al. (2022). Acoustic emission-based numerical simulation of tectonic stress field for tectoclase prediction in shale reservoirs of the northern Guizhou area, China. *Energy Geosci.* 3 (4), 436–443. doi:10.1016/j.engeos.2021.10.005

Xia, D. L., Wu, Y., Zou, M., Xia, D. D., and Pang, W. (2022). Quality characterization of tight sandstone reservoirs in the yanchang formation of the honghe oilfield, ordos basin, central China. *Energy Geosci.* 3 (4), 444–452. doi:10.1016/j.engeos.2021.07.001

Xiao, Dai., Cao, J., Luo, B., Tan, X. C., Liu, H., Zhang, B. J., et al. (2020). On the dolomite reservoirs formed by dissolution: Differential eogenetic versus hydrothermal in the lower Permian Sichuan Basin, southwestern China. *AAPG Bull.* 104 (7), 1405–1438. doi:10.1306/02262018242

Zhang, K., Jiang, S., Zhao, R., Wang, P., Jia, C., and Song, Y. (2022a). Connectivity of organic matter pores in the Lower Silurian Longmaxi Formation shale, Sichuan Basin, Southern China: Analyses from helium ion microscope and focused ion beam scanning electron microscope. *Geol. J.* 57 (5), 1912–1924. doi:10.1002/gj.4387

Zhang, K., Jiang, Z. X., Song, Y., Jia, C., Yuan, X., Wang, X., et al. (2022b). Quantitative characterization for pore connectivity, pore wettability, and shale oil mobility of terrestrial shale with different lithofacies - A case study of the Jurassic Lianggaoshan Formation in the Southeast Sichuan Basin of the Upper Yangtze Region in Southern China. *Front. Earth Sci.* 2022, 864189. doi:10.3389/feart.2022.864189

Zhang, K., Song, Y., Jiang, Z. X., Yuan, X., Wang, X., Han, F., et al. (2022c). Research on the occurrence state of methane molecules in postmature marine shales A case analysis of the Lower Silurian Longmaxi Formation shales of the upper Yangtze region in Southern China. *Front. Earth Sci.* 2022, 864279. doi:10.3389/feart.2022.864279

Zhang, Y. B., Zhao, Z. J., Wang, G. H., Jiang, Z. X., Wang, M. J., Zheng, M., et al. (2014). Type division and controlling factor analysis of 3rd-order sequences in marine carbonate rocks. *Geosci. Front.* 5 (2), 289–298. CNKI:SUN:GSFT.0.2014-02-013. doi:10.1016/j.gsf.2013.07.002

Zhang, Y. X., Chen, J. W., Zhou, J. Y., and Yuan, Y. (2019). Sedimentological sequence and depositional evolutionary model of lower triassic carbonate rocks in the south yellow sea basin. *China Geol.* 2 (3), 299–312. doi:10.31035/cg2018113

Zhang, Y. X., Wang, L. C., and Tan, X. C. (2020). Microfacies and sedimentary environment of Qixia Formation in xiaonanhai section, northern sichuan. *Acta Sedimentol. Sin.* 38 (05), 1049–1060. doi:10.14027/j.issn.1000-0550.2019.094

frontiers | Frontiers in Earth Science

TYPE Original Research
PUBLISHED 22 March 2023
DOI 10.3389/feart.2023.1133413

OPEN ACCESS

EDITED BY
Shuai Yin,
Xi'an Shiyou University, China

REVIEWED BY
Kun Zhang,
Southwest Petroleum University, China
Qrong Qin,
Southwest Petroleum University, China

*CORRESPONDENCE
Lin Qi,
ejiqimao@163.com

SPECIALTY SECTION
This article was submitted to Structural Geology and Tectonics, a section of the journal Frontiers in Earth Science

RECEIVED 28 December 2022
ACCEPTED 20 February 2023
PUBLISHED 22 March 2023

CITATION
Lai Q, Qi L, Chen S, Ma S, Zhou Y, Fang P, Yu R, Li S, Huang J and Zheng J (2023), Resercoir space characteristics and pore structure of Jurassic Lianggaoshan Formation lacustrine shale reservoir in Sichuan Basin, China: Insights into controlling factors.
Front. Earth Sci. 11:1133413.
doi: 10.3389/feart.2023.1133413

Resercoir space characteristics and pore structure of Jurassic Lianggaoshan Formation lacustrine shale reservoir in Sichuan Basin, China: Insights into controlling factors

Qiang Lai[1], Lin Qi[1]*, Shi Chen[1], Shaoguang Ma[2], Yuanzhi Zhou[3], Pingchao Fang[3], Rui Yu[1], Shuang Li[4], Jun Huang[5] and Jie Zheng[6]

[1]Geology Exploration and Development Research Institute, CNPC Chuanqing Drilling Engineering Co., Ltd, Chengdu, China, [2]Development Department, PetroChina Southwest Oil and Gas Field Company, Chengdu, China, [3]Exploration Division, PetroChina Southwest Oil and Gas Field Company, Chengdu, China, [4]Sichuan Yuesheng Energy Group Co., Ltd, Chengdu, China, [5]Chengdu Geoservice Oil and Gas Technology Development Company, Chengdu, China, [6]Chengdu Caledonian Oil and Gas Technology Development Co., Ltd, Chengdu, China

The Jurassic Lianggaoshan Formation lacustrine shale oil is the most potential exploration target of unconventional hydrocarbon resource in Southwest China. In this study, nuclear magnetic resonance (NMR), scanning electron microscopy (SEM), low-temperature N_2 adsorption (LTNA), and high pressure mercury intrusion mercury injection capillary pressure are intergrated to reveal pore structure and its controlling factors of Lianggaoshan Formation lacustrine shale reservoir. Results indicate that three types of lithology combination are classified in the Jurassic Liangggaoshan lacustrine shale reservoir. Type A comprises pure shale. Type B is characterized by frequent shell limestone interbedding. Type C is characterized by frequent siltstone interbedding. The Type C shale is characterized by relatively high proportion of organic pores, high development and good connectivity of nanopores, and highest pore volume and Surface area. The nanopores of Lianggaoshan lacustrine shales are mainly dominated by mesopores and part of the macropores. Among them, the PV and SA are both mainly dominated by micropores. The enrichment of organic matter has little effect on the development of micropores, and does not affect the mesopore and macropore development. Quartz particles in Lianggaoshan lacustrine shale do not clearly facilitate the development of micropore and mesopore-macropore. Intraparticle pore in feldspar clast is an important component of mesopore and macropore. Clay minerals has no positive effect on the formation of micropore and mesopore-macropore.

KEYWORDS

fractal dimension, lacustrine shale, pore structure, lithology combination, lianggaoshan formation, Sichuan Basin

Introduction

Organic matter can be enriched in fine sediments in marine, transitional and lacustrine environments to form oil-bearing and natural gas-bearing organic shale (Gu et al., 2022a; Gu et al., 2022b; Gu et al., 2022c; Dong et al., 2022; Sun et al., 2022). At present, marine shale gas has achieved large-scale and efficient development (Zou et al., 2019; Li et al., 2022; Li et al., 2022; Li, 2022; Yuan et al., 2022). Fuling, Changning, Weiyuan, Zhaotong and other 100 billion square gas fields have been found in Sichuan Basin (Jiang et al., 2016; Jiang et al., 2018; Dong et al., 2022), forming the first 10 trillion square natural gas area in the history of China's petroleum industry in southern Sichuan (Fan et al., 2020; Fu et al., 2021; Fan et al., 2022). The exploration and development of lacustrine shale oil in China started relatively late, but due to the deepening of basic geological theory and the progress of engineering technology (Fu et al., 2020), significant exploration progress has been made in many sets of shale strata, such as the Paleogene Kongdian Formation and Shahejie Formation in the Bohai Bay Basin, the Permian Lucaogou Formation in Jimusar Sag, the Cretaceous Qingshankou shale of Songliao Basin, the Jurassic Dongyuemiao Member in Eastern Sichuan Basin, and the Triassic Yanchang shale in Ordos Basin (Yang et al., 2019; Wei et al., 2021; Peng et al., 2022; Qiu and He, 2022). Lacustrine shale oil in several basins has entered the stage of industrial development (Xu et al., 2017; Chen et al., 2018; Han et al., 2021; Zhao et al., 2022).

Due to the relatively small proportion of organic pores, lacustrine shale has more complex pore structure and stronger heterogeneity than marine shale (Zhang et al., 2021; Zhang et al., 2023). Intraparticle pores in clay aggregates, interparticle pores between or at the edges of brittle minerals (quartz or feldspar), and dissolution pores in calcite and dolomite are thought to provide the main storage space required for lacustrine shale oil (Zhang et al., 2020). The shale oil resources in the Sichuan Basin exceed two billion tons, and the shale quality is similar to that of other basins (Xu et al., 2017; Liu et al., 2021; Shu et al., 2021). Suggesting good exploration and development prospects (Wang et al., 2020). To date, the petroleum geologists have launched a new round of exploration work for the Lianggaoshan Formation shale oil. However, the study of lacustrine shale oil in the Sichuan Basin has just started, and the understanding is not deep (Xu et al., 2017; Liu et al., 2020). The Lianggaoshan Formation lacustrine shale experiences complex sedimentation and structural evolution, forming a large number of multiscale pore and fracture systems, so the heterogeneity of the reservoir pore structure is strong. Based on scanning electron microscopy (SEM), nuclear magnetic resonance (NMR), and related geochemical experiments, combined with low-temperature N_2 adsorption (LTNA) and mercury injection capillary pressure (MICP) measurement, this study quantitatively characterized the reservoir space and pore structure of the Lianggaoshan lacustrine shale in the Sichuan Basin by using the commonly used FHH model and analyzed the main influencing factors of the fractal dimension.

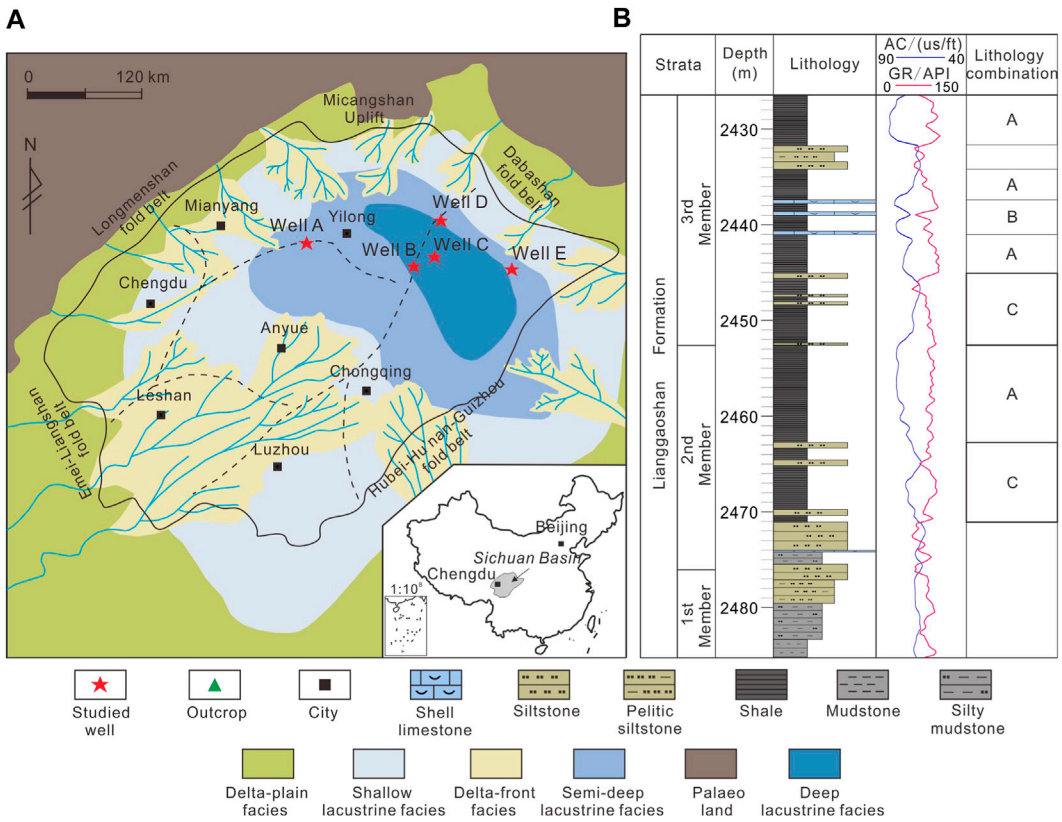

FIGURE 1
(A) Sedimentary facies of the Sichuan Basin during Lianggaoshan Formation deposition, Southwest China. **(B)** Generalized stratigraphy of Jurassic Lianggaoshan Formation Sichuan Basin (based on the Well B).

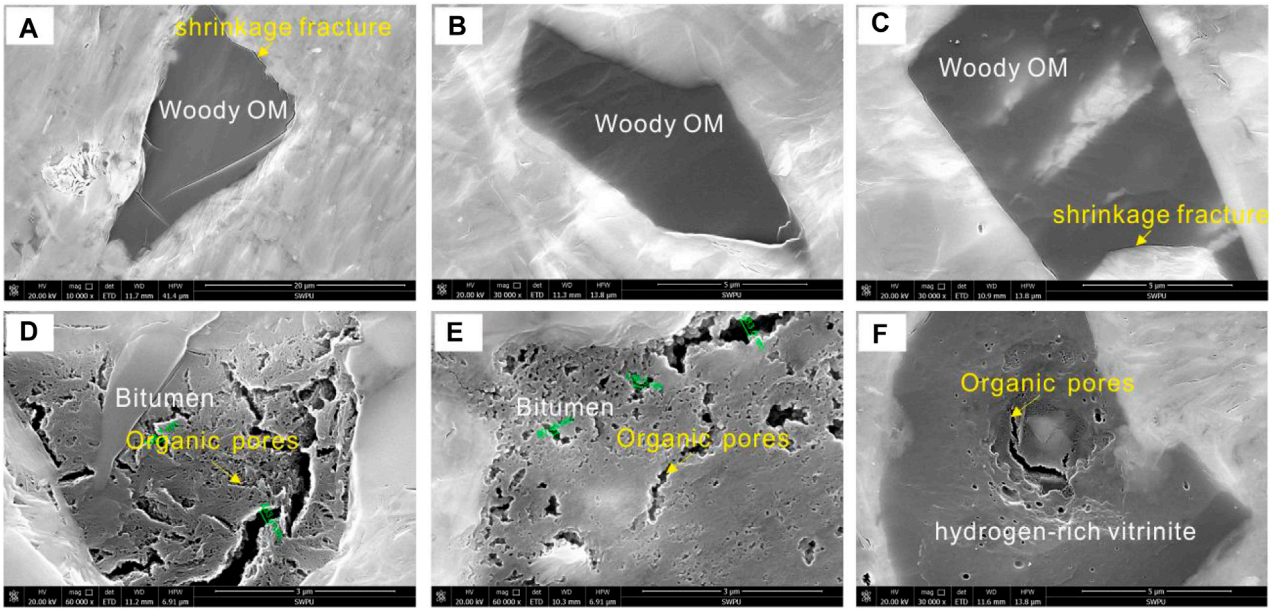

FIGURE 2
High-resolution SEM image of organic matters in Lianggaoshan Formation lacustrine shale reservoir. **(A)** No organic pores are developed in woody organic matter (OM), Type A shale, Well C, 2455.06m; **(B)** No organic pores are developed in woody organic matter (OM), Type A shale,Well B, 1896.13 m; **(C)** Only shrinkage fracture are oberved at the edge of woody organic matter (OM), Type B shale, Well C, 2452.29m; **(D)** Organic pores in bitumen, Type B shale, Well A, 1751.71 m; **(E)** Organic pores in bitumen, Type C shale, Well C, 2465.48m; **(F)** Organic pores in hydrogen-rich vitrinite, Type C shale, Well B, 1928.58 m

This study has guiding significance for geological evaluation of lacustrine shale reservoir.

Geological background

Sichuan Basin is located in the Southwest China (Figure 1A), and the area is about 260,000 km^2 (Figure 1A). In the Early-Middle Jurassic, the Sichuan Basin were dominated by a delta-lake sedimentary system and experienced four lake transgressions during this period (Cheng et al., 2023; Lei et al., 2023). From the bottom to the top, four sets of organic-rich shales formed in the Zhenzhuchong Member, Dongyuemiao Member, Da'anzhai Member, and Lianggaoshan Formation. The Lianggaoshan Formation comprises three members: first Member, second Member, and third Member. Within the range of lake deposition, the first Member and lower part of second Member are dominated by shore-shallow lake, and the third Member and upper part of second Member are dominated by semi-deep lake facies. Organic-rich shale is mainly developed in the upper part of second Member and third Member. According to the combination of rock types, the organic-rich shale can be divided into three types: Type A, Type B and Type C. Type A comprises pure shale, with clay content ranging between 20.4% and 65.4%. Type B is characterized by frequent shell limestone interbedding, with clay content ranging between 7.2% and 49.8%. Type C is characterized by frequent siltstone interbedding, with clay content ranging between 26.1% and 40.9% (Figure 1B).

Samples and methods

A total of 135 samples of Lianggaoshan lacustrine shale were acquired from drilling cores for SEM analysis, X-ray diffraction and TOC test. All experiments and measurements are finished in the PetroChina Exploration and Development Research Institute. The whole-rock and clay mineral X-ray diffraction measurement was carried out using a Malvern Panalytical X'Pert^3 MRD X-ray diffractometer. TOC test was finished through a LECO CS230 Series Carbon and Sulfur Analyzer. Mercury intrusion was finished through a Quantachrome Poremaster. Samples were prepared with an approximate size of 20 × 20 mm^2 and weighed out to 10–20 g, and then, the samples were dried at 110°C for at least 24 h under vacuum in an oven. The MICP ranged from 0 Mpa to 215 Mpa during this measurement. For low-temperature N_2 adsorption, the samples were crushed into 60–80 mesh, dried in an oven at 110°C for 12 h, and then placed in an Autosorb-IQ3 specific surface and a pore size distribution analyzer (Cantor Company, United States). The pretreatment was completed by degassing at 110°C for 12 h in the vacuum condition, and then nitrogen carbon adsorption was carried out. After the experiment, the Brunauer–Emmett–Teller (BET) model was used to calculate the specific surface area, and the Barrett–Joyner–Halenda (BJH) model was employed to obtain the pore size distribution and volume. The reservoir space classification is based on schemes proposed by Loucks et al. (2012). The pore size was divided into three categories according to the pore size distribution (Rouquerol et al., 1994): micropores (pore size < 2 nm), mesopores (pore size between 2nm and 50 nm), and macropores (pore size >50 nm).

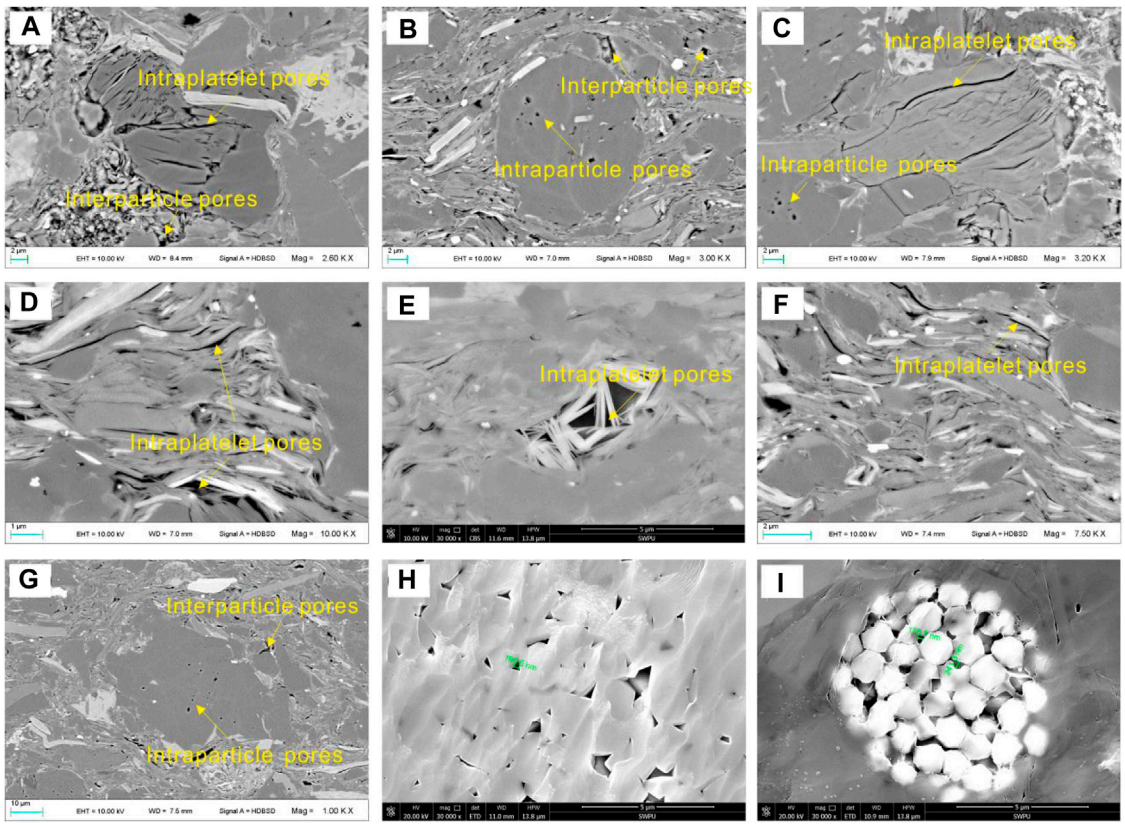

FIGURE 3
High-resolution SEM image of inorganic pores in Lianggaoshan Formation lacustrine shale reservoir. **(A)** Intraparticle pores in clay mineral aggregates, Type A shale, Well A, 2161.25m; **(B)** Intraparticle dissolution pores in feldspar granules, Type A shale, Well B, 2455.06m; **(C)** Type A shale, Well C, 1764.7m; **(D)** Intraparticle pores in clay mineral aggregates, Type B shale, Well D,2437.33 m; **(E)** Type B shale, Well B, 2452.29 m; **(F)** Type B shale, Well E, 1751.71 m; **(G)** Type C shale, Well A, 2164.49 m; **(H)** Type C shale, Well C, 1928.58 m; **(I)** Intercrystalline pores in strawberry pyrite aggregates, Type C shale, Well D, 2465.48 m

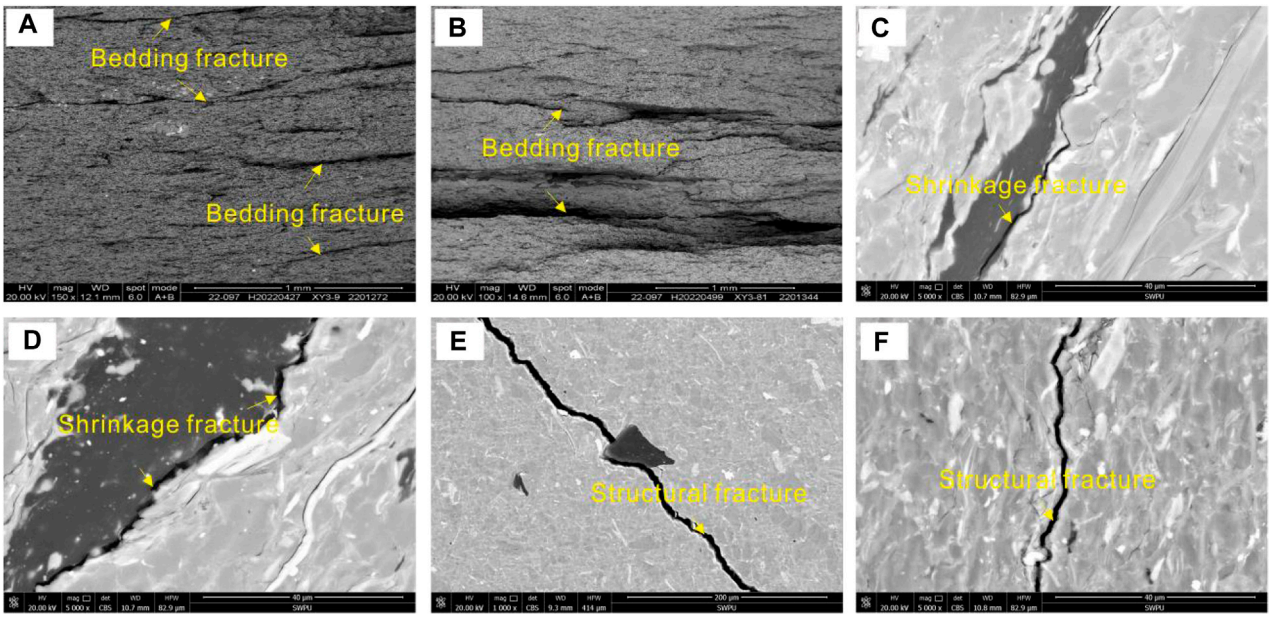

FIGURE 4
High-resolution SEM image of microfractures in Lianggaoshan Formation lacustrine shale reservoir. **(A)** Multiple bedding fracture are parallel to each other, Type A shale,Well C, 2455.06 m; **(B)** Bedding fracture in Type A shale,Well B, 1896.13 m; **(C)** Shrinkage fracture between organic matter and clay mineral, Type B shale,Well C, 2452.29 m; **(D)** Shrinkage fracture between organic matter and clay mineral, Type B shale,Well A, 1751.71 m; **(E)** Structural fracture in Type C shale, Well C, 2465.48 m; **(F)** Structural fracture in Type C shale, Well B, 1928.58 m.

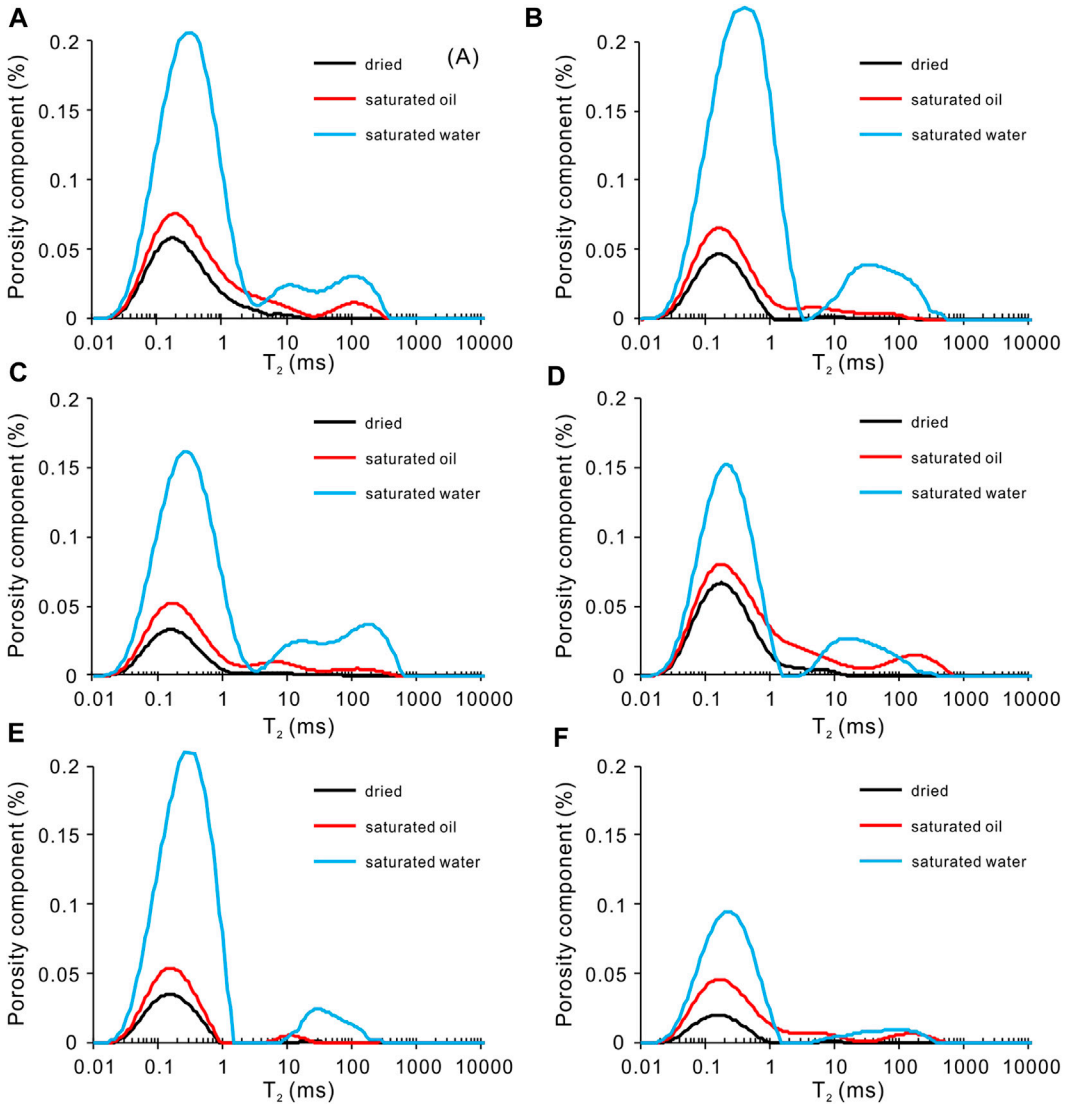

FIGURE 5
NMR T_2 spectra of Jurassic Lianggaoshan Formation lacustrine shale in different lithology combination under different states. **(A)** Type A shale,Well C, 2455.06m; **(B)** Type A shale,Well B, 1896.13 m; **(C)** Type B shale,Well C, 2452.29 m; **(D)** Type B shale,Well A, 1751.71 m; **(E)** Type C shale, Well C, 2465.48 m; **(F)** Type C shale, Well B, 1928.58 m.

When P/Po = 0.5, hysteresis loops of most samples begin to be observed, suggesting the great variation in pore size distribution (or morphology) causing different adsorption behaviors at this pressure (Guo et al., 2022a; Guo et al., 2022b; Li et al., 2022; Huang et al., 2022). The relative pressure (P/Po) was set as the threshold to divided the pore size distribution into two groups. The first group with P/Po=0-0.5 is subjected to the monolayer-multilayer adsorption process controlled by van der Waals force, while the second group with P/Po=0.5-1.0 experiences the capillary condensation adsorption process controlled by surface tension (Sun et al., 2015; Wang et al., 2015). In this paper, the Frenkel-Halsey-Hill (FHH) model is used to calculate the fractal dimensions of these two groups of samples separately, which are denoted as D_2 and D_1 for the first and second groups, respectively.

Results

Reservoir space characteristics

Organic pore

Organic pores are generally considered to be the main pore type of shale reservoirs and one of the key factors for shale gas enrichment (Xi et al., 2018; Cai et al., 2022; Wang et al., 2022; Xi et al., 2022). Organic matters in Lianggaoshan shale is mainly woody organic matter, followed by solid bitumen. The results of argon ion polishing scanning electron microscope show that the development of organic pores is different with different micro components. There are no organic pores in the woody organic matter (Figures 2A, B), but only shrinkage fracture at the edge of woody organic matter (Figure 2C). Both hydrogen-rich vitrinite and solid bitumen contain

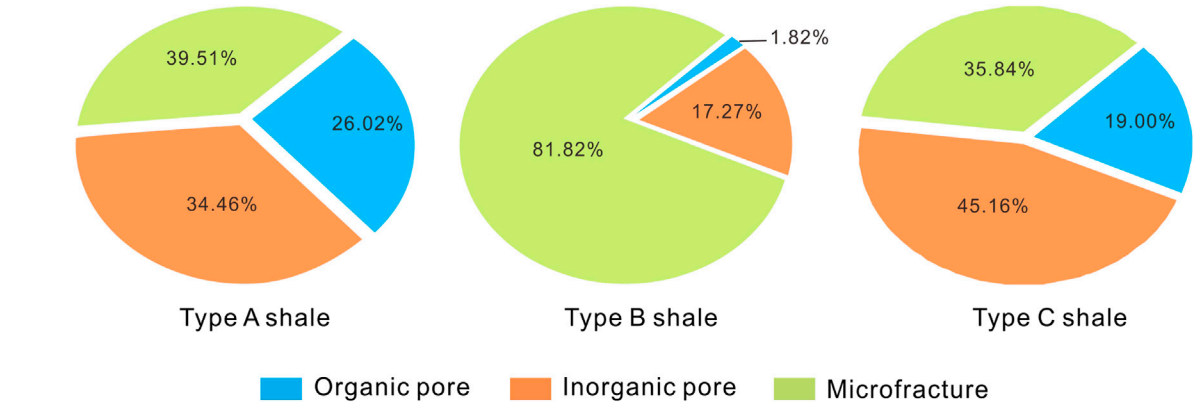

FIGURE 6
Histogram showing proportion of reservoir spaces of Jurassic Lianggaoshan Formation lacustrine shale in different lithology combination.

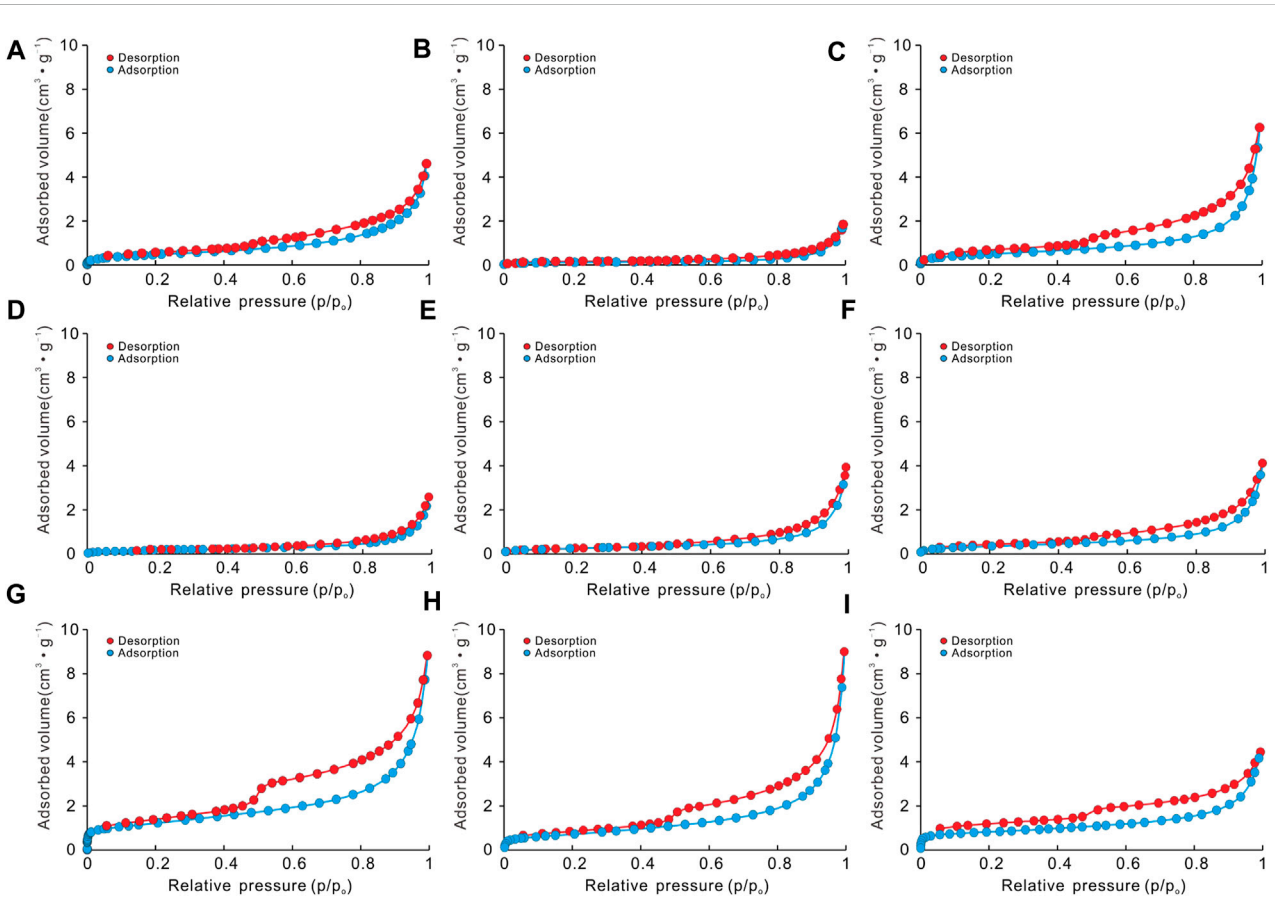

FIGURE 7
LTNA isotherms curves for the Lianggaoshan Formation lacustrine shale reservoir. **(A)** Type A shale, Well A, 2161.25 m; **(B)** Type A shale, Well B, 2455.06 m; **(C)** Type A shale, Well C, 1764.7 m; **(D)** Type B shale, Well D,2437.33 m; **(E)** Type B shale, Well B, 2452.29 m; **(F)** Type B shale, Well E, 1751.71 m; **(G)** Type C shale, Well A, 2164.49 m; **(H)** Type C shale, Well C, 1928.58 m; **(I)** Type C shale, Well D, 2465.48 m

varying degrees of round organic pores (Figures 2D, F). The development degree of shale organic pores in Type A and Type C shale is slightly higher (Figures 2D, E), mostly irregular, and the pore size is mostly 100nm–500 nm (Figure 2D). Type A shale locally develops honeycomb organic pores (Figure 2E), and the Type B shale organic pores are less developed (Figure 2F).

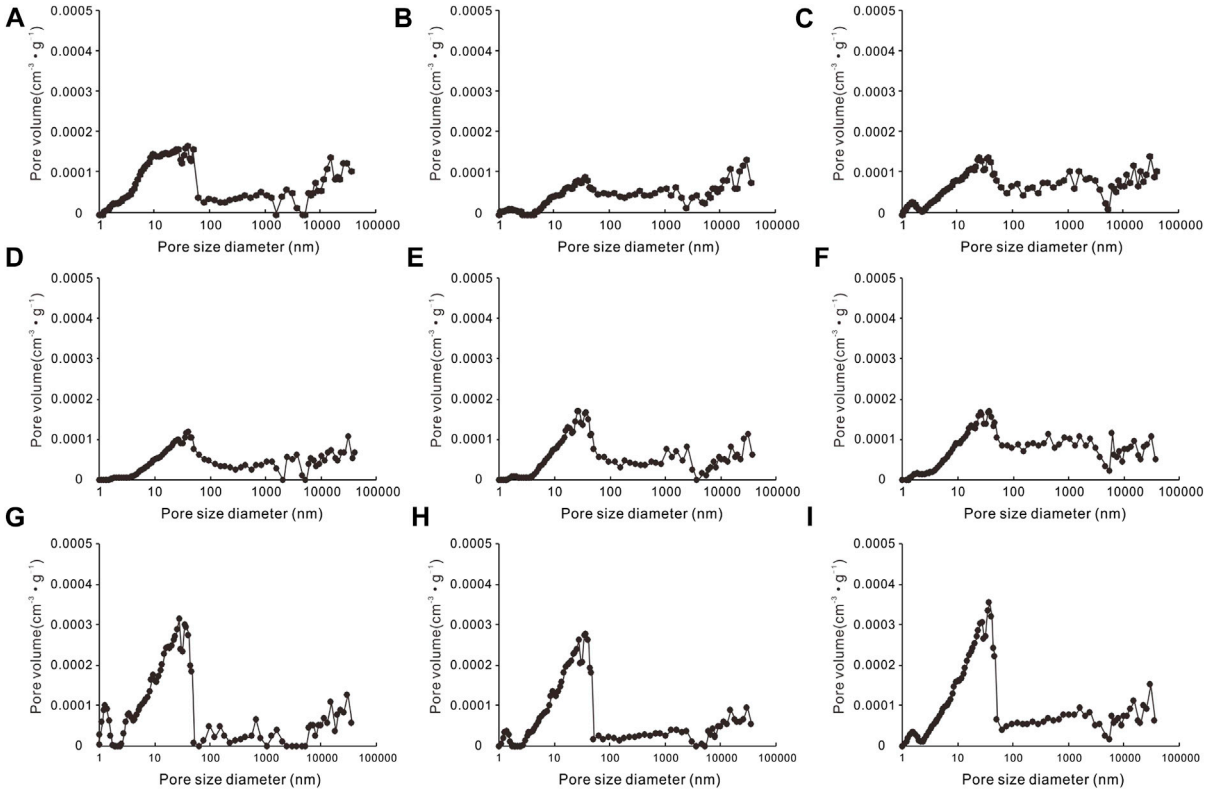

FIGURE 8
Pore-size distribution with MICP and LTNA for Jurassic Lianggaoshan Formation lacustrine shale in different lithology combination. **(A)** Type A shale, Well A, 2161.25 m; **(B)** Type A shale, Well B, 2455.06 m; **(C)** Type A shale, Well C,1896.18 m; **(D)** Type B shale, Well D, 2437.33 m; **(E)** Type B shale, Well B, 2452.29 m; **(F)** Type B shale, Well E, 1751.71 m; **(G)** Type C shale, Well A, 2164.49 m; **(H)** Type C shale, Well D, 2447.33 m; **(I)** Type C shale, Well E,1750.73 m.

Inorganic pore

According to the observation of argon ion polishing scanning electron microscopy, there are four types of inorganic pores developed in the lacustrine shale of Lianggaoshan Formation in the study area, including interparticle pore between grains, intraplatelet pore within clay aggregates, intercrystalline pore within pyrite framboids and intraparticle pore (Figure 3).

The interparticle pore is one of the main pore types of lacustrine shale in the Lianggaoshan Formation (Figure 3A). It is a primary pore between quartz, feldspar, clay minerals (such as illite, chlorite, etc.) and other particles arranged and accumulated, and remained after diagenetic compaction (Figure 3B). Through observation and analysis, it is shown that the micro-pores developed between mineral particles and between mineral particles and clay minerals in the study area are mainly triangular, polygonal, elongated and irregular in shape. The pore size range is large, nano-scale and micron-scale pores are developed, mainly formed by the contact of brittle particles and plastic particles. Since most of the intergranular pores with large pore size in the early stage were filled with asphalt, only part of the intergranular pores with relatively small pore size remained, which were preserved by a certain compressive supporting structure formed by the disorderly accumulation of clay minerals and brittle particles or clay minerals.

Intraplatelet pore is the micropore within illite and chlorite (Figure 3A). When shale pore water is alkaline and rich in potassium ions, montmorillonite will convert to illite as the burial depth increases, accompanied by a decrease in volume, resulting in intraplatelet pore. Intraplatelet pores are widely developed in lacustrine shale of Lianggaoshan Formation (Figure 3C), which are generally developed between illite lamellae and between illite and mica lamellae (Figure 3D). This type of pore morphology can be slit, triangle or polygon (Figure 3E). The formation of this kind of pores is caused by the early clay mineral pores (Figure 3F). With the increase of burial depth, the intraplatelet pore decreases rapidly under strong compaction.

Intraparticle pore is a secondary pore generated by the dissolution of soluble minerals such as feldspar and carbonate by acidic fluid produced after decarboxylation of organic matter (Figure 3B). The intraparticle pore size is relatively small, mainly between 0.05um and 4um (Figure 3G).

Intercrystalline pore within pyrite framboids is an intergranular micropore formed by mineral crystallization under stable environment and suitable medium conditions (Figures 3H, I). In general, the inorganic pores in Type A shale are mainly intraparticle pore, intercrystalline pore within pyrite framboids and interparticle pore, and the pore size of inorganic pores is more than 1 μm. The inorganic pores of Type C shale are mainly intraparticle pore, interparticle pore and intercrystalline pore within pyrite framboids. In contrast, Type B shale has the lowest development of inorganic pores.

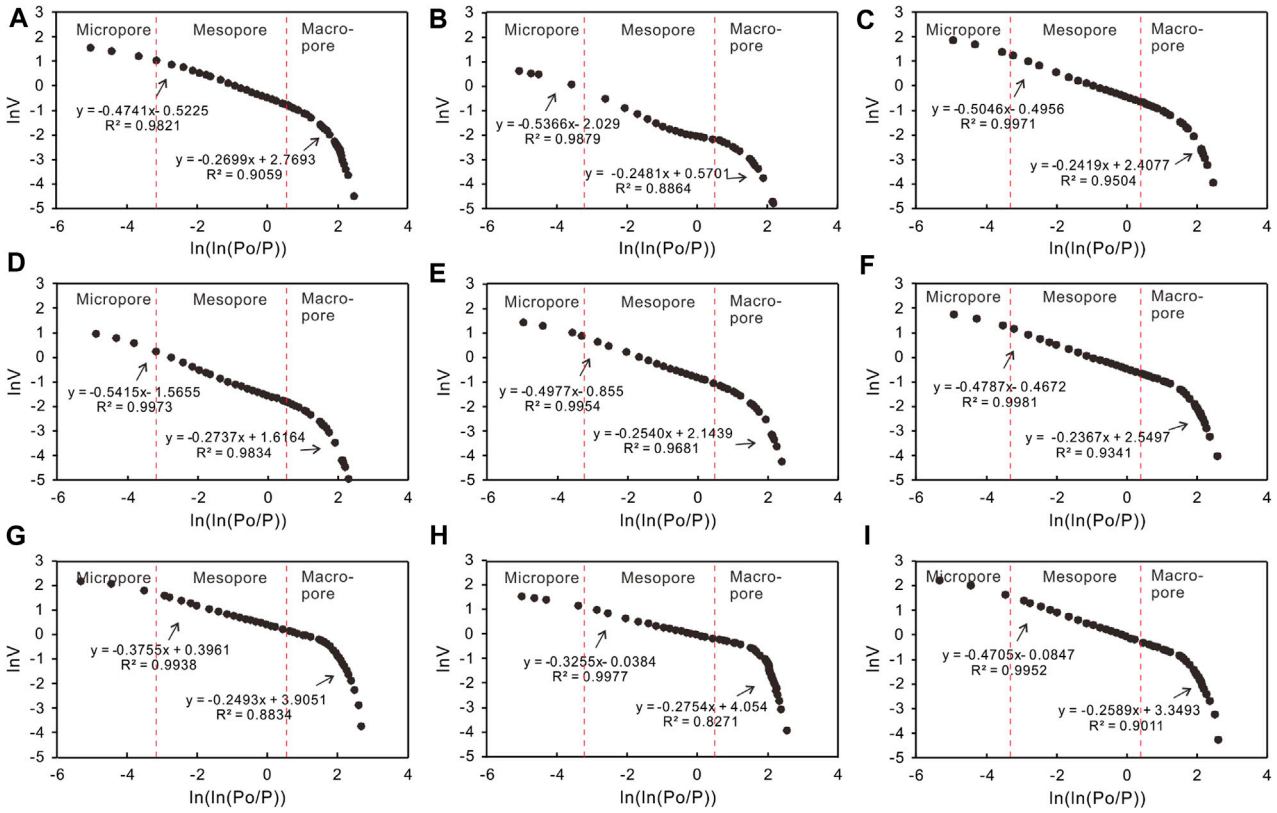

FIGURE 9
Schematic diagram showing fractal fitting of Jurassic Lianggaoshan Formation lacustrine shale in different lithology combination. Micropore, mesopore, and macropore are represented as the blue, red, and black hollow circles, respectively. **(A)** Type A shale, Well A, 2161.25 m; **(B)** Type A shale, Well B, 2455.06 m; **(C)** Type A shale, Well C, 1764.7 m; **(D)** Type B shale, Well D, 2437.33 m; **(E)** Type B shale, Well E, 1751.71 m; **(F)** Type B shale, Well C, 1894.02 m; **(G)** Type C shale, Well A, 2164.49 m; **(H)** Type C shale, Well D, 2465.48 m; **(I)** Type C shale, Well C, 1928.58 m

Microfracture

The microfractures developed in shale reservoirs are not only conducive to the enrichment of free gas, but also the main channel for shale gas seepage and migration, which plays a key role in the development of shale gas. According to the genesis of fractures, the microfractures in lacustrine shale of Lianggaoshan Formation can be divided into bedding fracture, shrinkage fracture and structural fracture (Figure 4).

Proportion of different reservoir spaces

Organic pores are generally lipophilic, while inorganic pores are mostly hydrophilic (Li et al., 2016). Tinni et al. (2014) used nuclear magnetic resonance experiments to identify the distribution characteristics of transverse relaxation time (T_2) of oil-wet pores and hydrophilic pores in shale gas reservoirs. It is generally believed that organic pores in shale gas reservoirs have strong oil wettability, while inorganic pores have strong water wettability. Accordingly, NMR experiments were conducted under water- and oil-saturated conditions, respectively, to observe the signal characteristics on the transverse relaxation time (T_2) distribution spectra of the two types of pores. The presence of three peaks in the T_2 spectra of lipophilic pores indicates three types of organic pores: volumetrically dominant small pores with short T_2, large pores with long T_2, and microfracture developed in organic matter (Figure 5). Based on the above theoretical understanding, Fu et al. (2021) proposed a method for calculating the proportion of organic and inorganic pores based on the wettability of shale pores.

The T_2 spectrum shows that the Type A shale saturated by oil exhibits unimodal characteristics, and the corresponding amplitude is high. The calculation results suggest that the organic pores account for 26.02% of all reservoir spaces, and the inorganic pores account for 34.46%. The T_2 spectrum shows that the Type B shale saturated by oil is also unimodal shape, the corresponding amplitude is low, and the organic pores only account for 1.82%. The T_2 spectrum shows that the Type C shale saturated by oil is unimodal shape. The corresponding amplitude is relatively higher than Type B shale. When shale sample is saturated with water, the corresponding amplitude exhibits much higher than shale sample saturated with oil. The organic pores in Type C shale account for 19.00% (Figure 6).

Pore structure quantitative characteristics

LTNA isotherms

The IUPAC classification of LTNA curves and hysteresis loops divides nanoscale pores into four different categories, i.e., cylindrical pores, ink bottle pores, parallel plate pores, and slit pores (Thommes et al., 2015). Results suggest that Type C shale

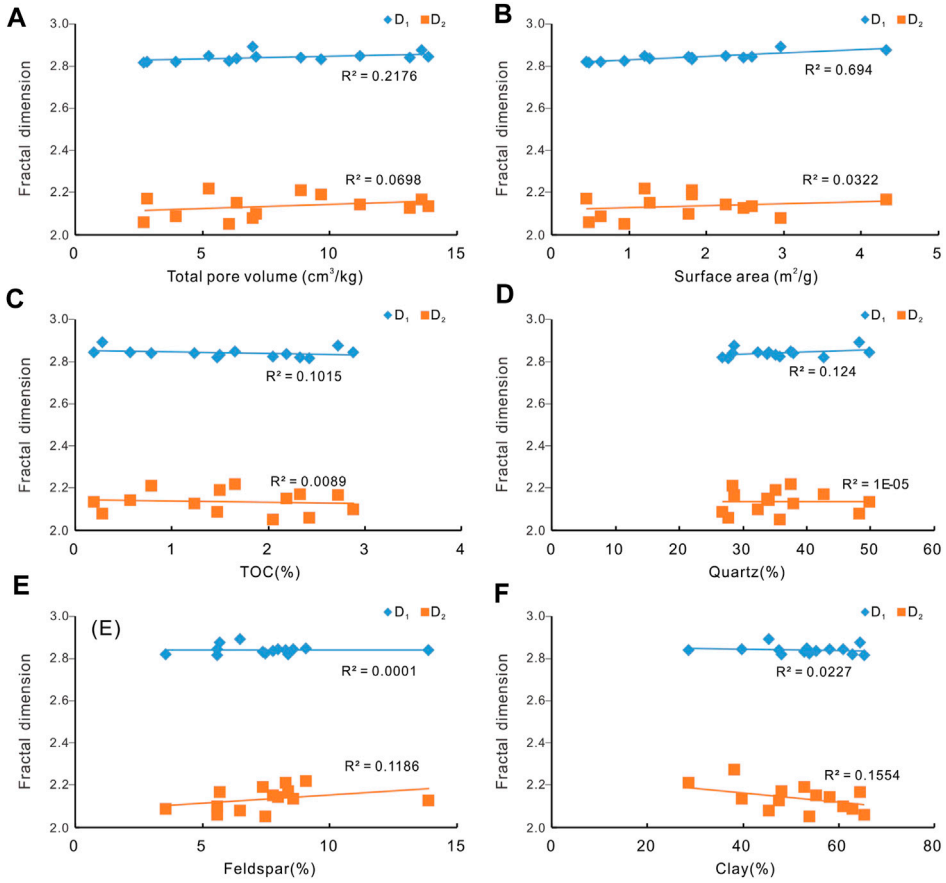

FIGURE 10
Correlation between the shale mineral composition and fractal dimension of the Jurassic Lianggaoshan Formation lacustrine shale. **(A)** Correlation between fractal dimensions and total pore volumn; **(B)** Correlation between fractal dimensions and surface area; **(C)** Correlation between fractal dimensions and TOC content; **(D)** Correlation between fractal dimensions and quartz content; **(E)** Correlation between fractal dimensions and feldspar content; **(F)** Correlation between fractal dimensions and clay content.

is dominated by parallel plate pores with high development and good connectivity. The Type A shale is dominated by parallel plate pores with lower development than Type C. The Type B shale is dominated by parallel plate pores with lowest development. Figures 7, 8.

Surface area (SA) and pore volume (PV)

The surface area of the Lianggaoshan shale samples were acquired through the BET model. The surface area of the Type C shale ranges from 0.48 m^2/g to 4.32 m^2/g and the SA of the Type B ranges from 0.63 m^2/g to 1.82 m^2/g. The surface area of the Type A shale ranges from 0.44 m^2/g to 1.81 m^2/g.

The pore volume range of the Lianggaoshan shale is between 2.73 cm^3/kg and 13.90 cm^3/kg (average value 7.99 cm^3/kg). The average pore volume of the Type A and Type B is 6.23 cm^3/kg and 6.33 cm^3/kg, lower than that of the Type C shale (10.28 cm^3/kg).

Pore-size distribution (PSD)

The PSD between 2nm and 100000 nm was acquired by integrating MICP and LTNA experiments. The results show that although the reservoir space of Lianggaoshan lacustrine shale is mainly mesopores ranging between 10nm and 50 nm and macropores ranging between 50nm and 100 nm.

Discussion

Through correlationship between shale reservoir key parameters and fractal dimension, the main controlling factors of pore structure are discussed. The fractal dimension D_1 reflects relative pressure (P/P_o) > 0.5, representing capillary condensation. The fractal dimension D_2 reflects relative pressure (P/P_o) < 0.5, representing mono- and multi-layer adsorption (Figure 9).

For Lianggaoshan shale, the D_1 reflects the micropore development, and D_2 reflects the development degree of mesopore-macropore. D_2 is generally larger than D_1 and is closer to 3, suggesting that the mesopore-macropore has a simpler pore structure than micropore, and its heterogeneity is weaker. D_1 is characterized by clearly positive correlation with SA and PV, suggesting micropores are major contributors to SA and PV of Lianggaoshan shale (Figures 10A, B).

The correlation between TOC and D_1 is slightly positive, indicating that the enrichment of organic matter has little effect on the formation of micropores (Figure 10C). In addition, the enrichment of organic matter does not affect the mesopore-macropore development as well. Due to the low content of quartz in Lianggaoshan lacustrine shale, which is mainly detrital quartz, it does not significantly affect the formation of micropore and mesopore-macropore (Figure 10D). A slight positive correlation exists between D_2 and feldspar content, indicating that intraparticle pores developed in feldspar particles provide partial mesopore-macropore but not micropores (Figure 10E). There is no correlationship between clay mineral content and D_1, suggesting clay minerals has no perceptible effect on the formation of micropore. Meanwhile, there is a slightly negative correlationship between clay mineral and D_2, suggesting the existence of clay minerals is unfavorable to the development of mesopore-macropore (Figure 10F).

Conclusions

1) Three types of lithology combination developed in the Jurassic Liangggaoshan lacustrine shale. Type A comprises pure shale. Type B is characterized by frequent shell limestone interbedding. Type C is characterized by frequent siltstone interbedding.

2) Organic pore, inorganic pore (including intraparticle pore in feldspar, interparticle pore, and intercrystalline pore between pyrite crystals), and microfractures compose reservoir spaces of Jurassic Liangggaoshan lacustrine shale. Type A shale has the highest proportion of organic pores, while Type B has the lowest proportion. The pores of Lianggaoshan lacustrine shales are dominated by mesopores and part of the macropores. Among them, the PV and SA are both mainly dominated by micropores.

3) The enrichment of organic matter has little effect on the development of micropores, and does not affect the mesopore and macropore development as well. Quartz particles in Lianggaoshan lacustrine shale do not clearly facilitate the development of micropore and mesopore-macropore. Intraparticle pore in feldspar clast is an important component of mesopore and macropore. Clay minerals has no positive effect on the formation of micropore and mesopore-macropore.

Data availability statement

The raw data supporting the conclusion of this article will be made available by the authors, without undue reservation.

Author contributions

QL contributed as the major author of the article. SM, YZ, and PF conceived the project. SL, JH, and JZ collected the samples. RY and SC analyzed the samples. All authors contributed to the article and approved the submitted version.

Funding

The study was funded by the National Science Foundation of China (Grant Nos. 41302101 and 41330313), the Chuanqing Drilling Engineering Co., Ltd. E Class Scientific Research Project (Grant No. CQ2022B-Y-1-1) and the 973 Prophase Special Program of China (Grant No. 2011CB211701) is acknowledged. The authors declare that this study received funding from the Chuanqing Drilling Engineering Co., Ltd. The funder was not involved in the study design, collection, analysis, interpretation of data, the writing of this article or the decision to submit it for publication.

Conflict of interest

Authors QL, LQ, SC, and RY were employed by the CNPC Chuanqing Drilling Engineering Co., Ltd; Authors SM, YZ, and PF were employed by the PetroChina Southwest Oil and Gas Field Company; Author SL was employed by the Sichuan Yuesheng Energy Group Co., Ltd; Author JH was employed by the Chengdu Geoservice Oil and Gas Technology Development Company; Author JZ was employed by the Chengdu Caledonian Oil and Gas Technology Development Co., Ltd.

Publisher's note

References

Cai, G., Jiang, Y., Li, X., Sun, S., Fu, Y., Gu, Y., et al. (2022). Comparison of characteristics of transitional and marine organic-rich shale reservoirs. *Acta Sedimentol. Sin.* 40 (4), 1030–1042. doi:10.14027/j.issn.1000-0550.2021.069

Chen, D., Zhang, J., Wang, X., Lan, B., Li, Z., and Liu, T. (2018). Characteristics of lacustrine shale reservoir and its effect on methane adsorption capacity in Fuxin Basin. *Energy and Fuels* 32 (11), 11105–11117. doi:10.1021/acs.energyfuels.8b01683

Cheng, D., Zhang, Z., Hong, H., Zhang, S., Qin, C., Yuan, X., et al. (2023). Sedimentary and provenance characteristics and the basin-mountain relationship of the jurassic Lianggaoshan Formation in eastern Sichuan Basin, SW China. *Petroleum Explor. Dev.* 50 (2), 1–11. doi:10.11698/PED.20220412

Dong, D., Liang, F., Guan, Q., Jiang, Y., Zhou, S., Yu, R., et al. (2022). Development model and identification evaluation technology of Wufeng-Longmaxi Formation quality shale gas reservoirs in the Sichuan Basin. *Nat. Gas. Ind.* 42 (8), 96–111. doi:10.3787/j.issn.1000-0976.2022.08.008

Fan, C., Li, H., Qin, Q., He, S., and Zhong, C. (2020). Geological conditions and exploration potential of shale gas reservoir in Wufeng and Longmaxi Formation of southeastern Sichuan Basin, China. *J. Petroleum Sci. Eng.* 191, 107138. doi:10.1016/j.petrol.2020.107138

Fan, C., Xie, H., Li, H., Zhao, S., Shi, X., Liu, J., et al. (2022). Complicated fault characterization and its influence on shale gas preservation in the southern margin of the Sichuan Basin, China. *Lithosphere* 2022, 8035106. doi:10.2113/2022/8035106

Fu, Y., Jiang, Y., Dong, D., Hu, Q., Lei, Z., Peng, H., et al. (2021). Microscopic pore-fracture configuration and gas-filled mechanism of shale reservoirs in the Western chongqing area, Sichuan Basin, China. *Petroleum Explor. Dev.* 48 (5), 1063–1076. doi:10.1016/S1876-3804(21)60091-5

Fu, Y., Jiang, Y., Xia, G., Chen, H., Zhou, K., Wang, J., et al. (2020). Optimization of GRI porosity determination method for marine shale. *Nat. Gas. Ind.* 40 (10), 20–28. doi:10.3787/j.issn.1000-0976.2020.10.003

Gu, Y., Cai, G., Hu, D., Wei, Z., Liu, R., Han, J., et al. (2022c). Geochemical and geological characterization of upper permian linghao Formation shale in nanpanjiang basin, SW China. *Front. Earth Sci.* 10, 883146. doi:10.3389/feart.2022.883146

Gu, Y., Hu, D., Wei, Z., Liu, R., Hao, J., Han, J., et al. (2022b). Sedimentology and geochemistry of the upper permian linghao formation marine shale, central nanpanjiang basin, SW China. *Front. Earth Sci.* 10, 914426. doi:10.3389/feart.2022.914426

Gu, Y., Li, X., Qi, L., Li, S., Jiang, Y., Fu, Y., et al. (2022a). Sedimentology and geochemistry of the lower permian shanxi formation Shan 2^3 submember transitional shale, eastern Ordos Basin, north China. *Front. Earth Sci.* 10, 859845. doi:10.3389/feart.2022.859845

Guo, X., Borjigin, T., Wei, X., Yu, L., Lu, X., Sun, L., et al. (2022b). Occurrence mechanism and exploration potential of deep marine shale gas in Sichuan Basin. *Acta Pet. Sin.* 43 (4), 453–468. doi:10.7623/syxb202204001

Guo, X., Hu, D., Shu, Z., Li, Y., Zheng, A., Wei, X., et al. (2022a). Exploration, development and construction in the Fuling national shale gas demonstration area in Chongqing: Progress and prospect. *Nat. Gas. Ind.* 42 (8), 14–23. doi:10.3787/j.issn.1000-0976.2022.08.002

Han, H., Dai, J., Guo, C., Zhong, N., Pang, P., Ding, Z., et al. (2021). Pore characteristics and factors controlling lacustrine shales from the upper cretaceous Qingshankou formation of the Songliao Basin, northeast China: A study combining SEM, low-temperature gas adsorption and MICP experiments. *Acta Geol. Sin. Engl. Ed.* 95 (2), 585–601. doi:10.1111/1755-6724.14419

Huang, H., Li, R., Lyu, Z., Cheng, Y., Zhang, B., Jiang, Z., et al. (2022). Comparative study of methane adsorption of Middle-Upper Ordovician marine shales in the Western Ordos Basin, NW China: Insights into impacts of moisture on thermodynamics and kinetics of adsorption. *Chem. Eng. J.* 446, 137411. doi:10.1016/j.cej.2022.137411

Jiang, Y., Chen, L., Qi, L., Luo, M., Chen, X., Tao, Y., et al. (2018). Characterization of the lower silurian longmaxi marine shale in changning area in the south Sichuan Basin, China. *Geol. J.* 53, 1656–1664. doi:10.1002/gj.2983

Jiang, Y., Song, Y., Qi, L., Chen, L., Tao, Y., Gan, H., et al. (2016). Fine lithofacies of China's marine shale and its logging prediction: A case study of the lower silurian longmaxi marine shale in weiyuan area, southern Sichuan Basin, China. *Earth Sci. Front.* 23 (1), 107–118. doi:10.13745/j.esf.2016.01.010

Lei, W., Chen, D., Liu, Z., and Cheng, M. (2023). Paleoenvironment-driven organic matter accumulation in lacustrine shale mixed with shell bioclasts: A case study from the jurassic da'anzhai member, Sichuan Basin (China). *J. Petroleum Sci. Eng.* 220, 111178. doi:10.1016/j.petrol.2022.111178

Li, H. (2022). Research progress on evaluation methods and factors influencing shale brittleness: A review. *Energy Rep.* 8, 4344–4358. doi:10.1016/j.egyr.2022.03.120

Li, H., Zhou, J., Mou, X., Guo, H., Wang, X., An, H., et al. (2022a). Pore structure and fractal characteristics of the marine shale of the longmaxi Formation in the changning area, southern Sichuan Basin, China. *Front. Earth Sci.* 10, 1018274. doi:10.3389/feart.2022.1018274

Li, J., Jin, W., Wang, L., Wu, Q., Lu, J., and Hao, S. (2016). Quantitative evaluation of organic and inorganic pore size distribution by NMR: A case from the silurian longmaxi formation gas shale in fuling area,Sichuan Basin. *Oil Gas Geol.* 37 (1), 129–134. doi:10.11743/ogg20160118

Li, J., Li, H., Yang, C., Wu, Y., Gao, Z., and Jiang, S. (2022b). Geological characteristics and controlling factors of deep shale gas enrichment of the Wufeng-Longmaxi Formation in the southern Sichuan Basin, China. *Lithosphere* 2022 (12), 4737801. doi:10.2113/2022/4737801

Li, Y., Zhou, A., Xie, W., Qiu, X., Dai, Y., Hu, X., et al. (2022c). Lithofacies divisionand main controlling factors of reservoir development in Wufeng Formation-Longilsub-member shale in the Luzhou region, South Sichuan Basin. *Nat. Gas. Ind.* 42 (8), 112–123. doi:10.3787/j.issn.1000-0976.2022.08.009

Liu, Y., Huang, C., Zhou, Y., Lu, Y., and Ma, Q. (2020). The controlling factors of lacustrine shale lithofacies in the Upper Yangtze Platform (South China) using artificial neural networks. *Mar. Pet. Geol.* 118, 104350. doi:10.1016/j.marpetgeo.2020.104350

Liu, Z., Hu, Z., Liu, G., Liu, Z., Liu, H., Hao, J., et al. (2021). Pore characteristics and controlling factors of continental shale reservoirs in the Lower Jurassic Ziliujing Formation, northeastern Sichuan Basin. *Oil Gas Geol.* 42 (1), 136–145. doi:10.11743/ogg20210112

Loucks, R. G., Reed, R. M., Ruppel, S. C., and Hammes, U. (2012). Spectrum of pore types and networks in mudrocks and a descriptive classification for matrix-related mudrock pores. *AAPG Bulltin* 96 (6), 1071–1098. doi:10.1306/08171111061

Peng, J., Hu, Z., Feng, D., and Wang, Q. (2022). Sedimentology and sequence stratigraphy of lacustrine deep-water fine-grained sedimentary rocks: The lower jurassic Dongyuemiao Formation in the Sichuan Basin, western China. *Mar. Petroleum Geol.* 146, 105933. doi:10.1016/j.marpetgeo.2022.105933

Qiu, Z., and He, J. (2022). Depositional environment changes and organic matter accumulation of Pliensbachian-Toarcian lacustrine shales in the Sichuan basin, SW China. *J. Asian Earth Sci.* 232, 105035. doi:10.1016/j.jseaes.2021.105035

Rouquerol, J., Avnir, D., Fairbridge, C. W., Everett, D. H., Haynes, J. H., Pernicone, N., et al. (1994). Recommendations for the characterization of porous solids (Technical Report). *Pure Appl. Chem.* 66, 1739–1758. doi:10.1351/pac199466081739

Shu, Z., Zhou, L., Li, X., Liu, H., Zeng, Y., Xie, H., et al. (2021). Geological characteristics of gas condensate reservoirs and their exploration and development prospect in the Jurassic continental shale of the Dongyuemiao Member of Ziliujing Formation, Fuxing area, eastern Sichuan Basin. *Oil Gas Geol.* 42 (1), 212–223. doi:10.11743/ogg20210118

Sun, W., Feng, Y., Jiang, C., and Chu, W. (2015). Fractal characterization and methane adsorption features of coal particles taken from shallow and deep coalmine layers. *Fuel* 155, 7–13. doi:10.1016/j.fuel.2015.03.083

Sun, Y., Jiang, Y., Xiong, X., Li, X., Li, S., Qiu, Z., et al. (2022). Lithofacies and sedimentary environment evolution of the Shan23 Submember transitional shale of the Shanxi Formation in the Danilng-Jixian area, eastern Ordos Basin. *Coal Geol. Explor.* 50 (9), 104–114. doi:10.12363/issn.1001-1986.21.12.0821

Thommes, M., Kaneko, K., Neimark, A. V., Olivier, J. P., Rodriguez-Reinoso, F., Rouquerol, J., et al. (2015). Physisorption of gases, with special reference to the evaluation of surface area and pore size distribution (IUPAC Technical Report). *Pure Appl. Chem.* 87, 1051–1069. doi:10.1515/pac-2014-1117

Tinni, A., Odusina, E., and Sulucamain, I. (2014). "NMR response of brine, oil, and methane in organic rich shales," in *SPE USA unconventional resources conference: The woodlands* (Texas, USA: SPE), 98–106.

Wang, M., Xue, H., Tian, S., Wilkins, R. W. T., and Wang, Z. (2015). Fractal characteristics of upper cretaceous lacustrine shale from the Songliao Basin, NE China. *Mar. Petroleum Geol.* 67, 144–153. doi:10.1016/j.marpetgeo.2015.05.011

Wang, X., Jin, Z., Zhao, J., Zhu, Y., Hu, Z., Liu, G., et al. (2020). Depositional environment and organic matter accumulation of Lower Jurassic nonmarine fine-grained deposits in the Yuanba Area, Sichuan Basin. SW China. *Mar. Petroleum Geol.* 116, 104352. doi:10.1016/j.marpetgeo.2020.104352

Wang, Z., Jiang, Y., Fu, Y., Lei, Z., Xu, C., Yuan, J., et al. (2022). Characterization of pore structure andheterogeneity of shale reservoir from Wufeng Formation-Sublayers Long-1, in Western Chongqing based on nuclear magnetic resonance. *Earth Sci.* 47 (2), 490–504. doi:10.3799/dqkx.2021.076

Wei, G., Wang, W., Feng, L., Tan, X., Yu, C., Zhang, H., et al. (2021). Geological characteristics and exploration prospect of black shale in the Dongyuemiao member of lower jurassic, the eastern Sichuan Basin, China. *Front. Earth Sci.* 9, 765568. doi:10.3389/feart.2021.765568

Xi, Z., Tang, S., Wang, J., Yang, G., and Li, L. (2018). Formation and development of pore structure in marine-continental transitional shale from northern China across a maturation gradient: Insights from gas adsorption and mercury intrusion. *Int. J. Coal Geol.* 200, 87–102. doi:10.1016/j.coal.2018.10.005

Xi, Z., Tang, S., Zhang, S., Lash, G. G., and Ye, Y. (2022). Controls of marine shale gas accumulation in the eastern periphery of the Sichuan Basin, South China. *Int. J. Coal Geol.* 251, 103939. doi:10.1016/j.coal.2022.103939

Xu, Q., Liu, B., Ma, Y., Song, X., Wang, Y., and Chen, Z. (2017). Geological and geochemical characterization of lacustrine shale: A case study of the jurassic Da'anzhai member shale in the central Sichuan Basin, Southwest China. *J. Nat. Gas Sci. Eng.* 47, 124–139. doi:10.1016/j.jngse.2017.09.008

Yang, R., Hu, Q., Yi, J., Zhang, B., He, S., Guo, X., et al. (2019). The effects of mineral composition, TOC content and pore structure on spontaneous imbibition in Lower Jurassic Dongyuemiao shale reservoirs. *Mar. Petroleum Geol.* 109, 268–278. doi:10.1016/j.marpetgeo.2019.06.003

Yuan, T., Wei, X., Zhang, H., Li, C., Wei, F., Lu, L., et al. (2022). Shale petrofacies division of Wufeng-Longmaxi formations in Sichuan Basin and its periphery. *Petroleum Geol. Exp.* 42 (3), 371–414. doi:10.11781/sysydz202003371

Zhang, P., Lu, S., Li, J., Wang, J., Zhang, J., Chen, G., et al. (2023). Microscopic characteristics of pore-fracture system in lacustrine shale from Dongying Sag, Bohai Bay Basin, China: Evidence from scanning electron microscopy. *Mar. Petroleum Geol.* 150, 106156. doi:10.1016/j.marpetgeo.2023.106156

Zhang, P., Lu, S., Li, J., Chang, X., Li, J., Li, W., et al. (2020). Broad ion beam-scanning electron microscopy pore microstructure and multifractal characterization of shale oil reservoir: A case sample from dongying sag, Bohai Bay Basin, China. *Energy Explor. Exploit.* 38, 613–628. doi:10.1177/0144598719893126

Zhang, P., Misch, D., Hu, F., Kostoglou, N., Sachsenhofer, R. F., Liu, Z., et al. (2021). Porosity evolution in organic matter-rich shales (Qingshankou Fm.; Songliao Basin, NE China): Implications for shale oil retention. *Mar. Petroleum Geol.* 130, 105139. doi:10.1016/j.marpetgeo.2021.105139

Zhao, X., Zhou, L., Pu, X., Jin, F., Han, W., Shi, Z., et al. (2022). Theories, technologies and practices of lacustrine shale oil exploration and development: A case study of Paleogene Kongdian Formation in cangdong sag, Bohai Bay Basin, China. *Petroleum Explor. Dev.* 49 (3), 707–718. doi:10.1016/s1876-3804(22)60059-4

Zou, C., Zhu, R., Chen, Z., Ogg, J. G., Wu, S., Dong, D., et al. (2019). Organic-matter-rich shales of China. *Earth Sci. Rev.* 189, 51–78. doi:10.1016/j.earscirev.2018.12.002

frontiers | Frontiers in Earth Science

TYPE Original Research
PUBLISHED 28 March 2023
DOI 10.3389/feart.2023.1119600

OPEN ACCESS

EDITED BY
Hu Li,
Southwest Petroleum University, China

REVIEWED BY
Guodong Yang,
Wuhan University of Science and Technology, China
Dan Yong,
Chengdu Geological Survey Center, China

*CORRESPONDENCE
Wanli Yu,
yuwl_sc@cnpc.com.cn

SPECIALTY SECTION
This article was submitted to Structural Geology and Tectonics, a section of the journal Frontiers in Earth Science

RECEIVED 09 December 2022
ACCEPTED 28 February 2023
PUBLISHED 28 March 2023

CITATION
Hu X, Yu W, Yi C, Xiao C, Li J and Wang B (2023), Seismic prediction of shale reservoir quality parameters: A case study of the Longmaxi–Wufeng formation in the WY area.
Front. Earth Sci. 11:1119600.
doi: 10.3389/feart.2023.1119600

Seismic prediction of shale reservoir quality parameters: A case study of the Longmaxi–Wufeng formation in the WY area

Xiuquan Hu[1,2], Wanli Yu[3]*, Chi Yi[1,2], Chenjing Xiao[4], Jianghan Li[1,2] and Boqiang Wang[1,2]

[1]College of Energy, Chengdu University of Technology, Chengdu, China, [2]State Key Laboratory of Oil and Gas Reservoir Geology and Exploitation, Chengdu University of Technology, Chengdu, China, [3]Geological Exploration and Development Research Institute, CNPC Chuanqing Drilling Engineering Company Limited, Chengdu, China, [4]Sinopec Northwest Oilfield Branch, Urumchi, China

Shale is a crucial natural gas resource, attracting global exploration and development interest. China has abundant shale gas resources that will drive future oil and gas exploration advances by increasing reserves and production. The WY shale gas field is the most productive and has the greatest potential for exploration and development. This study analyzed high-quality shale logging response characteristics and drilling logging, seismic, and analytical test data in the WY area to establish a rock physical model of seismic attribute parameters and shale reservoir quality parameters. Seismic elastic parameters were converted into indicators that directly reflect shale reservoir quality, such as total organic carbon (TOC), high-quality reservoir thickness, porosity, brittleness index, and crack development strength. Corresponding regression equations were established to predict quality parameters.The results showed that shale reservoir quality parameters have a good correlation with seismic parameters. The TOC distribution ranged from 2% to 5% in the study area and was generally high in the north but low in the south. The high-quality shale reserve had a thickness of over 40 meters, and except for the northwest region, the porosity was nearly over 4%. The overall brittleness of the study area was favorable, and the brittleness index was over 35%, which is suitable for network fractures formation in subsequent fracturing operations. The anisotropy of shale in S_1l^{1} was small, and the overall fractures were underdeveloped in the study area. Drilling verifications showed that the prediction results of the quality parameters of high-quality shale reservoirs were consistent with actual drilling test results with high reliability. This study provides guidance for comprehensive prediction of sweet spots and subsequent fracturing and well location deployment.In summary, this study provides valuable insights into shale gas exploration and development in the WY area by establishing a rock physical model, predicting quality parameters, and offering guidance for fracturing and well location deployment.

KEYWORDS

seismic inversion, shale gas, Longmaxi-Wufeng formation, brittleness index, OVT gather, prestack-anisotropy

1 Introduction

As today's society and economy grow rapidly, the current exploitation of conventional oil and gas reservoirs has become insufficient in meeting the demand for oil and gas resources. Thus, the development and utilization of non-fossil and non-conventional oil and gas energy have been a new approach considering the rapid consumption and shortage of fossil energy. Natural gas resources are a type of clean energy with low carbon emission, high calorific value, large reserves, and wide distribution. The energy type is environmentally friendly, has a wide range of uses, and has good stability. These attributes play a unique role in energy conservation and emission reduction, coping with global climate change, and avoiding smog. For example, shale gas is an important natural gas resource that emits lower greenhouse gases than fossil fuels such as oil and coal; the emission levels are consistent with the general trend of low-carbon sustainable development in various countries. Recently, many countries have shown a keen interest in the exploration and development of shale gas. This follows the success of shale oil and gas development in North America, which not only helped the United States to realize the reversal of natural gas imports and exports, but also provided the country with a sustainable green development path while boosting shale gas development in other countries (Jiang et al., 2012; Teng and Liu 2013; Sarkar et al., 2018; Zou et al., 2021). Access to mature technology and massive output has helped the United States and Canada to achieve large-scale commercial exploitation of shale gas (Liss, 2014; Selçuk and İkbal 2016; Jasmin et al., 2016; Soeder 2017; Ladevèze et al., 2019; Fahad et al., 2021). Although the exploration and development of shale gas in China started late, it has developed rapidly, especially in the upper Yangtze region of south Sichuan, east Sichuan, southeast Chongqing, north Guizhou, and west Hubei, which is the main prospect area of shale gas in China (Jia et al., 2016; He et al., 2017; Ma and Xie., 2018). Considering the Sichuan Basin as an example, the shale gas reserve in the two shale sets in the Cambrian and Silurian systems are equivalent to 1.5–2.5 times the conventional natural gas resources in the basin. Therefore, a strong prospect exists for the exploration and development of shale gas resources in China, and a substantial resource base is available for expediting the exploration and development. The Changning–Weiyuan National Shale Gas Demonstration Zone and the Fuling National Shale Gas Demonstration Zone are China's largest shale gas production bases, with a daily output of 2.011×10^7 m^3. As the earliest shale gas discovery area in China, WY has developed an excellent shale gas production capacity after more than 10 years of exploration and development research, and its development prospects are relatively good (Wang et al., 2018; Zeng et al., 2018; Fan et al., 2020; Li et al., 2022). To promote the large-scale production construction in this area and the increase in shale gas production in Southwest China, it remains crucial to evaluate the favorable exploration spots in this area.

As an important unconventional oil and gas reservoir, shale has geological characteristics, such as self-generation, self-storage, adsorption accumulation, and hidden accumulation. Its reservoir evaluation and exploitation are significantly different from those of conventional natural gas (Zhang et al., 2021; Wang et al., 2016; Yang et al., 2016). Practical shale gas exploration and development have shown that this type of reservoir lacks natural productivity and requires reservoir stimulation through horizontal drilling, hydraulic fracturing, and other stimulants to achieve high production. The quality parameters of shale gas reservoirs are the key factors for shale gas drilling and fracturing selection evaluation and can indicate the shale gas resource potential. These parameters include organic carbon content, reservoir effective thickness, porosity, and brittleness index. For shale reservoirs with self-generation and self-storage properties, the development and distribution of fractures play a crucial role in the storage and migration of the shale gas, and a certain degree of the micro-fracture development zone is crucial to the construction of fracture networks in later fracturing construction (Wu, 2017; Li J. et al., 2022). Consequently, fracture prediction is also a major issue in shale gas exploration.

Previous studies have shown that through the abundance of organic matter and the effective thickness of the reservoir, the distribution and potential of the shale reservoir can be determined. Determine the oil and gas enrichment area through factors such as lithology and physical properties (porosity); And, determine the reservoir engineering quality through brittleness and fracture prediction, and select the appropriate fracturing section (Zheng et al., 2021; Li, 2022; Li et al., 2022). Therefore, research on the quality parameters of shale reservoirs is vital for predicting favorable zones, subsequent fracturing, and well site deployment. Previous studies on shale gas in the WY area have mainly focused on examining shale reservoir characteristics, while only a few have investigated the quality parameters of shale reservoirs. Moreover, only a few researchers have comprehensively predicted sweet spots through the seismic prediction of shale reservoir quality parameters while restricting further developments to subsequent exploration and development work. To estimate shale reservoir quality parameters accurately, we selected the Longmaxi–Wufeng Formation shale in the W204 well area as the research object in this study. The relationship between seismic elastic parameters and reservoir quality parameters was established by analyzing the shale reservoir's petrophysical properties in the work area through the analysis of high-quality shale logging response characteristics. The seismic data were converted into shale gas reservoir quality data. Meanwhile, pre-stack fracture prediction was performed, providing a basis for evaluating shale gas area selection in the work area and guiding the subsequent fracturing construction and well site deployment.

2 Geological background

The Sichuan Basin is located on the northwestern margin of the upper Yangtze platform and has experienced multiple periods of tectonic movement since the Sinian period. The Late Ordovician Five Peaks–Early Silurian Longmaxi period was a period of intense extension in southern China (Zhao et al., 2016; Niu et al., 2021; Li et al., 2023). The Longmaxi–Wufeng Formation in the Sichuan Basin is mainly exposed in southeastern Sichuan, Daba Mountain, Micang Mountain, Longmen Mountain, and the eastern side of the Kangdian ancient land on the basin's edge, where only the Huaying Mountain is exposed. The stratum is mainly buried at a depth of 2,000–4,000 m. The WY shale gas field is located in the low-fold structural belt in southwestern Sichuan (Figure 1), adjacent to the Weiyuan structure in the north and the Ziliujing anticline in the southeast; moreover, it is generally controlled by the large-scale

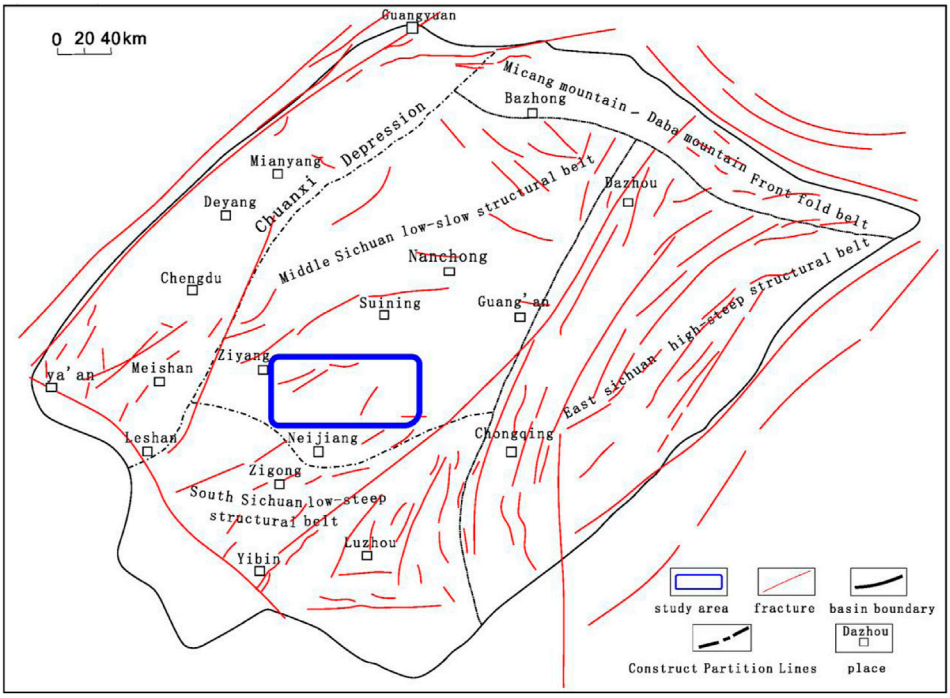

FIGURE 1
Structure location map of WY shale gas field.

dome anticline in Weiyuan (Dai et al., 2020). Several wells were drilled through the Silurian strata in Weiyuan, Luzhou, and eastern Sichuan, and the drilling shows that the Upper Ordovician Wufeng Formation–Lower Silurian Longmaxi Formation is in conformity contact; the lithological boundary is the Guanyinqiao section shell limestone at the top of the Wufeng Formation limestone. Organic-rich mud shale is 30–120 m thick and is the main target formation for exploration in the WY shale gas field (Figure 1).

The Longmaxi-Wufeng Formation in the study area is controlled by three paleo-uplifts affected by the Caledonian movement, namely the Central Sichuan paleo-uplift, the Central Guizhou paleo-uplift and the Kangdian ancient land. It is mainly a set of deep-water shelf facies deposits. The lithology is carbonaceous shale and argillaceous siltstone, which are widely distributed and relatively stable (Mou et al., 2016; Yang et al., 2019). The organic type is a sapropel-type organic formed by lower aquatic plankton and algae, mainly type I kerogen, with a kerogen index of more than 90%, mainly amorphous sapropel and algae. The sapropel group accounts for more than 95%.The Wufeng Formation in the study area can be divided into two members according to lithology and biological assemblage from bottom to top: the first and second members of the Wufeng Formation (Hu, 2021). The first member of the Wufeng Formation is black carbonaceous shale, which is rich in graptolite, slightly sandy, and siliceous, and it contains three graptolite belts. The depositional time limit was 2.46 Ma, with little lateral change. The second member of the Wufeng Formation is the original Guanyinqiao Formation. The main lithology is gray, gray-black, and medium-thick marl or argillaceous limestone. The deposition time limit was 0.73 Ma, and the lateral distribution was uneven. The Longmaxi Formation in the study area can be divided into two members according to lithology and biological assemblages (Shi et al., 2022). The first member is mainly black carbonaceous shale at the bottom, gray-black-dark gray shale and sandy shale in the middle, and dark gray-yellow-green calcareous shale in the upper part, including eight graptolite belts with a depositional time limit of 5.94 Ma. The second member of the Longmaxi Formation is a dark gray calcareous shale or gray-green sandy shale, and graptolites are rare here. The first Long segment is subdivided into subsegments Longyi 1 (S_1l^{1I}) and Longyi 2 (S_1l^{1II}). By comprehensively utilizing petrology, sedimentary structure, paleontology, and electrical properties, the Longyi 1 sub-member was subdivided into the Longyi 1^1 sub-member (S_1l^{1I-1}), Longyi 1^2 sub-member (S_1l^{1I-2}), Longyi 1^3 sub-member (S_1l^{1I-3}), and Longyi 14 sub-member (S_1l^{1I-4}). The Longyi 1^1 sub-member was in the most favorable microphase, with high organic matter abundance, well-developed organic pores, and high gas content while being the main sub-member for development (Table 1).

3 Methods and tests

According to the collected drilling logging data and the test analysis of core samples, we analyzed the high-quality shale logging response characteristics and conducted the rock physics analysis of organic carbon content, porosity, brittleness index, and other rock physics analyses of shale reservoirs. The relationship between seismic elastic parameters and reservoir quality parameters was established from the analysis of shale reservoir geological and logging response characteristics, combined with the rock physics analysis results. The post-stack inversion and pre-stack simultaneous

TABLE 1 Comprehensive stratigraphic division table of WY area.

Stratum				Characteristics	Thickness (m)	Sea level	Graptolite belt
Set	Segment	Sub-member	Thin layer				
Liangshan Group/Stone Niulan Group (P_1l/S_1sh)				The carbonaceous mud shale is bounded by the grey-green silty mudstone at the top of the Longmaxi Formation, with high GR, AC, CNL, low RT, and DEN	2–10		
Longmaxi Formation (S_1l)	Long2 segment (S_1l^2)			The gray-black shale at the bottom of the Long 2 Member and the rhythmic layer boundary between the black shale and gray silty shale overlay the Long 1 Member below; the DEN boundary is obvious	100–250	Marine transgression again	LM7-9
	Longyi segment (S_1l^1)	Longyi 2 (S_1l^{1l1})		The lithology is demarcated by the dark gray shale at the bottom of Longyi 2 and the gray-black shale at the bottom of Longyi 1. The overall GR and AC are lower than those of Longyi 1, the overall DEN is higher than that of Longyi 1, and the overall TOC of Longyi 2 is less than 2%	100–150	Stage of the marine retreating	
		Longyi 1 (S_1l^{1l})	4 (S_1l^{1l-4})	Thick, black silty shale, calcareous shale, GR is relatively low and flat-box type, 140–180 (API), AC, CNL lower than 3, DEN higher than 3, TOC lower than 3%	20–30		LM6
			3 (S_1l^{1l-3})	Marker layer, black carbonaceous, siliceous shale, GR gyro-type protruding from sublayers 4 and 2, 160–270 (API), high AC, low DEN, TOC similar to GR	4–10	Stage of the marine transgression	LM5
			2 (S_1l^{1l-2})	Thick, black carbonaceous shale, GR is low-flat box-shaped relative to sublayers 3 and 1, similar to sublayer 4, GR140–180 (API), stable TOC distribution, lower than sublayers 1 and 3	3–8		LM2-4
			1 (S_1l^{1l-1})	The marker layer is black carbonaceous and siliceous shale. The GR at the bottom shows the highest value in the Longmaxi Formation, at 170–500 (API), the TOC is 4%–12%, and the lower half of the maximum GR value is 1 at the bottom boundary	2–6		LM1
Wufeng Formation (O_3w)	Wu2 segment (O_3w^2)			The top boundary is the shell limestone of the Guanyinqiao Member, with a thickness of less than 1 m, and the carbonaceous siliceous shale of the Wufeng Formation below; the boundary is the lower half-amplitude point of the GR finger-shaped peak, and the high GR is delineated into the Longmaxi Formation, and this interval presents the characteristics of low GR	0.5–15	Initial stage of the marine transgression	WF4
	Wu1 segment (O_3w^1)						WF1-3
Linxiang Group (O_3l)				Gray Nodular limestone, low GR, and Wufeng shale are demarcated, the shale decreases downward, the limestone is purer, and the electrical properties are low GR and high RT	5–20		

inversion technology of constrained sparse pulse were used to convert the seismic data into shale gas reservoir quality parameters, including organic carbon content, high-quality shale reservoir thickness, porosity, and brittleness content. Error statistics were then performed to illustrate the reliability of the method. Pre-stack anisotropic fracture prediction based on seismic data in the Offset-vector tiles (OVT) domain provides a basis for shale gas selection evaluation in the work area and guides subsequent well placement and fracturing operations. W204 is used as a drilling well for seismic inversion. W211 and W213 are used as wells for verification of seismic prediction results.

3.1 Sample tests

The Longmaxi Formation–Wufeng Formation shale reservoir in the WY area was systematically studied, three wells (W204, W211,

and W213) were considered, and one well core (W204) was observed in detail. We selected 69 core samples from the Longmaxi–Wufeng Formation shale section in the W204 well area for testing and analysis of total organic carbon (TOC), six samples for testing and analysis of total gas content, 75 samples for porosity testing, and 62 samples for brittleness index testing. The collected three-dimensional work area was approximately 383.72 km^2. Shale reservoir prediction was performed synthetically using the test, logging, and seismic data.

3.2 Rock physics

Models of rock physics link logging and seismic waves. The models provide basic data for rock physics sensitive parameter analysis and pre-stack inversion; they also transform seismic information into reservoir description parameters such as lithology, physical properties, and oil and gas properties to describe oil and gas reservoirs quantitatively and reduce reservoir prediction risks in rock physics research (Wang, 2015; Liu et al., 2017; Zhou et al., 2021; Miele et al., 2022). Through the intersection analysis of the quality and seismic parameters of the drilling shale reservoir in the W204 well area, we established various rock physical editions, such as the rock physical edition of the ratio of compressional and shear wave velocity and TOC, density and TOC, compressional wave impedance and porosity, density and porosity, brittleness index and density, the ratio of brittleness index to compression and shear wave velocity. These rock physical editions provides a basis for subsequent predictions of reservoir quality parameters.

3.3 Seismic inversion

Seismic inversion is a core technology for reservoir prediction (Zhou, 2015). We established the relationship between the seismic and evaluation parameters and proposed using Jason's constrained sparse pulse post-stack inversion and pre-stack simultaneous inversion to predict the quality parameters of shale gas reservoirs. These were based on the analysis of the geological characteristics and logging response characteristics of the Longmaxi–Wufeng Formation shale in the WY area, combined with the analysis results of the rock physical characteristics of the reservoir. The thickness and porosity of shale reservoirs can be predicted through post-stack impedance inversion. Similarly, pre-stack impedance inversion can be performed to obtain density, Young's modulus, Poisson's ratio, and brittleness index for TOC and brittleness prediction.

Because there are only three wells in the study area, post-stack inversion mainly adopts the constrained sparse pulse inversion method based on Jason. Constrained sparse pulse inversion is not based on the initial model but simply determines the reflection coefficient value according to the waveform relationship of the seismic waveform trace. It uses the well control interpolation model to control the low-frequency impedance trend and finally obtains the wave impedance inversion results (Helgesen et al., 2000; Taylor et al., 2015; Zhang and Yin, 2015; Yuan et al., 2016). Although a low wave impedance resolution is obtained by this inversion type because it does not depend on the number of wells and the initial model, the inversion error caused by the deviation of the initial model is avoided due to the small number of wells. The impedance difference depends more on the seismic reflection energy difference; therefore, it can depict the formation's horizontal and vertical variations more accurately. Compared with post-stack inversion, simultaneous pre-stack inversion can obtain not only the P-wave impedance, but also the shear-wave impedance, density, and a series of elastic parameters derived accordingly (Figure 2). Therefore, pre-stack inversion can yield rich seismic elastic properties, which considerably increases the amount of information and number of methods for comprehensive geological and seismic interpretation.

3.4 Fracture prediction

Currently, seismic data are commonly used for fracture prediction, which can be roughly divided into three categories: multi-component converted wave fracture detection, post-stack seismic attribute analysis, and pre-stack anisotropic fracture detection (Dang et al., 2016; Bhattacharya and Mishra, 2018; Ge et al., 2021; Li H. et al., 2022; Ma et al., 2018; Zahm and Hennings, 2009; Zhang, 2010). However, multi-wave and multi-component data are rarely collected, and the resolution of the horizontal component data is typically lower than that of the vertical component. Hence, the horizontal component data cannot meet the general needs of fracture exploration. The post-stack seismic attribute detection fracture method is more suitable for inferring the general appearance of the fracture development area, and the calculated fracture accuracy is low. The use of pre-stack fracture prediction based on the OVT domain can improve the reliability and accuracy of the prediction results while addressing the problems of fracture orientation and fracture density or strength (Wu, 2017).

In this study, we used the pre-stack anisotropy of the amplitude variation with azimuth angle (AVAZ) based on OVT domain seismic data to perform fracture prediction investigations. Seismic waves produce certain anisotropic characteristics when passing through a fracture development zone (Ajaz et al., 2021), including AVAZ, apparent velocity variation with azimuth angle (VVAZ), wavelet frequency variation with azimuth angle (FVAZ), and frequency attenuation changes with azimuth angle (QVAZ) (Han et al., 2020). Monitoring these changes can help detect the orientation and development density of fractures (especially high-angle, high-density fractures). The azimuth variation characteristics of the bottom interface travel time and top interface amplitude of the fracture-developed layer and isotropic formation are simulated under a fixed offset. The simulation shows that in the presence of fracture-induced azimuthal anisotropy, the P-wave travel time and amplitude undergo approximately elliptical changes. In the direction of the fracture strike, the amplitude is large, whereas the travel time is short; in the vertical fracture direction, the travel time is large, whereas the amplitude value is small. Traditional common shot offset technology can be used to address the problem of VTI anisotropy. However, because the azimuth information cannot be saved by the common shot domain, the subsequent azimuthal anisotropy analysis is not feasible (Wu, 2017). OVT gather is a data domain method, which is a subdivision and reintegration form of cross-arranged

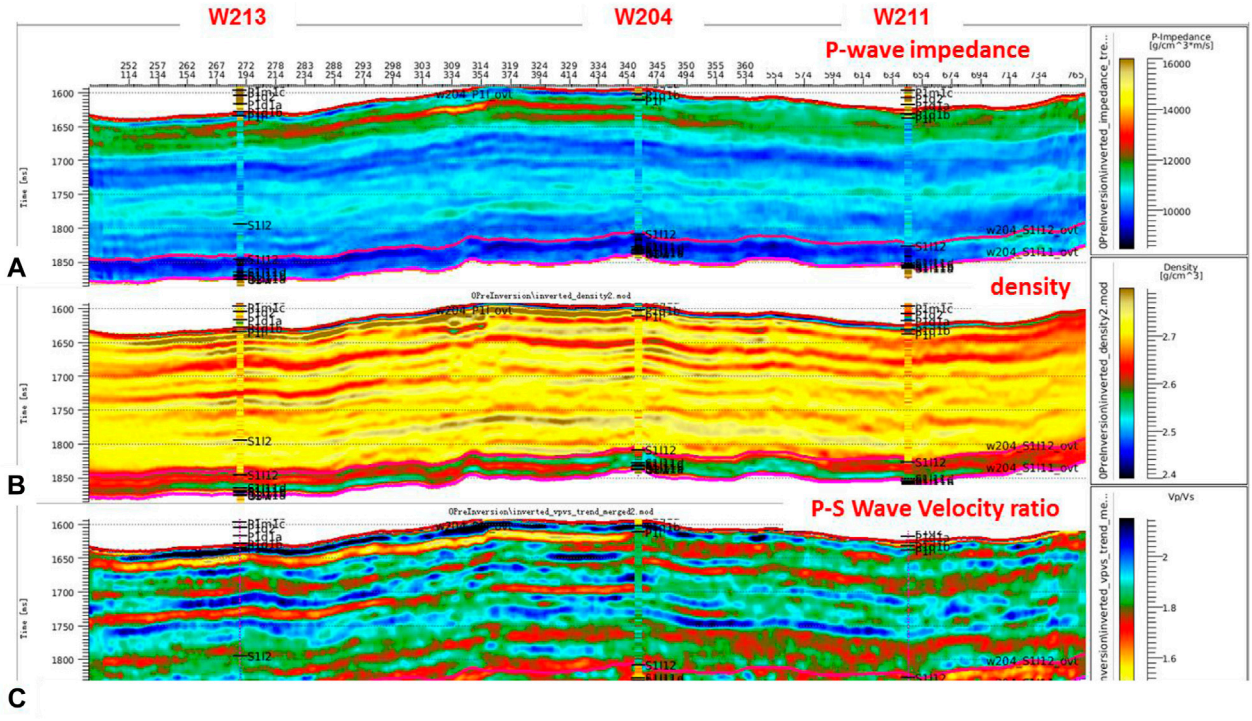

FIGURE 2
Seismic inversion section [**(A)** P-wave impedance inversion section, **(B)** density inversion section, **(C)** P-S Wave Velocity ratio inversion section].

subsets (Starr, 2000) that can be regarded as a single coverage of the entire work area. In the data volume, all seismic traces in the gather have roughly the same offset and azimuth (Cai, 2021), meaning OVT can be directly used for azimuth analysis after migration. This attribute is a major advantage of OVT technology (Dang et al., 2016; Wu, 2017). In addition, the number of gathers after OVT migration is large; the overall energy is more balanced; and the energy of near, medium, and far tracks tends to be consistent. OVT gathers can suppress multiple waves, highlight the energy of significant waves, and satisfy the impact of fracture prediction on the quality of seismic data requirements (Dang et al., 2016). Therefore, the pre-stack anisotropic fracture prediction based on the AVAZ was performed in the W204 well area using OVT gathers. The relevant data obtained can directly reflect vital information, such as reservoir fracture direction and density, which is helpful for drilling and developing oil wells.

4 Applications

4.1 Logging response characteristics of high-quality shale

We conducted a comprehensive logging evaluation, including physical property calculation, organic carbon content evaluation, gas content analysis, and brittleness coefficient evaluation. It was found that the high-quality shale in the WY area had the characteristics of "four highs": high organic matter, porosity, air content, and brittleness index. The logging response characteristics are low density and low P-wave velocity ratio. The specific high-quality shale logging response range is: density <2.66 g/cm^3, P-S wave velocity ratio <1.70, S-wave impedance <9500 m/s * g/cm^3. Well W204 was sampled to determine the log response characteristics of the high-quality shale member of Longyi 1 sub-members and Wufeng Group (Table 2; Figure 3).

4.1.1 Longyi 1^4 sub-member (S_1l^{1l-4})

The organic carbon content is between 1.0% and 2.7%, with an average of 2.2%; the porosity is between 4.0% and 6.5%, with an average of 5.7%; the gas content varies greatly and is within 1.1–3.3 m^3/t; the brittleness index is between 40% and 45%, and the overall fracturing ability is relatively general.

4.1.2 Longyi 1^3 sub-member (S_1l^{1l-3})

The organic carbon content is between 2.5% and 4.0%, with an average of 3.3%; the porosity is between 4.5% and 7.0%, with an average of 6.2%; the gas content is 2.5–4.0 m^3/t, with an average of 3.5 m^3/t; the brittleness index is between 45% and 60%, with an average of 50%, and the overall fracturing ability is excellent.

4.1.3 Longyi 1^2 sub-member (S_1l^{1l-2})

The organic carbon content is between 2.0% and 3.5%, and the distribution is stable, with an average of 2.8%; the porosity is between 4.5% and 7.0%, with an average of 6.0%; the gas content is 2.5–4.5 m^3/t, with an average of 3.5 m^3/t; the brittleness index is between 50% and 55%, and the overall fracturing ability is good.

TABLE 2 Statistical table of logging response characteristics of well W204.

Stratum	TOC (%)		Porosity (%)		Gas content (m^3/t)		Brittleness index (%)
	Range value	Average	Range value	Average	Range value	Average	
S_1l^{II1-1}	1.0–2.7	2.2	4.0–6.5	5.7	1.1–3.3		40–45
S_1l^{II1-2}	2.5–4.0	3.3	4.5–7.0	6.2	2.5–4.0	3.5	45–60
S_1l^{II1-3}	2.0–3.5	2.8	4.5–7.0	6.0	2.5–4.5	3.5	50–55
S_1l^{II1-4}	5.0–7.0	2.5	6.0–8.5	5.8	4.0–10.0	5.5	50–55
Wufeng Formation	1.0–2.5		2.0–5.0	4.0	1.0–4.5	2.0	45–50

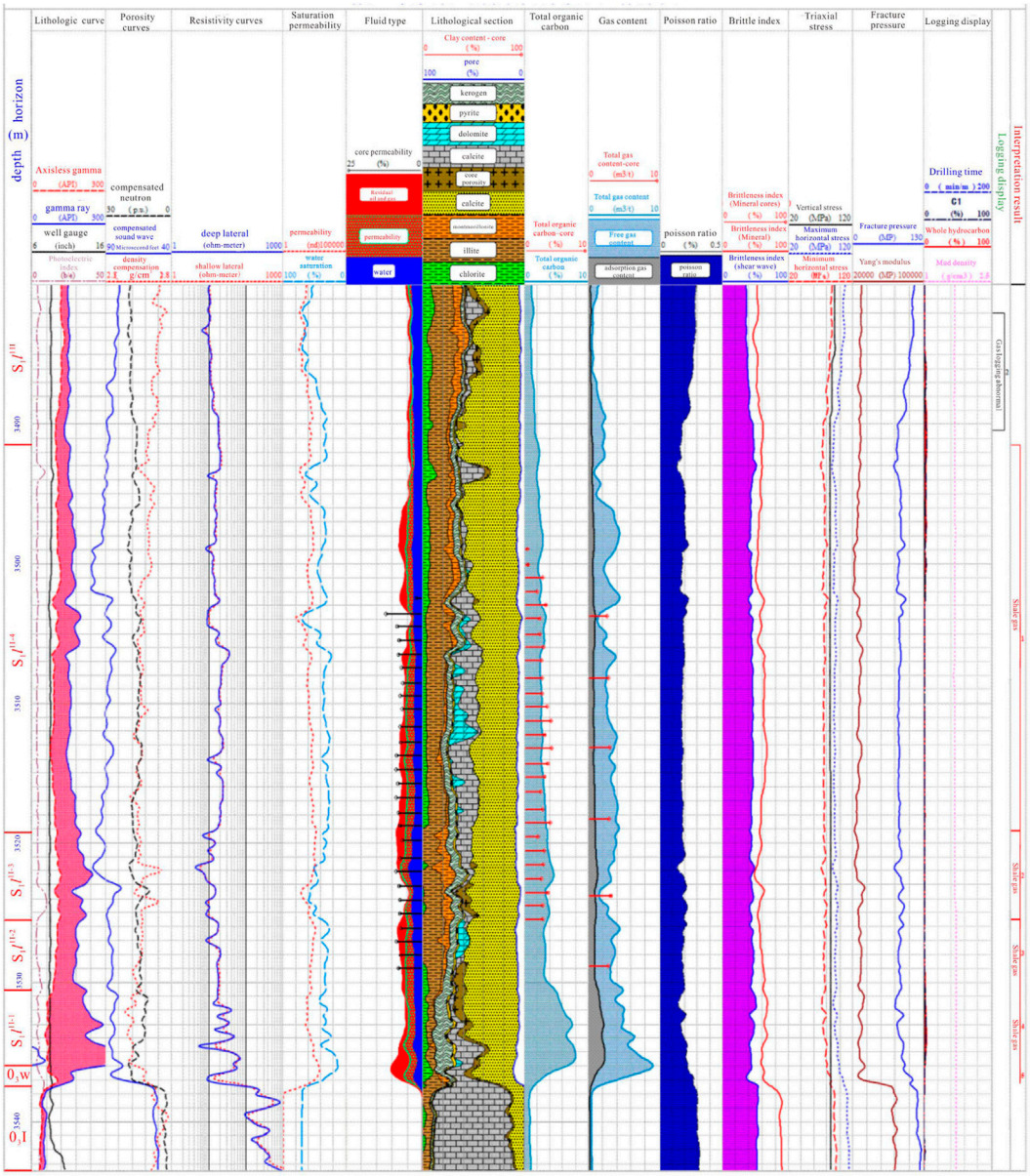

FIGURE 3
Logging curve characteristics and results of well W204.

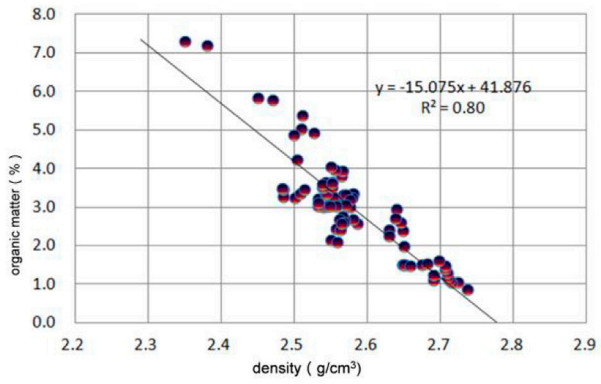

FIGURE 4
Cross plot of density and TOC.

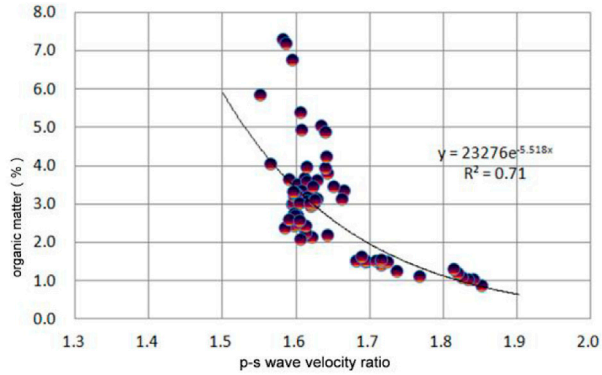

FIGURE 5
Cross plot of P-S wave velocity ratio and TOC.

4.1.4 Longyi 11 sub-member (S_1l^{11-1})

The organic carbon content is between 5.0% and 7.0%, with an average of 5.5%; the porosity is between 6.0% and 8.5%, with an average of 5.8%; the gas content is 4–10 m^3/t, with an average of 5.5 m^3/t; the brittleness index is between 50% and 55%, and the overall fracturing ability is outstanding.

4.1.5 Wufeng formation

The organic carbon content is between 1.0% and 2.5%; the porosity is between 2.0% and 5.0%, with an average of 4.0%; the gas content is 1.0–4.5 m^3/t, with an average of 2.0 m^3/t; the brittleness index is generally between 45% and 50%, and the overall fracturing ability is relatively general.

4.2 Total organic carbon prediction

4.2.1 Rock physical analysis of organic carbon content

The rock organic matter forms the material basis for the oil and gas formation. The amount of organic matter in the rock (i.e., the abundance of organic matter) mainly determines the hydrocarbon-generation capacity of the source rocks, and the TOC is often used to measure the abundance of organic matter. The TOC (%) in the rock refers to the ratio of the residual organic carbon content to the unit rock mass after a series of geological historical events in the rock (Xu et al., 2012). Therefore, the quality of shale gas reservoirs can be determined according to the TOC. The cross-analysis of TOC, gamma, density, neutron porosity, and acoustic time difference of the Longmaxi–Wufeng Formation shale reservoir in the W204 well block showed a good linear positive correlation between TOC and density in the target interval of this study. Moreover, the correlation coefficient reached 0.80 (Figure 4). Meanwhile, the TOC of the target interval in the study area has a good (correlation coefficient = 0.71) exponential relationship with the ratio of the compressional and shear wave velocity (Figure 5). According to the above analysis results, we developed a multiple regression model for organic matter, density, and velocity ratio of the longitudinal and shear waves, with a correlation coefficient of 0.84. The model is expressed as follows:

$$TOC = 35.44 - 12.08 \times DEN - 0.2587 \times e^{Vp/Vs};\ R^2 = 0.84,$$

where DEN is density [g/cm^3], and Vp/Vs is the ratio of longitudinal to shear wave velocity [non-dimensional].

4.2.2 Plane prediction of organic carbon content

The TOC is an index of the abundance of organic matter; it refers to the carbon content of the remaining organic matter in the rock after the oil and gas in the source rock escape. The TOC can adequately represent the gas production potential of the shale gas reservoir and is a key parameter for predicting the spatial and planar distributions of shale gas reservoirs by the seismic method. The test results of drilling samples show that the TOC content of shale reservoir in the study area is relatively high, ranging from 0.17% to 5.52%, with an average of 2.28%, which is medium-high organic carbon content. The samples with TOC greater than 1% account for 92.52% of the total. According to the previous rock physics analysis, the TOC and density have a good linear positive correlation (correlation coefficient = 0.71) in the WY area. Additionally, it has a good exponential correspondence with the ratio of compression and shear wave velocity. Therefore, as expressed above, we established a multivariate linear relationship between TOC, density, and the ratio of compression to shear wave velocity to predict the TOC (Figure 6A): $TOC=35.44–12.08\times DEN–0.2587\times e^{Vp/Vs}$, $R^2=0.84$. The TOC distribution map of the Longmaxi–Wufeng Formation shale in the W204 well area (Figure 7) shows that the TOC distribution ranges from 2.0% to 5.0%, and the average TOC is above 2.5%. The TOC was highest in the north and lowest in the south, with the characteristics in the part of southeast region being high TOC values. The actual TOC test and predicted data of the three wells in the study area were compared for error analysis (Table 3). The absolute and relative errors of wells W204, W211, and W213 were 0.3, 0.27, and 0.31, as well as 8.3%, 8.2%, and 9.4%, respectively. The overall relative error did not exceed 10%. Thus, the prediction results are credible.

4.3 Thickness prediction of high-quality reservoir

The thickness of the shale gas reservoir determines the gas content potential of the shale gas reservoir. High-quality shale reservoirs were classified according to the evaluation standard of

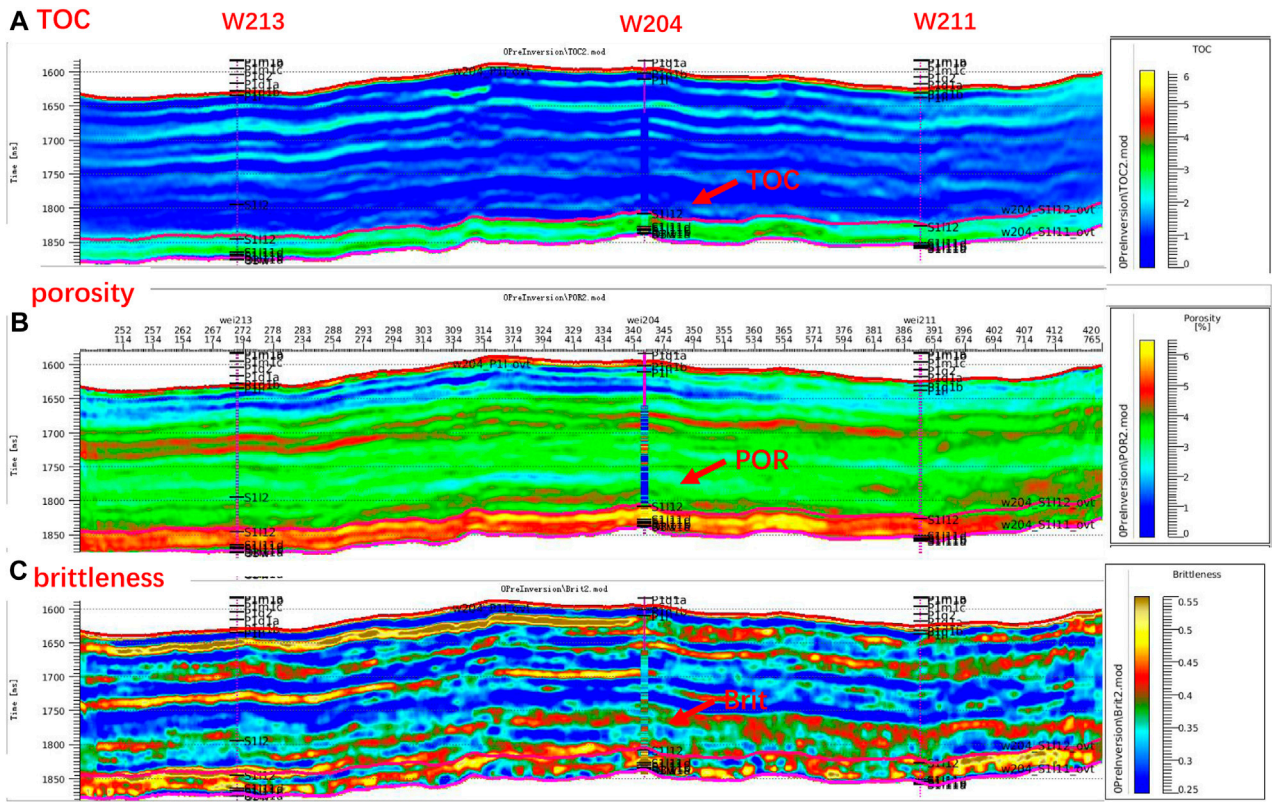

FIGURE 6
Shale reservoir quality parameters section [**(A)** TOC prediction section, **(B)** porosity prediction section, **(C)** brittleness index prediction section].

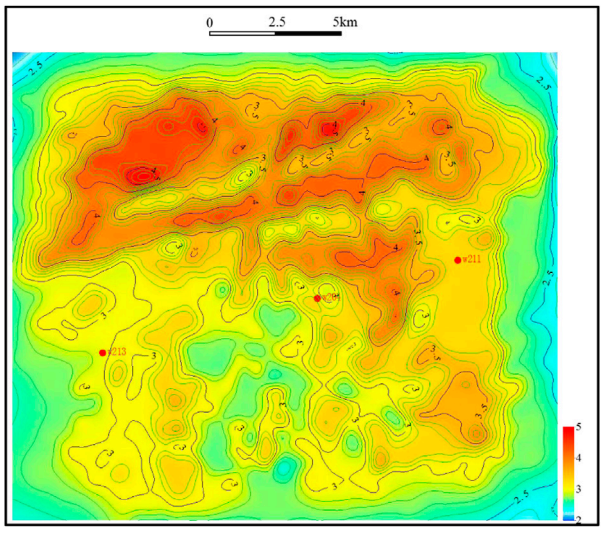

FIGURE 7
Planar distribution map of shale TOC in the W204 well area (%).

organic matter in the key geological parameters of the shale gas (Poor: TOC <1%; Average: TOC 1%–2%; Good: TOC >2%) (Dong et al., 2016). The thickness distribution range of high-quality shale reservoirs in the Longmaxi–Wufeng Formation was obtained using the threshold value TOC ≥2% (Figure 8). According to the analysis, the high-quality shale reservoirs in the Longmaxi–Wufeng Formation in the W204 well area are laterally stable, with an overall thickness of more than 40 m and local thicknesses ranging from 30 to 40 m and rarely thinner than 30 m. These values are consistent with the regional geological sedimentary law. For the error analysis, the thicknesses of the high-quality shale reservoirs in the three wells in the study area were compared with the predicted data (Table 4). The absolute and relative errors of wells W204, W211, and W213 were 2, 3.7, and 4.4 m, as well as < 4%, 6.6%, and slightly >8.3%. The relative error of the three wells was less than 9%, indicating that the prediction results are reliable.

4.4 Porosity prediction

4.4.1 Porosity rock physical analysis

The porosity of a rock refers to the ratio of the rock pore volume to rock volume (φ, %) (Xu et al., 2012). From the seismic perspective, porosity prediction primarily uses seismic technology to establish a correlation between porosity and rock physics characteristics to explain the reservoir's physical properties indirectly. Our intersection analysis showed that porosity had a good linear correlation with the density and P-wave impedance

TABLE 3 Statistical table of average TOC seismic prediction errors of shale in the W204 well area.

Well number	Average TOC (%)	Predicted average TOC (%)	Absolute error	Relative error (%)
W204	3.6	3.3	−0.3	8.3
W211	3.3	3.03	−0.27	8.2
W213	3.3	2.99	−0.31	9.4

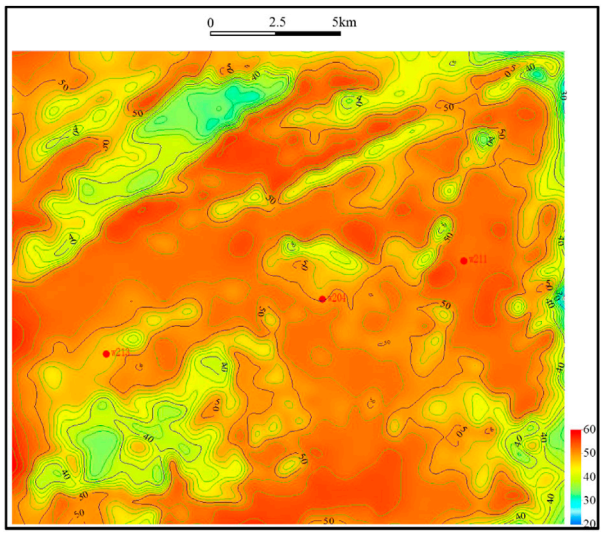

FIGURE 8
Planar distribution map of high-quality shale thickness in the W204 well area (m).

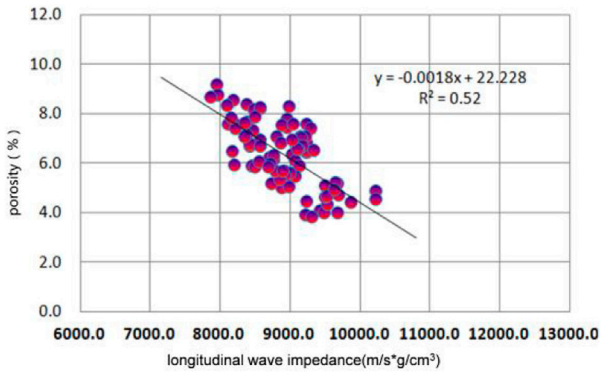

FIGURE 9
Cross plot of P-wave impedance and porosity.

(Figures 9, 10), and the correlation with other parameters is average. Porosity can be predicted by the P-wave impedance data volume and density velocity volume obtained by seismic inversion. According to the above intersection relationship, we developed the following multiple regression model of porosity, density, and P-wave impedance:

$$\varphi = 37.80 - 8.22 \times \mathrm{DEN} - 0.00114 \times \mathrm{ZVP};\ R^2 = 0.61,$$

where DEN is density [g/cm^3], and ZVP is longitudinal wave impedance [m/s · g/cm^3].

4.4.2 Porosity plane prediction

Organic pores are important storage spaces for shale gas. The development degree of organic pores is proportional to the gas content of shale gas and the gas production of a single well. The sample test in the study area shows that the physical properties of the shale layer are good. The porosity is between 2.02% and 10.05%, with an average of 5.75%. The pore types include organic pores, inorganic pores and microcracks. Thus, the accurate prediction of the porosity distribution can help understand the possible enrichment areas of shale gas. According to our rock physics analysis, porosity had the good positive correlation with P-wave impedance and density to predict the Porosity (Figure 6B). We established a multivariate linear relationship between porosity, P-wave impedance, and density: $\varphi = 37.80–8.22 \times \mathrm{DEN}—0.00114 \times \mathrm{ZVP}$; $R^2 = 0.61$. From the porosity plane distribution map of the high-quality shale reservoirs in the Longmaxi–Wufeng Formation in the W204 well block (Figure 11), it can be concluded that the overall porosity of the high-quality shale in the Longmaxi–Wufeng Formation changes slightly; the distribution range is 3%–7%, and the porosity of the rest of the region is almost greater than 4%, except for the northwest region, where the porosity is less than 4%. The high-quality shale porosity test data of the three wells in the study area were compared with seismic predictions (Table 5). The absolute

TABLE 4 Statistical table of the prediction error of high-quality shale reservoir thickness.

Well number	Thickness of high-quality shale reservoirs (m)	Predicted thickness of high-quality shale reservoirs (m)	Absolute error	Relative error (%)
W204	50	48	−2	4
W211	56	52.3	−3.7	6.6
W213	52.7	48.3	−4.4	8.3

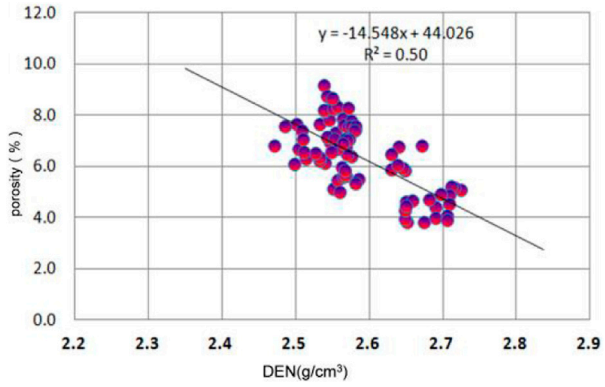

FIGURE 10
Cross plot of density and porosity.

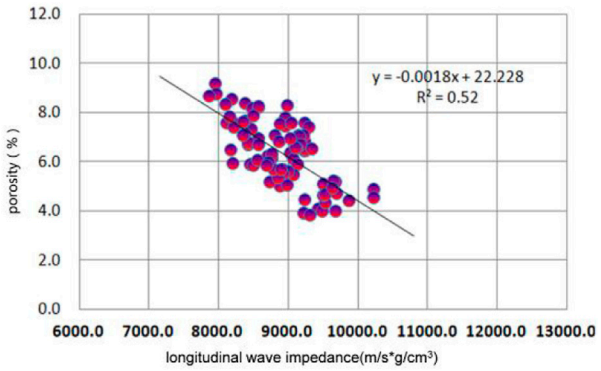

FIGURE 12
Cross plot of brittleness index and P-S wave velocity ratio.

and relative errors of wells W204, W211, and W213 were 0.61, 0.43, and 0.62, as well as 7.2%, 11.1%, and 10%, respectively. Thus, the porosity prediction results are more reliable.

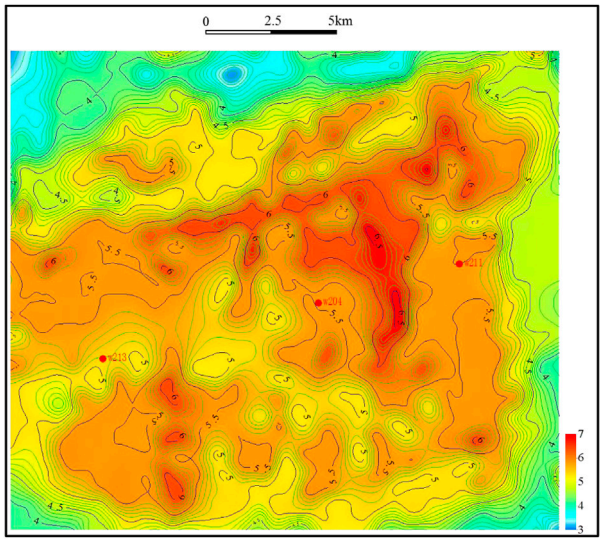

FIGURE 11
Planar distribution of porosity in W204 well area.

4.5 Brittleness prediction

4.5.1 Rock physical analysis of brittleness index

The brittleness index of shale reservoirs is a reliable basis for selecting well sections for horizontal fracturing. The Poisson's ratio and Young's modulus are important parameters of brittle minerals in shale reservoirs but do not directly reflect rock brittleness. The reservoir brittleness is expressed by normalizing both parameters; the larger Young's modulus, the smaller the Poisson's ratio, and the greater the reservoir brittleness. After the rock density, shear wave transit time, and longitudinal wave transit time are determined, both parameters are calculated, and the brittleness index of the reservoir is obtained (Qin and Yang, 2019). We determined the intersection of the brittleness index and parameters such as the ratio of longitudinal to shear wave velocities, wave impedance, and density; the parameters related to the brittleness index were optimized. The results show that the shale brittleness index in this area has a good correlation with the ratio of compression to shear wave velocity and density (Figures 12, 13); that is, a low ratio of compression to shear wave velocity and low density corresponds to a high brittleness index. Hence, we established a multiple regression model of the brittleness index, density, and ratio of longitudinal to shear wave velocities. The model is expressed as follows:

$$\text{Brittleness index} = 1.996 - 0.81 \times (\text{Vp/Vs}) - 0.061 \times \text{DEN};\ R^2 = 0.73,$$

where DEN is density [g/cm^3], and Vp/Vs is the ratio of longitudinal to shear wave velocities [non-dimensional].

TABLE 5 Statistical table of porosity prediction error of high-quality shale.

Well number	Average porosity (%)	Predicted average porosity (%)	Absolute error	Relative error (%)
W204	6.2	5.59	−0.61	9.8
W211	6	5.57	−0.43	7.2
W213	5.6	4.98	−0.62	11.1

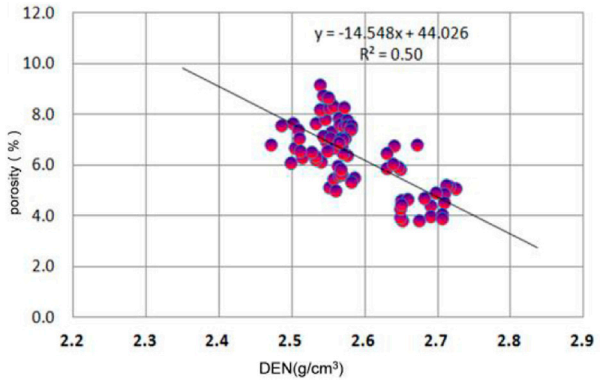

FIGURE 13
Cross plot of brittleness index and density.

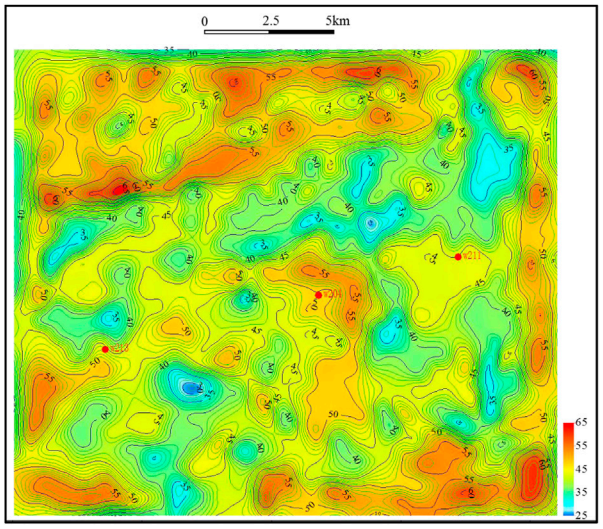

FIGURE 14
Planar distribution map of brittleness index in W204 well area.

4.5.2 Brittleness index plane prediction

The shale gas in a shale gas reservoir is trapped in mudstone and shale formations with hydrocarbon-generating ability in the adsorption or free states. The gas flow resistance in the reservoir is larger than that of conventional natural gas. Thus, fracturing technology is key for the commercial exploitation of shale gas, in which the brittleness of shale reservoirs has a significant influence on the effect of shale gas fracturing (Shi et al., 2015; Yan et al., 2021), and high brittle mineral content is the basis for natural fractures and fracturing in later developments. A rock structure with highly brittle minerals results in shale rock with a high Young's modulus and low Poisson's ratio. Moreover, it is easy to form natural fractures and artificially induced fractures, which is advantageous for the migration and enrichment space of shale gas. Therefore, it is important to estimate the brittleness index of shale gas reservoirs, which is crucial to subsequent fracturing.

The measured brittle mineral content of the samples in the study area is between 66.2% and 92.3%, with slight differences in each small layer. The brittle mineral content is generally stable on the plane, and the average value of each well area is generally greater than 60%. The reservoir compressibility is generally good. According to previous rock physics analysis results, the shale brittleness index in this area has a good correlation with the ratio of compression and shear wave velocity and density. Hence, a multiple regression model of the brittleness index, density, and ratio of compression to shear wave velocity was established to predict the Brittleness (Figure 6C): Brittleness index = 1.996–0.81 × (Vp/Vs)—0.061 × DEN; R^2 = 0.73. Through pre-stack simultaneous inversion, data volumes such as the ratio of P-to-shear wave velocity and density were obtained, and the brittleness index could be calculated by introducing it into the multivariate regression model of the brittleness index. The planar distribution of the brittleness index (Figure 14) revealed the following conclusions: The overall brittleness of the Longmaxi–Wufeng Formation shale in the study area was good. The brittleness index in most areas was greater than 35%, while it reached 65% in some areas. The overall compressibility was good, which was suitable for subsequent fracturing operations. The error analysis of the high-quality shale brittleness index and the predicted data of the three wells in the study area (Table 6) showed that the absolute error of the brittleness index of well W204 was small at 0.8, and the relative error was 1.5%; the absolute error of the brittleness indexes of wells W211 and W213 were highly similar, at 4.4 and 4, respectively, and the relative errors were 8.8% and 7.8%, respectively. The relative errors of the three wells were less than 10%, indicating that the porosity prediction results were reliable.

4.6 Fracture prediction

The hydrocarbon-generation potential of shale is the basis for shale gas production, and fracture development is the key to shale gas production. In low-permeability reservoirs, fracture development can improve reservoir performance and infiltration capacity, provide good channels for oil and gas migration, and control the distribution of oil and gas reservoirs. These factors are vital for studying formation pressure distribution and oil and gas development (Starr, 2000; Cai, 2021). The large-scale faults in the study area are not developed, but through the observation of the surrounding well rock cores, the fractures are developed (Figure 15). There are mainly two or more groups of cracks, among which the cracks in the near NS and near EW directions are the main ones. We performed the pre-stack anisotropic fracture prediction based on OVT data in the W204 well area.

First, we analyzed the OVT gathers, coverage time, and offset distance–azimuth angle of the 204 well in the W204 well area. In the 30 m × 30 m area, the maximum coverage time in the central area was 256 times, and the coverage time at the edge of the work area was short. The minimum and maximum offset distances were 1.414 m and 4476.45 m, respectively. The coverage time for each azimuth angle at medium and small offset distances was relatively uniform. In general, the gathers met the azimuth anisotropy analysis. Finally,

TABLE 6 Statistical table of the prediction error of high-quality shale brittleness index.

Well number	Brittleness index (%)	Predicted brittleness index (%)	Absolute error	Relative error (%)
w204	52	52.8	0.8	1.5
w211	50	45.6	−4.4	8.8
w213	51	47	−4	7.8

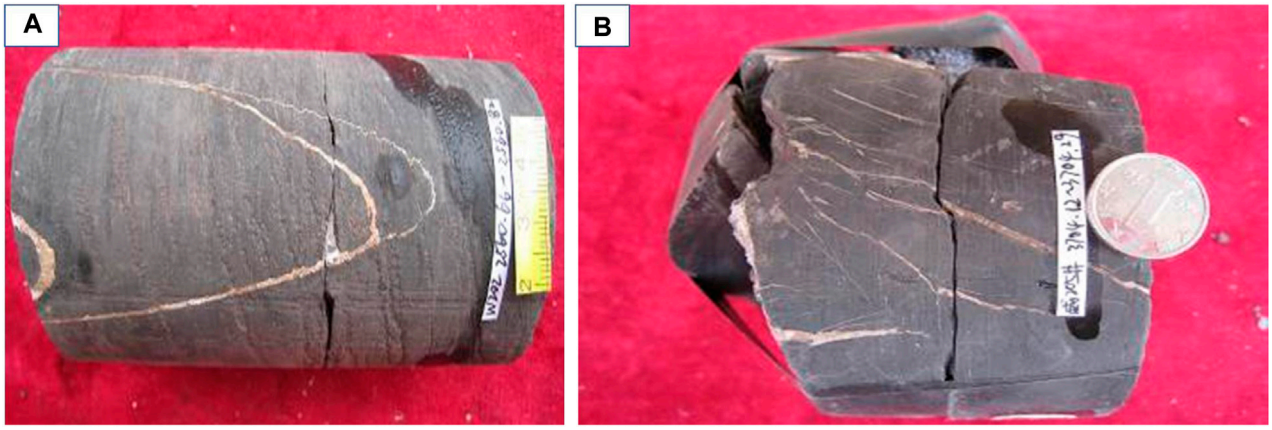

FIGURE 15
Rock core photos [**(A)** calcite full-filled high-angle fractures, W202 well, 2560 m **(B)** calcite full-filled multiple high-angle fractures, oblique fractures, W205 well, 3704 m].

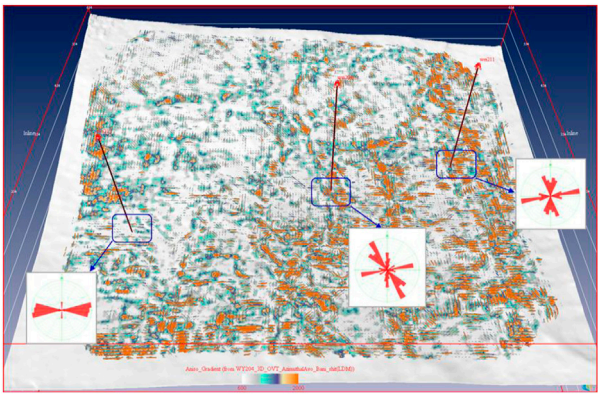

FIGURE 16
Three drilling locations of S_1l^{11} fracture direction statistics in the W204 well area.

the OVT data is used for superposition. The maximum incident angle of the target layer of the OVT gather reaches 30°, and five partial superpositions are determined, which are 1–9°, 6–14°, 11–19°, 16–24°, 21–29°, respectively. The wavelet morphology of the superimposed data at different angles is consistent. Finally, we used OVT data to perform pre-stack fracture inversion based on the AVAZ to obtain the density and orientation of the fracture development (Figure 16). The analysis showed that the anisotropy in the study area was generally weak, and the fractures in the shale section of the Longyi 1 sub-member (S_1l^{11}) were underdeveloped as a whole. Fractures were mainly developed in the EW and NS directions, and some were developed in the NW direction. Three groups of fractures were in the W204 well area, two in the W211 well area, and one in the EW direction in the W213 well area.

5 Conclusion

(1) The TOC distribution range of the Longmaxi–Wufeng Formation shale in the WY area was between 2% and 5%, with high TOC in the north and southeastern parts while low TOC is in the south. With 2% as the threshold value, the overall thickness of high-quality reservoirs was more than 40 m, and the thickness distribution in local areas was between 30 m and 40 m, extending in the direction of the NE–SW banding.

(2) The porosity of the Longmaxi–Wufeng Formation shale in the WY area changed slightly with a distribution range of 3%–7%. Except for the northwest region, almost all other areas had a porosity greater than 4%. The overall brittleness of the study area was relatively good. The brittleness index in most areas was greater than 35%, and the local brittleness index reached 65%, which is suitable for the formation of network fractures in subsequent fracturing operations. A comparison of the prediction results of this time with the

drilling test data showed that the relative error was almost less than 10%, and the reliability was high.

(3) The pre-stack anisotropic fracture prediction of AVAZ based on OVT data was performed in the WY area. The anisotropy in the study area was generally weak. The fractures in the shale of the Longyi 1 sub-member were underdeveloped as a whole, and the fracture development orientations were mainly east-west and north-south, followed by some fractures in the NW direction. Three groups, two groups, and one group of fractures were developed in the W204, W211, and W213 well areas, respectively.

(4) This study comprehensively studied quality parameters sensitive to shale reservoir productivity, such as TOC, reservoir thickness, porosity, brittleness index, and fracture development strength. Seismic prediction of quality parameters was performed to provide a comprehensive prediction for sweet spots and subsequent wells. This work provides an important basis for bit deployment and fracturing. Compared with the uncertainty of previous single method or single reservoir quality parameter prediction, this study uses a variety of methods including pre-stack and post-stack to carry out comprehensive prediction of various reservoir quality parameters, which is more reliable and worthy of promotion.

Data availability statement

The original contributions presented in the study are included in the article/supplementary material, further inquiries can be directed to the corresponding author.

Author contributions

XH and WY contributed to the conception and design of the study. XH and WY wrote the first draft of this manuscript. CX and CY conducted the investigations and data collation. JL and BW reviewed and edited the manuscript. All authors contributed to the revision of the manuscript and read and approved the version submitted.

Funding

This study was supported financially by the National Natural Science Foundation of China (Grant No. 42172175).

Acknowledgments

We would like to thank Chuanqing Drilling Engineering Co., Ltd. for providing data and allowing the publication of this article.

Conflict of interest

Author WY was employed by the company CNPC Chuanqing Drilling Engineering Company Limited. Author CX was employed by the company Sinopec Northwest Oilfield Branch.

The remaining authors declare that the research was conducted in the absence of any commercial or financial relationships that could be construed as a potential conflict of interest.

Publisher's note

All claims expressed in this article are solely those of the authors and do not necessarily represent those of their affiliated organizations, or those of the publisher, the editors and the reviewers. Any product that may be evaluated in this article, or claim that may be made by its manufacturer, is not guaranteed or endorsed by the publisher.

References

Ajaz, M., Ouyang, F., Wang, G. H., Liu, S. L., Wang, L. X., and Zhao, G. (2021). Fluid identification and effective fracture prediction based on frequency-dependent AVOAz inversion for fractured reservoirs. *Petroleum Sci.* 18 (4), 1069–1085. doi:10.1016/j.petsci.2021.07.011

Bhattacharya, S., and Mishra, S. (2018). Applications of machine learning for facies and fracture prediction using Bayesian Network Theory and Random Forest: Case studies from the Appalachian basin, USA. *J. Petroleum Sci. Eng.* 170, 1005–1017. doi:10.1016/j.petrol.2018.06.075

Cai, W. R. (2021). Application of five-dimensional regularization in OVT domain in high-density data processing of coal fields. *Coal Technol.* 40 (12), 86–90. doi:10.13301/j.cnki.ct.2021.12.021

Dai, X., Dong, D. Z., and Ni, Y. Y. (2020). Some essential geological and geochemical issues about shale gas research in China. *Nat. Gas. Geosci.* 31 (6), 745–760. doi:10.11764/j.issn.1672-1926.2020.05.016

Dang, Q. N., Cui, Y. F., Chen, M., Zhao, R. R., Liu, W. M., and Li, Y. (2016). Fracture detection with prestack seismic data in OVT domain: A case study of the ordovician carbonate reservoir in zg area of tazhong district in tarim basin. *Geophys. Geochem. Explor.* 40 (2), 398–404. doi:10.11720/wtyht.2016.2.27

Dong, D. Z., Wang, Y. M., and Huang, X. N. (2016). Discusion about geological characteristics, resource evaluation methods and its key parameters of shale gas in China. *Nat. Gas. Geosci.* 27 (9), 1583–1601. doi:10.11764/j.isn.1672-1926.2016.09.1583

Fahad, I. S., Salem, A., Temoor, M., Amirmasoud, K. D., and Shahin, N. (2021). Smart shale gas production performance analysis using machine learning applications. *Petroleum Res.* 7 (1), 21–31. doi:10.1016/j.ptlrs.2021.06.003

Fan, C. H., Li, H., Qin, Q. R., He, S., and Zhong, C. (2020). Geological conditions and exploration potential of shale gas reservoir in Wufeng and Longmaxi Formation of southeastern Sichuan Basin, China. *Petrol. Sci. Eng.* 191, 107138. doi:10.1016/j.petrol.2020.107138

Ge, X. Y., Mou, C. L., Yu, Q., Liu, W., Men, X., He, L., et al. (2021). A study on the enrichment of organic materials in black shales of the Wufeng to Longmaxi Formations in eastern Sichuan Basin. *Sediment. Tethys Geol.* 41 (03), 418–435. doi:10.19826/j.cnki.1009-3850.2020.12001

Han, Y., Zhao, Z., Wang, S. X., Qi, K. B., and Zhou, B. D. (2020). "Shale oil fracture prediction technology and application based on OVT seismic data," in SPG/SEG Nanjing 2020 International Geophysical Conference Papers, 1314–1317. doi:10.26914/c.cnkihy.2020.015057

He, L., Liu, W., Yang, P., Yu, Q., Wang, J., Wang, Z. J., et al. (2017). Genetic conditions of the shale gas and delineation of the favourable areas in the Wufeng Formation-Longmaxi Formation on the southwestern margin of the Sichuan Basin. *Sediment. Tethys Geol.* 37 (03), 50–58. Available at: https://kns.cnki.net/kcms/detail/detail.aspx?FileName=TTSD201703006&DbName=CJFQ2017.

Helgesen, J., Magnus, I., Prosser, S., Saigal, G., Aamodt, G., Dolberg, D., et al. (2000). Comparison of constrained sparse spike and stochastic inversion for porosity prediction at Kristin Field. *Soc. Explor. Geophys.* 19 (4), 400–407. doi:10.1190/1.1438620

Hu, K. (2021). Reservoir and sweet pot distribution characteristics of shale gas in Wufeng-Longmaxi Formation,southwest of Sichuan Basin. *Nconcentional oil&Gas* 8 (05), 34–44. doi:10.9901/j.fcgyq.2021.05.05

Jasmin, C., Dr, L. S., and Prof, A. A. (2016). Shale gas: A review of the economic, environmental, and social sustainability. *Energy Technol.* 4 (7), 772–792. doi:10.1002/ente.201500464

Jia, A. L., Wei, Y. S., and Jin, Y. Q. (2016). Progress in key technologies for evaluating marine shale gas development in China. *Petroleum Explor. Dev.* 43 (06), 1035–1042. doi:10.1016/s1876-3804(16)30120-3

Jiang, F. J., Pang, X. Q., and Ouyang, X. C. (2012). The main progress and problems of shale gas study and the potential prediction of shale gas exploration. *Earth Sci. Front.* 19 (02), 198–211. Available at: https://kns.cnki.net/kcms/detail/detail.aspx?FileName=DXQY201202030&DbName=CJFQ2012.

Ladevèze, P., Rivard, C., Lavoie, D., Séjourné, S., Lefebvre, R., and Bordeleau, G. (2019). Fault and natural fracture control on upward fluid migration: Insights from a shale gas play in the st. Lawrence platform, Canada. *Hydrogeology J.* 27, 121–143. doi:10.1007/s10040-018-1856-5

Li, H. (2022). Research progress on evaluation methods and factors influencing shale brittleness: A review. *Energy Rep.* 8, 4344–4358. doi:10.1016/j.egyr.2022.03.120

Li, H., Zhou, J. L., Mou, X. Y., Guo, H. X., Wang, X. X., An, H. Y., et al. (2022). Pore structure and fractal characteristics of the marine shale of the Longmaxi Formation in the changning area, southern Sichuan Basin, China. *Front. Earth Sci.* 10, 1018274. doi:10.3389/feart.2022.1018274

Li, J., Li, H., Xu, J. L., Wu, Y. J., and Gao, Z. (2022). Effects of fracture formation stage on shale gas preservation conditions and enrichment in complex structural areas in the southern Sichuan Basin, China. *Front. Earth Sci.* 9, 823855. doi:10.3389/feart.2022.921988

Li, J., Li, H., Yang, C., Ren, X. H., and Li, Y. D. (2023). Geological characteristics of deep shale gas and their effects on shale fracability in the Wufeng–Longmaxi Formations of the southern Sichuan Basin, China. *Lithosphere* 2023 (1), 4936993. doi:10.2113/1970/4936993

Li, J., Li, H., Yang, C., Wu, Y. J., Gao, Z., and Jiang, S. L. (2022). Geological characteristics and controlling factors of deep shale gas enrichment of the Wufeng-Longmaxi Formation in the southern Sichuan Basin, China. *Lithosphere* 2022, 4737801. doi:10.2113/2022/4737801

Liss, W. E. (2014). Impacts of shale gas advancements on natural gas utilization in the United States. *Energy Technol.* 2 (12), 953–967. doi:10.1002/ente.201402061

Liu, X. X., Guo, Z. Q., Liu, C., and Liu, Y. W. (2017). Anisotropy rock physics model for the Longmaxi shale gas reservoir, Sichuan Basin,China. *AppliedGeophysics* 14 (01), 21–30. doi:10.1007/s11770-017-0609-x

Ma, X. H., and Xie, . (2018). The progress and prospects of shale gas exploration and exploitation in southern Sichuan Basin, NW China. *Petroleum Explor. Dev.* 45 (01), 161–169. doi:10.11698/PED.2018.01.18

Ma, Y. S., Cai, X. Y., and Zhao, P. R. (2018). China's shale gas exploration and development: Understanding and practice. *Petroleum Explor. Dev.* 45 (04), 589–603. doi:10.1016/s1876-3804(18)30065-x

Miele, R., Barreto, B. V., Yamada, P., Varell, L. E. S., Pimentel, A. L., Costa, J. F., et al. (2022). Geostatistical seismic rock physics AVA inversion with data-driven elastic properties update. *IEEE Trans. Geoscience Remote Sens.* 60, 1–15. doi:10.1109/TGRS.2021.3135718

Mou, C. L., Wang, X. P., and Wang, Q. Y. (2016). Relationship between sedimentary facies and shale gas geological conditions of the Lower Silurian Longmaxi Formation in southern Sichuan Basin and its adjacent areas. *J. Palaeogeogr.* 18 (3), 457–472. doi:10.7605/gdlxb.2016.03.032

Niu, W. T., Zhu, D. X., and Jiang, L. W. (2021). Sweet spot"comprehensive evaluation technology of complex mountain shale gas reservoir: Taking the Zhaotong National Shale Gas Demonstration Zone as an example. *Nat. Gas. Geosci.* 32 (10), 1546–1558. doi:10.11764/j.issn.1672-1926.2021.07.0012021

Qin, H., and Yang, X. L. (2019). Long interpretation methods for measuring the brittleness of tight reservoir. *Well logging Technol.* 43 (05), 509–513+530. doi:10.16489/j.issn.1004-1338.2019.05.013

Sarkar, P., Singh, K. H., Ghosh, R., and Singh, T. N. (2018). Estimation of elastic parameters, mineralogy and pore characteristics of Gondwana shale in Eastern India for evaluation of shale gas potential. *Curr. Sci.* 115 (4), 710–720. https://www.jstor.org/stable/26978280. doi:10.18520/cs/v115/i4/710-720

Selçuk, B., and İkbal, S. (2016). New horizon in energy: Shale gas. *J. Nat. Gas Sci. Eng.* 35, 637–645. doi:10.1016/j.jngse.2016.09.014

Shi, X. S., Liu, D. A., and Cui, Z. D. (2015). Analysis and thinking on fracturing technology of shale gas exploitation. *Nat. gas Explor. Dev.* 38 (03), 62–65+69+12-13. Available at: https://kns.cnki.net/kcms/detail/detail.aspx?FileName=TRKT201503014&DbName=CJFQ2015.

Shi, Z. S., Zhou, T. Q., Guo, W., Liang, P. P., and Cheng, F. (2022). Quantitative paleogeographic mapping and sedimentary microfacies division in a deep-water marine shale shelf: Case study of wufeng-longmaxi shale, southern Sichuan Basin, China. *Acta Sedimentol. Sin.* 2023, 1–22. doi:10.14027/j.issn.1000-0550.2021.162

Soeder, D. (2017). The successful development of gas and oil resources from shales in North America. *J. PetroleumScience Eng.* 163, 399–420. doi:10.1016/j.petrol.2017.12.084

Starr, J. (2000). *Method of creationg common-offset/common azimuthe gathers in 3D seismic Survey and method of conducting Re-flection attribute variation analysis*. U S Patent:6026059,2000, American patent.

Taylor, J. C., Bill Richards, F. W., Ricardo, L. S., Grant, W., and Leslie, E. (2015). Interpretation of the Penobscot 3D seismic volume using constrained sparse spike inversion, Sable sub-Basin, offshore Nova Scotia. *Mar. Petroleum Geol.* 68, 73–93. doi:10.1016/j.marpetgeo.2015.08.009

Teng, W., and Liu, Y. S. (2013). Analysis of distribution,storage potential land prospect for shale oil and gas in China. *Prog. Geophys.* 28 (03), 1083–1108. doi:10.6038/pg20130301

Wang, J., Luo, H. S., Liu, H. Q., Lin, J., Li, L., and Lin, W. (2016). Influences of adsorption/desorption of shale gas on the apparent properties of matrix pores. *Petroleum Explor. Dev.* 43 (01), 158–165. doi:10.1016/s1876-3804(16)30019-2

Wang, Y. G. (2015). Integrating the latest achievements of scientific research and production, founding the first class platform of Petroleum geophysical exploration——review of ' Petroleum geophysical exploration ' in 2014. *Geophys. Pet. Explor.* 50 (04), 776–808+8. doi:10.13810/j.cnki.issn.1000-7210.2015.04.027

Wang, Z. J., Yu, Q., Yang, P., Liu, W., Yang, F., Liu, J, H., et al. (2018). The main controlling factors of shale gas enrichment and exploration prospect areas in the Sichuan-Yunnan-Guizhou border areas, southwestern China. *Sediment. Geol. Tethyan Geol.* 38 (03), 1–15. Available at: https://kns.cnki.net/kcms/detail/detail.aspx?FileName=TTSD201803001&DbName=CJFQ2018.

Wu, T. (2017). Analysis on application effect of pre-stack fracture prediction using offset vector slice (OVT) technology in shale gas area. *West-china Explor. Eng.* 29 (08), 69–72.

Xu, G. S., Li, Z. D., and Luo, X. P. (2012). *Petroleum geology*. Beijing: Geological Publishing House, 88–91.

Yan, Y. Q., Li, Y., Guo, S. H., Yang, X. X., and Hao, H. Y. (2021). Study and application of rock brittleness evaluation method based on compressive deformation characteristics. *Xinjiang Oil Gas* 17 (04), 21–27. Available at: https://kns.cnki.net/kcms/detail/detail.aspx?FileName=XJSY202104005&DbName=CJFQ2021.

Yang, Y. N., Wang, J., and Xiong, G. Q. (2016). Controls of sedimentary environments on shale gas reservoirs: A case study of the Wufeng and longmaxi formations in northeastern chongqing. *Sediment. Geol. Tethyan Geol.* 36 (03), 91–97. Available at: https://kns.cnki.net/kcms/detail/detail.aspx?FileName=TTSD201603012&DbName=CJFQ2016.

Yang, Z. H., Han, Z. Y., and Teng, G. E. (2019). Characteristics of Wufeng-Longmaxi For-mations shale sweet layer:Case study of Weiyuan-Rongchang block of SINOPEC. *Nat. Gas. Geosci.* 30 (7), 1037–1044. doi:10.11764/j.issn.1672—1926.2019.04.006

Yuan, H. J., Meng, E., Li, D. P., and Leng, C. (2016). Application of constrained sparse pulse inversion technology in reservoir prediction of Xinmin Oilfield. *Inn. Mong. Petrochem. Ind.* 42 (04), 82–84.

Zahm, C. K., and Hennings, P. H. (2009). Complex fracture development related to stratigraphic architecture: Challenges for structural deformation prediction, Tensleep Sandstone at the Alcova anticline, Wyoming. *AAPG Bull.* 93 (11), 1427–1446. doi:10.1306/08040909110

Zeng, Q,C., Chen, S., and He, P. (2018). Quantitative seismic prediction of shale gas sweet spots in lower silurian Longmaxi Formation, weiyuan area, Sichuan Basin, SW China. *Petroleum Explor. Dev.* 45 (03), 406–414. doi:10.11698/PED.2018.03.05

Zhang, D. W. (2010). Strategic concepts of accelerating the survey "exploration and exploitation of shale gas resources in China". *Oil Gas Geol.* 31 (02), 135–139+150. Available at: https://kns.cnki.net/kcms/detail/detail.aspx?FileName=SYYT201002004&DbName=CJFQ2010.

Zhang, L. H., Hu, Y., and Li, X. G. (2021). History and key technological progress of natural gas development in the Sichuan Basin. *Nat. Gas. Ind.* 41 (12), 60–72. doi:10.3787/j.issn.1000-0976.2021.12.007

Zhang, Y., and Yin, Y. S. (2015). Application of constrained sparse spike inversion in the third member of Hetaoyuan Formation in Dupo Oilfield. *Lithol. Reserv.* 27 (03), 103–107.

Zhao, S. X., Yang, Y. M., and Zhang, . (2016). Micro-layers division and fine reservoirs contrast of Lower silurian longmaxi formation shale,Sichuan Basin,SW China. *Nat. Gas. Ind.* 27 (03), 470–487. doi:10.11764/j.issn.1672-1926.2016.03.0470

Zheng, D., Wang, C. Y., Zhang, H. B., Wang, X. L., and Zhu, H. (2021). Logging evaluating methods of seven property parameters and enriched layers for Gulong shale oil reservoir in Songliao Basin. *Petroleum Geol. Oilfield Dev. Daqing* 40 (05), 87–97. doi:10.19597/J.ISSN.1000-3754.202107003

Zhou, H. (2015). *The application of reservoir prediction technique in Fuyu reservoir of the central depression in Jilin oil field*. Northeast petroleum university, Daqing city, Heilongjiang Province.

Zhou, Y. X., Zhao, A. K., Yu, Q., Zhang, D., Zhang, Q., and Lei, Z. H. (2021). A new method for evaluating favorable shale gas exploration areas based on multi-linear regression analysis: A case study of marine shales of wufeng-longmaxi formations, upper Yangtze region. *Sediment. Geol. Tethyan Geol.* 41 (03), 387–397. doi:10.19826/j.cnki.1009-3850.2021.05001

Zou, C. N., Zhao, Q., Cong, L. Z., Wang, H. Y., Shi, Z. S., Wu, J., et al. (2021). Development progress, potential and prospect of shale gas in China. *Nat. Gas. Ind.* 41 (01), 1–14. doi:10.3787/j.issn.1000-0976.2021.01.001

frontiers | Frontiers in Earth Science

TYPE Original Research
PUBLISHED 29 March 2023
DOI 10.3389/feart.2023.1134260

OPEN ACCESS

EDITED BY
Shuai Yin,
Xi'an Shiyou University, China

REVIEWED BY
Zhu Baiyu,
Yangtze University, China
Meng Wang,
Chongqing University of Science and Technology, China
Kongyang Wang,
Tianjin Branch, CNOOC Co. Ltd, China
Shiming Wei,
China University of Petroleum, Beijing, China

*CORRESPONDENCE
Yutian Feng,
fengtiantian0130@163.com
Hongming Tang,
swpithm@vip.163.com

SPECIALTY SECTION
This article was submitted to Structural Geology and Tectonics, a section of the journal Frontiers in Earth Science

RECEIVED 30 December 2022
ACCEPTED 14 March 2023
PUBLISHED 29 March 2023

CITATION
Feng Y, Tang H, Tang H, Leng Y, Shi X, Liu J, Wang Z and Deng C (2023), Influence of geomechanics parameters on stress sensitivity in fractured reservoir. *Front. Earth Sci.* 11:1134260. doi: 10.3389/feart.2023.1134260

Influence of geomechanics parameters on stress sensitivity in fractured reservoir

Yutian Feng[1]*, Hongming Tang[1]*, Haoxuan Tang[1], Yijiang Leng[1], Xuewen Shi[2], Jia Liu[2], Zhao Wang[1] and Cong Deng[1]

[1]School of Geoscience and Technology, Southwest Petroleum University, Chengdu, China, [2]Shale Gas Research Institute, PetroChina Southwest Oil and Gas Field Company, Chengdu, China

The complex fractures aggravate stress sensitivity and heterogeneity of the reservoir and seriously restrict effective development. Therefore, it is of great significance to study and quantitatively evaluate the stress sensitivity of the fractured reservoir. Taking the typical block of the Longmaxi shale reservoir in southern Sichuan as the engineering background, one uses the finite element method to develop a numerical model of a two-dimensional fracture closure variation subjected to the non-hydrostatic stress field. It explores the influence of different fracture occurrences and rock mechanical parameters on stress sensitivity. The theoretical model verifies the numerical simulation results to reveal the stress sensitivity mechanism of the fractured reservoir. The results show that the influence of the dip angle of fracture on the stress sensitivity depends on the anisotropy of applied *in-situ* stresses. The stronger stress sensitivity occurs in low-dip angles where the lateral pressure coefficient is less than 1. One defines the lateral pressure coefficient. On the contrary, the stronger stress sensitivity occurs in high-dip angles where the lateral pressure coefficient is more significant than 1. It is because the normal stress differences under different stress fields apply to the fracture. Under a given stress condition, the stress sensitivity of fracture negatively correlates with aspect ratio, elastic modulus, and Poisson's ratio. Pressure maintenance may be more critical in a reservoir with a low aspect ratio and rich in soft minerals. The theoretical predicting model of fracture permeability under different conditions is established based on the linear elastic theory. The relative error between theoretically predicted results and numerical simulation ones is less than 10%, which verifies the accuracy of numerical simulation results. The fundamental reason for stress sensitivity in the fractured reservoir is the fracture geometry and mineral deformation change. The research results are of great significance for establishing the productivity equation considering the stress sensitivity, accurately evaluating the variation of reservoir seepage capacity, and formulating reasonable drainage and production system.

KEYWORDS

fractured reservoir, stress sensitivity, aspect ratio, elastic modulus, Poisson's ratio

1 Introduction

With the decrease of pore pressure in the process of reservoir exploitation, the effective stress on the reservoir significantly increases, resulting in the geometry deformation of pores and fractures in the rock and the change of reservoir permeability (Gutierrez et al., 2000; Liu et al., 2009; Chen et al., 2015; Gutierrez

et al., 2015; Pan et al., 2015; Tao et al., 2018; Zhou et al., 2019). It is often referred to as the stress sensitivity of reservoir rocks. Fatt and Davis (1952) first proposed the stress sensitivity of rock, and found that the decreased rate of rock permeability with the increase of effective stress was 11%–41%. Since then, experts have conducted extensive research on the stress sensitivity of rocks through experimental and theoretical methods (Tan et al., 2021). Stress sensitivity varies with rock type (Zhu et al., 2018). The permeability of tight sandstone and shale usually suffers from more significant loss as the effective stress increases (Warplnski and Teufel, 1992; Suri et al., 1997; Han and Dusseault, 2003; İşcan et al., 2006; Worthington, 2008; Turcio et al., 2013; Li et al., 2014; Meng et al., 2015; Luo et al., 2018; Li et al., 2019; Wang et al., 2019; Li, 2022). It is because of the poor relative physical properties, complex pore structure, and rich natural fractures. Natural fracture is an essential part of a low permeability reservoir, which will aggravate the stress sensitivity and heterogeneity of the reservoir (Wu et al., 2022; Li et al., 2023; Sun, 2023). The intensity of stress sensitivity affects the depletion rate of reservoirs, and seriously restricts the seepage and practical development of the reservoir. When formulating the development plan for oil and gas reservoirs, it is necessary to consider the stress sensitivity of fractures to accurately evaluate the percolation capacity of reservoirs, develop a reasonable production system and predict the productivity of oil and gas wells. Therefore, it is essential to study and quantitatively evaluate the stress sensitivity of fractured reservoirs.

Currently, the methods to analyze the stress sensitivity of fractured reservoirs include indoor experiments, theoretical research, and micro-scale analysis (Zhang et al., 2014; Zhang et al., 2015a; Zhang et al., 2015b; Duan et al., 2017; Foroozesh et al., 2021; Wu et al., 2022). Evaluation methods by indoor experiment mainly include the changes in confining pressure and pore pressure. The former approach is often adopted, but the latter is difficult to control the pressure variation and is rarely used (Kang et al., 2020). The naturally fractured rock has a stronger stress sensitivity than that of the intact rock (Warplnski and Teufel, 1992; Suri et al., 1997; Han and Dusseault, 2003; İşcan et al., 2006; Worthington, 2008; Li et al., 2011; Turcio et al., 2013; Li et al., 2014; Meng et al., 2015; Luo et al., 2018; Wang et al., 2019) conducted a visual experiment to measure the variation of fracture width subjected to increasing effective stress. Zhao et al. (2013) studied the stress sensitivity of the fractured rock samples to different filled extents of fractures. The experiment results show that the decreasing stress sensitivity depends on increasing filling extents. Dong et al. (2010) studied the stress sensitivity related to the physical properties of ultra-low permeability gas reservoirs. They showed that the stress sensitivity of shale is more than two times of sandstone. The experimental results of Kassis and Sondergeld (2010) show that the stress sensitivity of fracture is influenced by the loading path of effective stress, fracture development status, and proppant properties.

In terms of theoretical research, Greenwood and Williamson (1996) first proposed the G&W model using the classical Hertz elastic contact theory to describe the mechanical process of contact surfaces between rough and smooth cracks (Greenwood and Williamson, 1966). Walsh and Grosenbaugh (1979) further studied the variation of the fracture deformation based on the abovementioned model. They found that a specific functional relationship occurs between the fracture closure and the standard deviation of the height concerning the micro-convex surface. Brown and Scholz (1986) proposed the B & S model that the fracture closure problem addresses a contact problem between the rough and smooth surfaces of fracture. The pressure-related permeability models include exponential (Reyes and Osisanya, 2002), power (Xiao et al., 2015), logarithmic (Xiao et al., 2016), and binomial (Halsey et al., 1986).

Many further studies discuss the influence of pore throat and fracture structure, mineral components, and rock characteristics on stress-sensitive behavior (Cai, 2020; Tan et al., 2021; Zhu et al., 2022). Kang et al. (2020) pointed out that the stress sensitivity of low permeability reservoir is affected by burial depth, pore throat structure, mineral type, and fracture development scale. Sheng et al. proposed that the content of plastic minerals, the width, and the number of fractures in low and ultra-low permeability reservoirs are critical factors in determining stress sensitivity. The stress sensitivity is more robust than the medium and high permeability reservoirs because of the threshold pressure gradient (Sheng et al., 2016). A study conducted by Chalmers et al. (2012) shows that the geological control factors of permeability on the change in effective stress are the properties of the pore structure, mineral type, and anisotropy and that the sensitivity of permeability increases as the increasing aspect ratio and decreased elastic modulus of the rock. Wang et al. (2022) pointed out that fracture permeability is not only related to fracture compressibility but also influenced by the fracture direction, reservoir shape, and elastic properties of the reservoir and surrounding rock.

In terms of the finite element model, Walsh (1981) found a linear relationship between the cube root concerning permeability and the natural logarithm of confining pressure through numerical simulation. Warpinski and Teufel (1993) found that the fracture will shrink and close with increasing effective stress on the rock sample. Kang et al. (2014) studied the influencing factors of changing fracture width by using a finite element method and established a prediction model for fracture width. Wang et al. (2016) used a finite element model to obtain the closure variations of fractures with different occurrences under different conditions, which provided a theoretical basis for oil exploitation in fracture-vuggy reservoirs.

Therefore, previous studies on the stress sensitivity of fractured reservoirs have primarily used experimental analysis and theoretical models. In contrast, few comprehensive studies have considered the effects of the parameters of the fracture system and rock mechanics parameters on the stress sensitivity of reservoirs. Most of them are limited to the study on the stress sensitivity of fractures under a uniaxial stress state, which cannot reflect the deformation characteristics of fractures under complex *in-situ* stress conditions. Based on the *in-situ* stress parameters of the typical block of the Longmaxi shale reservoir in the southern Sichuan area, this paper provides a theoretical model to study the influence of different fracture occurrences and rock mechanical parameters on the closure variation of fractures under the action of *in-situ* stress. One evaluates their stress sensitivity, comprehensively analyzes the main control factors of stress sensitivity and reveals the stress sensitivity mechanism of fractured reservoirs. The results of the numerical model verify this theoretical model. The research results of this paper are of great significance for establishing a productivity equation considering the influence of stress sensitivity, accurately

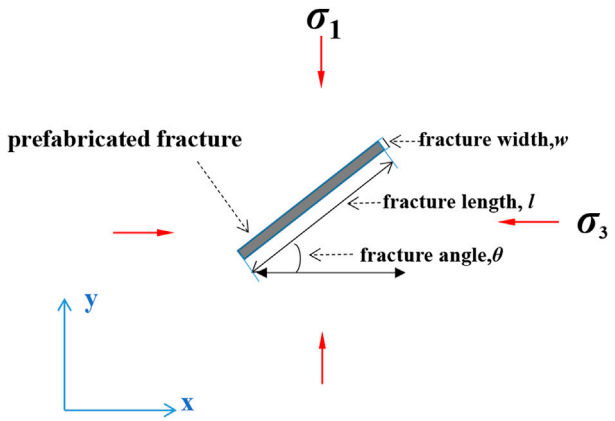

FIGURE 1
Diagram of the numerical analysis Model.

evaluating the change of reservoir seepage capacity, and formulating proper production scheduling and production system.

2 Model set-up and numerical procedure

Finite element simulation is a primary means to simulate fracture initiation and propagation. Based on the finite element method theory, the finite element inlays the analysis and solution process to make the simulation steps simple and convenient. The ideal fractured reservoir with a flaky fracture structure represents the complex fracture system. One uses ABAQUS to simulate the morphological characteristics of ideal fractures subjected to anisotropic *in-situ* stresses. The plane strain assumption holds within the discussion concerning the variation of the fracture closure in this work. Namely, the CPE4P element is used during the model development. Thus, the normal and shear strains are null along the width direction. A rectangle fracture shape is prefabricated by cutting a groove in the middle of the numerical model. Figure 1 shows the numerical model and boundary conditions. The fracture occurs in the *in-situ* stress field under the combined action of the σ_1 (Y direction) and σ_3 (X direction) of the overlying strata. The stresses σ_1 and σ_3 are prescribed as the $\sigma_1 > \sigma_3$ and depend on the *in-situ* stresses (σ_v, σ_H, and σ_h) in faulting stress regimes (see Figure 2). The stress ratio σ_3/σ_1 is called the coefficient of lateral pressure. The model analysis makes the following assumptions. 1) The crack closure is simulated by loading stress on the upper, lower, left, and right sides of the prefabricated crack surface, which is equivalent to considering the simultaneous action of horizontal and vertical stresses; 2) The contact deformation of the crack surface behaves as elastic deformation. One explores the variation of the rock mechanical parameters (Elastic modulus E, Poisson's ratio ν), fracture angle θ, and fracture aspect ratio ε (w/l) impact on the stress sensitivity of fractured reservoirs.

2.1 Model design and material parameters

The model variables include the characteristic parameters of fracture (fracture angle θ, fracture aspect ratio ε) and rock mechanics parameters (Elastic modulus E, Poisson's ratio ν). Considering the complex geological processes, the angle between the fracture and the vertical stress is usually random, so the model finds the fracture with different angles of 0°–90°. The aspect ratio characterizes the pore fracture morphology. According to the fracture size, one assigns the aspect ratio variable to be 0.001 to 0.1 in the model.

The rock mechanics parameters include elastic and strength characteristic parameters. Elastic properties to describe the elastic deformation of a material under loading, including Poisson's ratio and Young's modulus, determine the brittleness of rock. Rock strength characteristics, including compressive strength, shear strength, tensile strength, and internal friction angle, describe the plastic deformation of rock (Iferobia and Ahmad, 2020). Since the contact deformation of the fracture surface behaves as elastic deformation in the model, the elastic parameters are set as variables, but the strength parameters are fixed.

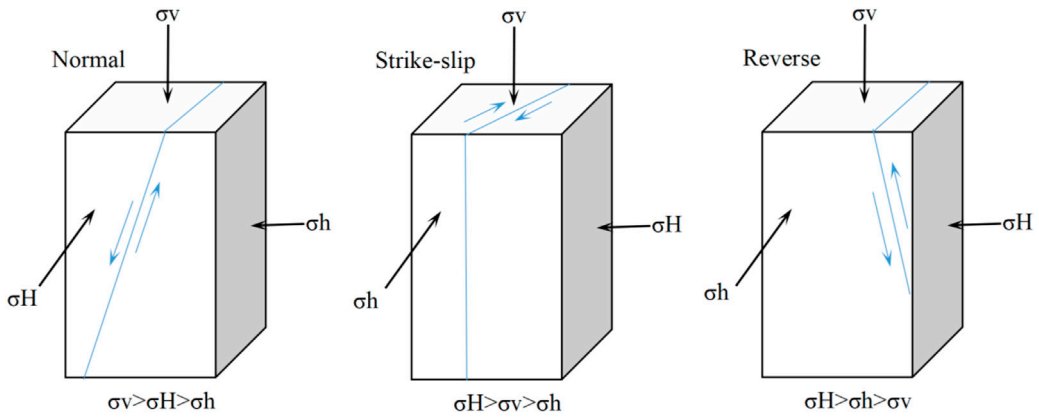

FIGURE 2
The distribution of principal *in-situ* stress (σ_v, σ_H, and σ_h) based on different stress magnitude and directions and the resulting fault types (normal fault, strike-slip fault, and reverse fault regimes).

The characteristics of the underground fluid and the magnitude of *in-situ* stress will affect the reservoir characteristics in a complex geological environment. The ground stress acting on the depth of the reservoir includes vertical and horizontal (minimum and maximum) *in-situ* stress. Vertical stress (σ_v) results from the overlying weight of the strata and the fluid contained in the pore space, which causes the underlying strata to expand and expand horizontally and laterally due to Poisson's ratio effect. The horizontal stresses (σ_h, σ_H) are formed by surrounding rock and lateral movement caused by caprock stress (Djurhuus and Aadnøy, 2003). Iferobia and Ahmad (2020) classified different faults (normal, strike-slip, and reverse). Figure 2 shows the fault types and their corresponding stresses. For the two-dimensional plane strain model, the cracks are mainly affected by the external forces of the vertical and horizontal stresses. Therefore, two cases are considered. The vertical stress is greater than the horizontal one, and the vertical stress is less than the horizontal one, namely, the normal fault and reverse fault (or strike-slip fault). The principal stress of the model is set according to the measured value of the target block. According to the triaxial rock mechanics analysis and test of 12 wells (95 samples) in the Longmaxi Formation in southern Sichuan, the distribution range of elastic modulus (Young's modulus) is 11.02–78.33 GPa, with an average value of 45.35 GPa. Poisson's ratio ranges from 0.154 to 0.335, with an average of 0.251; The average uniaxial compressive strength is 176.85 MPa, the average tensile strength is 12.38, and the average values of internal friction angle and cohesion are 45.59°and 2 MPa respectively. The strike-slip fault is easy to form in Weiyuan Block, and the vertical stress of typical wells ranges from 83.4 to 102.6 MPa, with an average of 95.7 MPa. The maximum horizontal principal stress is 96.2–120.2 MPa, with an average of 105.8 MPa. Normal faults are easy to form in Changning Block. The vertical stress of typical wells ranges from 82.5 to 96.2 MPa, with an average of 91.0 MPa; The maximum horizontal principal stress is 65.4–88.2 MPa, with an average of 79.5 MPa.

2.2 Evaluation criteria

Evaluating the element damage uses the maximum tensile strength criterion and the damage threshold of the Mohr-Coulomb criterion. The expression with tensile failure criterion is as follows

$$\begin{cases} \sigma_v - \frac{1+\sin\varphi}{1-\sin\varphi}\sigma_H \geq \sigma_c,\ \sigma_v > \sigma_c - \lambda\sigma_t \\ \sigma_H \leq -\sigma_t,\ \sigma_v \leq -\sigma_c - \lambda\sigma_t \end{cases} \quad (1)$$

where, σ_v, σ_H is the principal *in-situ* stress, MPa; φ is the friction angle, (°); λ is the residual strength coefficient; σ_t is the tensile strength, MPa; σ_c is the uniaxial compressive strength under ultimate stress, MPa.

The whole process of fracture closure is predicted and dynamically demonstrated. The vertical and horizontal output stress values are converted into the constant change of fracture effective stress P, and the fracture flow space of each closure step is output to calculate the fracture permeability under different closure degrees.

TABLE 1 Evaluation index of stress sensitivity coefficient.

S_s	Degree of stress sensitivity
S_s<0.05	No
0.05≤S_s≤0.30	Weak
0.30<S_s≤0.50	Medium to weak
0.50<S_s≤0.70	Medium to strong
0.70<S_s≤1.00	Strong
S_s>1.00	Extremely strong

2.3 Simulation design and data processing

Jiang and Yang (2018) evaluated the stress sensitivity of the fracture by deducting the fracture pore size in the model and converting it into fracture permeability according to the classical cubic law. The evaluation method concerning the stress sensitivity of fractured reservoirs is different from that of matrix reservoirs. The data processing and evaluation standard of stress sensitivity in industry standards (SY/T5358-2010) is also controversial (Kang et al., 2020). Therefore, the stress sensitivity coefficient is used to evaluate the stress sensitivity of the fractured reservoir. The stress sensitivity coefficient S_s is expressed in Eq. 2, and the evaluation indexes are shown in Table 1 (Jones, 1975; Jones and Owens, 1980).

$$S_s = \frac{1 - \left(\frac{K_i}{K_o}\right)^{1/3}}{\lg\frac{\sigma_i}{\sigma_o}} \quad (2)$$

The above symbols include stress sensitivity coefficient S_s, dimensionless; initial stress value σ_o, MPa; Initial permeability value K_o, 10^{-3} μm^2; Effective stress value of each experimental point σ_i, MPa; Corresponding permeability value of each practical point K_i, 10^{-3}μm^2.

3 Characteristics of fracture deformation and influencing factors

Although many experiments have proved the high dependence of fracture permeability on effective stress, it is difficult to be characterized by a formula due to the difference in rock type and pore structure, and theoretical studies on numerical models are still insufficient (Chen et al., 2015). In this section, the fracture permeability model is derived based on the simulation variables, and the theoretical model is used to fit the numerical simulation results. One also discusses the influencing factors and characteristics of stress sensitivity.

3.1 Fracture angle

Under the same underground stress condition, the closure variation of fractures with different occurrences, such as low-angle and high-angle fractures, are significantly different. The closure variation usually depends on the *in-situ* stress, fracture dip angle, and the angle between

TABLE 2 List of performed numerical experiments.

serial number	variables	number of analog groups	fracture parameters			
			Angle θ,°	Aspect ratio ε	Elastic modulus E, GPa	Poisson's ratio, ν
1	fracture angle	14	0 to 90	0.001	45	0.25
2	fracture aspect ratio	22	45	0.001 to 0.1	45	0.25
3	elastic modulus	16	45	0.001	10 to 80	0.25
4	Poisson's ratio	18	45	0.001	45	0.15 to 0.35

*1) The selection of rock mechanics parameters is based on the range and average value of measured values in the target block; 2) Vertical stress is greater than horizontal stress (typical Wells in Changning Block: vertical stress 91.0 MPa, horizontal stress 79.5 MPa) and vertical stress is less than horizontal stress (typical Wells in Weiyuan Block: The vertical stress is 95.7 MPa, the horizontal stress is 105.8 MPa), that is, the coefficient of lateral pressure K (the ratio of horizontal stress to vertical stress) is less than one and larger than one, respectively. 3) In simulations 2 to 4, the 45°fracture is kept to ensure that the fracture's vertical and horizontal stress components are consistent and to avoid the influence of angle.

TABLE 3 The related parameters of numerical simulation and the theoretical calculation result.

Simulation type	Inclination simulation							
Variables	Lateral pressure coefficient<1				Lateral pressure coefficient>1			
	Fitting Equation	R^2	Stress sensitivity coefficient S	The relative error between modular results (K_i/K_o)and theoretical results (K_i/K_o)	Fitting Equation	R^2	Stress sensitivity coefficient S	The relative error between modular results (K_i/K_o) and theoretical results (K_i/K_o)
Inclination0°	y=158233e-0.085x	0.8710	0.65	10.37	y = 204370e-0.108x	0.8026	0.55	9.19
Inclination 15°	y = 135921e-0.088x	0.8937	0.64	4.28	y = 150626e-0.106x	0.9179	0.55	8.03
Inclination 30°	y = 143396e-0.094x	0.9288	0.64	6.58	y = 123554e-0.102x	0.9450	0.56	9.34
Inclination 45°	y = 124218e-0.081x	0.945	0.63	6.68	y = 145246e-0.126x	0.8565	0.58	6.39
Inclination 60°	y = 147905e-0.089x	0.8813	0.63	10.14	y = 129879e-0.125x	0.9489	0.59	8.20
Inclination 75°	y = 159177e-0.086x	0.9000	0.55	7.75	y = 135980e-0.133x	0.9557	0.65	8.33
Inclination90°	y = 210665e-0.095x	0.7945	0.53	8.39	y = 159217e-0.16x	0.8917	0.72	7.74

the fracture strike and the maximum horizontal principal stress (Fan et al., 2020; Liu et al., 2021).

The following conditions are assumed to establish the predicting model of fracture deformation with different angles under non-hydrostatic stress. 1) The matrix is an isotropic linear continue. 2) A linear correlation occurs between stress and displacement of fractures. 3) The influence of shear stress is not considered.

According to the force analysis diagram (Figure 1), when the fracture angle is α, the normal force (σ_n) on the fracture surface is written as (Feng et al., 2021):

$$\sigma_n = \sigma_v \cos^2 \alpha + \sigma_H \sin^2 \alpha \tag{3}$$

According to the effective principle stress (Ma et al., 2020), the normal displacement of the fracture is given by

$$u_n = b_o \frac{\sigma_n}{E_f} = \frac{b_o\left(\sigma_v \cos^2 \alpha + \sigma_H \sin^2 \alpha - \alpha_f p\right)}{E_f} \tag{4}$$

The fracture width after stress deformation reads

$$b_f = b_o - u_n = b_o - \frac{b_o\left(\sigma_v \cos^2 \alpha + \sigma_H \sin^2 \alpha - \alpha_f p\right)}{E_f} \tag{5}$$

Based on the classical cubic law, the permeability retention rate is derived after stress-sensitive damage of fractures

10.3389/feart.2023.1134260

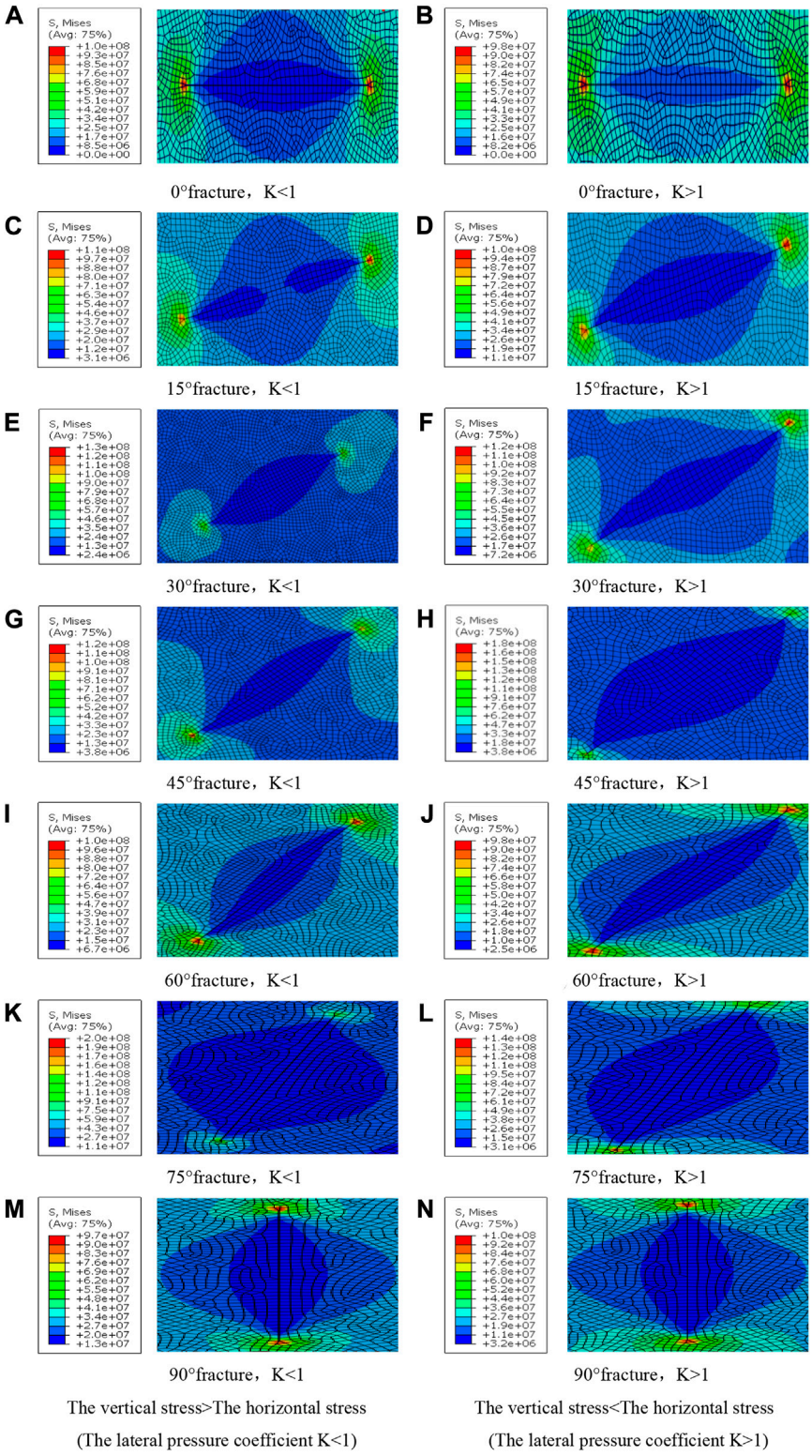

FIGURE 3
Stress nephogram of fractures with different angles under stress in two directions.

$$\frac{k_f}{k_o} = \frac{\left(b_o - \frac{b_o\left(\sigma_v \cos^2\alpha + \sigma_H \sin^2\alpha - \alpha_f p\right)}{E_f}\right)^2}{{b_o}^2} \times 100\% \quad (6)$$

In the above, the parameters include fracture permeability after deformation k_f, mD; Initial fracture permeability k_o, mD; The normal displacement of the fracture u_n, mm; Initial fracture

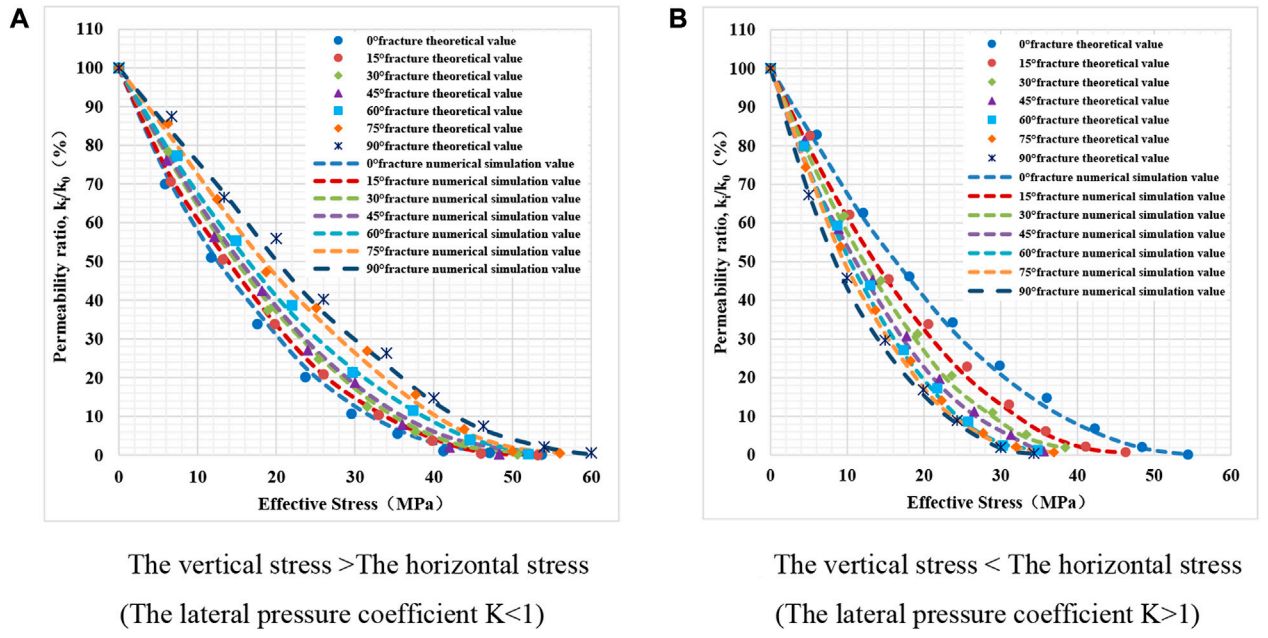

FIGURE 4
Variation curve of permeability ratio of fractures at different angles with effective stress.

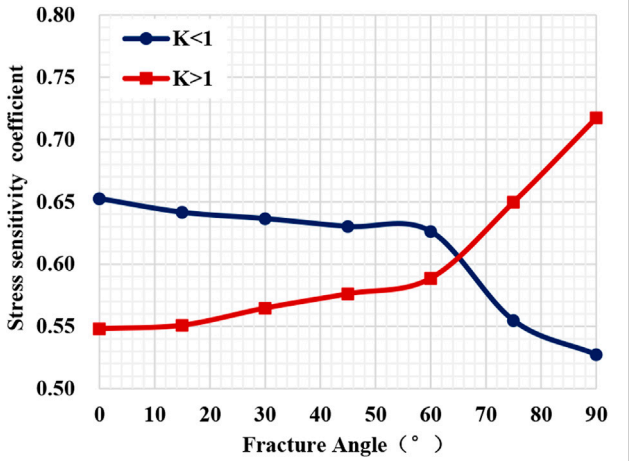

FIGURE 5
Curve of stress sensitivity coefficient changing with fracture angle.

width of the fracture b_o, mm; Fracture width after deformation b_f, mm; The normal force on the joint surface σ_n, MPa; the vertical and horizontal stress σ_v, σ_H, MPa; The elastic modulus of fracture E_f, MPa; the fracture effective stress coefficient α_f, default as 1; the angle of fracture α, °; The pore fluid pressure p, MPa.

Based on the simulation experiment scheme (see Table 2), one predicts the permeability decreasing tendency of fractures at different angles with changes in effective stress and compares it with the simulation results.

Under two *in-situ* stress condition, the use of ABAQUS finite element simulation obtains the stress nephogram of fractures at all angles. Figure 3 shows the stress and expansion state of fractures at different angles. When the non-equal stress is applied to the fracture, the pressure contour line is elliptic distribution, and the pressure emanates outward from the fracture. The pressure value gradually increases outward from the low-stress value near the fracture. In other words, the stress effect transfers pressure in an ellipse to the interior around the fracture.

Meanwhile, stress concentration appears at both ends of the fracture, decreasing outward and diverging. With the increasing stress in both directions, the formation pressure in the fracture continuously decreases, and the fracture gradually is compressed and deforms to reduce the width. Finally, the fracture is completely closed.

The fracture permeability ratio at different angles changes with effective stress (see Figure 4). The overall closure variation shows that the seepage capacity of the fracture decreases with increasing effective stress. The fracture width continuously decreases due to deformation closure when the fracture is subjected to the action of *in-situ* stress. As the effective stress begins to decline, the fracture deformation is relatively large, but the permeability rapidly decreases. Therefore, stress sensitivity is vital. When the stress decreases to a specific value, the fracture deformation tends to be stable, and the permeability slowly decreases. The correlation curve shows an exponential downward tendency. The fitting formula is shown in Table 3. R^2 reaches 0.7945–0.9450, with an average of 0.8943, consistent with previous research results (Dong et al., 2010; Metwally and Sondergeld, 2011; Chalmers et al., 2012; Ghanizadeh et al., 2014; Bhandari et al., 2015; Chen et al., 2019). When the coefficient of lateral pressure is less than 1, the fracture with a lower dip angle is easier to close (Figure 4A). The stress sensitivity coefficient S_s is 0.53–0.65, which belongs to medium to severe damage, and decreases with the increasing dip angle (Figure 5). In other words, the fracture with a greater dip dangle has weaker

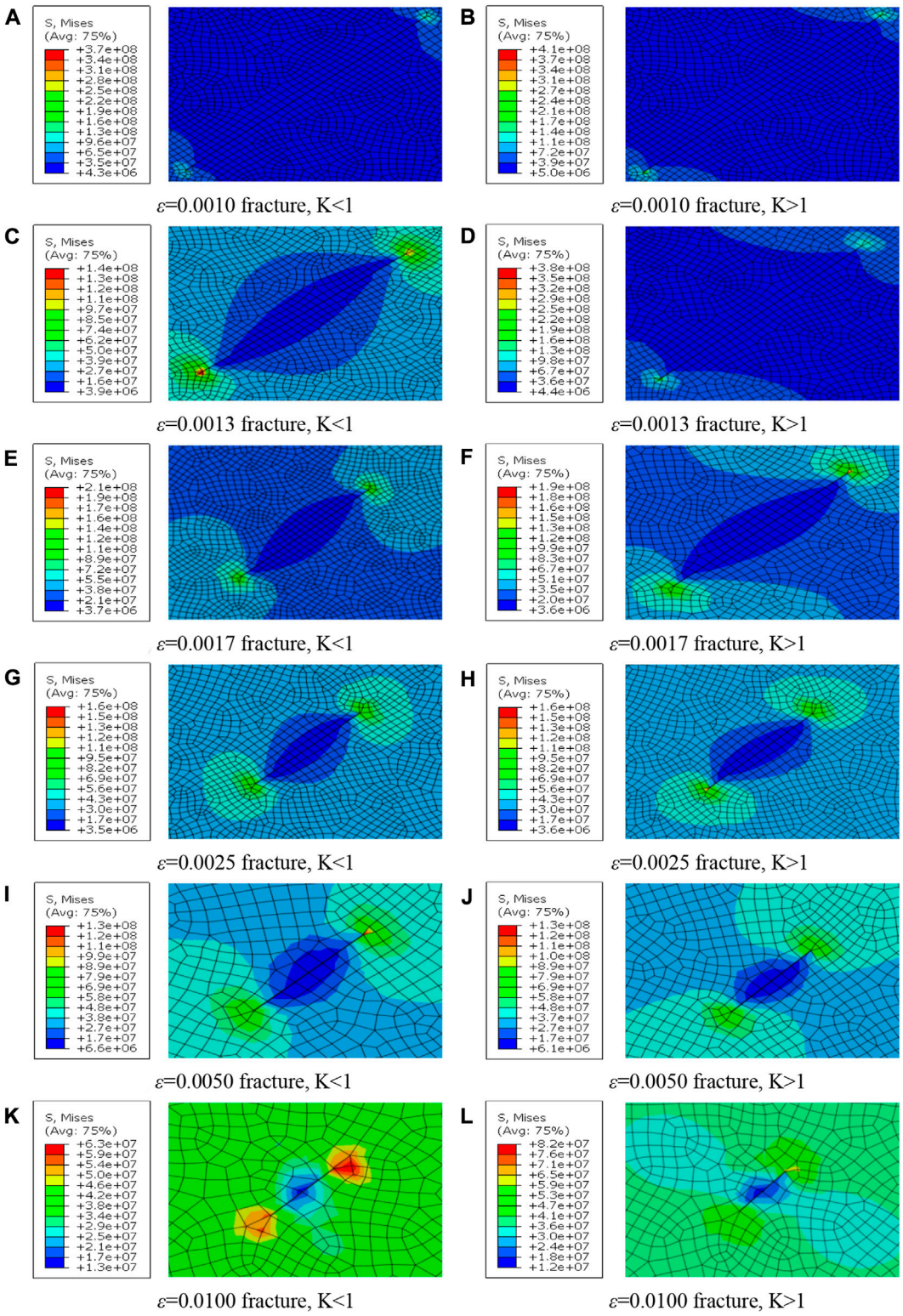

FIGURE 6
(Continued).

stress sensitivity damage. When the lateral pressure coefficient is larger than one, the fracture with a higher dip angle is easier to close (Figure 4B). The stress sensitivity coefficient S_s is 0.55–0.72, which belongs to medium to severe damage, and increases with the increasing dip angle (Figure 5). The fracture with a greater dip dangle has more serious stress sensitivity damage.

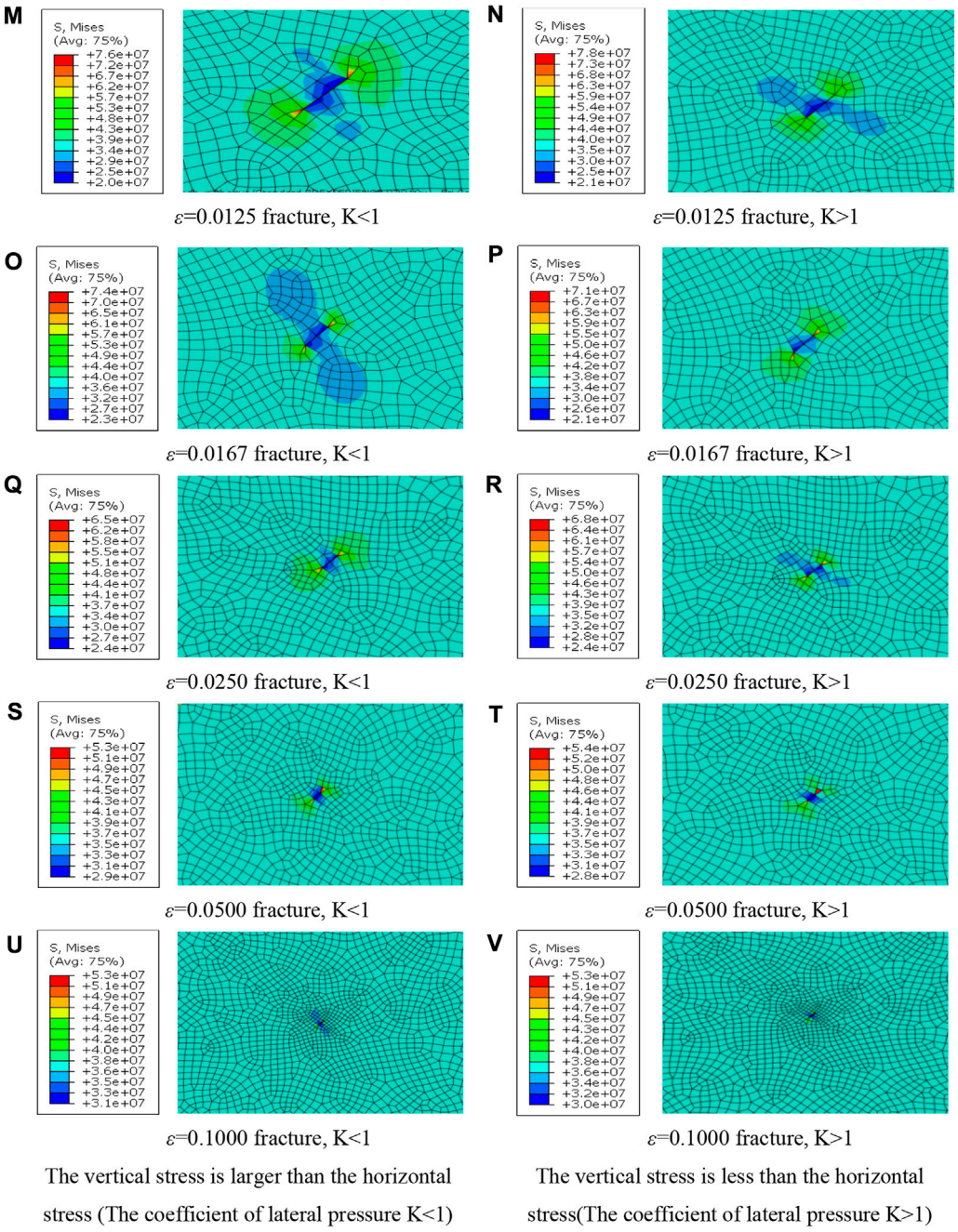

FIGURE 6
(Continued). Stress nephogram of fractures with different aspect ratios under non-hydrostatic stress.

Figure 4 shows the fitting curve based on the numerical simulation and the theoretically predicted results. The average relative errors of numerical simulation and theoretically predicted ones are 7.74% and 8.17%, respectively (see Table 3), indicating a high degree of agreement. Under the same stress condition, the normal effective stress of fracture surfaces is different. Thus, the fracture permeability presents different response characteristics and stress sensitivity coefficients during loading. When vertical stress is larger than horizontal stress, the permeability change of the fracture is lower for a larger angle, since the vertical stress component applied to the fracture with a large angle is smaller than that of a slight dip angle. On the contrary, when the vertical stress is less than the horizontal stress, the vertical stress component applied to the fracture with a large angle is greater than that of a slight angle. The results of numerical simulation and theoretical prediction are in good agreement, which verifies the accuracy and practicability of the predicting model for fracture deformation based on different angles, and can be further used to deduce the natural fracture network deformation and productivity prediction.

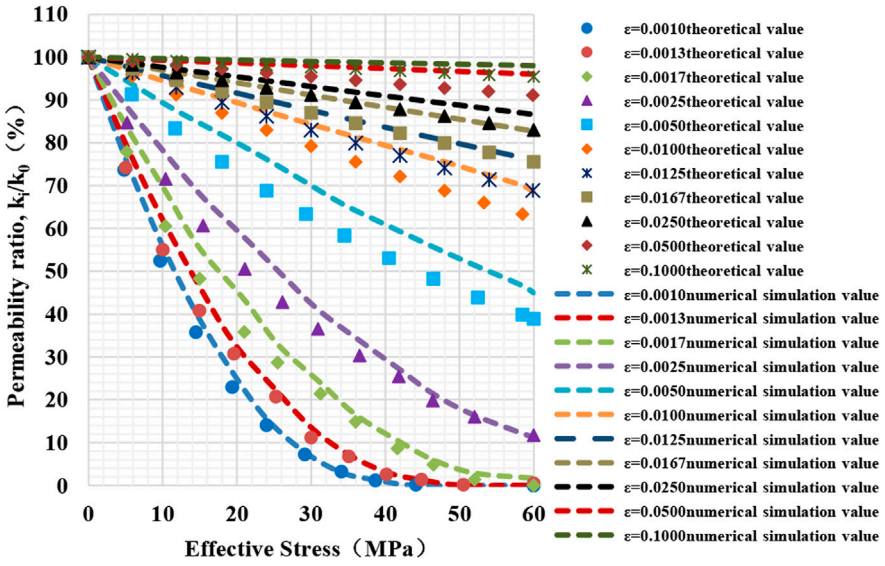

FIGURE 7
Variation curve of permeability ratio of fractures with different aspect ratios with effective stress.

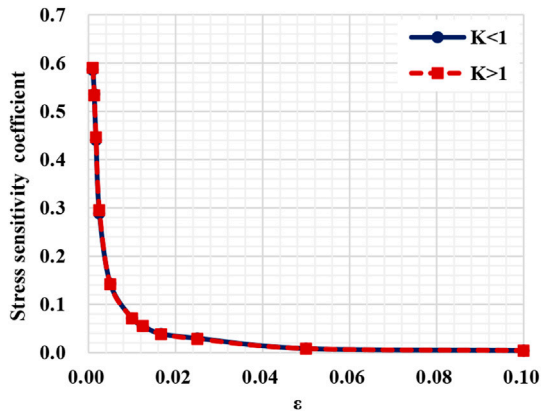

FIGURE 8
Variation of stress sensitivity coefficient with the fracture aspect ratio.

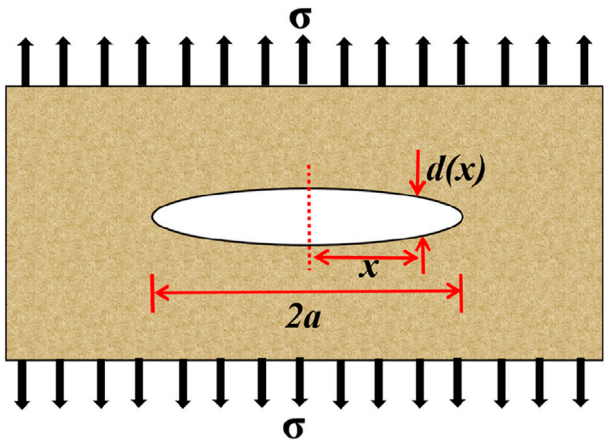

FIGURE 9
Schematic of the growth conditions derivation of Griffith crack.

3.2 Aspect ratio

The compressibility of reservoir pore space also depends on the geometric shape. Generally, the flow path can be described as a circular pipe, an ellipsoidal pore, or a plane fracture (Bernabe et al., 1982; Sisavath et al., 2000; Izadi et al., 2011; Schwartz et al., 2019; Li et al., 2022). The aspect ratio ε (ε = w/l) is the main parameter to distinguish the type and size of the pore spaces, which w is the minor axis length and l is the major axis length. In this study, the aspect ratio variable of 0.001–0.1 based on the crack size is considered in the model.

The general expression of the pore compression coefficient of elliptic pores is usually described as Eq. 7 under plane strain condition (Schwartz et al., 2019). The pore is considered a fracture when the aspect ratio is small. The aspect ratio is the ratio of the width and length of the fracture. According to Eq. 7, rock compressibility is mainly affected by aspect ratio, young's modulus, and Poisson's ratio, which respectively reflect the influence of fracture occurrence and rock mechanical properties on the stress sensitivity of a fractured reservoir.

$$C_p = \frac{2(1-\nu)}{E}\left(\varepsilon + \frac{1}{\varepsilon}\right) \tag{7}$$

where C_p is the coefficient of pore compression, other definitions include Poisson's ratio ν, elastic modulus E, and fracture aspect ratio ε. As ε is much smaller than unity, Eq. 7 can be simplified as

$$C_p = \frac{2(1-\nu)}{E\varepsilon} \tag{8}$$

Strain in the pore space is defined as:

$$\varepsilon_p = \sigma C_p \tag{9}$$

where ε_p is the pore strain, and σ is the applied stress. We invoke the constraint that the aspect ratio ε can be assumed constant under hydrostatic pressure. According to the two-dimensional pore strain formula rederived by B. Schwartz et al. (2019), and considering the seepage characteristics of parallel plate fractures in the model, the permeability retention rate after stress-sensitive fracture damage can be characterized as follows

$$\frac{K_i}{K_o} = \left(1 - \triangle\sigma C_p\right)^{\frac{3}{2}} \tag{10}$$

In the case that the aspect ratio does not hold constant, by changing the area change of the elliptic model, the following formula is derived

$$\frac{K_i}{K_o} = \left(1 - \triangle\sigma C_p\right)^{3} \tag{11}$$

Based on the simulation experiment scheme, the permeability decreasing tendency of fractures is predicted according to Eq. 11 and compared with the simulation results for different aspect ratios under different effective stress.

Figure 6 shows the stress nephogram of fractures with different aspect ratios under non-hydrostatic stress conditions. Figure 7 presents the variation of fracture permeability ratio against effective stress (since the lateral pressure coefficient does not affect the variation tendency of fracture aspect ratio with effective stress, one selects any stress condition is herein only fitted). The fracture permeability decreases with the increasing effective stress, and the coefficient of lateral pressure does not affect the variation tendency of the fracture aspect ratio with the effective stress. The permeability decreases with decreasing aspect ratio (see Figure 7). When the aspect ratio is $\varepsilon \leq 0.0025$, the fracture permeability ratio decreases exponentially with the increasing effective stress. The fracture permeability ratio decreases linearly when the aspect ratio is $\varepsilon > 0.0025$. Under the non-hydrostatic stress conditions, the variation tendency of the stress sensitivity coefficient coincides (see Figure 8). S_s ranges from 0.004 to 0.586, and shows an exponential downward trend with the increasing aspect ratio. When the aspect ratio $\varepsilon \leq 0.0025$, S_s ranges from 0.302 to 0.586 with an average value of 0.463, corresponding to medium-weak and medium-strong damage. When the aspect ratio $\varepsilon > 0.0025$, S_s ranges from 0.004 to 0.143, with an average value of 0.049, indicating no damage. In other words, the stress-sensitive damage degree of fractures with an aspect ratio $\varepsilon \leq 0.0025$ is significantly higher than that of fractures with an aspect ratio $\varepsilon > 0.0025$, which is consistent with previous studies. Namely, the rock is richer in fractures, and the stress sensitivity of the reservoir is stronger (Schwartz et al., 2019).

Figure 7 shows the fitting curve based on the numerical simulation and theoretically predicted results. When the aspect ratio is less than 0.0025, the numerical and theoretical values exponentially decrease with the increasing effective stress.

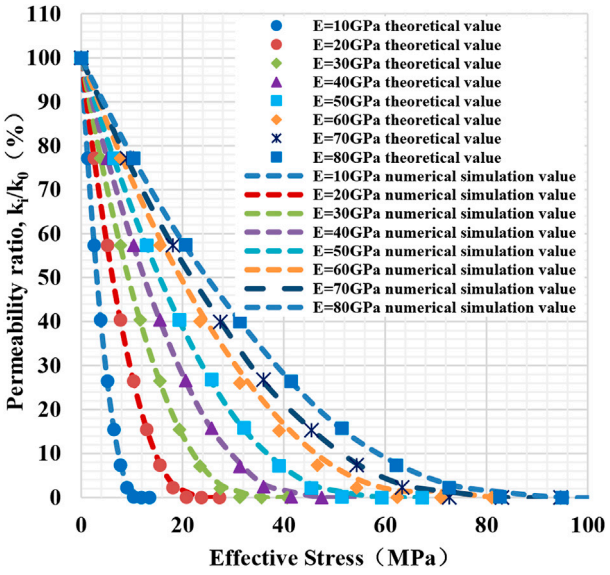

FIGURE 10
Curve of permeability ratio of fractures with different elastic modulus changing with effective stress.

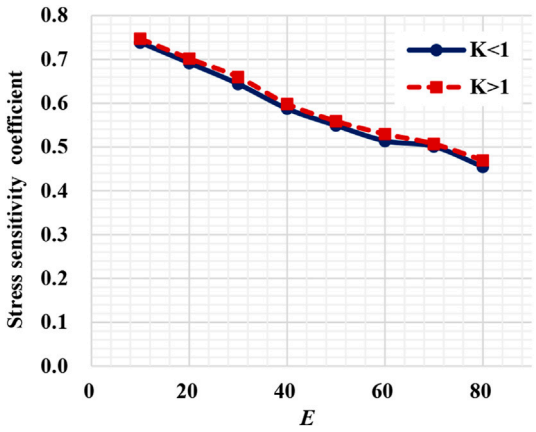

FIGURE 11
Variation of stress sensitivity coefficient against the elastic modulus.

Still, the aspect ratio is more significant than 0.0025, and the numerical and theoretical values decrease linearly. When the aspect ratio is less than 0.01, the relative error between the numerical simulation value and the theoretically predicted value is more significant, ranging from 6.13% to 13.45%, with an average of 9.45%. On the contrary, when the aspect ratio is less than 0.01, the relative error value of the two decreased significantly, ranging from 1.46% to 4.92%, with an average of 3.24%. In other words, the theoretical prediction has higher fitting accuracy and minor relative error in the case of modeling with a larger aspect ratio.

The influence of fracture aspect ratio on stress sensitivity is usually more important than the mechanical properties of the rock.

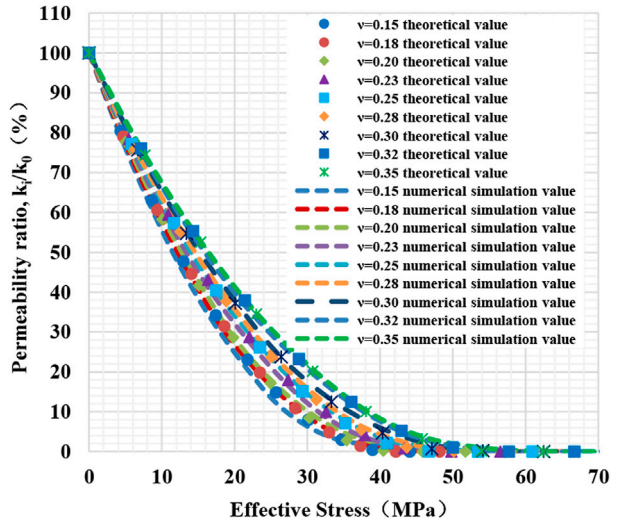

FIGURE 12
Variation curve of permeability ratio of fractures with different Poisson's ratios as a function of effective stress.

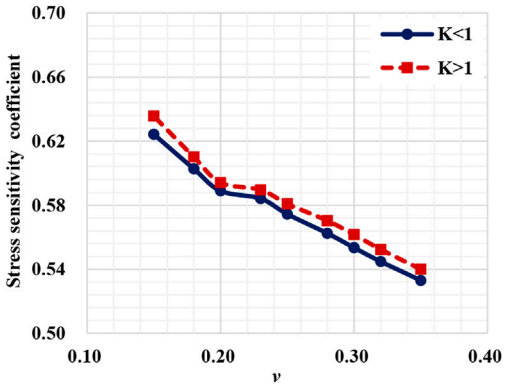

FIGURE 13
Variation of stress sensitivity coefficient against Poisson's ratio.

It suggests pressure maintenance may be more critical in a fractured reservoir with a low aspect ratio.

3.3 Elastic modulus

Griffith (1920) was the first to derive the formula of fracture propagation in elliptic holes by the theory of elastic energy conversion. As shown in Figure 9, the variation $d(x)$ of the ellipse's short axis width is described as under effective stress

$$d(\chi) = \frac{4\sigma}{E'}\sqrt{\alpha^2 - \chi^2} \tag{12}$$

where σ is the effective stress, E' is the elastic energy, α is the radius of the long axis of the ellipse hole, and the value of the horizontal coordinate x of the ellipse hole is $[-\alpha, \alpha]$ under the plane strain condition $E' = \frac{E}{1-\nu^2}$.

When the ratio of the short axis to the long axis (the aspect ratio) of the elliptical pore gradually decreases, it can be approximated as a fracture. Therefore, the model is usually assumed to be an elliptical hole, and its stress deformation is derived. Based on the above theory, Du et al. (2022) obtain the permeability expression with one fracture can be ed from the Poiseuille equation and Darcy's law

$$K = \frac{\phi b^2}{3} \tag{13}$$

where b is the radius of the short axis of the elliptical hole. The expressions of initial permeability and permeability are under different effective stress states

$$K_o = \frac{\phi {b_o}^2}{3}; \quad K_i = \frac{\phi {b_i}^2}{3} \tag{14}$$

where b_o is the initial short axis radius of the elliptical hole, and b_i is the short axis radius after stress deformation. The formula of permeability retention rate after stress-sensitive fracture damage is further derived:

$$\frac{K_i}{K_o} = \left[1 - \frac{1}{\varepsilon}\frac{2(1-\nu^2)(\sigma_e + \sigma_{eo})}{E}\right]^2 \tag{15}$$

where σ_e is the effective stress, and σ_{eo} is the initial effective stress.

Based on the simulation experiment scheme, the permeability decreasing tendency of fractures is predicted according to Eq. 15 and compared with the simulation results with different elastic modulus under different effective stress.

The stress nephograms of fractures with different elastic modulus under non-hydrostatic stress conditions are obtained by numerical simulation. Figure 10 shows the variation of the fracture permeability ratio with stress (since the lateral pressure coefficient does not affect the variation tendency of fracture elastic modulus with effective stress, one selects any stress condition is herein only fitted). The fracture permeability decreases with increasing effective stress, and the permeability ratio shows an exponential downward tendency. The coefficient of lateral pressure does not influence the variation of the fracture aspect ratio against the effective stress. The changing tendency of the stress sensitivity coefficient coincides under the non-hydrostatic stress conditions (see Figure 11). Figure 10 shows a more obvious permeability decrease for a smaller elastic modulus. With the elastic modulus increase, a linear downward tendency with S_s of 0.45–0.74 shows medium, weak, severe fracture damage. The smaller elastic modulus of the fracture has stronger stress sensitivity.

Figure 10 shows the fitting curve based on the numerical simulation and theoretically predicted results. With the increase of elastic modulus, the decreasing tendency of permeability becomes slow, and the stress sensitivity uniformly decreases. That is to say, the fracture with a larger Young's modulus is harder to compress. The relative error between the numerical simulation value and the theoretically predicted one is 4.22%–9.63%, with an average of 5.46%, which is in good agreement.

The stress sensitivity of rock is essentially caused by the change in pore structure and mineral deformation, which reflects the change in pore-throat connectivity and electrical conductivity. The elastic modulus is the internal factor that affects stress sensitivity. Harder mineral components are harder to compress than softer ones (Xu et al., 2018a; Xu et al., 2018b). The quartz and calcite minerals with high elastic modulus are difficult to deform under loading, so the increase in the content of these brittle minerals reduces the stress sensitivity of the rock (Li et al., 2014). On the contrary, plastic minerals such as gypsum and clay have better toughness and lower elastic modulus. Research indicates that clay minerals play a significant role in rock deformation, and the stress sensitivity is 25 times that of quartz. Therefore, the higher content of clay minerals possesses stronger stress sensitivity (Xu et al., 2018a,; Xu et al., 2018b). Meanwhile, the type of clay minerals will also affect stress sensitivity. For example, kaolinite reduces stress sensitivity, but the illite or mixed layer enhances the stress sensitivity (Xiao et al., 2016).

3.4 Poisson's ratio

According to Eq. 15, the decreasing tendency of fracture permeability is predicted with different Poisson's ratios and effective stress and is further compared with the simulation results.

Stress nephograms of fractures against different Poisson's ratios under non-hydrostatic conditions are obtained by numerical simulation. Figure 12 shows the variation of the fracture permeability ratio against the effective stress. The fracture permeability decreases with the effective stress increase, and the permeability ratio shows an exponential downward tendency. The coefficient of lateral pressure does not affect the changing preference of the fracture aspect ratio with the effective stress, indicating that the permeability decrease is more evident for smaller Poisson's ratio ν. Still, the change range is small (see Figure 12). Figure 13 shows the variation tendency of stress sensitivity coefficients is the same under non-hydrostatic stress conditions. With the increase of Poisson's ratio ν, there is an approximate linear downward tendency with S_s 0.53 to 0.64, which is medium to severe damage. The smaller Poisson's ratio of the fracture presents stronger stress sensitivity.

Figure 12 shows the fitting curve based on the theoretical model's numerical simulation and calculation results. Noting that the coefficient of lateral pressure does not influence the changing tendency of fracture elastic modulus with effective stress, herein, the model is only fitted under any stress condition. With the increase of Poisson's ratio, the decreasing tendency of permeability progressively slows down, and the stress sensitivity uniformly decreases. The fracture is more challenging to be compressed where the rock has a larger Poisson's ratio, while the decreased range is generally reduced. It is not significant the influence of Poisson's ratio on the stress sensitivity of fracture. The relative error between the numerical simulation value and the theoretical calculation value ranges from 3.48% to 11.98% and averages 8.53%, which is in good agreement.

In terms of mechanical properties, Poisson's ratio varies with rock properties. For example, the elastic modulus of calcite and quartz are similar. Still, Poisson's ratio is much higher than quartz, which has higher compressive resistance and can play a better-supporting role on the fracture surface. The stress sensitivity is weaker when the reservoir has a higher calcite content. Clay minerals are typical minerals with low elastic modulus and high Poisson's ratio. Still, compared to elastic modulus, Poisson's ratio has much less influence on rock stress sensitivity, so clay minerals still have strong plasticity.

The internal factor of rock is the most critical factor affecting the stress sensitivity of fracture. The internal factors are mineral composition, grain structure, pore structure, water saturation, mechanical morphology, geometric structure, and filling degree. External factors mainly comprise the effective stress, reservoir temperature, loading mode, threshold pressure, and working fluid invasion. Specifically, under external stress, the stress sensitivity increases with the decreasing hardness of minerals. For example, the experimental studies from Zhang Rui et al. show that the pore compressibility of shale is 1–2 orders of magnitude higher than that of sandstone. That is, the porosity of shale decreases more significantly than sandstone under the given stress. It is because shale reservoirs develop microfractures, and the nanopores have a low aspect ratio. In addition, shale is rich in clay and organic matter, so the elastic modulus is usually lower than that of sandstone. The low aspect ratio of pore and young's modulus leads to high pore compressibility, which is why shale permeability is more sensitive to effective stress (Zhang et al., 2015a; Zhang et al., 2015b). For example, dolomite has the highest elastic modulus among common carbonate minerals, followed by calcite and clay. When dolomite and calcite contain a certain amount of clay, the reservoir is more sensitive to stress. Therefore, the stress sensitivity of fracture in micritic limestone and micritic dolomite is more robust than that of natural and bioclastic limestone (Feng et al., 2019).

During the development of a fractured reservoir, it is necessary to carry out detailed research on the distribution characteristics of reservoir lithology, pore structure parameters, mechanical properties, natural fractures, and fractured fractures, and obtain a full understanding of the variation, including fracture closure, fracture deformation and seepage characteristics of fracture, and influencing factors under *in-situ* stress state. Meanwhile, it is also required to consider both internal and external influencing factors and combine them with the characterization and development demand of the reservoir. Thus, formulating reasonable development modes and exploitation speed ensures efficient and stable production of oil and gas reservoirs and maximizes economic benefits.

4 Conclusion

1. Taking the typical block of the Longmaxi shale reservoir in southern Sichuan as the engineering background, one uses the linear elastic theory to establish theoretical models to simulate the variation of fracture closure under the two-directional stress loading. There is an exponential relationship between permeability and effective stress with different applied angles to fractures, and the influence of applied angle on stress sensitivity is related to the local stress

field. When the coefficient of lateral pressure is less than one, and the applied angle is smaller, the stress sensitivity is more robust, and the coefficient of stress sensitivity S_s ranges from 0.53 to 0.65. When the coefficient of the lateral pressure is greater than one, and the applied angle is larger, the stress sensitivity is greater, and the coefficient of stress sensitivity S_s is 0.55–0.72. The abovementioned difference depends on the difference between normal stresses with different angles applied to fractures under different stress field conditions. Under the normal faulting stress regime, the fractured reservoirs with horizontal and low-angle fractures are suggested to exploit while timely maintaining formation pressure. On the contrary, attention should be paid to high-angle fractures under the reverse or strike-slip faulting regimes.

2. Under the same stress state, the stress sensitivity of fracture correlates with aspect ratio, elastic modulus, and Poisson's ratio. Geometry determines the compressibility of pore space. The aspect ratio of fracture much more influence the stress sensitivity than the mechanical properties of rock. Meanwhile, elastic modulus and Poisson's ratio act as the internal factors to affect stress sensitivity, and the affecting intensity depends on the type and content of mineral components. Pressure maintenance is more critical for fractured reservoirs with low aspect ratios and rich in soft minerals.
3. Based on the linear elastic deformation theory and the stress analysis applied to the fracture surface, one develops a theoretical model of fracture permeability under different conditions. The results show that the values of relative error between the numerical simulation and the theoretical model are less than 10%, which has a good consistency and verifies the accuracy of the simulation results. Meanwhile, the theoretical model considers the fracture occurrence and elastic parameters and has broader applicability than the standard empirical formulas. Thus, the theoretical model can be further applied to describe the deformation of real fracture networks and productivity prediction.
4. Both internal and external factors determine the strong stress sensitivity of a fractured reservoir, and the internal factor is the most important one. The change in fracture geometry and mineral deformation essentially causes stress sensitivity. In developing a fractured reservoir, it is necessary to conduct detailed research on the lithologic characteristics, pore structure, mechanical properties, and fracture distribution characteristics—A complete understanding of the variation of deformation and seepage characteristics of fracture and the corresponding influencing factors. Based on the reservoir features and development demands, formulating a reasonable development method and production speed ensures the efficient and stable production of the reservoir and maximizes the economic benefits.

Data availability statement

The original contributions presented in the study are included in the article/supplementary material, further inquiries can be directed to the corresponding authors.

Author contributions

YF: Research idea, conceptualization and technical implementation, data interpretation, drafted and revised the work. HoT: Suggestions and supervisions for the work. HaT: Suggestions and technical supports for the work. YL: Suggestions and data interpretation for the work. XS: Data interpretation, drafted and revised the work. JL: Data interpretation, drafted and revised the work. ZW: Polishgrammar, suggestions, and technical supports for the work. CD: Polishgrammar, suggestions, and technical supports for the work.

Funding

This research is supported by the Innovation Consortium Project of China National Petroleum Corporation and Southwest Petroleum University (Grant No. 2020CX020102).

Conflict of interest

Authors XS and JL are employed by PetroChina Southwest Oil and Gas Field Company. This study received funding from the Innovation Consortium Project of China National Petroleum Corporation and Southwest Petroleum University (Grant No. 2020CX020102). The funder had the following involvement with the study design, data collection, and analysis.

The remaining authors declare that the research was conducted in the absence of any commercial or financial relationships that could be construed as a potential conflict of interest.

Publisher's note

References

Bernabe, Y., Brace, W. F., and Evans, B. (1982). Permeability, porosity and pore geometry of hot-pressed calcite. *Mech. Mater* 1 (3), 173–183. doi:10.1016/0167-6636(82)90010-2

Bhandari, A. R., Flemings, P. B., Polito, P. J., Cronin, M. B., and Bryant, S. L. (2015). Anisotropy and stress dependence of permeability in the barnett shale. *Transp. Porous Med.* 108 (2), 393–411. doi:10.1007/s11242-015-0482-0

Brown, S. R., and Scholz, C. H. (1986). Closure of rock joints. *J. Geophys. Res.* 91 (91), 4939–4948. doi:10.1029/jb091ib05p04939

Cai, M. F. (2020). Key theories and technologies for surrounding rock stability and ground control in deep mining. *J. Min. Strata Control Eng.* 2 (3), 033037. doi:10.13532/j.jmsce.cn10-1638/td.20200506.001

Chalmers, G. R. L., Ross, D. J. K., and Bustin, R. M. (2012). Geological controls on matrix permeability of devonian gas shales in the horn river and liard basins, northeastern British columbia, Canada. *Int. J. Coal Geol.* 103, 120–131. doi:10.1016/j.coal.2012.05.006

Chen, D., Pan, Z., and Ye, Z. (2015). Dependence of gas shale fracture permeability on effective stress and reservoir pressure: Model match and insights. *Fuel* 139, 383–392. doi:10.1016/j.fuel.2014.09.018

Chen, Y., Jiang, C., Yin, G., Zhang, D., Xing, H., and Wei, A. (2019). Permeability evolution under true triaxial stress conditions of Longmaxi shale in the Sichuan Basin, Southwest China. *Powder Technol.* 354, 601–614. doi:10.1016/j.powtec.2019.06.044

Djurhuus, J., and Aadnøy, B. S. (2003). *In situ* stress state from inversion of fracturing data from oil wells and borehole image logs. *J. Petrol Sci. Eng.* 38 (3), 121–130. doi:10.1016/S0920-4105(03)00026-3

Dong, J., Hsu, J., Wu, W., Shimamoto, T., Hung, J., Yeh, E., et al. (2010). Stress-dependence of the permeability and porosity of sandstone and shale from TCDP Hole-A. *Int. J. Rock Mech. Min.* 47 (7), 1141–1157. doi:10.1016/j.ijrmms.2010.06.019

Du, S. H., Shen, W. H., and Zhao, Y. B. (2022). Quantitative evaluation of stress sensitivity in shale reservoirs: Ideas and applications. *Chin. J. Theor. Appl. Mech.* 54 (8), 2235–2247. doi:10.6052/0459-1879-22-262

Duan, X. G., An, W. G., Hu, Z. M., Gao, S. S., Ye, L. Y., and Chang, J. (2017). Experimental study on fracture stress sensitivity of Silurian Longmaxi shale formation, Sichuan Basin. *Nat. Gas. Geosci.* 28 (9), 1416–1424. doi:10.11764/j.issn.1672-1926.2017.07.013

Fan, C. H., Li, H., Qin, Q. R., He, S., and Zhong, C. (2020). Geological conditions and exploration potential of shale gas reservoir in Wufeng and Longmaxi Formation of southeastern Sichuan Basin, China. *J. Petroleum Sci. Eng.* 191, 107138. doi:10.1016/j.petrol.2020.107138

Fatt, I., and Davis, D. (1952). Reduction in permeability with overburden pressure. *J. Petrol. Technol.* 4 (12), 16. doi:10.2118/952329-g

Feng, J. W., Sun, Z. X., Wang, Y. D., and She, J. F. (2019). Study on stress sensitivity of ordovician fractures in hetianhe gas field, tarim basin. *Geol. J. China Univ.* 25 (02), 276–286. doi:10.16108/j.issn1006-7493.2018059

Feng, Y. L., Liu, Y. T., Ding, Z. P., Chen, J., and Mao, X. L. (2021). Deformation characteristics of fractures in different directions under anisotropic stress boundary conditions. *Sci. Technol. Eng.* 21 (2), 694–702.

Foroozesh, J., Mohamed Abdalla, A. I., Zivar, D., and Douraghinejad, J. (2021). Stress-dependent fluid dynamics of shale gas reservoirs: A pore network modeling approach. *J. Nat. Gas. Sci. Eng.* 95, 104243. doi:10.1016/j.jngse.2021.104243

Ghanizadeh, A., Gasparik, M., Amann-Hildenbrand, A., Gensterblum, Y., and Krooss, B. M. (2014). Experimental study of fluid transport processes in the matrix system of the European organic-rich shales: I. Scandinavian alum shale. *Mar. Petrol Geol.* 51, 79–99. doi:10.1016/j.marpetgeo.2013.10.013

Greenwood, J., and Williamson, J. (1966). Contact of nominally flat surfaces. *Proc. R. Soc. Lond. Ser. A Math. Phys. Sci.* 295 (1442), 300–319.

Griffith, A. A. (1920). The phenomenon of rupture and flow in solids. *Philosophical Trans. R. Soc. A* 221, 163–198.

Gutierrez, M., Katsuki, D., and Tutuncu, A. (2015). Determination of the continuous stress-dependent permeability, compressibility and poroelasticity of shale. *Mar. Petrol Geol.* 68, 614–628. doi:10.1016/j.marpetgeo.2014.12.002

Gutierrez, M., øino, L. E., and Nygard, R. (2000). Stress-dependent permeability of a de-mineralised fracture in shale. *Mar. Petrol Geol.* 17 (8), 895–907. doi:10.1016/S0264-8172(00)00027-1

Halsey, T. C., Meakin, P., and Procaccia, I. (1986). Scaling structure of the surface layer of diffusion-limited aggregates. *Phys. Rev. Lett.* 56 (8), 854–857. doi:10.1103/PhysRevLett.56.854

Han, G., and Dusseault, M. B. (2003). Description of fluid flow around a wellbore with stress-dependent porosity and permeability. *J. Petrol Sci. Eng.* 40 (1), 1–16. doi:10.1016/S0920-4105(03)00047-0

Iferobia, C. C., and Ahmad, M. (2020). A review on the experimental techniques and applications in the geomechanical evaluation of shale gas reservoirs. *J. Nat. Gas. Sci. Eng.* 74, 103090. doi:10.1016/j.jngse.2019.103090

İşcan, A. G., Kök, M. V., and Bagcı, A. S. (2006). Estimation of permeability and rock mechanical properties of limestone reservoir rocks under stress conditions by strain gauge. *J. Petrol Sci. Eng.* 53 (1), 13–24. doi:10.1016/j.petrol.2006.01.008

Izadi, G., Wang, S., Elsworth, D., Liu, J., Wu, Y., and Pone, D. (2011). Permeability evolution of fluid-infiltrated coal containing discrete fractures. *Int. J. Coal Geol.* 85 (2), 202–211. doi:10.1016/j.coal.2010.10.006

Jiang, J., and Yang, J. (2018). Coupled fluid flow and geomechanics modeling of stress-sensitive production behavior in fractured shale gas reservoirs. *Int. J. Rock Mech. Min.* 101, 1–12. doi:10.1016/j.ijrmms.2017.11.003

Jones, F. O. (1975). A laboratory study of the effects of confining pressure on fracture flow and storage capacity in carbonate rocks. *J. Petroleum Technol.* 27 (01), 21–27. doi:10.2118/4569-PA

Jones, F. O., and Owens, W. W. (1980). A laboratory study of low-permeability gas sands. *J. Petroleum Technol.* 32 (09), 1631–1640. doi:10.2118/7551-PA

Kang, Y. L., Li, C. J., You, L. J., Li, J. X., Zhang, Z., and Wang, T. (2020). Stress sensitivity of deep tight gas-reservoir sandstone in Tarim Basin. *Nat. Gas. Geosci.* 31 (4), 532–541. doi:10.11764/j.issn.1672-1926.2020.01.002

Kang, Y., Xu, C., You, L., Yu, H., and Zhang, B. (2014). Comprehensive evaluation of formation damage induced by working fluid loss in fractured tight gas reservoir. *J. Nat. Gas. Sci. Eng.* 18, 353–359. doi:10.1016/j.jngse.2014.03.016

Kassis, S., and Sondergeld, C. H. (2010). "Fracture permeability of gas shale: Effects of roughness, fracture offset, proppant, and effective stress," in *International oil and gas conference and exhibition in China* (Beijing. SPE-131376-MS.

Li, D. Q., Kang, Y. L., and You, L. J. (2014). Experimental study on permeability stress sensitivity of carbonate rocks. *Nat. Gas. Geosci.* 25 (03), 409–413. doi:10.11764/j.issn.1672-1926.2014.03.0409

Li, D. Q., Kang, Y. L., and Zhang, H. (2011). New evaluation method of permeability stress sensitivity based on visual fracture aperture measurement. *Nat. Gas. Geosci.* 22 (3), 494–500.

Li, H. (2022). Research progress on evaluation methods and factors influencing shale brittleness: A review. *Energy Rep.* 8, 4344–4358. doi:10.1016/j.egyr.2022.03.120

Li, H., Tang, H. M., Qin, Q. R., Zhou, J. L., Qin, Z. J., Fan, C. H., et al. (2019). Characteristics, formation periods and genetic mechanisms of tectonic fractures in the tight gas sandstones reservoir: A case study of xujiahe Formation in YB area, sichuan basin, China. *J. Petroleum Sci. Eng.* 178, 723–735. doi:10.1016/j.petrol.2019.04.007

Li, H., Zhou, J. L., Mou, X. Y., Guo, H. X., Wang, X. X., An, H. Y., et al. (2022). Pore structure and fractal characteristics of the marine shale of the Longmaxi Formation in the changning area, southern sichuan basin, China. *Front. Earth Sci.* 10, 1018274. doi:10.3389/feart.2022.1018274

Li, J., Li, H., Yang, C., Ren, X. H., and Li, Y. D. (2023). Geological characteristics of deep shale gas and their effects on shale fracability in the Wufeng–Longmaxi Formations of the southern Sichuan Basin, China. *Lithosphere* 2023 (1), 4936993. doi:10.2113/1970/4936993

Liu, H., Rutqvist, J., and Berryman, J. G. (2009). On the relationship between stress and elastic strain for porous and fractured rock. *Int. J. Rock Mech. Min.* 46 (2), 289–296. doi:10.1016/j.ijrmms.2008.04.005

Liu, Q., Cheng, Q., Sun, Z. G., and Hu, Q. T. (2021). Stress sensitivity of coal seam with different fractures: Case study of Fuxin Basin. *Nat. Gas. Geosci.* 32 (3), 437–446. doi:10.11764/j.issn.1672-1926.2020.11.016

Luo, W., Tang, C., Feng, Y., and Zhu, M. (2018). Mechanism of fluid flow along a dynamic conductivity fracture with pressure-dependent permeability under constant wellbore pressure. *J. Petrol Sci. Eng.* 166, 465–475. doi:10.1016/j.petrol.2018.03.059

Ma, J., Querci, L., Hattendorf, B., Saar, M. O., and Kong, X. Z. (2020). The effect of mineral dissolution on the effective stress law for permeability in a tight sandstone. *Geophys Res. Lett.* 47 (15). doi:10.1029/2020GL088346

Meng, Y., Li, Z., and Lai, F. (2015). Experimental study on porosity and permeability of anthracite coal under different stresses. *J. Petrol Sci. Eng.* 133, 810–817. doi:10.1016/j.petrol.2015.04.012

Metwally, Y. M., and Sondergeld, C. H. (2011). Measuring low permeabilities of gas-sands and shales using a pressure transmission technique. *Int. J. Rock Mech. Min.* 48 (7), 1135–1144. doi:10.1016/j.ijrmms.2011.08.004

Pan, Z., Ma, Y., Connell, L. D., Down, D. I., and Camilleri, M. (2015). Measuring anisotropic permeability using a cubic shale sample in a triaxial cell. *J. Nat. Gas. Sci. Eng.* 26, 336–344. doi:10.1016/j.jngse.2015.05.036

Reyes, L., and Osisanya, S. O. (2002). Empirical correlation of effective stress dependent shale rock properties. *J. Can. Petroleum Technol.* 41 (12). doi:10.2118/02-12-02

Schwartz, B., Huffman, K., Thornton, D., and Elsworth, D. (2019). The effects of mineral distribution, pore geometry, and pore density on permeability evolution in gas shales. *Fuel* 257, 116005. doi:10.1016/j.fuel.2019.116005

Sheng, Y. S., Hu, Q. X., Gao, H., Shi, Y. M., Dang, Y. C., Shao, F., et al. (2016). Evaluation on stress sensibility of low reservoir *in situ* conditions. *Acta Sci. Nat. Univ. Pekin.* 52 (06), 1025–1033. doi:10.13209/j.0479-8023.2016.050

Sisavath, S., Jing, X. D., and Zimmerman, R. W. (2000). Effect of stress on the hydraulic conductivity of rock pores. *Phys. Chem. Earth, Part A Solid Earth Geodesy* 25 (2), 163–168. doi:10.1016/S1464-1895(00)00026-0

Sun, Z. M. (2023). Superimposed hydrocarbon accumulation through multi-source and multi-stage evolution in the cambrian xixiangchi group of eastern sichuan basin: A case study of the pingqiao gas-bearing anticline. *Energy Geosci.* 4 (1), 131–142. doi:10.1016/j.engeos.2022.09.001

Suri, P., Azeemuddin, M., Zaman, M., Kukreti, A. R., and Roegiers, J. C. (1997). Stress-dependent permeability measurement using the oscillating pulse technique. *J. Petrol Sci. Eng.* 17 (3), 247–264. doi:10.1016/S0920-4105(96)00073-3

Tan, Q., Kang, Y., You, L., Xu, C., Zhang, X., and Xie, Z. (2021). Stress-sensitivity mechanisms and its controlling factors of saline-lacustrine fractured tight carbonate reservoir. *J. Nat. Gas. Sci. Eng.* 88, 103864. doi:10.1016/j.jngse.2021.103864

Tao, S., Chen, S., Tang, D., Zhao, X., Xu, H., and Li, S. (2018). Material composition, pore structure and adsorption capacity of low-rank coals around the first coalification jump: A case of eastern junggar basin, China. *Fuel* 211, 804–815. doi:10.1016/j.fuel.2017.09.087

Turcio, M., Reyes, J. M., Camacho, R., Lira-Galeana, C., Vargas, R. O., and Manero, O. (2013). Calculation of effective permeability for the BMP model in fractal porous media. *J. Petrol Sci. Eng.* 103, 51–60. doi:10.1016/j.petrol.2013.02.010

Walsh, J. B. (1981). Effect of pore pressure and confining pressure on fracture permeability. *Int. J. Rock Mech. Min. Sci. Geomechanics Abstr.* 18 (5), 429–435. doi:10.1016/0148-9062(81)90006-1

Walsh, J. B., and Grosenbaugh, M. A. (1979). A new model for analyzing the effect of fractures on compressibility. *J. Geophys. Res. Solid Earth* 84 (B7), 3532–3536. doi:10.1029/jb084ib07p03532

Wang, C., Zhang, Q. Y., Liu, Z. C., Zhang, Y., and Li, X. J. (2016). Prediction model for fracture width changes in vug-fracture oil reservoirs and its application. *J. China Univ. Petroleum(Edition Nat. Sci.* 40 (1), 86–91. doi:10.3969/j.issn.1673-5005.2016.01.012

Wang, M. Y., Li, L. X., Peng, X., Hu, Y., Wang, X., Luo, Y., et al. (2022). Influence of stress redistribution and fracture orientation on fracture permeability under consideration of surrounding rock in underground gas storage. *ENERGY Rep.* 8, 6563–6575. doi:10.1016/j.egyr.2022.04.076

Wang, X. Q., Zhu, Y. M., and Fu, C. Q. (2019). Experimental investigation of the stress-dependent permeability in the Longmaxi Formation shale. *J. Petrol Sci. Eng.* 175, 932–947. doi:10.1016/j.petrol.2019.01.037

Warpinski, N. R., and Teufel, L. W. (1993). Laboratory measurements of the effective-stress law for carbonate rocks under deformation. *Int. J. Rock Mech. Min. Sci. Geomechanics Abstr.* 30 (7), 1169–1172. doi:10.1016/0148-9062(93)90088-U

Warplnski, N. R., and Teufel, L. W. (1992). Determination of the effective stress law for permeability and deformation in low-permeability rocks. *SPE Form. Eval.* 7 (02), 123–131. doi:10.2118/20572-PA

Worthington, P. F. (2008). A diagnostic approach to quantifying the stress sensitivity of permeability. *J. Petrol Sci. Eng.* 61 (2), 49–57. doi:10.1016/j.petrol.2008.03.003

Wu, J. F., Fan, H. C., Zhang, J., Hu, H. R., Yuan, S. S., and Li, J. J. (2022). An experimental study on stress sensitivity of hydraulic fractures in shale: A case study on Longmaxi Formation shale in the southern sichuan basin. *Nat. Gas. Ind.* 42 (2), 71–81. doi:10.3787/j.issn.1000-0976.2022.02.008

Xiao, W., Jiang, L., Li, M., Zhao, J., Zheng, L., Li, X., et al. (2015). Effect of clay minerals on the effective pressure law in clay-rich sandstones. *J. Nat. Gas. Sci. Eng.* 27, 1242–1251. doi:10.1016/j.jngse.2015.09.067

Xiao, W., Li, T., Li, M., Zhao, J., Zheng, L., and Li, L. (2016). Evaluation of the stress sensitivity in tight reservoirs. *Petrol Explor Dev+* 43 (1), 115–123. doi:10.1016/S1876-3804(16)30013-1

Xu, C. Y., Lin, C., Kang, Y. L., and You, L. J. (2018a). An experimental study on porosity and permeability stress-sensitive behavior of sandstone under hydrostatic compression: Characteristics, mechanisms and controlling factors. *Rock Mech. Rock Eng.* 51 (8), 2321–2338. doi:10.1007/s00603-018-1481-6

Xu, C. Y., You, Z. J., Kang, Y. L., and You, L. J. (2018b). Stochastic modelling of particulate suspension transport for formation damage prediction in fractured tight reservoir. *Fuel* 221, 476–490. doi:10.1016/j.fuel.2018.02.056

Zhang, R., Ning, Z. F., Yang, F., Zhao, H. W., Du, L. H., and Liao, X. W. (2014). Experimental study on microscopic pore structure controls on shale permeability under compaction process. *Nat. Gas. Geosci.* 25 (8), 1284–1289. doi:10.11764/j.issn.1672-1926.2014.08.1284

Zhang, R., Ning, Z. F., Yang, F., and Zhao, H. W. (2015a). Shale stress sensitivity experiment and mechanism. *Acta Pet. Sin.* 36 (2), 224–231. doi:10.7623/syxb201502012

Zhang, R., Ning, Z., Yang, F., Wang, X., Zhao, H. W., and Wang, Q. (2015b). Impacts of nanopore structure and elastic properties on stress-dependent permeability of gas shales. *J. Nat. Gas. Sci. Eng.* 26, 1663–1672. doi:10.1016/j.jngse.2015.02.001

Zhao, L., Chen, Y., Ning, Z., Wang, X., Zhao, H. W., Wang, Q., et al. (2013). Stress sensitive experiments for abnormal overpressure carbonate reservoirs: A case from the Kenkiyak low-permeability fractured-porous oilfield in the littoral Caspian Basin[J]. *Pet. Explor. Dev.* 40 (2), 194–200.

Zhou, J., Zhang, L., Li, X., and Pan, Z. (2019). Experimental and modeling study of the stress-dependent permeability of a single fracture in shale under high effective stress. *Fuel* 257, 116078. doi:10.1016/j.fuel.2019.116078

Zhu, Q. Y., Dai, J., Yun, F. F., Zhai, H. H., Zhang, M., and Feng, L. R. (2022). Dynamic response and fracture characteristics of granite under microwave irradiation. *J. Min. Strata Control. Eng.* 4 (1), 019921. doi:10.13532/j.jmsce.cn10-1638/td.20210926.001

Zhu, S. Y., Du, Z. M., Li, C. L., Salmachi, A., Peng, X. L., Wang, C. W., et al. (2018). A semi-analytical model for pressure-dependent permeability of tight sandstone reservoirs. *Transp. Porous Med.* 122 (2), 235–252. doi:10.1007/s11242-018-1001-x

frontiers | Frontiers in Earth Science

TYPE Original Research
PUBLISHED 11 April 2023
DOI 10.3389/feart.2022.1067316

OPEN ACCESS

EDITED BY
Shuai Yin,
Xi'an Shiyou University, China

REVIEWED BY
Xiangliang Qiu,
Xi'an Shiyou University, China
Fuhua Shang,
Inner Mongolia University of Technology, China

*CORRESPONDENCE
Kaijun Tan,
tankaijun20@126.com

SPECIALTY SECTION
This article was submitted to Structural Geology and Tectonics, a section of the journal Frontiers in Earth Science

RECEIVED 11 October 2022
ACCEPTED 19 December 2022
PUBLISHED 11 April 2023

CITATION
Tan K, Wu Q, Chen J, Yao J, Qin Y and Zhang Y (2023), Development characteristics and controlling factors of dolomite reservoirs of permian Qixi a Formation in central Sichuan Basin. *Front. Earth Sci.* 10:1067316. doi: 10.3389/feart.2022.1067316

Development characteristics and controlling factors of dolomite reservoirs of permian Qixi a Formation in central Sichuan Basin

Kaijun Tan*, Qingpeng Wu, Juan Chen, Jun Yao, Yang Qin and Yongfeng Zhang

Research Institute of Petroleum Exploration and Development Northwest Branch, Lanzhou, China

In recent years, with the fine exploration of carbonate reservoirs in the Qixia Formation, central Sichuan Basin, researchers have made important oil and gas discoveries in the dolomite reservoirs. However, the characteristics, genesis and controlling factors of dolomite reservoirs in the Qixia Formation in this area are still unclear. In this paper, the petrology, pore structures, physical properties and geochemical characteristics of the dolomite reservoirs in the Permian Qixia Formation in the central Sichuan Basin have been systematically studied based on a large number of cores, thin sections, physical property and geochemical tests. Furthermore, the genesis and main controlling factors of dolomite reservoirs are clarified. The study shows that the dolomites have the characteristics of small single-layer thickness and multi-layer development, and they are usually interbeded with the limestones. The reservoir types are mainly fine crystal and fine medium crystal dolomite, and the reservoir spaces include intercrystalline pores and dissolution pores (or caves). Moreover, the reservoir physical properties are characterized by medium porosity and medium to high permeability. Quasi-syngenetic dolomitization is the main origin of dolomite in the target layer, and the dolomite was slightly modified by hydrothermal solution at the end of the Maokou Formation period. The development of dolomite reservoirs in the Qixia Formation in the study area is affected by palaeogeomorphology, sedimentation and diagenesis. The granular shoal facies developed in the high parts of the paleogeomorphology provides the material basis for the formation of dolomite reservoirs. The high frequency sequence interface controls the development of dolomite reservoirs in the highstand systems tract. In addition, the quasi-syngenetic dissolution promots the development of the early secondary pores and provids an effective channel for the migration of the diagenetic fluids in the later stage. In the direction of orthogonal horizontal deposition, the dolomites have the characteristics of thin monolayer thickness, multiple sequences and are interbedded with limestone. The dolomite shoals in the study area are distributed as clumps in the plane, which has great potential for hydrocarbon exploration.

KEYWORDS

sichuan basin, qixia formation, dolomite reservoir, geochemical characteristics, origin of dolomite, exploration potential

1 Introduction

Carbonate reservoir is a kind of unconventional tight reservoir with low porosity, low permeability and strong heterogeneity. Carbonate reservoirs are developed in the Tarim Basin, Sichuan Basin, Qaidam Basin, Bohai Bay Basin and Ordos Basin in China (Hong et al., 2004; Chen et al., 2012; Jiang et al., 2018; Xie et al., 2022). Dolomite is usually deposited in the closed water environment with strong evaporation, and its physical properties are usually good (Huang et al., 2001; Chen et al., 2012). Therefore, it is a typical high-quality carbonate reservoir. A large number of studies have shown that the factors affecting the quality of dolomite reservoir include sedimentary facies, diagenesis, tectonic activity and paleogeomorphology (Xiong et al., 2017; Jiang et al., 2018).

In recent years, with the fine exploration of carbonate reservoirs in the Qixia Formation, central Sichuan Basin, researchers have made important oil and gas discoveries in the dolomite reservoirs. Recently, several wells have obtained high-yield gas flows in the Qixia Formation of the Moxi and Gaoshiti areas in the central Sichuan Basin, which shows that the Qixia Formation has great potential for oil and gas exploration and development. At present, some scholars have carried out a lot of research on the characteristics and genesis of dolomite reservoirs in the Permian Qixia Formation, Sichuan Basin (Bau and Dulski., 1996; Veizer and Azmy., 1999; Meyer et al., 2013; Geske et al., 2015). Generally, the genesis of dolomite reservoir mainly includes syngenetic dolomitization, burial dolomitization, mixed water dolomitization, structural hydrothermal dolomitization, and multi-stage superimposed dolomitization (Burke et al., 1982; Crozaz et al., 2003; Mazumdar et al., 2003; Morozov et al., 2021; Richardson et al., 2022; Gao et al., 2023). It is generally believed that the development of dolomite reservoirs in the Permian Qixia Formation in the Sichuan Basin is mainly controlled by sedimentary facies, tectonic-hydrothermal and early karst controlled by multiple sequence interfaces. However, these viewpoints can not accurately explain the phenomena of thin layer thickness and strong lateral heterogeneity of dolomite reservoirs in the Qixia Formation in central Sichuan Basin. At present, there is no systematic study on the characteristics, genesis and controlling factors of dolomite reservoirs in the Qixia Formation in the central Sichuan Basin, and it is difficult to accurately predict the distribution of dolomite reservoirs. In this paper, the petrology, pore structures, physical properties and geochemical characteristics of the dolomite reservoirs in the Permian Qixia Formation in the central Sichuan Basin have been systematically studied based on a large number of cores, thin sections, physical property and geochemical tests. This study can provide theoretical and technical supports for gas exploration and development of the Qixia Formation in this area.

2 Geological background

The Sichuan Basin is a large hydrocarbon superimposed basin in western China. It covers an area of about 18×10^4 km^2 and is a rhomboid petrol-bearing basin extending in the northeast direction. The tectonic units of the Sichuan Basin include the West Sichuan Foreland Depression, the Middle Sichuan Gentle Fold Area, the North Sichuan Thrust Fold, the East Sichuan High and Steep Structural Area, the South Sichuan Low and Steep Fold Area and the Southwest Sichuan Uplift Area. The study area is located in the Middle Sichuan Gentle Fold Area of the Sichuan Basin (Figure 1).

From bottom to top, the Liangshan and Qixia Formations are developed in the Lower Permian in the central Sichuan Basin, and the overlying strata is the Middle Permian Maokou Formation (Figure 2). The Liangshan Formation is in unconformity contact with the underlying strata, while it is in conformity contact with the Qixia Formation. The Liangshan Formation is a set of shore-marsh facies sand and mudstone deposits interbeded with coal lines. The bottom of the Maokou Formation is a set of bioclastic limestone and micritic bioclastic limestone deposits rich in argillaceous components, which are in parallel unconformity contact with the Qixia Formation. The Qixia Formation is divided into the Qi one and Qi two sub-members. Dark grey-black gray argillaceous and bioclastic micritic limestones are developed in the Qi one sub-member. While gray bioclastic limestone, dolomite and a small amount of black siliceous mass are usually found in the Qi two sub-member. The thickness of the Qixia Formation is 100–150 m, and it belongs to the facies of open platform, grain shoal and open sea (or intershoal sea) of carbonate rocks. According to statistics, the average thickness of the single shoal body in the granular shoal is mostly between .5 m and 1.2 m, and the thickest can reach 2.1 m. The granular shoal is mainly developed in the top of the Qi one sub-member and the middle and upper parts of the Qi two sub-member.

3 Materials and methods

The experimental samples of this study were collected from the Wells MX42 and MX108 in the central Sichuan Basin. The carbon and oxygen isotopes were determined using an isotope ratio mass spectrometer, Delta V Advantage. The standard 100% phosphate method was used to perform carbon and oxygen isotope tests. The test accuracy meets: $\delta^{13}C<.01‰$, $\delta^{18}O<.02‰$. The strontium isotope was determined *via* a thermoionization isotope ratio mass spectrometer TRITON PLUS. The ambient temperature was 22 °C, the relative humidity was 66%, and the error range was between .000014 and .000084. The cerium and europium isotopes were determined using a solid isotope mass spectrometer ThermoFisher TRITON TI. The heating temperature was 1,000°C, the vacuum degree of ion source was 1.1×10^{-7} mbar, and the mass stability was less than .00001. Exponential laws were used for isotopic ratio corrections.

4 Results

4.1 Petrological characteristics

The lithology of the Permian Qixia Formation in the central Sichuan Basin is mainly bioclastic limestones and argillaceous bioclastic limestones, followed by dolomites with good reservoir properties. According to the crystal size, the dolomites in the Qixia Formation are mainly fine crystal and fine-medium crystal dolomites (Figures 3A,B), followed by coarse-crystal dolomites (Figure 3C), mud-silt crystal dolomites (Figure 3E) and saddle-shaped dolomites (Figure 3F) are rare.

Grain dolomites are mainly medium—thin layer light gray—gray dolomites. Under the microscope, the dolomite crystals appear as hedral and semi-hedral crystals. The heteromorphic crystals mostly

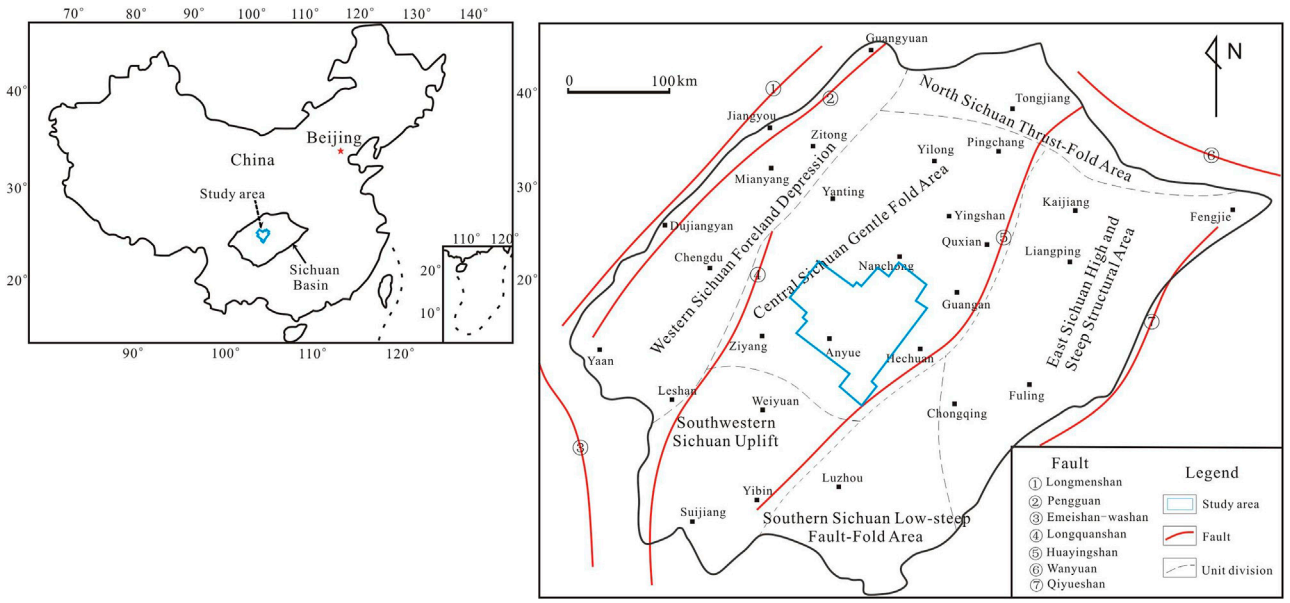

FIGURE 1
Structural location of the study area (modified according to Tan et al., 2022).

have non-flat crystal planes, and the crystal morphology and contour are not clear (Figure 3C). In addition, the morphology of some crystals can only be recognized under orthogonal light, and most crystals have wave-like extinction characteristics. Residual biodebris can occasionally be found. Distinct bioclastic structures can be observed when a fraction of hedral crystalline dolomites are restored (Figure 3D), including foraminifera, terraines, and corals. According to the observation results, the semi-hedral and hedral crystals have flat crystal planes, which are mostly found in the medium coarse crystal dolomites. The grain core is dirty and the color of the ring edge is usually bright. If the crystal shape is good, the bright edge fog center structure is obvious (Briais et al., 1993; Budd, 1997; Hong et al., 2004; Ma et al., 2023).

Mud-silty dolomite can be observed only in the upper part of the Qixia Formation in Well Heshen 2. The mud-silt particles are sand-like and mostly surrounded by sparry dolomite ring edges (Figure 3E). The pores of fine crystal dolomite are usually filled or semi-filled with asphalt. In addition, it can be observed in the cores and under the microscope that the caves or soluble seams are always filled with saddle-shaped dolomites with non-flat crystal plane (Hu and Wang., 1990; Chacko and Deines., 2008). The dolomites have coarse grains and large curved crystal surfaces, and they have wavy extinction characteristics under orthogonal polarization conditions (Figure 3F).

4.2 Developmental characteristics of pores

The reservoir space of dolomite reservoirs of the Qixia Formation in the central Sichuan is mainly composed of intergranular pores, intergranular dissolution pores and caves, accounting for 60%–80%; followed by the residual intergranular pores and residual intra granular pores, accounting for 20%–40%. In addition, a few micro-fractures and dissolution expansion fractures are also developed.

Intercrystalline pores are unfilled pores between grains of dolomite, and the dolomites have flat edges. The intercrystalline pores have irregular polygonal shape, and often appear as triangular pores. This type of pores have a high development frequency with pore sizes ranging from .01 mm to .5 mm (Figure 4A). There are obvious dissolution traces on the inner edges of some pores, and the surface ratios are between 1% and 8%. Intercrystalline pores exist in all kinds of crystalline dolomites. They are mostly found in fine-mesocrystalline and mesocrystalline dolomites, and their main throat types are constricted or flaky throats.

The intercrystalline pores can be strongly dissolved under the action of acidic fluids, and then the intercrystalline dissolved pores are formed (Figures 4B,C). The dolomite grains at the pore edges have obvious cove—shaped dissolution edges. According to the statistics, the pore size of the intercrystalline dissolved pores is in the range of .05–1.0 mm, and the surface ratio is in the range of 2%–11%. Intercrystalline dissolved pores are mainly developed in cave-filled dolomites and pinhole matrix dolomites.

Dissolution pore is the most developed pore type in the Permian Qixia Formation in the central Sichuan Basin. They appear as residual dissolution pores filled with dolomite or bitumen. The pore sizes of the dissolution pores vary greatly, with the main pore sizes ranging from .1 cm to 4 cm (Figures 4D–F). The millimeter-level spiculate dissolution pores are distributed uniformly in local layers, while the centimeter-level dissolution pores have irregular and heterogeneous distribution characteristics. The caves are mostly filled with macrocrystalline calcite, medium coarse-grained dolomite, saddle-shaped dolomite, quartz and asphalt.

4.3 Physical characteristics

According to the physical test results of samples taken from the target layer (Figure 5), the minimum porosity of the limestone samples

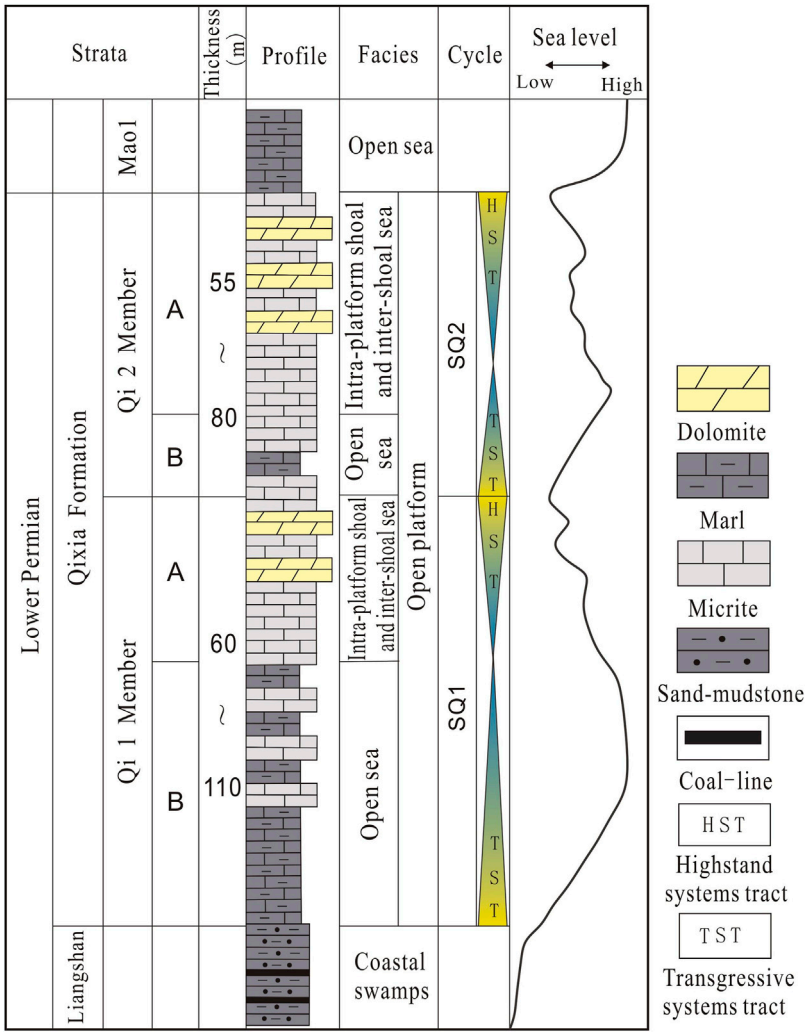

FIGURE 2
Stratigraphic integrated histogram of Qixia Formation in the study area.

is .04%, while the maximum porosity is 9.06%, and the average porosity is .57%. The samples with porosity less than 1% account for 88.9% of the total samples; while the samples with porosity greater than 4% account for only .6% of the total samples. The minimum permeability of the limestone samples is close to 0, while the maximum permeability is 4.75×10^{-3} μm^2, and the average permeability is 1.05×10^{-3} μm^2. The samples with permeability less than 1×10^{-3} μm^2 accounted for 83.4% of the total samples. For the dolomite samples, the minimum porosity is .43%, the maximum porosity is 10.86%, and the average porosity is 4.12%. The samples with porosity greater than 2% accounted for 70.3% of the total samples. In addition, the minimum permeability is close to 0, the maximum is 101.6×10^{-3} μm^2, and the average is 6.32×10^{-3} μm^2. The samples with permeability greater than 1×10^{-3} μm^2 accounted for about 62.1% of the total samples.

The dolomite of the Qixia Formation in the study area has better reservoir performance than limestone. This is because the dolomite is formed on the basis of bioclastic limestone and other granular rocks by dolomitization. Under the action of dolomitization, the gray matter minerals are transformed into dolomite, and the strength and pressure solubility of the rock are increased. At the same time, the dissolution pores and caves are easy to form in dolomite after the dissolution in the quasi-syngenetic period.

4.4 Carbon and oxygen isotopes

The fractionation effect of carbon isotopes in carbonate rocks is little affected by temperature and pH. In the process of carbonate precipitation, carbon isotope changes only slightly, so it can objectively reflect the original carbon isotope composition of seawater. The oxygen isotopic composition of carbonate rocks is mainly controlled by fluid fractionation during deposition, open-seal degree of sedimentary environment, hydrothermal process and temperature during diagenesis. The higher the temperature, the more negative the oxygen isotopes of the precipitated minerals.

The $\delta^{13}C$ values of the Permian Qixia Formation limestones in the central Sichuan Basin range from 2.89‰ to 5.23‰, with an average of 4.21‰; while the $\delta^{18}O$ values range from −6.85‰ to −5.31‰, with an average of −6.22‰. In addition, the $\delta^{13}C$ values of dolomites range

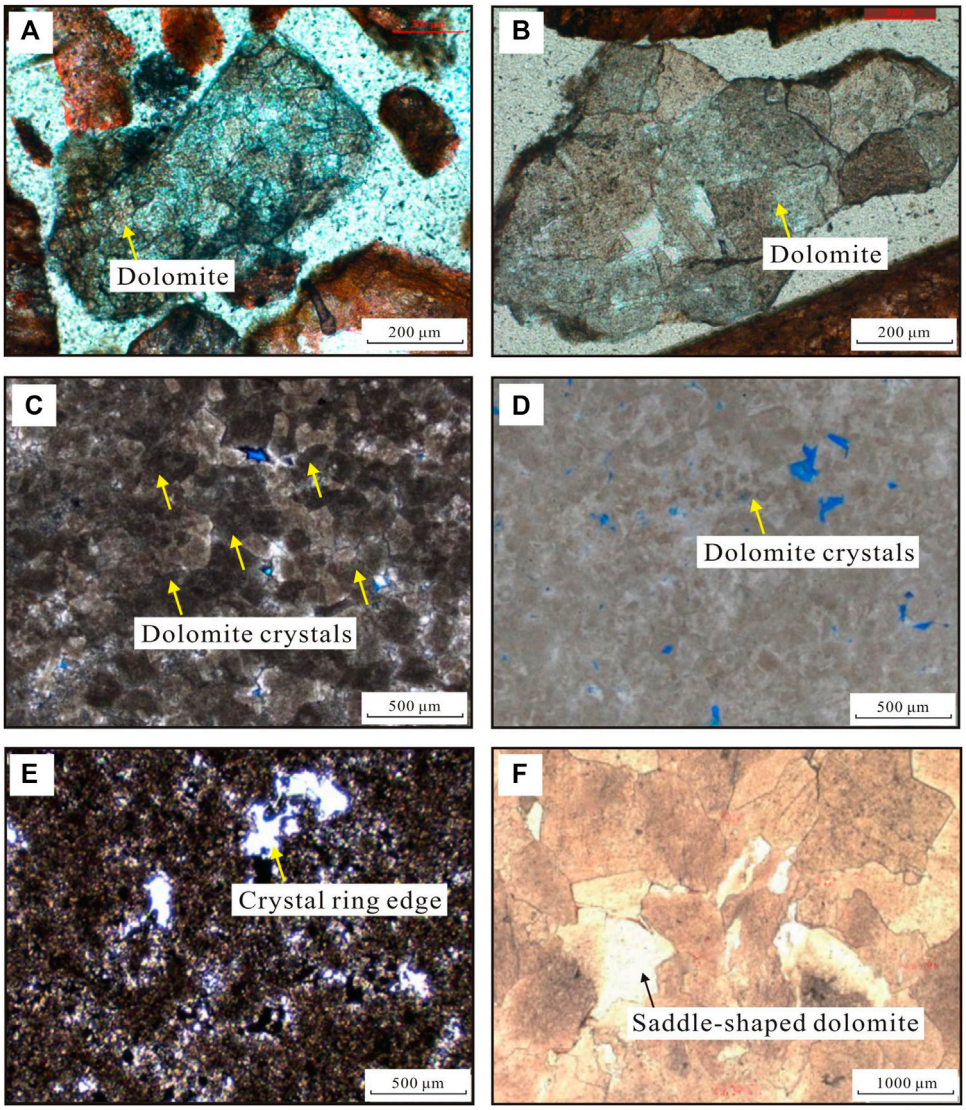

FIGURE 3
Microcosmic characteristics of dolomites of Permian Qixia Formation in central Sichuan Basin. **(A)** Moxi well 131X1, 4,291 m, mesocrystalline dolomite; **(B)** Gaoshi 128 well, 4,288 m, fine—medium crystalline dolomite; **(C)** Moxi 42 well, 4651.43 m, medium coarse crystal dolomite with blurred crystal edge; **(D)** Moxi 42 well, 4651.43 m, with obvious biodebris; **(E)** Heshen two well, mud-silty sand-clastic dolomite, 4357.5 m, with sparry ring edges on grain edges; **(F)** Gaoshi 16 well, saddle-shaped dolomite, 4556.4 m, coarse crystal, curved crystal surface and dissolution pores.

from 3.68‰ to 5.25‰, with an average of 4.73‰, and the $\delta^{18}O$ values range from −8.35‰ to −7.02‰, with an average of −6.52‰. As a whole, the $\delta^{13}C$ values of the dolomites and limestones are located in the Early Permian seawater, while the $\delta^{18}O$ values are roughly or slightly lower than those of the contemporaneous seawater (Figure 6). The negative oxygen isotope indicates the existence of obvious thermodynamic fractionations. Moreover, the formation of dolomites may be influenced by the hydrothermal processes, namely, hydrothermal dolomitization.

4.5 Strontium isotope

In geological history, the composition of strontium isotopes in seawater is a function of time. The change of strontium isotope with time is mainly controlled by two strontium sources: ① Strontium of relatively radioactive origin is provided to seawater by weathering of ancient continental siliceous aluminaceous rocks through rivers. It has a high $^{87}Sr/^{86}Sr$ ratio (Huang et al., 2006). ② Relatively radiation-depleted strontium that is supplied by mid-ocean ridge hydrothermal systems through seafloor spreading or volcanic activities. It has a low $^{87}Sr/^{86}Sr$ value (Huang et al., 2006). The mixing time of strontium in seawater (about .001 Ma) is much less than the residual time of strontium in seawater (about 1 Ma). Therefore, the isotopic composition of marine strontium is the same all over the world at any time. Unlike carbon and oxygen isotopes, strontium isotopes do not fractionate due to temperature, pressure and microbial effects, and minerals can directly reflect the isotopic composition of fluids (Mazzullo, 2000; Li and Liu., 2013; Pajdak et al., 2017).

According to statistics, the $^{87}Sr/^{86}Sr$ values of micritic limestone of the Permian Qixia Formation in the central Sichuan range from

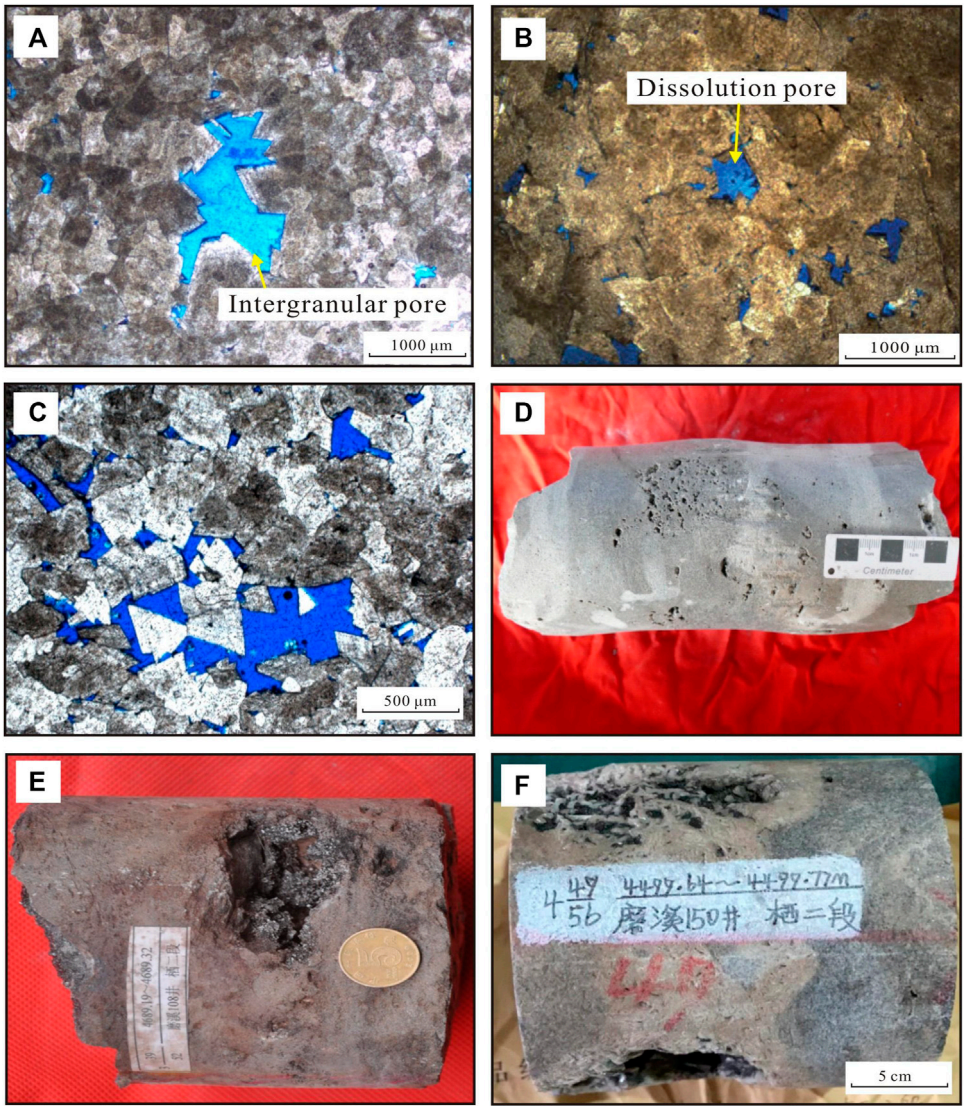

FIGURE 4
Development characteristics of pores developed in dolomite reservoirs of Permian Qixia Formation in central Sichuan Basin. **(A)** Moxi 42 well, 4,656 m, crystalline dolomite, intercrystalline pores; **(B)** Moxi 108 well, medium granular dolomite, 4671.25 m, intercrystalline dissolved pores; **(C)** Moxi 150 well, 4500.7 m, mesocrystalline dolomite, intercrystalline pores and intercrystalline dissolved pores; **(D)** Moxi 151 well, granular dolomite, 4483.70–4483.93 m, dissolution pores; **(E)** Moxi 108 well, granular dolomite, 4689.19–4689.32 m, dissolution pores; **(F)** Moxi 150 well, granular dolomite, 4499.64–4499.77 m, dissolution pores.

.70661 to .70755, with an average value of .70712; the $^{87}Sr/^{86}Sr$ values of micritic bioclastic limestones in the Permian Qixia Formation range from .707,009 to .70767, with an average of .70748; the $^{87}Sr/^{86}Sr$ values of the granular dolomites range from .70765 to .71045, with an average of .70844; in addition, the $^{87}Sr/^{86}Sr$ values of the saddle-shaped dolomites range from .70765 to .70939, with an average of .70832.

By comparing the $^{87}Sr/^{86}Sr$ values of the global Permian seawater, it is found that the $^{87}Sr/^{86}Sr$ values of the micritic limestones and micritic bioclastic limestones fall within the seawater range of the same period, while that of the granular and the saddle-shaped dolomites are higher than the seawater range of the same period (Figure 7) (Huang et al., 2001; Jiang et al., 2018). Therefore, the formation of granular and saddle-shaped dolomites may be modified by strontium-rich fluids.

The large scale magmatic activities in the late Early Permian in the Sichuan Basin is the eruption and intrusion of basic rocks. In turn, the hydrothermal dolomites have other sources of ^{87}Sr-rich strontium isotopes. When the deep hydrothermal fluids passed through the underlying Cambrian Qiongzhusi Formation shale, it probably mixed with the ^{87}Sr-rich pore fluids in clastic rocks, and migrated upward to the Permian system. Finally, recrystallization and hydrothermal precipitation resulted in ^{87}Sr-rich in granular and saddle-shaped dolomites inside the fractures and caves.

4.6 Cerium and europium isotopes

Eu and Ce are abnormal in different diagenetic environments due to the change of valence state (Vasconcelos et al., 1995; Machel,

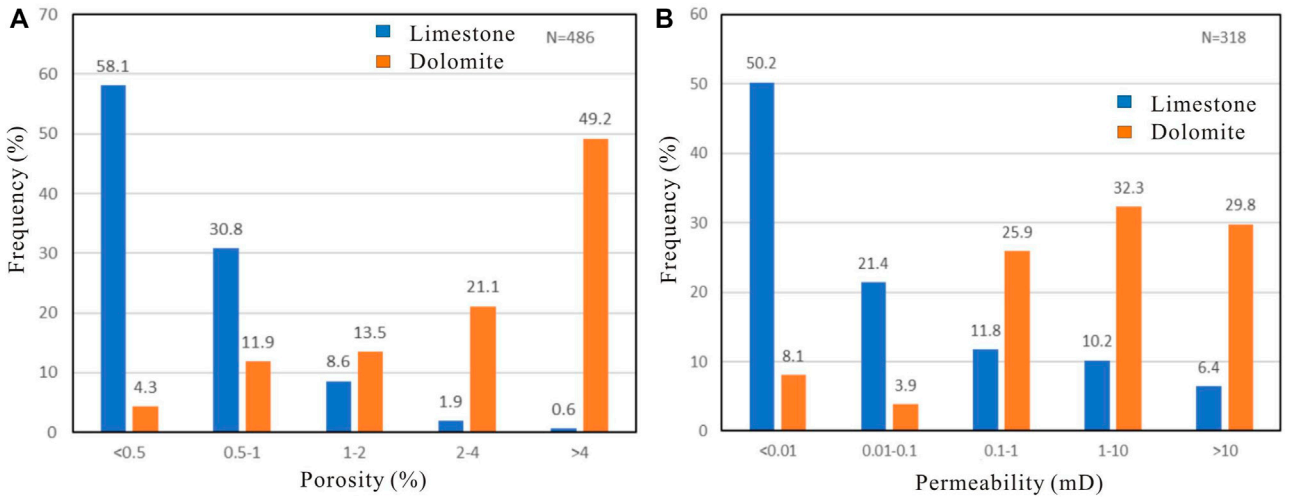

FIGURE 5
Histograms of physical property distribution of limestones and dolomites in Permian Qixia Formation in central Sichuan Basin. **(A)** Porosity distribution histogram; **(B)** Permeability distribution histogram.

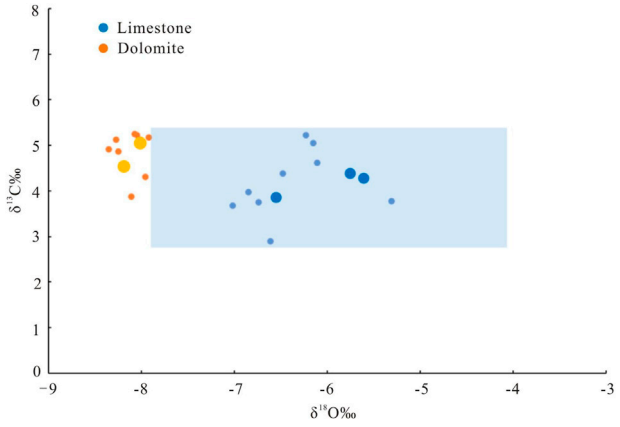

FIGURE 6
Carbon and oxygen isotope characteristics of limestones and dolomites of Permian Qixia Formation in Central Sichuan Basin (partial data from Chen et al., 2012). The blue area represents the range of carbon and oxygen isotopes in early Permian seawater; the enlarged symbol data comes from Chen et al., 2012.

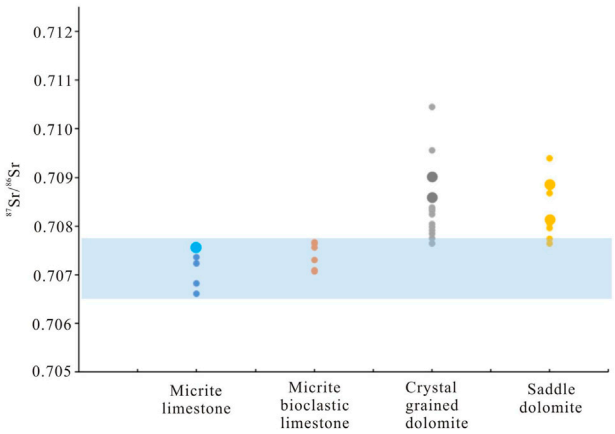

FIGURE 7
$^{87}Sr/^{86}Sr$ isotopic characteristics of different lithologies of Permian Qixia Formation in Central Sichuan Basin (partial data from Jiang et al., 2018). The blue area represents the $^{87}Sr/^{86}Sr$ range (.70662–.70774) of Permian seawater; the enlarged symbol data comes from Jiang et al., 2018.

2004; Haas et al., 2017). Thus, they can be used to indicate different diagenetic environments. For example, Ce is sensitive to environmental redox properties in aqueous solution and precipitation process, and it often fractionates with other trivalent rare Earth elements. Ce^{3+} is oxidized to Ce^{4+} under oxidizing conditions. Ce^{4+} is less soluble and more thermodynamically stable than other trivalent rare Earth elements (Davies and Smith., 2006; Cheng et al., 2022). The insolubility and preferential adsorption of Ce^{4+} on the particle surface lead to the separation of $Ce^{4+}$from other rare Earth elements, and this process leads to the negative anomaly of Ce.

The δCe values of the Permian Qixia Formation limestones in the central Sichuan Basin range from .73 to 1.01, with an average of .85; while the δEu values range from .94 to 1.3, with an average of 1.09. The δCe values of dolomites range from .73 to 1.01, with an average of .89, and the δEu values range from .97 to 1.98, with an average of 1.23. The δCe and δEu values of micritic limestone are .68 and .73, respectively. As can be seen from Figure 8, when δCe is less than 1 and δEu is greater than 1, the Ce element has a slight negative anomaly, while the Eu element has a slight positive anomaly. The δCe and δEu values of all the samples are higher than those of the micritic limestones under the seawater of the same period. It reflects that the

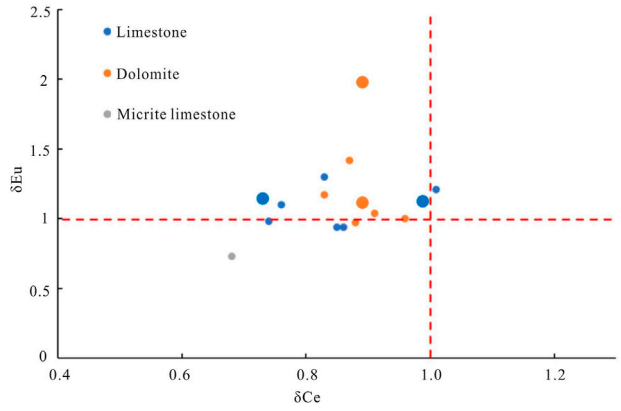

FIGURE 8
Distribution of Eu and Ce in dolomites of Permian Qixia Formation in Central Sichuan Basin (partial data from Duan et al., 2021). The enlarged symbol data comes from Duan et al., 2021.

formation environment of dolomites is oxidation and high temperature.

5 Discussion

5.1 Origin of dolomite

According to the microscopic and geochemical characteristics of the dolomites in the Permian Qixia Formation, central Sichuan Basin, it is believed that the dolomites are mainly formed in the quasi-syngenetic period, and are transformed by hydrothermal actions in the shallow burial period. The basis is as follows:

① Direct contact between dolomite and limestone can be seen in the Qixia Formation in the central Sichuan Basin, for example, the coring section of Well Moxi 42 at 4,653.46 m (Figure 9). This indicates that dolomitization occurred at least before massive pressure dissolution.

② From the perspective of chronology, previous studies have found that the age of surrounding dolomite rocks of the Permian Qixia Formation in the central Sichuan Basin is (274.5 ± 9.9) Ma, and the age of the Qixia Formation is (283.5 ± .6) Ma ~ (272.95 ± .11) Ma. The age of dolomite falls in the Qixia Formation, which is the most direct evidence that the surrounding dolomite rocks are formed in the quasi-syngenetic period.

③ From the perspective of geochemical properties, the degree of order of dolomites in the Qixia Formation in the study area is generally low, which is in line with the characteristics of quasi-syngenetic dolomitization (Tan et al., 2022). The values of $^{87}Sr/^{86}Sr$ and $\delta^{13}C$ of dolomites and limestones fall within the range of the Permian seawater. It reflects that the diagenetic fluids of limestone and dolomitization are of the same origin. Dolomites have lower $\delta^{18}O$ values and higher $^{87}Sr/^{86}Sr$ values than limestones due to slight modifications by later diagenetic fluids. In addition, the δEu element of dolomites shows a slight positive anomaly. The positive anomaly only appears in the extreme reduction environment. Therefore, it reflects that the fluids by dolomite transformation in the late stage is hydrothermal fluids with high temperature, and the hydrothermal fluid came from the volcanic event of Mount Emei at the end of the Maokou Formation (Tan et al., 2022).

5.2 Controlling factors of dolomite reservoir development

(1) Influence of granular shaol on reservoir development

The Permian Qixia Formation in the Sichuan Basin is mainly developed in platform margin, open platform and sag conditions. The most dominant microfacies assemblages of the Permian Qixia Formation in the central Sichuan area are the sedimentary sequences of interbeded interbeach-sea and intra-platform shoal in the open platform. In addition, it is longitudinally reflected as a rock assemblage type consisting of micritic rocks gradually transitioning upward to granular rocks (Figure 2). The granular shoal within the platform is mainly distributed in the Longnusi, Moxi and Gaoshiti areas, and its lithology mainly includes granular limestone, residual granular dolomite, dolomitic limestone and callitic dolomite. The low energy non-granular rocks have high original porosity in the sedimentary stage. However, under the influence of compaction and cementation in the early stage of shallow burial, the original pores are difficult to be preserved due to rapid compaction. Therefore, it is difficult for karst water to enter the reservoir in the diagenetic stage. Granular rocks represent strong water energy. After winnowing, the proportion of fine sediments is very low, and the contacts between particles are often point-line type. Therefore, the original pores are well preserved in the shallow burial stage. The pore development layer is a high permeability layer that allows karst water to pass through, which can promote the full water-rock interactions of karst water along the intergranular pores. Furthermore, the pore-cave or fracture-cave type reservoirs with good permeability are formed.

The study shows that the granular shoals are controlled by the sedimentary paleogeomorphology. Granular shoal are generally developed in the high parts of paleogeomorphology where the energy of the sedimentary water is high. The thickness of the shoal facies in the high parts is larger than that in the slope areas. Granular shoals are not only the material base of reservoir development, but also provide an important carrier of primary reservoir space. Bioclastic particles themselves contain coelomic pores, and intergranular pores are formed by particle accumulation. These primary pores are an important part of the effective reservoir space, and also promote the development of dissolution pores in the quasi-syngenesis.

(2) Effect of sequence interface on longitudinal distribution of reservoirs

The sedimentary cycles of the Permian Qixia Formation in the central Sichuan Basin are very clear (Figure 9). In the highstand systems tract of each cycle, high-energy deposits such as sparry clastic limestones and dolomites are developed. During the period of sea level decline in the highstand systems tract, the granular shoals developed in the high parts of the paleogeomorphology are easily exposed. At this time, some soluble minerals such as aragonite and high-magnesium calcite are dissolved by atmospheric fresh water, and pore layers and

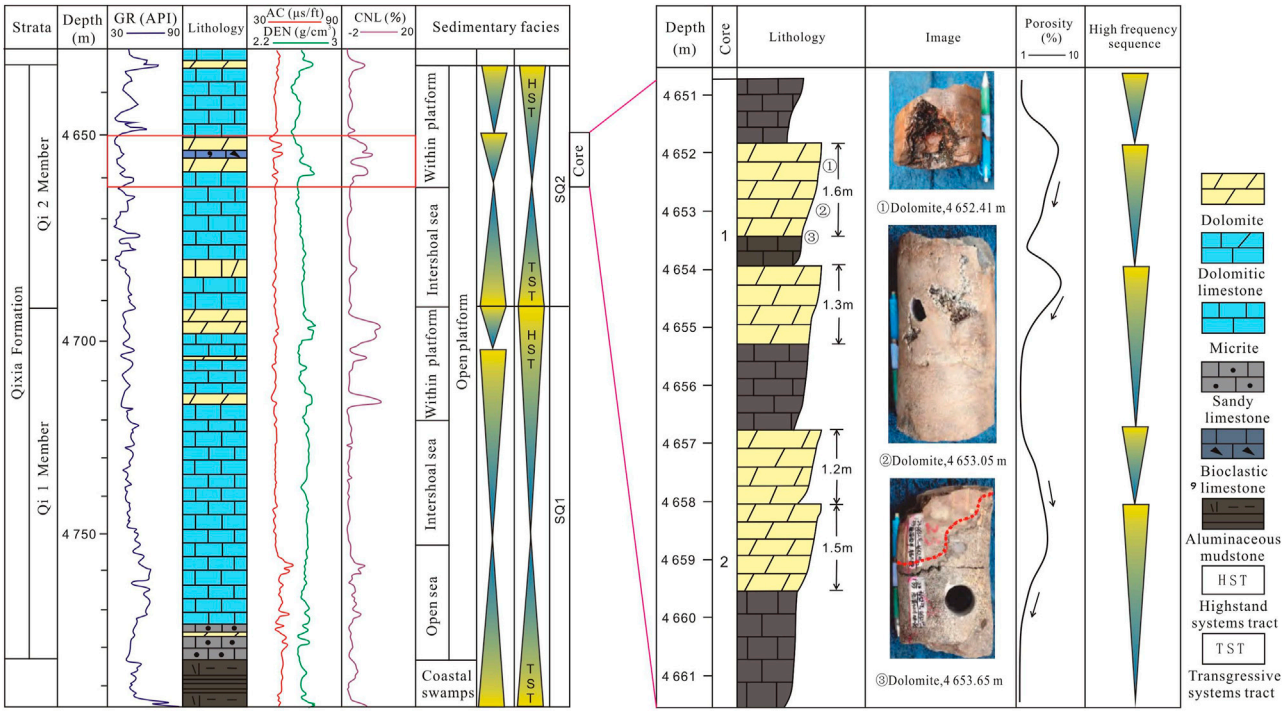

FIGURE 9
Comprehensive lithologic histogram of ixia Formation in Well Moxi 42 (modified after Duan et al., 2021).

dissolution pores are formed along the bedding. At the top of the sequence interface, the dissolution pores are large, and at the bottom, there are almost no dissolution pores in the bioclastic micritic limestones. Then, a typical high-frequency cycle is formed (Figure 9). It should be noted that not every high frequency cycle will have dolomite development at the top, but the dolomite is all developed at the top of the high frequency cycle. This is well confirmed by the $\delta^{18}O$ analysis data, which shows that dolomite (mean −6.52%) is more negative than limestone (mean −6.22%). This is because the dolomite of the Qixia Formation in the study area is usually developed at the end of the high frequency cycle, that is, the top of the high frequency cycle. At the same time, the decline of sea level inevitably leads to the gradually restricted water body in the high parts of the ancient landforms. Due to the gradual enrichment of Mg^{2+} in seawater by evaporation, the Mg^{2+}-rich fluids enter the granular shoal limestones along the pre-existing dissolution pores, and then lead to the percolation and reflux dolomitization of the granular shoal limestones. This is also the reason why dissolution pores of the Qixia Formation mainly exist in dolomites.

(3) Effect of quasi-syngenetic dissolution on reservoir development

Quasi-syngenetic dissolution is one of the key diagenesis processes for the formation of high quality carbonate reservoirs. Granular shoals are exposed to atmospheric freshwater diagenetic environments under high frequency sea-level changes. At this time, the fluids in the pore of rock are mainly atmospheric fresh water, and the dissolution is significant at this stage. Unstable minerals are prone to selective dissolution of fabrics, which promotes the formation of secondary dissolution pores. The quasi-syngenetic dissolution not only promotes the development of early secondary pores, but also provides a good percolation channel for later diagenetic fluids.

The reservoirs formed by quasi-syngenetic dissolution have strong longitudinal differences. Due to the frequent rise and fall of sea level, the time of quasi-syngenetic dissolution is very limited, and the karstification of each stage of granular shoal can only reach a certain depth. Under the surface of dissolution, the dissolution of atmospheric fresh water is strong, and a large number of dissolution pores and caves are formed. However, for the lower granular shoal far from the dissolution surface, the dissolution pores are less developed due to the weak dissolution. Dissolved pores are the main pore type. Furthermore, there is a positive correlation between the sedimentary cycle of the granular shoals and the development degree of pores and the physical properties.

Through the observations of the cores of Well Moxi 42, it is found that the pores are generally developed in the middle and upper cycle of the granular shoals. The changes of core porosity and permeability have obvious characteristics of multiple sedimentary cycles (Figure 9). The development of dissolution in dolomite reservoir is closely related to the change of high frequency sea level, that is, it shows the characteristics of quasi-syngenetic dissolution. The main reasons are: 1) From the point of view of the cores, the quasi-syngenetic dissolution is manifested as the formation of dissolution pores distributed along the beddings, and most of the pores are developed in the upper cycle of the shoal; 2) From thin section observations, the quasi-syngenetic dissolution is manifested as the expansion of the primary pores such as intergranular and biocoelomic pores. Dissolution pores of different grades are well developed (Figures 3F,4B).

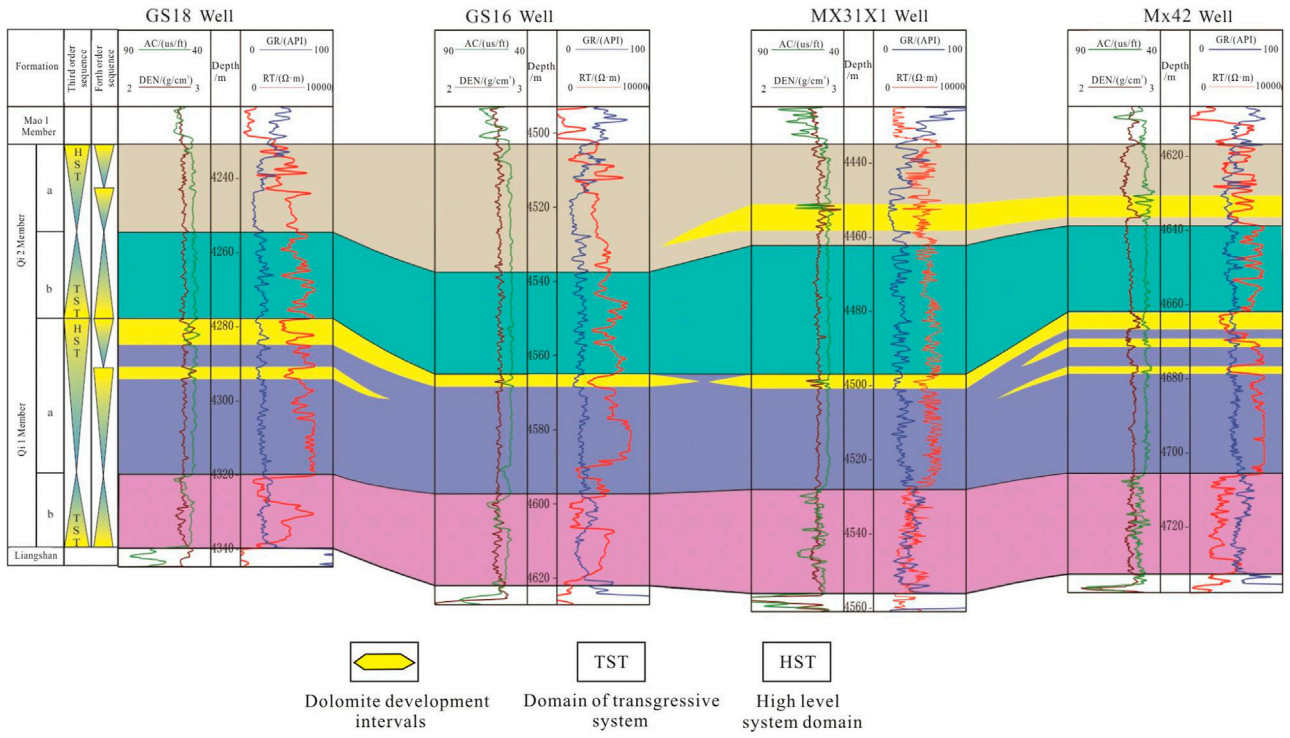

FIGURE 10
Interwell correlation profile of dolomite reservoirs of Permian Qixia Formation in central Sichuan Basin.

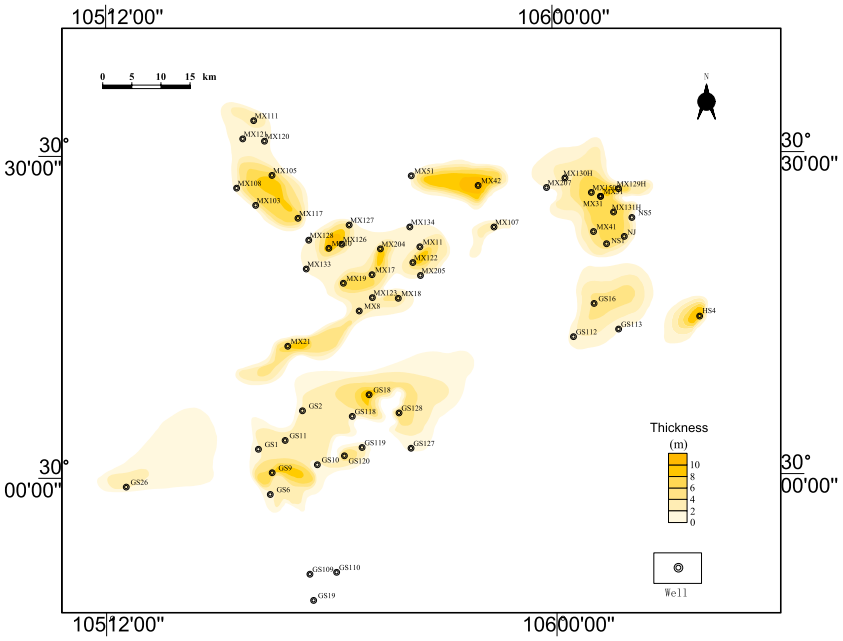

FIGURE 11
Thickness distribution of dolomite reservoirs of Permian Qixia Formation in central Sichuan Basin.

5.3 Distribution law of dolomite reservoirs

According to previous studies, the dolomites of the Permian Qixia Formation in the Sichuan Basin are characterized by thin single layer thickness and strong lateral heterogeneity (Tian et al., 2015). However, in this study, dolomites with thickness of several meters to 10 m were developed in the Permian Qixia Formation in central Sichuan Basin. For example, the thickness of dolomites in the areas where Wells Moxi

42, Moxi 10, Moxi 11, and Moxi 21 are located is all greater than 10 m. According to the well-connecting profile in Figure 10, dolomites are developed in the HST of SQ1 in Wells Gaoshi 18 and Gaoshi GS16. The dolomites are generally located in the middle part of the Qixia Formation. In addition, dolomites are developed in the HST of SQ2 in Wells Moxi 31X1 and Moxi 42. The dolomites are generally located 10–20 m away from the top of the Qixia Formation. The dolomite reservoirs of the two adjacent wells have similar development positions. This indicates that the dolomites of the Permian Qixia Formation in the central Sichuan Basin have good transverse continuity in a certain area.

According to the above research, the development of dolomite reservoirs is affected by many factors. The paleogeomorphic highlands in the paleo-sedimentary period are the dominant topographic units for the development of grain shoals. During the period of sea level decline in the high level domain, the grain shoals in the high position are most prone to be exposed and then dissolved to form early pores. These pores provide channels for early dolomitization, and early dolomitization is conducive to the preservation of early pores. On the other hand, the water energy in the high parts of paleogeomorphology during the deposition period was high, so the deposition thickness was significantly higher than that in the surrounding areas. Therefore, the areas with large sedimentary thickness of the Qixia Formation is the favorable areas for the development of dolomite reservoirs. The planar distribution of dolomite reservoirs is shown in Figure 11.

Firstly, the macro distribution range of dolomite of the Qixia Formation is predicted by the palaeogeomorphology restoration. In addition, the planar distribution of dolomite reservoir can be predicted according to the seismic response of dolomite reservoirs. Finally, the distribution of dolomite reservoirs is predicted by the geological and seismic results. The dolomite shoals in the study area are distributed as clumps in the plane, and they cover a total area of 1,940 km^2. The thickness of dolomite reservoirs exposed by drillings is distributed in 6 m–12 m, and the thickness of dolomite reservoirs revealed by the Gaoshi 128 well is 16.7 m. Moreover, several wells, such as Wells Moxi 31X1, Moxi 42, Gaoshi 18, Heshen two and Heshen 4, have obtained high production gasflows. It shows that the dolomites of the Permian Qixia Formation in central Sichuan Basin has great potential for oil and gas exploration and development.

6 Conclusion

(1) The dolomites developed in the Permian Qixia Formation in the central Sichuan Basin have the characteristics of small single-layer thickness and multi-layer development, and they are interbeded with the limestones. The reservoir types are mainly fine crystal dolomite and fine medium crystal dolomite, and the reservoir spaces are mainly intercrystalline pores and caves. Moreover, the reservoir physical properties are characterized by medium porosity and medium to high permeability.

(2) Quasi-syngenetic dolomitization is the main origin of dolomite in the target layer, and the dolomite was slightly modified by hydrothermal solution at the end of the Maokou Formation period. The development of dolomite reservoirs in the Qixia Formation in the study area is affected by palaeogeomorphology, sedimentation and diagenesis.

(3) The granular shoal facies developed in the high parts of paleogeomorphology provides the material basis for the formation of dolomite reservoirs. The high frequency sequence interface controls the development of dolomite reservoirs in highstand systems tract. In addition, the quasi-syngenetic dissolution promotes the development of the early secondary pores and provids an effective channel for the migration of diagenetic fluids in the later stage.

(4) In the direction of orthogonal horizontal deposition, the dolomites have the characteristics of thin monolayer thickness, multiple sequences and are interbedded with limestone. The dolomite shoals in the study area are distributed as clumps in the plane, which has great potential for hydrocarbon exploration.

Data availability statement

The original contributions presented in the study are included in the article/Supplementary Material, further inquiries can be directed to the corresponding author.

Author contributions

KT is responsible for the idea of this paper and QW, JC, JY, YQ, and YZ are responsible for the experiments.

Conflict of interest

Authors KT, QW, JC, JY, YQ, and YZ are employed by the Research Institute of Petroleum Exploration and Development Northwest Branch.

Publisher's note

References

Bau, M., and Dulski, P. (1996). Distribution of yttrium and rare-Earth elements in the penge and kuruman iron-formations, transvaal supergroup, South Africa. *Precambrian Res.* 79 (1/2), 37–55. doi:10.1016/0301-9268(95)00087-9

Briais, A., Patriat, P., and Tapponnier, P. (1993). Updated interpretation of magnetic anomalies and seafloor spreading stages in the South China Sea: Implications for the Tertiary tectonics of Southeast Asia. *J. Geophys. Res. Solid Earth* 98 (B4), 6299–6328. doi:10.1029/92JB02280

Budd, D. A. (1997). Cenozoic dolomites of carbonate islands: Their attributes and origin. *Earth-Science Rev.* 42, 1–47. doi:10.1016/S0012-8252(96)00051-7

Burke, W. H., Denison, R. E., Hetherington, E. A., Koepnick, R. B., Nelson, H. F., and Otto, J. B. (1982). Variation of seawater $^{87}Sr/^{86}Sr$ throughout Phanerozoic time. *Geology* 10 (10), 516–519. doi:10.1130/0091-7613(1982)10<516:vosstp>2.0.co;2

Chacko, T., and Deines, P. (2008). Theoretical calculation of oxygen isotope fractionation factors in carbonate systems. *Geochimica Cosmochimica Acta* 72 (15), 3642–3660. doi:10.1016/j.gca.2008.06.001

Chen, X., Zhao, W., and Zhang, L. (2012). Discovery and exploration significance of the Middle Permian tectonic hydrothermal dolomite in the central Sichuan Basin. *Acta Pet. Sin.* 33 (4), 562–569. doi:10.3969/j.issn.1672-9854.2021.04.007

Cheng, Z., Yong, S., Yiren, F., Peiqiang, Y., Xinmin, G., Fei, W., et al. (2022). Application and prospect of low-field nuclear magnetic resonance technology in accurate characterization of coal pore structure. J. *J. China Coal Soc.* 47 (02), 828–848. doi:10.13225/j.cnki.jccs.xr21.1766

Crozaz, G., Floss, C., and Wadhwa, M. (2003). Chemical alteration and REE mobilization in meteorites from hot and cold deserts. *Geochimica Cosmochimica Acta* 67 (24), 4727–4741. doi:10.1016/j.gca.2003.08.008

Davies, G. R., and Smith, L. B. (2006). Structurally controlled hydrothermal dolomite reservoir facies: An overview. *AAPG Bull.* 90 (11), 1641–1690. doi:10.1306/05220605164

Duan, J., Zheng, J., and Shen, A. (2021). Characteristics and Genesis of dolomite reservoir of lower permian Qixia Formation in central Sichuan Basin. *Mar. oil gas Geol.* 26 (4), 345–356. doi:10.3969/j.issn.1672-9854.2021.04.007

Gao, C., Meng, S., Zhang, J., Wang, J., and Sun, Y. (2023). Effects of cementation on physical properties of clastic rock-originated weathering crust reservoirs in the Kexia region, Junggar Basin, NW China. *Energy Geosci.* 4 (1), 74–82. doi:10.1016/j.engeos.2022.08.006

Geske, A., GoldsteinMavromatis, R. H, V., Richter, D., Buhl, D., Kluge, T., et al. (2015). The magnesium isotope (δ^{26}Mg) signature of dolomites. *Geochimica Cosmochimica Acta* 149, 131–151. doi:10.1016/j.gca.2014.11.003

Haas, J., Hips, K., Budai, T., Gyori, O., Lukoczki, G., Kele, S., et al. (2017). Processes and controlling factors of polygenetic dolomite Formation in the transdanubian range, Hungary: A synopsis. *Int. J. Earth Sci.* 106 (3), 991–1021. doi:10.1007/s00531-016-1347-7

Hong, H., Su-ping, P., and Long-yi, S. (2004). Trace elements and sedimentary settings of Cambrian-Ordovician carbonates in Bachu area, Tarim Basin. *Xinjiang Pet. Geol.* 25 (6), 631.

Hu, X. M., and Wang, C. S. (1990). Several major geological events and global climate change since 100 Ma. *Escploration Nat.* 18 (67), 53–58. doi:10.1016/0375-6742(81)90109-6

Huang, C. G., Huang, S. J., and Wu, S. J. (2006). Evolution and main controlling factors of strontium isotopic composition in seawater from 100 Ma. *J. Earth Sci. Environ.* 28 (2), 19–25. doi:10.3969/j.issn.1672-6561.2006.02.004

Huang, S., Shi, H., and Zhang, M. (2001). Strontium isotope evolution and global sea level change of Carboniferous-Permian Marine carbonates in the Upper Yangtze Basin. *Acta Sedimentol. Sin.* 19 (4), 481–487.

Jiang, Y., Gu, Y., and Li, K. (2018). Types and Genesis of reservoir and permeability space of Middle Permian hydrothermal dolomite in the central Sichuan Basin. *Nat. Gas. Ind.* 38 (2), 16–24. doi:10.3787/j.issn.1000-0976.2018.02.003

Li, H., and Liu, Y. (2013). Dolomite problem" and research of ancient lacustrine dolostones. *Acta Sedimentol. Sin.* 3 (2), 302–315. doi:10.14027/j.cnki.cjxb.2013.02.017

Ma, L., Song, M., Wang, Y., Wang, Y., and Liu, H. (2023). Exploration progress of the paleogene in jiyang depression, Bohai Bay Basin. *Energy Geosci.* 4 (1), 42–50. doi:10.1016/j.engeos.2022.07.004

Machel, H. G. (2004). Concepts and models of dolomitization: A critical reappraisal. *Geol. Soc. Lond. Spec. Publ.* 235 (1), 7–63. doi:10.1144/gsl.sp.2004.235.01.02

Mazumdar, C., Alleno, E., Sologub, O., Salamakha, P., Noel, H., Potel, M., et al. (2003). Investigations of the structural, magnetic and Ce-valence properties of quaternary CeM_2B_2C compounds (M: Co, Ni Rh, Pd Ir and Pt). *ChemInform* 34 (11), 18–25. doi:10.1016/S0925-8388(01)01979-X

Mazzullo, S. J. (2000). Organogenic dolomitization in peritidal to deep-sea sediments. *J. Sediment. Res.* 70 (1), 10–23. doi:10.1306/2dc408f9-0e47-11d7-8643000102c1865d

Meyer, E. E., Quicksall, A. N., Landis, J. D., Link, P. K., and Bostick, B. C. (2013). Trace and rare Earth elemental investigation of a sturtian cap car▪bonate, pocatello, Idaho: Evidence for ocean redox conditions before and during carbonate deposition. *Precambrian Res.* 192 (1), 89–106. doi:10.1016/j.precamres.2011.09.015

Morozov, V. P., Jin, Z., Liang, X., Korolev, E. A., Liu, Q., Kolchugin, A. N., et al. (2021). Comparison of source rocks from the lower silurian longmaxi Formation in the yangzi platform and the upper devonian semiluksk Formation in East European platform. *Energy Geosci.* 2 (1), 63–72. doi:10.1016/j.engeos.2020.10.001

Pajdak, A., Godyn, K., Kudasik, M., and Murzyn, T. (2017). The use of selected research methods to describe the pore space of dolomite from copper ore mine, Poland. *Environ. Earth Sci.* 76 (10), 389–416. doi:10.1007/s12665-017-6724-4

Richardson, M., Abraham-A, F., and Anthony, I. (2022). Physical properties of sandstone reservoirs: Implication for fluid mobility. *Energy Geosci.* 3 (4), 349–359. doi:10.1016/j.engeos.2022.06.001

Tan, K., Yao, J., Chen, J., Tang, D., Qin, Y., and Wu, Q. (2022). Controlling effect of source-reservoir assemblage on natural gas accumulation: A case study of the upper triassic xujiahe Formation in the Sichuan Basin. *Front. Earth Sci.* 10, 1–15. doi:10.3389/feart.2022.1028439

Tian, Y., Liu, S., and Zhao, Y. (2015). Formation mechanism of high quality reservoirs of lower cambrian longwangmiao Formation in central Sichuan Basin. *J. Guilin Univ. Technol.* 35 (2), 217–226. CNKI:SUN:GLGX.0.2015-02-001.

Vasconcelos, C., McKenzie, J. A., Bernasconi, S., Grujic, D., and Tiens, A. J. (1995). Microbial mediation as a possible mechanism for natural dolomite formation at low temperatures. *Nature* 377 (6546), 220–222. doi:10.1038/377220a0

Veizer, A., Azmy, K., Bruckschen, P., Buhl, D., Bruhn, F., et al. (1999). 87Sr/86Sr, δ^{13}C and δ^{18}O evolution of Phanerozoic seawater. *Chem. Geol.* 161 (1/3), 59–88. doi:10.1016/S0009-2541(99)00081-9

Xie, R., Luo, Z., Zhang, M., Wang, Y., Chen, J., and Zhu, M. (2022). Factors controlling tight oil and gas reservoir development in the Jurassic siliciclastic-carbonate rocks in Sichuan Basin, China. *Energy Geosci.* 3 (4), 453–464. doi:10.1016/j.engeos.2021.08.001

Xiong, L., Yao, G., Ni, C., Xiong, S., Shen, A., Zhou, G., et al. (2017). Characteristics, controlling factors and evolution of the middle devonian guanwushan formation reservoirs in longmenshan area, northwestern sichuan, China. *Nat. Gas. Geosci.* 28 (7), 1031–1042. doi:10.11764/j.issn.1672-1926.2017.06.010

frontiers | Frontiers in Earth Science

TYPE Original Research
PUBLISHED 09 May 2023
DOI 10.3389/feart.2023.1182711

OPEN ACCESS

EDITED BY
Hu Li,
Southwest Petroleum University, China

REVIEWED BY
Dianshi Xiao,
China University of Petroleum, Huadong, China
Xixin Wang,
Yangtze University, China
Huafeng Tang,
Jilin University, China

*CORRESPONDENCE
Qingyou Yue,
yueqingyou@lnpu.edu.cn

RECEIVED 09 March 2023
ACCEPTED 14 April 2023
PUBLISHED 09 May 2023

CITATION
Yue Q, Wang B, Ren X, Cang Z, Han J, Li C, Zhao R and Wang H (2023), Classification, identification, and reservoir characteristics of intermediate mafic lava flows: a case study in Dongling area, Songliao Basin.
Front. Earth Sci. 11:1182711.
doi: 10.3389/feart.2023.1182711

Classification, identification, and reservoir characteristics of intermediate mafic lava flows: a case study in Dongling area, Songliao Basin

Qingyou Yue[1]*, Baozhu Wang[1], Xianjun Ren[2], Zhengyi Cang[3], Jiaoyan Han[2], Cunlei Li[1], Ranlei Zhao[1] and Haidong Wang[1]

[1]College of Petroleum and Natural Gas Engineering, Liaoning Petrochemical University, Fushun, China, [2]Northeast Oil & Gas Branch of Sinopec, Changchun, China, [3]Chengdu Exploration and Development Research Institute, Petro China Daqing Oilfield Company LTD, Chengdu, China

Intermediate mafic lava is a special oil and gas reservoir. While its internal structure is an important factor affecting the reservoir properties, the identification of facies and understanding of the relationship between facies architecture and reservoir are limited. This study evaluated the intermediate mafic lava flows of the Yingcheng Formation in the Dongling area of Songliao Basin by analyzing drilling cores, corresponding thin sections, and scanning electron microscope (SEM) images, as well as well-logging and seismic attributes. We also performed helium gas experiments and high-pressure mercury intrusion (HPMI) analysis to assess the physical properties and pore structure of the reservoir, respectively. The results showed that intermediate mafic lava flows develop tabular lava flow, compound lava flow, and hyaloclastite. Three facies showed present diverse well-logging and seismic responses. The intermediate mafic lava facies architecture was divided into crater-proximal facies (CF-PF), medial facies (MF), and distal facies (DF), which were characterized by their vesicles and joints and could be identified through their seismic attributes. The reservoir spaces including vesicles, amygdale inner pores, joint fissures, and dissolution pores predominantly showed oil and gas accumulation. The results of the tests of the reservoir's physical properties showed that the reservoir quality was best in the CF-PF, which is the main target of oil and gas exploration.

KEYWORDS

intermediate mafic lava flows, Dongling area, Yingcheng Formation, facies architecture, reservoir characteristics

1 Introduction

Volcanic reservoirs are widely distributed in many basins worldwide and have been the target of oil and gas exploration and development for more than 130 years (Zou et al., 2008). A small number of volcanic reservoirs are composed of acidic volcanic rocks, such as the Yo-shii Kashiwazaki rhyolite gas field in Niigata Basin in Japan (Zhao et al., 2009). Most volcanic reservoirs are dominated by intermediate mafic volcanic rocks, such as basalt in the Scott Reef oil fields and the gas fields in Australia; basalt and basaltic agglomerates in the West Rozel oil field in North Basin, USA; and vesicle basalt in the YPF Palmar Largo oil field in Noro Este Basin, Argentina (Passey et al., 2007). Since the discovery of basaltic oil and gas reservoirs in the

northwestern margin of the Junggar Basin in 1957, volcanic oil and gas reservoirs in China have become the focus of comprehensive exploration (Zhao et al., 2009). The lithology of volcanic reservoirs differs between the eastern and western basins of China. The western basin is mainly composed of intermediate mafic volcanic rocks, while the eastern basin is acidic volcanic rocks (Hou et al., 2013). The intermediate mafic volcanic reservoirs in the western basins are mostly secondarily weathered or composed of volcanic pyroclastic rocks (Hou et al., 2003; Wang et al., 2011; Fan et al., 2020). With the increasing development of volcanic oil and gas fields in Songliao Basin, outcrop surveys and drilling have confirmed that the intermediate mafic reservoirs developed in the Early Cretaceous Yingcheng Formation in Songliao Basin (Huang et al., 2010; Shan et al., 2012; Zhang et al., 2018). Different from the western basin, the intermediate mafic lava reservoir is buried *in situ* with weak secondary reformation, making it a good material for the study of intermediate mafic lava flow structure and reservoir characteristics.

Intermediate mafic lava flows with vast extent and emplacement on low slopes are consistent with an eruption from point sources or along fissures (Walker et al., 1993; Marsh et al., 2001). The range of lava flows is wide and multiple eruption units overlap. For example, the basalt lava flows in the Faroe Islands extend at least 6.6 km (Self et al., 2013; Yi et al., 2016), and three different types of basalt flows (tabular, compound, and hyaloclastite) display a range of facies onshore (Greeley et al., 1982; Nelson et al., 2009). According to the maximum average slope, the volcanic basalt lava seismic facies are divided into three types: mounded seismic facies units (MSFUs), tabular seismic facies units (TSFUs), and mounded-tabular seismic facies units (M-TSFUs) (Tang et al., 2023). Based on petrographic studies of Mesozoic intermediate mafic volcanic rocks, Cenozoic Changbaishan basalt, and Wudalianchi basalt encountered in Songliao Basin, the intermediate mafic lava flows can be divided into braided, tabular, and fan lava flows (Wang et al., 2018). Significant progress has also been made in the study of the diagenesis and reservoir characteristics of intermediate mafic lavas (Huang et al., 2010; Liu et al., 2010; Ren et al., 2015). Previous studies based on thin section observations, SEM, MIP, and low-temperature nitrogen adsorption (LTNA) revealed the pore structure characteristics of intermediate mafic volcanic reservoirs (Cang et al., 2021). The internal structure of oil reservoirs has mostly focused on tight sandstone and shale reservoirs (Li et al., 2019; 2020; Shan et al., 2021; Li et al., 2023). Previous studies showed that the primary vesicles and fractures of intermediate mafic lava flows can form high-quality reservoirs for oil and gas migration and storage (Liu et al., 2010; Yue et al., 2021). However, several studies have reported the inner structure of intermediate mafic lava flows corresponds to the geophysical method.

Therefore, taking the intermediate mafic lava flows of the Yingcheng Formation in the Dongling region as an example, this study classified the types of lava flows by field outcrop observation and identified them based on the combination of drilling cores, logging curves, and 3D seismic profiles. The reservoir space types of different lava flows were observed by casting thin sections and SEM, and the micropore structure was analyzed by HPMI. In addition, the reservoir properties and pore structure of different lava flows were clarified. Combined with the analysis of reservoir space type and diagenesis, we established a reservoir geological model of intermediate mafic lava flows. This study has a practical significance for recognizing the distribution of intermediate mafic lava flow reservoirs.

2 Geological setting and samples

2.1 Geological setting

The study region (Figures 1A, B) is located in the southern part of the Changling fault depression of Songliao Basin, controlled by a series of NNE- or NE-trending basement fractures under the consumption effect of ocean-continent subduction in the Meso-Cenozoic (Ren et al., 2002; Wei et al., 2010; Feng et al., 2014). Fault activity controls the development of the fault depression and volcanic eruption intensity. The fault development scale is different and can be divided into three levels, F1, F2, and F3 (Figure 2). The F1 faults run from south to north, extending up to 16 km, with large fault distances, and control the development of the fault depression. The F2 fault is the secondary fault, with a smaller scale and extension than those of F1, and generally 20–50 m between faults. The F3 fault is the branch fault of F1 and F2, with a small fault distance and short extension, which develops in a nearly north-south direction. The faults are distributed in an echelon from west to east, and the section shows a negative flower structure. The strata on the lower side of the fault are fully developed and thick, while those on the upper side gradually become thinner, with some missing strata.

Large-scale volcanic eruptions occurred in Songliao Basin during the Late Jurassic-Early Cretaceous Period (Figure 2). The strata from bottom to top are the Huoshiling Formation, Shahezi Formation, and Yingcheng Formation, respectively (Tang et al., 2008; Wang et al., 2015). The study region experienced extension during the Huoshiling stage, along with volcanic and continental deposits. During the Shahezi stage, the strata continued to be subjected to the east-west tension, and the water body gradually became deeper so that the sedimentary environment evolved from a shore-shallow lake to a deep lake (Zhang et al., 2012). As a result, it provides a good oil and gas supply for the Yingcheng Formation volcanic reservoirs. Based on 19 wells penetrating the volcanic rocks of the Yingcheng Formation, the maximum thickness of lava flows in the Yingcheng Formation is >400 m. The first member of the Yingcheng Formation consists of the main lava flows that are primarily composed of basalt, basaltic andesite, and a thin layer of pyroclastic rocks. These can be divided into three eruption stages according to the thick deposition layers, which are mainly gray and black shale (Figure 1C).

2.2 Samples and methods

A total of 12 representative core samples were collected from six wells in the study region, including basalt, basaltic andesite, and trachybasalt. Among them, the lava samples contained vesicle lava and dense lava. The samples represented the characteristics of different lava flows, and core sample pictures are shown in Figure 3. The porosity and permeability data were obtained by helium gas assessments of the high-pressure physical properties. Information on the rock samples including well, depth, lithology, and physical properties is shown in Table 1.

The samples were cut into standard cylinders (3 cm in length, 2.54 cm in diameter). After washing and drying, helium gas

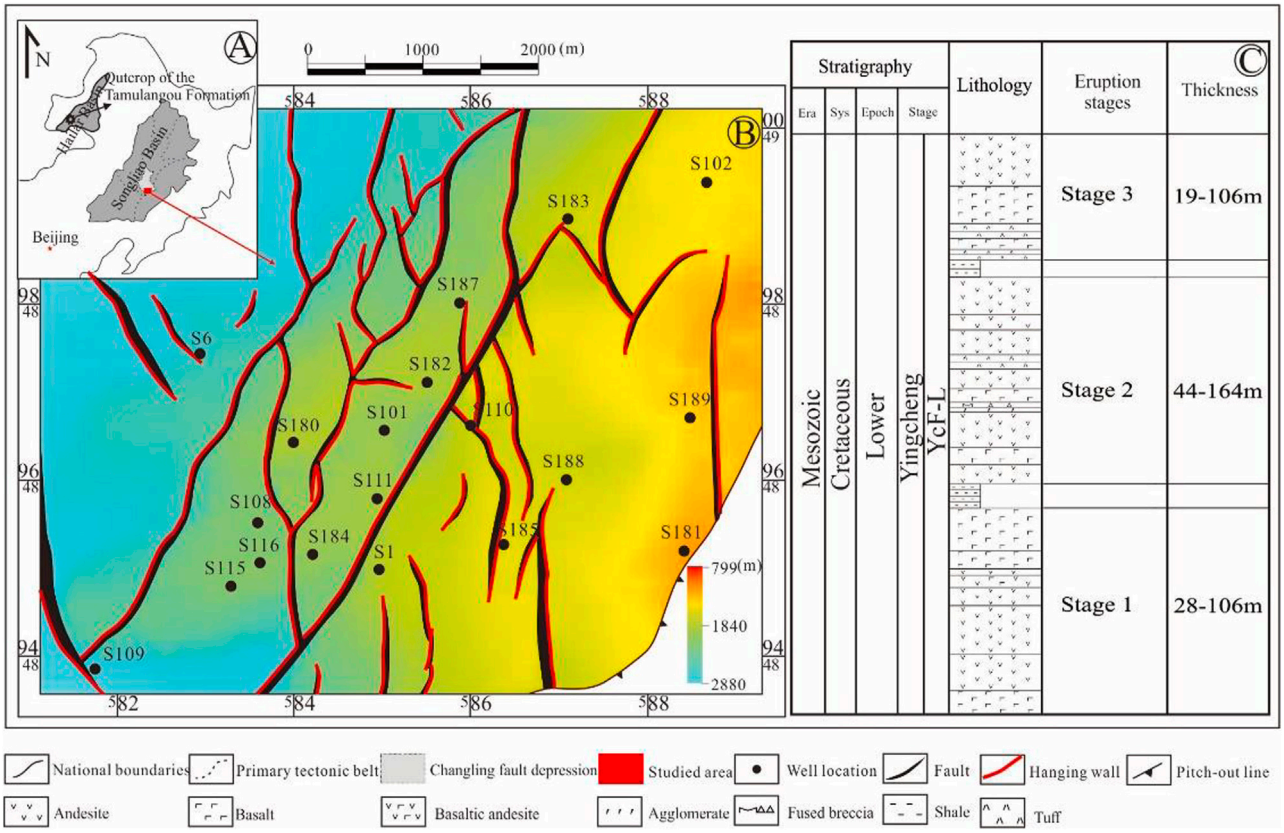

FIGURE 1
(A) Location of the Songliao and Hailar basins and the area of outcrop of the Tamulangou Formation. **(B)** Location of the Dongling area, wells, and faults in the Changling Depression in Songliao Basin. **(C)** Stratigraphic column of volcanic rocks in the Yingcheng Formation, Lower Cretaceous. YcF-L, Lower Yingcheng Formation.

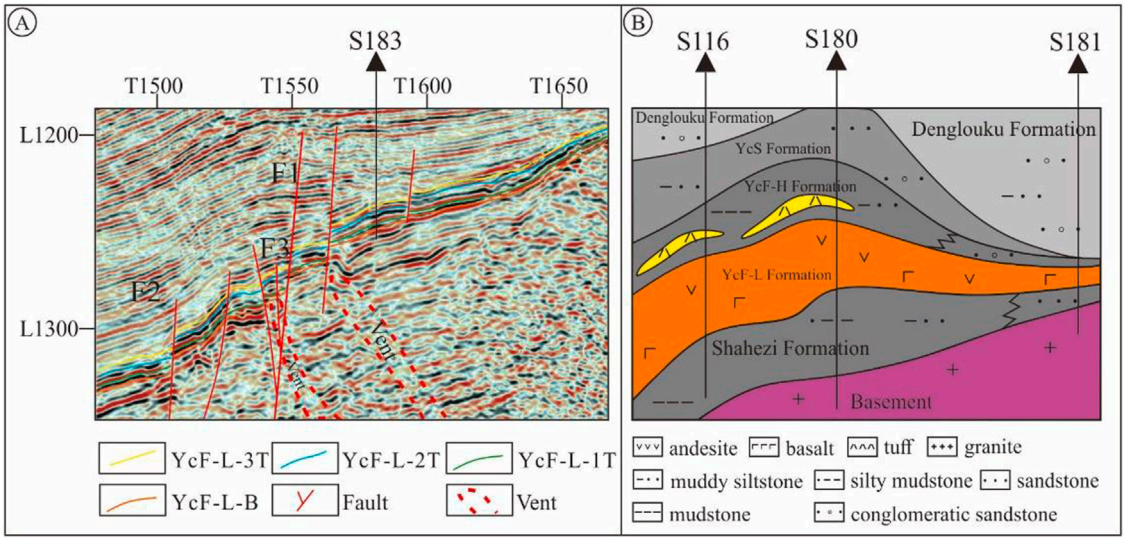

FIGURE 2
Characterization of volcanic strata through seismic profiles. **(A)** Distribution characteristics of the target layer faults in the study area, showing an echelon distribution, with some showing negative flower-shaped faults. **(B)** Volcanic lava flows mainly distributed in the YcF-L Formation. The underlying stratum of the volcanic formation is the source rock of the Shahezi Formation.

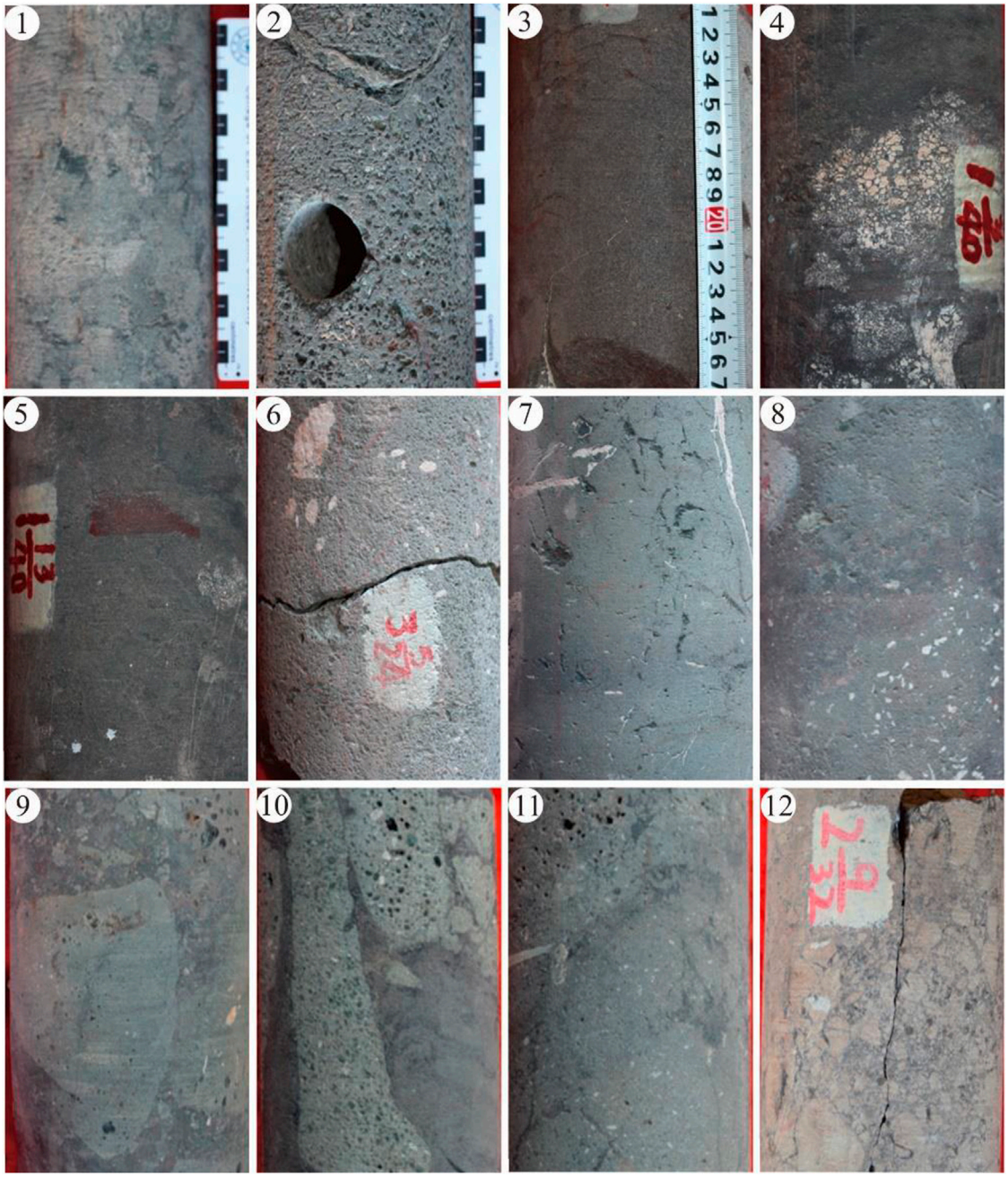

FIGURE 3
Pictures of 12 volcanic core samples obtained from the Yingcheng Formation. All core samples are full-hole cores from six wells.

experiments, casting thin sections, SEM, and HPMI experiments were performed successively. The helium gas experiments, casting thin sections, and SEM were carried out at the Laboratory at Jilin University. The HPMI experiments were performed on a Pore Master-60 GT at the Beijing Center for Physical and Chemical Analysis, according to the National Standard GB/T 21650.1. The pore size range of the HPMI was >9 nm, which can be used to characterize the pore structure of the samples. In addition, basalt field outcrop profiles, seismic data, and well logging data in the study region were obtained from Sinopec Northeast Oil and Gas Branch.

3 Results

3.1 Intermediate mafic lava flows in outcrops

Based on the observations of the basalt outcrop, including morphology, dimension, and internal structure in the middle

TABLE 1 Wells, depths, lithology, porosity, and permeability of 12 rock samples.

Sample	Well	Depth (m)	Lithology	Porosity (%)	Permeability (mD)
1	S1	2,402.2	Andesite	5.6	0.37
2	S1	2,408.2	Trachybasalt	9.9	0.5
3	S102	1857.1	Basalt	5.9	0.87
4	S116	2,709.7	Basalt	13.2	1.2
5	S116	2,711.7	Basalt	4.3	0.1
6	S187	2,432.9	Basaltic andesite	10.7	0.5
7	S187	2,453.3	Basaltic andesite	8.1	0.3
8	S187	2,436.1	Basalt	8.1	0.7
9	S180	2,480.2	Basaltic agglomerated lava	9.7	3.8
10	S180	2,471.5	Basaltic andesite	8.9	1.2
11	S180	2,472.9	Basaltic andesite	4.2	0.3
12	S183	1,986.6	Trachyandesite	12.8	2.56

Jurassic Tamulangou Formation at Hulun Lake in Inner Mongolia, the intermediate mafic lava flows at the Hailer Basin margin (Figure 1) can be divided into three representative lava flow units, including tabular lava flow, compound lava flow, and hyaloclastite.

The external shape of the tabular lava flows was similar to plate-like, with overlapping layers and large single-layer thickness, up to several tens of meters, with the extension of good continuity reaching several kilometers (Byrnes et al., 2002; Hachimi et al., 2010). It mainly formed in the phase of powerful volcano eruption and is the largest accumulation of the intermediate mafic lava flows (Figure 4A). A mass of primary pores of large size developed at the top of the tabular lava flows, while the bottom is mostly residual pores. The middle part shows a dense massive structure and columnar joints (Figure 4B).

The flow lobe of the compound lava flows is thin, similar to the braided channel. It is also interlaced overlapped and has a lineoid section (Figure 4A). Individual flow lobes comprise a lower crust, a core, and an upper vesicle belt. The core is compact with irregular jointing (Figure 4B). Compound lava flow often presents multiple layers of flow lobes in different volcanoes.

Hyaloclastite is common in the initial formation of underwater volcanic eruptions (Clague et al., 2013). After volcanic eruptions, the subaerial lava flow is quenched by water at the distal facie of the facies architecture (Caroff et al., 2019; Angulo et al., 2021). The hyaloclastite structure shows a glassy texture and broken breccia structure. When the lava flow encounters quenching condensation on the water, the internal lava maintains a higher temperature (Nichols et al., 2012). Under the influence of external temperature and pressure differences, the internal lava extrudes and condenses, forming a new condensation crust. Thus, the hyaloclastite is generally pillow-shaped (Figure 4A). The hyaloclastite has radioactive joints, and the vesicles are mostly developed in the outer ring zone (Figure 4B).

3.2 Geophysical identification of lava flows

Intermediate mafic lava flows are distributed on the surface in shield-like or sheet-like shapes, with weak eruption intensity, and are generally formed by overflowing fissures (Walker et al., 1993; Single et al., 2004). Field geological surveys of volcanic architecture in Songliao Basin divided the volcanic institutions horizontally into CF-PF, PF, and DF (Wang et al., 2015). Wells S180, S183, and S1 in the study area revealed CF-PF, MF, and DF, respectively (Figures 5A–C). The CF-PF is mainly dominated by thick tabular lava, and compound lava flows are formed in the early stage of magma eruption. Hyaloclastite can form at the bottom of lava flows if the crater is in a lacustrine environment. The MF and DF are mainly composed of thin tabular and compound lava, respectively. The lava flows were quenched with water to form hyaloclastite.

The seismic reflection pattern of tabular lava is similar to sedimentary strata with parallel or subparallel features, characterized by strong amplitude and high frequency due to the dense block structure (Figure 5). The compound lava was a braided shape, with a medium frequency, medium amplitude, and subparallel type. The thin compound lava flows overlapped; thus, it was difficult to discern single lava lobes on the seismic sections. There are two forms of hyaloclastite formation; namely, when the lava flow overflows from the crater into the lake, in which the seismic reflection is characterized by a forest filling, and underwater volcanic eruption, in which the lava flow is quenched to form mushroom- or pillow-like structures. The internal seismic reflection is characterized by low frequency and weak amplitude.

Well-logging can represent the physical properties of different lava flows and their internal structural characteristics (Figure 5). Tabular lava showed high resistivity (LLD and LLS) in the range of

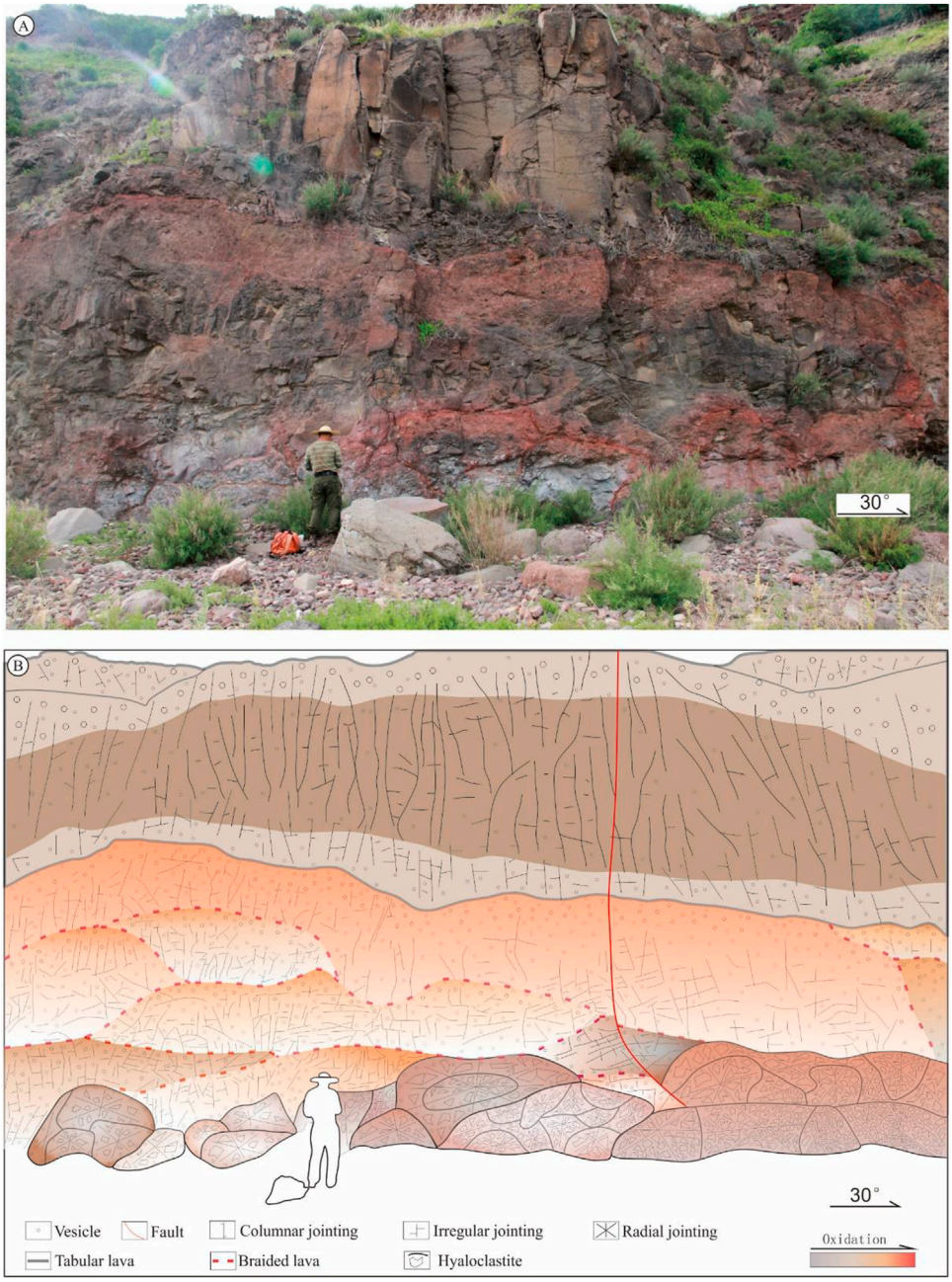

FIGURE 4
(A) Geological profile of lava flows in the upper Jurassic Tamulangou Formation of Hulun Lake, Inner Mongolia. **(B)** Sketch of different facies of intermediate mafic lava flows with corresponding vesicle, jointing, and geological morphology.

22 to 508 Ω•m (average 268 Ω•m), high density (DEN) from 2.5 to 2.9 g/cm^3, low acoustic (AC) from 190 to 272 μs/m, and showed box-shape. The resistivity at the top of the tabular lava was generally lower than other portions due to the pore development. The resistivity of the compound lava flow was generally smaller than that of the tabular lava flow, with a range of 10–100 Ω•m, AC 210–270 μs/m, and DEN is 2.3–2.7 g/cm^3. The compound lava flow was characterized by interlaced overlapping thin-layer lava flows, with much smaller scales of pore and dense zones. The curves showed obvious finger shapes. The hyaloclastite showed lower LLD or LLS, higher AC, and lower DEN than other lava flows, as well as a jagged shape due to the internal structure.

3.3 Identification of intermediate mafic lava architecture

The intermediate mafic lava has the characteristics of a wide flow range and multiple eruption units that interlace and overlap. For example, the basalt lava flow of the Faroe Islands extends at least

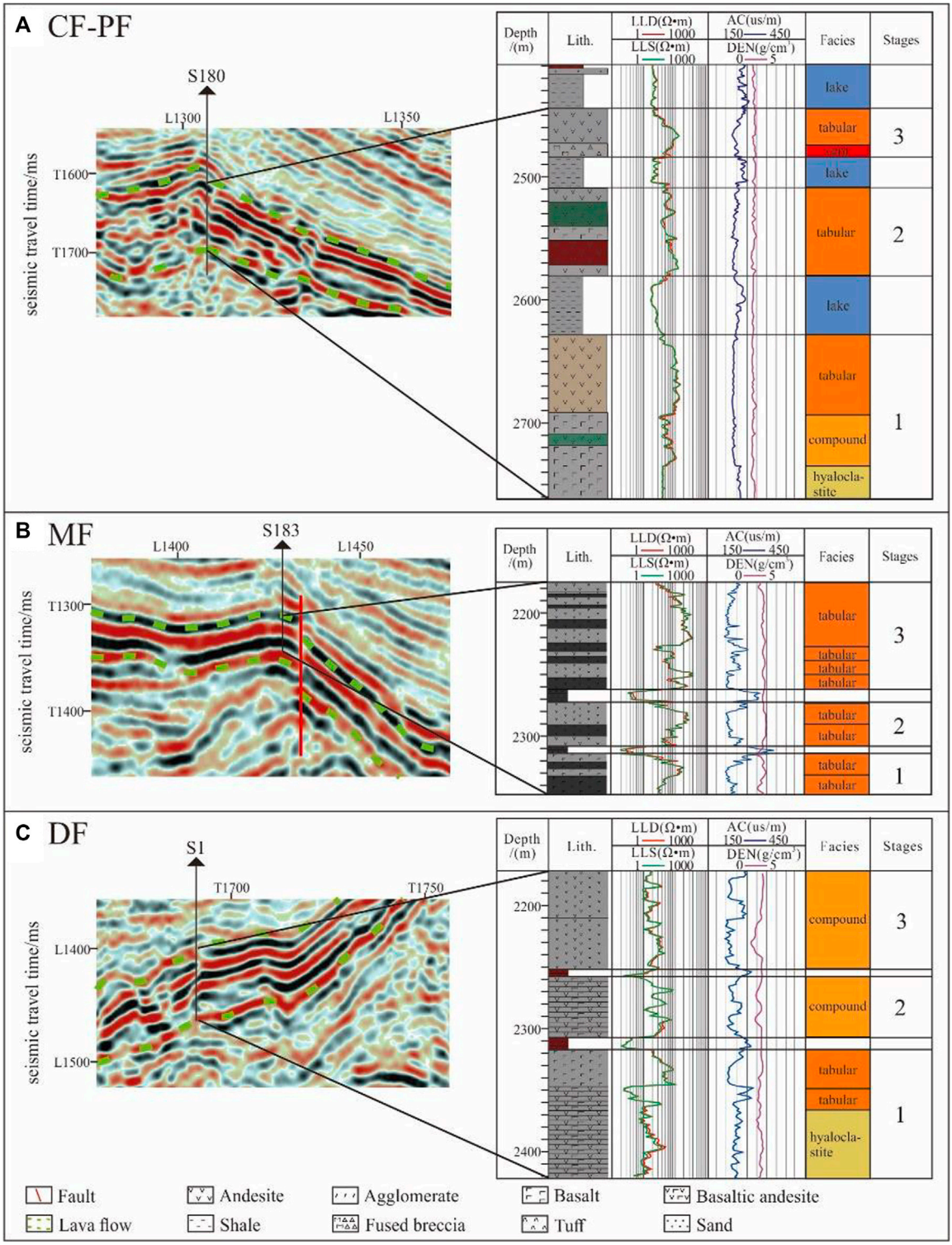

FIGURE 5
Conventional logging response of different lava flows in CF-PF **(A)**, MF **(B)** and DF **(C)**, respectively. LLD, Deep lateral resistivity logging, LLS, Shallow resistivity logging, AC, Acoustic logging, DEN, Density logging.

6.6 km (Jerram et al., 2009). Intermediate mafic volcanoes may be affected by the superimposition of other volcanic lavas, which makes it impossible to reflect the distribution characteristics of volcanic craters according to the thickness and scale of the lava flows.

Well S180 showed basaltic agglomerated lava 2480 m in depth. The core showed a breccia structure. Observation of the core showed that the size of the blasted breccia was uneven. The seismic profile showed that the volcanic channel formed along the fault near the

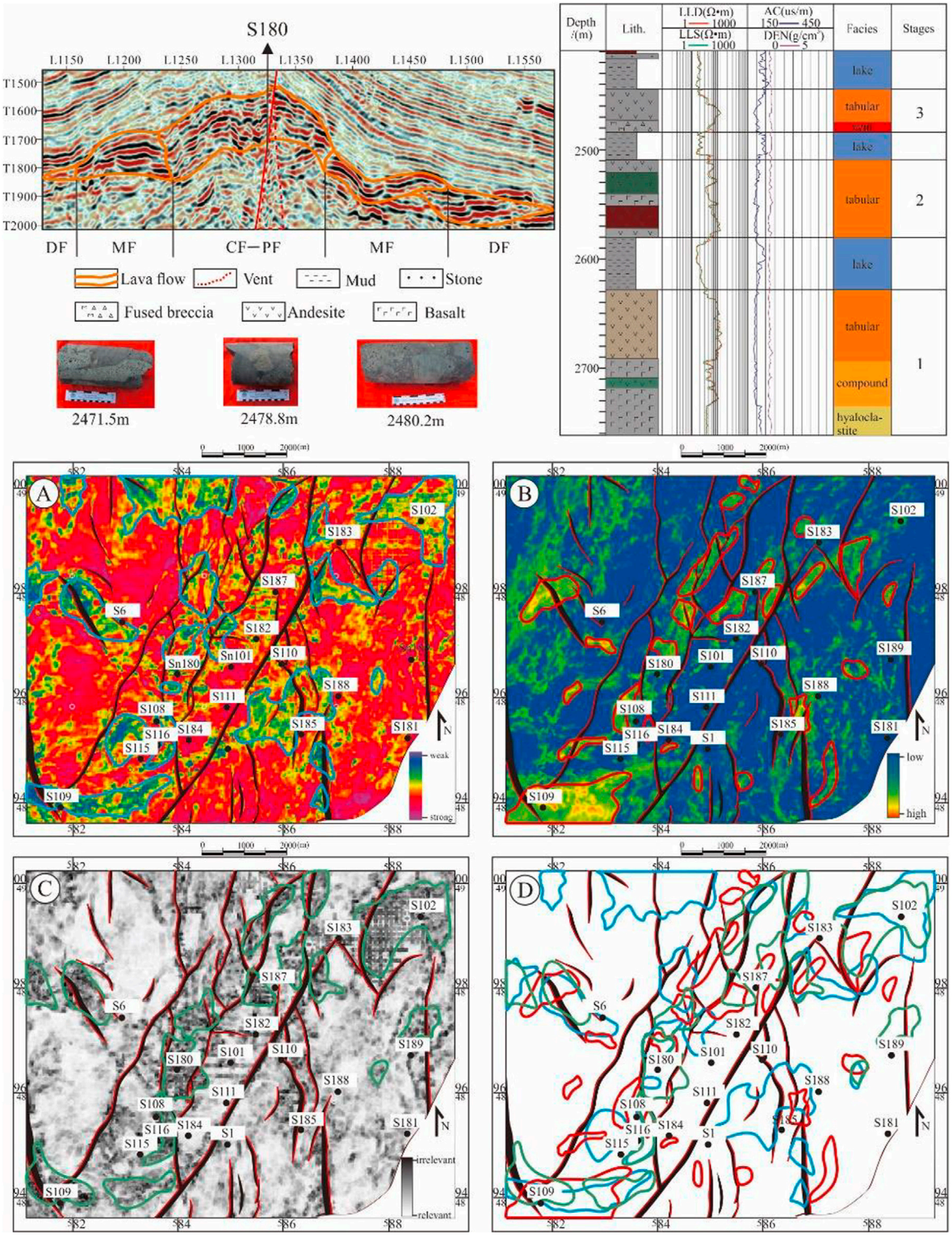

FIGURE 6
Identification of craters through core, well logging, and seismic attributions. **(A)** Root mean square (RMS) amplitude. Blue circles, craters. **(B)** Stratigraphical dip attribution. Red circles, craters. **(C)** Coherence attribution. Green circles, craters. **(D)** Combination of the three methods to identify craters.

drilling well, which was characterized by time-lapse, poor stratigraphic continuity, medium weak amplitude, and high dip angle (Figure 6). Crater identification is an important factor in the description of volcanic architecture. Based on the seismic response characteristics, the distribution of craters was characterized according to amplitude, dip angle, and coherence, respectively.

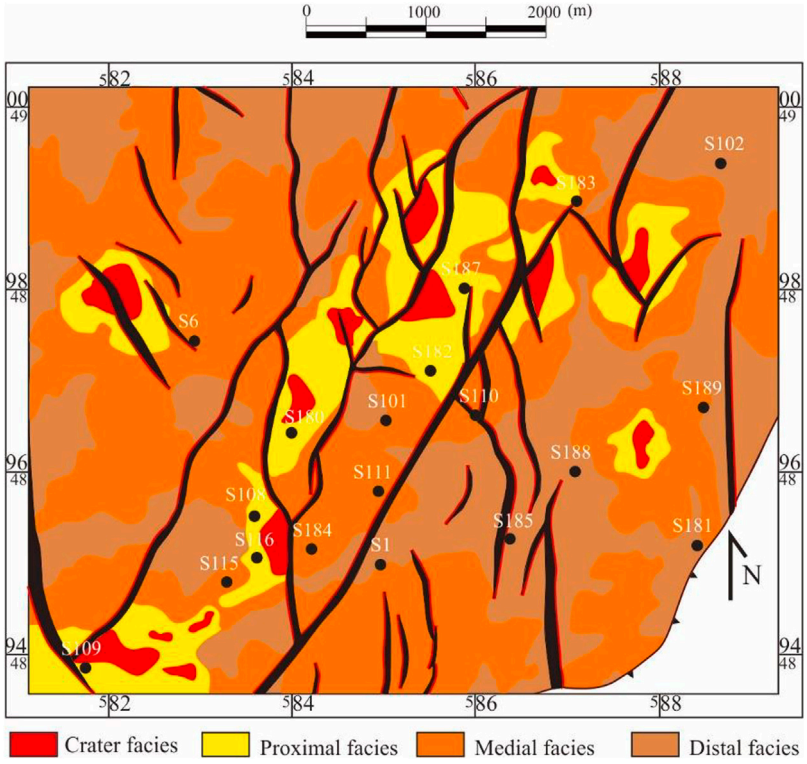

FIGURE 7
Distributions of the facies zones of intermediate mafic lava flows.

Finally, the distribution of craters was determined based on the combination of the aforementioned three attributes (Figure 6). The distribution of volcano craters showed that most intermediate mafic volcanoes were formed by the progress of the lava overflow through the faults, especially at crossing faults.

According to the volcanic seismic facies characteristics of well S180, the volcanic architecture can be divided into CF-PF, MF, and DF. The seismic response characteristics of CF-PF included a weak root mean square amplitude, high dip angle, and poor coherence. The seismic response characteristics of the MF were a strong root mean square amplitude and good correlation. The seismic response characteristics of the DF were weak root mean square amplitude, poor correlation, and small dip angle (Figure 6). The distributions of the facies zone of intermediate mafic lava flows are shown in Figure 7.

4 Discussion

4.1 Formation mechanisms of the reservoirs

The volatile gas content of mafic magma is relatively high, and the magma temperature can reach >1,100°C (Iio et al., 2018). During overflow along the surface after magma eruption, gas escapes and forms many vesicles under the dual effects of temperature and pressure (He et al., 2019). Due to the instability of plagioclase and other mafic minerals in the mafic lava, alteration is easy to occur in the presence of fluid (Figure 8E). Different types of secondary minerals, mainly calcite and chlorite, fill the vesicles and form the amygdales (Figures 8A, D, F). These may originate from the precipitation of iron and calcium ions during the dissolution of intermediate mafic lava, providing a material basis for the formation of calcite and chlorite in the open spatial pores and fissures. Volcanic eruptions are greatly affected by tectonic activities (Li et al., 2022). Volcanic institutions are mostly distributed near faults, and structural fissures of different sizes can be observed at the core (Figure 8I). Basaltic agglomerated lava develops blast cracks filled with mafic magma liquid (Figure 8H). In addition to primary pores and fissures, the main reservoir space of natural gas is secondarily dissolved pores and fissures, including mineral-dissolved pores, filling-dissolved pores, and some glassy devitrification pores (Figures 8C, G). The minerals on the edge of the vesicles are prone to chloritization due to their contact with the fluid (a chlorite ring around the vesicle is visible in Figures 8A, B).

4.2 Reservoir geological model

The energy of fissure overflow-type mafic volcanoes is weak in the initial stage of eruption. The volcanic eruption gradually increases with the upwelling of volatile gas before later decreasing (Ni et al., 2014). A lava flow is rich in volatiles near the volcano crater, mostly porous lava, lava with foam structure, and welded breccia. The upper part of the tabular lava flow is mainly distributed with a large pore zone; the volatile escapes upward, the middle part forms a dense block, and the columnar joint develops after condensation and contraction (Walker et al., 1971). Volatiles that cannot easily escape remain at the bottom, forming a sparse

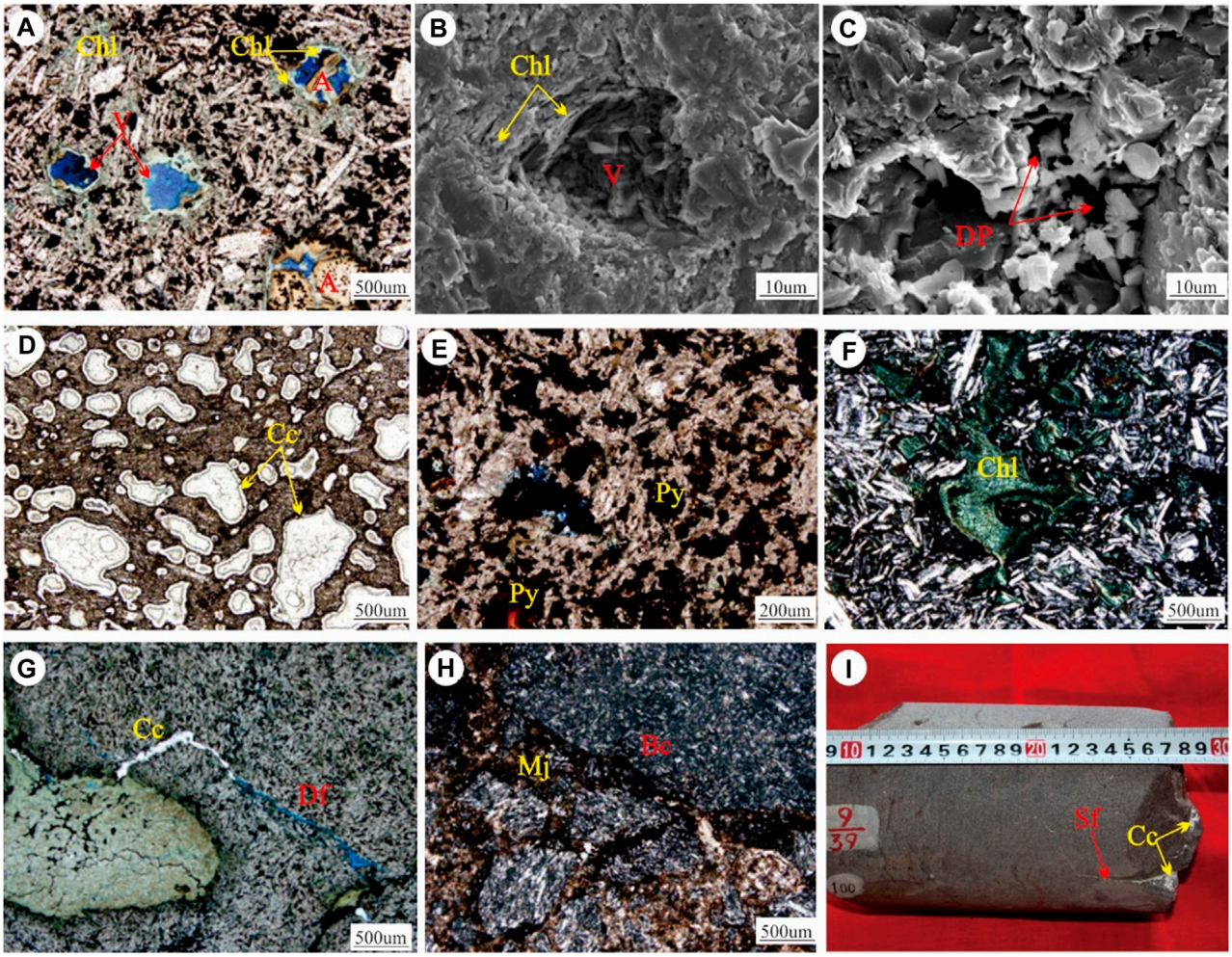

FIGURE 8
Space types of intermediate mafic lava reservoirs in the Yingcheng Formation of the Changling fault depression. **(A)** S116 well, 2,714.2 m, basalt, vesicle, and amygdale development, **(B)** S116 well, 2,715.2 m, basalt, micron vesicle. **(C)** S1 well, 2,403.3 m, andesite, dissolved pores. **(D)** S116 well, basalt, vesicle filled with calcite. **(E)** S102 well, 1857.1 m, basalt, mafic minerals. **(F)** S180 well, 2,471.5 m, basaltic andesite, chlorite-filled pores, and chloritization of some mafic minerals. **(G)** S1 well, 2,402 m, andesite, fissure filled with calcite and dissolution. **(H)** S180 well, 2,480.2 m, basaltic agglomerated lava, mafic magma juice filling the blast crack. **(I)** S187 well, 2,436.1 m, basalt, structural fissures filled with calcite. V, vesicle; Dp, dissolved pore; A, amygdale; Df, dissolved fissure; Bc, blast crack; Sf, structural fissure; Cc, calcite; Chl, chlorite; Py, pyroxene; Mj, mafic magma juice.

pore zone with small pores. The erupted magma flows from the crater to far distances, which in the MF is relatively dense and thick, with some sparse and smaller pores on the lava flow surface. The internal structure characteristics of single lava flows are the same as those of near-source lava flows, with upper pore zones, middle dense zones, and lower sparse pore zones. The thin-layer lava flow in the DF is interlaced and overlapped. The volatile content in DF is low, and the pores are very small. The facies architecture shows two situations of hyaloclastite were formed by magma quenching in water. One is volcanic eruption at the bottom of the lake, which formed near the bottom of the crater; the other is onshore eruption, in which the lava flowed into the lake at the distal end to form. The hyaloclastite recrystallized to form devitrification pores (Zhao et al., 2009). Based on the aforementioned understanding of the morphology, occurrence, and lithofacies combination characteristics of different facies belts of volcanic institutions, and the internal structure of the intermediate mafic lava flows unit, the lithofacies model of the intermediate mafic lava flows is established (Figure 9).

4.3 Relationships between reservoir physical characteristics and facies architecture

The volcanic lava in the study area is a low-porosity and ultra-low permeability reservoir, in which the physical properties of the reservoir in different facies zones vary greatly (Figure 10). The porosity distribution of the CF-PF ranges from 3% to 14%, the average porosity of the top vesicle zone is as high as 12.4%, and the permeability is approximately 1 mD. This is the main target area for oil and gas exploration. According to the mercury injection curve characteristics of the rock samples, the maximum mercury injection saturation of rock samples reached 80%, further indicating the high reservoir porosity and good connectivity. The rising section of the

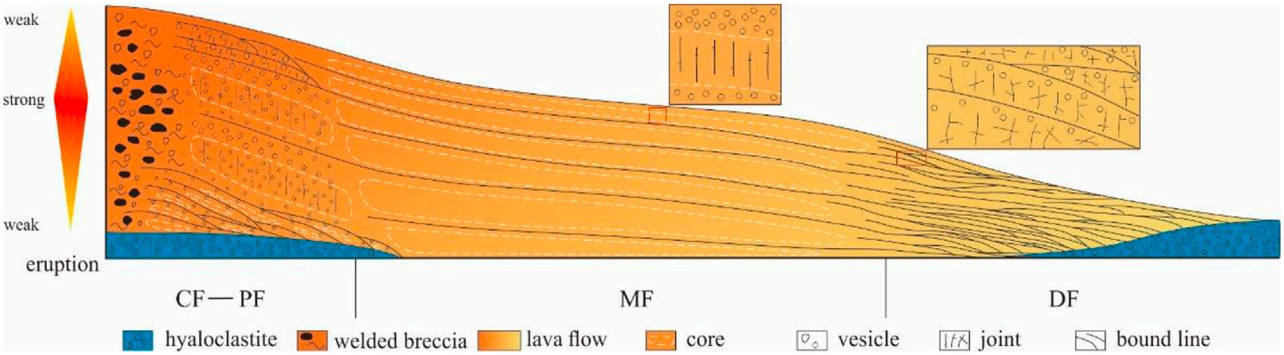

FIGURE 9
Facies architecture of intermediate mafic lava flows.

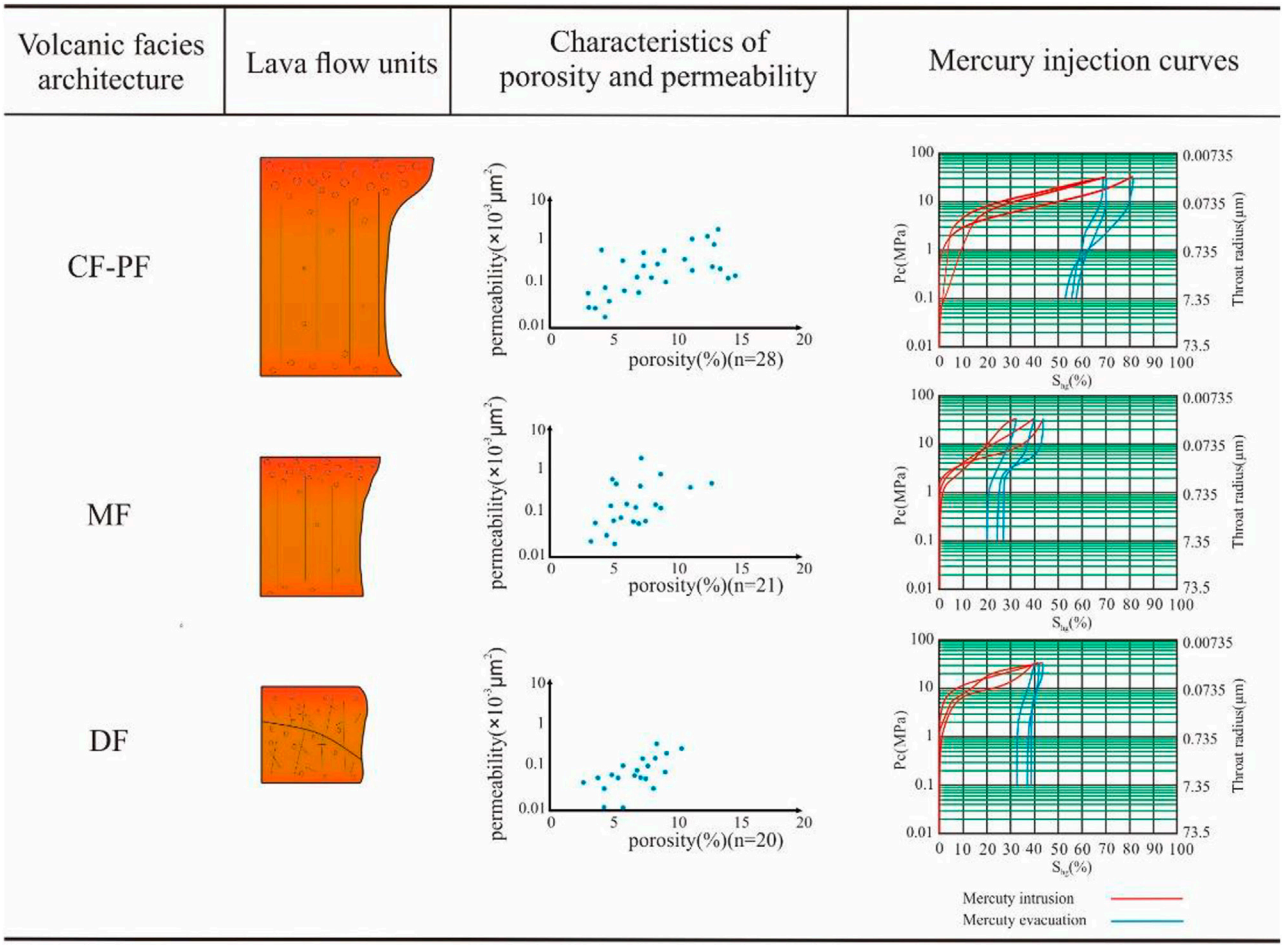

FIGURE 10
Reservoir characteristics of different volcanic facies architectures.

mercury injection curve shows the presence of micro-sized pores in the rock samples. The porosity of the reservoir in the MF was mostly distributed between 5% and 8% and the permeability was <1 mD. The mercury injection curve showed strong heterogeneity, with a mercury injection saturation of <40%. Moreover, the connectivity of the pores and fractures was not good, which verified the characteristics of small pores and micro-fractures, consistent with the lava flow structure of the original facies zone. The reservoir porosity and permeability

characteristics of the DF were similar to those of the MF. The mercury injection curve was characterized by nano-pores, a low maximum mercury injection saturation, and a mercury removal rate far lower than those of other facies zones, which further indicated the poor connectivity of its reservoir space. The reservoir space of the DF may be mainly composed of dissolution micropores and devitrification pores.

5 Conclusion

1) Intermediate mafic lava flows can be divided into tabular lava flow, compound lava flow, and hyaloclastite, which can be identified by seismic attributes such as seismic profile morphology (parallel, sub-parallel, braided, or pillow-shaped), amplitude (strong, medium, or weak), and frequency (high, medium, or low), and can also be identified by logging response characteristics (resistivity, AC, and DEN).
2) Craters characterized by time-lapse showed poor stratigraphic continuity, medium-weak amplitude, and high dip angle, which is one important factor in the description of volcanic architecture. The facies architectures consisted of CF-PF, MF, and DF (far away from the crater). The seismic response characteristics of the CF-PF included a weak root mean square amplitude, high dip angle, and poor coherence. The MF showed a strong root mean square amplitude and good correlation, while the DF showed a weak root mean square amplitude, poor correlation, and small dip angle.
3) The types of reservoir space were mainly vesicles, amygdale inner pores, dissolved pores, devitrification pores, and other fissures. Compared with other volcanic rocks, the alteration of mafic minerals is an important factor leading to secondary mineral filling. The physical properties of intermediate mafic lava reservoir mainly depended on three factors, namely, primary pore development, secondary mineral filling, and dissolution.
4) Comparison of the gas physical property analyses and the mercury intrusion curve characteristics showed that the porosity and permeability of the CF-PF were higher than those of the MF and DF, the proportion of micro-scale pores was relatively high, and the pore connectivity was the best, especially the top vesicle zone, in the CF-PF, with porosity as high as 12.4%, and permeability of approximately 1 mD, making it the main target area for oil and gas exploration.

Data availability statement

The original contributions presented in the study are included in the article/Supplementary Material. Further inquiries can be directed to the corresponding author.

Author contributions

Software, ZC and JH; investigation, BW and HW; data curation, XR; writing—original draft, QY; writing—review and editing, CL; visualization, RZ. All authors have read and agreed to the published version of the manuscript.

Funding

This research was funded by financial support from the Educational Department of Liaoning Province (grant numbers LJKZ0392, LJKZ0394, and L2020047) and a Liaoning Marine Economy Development Project (grant number HYZX202110).

Conflict of interest

Author ZC was employed by the Chengdu Exploration and Development Research Institute of Petro China Daqing Oilfield Company Ltd., China. Authors XR and JH were employed by the Northeast Oil & Gas Branch of Sinopec.

The remaining authors declare that the research was conducted in the absence of any commercial or financial relationships that could be construed as a potential conflict of interest.

Publisher's note

References

Angulo-Preckler, C., Pernet, P., García-Hernández, H., Kereszturi, G., Álvarez-Valero, A. M., Hopfenblatt, J., et al. (2021). Volcanism and rapid sedimentation affect the benthic communities of Deception Island, Antarctica. *Cont. Shelf Res.* 220 (71), 104404. doi:10.1016/J.CSR.2021.104404

Byrnes, R., and Jeffrey, M. (2002). Morphology, stratigraphy, and surface roughness properties of Venusian lava flow fields. *J. Geophys. Res.* 107 (10), 5079. doi:10.1029/2001je001828

Cang, Z., Shan, X., Yi, J., Yue, Q., Xu, C., Zou, X., et al. (2021). Fractal characterization of nanoscale pores of volcanic reservoirs in the Dongling area, Changling fault depression, Songliao Basin. *Nat. Resour. Res.* 30, 3483–3502. doi:10.1007/S11053-021-09867-9

Caroff, M. (2019). Emplacement of lobate sheet flows with hyaloclastites onto soft sediment: The Erquy Neoproterozoic lava pile, Armorican Massif (France). *Precambrian Res.* 334, 105454. doi:10.1016/j.precamres.2019.105454

Clague, D., Moore, J., and Alicé, S. (2013). *Volcanic breccia and hyaloclastite in blocks from the nuuanu and wailau landslides*. Hawaii: American Geophysical Union AGU.

Fan, C., Qin, Q., Lou, X., Pretorius, D., and Menasche, P. (2020). Formation mechanisms and distribution of weathered volcanic reservoirs: A case study of the carboniferous volcanic rocks in northwest Junggar Basin, China. *Energy Sci. Eng.* 8 (8), 1–10. doi:10.1016/j.yjmcc.2020.03.003

Feng, Z., Yin, C., Liu, J., Zhu, Y., Lu, J., and Li, J. (2014). Formation mechanism of *in-situ* volcanic reservoirs in eastern China: A case study from xushen gasfield in Songliao Basin. *Sci. China Earth Sci.* 57 (12), 2998–3014. doi:10.1007/s11430-014-4969-2

Greeley, R. (1982). The snake river plain, Idaho: Representative of a new category of volcanism. *J. Geophys. Res.* 87 (B4), 2705–2712. doi:10.1029/JB087iB04p02705

Hachimi, H., Youbi, N., and Madeira, J. (2010). "Morphology and emplacement mechanisms of the lava flows of the central atlantic magmatic province (CAMP) of Morocco," in *II central and north atlantic conjugate margins conference*. Editors R. Pena dos Reis and N. Pimentel (Lisbon, Portugal: Rediscovering the Atlantic: New ideas for an old sea). doi:10.1144/SP357.9

He, Q., Li, Y., and She, S. (2019). Mechanical properties of basalt specimens under combined compression and shear loading at low strain rates. *Rock Mech. Rock Eng.* 52, 4101–4112. doi:10.1007/s00603-019-01806-8

Hou, L., Luo, X., Wang, J., Yang, F., Zhao, X., and Mao, Z. (2013). Weathered volcanic crust and its petroleum geological significance: A case study of the carboniferous volcanic crust in northern xinjiang, NW China. *Petroleum Explor. Dev.* 40 (7), 277–286. doi:10.1016/S1876-3804(13)60034-8

Huang, Y., Wang, P., Shu, P., Xu, C., Lu, X., Zhang, W., et al. (2010). Avian influenza virus and Newcastle disease virus (NDV) surveillance in commercial breeding farm in China and the characterization of Class I NDV isolates. *Acta Petrol. Sin.* 26 (1), 82–86. doi:10.1016/j.vetmic.2010.01.003

Iio, Y., Sibson, R., Takeshita, T., Sagiya, T., Shibazaki, B., and Nakajima, T. J. (2018). Crustal dynamics: Unified understanding of geodynamic processes at different time and length scales. *Earth Planets Space* 70 (1), 97. doi:10.1186/s40623-018-0869-6

Jerram, D., Single, R., Hobbs, R., and Nelson, C. E. (2009). Understanding the offshore flood basalt sequence using onshore volcanic facies analogues: An example from the faroe–shetland basin. *Geol. Mag.* 146 (3), 353–367. doi:10.1017/S0016756809005974

Li, H., Qin, Q. R., Zhang, B. J., Ge, X. Y., Hu, X., Fan, C. H., et al. (2020). Tectonic fracture Formation and distribution in ultradeep marine carbonate gas reservoirs: A case study of the maokou Formation in the jiulongshan gas field, sichuan basin, southwest China. *Energy and Fuels* 34, 14132–14146. doi:10.1021/acs.energyfuels.0c03327

Li, H., Tang, H. M., Qin, Q. R., Zhou, J. L., Qin, Z. J., Fan, C. H., et al. (2019). Characteristics, formation periods and genetic mechanisms of tectonic fractures in the tight gas sandstones reservoir: A case study of xujiahe Formation in YB area, sichuan basin, China. *J. Petroleum Sci. Eng.* 178, 723–735. doi:10.1016/j.petrol.2019.04.007

Li, H., Zhou, J., Mou, X., Guo, H., and Wang, X. (2022). Pore structure and fractal characteristics of the marine shale of the longmaxi Formation in the changning area, southern sichuan basin, China. *Front. Earth Sci.* 10, 1018274. doi:10.3389/FEART.2022.1018274

Li, J., Li, H., Yang, C., Ren, X. H., and Li, Y. D. (2023). Geological characteristics of deep shale gas and their effects on shale fracability in the Wufeng–Longmaxi Formations of the southern Sichuan Basin, China. *Lithosphere* (1), 4936993. doi:10.2113/1970/4936993

Liu, W., Huang, Y., and Pang, Y. (2010). Diagenesis of intermediate and mafic volcanic rocks of Yingcheng Formation (K1y) in the Songliao Basin: Sequential crystallization, amygdule filling and reservoir effect. *Acta Petrol. Sin.* 26 (1), 158–164. doi:10.1000-0569/2010/026(01)-0158-64

Marsh, J., Ewart, A., Milner, S., Duncan, A., and Miller, R. (2001). The etendeka igneous Province: Magma types and their stratigraphic distribution with implications for the evolution of the paraná-etendeka flood basalt province. *Bull. Volcanol.* 62 (6-7), 464–486. doi:10.1007/s004450000115

Nelson, C., Jerram, D., and Hobbs, R. (2009). Flood basalt facies from borehole data: Implications for prospectivity and volcanology in volcanic rifted margins. *Pet. Geosci.* 15 (4), 313–324. doi:10.1144/1354-079309-842

Ni, H., Keppler, H., Walte, N., Schiavi, F., Chen, Y., Masotta, M., et al. (2014). *In situ* observation of crystal growth in a basalt melt and the development of crystal size distribution in igneous rocks. *Contributions Mineralogy Petrology* 167 (5), 1003–1013. doi:10.1007/s00410-014-1003-9

Nichols, A., Potuzak, M., and Dingwell, D. (2012). Cooling rates of basaltic hyaloclastites and pillow lava glasses from the HSDP2 drill core. *Geochimica Cosmochimica Acta* 73 (4), 1052–1066. doi:10.1016/j.gca.2008.11.023

Passey, S., and Bell, B. (2007). Morphologies and emplacement mechanisms of the lava flows of the Faroe Islands basalt group, Faroe Islands, NE atlantic ocean. *Bull. Volcano* 70 (2), 139–156. doi:10.1007/s00445-007-0125-6

Ren, J., Tamaki, K., Li, S., and Junxia, Z. (2022). Late Mesozoic and Cenozoic rifting and its dynamic setting in Eastern China and adjacent areas. *Tectonophysics* 344 (3-4), 175–205. doi:10.1016/S0040-1951(01)00271-2

Ren, X., Shan, X., and Yi, J. (2017). Characteristics and quantitative evaluation of reservoir in lava flow units in the early cretaceous Yingcheng Formation in changling depression of Songliao Basin. *J. China Univ. Petroleum Ed. Nat. Sci.* 41 (5), 30–40. doi:10.3969/j.issn.1673-5005.2017.05.004

Self, S., Thordarson, T., and Keszthelyi, L. (2013). Emplace of continental flood basalt lava flows. *Geophys. Monogr. Ser.*, 381–410.

Shan, S. C., Wu, Y. Z., Fu, Y. K., and Zhou, P. H. (2021). Shear mechanical properties of anchored rock mass under impact load. *J. Min. Strata Control Eng.* 3 (4), 043034. doi:10.13532/j.jmsce.cn10-1638/td.20211014.001

Shan, X., Gao, X., and Xu, H. (2012). The main factors of intermediate and mafic volcanic gas reservoir forming of Yingcheng Formation in Anda Area of Songliao Basin. *J. Jilin Univ. (Earth Sci. Ed.* 42 (5), 1348–1357.

Single, R., and Jerram, D. (2004). The 3D facies architecture of flood basalt provinces and their internal heterogeneity: Examples from the palaeogene skye lava field. *J. Geol. Soc.* 161 (6), 911–926. doi:10.1144/0016-764903-136

Tang, H., Pang, Y., and Bian, W. (2008). Quantitative analysis on reservoirs in volcanic edifice of early cretaceous Yingcheng Formation in Songliao Basin. *Acta Pet. Sin.* 29 (6), 841–845.

Tang, H., Wang, L., Wu, H., Hu, J., Dai, X., Goh, T. L., et al. (2023). Possible geological interpretation of the volcanic seismic facies based on volcanostratigraphy elements: A case analysis of the Yingcheng Formation in the Changling fault depression, Songliao Basin, ne China. *Geoenergy Sci. Eng.* 225, 211668. doi:10.1016/j.geoen.2023.211668

Walker, G. (1993). Basaltic-volcano systems. *Geol. Soc. Lond. Spec. Publ.* 76 (1), 3–38. doi:10.1144/GSL.SP.1993.076.01.01

Walker, G. (1971). Compound and simple lava flows and flood basalts. *Bull. Volcanol.* 35 (3), 579–590. doi:10.1007/BF02596829

Wang, J., Jin, J., Zhu, R., Rabkin, S. D., and Liu, R. (2011). Oncolytic herpes simplex virus treatment of metastatic breast cancer. *Acta Pet. Sin.* 32 (5), 757–763. doi:10.3892/ijo.2011.1266

Wang, P., and Chen, S. (2015). Cretaceous volcanic reservoirs and their exploration in the Songliao Basin, northeast China. *AAPG Bull.* 99 (3), 499–523. doi:10.1306/09041413095

Wang, P., He, K., and Yi, J. (2018). Volcanostratigraphy, volcanic architecture and reservoir of intermediate-mafic volcanic rocks: A comparison between buried cretaceous volcanoes in the Songliao Basin and the modern volcanoes in changbai mountain. *Acta Pet. Sin.* 57 (5), 775–787. doi:10.3969/j.issn.1000-1441.2018.05.017

Wei, H., Liu, J., and Meng, Q. (2010). Structural and sedimentary evolution of the southern Songliao Basin, northeast China, and implications for hydrocarbon prospectivity. *AAPG Bull.* 94 (4), 533–566. doi:10.1306/09080909060

Yi, J., Tang, H., and Wang, P. (2016). Types, characteristics and reservoir significance of basic lava flow units. *J. Central South Univ. Sci. Technol.* 47 (1), 149–158. doi:10.11817/j.issn.1672-7207.2016.01.022

Yue, Q., Shan, X., Zhang, X., Xu, C., Yi, J., and Fu, M. (2021). Quantitative characterization, classification, and influencing factors of the full range of pores in weathering crust volcanic reservoirs: Case study in bohai Bay basin, China. *Nat. Resour. Res.* 30, 1347–1365. doi:10.1007/s11053-020-09774-5

Zhang, C., Wu, C., and Xie, L. (2012). Filling characteristics and evolution analysis of the early Cretaceous small fault depression in Dongling region, Songliao Basin. *Acta Sci. Nat. Univ. Pekin.* 48 (2), 253–261. doi:10.13209/j.0479-8023.2012.034

Zhang, X., Xia, Y., Zhang, Y., Chen, Y., Zhang, G., and Gao, W. (2018). Volcanic reservoir characteristics and hydrocarbon Genesis of Jiamuhe formation in Jinlong 2 wellblock, Junggar Basin. *Petroleum Sci. Technol.* 36 (19), 1516–1523. doi:10.1080/10916466.2018.1471486

Zhao, H., Huang, W., and Wang, C. (2009a). Micropores from devitrification in volcanic rocks and their contribution to reservoirs. *Oil Gas. Geol.* 30 (1), 47–58.

Zhao, W., Zou, C., Li, J., Feng, Z., Zhang, G., Hu, S., et al. (2009b). Comparative study on volcanic hydrocarbon accumulations in Western and eastern China and its significance. *Petroleum Explor. Dev.* 36 (1), 1–11. doi:10.1016/S1876-3804(09)60106-3

Zou, C., Zhao, W., Jia, C., Zhu, R. K., Zhang, G. Y., Zhao, X., et al. (2008). Formation and distribution of volcanic hydrocarbon reservoirs in sedimentary basins of China. *Petroleum Explor. Dev.* 35 (3), 257–271. doi:10.1016/S1876-3804(08)60071-3

frontiers | Frontiers in Earth Science

TYPE Original Research
PUBLISHED 09 May 2023
DOI 10.3389/feart.2023.1176929

OPEN ACCESS

EDITED BY
Hu Li,
Southwest Petroleum University, China

REVIEWED BY
Xiujian Ding,
China University of Petroleum (Huadong), China
Wei Yu,
The University of Texas at Austin, United States

*CORRESPONDENCE
Long Huang,
huanglong0919@126.com,
Yunbo Zhang,
zhangyb2014@foxmail.com

RECEIVED 01 March 2023
ACCEPTED 12 April 2023
PUBLISHED 09 May 2023

CITATION
Wang M, Huang L, Lei B, Zhang Y and Pan J (2023), Permian sedimentary evolution and hydrocarbon accumulation effects in the central-southern South Yellow Sea Basin.
Front. Earth Sci. 11:1176929.
doi: 10.3389/feart.2023.1176929

Permian sedimentary evolution and hydrocarbon accumulation effects in the central-southern South Yellow Sea Basin

Mingjian Wang[1,2], Long Huang[1]*, Baohua Lei[1], Yunbo Zhang[3]* and Jun Pan[1]

[1]Qingdao Institute of Marine Geology, China Geological Survey, Ministry of Natural Resources, Qingdao, China, [2]Laboratory for Marine Mineral Resources, Pilot National Laboratory for Marine Science and Technology, Qingdao, China, [3]Oil and Gas Survey, China Geological Survey, Beijing, China

The South Yellow Sea Basin (SYSB) is an extension of the Lower Yangtze Block to the sea. The basin has undergone a complex tectonic-sedimentary evolution, and there has been no breakthrough in oil and gas exploration. Based on newly collected and processed well drilling data, cores, and seismic data of the central-southern SYSB and adjacent areas, the understudy area is set in the Lower Yangtze Region (LYR) to compare the overall sequence division and sedimentary facies. The Permian isochronous stratigraphic framework is methodically established in the central-southern SYSB, and the corresponding sedimentary facies and their distribution are examined in some detail. Finally, together with the previous investigations of tectonic evolution, the potential Permian oil-gas accumulation modes are proposed. The achieved results reveal that the second-order Permian sequence developed in the central-southern SYSB is consistent with the LYR. There exists a relatively complete second-order sequence I developed in the middle-bottom section and the transgressive systems tract of sequence II in the upper section. The Permian sedimentary system in the central-southern SYSB can be compared to the LYR and is generally distributed in a northeast direction. The transgressive systems tract of sequence I is broadly developed with the restricted platform and open platform as the dominant facies. The highstand systems tract of sequence I has been only developed in the northwest of the understudy area, with the shelf as the dominant facies. The transgressive systems tract of sequence II is mostly dominated by delta facies and swamp-lagoon facies with thick coal-measure layers, which provide a material basis for the formation of large-scale oil and gas fields. The thermal evolution of Permian source rocks was controlled by a combination of tectonic evolution and paleothermal gradient. Permian source rocks may have experienced secondary hydrocarbon generation in the western part of the southern Depression, whereas source rocks elsewhere experience only one hydrocarbon generation in the Early Triassic. The obtained results reveal that there are significant differences in the accumulation mode of different structural units.

KEYWORDS

South Yellow Sea Basin (SYSB), central-southern part, Permian, sequence, sedimentary facies, oil and gas accumulation mode

1 Introduction

The South Yellow Sea Basin (SYSB) is a marine extension of the Lower Yangtze Plate and is a polycyclic superimposed basin that developed in the pre-Sinian metamorphic basement. Before the Indosinian movement, the LYR as a whole was a unified marine-dominated sedimentary basin, and the stratigraphic development of the Subei Basin in the onshore area was obviously consistent with that of the SYSB in the offshore area. After the Indosinian movement, the unified marine sedimentary basin in the LYR broke up and entered the stage of continental basin with differentiated tectonic-sedimentary evolution. The results of the present research reveal that the Mesozoic and Paleozoic marine strata in the SYSB are highly developed and the structural deformation is comparatively weak, which is a relatively stable block. Currently, a large number of oil and gas shows have been found in the Lower Triassic Qinglong Formation and Upper Carboniferous Chuanshan Formation in the Subei Basin. The regeneration gas fields originating from the Mesozoic and Paleozoic have been also detected in Zhujiadun, Yancheng City. The oil-seedlings were observed in the limestone fractures of the Lower Triassic Qinglong Formation in the CSDP-2 well in the central Uplift of the SYSB. A large amount of asphalt has been seen in the fractures of the Silurian sandstone. These exploration results indicate that there are generation-migration-accumulation processes of oil and gas in the Mesozoic and Paleozoic of the LYR, which has a good prospect for oil and gas exploration.

Many scholars have carried out research on the petroleum geological conditions of the SYSB, and have achieved rich research results. The latest research results mainly include the following aspects. Wang et al. (2014) carried out a systematic analysis of the Permian hydrocarbon accumulation conditions by using the drilling data and 2D seismic data of the southern depression of the SYSB. Based on the drilling and core data of CSDP-02 holes implemented on the central Uplift of the SYSB, Cai et al. (2018a), Cai et al. (2018b), Cai et al. (2021a) and Cai et al. (2021b) carried out a study on the upper Paleozoic sedimentary environment of the central Uplift, and the hydrocarbon generation stages of the Meso-Paleozoic source rocks are also discussed. Lei (2018) and Lei (2022) used 2D seismic data of the SYSB to carry out the study of structural deformation in the study area since the Indosinian period, analyzed the deformation mechanism, and discussed the exploration prospects of oil and gas resources on the central Uplift. Although SYSB has experienced many years of exploration, there are still no significant oil and gas discoveries so far. It is the only offshore sedimentary basin in China that has not achieved oil and gas breakthroughs. Based on preceding research results, the following major problems exist. The Mesozoic and Paleozoic marine strata in the SYSB are deeply buried, the physical property differences in carbonate strata are almost trivial, the quality of seismic reflection imaging is poor, and the common seismic reflection interface is difficult to laterally trace. The study area has experienced the superimposed transformation of multi-stage tectonic movements and has complex structural features that lead to the existence of multiple seismic interpretation schemes (Zhu et al., 2002; Yang et al., 2003; Yang and Chen, 2003; Ma, 2007; Lei, 2018; Liang, 2021; Lei, 2022; Wang, 2022). There is little deep drilling data in this area and the seismic profile network is sparse and

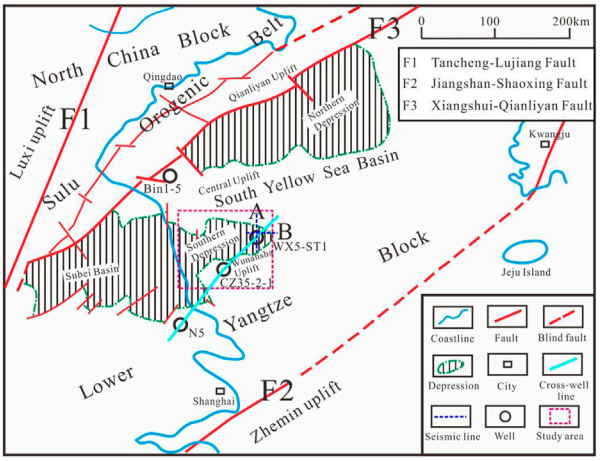

FIGURE 1
Tectonic location of the study area. The current tectonic relationship between SYSB and adjacent area is shown in this figure.

of poor quality (Ye, 2006; Wang, 2014; Wang, 2016; Wang, 2018; Wang, 2020). There is a lack of systematic understanding of the development of Permian sedimentary facies and the distribution of favorable source rocks (Wang, 2005; Wang, 2014; Qiu, 2018; Wang, 2018; Wang, 2020; Mi, 2022). The SYSB has not been generally investigated in the entire LYR, and a lack of comparative study on sequence division and sedimentary system development with other regions in the LYR is obvious (Ye, 2006; Hu, 2010; Cai, 2018a; Cai, 2021a). Different tectonic units in this region have different tectonic evolution histories, and the histories of hydrocarbon generation of the source rocks are also remarkably different (Wang, 2018; Chen, 2020). Up till now, hydrocarbon accumulation processes and modes of diverse tectonic units have not been systematically discussed (Dai, 2005; Wang, 2014; Wang, 2018; Zhang, 2018; Zhang, 2021; Li, 2022). These factors lead to the lack of oil and gas exploration goals, which limits the processes of oil and gas explorations in the study area. Among the many factors affecting oil and gas accumulation, sedimentation controls the development law of source rocks and reservoirs, which is the first basic problem to be solved (Radwan, 2021; Marghani, 2022).

2 Geological setting

From the point of view of the tectonic location, the SYSB is located in the eastern part of the LYR, in the east of the Tancheng-Lujiang fault, in the south of the Sujiao orogenic belt, in the north of the Jiangshan-Shaoxing fault belt and Zhemin Uplift. It is adjacent to the Korean Peninsula in the east and consists of five tectonic units from north to south, which are: Qianliyan Uplift, northern Depression, central Uplift, southern Depression, and Wunansha Uplift (Figure 1). The study area covers the central-southern part of the SYSB, including part of the central Uplift, the Southern Depression, and a portion of the Wunansha Uplift. The SYSB has experienced a drastic transformation with the evolution of the Indosinian Movement, the Yanshan Movement, and the

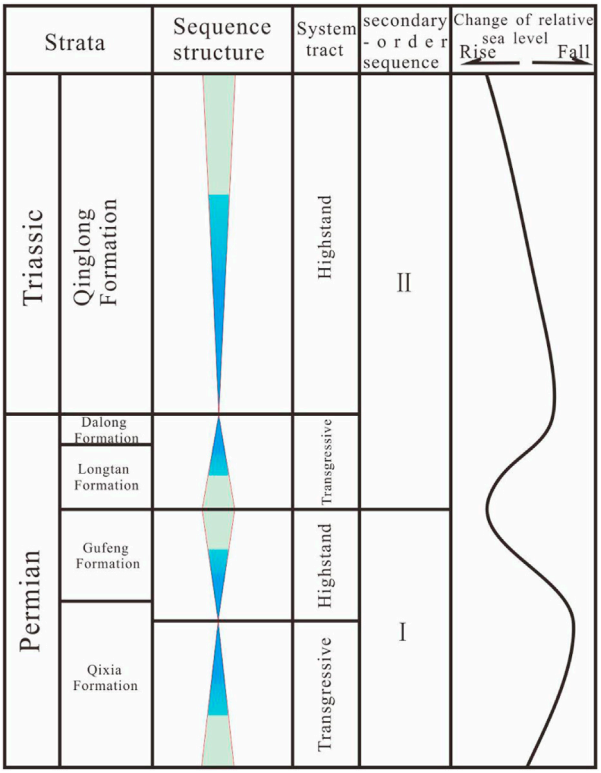

FIGURE 2
Division of the second-order sequence in the Permian system, LYR. Stratigraphic framework of Permian is shown in this figure (modified from Ma et al., 2009; Cai et al., 2018b; Cai, 2021a).

Himalayan Movement; hence, it exhibits complex structural features. Drilling data confirms that platform deposits are extensively developed in the SYSB from the Paleozoic to the Triassic (Wang, 2014; Wang, 2016; Cai, 2018b; Wang, 2018; Wang, 2020; Cai, 2021a; Cai, 2021b; Wang, 2022; Wang, 2023), and their lithology and seismic geological sequence in the SYSB are consistent with these on the land, which is a series of strata dominated by marine carbonate rocks (Figure 2). From bottom to top, the strata in order are Sinian, Cambrian, Ordovician, Lower Middle Silurian, Upper Devonian, Carboniferous, Permian, Lower Triassic, Upper Cretaceous, Paleogene, and Neogene-Quaternary. Among them, Upper Cretaceous and Paleogene are moderately limited in distribution and mainly occur in the depression, whereas in other areas, the Neogene directly overlies the Upper Paleozoic or Lower Triassic (Table 1).

3 Sequence division and sedimentary facies

3.1 Sequence division scheme

Referring to the previous research results of the LYR, three regional unconformities could be identified in the target layers of the study area. Among them, the unconformity between the Qixia Formation and the Carboniferous was configured by the Suwan tectonic movement, the regional unconformity between the Gufeng Formation and the Longtan Formation was formed by the Dongwu movement, and a regional angular unconformity was created on top of the Qinglong Formation by the Indosinian movement. The Permian-Triassic can be divided into two second-order sequences, namely, sequence I including the Qixia Formation and Gufeng Formation, and sequence II including the Longtan Formation, Dalong Formation, and Qinglong Formation (Figure 2). Sequences I and II developed only transgressive and highstand systems tract, and lacked lowstand systems tract (Figure 2). The object of this investigation is the Permian, which contains a well-developed sequence I and the transgressive systems tract of sequence II.

3.2 Single well sequence and sedimentary facies division

A total of 6 wells which drilled the Permian were collected in the study area and adjacent areas, and the sequence development features of wells WX5-ST1 and Bin 1–5 with relatively complete stratigraphic development are presented below.

3.2.1 Well Bin 1–5

The well Bin 1–5 is located on the west side of the central Uplift and was drilled deep into the Qixia Formation, and the overlying Gufeng Formation is directly overlain by the Neogene. Due to the effect of multi-stage tectonic movements, only sequence I is preserved in this well, and sequence II is denuded. Sequence I only develops the transgressive systems tract and highstand systems tract, and thereby, the lowstand systems tract is not developed.

The transgressive systems tract of sequence I in the Bin 1–5 well includes the middle and lower parts of the Qixia Formation. Lithologically, it is mostly composed of limestone and mudstone, containing calcified brachiopod fragments, less coral, encrinite fossils and common pyrite. This set of rocks is formed in relatively shallow water with a weak hydrodynamic environment, where the restricted platform facies is developed.

The highstand systems tract of sequence I in Bin 1–5 well includes the upper parts of the Qixia and Gufeng Formations, and the top of the sequence is a weathered denudation surface (Figure 3). The lithology is mainly gray-black mudstone, sandy mudstone, fine sandstone, and siltstone rich in carbon debris and ammonite fossils in local areas. Horizontal beds are broadly developed, followed by wavy beds. This formation is formed in a relatively weak hydrodynamic environment that can be affected by waves. This systems tract leads to the development of the lagoon facies in a coastal environment.

3.2.2 Well WX5-ST1

The WX5-ST1 well is located in the eastern part of the southern Depression of the SYSB and has been drilled in the Permian Longtan Formation. The Longtan Formation to the Qinglong Formation belongs to sequence II (Longtan Formation, Dalong Formation, and Qinglong Formation), and the upper sequence boundary is the top of Qinglong Formation, which represents a regional unconformity surface, and the lower boundary of the sequence cannot be revealed

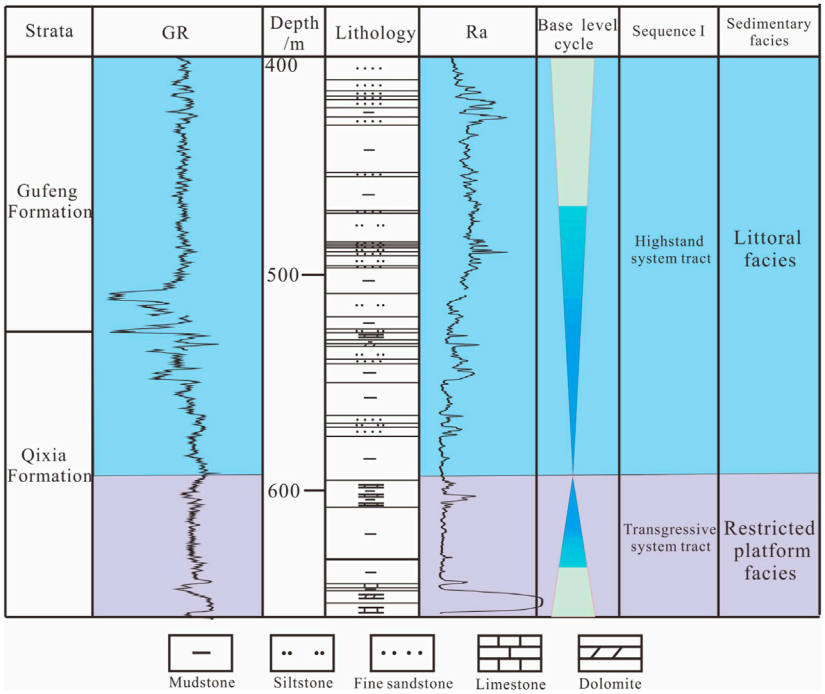

FIGURE 3
Division of sequence and sedimentary facies of sequence I in well Bin 1–5.

by digging. This sequence develops the transgressive systems tract and the highstand systems tract from the bottom up. The lowstand systems tract is undeveloped, and the highstand systems tract occupies the main body of the sequence, whereas the thickness of the transgressive systems tract (Longtan-Dalong Formation) is moderately thin (Figure 5).

The transgressive systems tract of sequence II in this well comprises the Longtan Formation and the middle-lower part of the Dalong Formation, which can be divided into three parts based on the lithology. The lower part is brown-dark gray siltstone and limestone. The middle part is gray-white-dark gray sandstone, of which the upper part possesses more coal seams. The upper part is dark gray, gray-black siltstone and mudstone, and pyrite is detected in mudstone. This systems tract has mostly incorporated into the development of delta facies and littoral facies.

3.3 Comparison of sequence stratigraphy and sedimentation

3.3.1 Comparison of logging sequence and logging facies

Based on the stratigraphic division of single well sequence in the study area and nearby areas, drilling wells in the Subei Basin and

TABLE 1 Seismic sequence and strata property since Devonian in the central-southern part of the SYSB.

Seismic sequence	Characteristic wave	Contact relation	Strata	Stratigraphic code	Lithology	Basin evolution
I	T_2	Angle unconformity	Neogene-Quaternary	N-Q	Mudstone, siltstone, argillaceous sandstone and glutenite	Continental depression basin
II	T_8	Angle unconformity	Cretaceous-Paleogene	K-E	Mudstone and siltstone	Extensional faulted basin
III	T_9	Conformity	Qinglong Formation of Triassic	Tq	Limestone and calcilutite	Epicontinental sea basin
IV	T_{10}	Parallel unconformity	Longtan-Dalong Formation of Permian	Pl-d	Sandstone, shale and coal seam	
V	T_{10}'	Parallel unconformity	Qixia-Gufeng Formation of Permian	Pq-g	Biolithite limestone and marl	
VI			Devonian-Silurian	D-C	Limestone and dolomite	

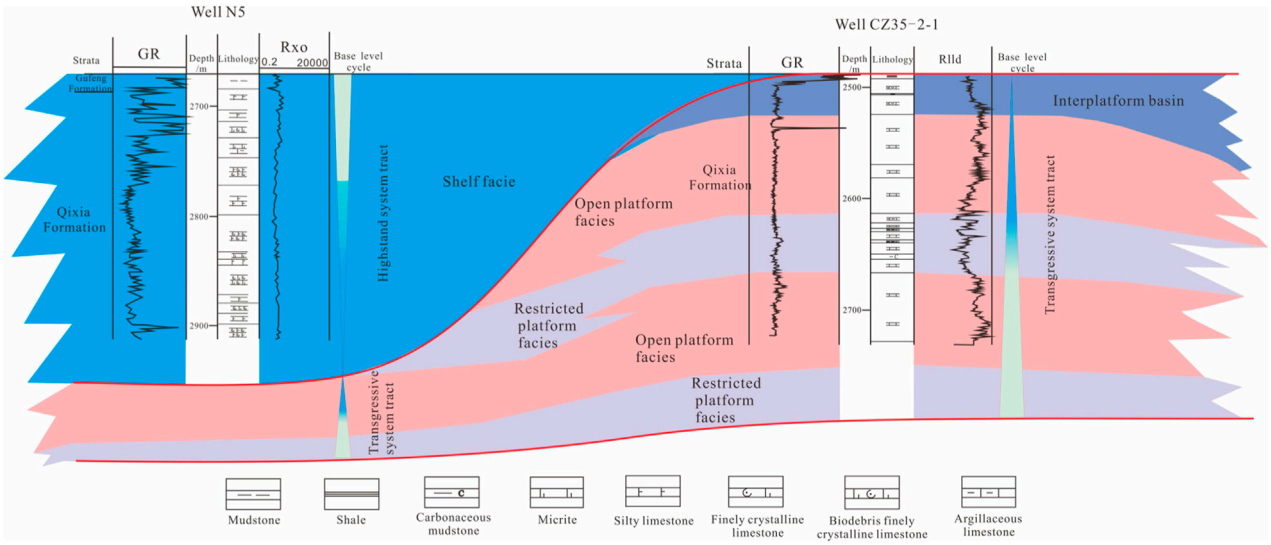

FIGURE 4
Sedimentary facies of sequence I in the cross-well profile (north-east direction). The fill colors represent different sedimentary facies. Stratigraphic framework and sedimentary facies are shown in this figure.

SYSB are chosen to perform the division and comparison of well-connected sequence stratigraphy. The following research focuses on two southwest-northeast well profiles.

3.3.1.1 Cross-well profile of sequence I in the southwest-northeast direction (well N5 to well CZ 35-2-1)

From the southwest-northeast well section of sequence I (Figure 4), it can be seen that the transgressive systems tract and highstand systems tract have been developed in the Lower Yangtze land area, whereas in the Lower Yangtze sea area (central-southern part of the SYSB) only the transgressive systems tract has been developed. From west to east, the transgressive systems tract thickness increases, which are essentially characterized by the alternating development of the restricted platform and the open platform, and the interplatform basin facies (Ma, 2009) is developed at the top. The highstand systems tract gradually thins to the sea area and disappears in the central-southern SYSB. The systems tract essentially developed shelf facies. Along with the regional geological background, during this period, the Dongwu tectonic movement occurred in the LYR with crustal uplift. Seawater gradually retreated from southern China to the south and southwest, and the early sedimentary layers were denuded in most parts of the LYR.

3.3.1.2 Cross-well profile of sequence II in the southwest-northeast direction

It can be observed from the cross-well profile of sequence II in the southwest-northeast direction (Figure 5) that the top and bottom boundaries of the sequence represent regional unconformity surfaces. After the Dongwu movement, the LYR was generally settled and received sediment. Transgressive and highstand systems tract are developed in both the land and sea areas of the LYR, whereas the lowstand systems tract is not developed. In the early and middle stages, the transgressive systems tract of sequence II incorporated into the development of the swamp-lagoon facies, delta facies, and swamp-lagoon facies from west to east. Further, the deep shelf facies and swamp-lagoon facies from west to east were developed in the late stage. In the initial stage of the highstand systems tract of sequence II, the water deepened and then became shallower from the Lower Yangtze land area to the southern Yellow Sea area. Along this direction, shallow shelf facies, deep shelf facies, shallow shelf facies, and swamp-lagoon facies are sequentially observable. In the middle and final stages, the restricted platform and the open platform were alternately developed. In the final stage of the highstand systems tract, the Yangtze plate and the North China plate collided from east to west, and the LYR generally rose with a decrease in relative sea level. The primary sedimentary strata were exposed to the surface and suffered from severe denudation.

3.3.2 Comparison of the seismic sequence and facies

Seismic profiles have the advantages of systematic, continuous, and regional distribution that can be employed to track and compare sequence and system boundaries in the basin. Line A is located in the central-eastern SYSB and crosses the Wunansha Uplift, the southern Depression and the central Uplift from south to north. Based on the seismic interpretation, both normal and reverse faults exist. Combined with the regional geological background and seismic interpretation, the reverse faults are essentially configured by the Indosinian movement, whereas the normal faults are mainly formed in the Late Cretaceous-Paleogene. Sequence I only has the transgressive systems tract, which corresponds to the Qixia Formation, and the highstand systems tract may exist in the western part of the study area, but its thickness should be moderately thin (Figure 6). The lithology of this systems tract chiefly exhibits carbonate rock, and the lithology difference between the consisting layers is very small, so it is difficult to form the effective wave impedance, and the characteristics of the wave group are not clear. The transgressive systems tract of sequence II roughly corresponds to the Longtan-Dalong Formation and produces marine clastic rocks. The lithology discrepancy between the constituent

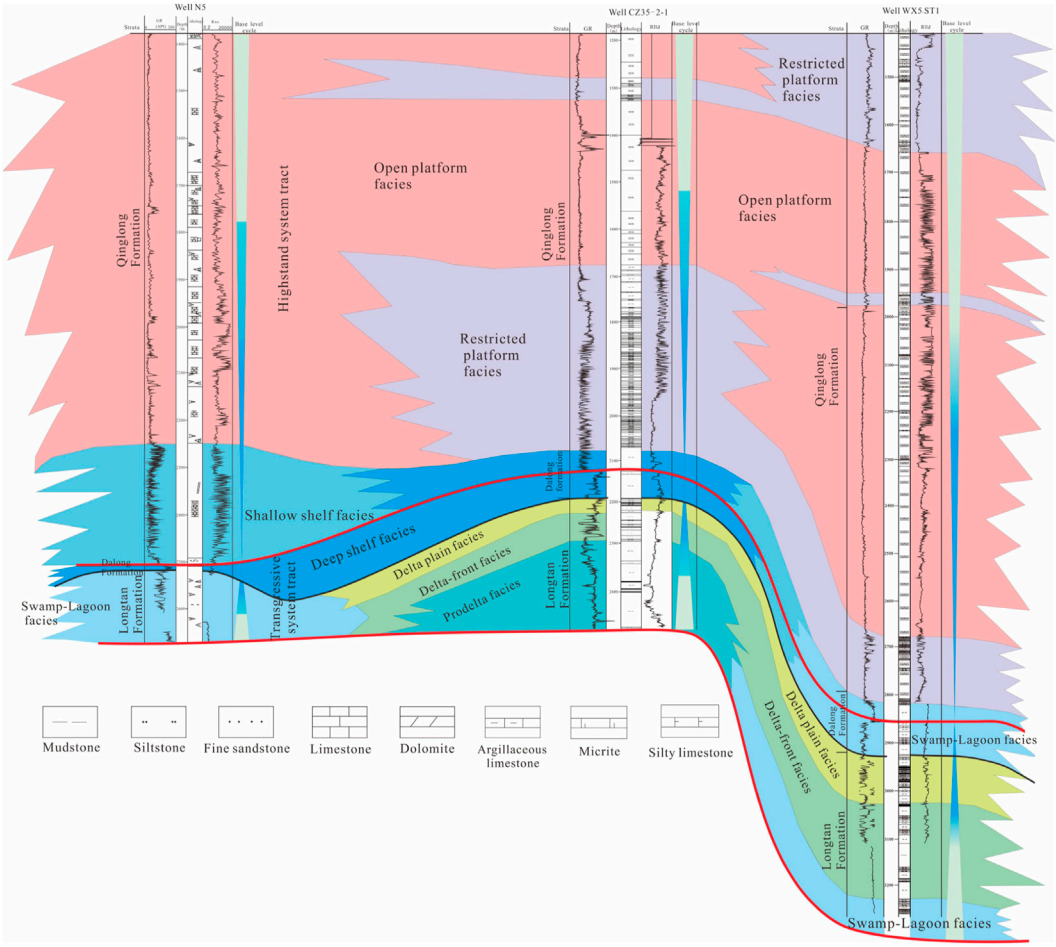

FIGURE 5
Sedimentary facies of sequence II in cross-well profile (north-east direction). The fill colors represent different sedimentary facies. Stratigraphic framework and sedimentary facies are shown in this figure.

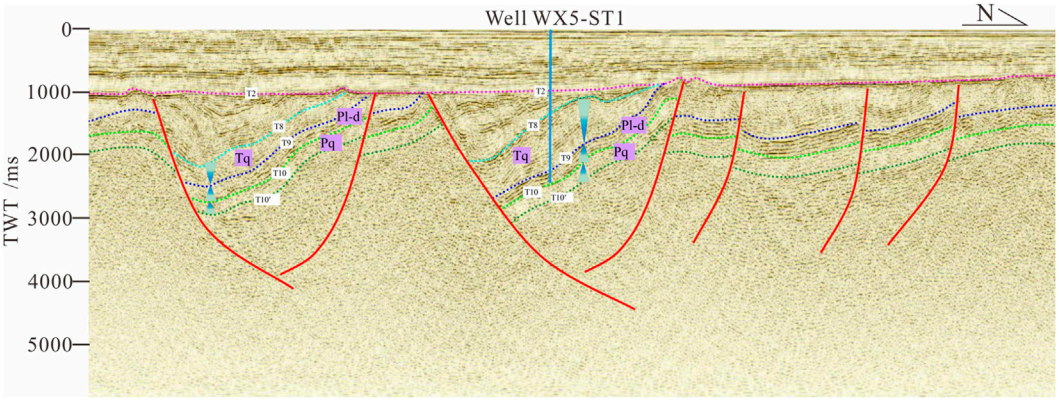

FIGURE 6
Seismic sequence in Line A (north-south direction). The Pq label represents the Qixia Formation of Permian; Pl-d represents the Longtan-Dalong Formation of Permian; Tq represents the Qinglong Formation of Triassic; T_2 represents the boundary between the Neogene and Paleogene; T_8 represents the top boundary of the Triassic; T_9 represents the boundary between the Triassic and Permian; T_{10} represents the boundary between the Longtan Formation and Qixia Formation; and T_{10}'represents the bottom boundary of Qixia Formation.

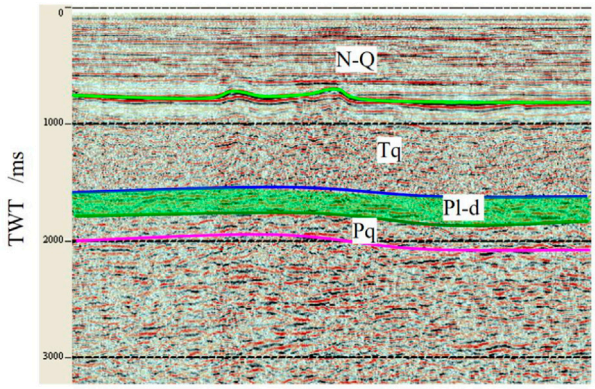

FIGURE 7
Shelf facies in the seismic profile. The Pq label represents the Qixia Formation of Permian; Pl-d represents the Longtan-Dalong Formation of Permian; Tq represents the Qinglong Formation of Triassic; and N-Q represents the Neogene–Quaternary.

layers is large, resulting in strong wave impedance and transparent wave group characteristics. It represents a set of medium-low frequency, medium-strong amplitude, and wave groups with good continuity, and the thickness of the formation is moderately stable.

Based on the sequence division and sedimentary facies analysis of drilling data in the understudy area as well as the nearby area, combined with the research results of the predecessors, the following seismic facies types are identified on the seismic profile by interpreting the seismic data in the central-southern part of the SYSB.

3.3.2.1 Parallel-subparallel, medium-medium strong amplitude, low-frequency, and intermittent-less continuous seismic facies

Seismic facies are sheet-like with a parallel-subparallel reflection structure inside. Seismic reflection is chiefly characterized by weak-moderate-moderate strong amplitude, low frequency, and intermittent-less continuous reflection (Figure 7). Combined with previous research on Permian sedimentary facies in the LYR and seismic data, these seismic wave groups are mainly consistent with shelf facies.

3.3.2.2 Progradation structure, medium-strong amplitude, low frequency-medium frequency, and less continuous-continuous seismic facies

Such seismic facies exhibit a progradation structure in the direction of the sediment source (Figure 8) and the seismic reflection demonstrates the characteristics of moderate strong amplitude, low-moderate frequency, and less continuous-continuous reflection. Combined with drilling data, these seismic reflection wave groups commonly represent for delta facies.

3.3.2.3 Parallel-subparallel, weak-medium amplitude, medium frequency, and less continuous-continuous seismic facies

Such seismic facies show that the hydrodynamic force of the sedimentary environment is weak and the wave impedance difference between the layers is relatively high. Together with drilling data and regional sedimentary evolution data, we conclude that such seismic reflection waves are associated with the restricted platform facies.

3.3.2.4 Weak reflection-blank reflection seismic facies

In combination with the drilling data in the study area, no effective reflection could be established due to the small lithological difference between the thick carbonate layers. These seismic reflection waves in the study area correspond to the facies of the open platform.

4 Distribution of the sedimentary facies

4.1 Sedimentary facies in the transgressive systems tract of sequence I

During this period, the Lower Yangtze Basin is distributed in the north-east direction restricted by the Xiangshui-Qianliyan Fault in the north, the Tancheng-Lujiang Fault in the west, and the Jiangshao Fault in the south (Figure 9). The water in this basin gradually deepens from northwest to southeast. In this regard, the basin has developed the tidal flat-lagoon facies, restricted platform facies, open platform facies, marginal slope facies, and shelf facies sequentially (Figure 9).

The central-southern SYSB is located in the eastern part of the LYR and exhibits the same sedimentary facies as the whole LYR with a northeasterly distribution (Figure 10). Based on the analysis of drilling, logging, and seismic data in the study area, it is concluded that tidal flat lagoon facies, restricted platform facies, open platform facies, marginal slope facies, and shelf facies have sequentially developed from northwest to southeast (Figure 10).

4.2 Sedimentary facies in the highstand systems tract of sequence I

The basin distribution in the LYR is inherited compared to the previous period and is still distributed in the northeast direction (Figure 11). However, compared to the previous period, the sedimentary system has been altered, mainly marine clastic rocks are developed, and carbonate rocks are moderately less developed. This basin is generally characterized by deep water in the middle and shallow water on both sides.

From northwest to southeast, the LYR led to the development of tidal flat-lagoon facies, foreshore-shoreface facies, shelf facies, and delta facies successively, and the shelf facies have developed the largest area (Figure 11). The sediment source in this period essentially originated from the ancient land on the north and south sides.

During this period, the sedimentary facies developed in the central-southern SYSB were similar to those in the LYR, and the water deepened from northwest to southeast. Only the western part of the study area presents a sedimentary process, and the central-eastern areas have been raised and denuded (Figure 12). By analyzing drilling, logging, and seismic data in the study area,

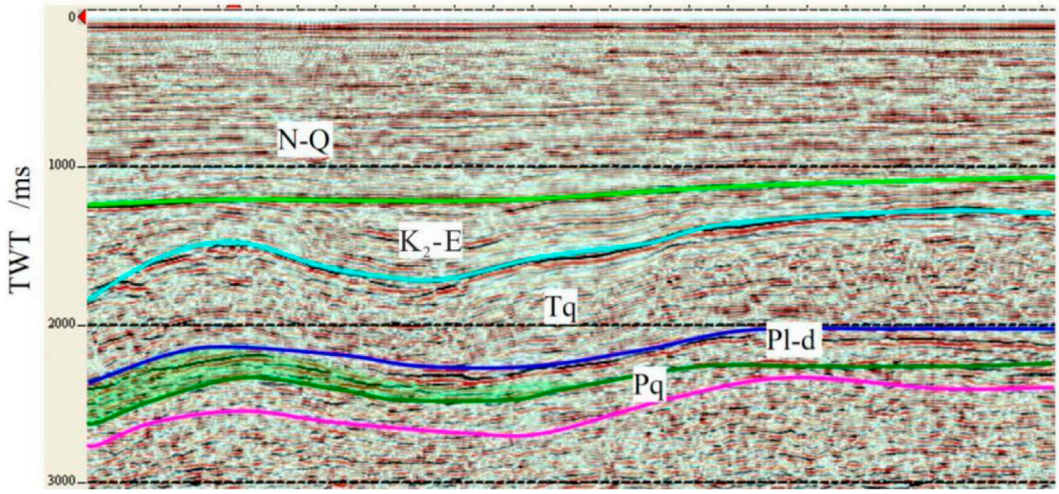

FIGURE 8
Delta facies in the seismic profile (perpendicular to the direction of the sediment source). The Pq label represents the Qixia Formation of Permian; Pl-d represents the Longtan-Dalong Formation of Permian; Tq represents the Qinglong Formation of Triassic; K_2-E represents the Late Cretaceous-Paleogene; and N-Q represents the Neogene–Quaternary.

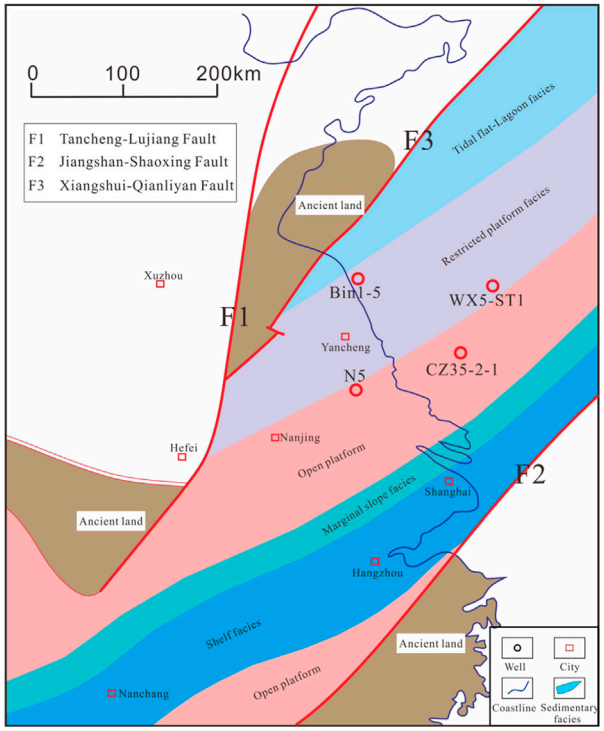

FIGURE 9
Sedimentary facies in the transgressive systems tract of sequence I in the Lower Yangtze [modified from (Ma, 2009)]. The fill colors represent different sedimentary facies. In the LYR area, tidal flat-lagoon facies, restricted platform facies, open platform facies, marginal slope facies, and shelf facies are developed.

tidal flat lagoon facies, foreshore-shoreface facies, and shelf facies were developed in the study area from northwest to southeast (Figure 12).

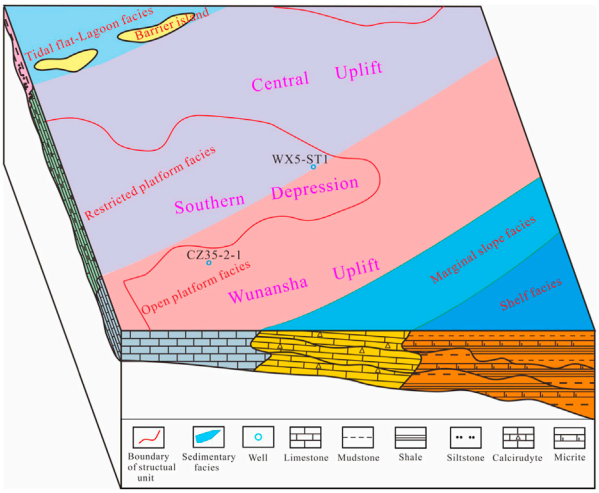

FIGURE 10
Sedimentary facies in the transgressive systems tract of sequence I in the central-southern SYSB. The fill colors represent different sedimentary facies. In the study area, tidal flat lagoon facies, restricted platform facies, open platform facies, marginal slope facies, and shelf facies are developed.

4.3 Sedimentary facies in the transgressive systems tract of sequence II

During the period of the transgressive systems tract of sequence II, the basin was still distributed in a northeast direction (Figure 13) and majorly developed with marine clastic rocks, with deep water in the middle part and shallow water in the north. The sedimentary system has also been changed, and the fluvial facies have developed in the northern region. Additionally, along the southeast direction, delta facies or

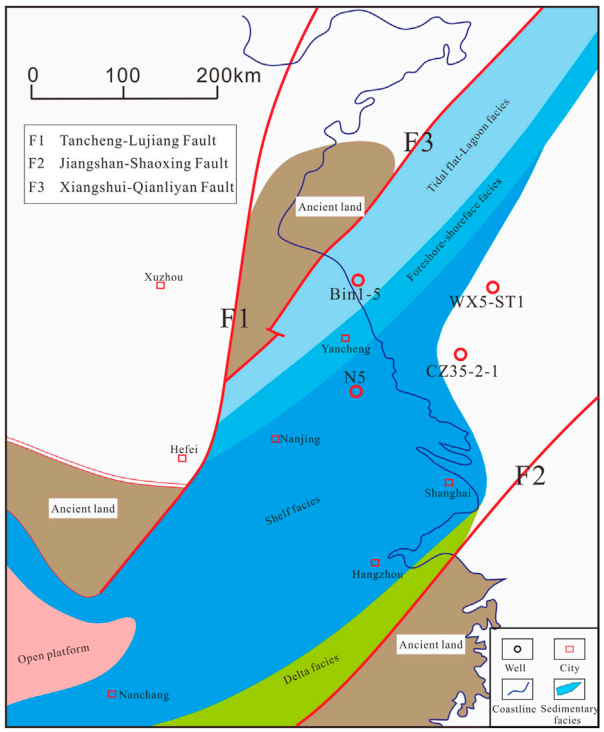

FIGURE 11
Sedimentary facies in the highstand systems tract of sequence I in the LYR [modified from (Ma, 2009)]. The fill colors represent different sedimentary facies. In the LYR area, tidal flat-lagoon facies, foreshore-shoreface facies, shelf facies, and delta facies are developed.

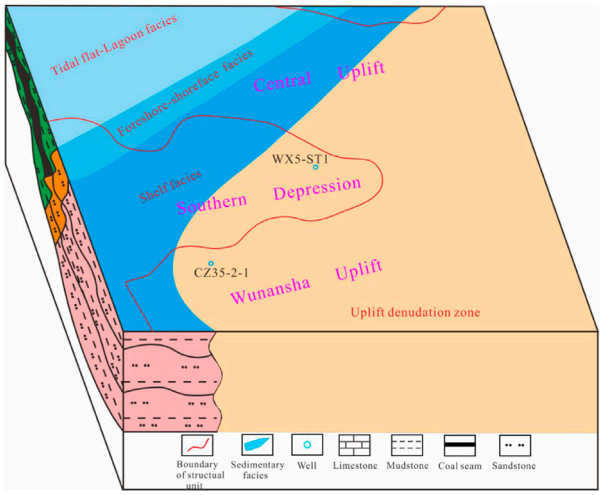

FIGURE 12
Sedimentary facies in the highstand systems tract of sequence I in the central-southern SYSB. The fill colors represent different sedimentary facies. In the study area, tidal flat lagoon facies, foreshore-shoreface facies, and shelf facies are developed.

littoral facies, shelf facies, and littoral facies have been successively developed (Figure 13). Sediment sources in this period all originated from the ancient lands of both sides.

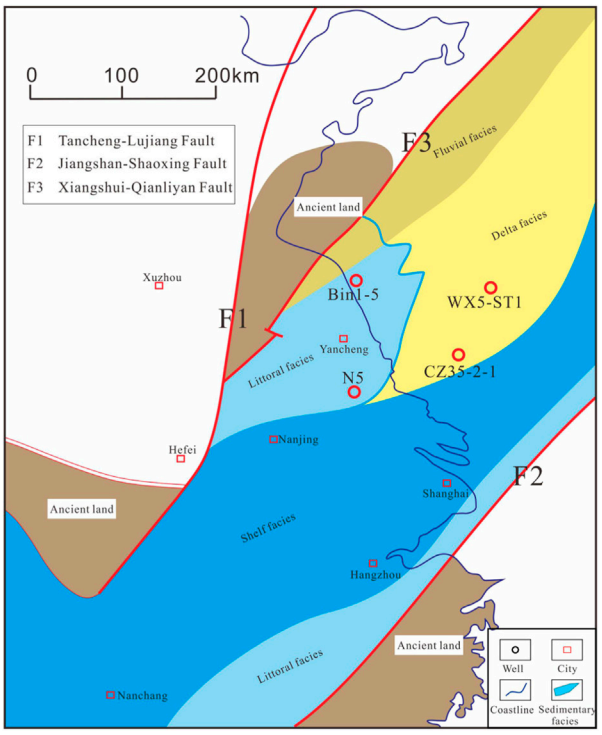

FIGURE 13
Sedimentary facies in the transgressive systems tract of sequence II in the LYR [modified from (Ma, 2009)]. The fill colors represent different sedimentary facies. In the LYR area, fluvial facies, delta facies or littoral facies, shelf facies, and littoral facies are developed.

During this period, the sedimentary system in the central-southern SYSB was still distributed in the northeast direction (Figure 14). From northwest to southeast, the water gradually gets deeper. By analyzing drilling, logging and seismic data in the study area, it is concluded that fluvial facies are developed in the northern area. Along the southeast direction, delta facies, swamp-lagoon facies, foreshore-shoreface facies and shelf facies are developed (Figure 14). The sedimentary sources in this period all originated from ancient lands on both sides (Figure 14).

5 Hydrocarbon accumulation mode

5.1 Control factors of oil and gas accumulation

Drilling and seismic data interpretation have revealed that the Permian Longtan-Dalong Formation has formed the tidal and swamp mudstone and coal seam in the understudy area. The kerogen type was mostly type III and the organic carbon content was high, generally in the range of 1.1%–3.2%, which represents a good medium source rock. The vitrinite reflectance (Ro) of source rocks in the Longtan Dalong Formation is in the interval of 1.2%–2.3% with an average of 1.95%, which has reached the stage of high maturity and overmaturity. The favorable reservoirs mainly include sandstones of delta facies and fluvial facies in the Permian Longtan

Formation, Upper Cretaceous and Paleogene systems, as well as carbonate rocks of platform facies, marginal slope facies, and platform marginal shoals in Lower Triassic Qinglong Formation. Most of the deep reservoirs are chiefly featured by their low-porous and low-permeability values, and the properties of the reservoir gradually enhance upward. Current studies show that tectonism controlled fracture development in tight reservoirs can significantly improve reservoir properties (Li, 2019; Li, 2020; Li, 2022a; Li, 2022b). Due to the multi-phase tectonic movements in the study area, this evolved secondary pores and cracks in the sedimentary layers (especially carbonate rocks), leading to porosity enhancement. The regional cap rocks mainly include mudstones of the Lower Permian Qixia Formation, Upper Permian Longtan Formation, and mudstones of the Cretaceous Pukou Formation, and many local cap rocks are also developed.

Former studies disclosed that the southern Depression of the SYSB experienced four evolutionary stages, which are: the epicontinental sea in Late Paleozoic-Early Triassic, uplift erosion in the Late Triassic-Early Cretaceous, the extensional faulted basin in the Late Cretaceous-Paleogene, and the continental depression basin in Neogene-Quaternary. However, the central Uplift and Wuansha Uplift experienced only three stages of evolution, which are the epicontinental sea in the Late Paleozoic-Early Triassic, uplift erosion in the Late Triassic-Paleogene, and the continental depression basin in Neogene-Quaternary. Due to various tectonic evolutionary histories, remarkable differences in hydrocarbon generation processes of Permian source rocks are detected. In the present investigation, typical wells of various structural units are selected for burial history analysis (Figure 15).

The WX5-ST1 well is located in the eastern part of the southern Depression of the SYSB, and the burial history indicates that the Permian source rocks only reached the first hydrocarbon generation in the Early Triassic. Although such rocks were reburied after the late Cretaceous–Paleogene and Neogene–Quaternary, they did not regenerate hydrocarbons due to the reduced geothermal gradient and insufficient burial depth (Wang, 2014). The western part of the southern Depression in the SYSB is the Late Cretaceous sedimentary center, with large strata thickness and secondary hydrocarbon generation from Permian source rocks that may occur in this area.

Well CZ35-2-1 is located in the Wunansha Uplift of the SYSB. The performed burial history analysis reveals that the Permian source rocks also experienced only one generation of hydrocarbons in the Early Triassic and did not produce hydrocarbons again in the next period. Similar to the tectonic evolution history of the Wunansha Uplift, the Permian source rocks in the central Uplift have only one hydrocarbon generation in the Early Triassic.

5.2 Accumulation mode

The tectonic activities in the understudy region at the Early Triassic and Neogene-Quaternary were mainly dominated by integrated uplift and subsidence, and faults were not well developed. The oil and gas produced by Permian source rocks in these two periods are mostly accumulated in the reservoirs close to the hydrocarbon generation centers, which mainly form self-generation and self-accumulation reservoirs of the Permian

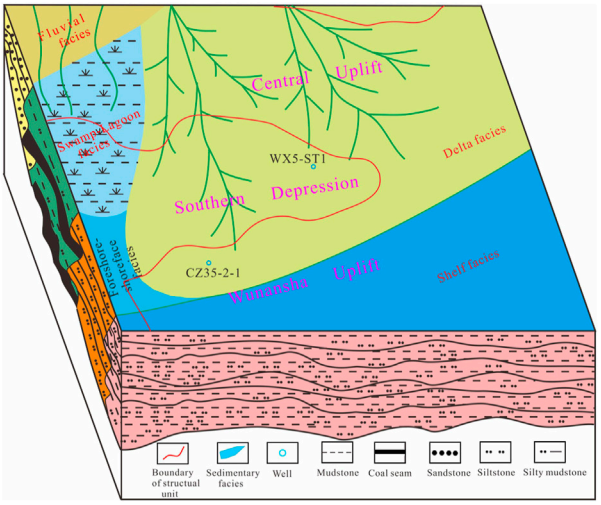

FIGURE 14
Sedimentary facies in the transgressive systems tract of sequence II in the central-southern SYSB. The fill colors represent different sedimentary facies. In the study area, fluvial facies, delta facies, swamp-lagoon facies, foreshore-shoreface facies, and shelf facies are developed.

(Figure 16). Among them, the early Tthe hydrocarbon productionriassic oil and gas reservoirs have been broadly distributed in the understudy region (including the central Uplift, the southern Depression, and the Wunansha Uplift), while the Neogene-Quaternary oil and gas reservoirs are only found in the western part of the southern Depression where secondary hydrocarbon generation may have occurred.

The southern Depression of the SYSB has been incorporated into the development of the extensional fault basin in the Late Cretaceous-Paleogene. On the one hand, the faults destroyed the oil and gas reservoirs formed in the early stages. On the other hand, the oil and gas produced by the secondary hydrocarbon production of Permian source rocks in the western part of the southern Depression can be transported along faults, unconformities, and other transport systems to shallow traps, which essentially constitute Permian generation-Mesozoic accumulation reservoirs and Permian generation-Cenozoic accumulation reservoirs generation (Figure 16). Such accumulation modes may only exist in the western part of the southern Depression.

6 Discussion and summary

Due to the comprehensive control of tectonic evolution and geothermal gradient, there are noticeable discrepancies in the process of hydrocarbon generation and favorable oil and gas accumulation modes of Permian source rocks among different structural units. The tectonic evolution history of the central SYSB Uplift is mostly similar to that of the Wunansha Uplift. Permian source rocks experienced only one hydrocarbon generation in the Early Triassic, and the strata suffered a severe squeeze and developed many reverse faults subjected to the Indosinian movement in the Late Triassic. The reverse fault destroyed the oil and gas reservoirs formed in the early stages.

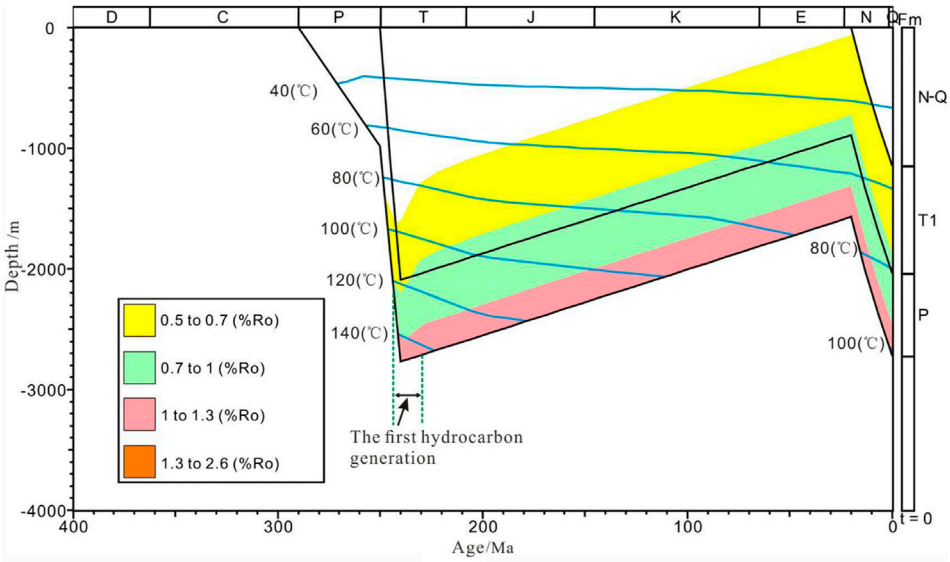

FIGURE 15
Burial history analysis of well CZ35-2-1 in the Wunansha Uplift of the SYSB. The fill colors represent different stages of maturity evolution. The P label represents Permian; Tq represents the Qinglong Formation of Triassic; and N-Q represents the Neogene–Quaternary.

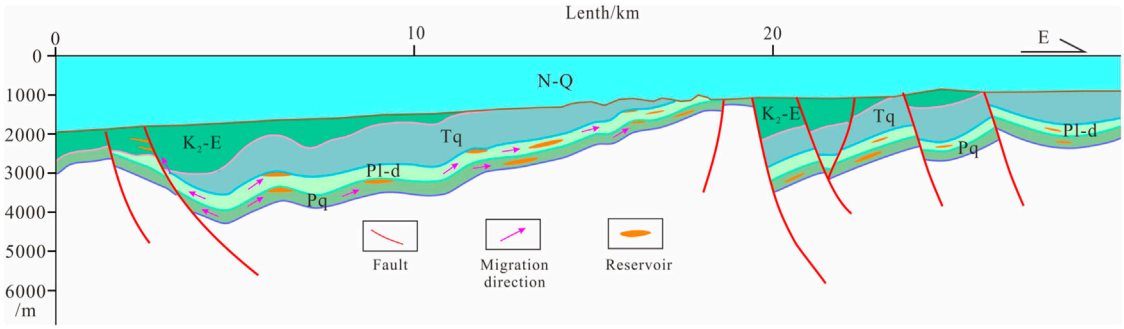

FIGURE 16
Predicted oil-gas accumulation mode of Permian in the central-southern SYSB (Line B position has been demonstrated in Figure 1). The fill colors represent different strata. The Pq label represents the Qixia Formation of Permian; Pl-d represents the Longtan-Dalong Formation of Permian; Tq represents the Qinglong Formation of Triassic; K_2-E represents the Late Cretaceous- Paleogene; and N-Q represents the Neogene–Quaternary.

For this reason, in the central Uplift and the Wunansha Uplift, we should focus on seeking tectonically stable blocks since the Early Triassic where Permian self-generation and self-accumulation oil and gas reservoirs may exist. In the eastern part of the southern Depression of the SYSB, due to the low tensile strength in the Late Cretaceous-Paleogene and thin stratigraphic sedimentation, only one hydrocarbon generation occurred in the early Triassic. Therefore, rigorous oil and gas exploration in this area should be focused on self-generation and self-accumulation Permian reservoirs. However, the high tensile strength and deposition of thick strata in the western areas of the southern Depression may have produced secondary hydrocarbons in the Late Cretaceous-Paleogene and Neogene-Quaternary. In this area, apart from searching for Permian self-generation and self-accumulation oil and gas reservoirs in stable blocks, we should also focus on finding Permian generation-Mesozoic accumulation and Permian generation-Cenozoic accumulation reservoirs formed by secondary hydrocarbon generation of Permian source rocks.

After a detailed analysis of sedimentary facies and oil and gas accumulation factors in the study area, we came to the following main conclusion:

(1) The Permian sequence in the central-southern SYSB is consistent with the LYR. The middle and lower parts of the Permian developed a relatively complete second-order sequence (i.e., sequence I), while the upper part of the Permian only developed the transgressive systems tract of another second-order sequence (i.e., sequence II).
(2) The sedimentary system in the central-southern SYSB can be compared with the LYR. The transgressive systems tract of

sequence I essentially developed restricted and open platform facies. The highstand systems tract is largely undeveloped in the study area and is predicted to develop only in the northwest of the southern Depression with shelf facies. The transgressive systems tract of sequence II essentially incorporates into the development of delta facies and swamp-lagoon facies.

(3) Thermal evolution of Permian source rocks was controlled by tectonic evolution and paleothermal gradient. Except for the possible presence of secondary hydrocarbon generation in the western part of the southern SYSB Depression, other areas experienced only one hydrocarbon generation in the Early Triassic.

(4) Different tectonic units exhibit different oil-gas accumulation modes. The central Uplift, Wunansha Uplift, and Southern Depression in the SYSB should focus on prospecting for Permian self-generation and self-accumulation reservoirs, and the western part of the Southern Depression of the SYSB should mainly look for Permian self-generation and self-accumulation reservoirs, as well as Permian generation-Mesozoic accumulation and Permian generation-Cenozoic accumulation reservoirs.

Data availability statement

The original contributions presented in the study are included in the article/Supplementary Material, further inquiries can be directed to the corresponding authors.

Author contributions

MW: substantial contributions to the conception and design of the work and writing of the original draft. LH: interpretation of the drilling data; construction of the stratigraphic framework; sedimentary evolution analysis. BL: interpretation of the seismic section; writing—review and editing; and supervision. YZ: evaluation of source rocks; establishment of the burial mode. JP: tectonic evolution analysis. All persons who have made substantial contributions to the work reported in the manuscript, including those who provided editing and writing assistance but who are not authors, are named in the Acknowledgments section of the manuscript.

Funding

This study was financially supported by the earthquake science and technology spark program of the China Earthquake Administration (XH22014A) and the National Natural Science Foundation of China (41606079).

Acknowledgments

The authors would like to thank the reviewers who gave many constructive suggestions on the manuscript. They would like to express their gratitude to EditSprings (https://www.editsprings.cn) for the expert linguistic services provided.

Conflict of interest

Authors MW, LH, BL, YZ, and JP were employed by Oil and Gas Survey and China Geological Survey.

Publisher's note

References

Cai, L., Guo, X., Xu, Z., Zhang, X., Li, W., Xiao, G., et al. (2018a). Depositional environment of upper paleozoic in the central uplift of the south Yellow Sea Basin. *ACTA SEDIMENTOL. SIN.* 36 (4), 695–705. doi:10.14027/j.issn.1000-0550.2018.124

Cai, L., Xiao, G., Guo, X., Wang, J., Wu, Z., and Li, B. (2018b). Evaluation of upper paleozoic and mesozoic source rocks in well CSDP-2 and marine oilandhas exploration prospect in the south Yellow Sea Basin. *ACTA PET. SINIA* 39 (6), 660–673. doi:10.7623/syx6201806005

Cai, L., Xiao, G., Wan, H., Zeng, Z., Zhang, X., Guo, X., et al. (2021a). Multi-stage accumulation of the meso-paleozoic marine hydrocarbon in central uplift of South Yellow sea: Exploration significance of borchole CSDP-2. *J. Jilin Univ.* 51 (2), 307–324. doi:10.13278/j.cnki.jjuese.20200256

Cai, L., Zhang, X., Guo, X., Zeng, Z., Wang, S., Pang, Y., et al. (2021b). Effective hydrocarbon-bearing geological conditions of the permian strata in the south Yellow Sea Basin, China: Evidence from borehole CSDP-2. *J. Petroleum Sci. Eng.* 196, 107815–107821. doi:10.1016/j.petrol.2020.107815

Chen, C., Xu, C., Qian, D., Yu, Q., Huang, M., Zhou, L., et al. (2020). Growth and health status of Pacific white shrimp, Litopenaeus vannamei, exposed to chronic water born cobalt. *J. East China Univ. Technol. Sci.* 43 (2), 137–145. doi:10.1016/j.fsi.2020.03.011

Dai, C., Yang, Y., and Yan, G. (2005). Modelling of burial and hydrocarbon-generation histories of Meso-Paleozoic marine residual basins in South Yellow Sea and its geologic significance. *Oil Gas Geol.* 26 (1), 49–56. doi:10.3321/j.issn:0253-9985.2005.01.008

Hu, F. (2010). Hydrocarbon resources potential study in mesozoic-palaeozoic marine strata in the south Yellow Sea Basin. *Offshore oil* 30 (3), 1–8. doi:10.396/j.issn.10008-2336.2010.03.001

Lei, B., Chen, J., Liang, J., Zhang, Y., and Li, G. (2018). Tectonic deformation and evolution of the south Yellow Sea Basin since indosinian movement. *Mar. Geol. Quat. Geol.* 38 (3), 45–54. doi:10.16562/j.cnki.0256-1492.2018.03.004

Lei, B., Zhang, Y., Wang, M., Chen, J., Liang, J., and Wang, W. (2022). Structural characteristics and hydrocarbon exploration prospect of the laoshan uplift in the south Yellow Sea Basin. *Mar. Geol. Quat. Geol.* 42 (2), 131–143. doi:10.16562/j.cnki.0256-1492.2021101201

Li, H., Qin, Q., Zhang, B., Ge, X., Hu, X., Fan, C., et al. (2020). Tectonic fracture Formation and distribution in ultradeep marine carbonate gas reservoirs: A case study of the maokou Formation in the jiulongshan gas field, sichuan basin, southwest China. *Energy & Fuels* 34, 14132–14146. doi:10.1021/acs.energyfuels.0c03327

Li, H. (2022a). Research progress on evaluation methods and factors influencing shale brittleness: A review. *Energy Rep.* 8, 4344–4358. doi:10.1016/j.egyr.2022.03.120

Li, H., Tang, H., Qin, Q., Zhou, J., Qin, Z., Fan, C., et al. (2019). Characteristics, formation periods and genetic mechanisms of tectonic fractures in the tight gas sandstones reservoir: A case study of xujiahe Formation in YB area, sichuan basin, China. *J. Petroleum Sci. Eng.* 178, 723–735. doi:10.1016/j.petrol.2019.04.007

Li, H., Zhou, J., Mou, X., Guo, H., Wang, X., An, H., et al. (2022b). Pore structure and fractal characteristics of the marine shale of the longmaxi Formation in the changning area, southern sichuan basin, China. *Front. Earth Sci.* 10, 1018274. doi:10.3389/feart.2022.1018274

Li, Z., Yang, B., Wang, J., Han, Z., and Wu, Q. (2022). Geochemical characteristics and hydrocarbon generation history of Mesozoic-Cenozoic lacustrine source rocks in the South Yellow Sea Basin,offshore eastern China. *Oil &Gas Geol.* 43 (2), 419–431. doi:10.11743/ogg20220214

Liang, J., Xu, M., Chen, J., Zhang, Y., Wang, J., Lei, B., et al. (2021). The response of the Indosinian Movement to the South Yellow Sea basin and its influence on the hydrocarbon geological conditions. *Geol. Bull. China* 40 (2/3), 252–259. doi:10.12097/j.issn.1671-2552.2021.2-3.002

Ma, L., Chen, H., Dong, Y., Xia, J., Sun, F., and Yang, L. (2007). A critical role for the loop region of the basic helix-loop-helix/leucine zipper protein Mlx in DNA binding and glucose-regulated transcription. *Oil Gas Geol.* 28 (1), 35–44. doi:10.1093/nar/gkl987

Ma, Y., Chen, H., and Wang, G. (2009). *Atlas of tectonic-lithofacies paleogeography in south China (Sinian-Neogene)*. Beijing, China: Science Press.

Marghani, M., Zairi, M., and Radwan, A. (2022). Facies analysis, diagenesis, and petrophysical controls on the reservoir quality of the low porosity fluvial sandstone of the Nubian formation, east Sirt Basin, Libya: Insights into the role of fractures in fluid migration, fluid flow, and enhancing the permeability of low porous reservoirs. *Mar. Petroleum Geol.* 147, 105986. doi:10.1016/j.marpetgeo.2022.105986

Mi, L., Wu, K., Liu, Z., Zhu, X., Geng, M., Zhang, Y., et al. (2022). Favorable exploration field analysis of Mesozoic-Paleozoic in South Yellow Sea basin from the distribution characteristics of marine source rocks in the Yangtze region. *China Offshore Oil Gas* 34 (2), 1–13. doi:10.11935/j.issn.1673-1506.2022.02.001

Qiu, E., Yang, F., Zhang, R., and Zhou, X. (2018). Seismic and sedimentary facies analysis and prediction of favorable Permian source rocks in the South Yellow Sea basin. *Mar. Geol. Quat. Geol.* 38 (3), 96–106. doi:10.16562/j.cnki.0256-1492.2018.03.009

Radwan, A. (2021a). Modeling the depositional environment of the sandstone reservoir in the middle miocene sidri member, badri field, gulf of suez basin, Egypt: Integration of gamma-ray log patterns and petrographic characteristics of lithology. *Nat. Resour. Res.* 30, 431–449. doi:10.1007/s11053-020-09757-6

Wang, L., Ye, J., and Wu, C. (2005). Petroleum geological characteristic of pre-Tertiary in south Yellow Sea Basin. *Nat. Gas. Ind.* 25 (7), 1–3.

Wang, M., Chen, X., Lei, B., and Zhu, X. (2018). Current status and problems of oil and gas exploration in South Yellow Sea basin. *Mar. Geol. Front.* 34 (11), 20–25. doi:10.16028/j.1009-2722.2018.11003

Wang, M., Jiang, X., Lei, B., Huang, L., and Pan, J. (2023). Tectonic evolution and its control on oil–gas accumulation in southern East China Sea since the Jurassic. *Front. Earth Sci.* 10, 1015832. doi:10.3389/feart.2022.1015832

Wang, M., Pan, J., Gao, H., Huang, L., and Li, X. (2022). Mesozoic basin evolution and hydrocarbon potential in north South China Sea and south East China Sea. *Earth Sci. Front.* 29 (2), 1–9. doi:10.13745/j.esf.sf.2021.7.8

Wang, M., Zhang, X., Meng, X., Chen, X., Zhu, X., and Lin, M. (2016). Hemagglutinin-esterase-fusion (HEF) protein of influenza C virus. *Mar. Geol. Front.* 32 (7), 28–45. doi:10.1007/s13238-015-0193-x

Wang, M., Zhang, X., Wu, Z., Xiao, G., Wang, J., and Wang, A. (2014). Tectonic evolution of southern depression in the South Yellow Sea basin and its hydrocarbon accumulation in Permian. *J. China Univ. Min. Technol.* 43 (2), 271–278. doi:10.13247/j.cnki.jcumt.2014.02.006

Wang, M., Zhang, Y., Pan, J., Huang, L., Chen, X., Luo, D., et al. (2020). Geological structure of the large section in eastern China's sea areas and its constraint on comprehensive stratigraphic division. *Geol. China* 47 (5), 1474–1485. doi:10.12029/gc20200513

Yang, Q., and Chen, H. (2003). Tectonic evolution of the North jiangsu-South Yellow Sea Basin. *Petroleum Geol. Exp.* 25 (Supplement), 562–565. doi:10.3969/j.issn.1001-6112.2003.z1.008

Yang, S., Hu, S., Cai, D., Feng, X., Gao, L., and Lu, J. (2003). Geothermal field and thermal-tectonic evolution of the southern part in the South Yellow Sea Basin. *Chin. Sci. Bull.* 48 (14), 1564–1569. doi:10.3321/j.issn:0023-074X.2003.14.017

Ye, Z., Liang, X., Ma, L., Zhang, T., and Xu, K. (2006). An approach to exploration direction of oil-gas in the marine residual basins of independent Lower Yangtze Block. *Chin. J. Geol.* 41 (3), 523–548. doi:10.3321/j.issn:0563-5020.2006.03.014

Zhang, M., Gao, S., and Tan, S. (2018). Geological characteristics of the meso-paleozoic in South Yellow Sea Basin and future exploration. *Mar. Geol. Quat. Geol.* 38 (3), 24–34. doi:10.16562/j.cnki.0256-1492.2018.03.002

Zhang, T., Zhu, W., Hu, S., Chen, C., Gao, S., Chen, Z., et al. (2021). Structural characteristic and its genetic mechanism of central uplift in South Yellow Sea Basin. *Earth Sci.* 46 (10), 3481–3495. doi:10.3799/dqkx.2020.380

Zhu, G., Liu, G., Li, S., and Niu, M. (2002). Four-story"structure of the basins in the Lower Yangtze region and their geodynamic setting. *J. Hefei Univ. Technol.* 23 (1), 47–52. doi:10.3969/j.issn.1008-2336.2010.03.001

frontiers | Frontiers in Earth Science

TYPE Original Research
PUBLISHED 11 May 2023
DOI 10.3389/feart.2023.1183734

OPEN ACCESS

EDITED BY
Shuai Yin,
Xi'an Shiyou University, China

REVIEWED BY
Dongxu Zhang,
Chengdu University of Technology, China
Zhu Baiyu,
Yangtze University, China

*CORRESPONDENCE
Zhanlei Wang,
28142547@qq.com

RECEIVED 10 March 2023
ACCEPTED 20 April 2023
PUBLISHED 11 May 2023

CITATION
Feng L, Jiang Y, Guo G, Yang C, Zhu X, Zeng Q, Cai G and Wang Z (2023), Pore structure and fractal characteristics of tight sandstone in meandering stream facies: a case study of the J_2s^2 member in the central Sichuan Basin, China. *Front. Earth Sci.* 11:1183734. doi: 10.3389/feart.2023.1183734

Pore structure and fractal characteristics of tight sandstone in meandering stream facies: a case study of the J_2s^2 member in the central Sichuan Basin, China

Linjie Feng[1,2], Yuqiang Jiang[1,2], Guian Guo[3], Changcheng Yang[3], Xun Zhu[3], Qinggao Zeng[4], Guangyin Cai[1,2] and Zhanlei Wang[1,2]*

[1]School of Geoscience and Technology, Southwest Petroleum University, Chengdu, China, [2]Unconventional Reservoir Evaluation Laboratory, PetroChina Key Laboratory of Unconventional Oil and Gas, Chengdu, China, [3]PetroChina Southwest Oil and Gas Field Company, Chengdu, China, [4]Tight Oil and Gas Exploration and Development Project Department of PetroChina Southwest Oil and Gas Field Company, Chengdu, China

Based on porosity and permeability tests, high-pressure mercury injection (HPMI), nuclear magnetic resonance (NMR) and centrifugal experiments, this study comprehensively analyzed the quality, pore structure and fractal characteristics of tight sandstone reservoir in meandering stream facies. The purpose is to reveal the relationship between physical properties, geometry and topological parameters of pores, fluid mobility and heterogeneity of pore system of tight sandstone reservoirs in meandering stream facies. The results show that the second member of the Middle Jurassic Shaximiao Formation (J_2S^2) in the central Sichuan Basin has developed tight sandstone reservoir of meandering fluvial facies, the pore radius of type I reservoir (K>0.3 mD) is mainly distributed at 0.01 μm~2 μm, the tortuosity ranges between 2.571 and 2.869, and the average movable fluid saturation is 70.12%. The pore radius of type II reservoir (0.08mD<K<0.3 mD) is mainly 0.003 μm~1 μm, the tortuosity ranges between 2.401 and 3.224, the average movable fluid saturation is 57.59%. The pore radius of type III reservoir (K<0.08 mD) is mainly 0.001 μm~0.4 μm, the tortuosity ranges between 0.905 and 2.195, and the average movable fluid saturation is 13.46%. Capillary-Paraachor point (CP point) and T2 cut-off value ($T_{2cutoff}$) are used to divide the fractal interval of capillary pressure curve and T_2 spectrum. The fractal dimension D_{h2} of small pores calculated by HPMI through 3D capillary tube model, the fractal dimension D_{n1} of large pores and D_{n2} of small pores calculated by NMR through wetting phase model can effectively characterize the heterogeneity of reservoir pores. Among them, D_{n1} has a strong negative correlation with porosity, permeability, pore radius and movable fluid saturation, indicating that the reservoir capacity, seepage capacity and pore size are mainly controlled by large pores, therefore, D_{n1} can be used as an effective reservoir evaluation parameter.

KEYWORDS

fractal dimension, tight sandstone, pore structure, meandering stream facies, shaximiao formation, sichuan basin

Introduction

In the past few decades, conventional oil and gas resources have continued to decrease. In view of the growing global demand for fossil energy, unconventional oil and gas resources such as tight gas have received widespread attention (Nelson, 2009; Zou et al., 2012a; Qu et al., 2020; Awan et al., 2021). China is rich in tight gas resources with reserves of about $21.85\times10^{12}m^3$ (Sun et al., 2019). Unlike conventional oil and gas bearing sandstone, the tight sandstone are characterized by low porosity and low permeability, and usually have complex micro-nano-scale pore systems and strong heterogeneity (Xiao et al., 2017; Li et al., 2018b; Zang et al., 2022a). Therefore, there are great challenges in the exploration and development of tight sandstone oil and gas reservoirs. Decades of production practice results show that pore structure is critical to the storage and seepage capacity of tight sandstone reservoir, and controls the distribution of oil and gas reservoir productivity and production effect (Wang et al., 2018b; Huang et al., 2018; Qu et al., 2020). Therefore, the study of pore structure and heterogeneity of tight sandstone is helpful to reveal the migration and enrichment mechanism of tight oil and gas and is of great significance to realize efficient development (Li et al., 2017; Nie et al., 2021).

In recent years, the pore structure characterization technology of tight sandstone has been developed rapidly, and many technical means have been used to study the two-dimensional and three-dimensional pore characteristics of tight reservoirs, mainly including image analysis technology, fluid injection technology and radiation detection technology (Li et al., 2019; Wu et al., 2022a). Through image analysis technology, the geometric characteristics such as pore throat shape and size, as well as the topological characteristics such as connectivity and coordination number of tight sandstone can be directly observed, and the main technologies include X-ray computed tomography (CT), scanning electron microscope (SEM), cast thin sections (CTS), etc (Zou et al., 2012b). Fluid injection technology is mainly used to characterize pore size and pore size distribution (PSD), and the main technical means include low-pressure nitrogen gas adsorption (N_2GA), high-pressure mercury intrusion (HPMI) and constant-rate mercury injection (CRMI) (Nooruddin et al., 2014; Li et al., 2019; Wu et al., 2022b). At present, the relatively widely used radiation detection technology in the quantitative study of unconventional reservoir pore structure is mainly small-angle scattering (SAS) and nuclear magnetic resonance (NMR), which also mainly characterizes geometric parameters such as pore size and distribution (Clarkson et al., 2012; Wu et al., 2022a). However, the pore size that can be characterized by any test technology is limited, and the full-size pore distribution cannot be characterized by a single method. Therefore, it is necessary to combine various means to describe the pore structure characteristics of the reservoir more comprehensively (Wang and Wang, 2022). The combination of HPMI and NMR is the most commonly used characterization method of full-size pore distribution in previous studies. Some scholars have proposed different methods to convert T_2 spectrum into PSD based on HPMI(Dai et al., 2019; Huang et al., 2020). In addition, the geometric parameters and topological parameters of pore throat can be obtained through the above techniques, but neither can directly and quantitatively characterize the heterogeneity of pores (Cui et al., 2022).

Fractal theory was proposed by Mandelbrot and Wheeler (1983) and was initially used to overcome the defects of Euclidean geometry in describing self-similar geometric structures. Pfeiferper and Avnir (1983) first introduced it into the study of porous media. Previous studies have demonstrated that the pore volume and PSD in sedimentary rocks have self-similarity, and its complexity can be evaluated by fractal dimension D) (Mandelbrot et al., 1984; Pfeifer, 1984). Fractal dimension is considered to be the bridge between micro heterogeneity and macro physical properties of reservoir (Li, 2010; Zhang and Weller, 2014; Li et al., 2017), which can be calculated based on NMR, HPMI, N_2GA and other experimental data (Amadu and Pegg, 2018; Schmitt Rahner et al., 2018; Cui et al., 2022). Generally, the fractal dimension of sandstone pore space is between 2.0 and 3.0 (Li and Horne, 2006). The larger the fractal dimension is, the stronger the pore heterogeneity is. It has obvious correlation with physical properties, pore size, PSD and connectivity (Amadu and Pegg, 2018; Zang et al., 2022a).

At present, the research on pore fractal characteristics of tight sandstone mainly focuses on the delta sedimentary environment, especially the underwater distributary channel sand in the delta front of the Triassic Yanchang Formation in the Ordos Basin, China. Many scholars have adopted a variety of fractal dimension calculation models, including geometry model, thermodynamics model, 3D capillary tube model, wetting phase model, etc., (Wang et al., 2018a; Wang et al., 2019; Wang et al., 2021b), to calculated the fractal dimension of pore-throat in different intervals based on the data obtained from HPMI, NMR, CRMI and other experiments, the applicability of different models is discussed, and the relationship between fractal dimension and mineral composition, reservoir physical properties, pore-throat structural parameters (Song et al., 2018; Guo et al., 2020; Qu et al., 2020; Zang et al., 2022a) and oil and gas properties (Cui et al., 2022) is deeply studied, and a reservoir evaluation scheme considering fractal characteristics is proposed. At present, a large number of academic achievements have been published. In addition, there are also some reports on fractal characteristics of pore throat of tight sandstone formed by lacustrine gravity flow (Guo et al., 2020; Wu et al., 2022a), however, the fractal characteristics of tight sandstone in meandering stream facies are still less studied.

Sandstone gas reservoirs of meandering stream facies developed in the second member of Middle Jurassic Shaximiao Formation (J_2S^2 member) are important tight gas exploration targets in Sichuan Basin, and the main gas producing blocks are located in the central area of Sichuan Basin. Since 2020, 724.16×10^8 m^3 of proved reserves have been discovered, which is at the initial stage of development, and the understanding of pore structure of reservoir has not been deepened. Therefore, this study takes J_2S^2 tight sandstone as the research object and takes its pore structure and fractal characteristics as the research content. The main research objectives include: 1) Combining HPMI and NMR to quantitatively characterize the pore structure of J_2S^2 tight sandstone in the study area; 2) Propose a reasonable pore type and fractal interval division scheme based on pore connectivity and fluid mobility; 3) Obtain fractal dimensions of different types of pores based on different experiments, and clarify the relationship between fractal dimensions and reservoir physical

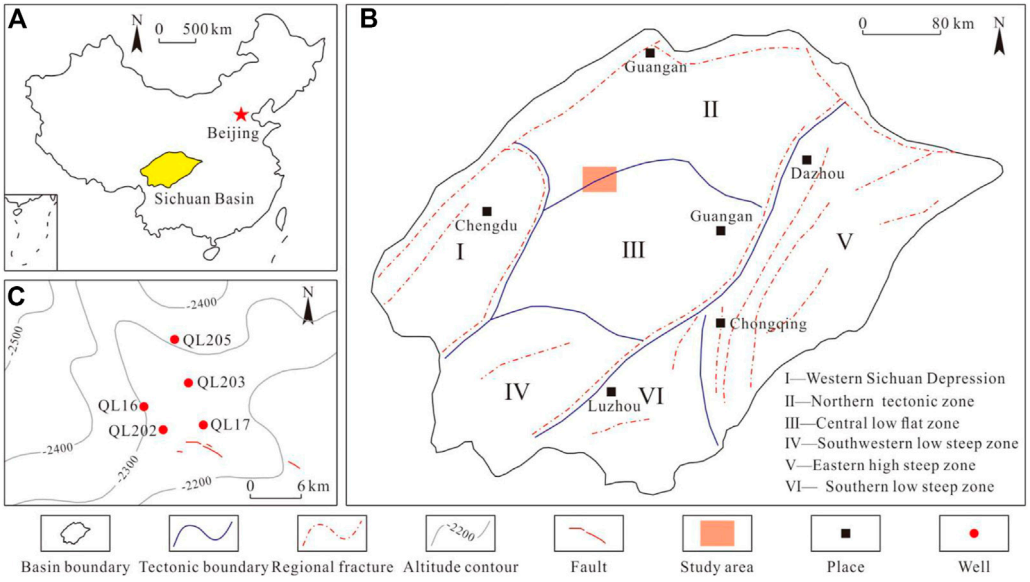

FIGURE 1
Location of the study area: **(A)**. Location of Sichuan Basin in China; **(B)**. Regional overview of the Sichuan Basin and the location of the study area; **(C)**. Location of sampling well and bottom structure of J_2s^2 member.

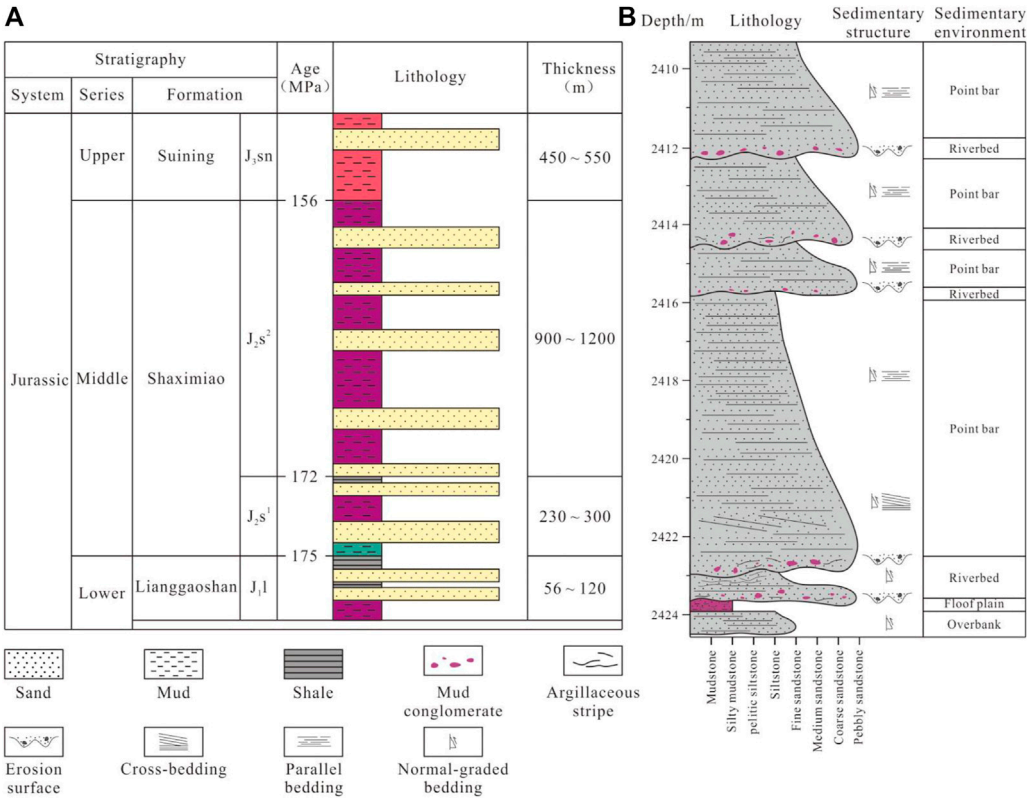

FIGURE 2
Stratigraphy and sedimentary characteristics of J_2S^2 member in the study area: **(A)**. Stratigraphic division and lithological characteristics; **(B)**. Sedimentary structure and environment based on Well QL16.

properties, geometric and topological parameters of pores, and fluid mobility.

Geological background

Sichuan Basin is located in southwest China (Figure 1A), with an area of about $19\times10^5 km^2$, is one of the most important petroliferous basins in China. The interior of the basin can be divided into 6 tectonic belts, including the Western Sichuan Depression, the northern tectonic belt, the central low flat zone, the southwestern low steep zone, the southern low steep zone, the eastern high-steep fold belt(Figure 1B) (Wang et al., 2021a). The location of the study area is shown in Figure 1B, which is located at the intersection of the southwest of the northern tectonic belt and the northwest of the central low flat zone. Since the Indosinian period, the tectonic movement in central Sichuan has been dominated by overall rise and fall. The current structural form of the target layer is generally a large gentle slope, with local nose bulge, In J_2s^2 member of the study area, a row of nose bulges is developed along the line from Well QL17 to Well QL205, and several faults are developed near the QL17 well block at the axis of the nose bulge (Figure 1C).

In the Late Triassic, under the influence of Indosinian tectonic movement, the collision between the North China Block and the South China Block caused the overall uplift of the Sichuan Basin (Li et al., 2020), ending the marine sedimentary stage of about 300 Ma from the Sinian to the Late Triassic, and opening the continental sedimentary stage of 65 Ma from the Late Triassic to the Late Cretaceous. During the sedimentary period of the Middle Jurassic Shaximiao Formation, meandering river deposits developed in the study area, forming a red stratum with a thickness of about 1500 m, mainly composed of purplish red mudstone, mixed with gray-green mudstone and gray sandstone (Figure 2A). A set of black shale with a thickness of about 2 m and rich in fossils is developed in the Shaximiao Formation in this area, representing a rapid lake transgression-lake regression. Taking the top of this set of shale as the boundary, the Shaximiao Formation can be divided into Sha1 member (J_2s^1) and Sha2 member (J_2s^2) from bottom to top. The thick sand body of J_2S^2 member is generally 15 m~20 m, with typical sedimentary characteristics of point bar in meandering stream. It is formed by the superposition of multiple sets of single sand bodies with positive grain sequence, and mainly develops parallel bedding. Scour surface is generally developed between single sand bodies, the purplish red and gray-green mudstone gravels can be seen at the bottom (Figure 2B).

Samples and experiments

Samples

A total of 12 tight sandstone samples from 5 wells in the study area are used in this paper and the location of the sample source wells are shown in Figure 1C. All samples are drilled on the core of J_2S^2 member, with burial depth of 2100 m~2400 m, and their initial shape are cylinder with a diameter of about 2.5 cm. Among them, Sample QL202-63 belongs to the riverbed sand body, Sample QL16-15 and QL203-13 belong to the overbank sand body, and the other samples are all point bar sand bodies.

Experiments

Based on the above samples, four tests including permeability and porosity measurement, NMR and HPMI were carried out successively, of which the permeability and porosity tests were carried out according to the National Standard of the PRC GB/T 29172-2012, the NMR was accroding to oil and gas industry standard of the RPC SY/T 6490-2014, and the HPMI was accroding to National Standard of the PRC GB/T 29171-2012. Before the test, the residual oil in all samples was cleaned with dichloromethane and distilled water, and then the samples were dried (110°C, 24 h). Also, the diameter, length and mass of the samples were accurately measured. In addition, all samples shall be dried once (110°C, 24 h) after each test.

Permeability test

The permeability of the sample was measured with the GRT-1 gas permeability tester, and helium was used as the carrier gas during the experiment. The final test results were not corrected for the Klinkenberg effect.

Porosity test

The porosity of the sample was determined by alcohol saturation method. Because the lithology of the sample is dense, it is necessary to vacuumize these samples for 18 h with vacuumizing instrument, then the alcohol was degassed and injected into a vacuum container containing above samples, which is maintained for 24 h under the pressure of 20 MPa to ensure that the samples were completely saturated. Then take out the samples, immerse them in alcohol, weigh them in turn with a hanging scale, and measure the density of alcohol. After weighing, take the samples out of the alcohol, carefully remove the excess liquid on the surface of samples, and weigh them in the air. The porosity of the sample can be calculated according to the following formula:

$$\varphi = \frac{m_1 - m_2}{m_1 - m_0} \times 100\% \quad (1)$$

Where: φ is the porosity, %; m_1 is the weight of the rock sample saturated with alcohol measured in the air, g; m_2 is the weight of the rock sample immersed in alcohol measured by the hanging scale, g; m_0 is the weight of dry rock sample, g.

NMR

Before the NMR experiment, the dry rock samples were vacuumized and saturated in the same way, the difference is that the saturated liquid used in the NMR experiment is deionized water. After the rock samples were completely saturated, take them out of the deionized water, carefully remove the excess water on the surface, and then weigh them in the air. Then the rock samples were wrapped in plastic paper and T_2 spectrums were determined by NMRC12-010V low field nuclear magnetic resonance instrument produced by Niumac.

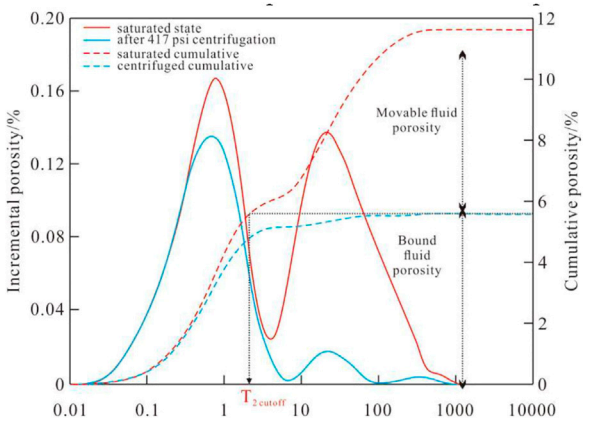

FIGURE 3
Illustration of the method to calculate the T_2 cutoff value, based on sample QL16-11.

The main parameters in the measurement process are set as follows: the test temperature is 32°C, the resonance frequency is 12 MHz, the number of echoes is 9000, the waiting time is 6000 ms, and the echo interval is 0.1 ms.

After the T_2 spectrum of the saturated samples are determined, they were placed in the centrifuge for centrifugation to determine the saturation of the movable fluid and the cut-off value of the relaxation time $T_{2(T2cutoff)}$. In the process of centrifugation, low centrifugal force or short centrifugal duration will cause some movable fluid to be unusable, while high centrifugal force will cause some bound fluid to come out, so it is necessary to select appropriate centrifugal force and centrifugal duration. In previous studies, the centrifugal force selected for tight sandstone is mostly 200~450psi, and the centrifugal duration is mostly 1~3 h (Liu et al., 2019; Wu et al., 2022b; Zang et al., 2022b; Dong et al., 2023). The centrifugal force selected for the tight sandstone of Yanchang Formation in Ordos Basin, which is close to the physical properties of the samples in this study, is usually 400~420 psi, and the centrifugal time is mostly 1~1.5 h. Therefore, in this experiment, the centrifugal force is 417psi and the centrifugal duration is 1.5 h.

After centrifugation, weigh the rock samples in the air and measure the T_2 spectrums. The movable fluid saturation can be obtained from the change of rock sample weight before and after centrifugation:

$$S_{wm} = \frac{m_3 - m_4}{m_3 - m_0} \times 100\% \quad (2)$$

Where: S_{wm} is the saturation of movable fluid,%; m_3 is the weight of saturated rock sample measured in the air, g; m_4 is the weight of rock sample after centrifugation, g. Put the cumulative porosity curve or cumulative signal curve of T_2 spectrum before and after centrifugation in the same coordinate system, extend the platform section of the cumulative curve of T_2 spectrum after centrifugation (Ge et al., 2015), and the corresponding relaxation time T_2 at the intersection of the cumulative curve of T_2 spectrum of saturated sample is the T_{cutoff} (Figure 3).

HPMI

AutoPore IV 9500mercury porosimeter is used in HPMI experiment, and the maximum mercury injection pressure is 200 MPa. The capillary pressure curve of samples obtained in the experiment can be converted into pore size by Washburn equation (Washburn, 1921), which is as follows:

$$P_c = \frac{2\sigma \cos\theta}{r} \quad (3)$$

Where: P_c is the capillary pressure, MPa; σ is the interfacial tension between mercury and air, which is 0.48N/m in this experiment; θ is the wetting angle of mercury and rock, which is 140° in this experiment; r is the pore radius, μm.

Methology description

Fitting method of NMR and mercury injection

According to NMR theory, the total relaxation time is the superposition of volume relaxation ($\frac{1}{T_{2B}}$), surface relaxation ($\rho\frac{S}{V}$) and diffusion relaxation ($\frac{D(\gamma G T_E)^2}{12}$), which can be expressed as:

$$\frac{1}{T_2} = \frac{1}{T_{2B}} + \rho\frac{S}{V} + \frac{D(\gamma G T_E)^2}{12} \quad (4)$$

Where: T_2 is the relaxation time, ms; T_{2B} is the volume relaxation time, ms; ρ is the surface relaxation strength, μm/ms; S is the pore surface area, μm^2; V is the pore volume, μm^3; D is the diffusion coefficient, μm^2/ms; γ is the rotational magnetic ratio, $(Tms)^{-1}$; G is the average magnetic field gradient, 10^{-4}T/cm; T_E is the echo time, ms.

For pores saturated by single-phase fluid in uniform magnetic field, the echo time is short enough, and the volume relaxation and diffusion relaxation are negligible, so Eq. 4 can be simplified as:

$$\frac{1}{T_2} = \rho\frac{S}{V} \quad (5)$$

For simplified spherical and cylindrical pores, the relationship between specific surface area and pore radius can be expressed as:

$$\frac{S}{V} = \frac{F_s}{r} \quad (6)$$

Where: F_s is the pore shape factor, $F_s = 2$ for cylindrical pores, $F_s = 3$ for spherical pores, dimensionless.

Combining Eq.5–6, the following formula can be obtained:

$$T_2 = \frac{r}{\rho F_s} \quad (7)$$

The relationship between pore radius and relaxation time T2 in the above formula is linear. However, previous research results show that there is a power function between relaxation time T_2 and pore radius and could be expressed as below:

$$T_2 = \frac{r^n}{\rho F_s} \quad (8)$$

Where: n is the power index, dimensionless. Transform Eq. 8 as follows:

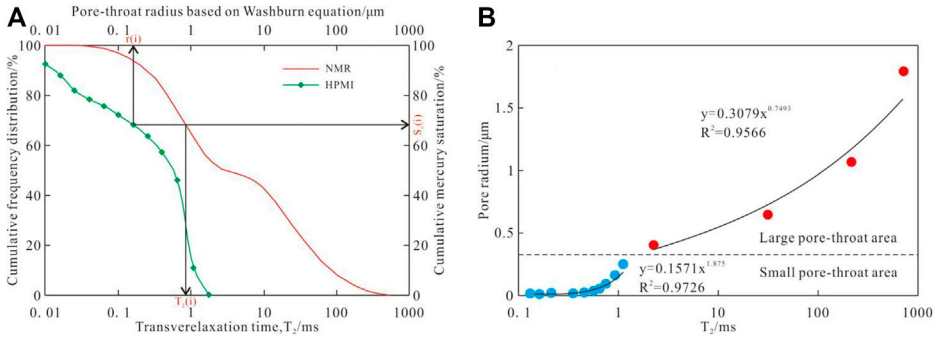

FIGURE 4
Conversion from NMR T_2 of Sample QL16-11 to pore–throat radius. **(A)** The corresponding relationship between T_2 and pore radius at a certain cumulative saturation. **(B)** The conversion relationship between the relaxation time and pore radius of different types of pores.

$$r = (T_2 \rho F_s)^{\frac{1}{n}} = T_2^{\frac{1}{n}} \cdot (\rho F_s)^{\frac{1}{n}} \tag{9}$$

It can be obtained by defining $C = (\rho F_s)^{\frac{1}{n}}$:

$$r = C T_2^{\frac{1}{n}} \tag{10}$$

According to Eq. 10, the relaxation time T_2 can be converted into pore radius r by determining the values of C and n. According to HPMI theory, mercury is a non-wetting phase for rocks. Driven by external pressure, mercury preferentially enters macropores and gradually enters smaller pores with the increase of pressure. Therefore, the increase of mercury saturation in capillary pressure curve is the accumulation from large pores to small pores. According to Eq. 8, the relaxation time T_2 is positively correlated with the pore radius, so the value obtained by accumulating the NMR signal frequency in the order of relaxation time T_2 from small to large still represents the accumulation from large pores to small pores. The cumulative curves obtained by the two methods have corresponding relaxation time $T_2(i)$ and pore radius $r(i)$ at the same node $S_c(i)$ (Figure 4A). The conversion relationship between relaxation time T_2 and pore radius can be obtained by power function regression. According to this relationship, T_2 spectrum can be converted into full-size pore distribution. It should be noted that in the power function regression analysis of the relaxation time and the corresponding pore radius, there is often an obvious turning point between the macropore and the micropore, dividing the scatter point into two parts with completely different trends (Figure 4B). Therefore, it is necessary to carry out regression analysis on large pores and small pores respectively to obtain more accurate pore size distribution curve.

Fractal theory

The pore space of tight sandstone has been proved to have self-similarity, according to fractal theory, this self-similarity can be described as the relationship between the number of pores and the radius of pores:

$$N(>r) = \int_{r}^{r_{max}} f(r) \propto r^{-D_f} \tag{11}$$

Where: $N(>r)$ is the number of pores with radius larger than r; r_{max} is the maximum pore radius, μm; $f(r)$ is the density function of pore radius, %; D_f is the fractal dimension. Take the logarithm of both sides of Eq. 11:

$$\lg N(>r) = -D_f \cdot lg\ r \tag{12}$$

According to Eq. 11, through the regression analysis of pore number and pore radius in double logarithmic coordinates, the fractal dimension can be described as:

$$D_f = -K \tag{13}$$

Where: K is the slope of $\lg N(>r)$ -lg r curve.

Fractal dimension based on HPMI

Many models for calculating pore fractal dimension based on capillary pressure curve have been proposed, including geometry model, thermodynamic model, 2D capillary tube model, 3D sphere model, 3D capillary tube model and wetting phase model, etc., (Wang et al., 2018a; Wang et al., 2018b; Wang et al., 2021b). In previous studies, the 3D capillary tube model and wetting phase model are the most commonly used. The 3D capillary model can be described by the relationship between the number of equivalent pores and the mercury saturated radius, or by the relationship between the mercury saturation and the mercury injection pressure. The comprehensive fractal dimensions obtained by these two expressions are consistent, but due to the differences in the data sets used, the results calculated based on mercury saturation and mercury injection pressure often have obvious multiple fractal intervals corresponding to different types of pores, while the results calculated based on the number of equivalent pores and mercury saturated radius generally do not have multi-segment fractal characteristics. In essence, the wetting phase model is to replace the wetting phase saturation with the non-mercury injection saturation, and calculates the fractal dimension through the relationship between the wetting phase saturation and capillary pressure. Many scholars have calculated the pore fractal dimension of tight sandstone based on the wetting phase model, and analyzed the relationship between fractal dimension and physical properties, pore structure parameters (Qu et al., 2020; Wu et al., 2022a; Wu et al., 2022b; Cui et al., 2022). At the same

time, some scholars have also proposed that the model is only applicable to the process of wetting phase fluid injection into porous media, and it is not appropriate to replace the wetting phase saturation with non-mercury injection saturation. The wetting phase model essentially calculates the fractal dimension of the remaining pore throat without mercury injection, and is not applicable to characterizing the pore throat fractal characteristics (Washburn, 1921; Zhang et al., 2017; Liu et al., 2018; Song et al., 2018).

Based on the analysis of the advantages and disadvantages of the 3D capillary model and the wetting phase model, this paper selects the 3D capillary model described by the mercury injection saturation and pressure to calculate the fractal dimension to determine the heterogeneity of the pore structure. The basic assumption of the 3D capillary tube model is that the pores in the rock are composed of capillaries with different radius r and length l, and the pore volume V can be expressed as:

$$V = \pi r^2 l \tag{14}$$

Since mercury preferentially enters large pores in rocks, the pore volume with radius greater than r is replaced by the cumulative mercury volume, and the number of pore throats with radius greater than r can be expressed as:

$$\mathrm{N}(>r) = \frac{V_{Hg}(r)}{\pi r^2 l} \tag{15}$$

The number of pores N(>r) obtained at this time is not true, but is actually the equivalent number of pores required for filling the accumulated mercury volume $V_{Hg}(r)$ with a capillary with radius equal to r. This model is the theoretical basis of 3D capillary tube model. Li (2010) combined the definition of self-similarity and washburn equation to transform the model, first, combining Eq.10–14:

$$\frac{V_{Hg}(r)}{\pi r^2 l} \propto r^{-D_h} \tag{16}$$

Where: D_h is the fractal dimension obtained based on HPMI. According to the algorithm, Eq. 16 can be simplified as:

$$V_{Hg}(r) \propto r^{-D_h} \tag{17}$$

Substitute the pore radius expressed by Washburn equation into Eq. 17:

$$V_{Hg}(r) \propto P_c^{-(2-D_h)} \tag{18}$$

The cumulative volume of mercury can be expressed by the following formula:

$$V_{Hg}(r) = S_{Hg} \cdot V_p \tag{19}$$

Where S_{Hg} is the mercury saturation,%; V_p is the sample pore volume. Combining Eq.18–19:

$$S_{Hg} \propto a P_c^{-(2-D_h)} \tag{20}$$

Take the logarithm of both sides of Eq. 20:

$$lg\ S_{Hg} \propto (D_h - 2) lg\ P_c + b \tag{21}$$

Where b is the newly obtained constant. Linear regression is performed on lg S_{Hg} and lg p in double logarithmic coordinates. Assuming the slope of the straight line is K_h, the fractal dimension is $D_h = 2 + K_h$.

Fractal dimension based on NMR

Deionized water is used as detection fluid in NMR experiment, which is usually a wetting phase fluid for rocks and enters into small pores preferentially, so the pore fractal dimension can be calculated using the wetting phase model. The pore in the wetting phase model is assumed to be spherical (Huang et al., 2017), and the accumulated pore volume of the wetting phase fluid can be expressed as:

$$V(<r) = \int_{r_{min}}^{r} f(r) \frac{4}{3} \pi r^3 dr \tag{22}$$

Where, V(<r) is the pore volume with radius less than r; r_{min} is the minimum pore radius. According to Eq. 11, f(r) can be expressed as:

$$f(r) = \frac{dN(>r)}{dr} \propto -D_n r^{-D_n - 1} \tag{23}$$

Where: D_n is the fractal dimension obtained based on NMR, dimensionless. Substitute Eq. 22 into Eq. 21:

$$V(<r) = \frac{4D_n}{3(3-D_n)} r^{3-D_f} \Big|_{r_{min}}^{r} = \frac{4D_n}{3(3-D_n)} \left(r^{3-D_n} - r_{min}^{3-D_n}\right) \tag{24}$$

Similarly, the total pore volume can be expressed as:

$$V = \frac{4D_n}{3(3-D_n)} \left(r_{max}^{3-D_n} - r_{min}^{3-D_n}\right) \tag{25}$$

Where r_{max} is the maximum pore radius. Based on Eq.22–25, wetting phase saturation can be expressed as:

$$S_w = \frac{V(<r)}{V} = \frac{r^{3-D_n} - r_{min}^{3-D_n}}{r_{max}^{3-D_n} - r_{min}^{3-D_n}} \tag{26}$$

Where S_w is the saturation of wetting phase,%. Since $r_{min} \ll r_{max}$, Eq. 26 can be simplified as follows:

$$S_w = \left(\frac{r}{r_{max}}\right)^{3-D_n} \tag{27}$$

By substituting Eq. 6 into Eq. 26, the following formula can be obtained:

$$S_w = \left(\frac{T_2}{T_{2max}}\right)^{3-D_n} \tag{28}$$

Where, T_{2max} is the maximum relaxation time, ms. Take the logarithm of both sides of Eq. 28:

$$lg\ S_w = (3 - D_n) lg\ T_2 - (3 - D_n) lg\ T_{2max} \tag{29}$$

Linear fitting of lg T_2 and lg S_w in double-logarithm coordination, assuming that the slope of the straight line is K_n, then $D_n = 3 - K_n$.

TABLE 1 Characteristic of physical property and pore structure parameters measured by HPMI and NMR.

Reservoir type	Sample ID	Depth m)	Porosity (%)	Permeability (mD)	S_{wm} (%)	HPMI							NMR					
						P_d (MPa)	r_d (μm)	P_{50} (MPa)	r_{50} (μm)	S_{Hg} (%)	Sorting coefficient	Skew coefficient	T_2 spectrum morphology	r_{max} (μm)	r_{median} (μm)	r_{mean} (μm)	τ	$T_{2cutoff}$ (ms)
I	QL16-13	2421.66	12.940	0.778	68.92	0.415	1.773	1.364	0.539	95.669	2.258	1.602	Bimodal	1.911	0.562	0.564	2.571	0.850
	QL17-1	2166.20	14.120	0.423	71.32	0.409	1.798	1.778	0.414	92.842	2.252	1.700	Bimodal	2.536	0.396	0.444	2.869	1.290
II	QL17-9	2177.40	12.740	0.235	67.43	0.685	1.072	2.162	0.340	94.999	2.175	1.632	Bimodal	1.698	0.337	0.367	3.020	0.740
	QL202-125	2276.90	11.710	0.167	65.61	0.680	1.081	2.872	0.256	93.015	2.084	1.783	Bimodal	1.673	0.242	0.302	2.832	1.047
	QL16-11	2415.93	11.700	0.104	54.19	1.118	0.657	3.525	0.209	92.409	2.091	1.810	Multi-modal	1.061	0.179	0.222	2.633	0.912
	QL203-5	2246.80	11.630	0.111	56.48	0.682	1.078	2.724	0.270	92.759	2.093	1.894	Bimodal	1.260	0.217	0.282	3.224	0.977
	QL205-1-41	2365.28	9.960	0.212	62.11	0.681	1.080	2.518	0.292	83.572	2.600	2.081	Multi-modal	1.081	0.283	0.315	2.416	1.203
	QL205-1-56	2368.36	8.530	0.129	39.7	0.681	1.079	2.901	0.253	89.345	2.158	1.927	Bimodal	0.923	0.237	0.264	2.401	2.583
III	QL202-69	2267.15	8.960	0.045	17.95	1.122	0.655	7.542	0.098	87.944	2.246	1.811	Unimodal	0.836	0.081	0.139	2.195	1.290
	QL202-63	2266.16	6.480	0.020	9.10	1.122	0.655	16.946	0.043	86.816	2.380	1.624	Unimodal	0.690	0.004	0.045	0.906	2.583
	QL16-15	2423.65	4.150	0.024	13.45	1.133	0.649	50.746	0.015	70.782	3.825	1.595	Unimodal	0.903	0.018	0.101	1.491	1.123
	QL203-13	2253.56	3.480	0.016	14.06	2.904	0.253	53.661	0.014	66.704	4.059	1.422	Unimodal	0.598	0.011	0.054	0.905	5.941

10.3389/feart.2023.1183734

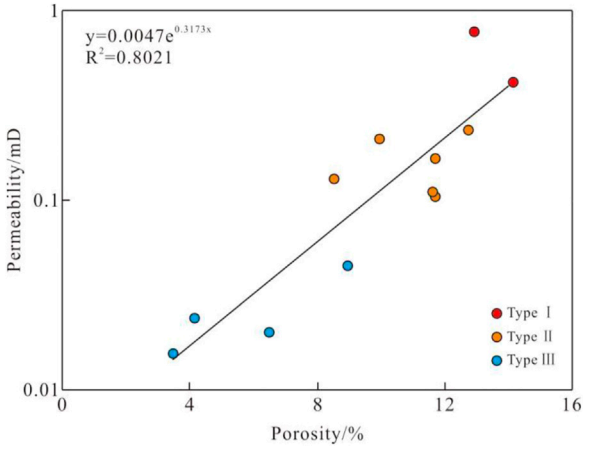

FIGURE 5
Relationship between porosity and permeability.

Results

Petro-physical characteristics

The porosity and permeability of each sample are shown in Table 1. The result shows that typical tight sandstone is developed in J_2S^2 member of central Sichuan Basin, the porosity of sample ranges 3.48%~14.12%, with an average of 9.7%, and the permeability ranges 0.016 mD~0.778 mD, with an average of 0.189 mD. In semi-logarithmic coordinates, porosity and permeability have relatively high positive correlation (Figure 5), and the coefficient of determination is 0.8021. With permeability as the main basis and porosity as the secondary reference, the reservoirs in J_2S^2 section of the study area can be divided into three types. The permeability of Class I reservoir is more than 0.3 mD, and the porosity is mainly more than 12%. The permeability of Class II reservoir is 0.08~0.3 mD, and the porosity is mainly 8%~12%. The permeability of Class III reservoir is less than 0.08 mD, and the porosity is mainly below 8%.

In addition, the $T_{2cutoff}$ and movable fluid saturation of each sample were obtained through the centrifugal experiment. The result shows that the $T_{2cutoff}$ of the sample had an increasing trend with the deterioration of physical properties, on the contrary, the movable fluid saturation had a decreasing trend with the deterioration of physical properties. $T_{2cutoff}$ of type I reservoir ranges 0.850 ms~1.290 ms, with an average of 1.070 ms, and the movable fluid saturation ranges 68.92%~71.32%, with an average of 70.12%. $T_{2cutoff}$ of type II reservoir ranges 0.740 ms~2.583 ms, with an average of 1.244 ms, and the movable fluid saturation ranges 39.70%~67.43%, with an average of 57.59%. $T_{2cutoff}$ of type III reservoir ranges 1.123 ms~5.941 ms, with an average of 2.734 ms, and the movable fluid saturation ranges 9.10%~17.95%, with an average of 13.46%.

Pore-throat structure parameters obtained by HPMI

The pore structure parameters, capillary pressure curve and pore size distribution curve obtained from HPMI experiment are shown in Table 1 and Figure 6. With the deterioration of reservoir physical properties, the platform section of capillary pressure curve gradually disappears (Figure 6A,C,E), the displacement pressure (P_d) and median pressure (P_{50}) gradually increase, and the maximum pore radius (r_d) and median pore radius ($r_{50\text{-}h}$) decrease accordingly. At the same time, the maximum mercury saturation (S_h) shows a decreasing trend, indicating that the total volume of pores decreases correspondingly, and the degree of connectivity decreases gradually. The displacement pressure of type Ⅰ reservoir ranges 0.409 MPa~0.415MPa, with an average of 0.412 MPa, and the median pressure ranges 1.364 MPa~1.778 MPa, with an average of 1.571 MPa. The corresponding maximum pore radius ranges 1.773 μm~1.798 μm, with an average of 1.785μm, the median pore radius ranges 0.414 μm~0.539 μm, with an average of 0.476 μm, the main pore radius is distributed at 0.5 μm~1.7 μm (Figure 6B), and the maximum mercury saturation is between 92.842% and 95.669%, with an average of 94.256%, indicating that the pore volume is large and the connectivity is good. The displacement pressure of type Ⅱ reservoir ranges 0.680 MPa~1.118MPa, with an average of 0.755 MPa, and the median pressure ranges 2.162 MPa~3.525MPa, with an average of 2.784 MPa. The corresponding maximum pore radius ranges 0.657 μm~1.081 μm, with an average of 1.008 μm, the median pore radius ranges 0.209 μm~0.340 μm, with an average of 0.270 μm, the main pore radius is distributed at 0.2 μm~1.8 μm (Figure 6D), and the maximum mercury saturation is between 83.572% and 94.999%, with an average of 91.017%, indicating that the pore volume is reduced and the connectivity is deteriorated compared with Type Ⅰ reservoir. The displacement pressure of type Ⅲ reservoir ranges 1.122 MPa~2.904 MPa, with an average of 1.570 MPa, and the median pressure ranges 7.542 MPa~53.661MPa, with an average of 32.224 MPa. The corresponding maximum pore radius ranges 0.253 μm~0.655 μm, with an average of 0.553 μm, the median pore radius ranges 0.014 μm~0.098 μm, with an average of 0.042 μm, the main pore radius is distributed at 0.05 μm~0.4 μm (Figure 6F), and the maximum mercury saturation is between 66.704% and 87.944%, with an average of 78.062%, indicating that the pore volume is small and the connectivity is poor.

Sorting coefficient and skewness coefficient are important parameters to describe the characteristics of pore size distribution, and their values have no obvious linear relationship with physical properties. The sorting coefficient reflects the concentration degree of pore distribution. The smaller the sorting coefficient, the higher the concentration degree of pore size within a certain size range. The sorting coefficient ranges 2.252~2.258 in type I reservoir, with an average of 2.255, and ranges 2.084~2.600 in type II reservoir, with an average of 2.200, and ranges 2.246~4.059 in type III reservoir, with an average of 3.128. The range of sorting coefficient of type II reservoir is significantly larger than that of type I reservoir, but the average value of the two types of reservoirs is close, mainly because the sorting coefficient of type II reservoir sample QL205-1-41 is significantly higher than that of other similar samples, and the sorting coefficient of the remaining type II reservoir samples is below 2.2. In general, the pore size distribution of type II reservoir is more concentrated than that of type I reservoir. The range and average value of sorting coefficient of type III reservoir are significantly larger than those of type I and II reservoirs, indicating

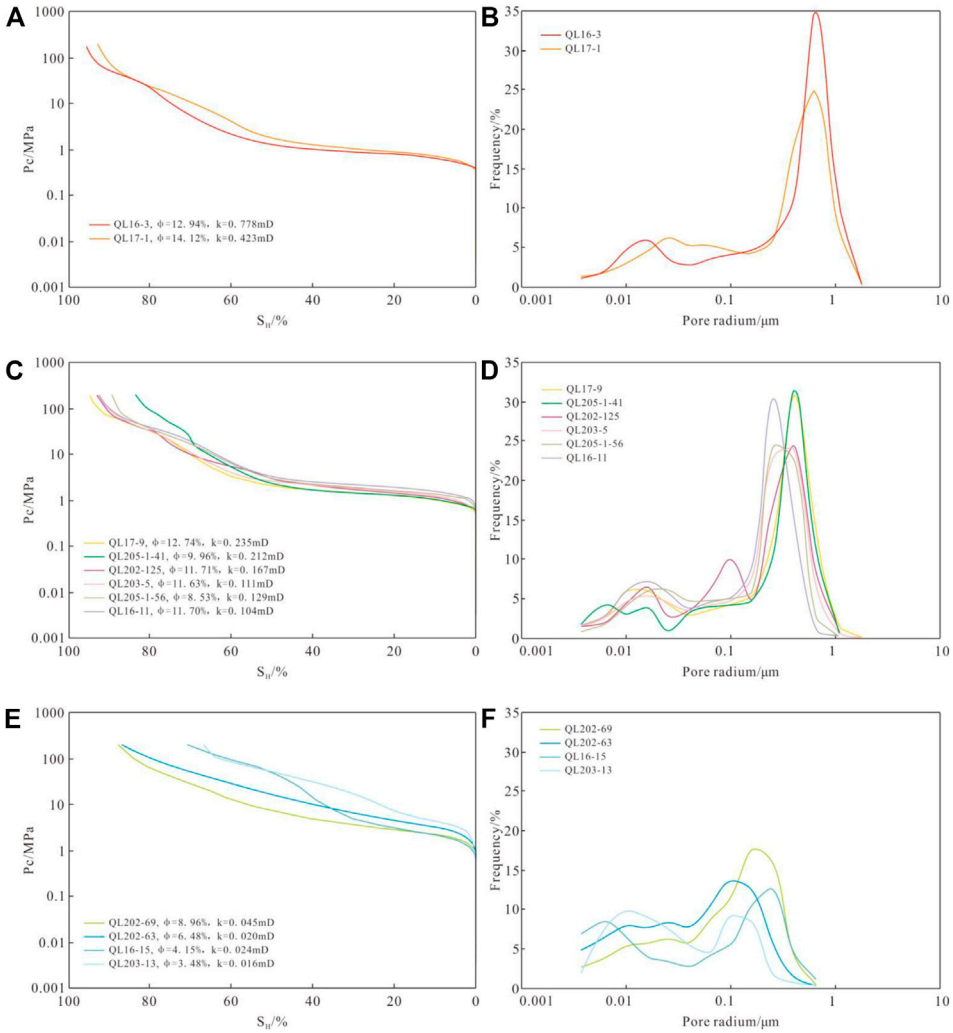

FIGURE 6
Capillary pressure curve and pore size distribution calculated by HPMI: **(A)** and **(B)**. Type I; **(C)** and **(D)**. Type II; **(E)** and **(F)**. Type III.

that the pore size distribution of type III reservoir is more dispersed. The skewness coefficient reflects the asymmetry of the PSD curve. When the skewness coefficient is greater than 0, it's coarse skewness, indicating that the PSD is more inclined to large pores compared to the average pore size, and when it is less than 0, it's fine skewness, indicating that the PSD is more inclined to small pores compared to the average pore size. The PSD of all kinds of reservoirs in J_2S^2 member shows coarse skewness, the skewness coefficient ranges 1.602~1.700 in type I reservoir, with an average of 1.651, and ranges 1.632~2.081 in type II reservoir, with an average of 1.854, and ranges 1.422~1.811 in type III reservoir, with an average of 1.613.

Pore-throat structure parameters obtained by NMR.

The pore structure parameters, T_2 spectrum obtained from NMR experiments and the full-size pore distribution curve obtained from fitting the capillary pressure curve are shown in Table 1 and Figure 7. The relaxation time of T_2 spectrum of water-saturated samples is between 0.01 and 1000 ms, and the T_2 spectrum of Type I and Type II reservoirs are mostly bimodal, with 8 ms as the dividing point of left and right peaks. Although the T_2 spectrum of Sample QL205-1-41 and Sample QL16-11 are multi-modal with three obvious peaks. The T_2 spectrum of type III reservoir is unimodal distribution, characterized by absolute predominance of left peak(Figure 7A,C,E). In general, with the physical properties of the sample getting worse, the peak value of T_2 spectrum has a tendency to decrease, and the right peak with relaxation time larger than 8 ms decreases rapidly, making T_2 spectrum transition from bimodal or multi-modal to unimodal.

The range of PSD obtained by NMR and HPMI fitting method is significantly wider than that calculated by Washburn equation, and the characterized pore size is more extensive, so the relatively real maximum pore radius (r_{max}), median pore radius (r_{median}) and average pore radius (r_{mean}) can be obtained. Pore radius of type I reservoir mainly ranges 0.01 μm~2 μm (Figure 7B), The maximum pore radius ranges 1.911 μm~2.536 μm With an average of 2.224 μm, The median pore radius ranges 0.396 μm~0.562 μm, with an average of 0.479 μm, the weighted mean pore radius ranges 0.444 μm~0.564 μm, with an average of 0.504 μm. Pore radius of type II reservoir mainly ranges

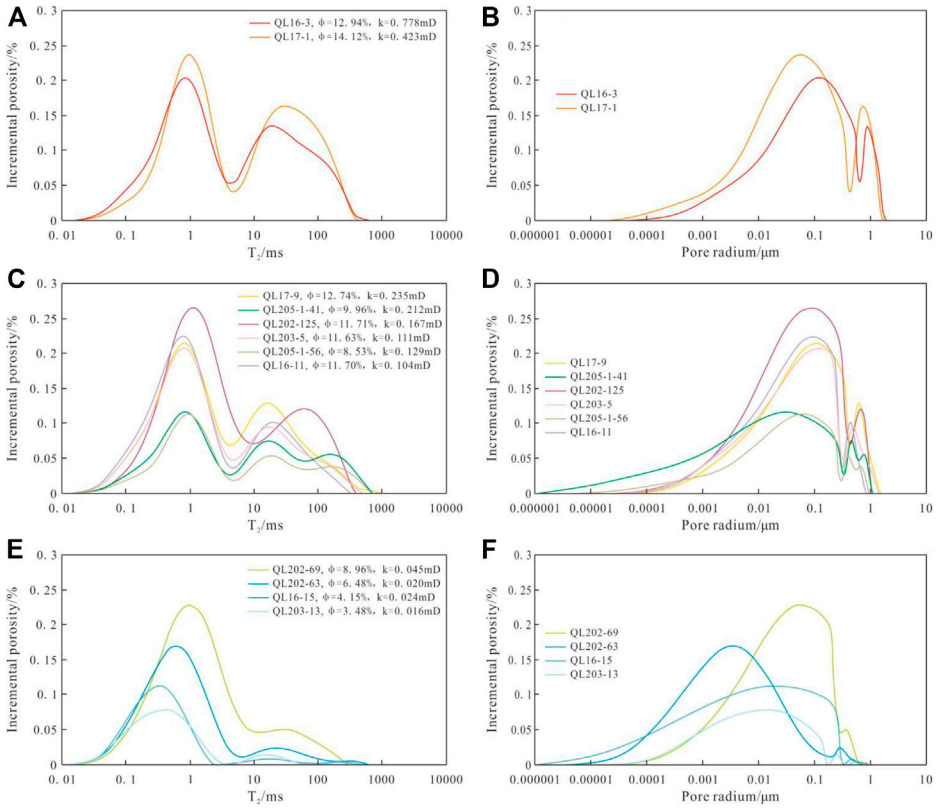

FIGURE 7
T_2 spectrum and full-size distribution of pores: **(A)** and **(B)**. Type I; **(C)** and **(D)**. Type II; **(E)** and **(F)**. Type III.

0.003 μm~1 μm(Figure 7D), The maximum pore radius ranges 0.923 μm~1.698 μm, with an average of 1.283μm, The median pore radius ranges 0.179 μm~0.337μm, with an average of 0.249 μm, the weighted mean pore radius ranges 0.222 μm~0.367 μm, with an average of 0.292 μm. Pore radius of type III reservoir mainly ranges 0.001 μm~0.4 μm (Figure 7F), only the main pore radius distribution of sample QL202-63 is significantly different from other similar samples with a range from 0.05 nm to 0.08 μm.The maximum pore radius of type III reservoir ranges 0.598 μm~0.903 μm, with an average of 0.757 μm, the median pore radius ranges 0.081 μm~0.114 μm, with an average of 0.029 μm, the weighted mean pore radius ranges 0.045 μm~0.139 μm, with an average of 0.085 μm.

The tortuosity is a description of the connectivity and complexity of the pores, and is one of the important pore topology parameters, which can be calculated by the following formula

$$\tau^2 = \frac{125\varphi r^2}{K} \tag{30}$$

Where, τ is the tortuosity, dimensionless; K is the permeability, mD. The calculation results show that the tortuosity of pores increases with the increase of reservoir physical properties, which is consistent with the results obtained by Qiao et al. (2020). The tortuosity of type I reservoir ranges 2.571~2.869, with an average of 2.720. The tortuosity of type II reservoir ranges 2.401~3.224, with an average of 2.754. The tortuosity of type III reservoir ranges 0.905~2.195, with an average of 1.374. Qiao et al. (2020) proposed that with the improvement of the physical properties of tight sandstone reservoirs, the coordination number of percolation channels increased, resulting in higher tortuosity of high-quality reservoirs.

Fractal dimensions based on HPMI

According to previous studies, when calculating the pore fractal dimension of tight sandstone by 3D capillary tube model described by mercury saturation and mercury injection pressure, there are generally two fractal intervals. Liu et al. (2018) proposed that when calculating fractal dimension based on this model, Capillary-Paraachor point (CPpoint) can be used as the segmentation point of different fractal intervals to better describe the fractal characteristics of pores in tight sandstone. According to the definition by Guo et al. (2004), the position of the maximum value of the plot of S_h/P_c^2 versus S_h is the CPpoint, which represents the node of transition from a well connected pores to poorly connected pores. According to the above theory, the CPpoints of capillary pressure curves of each sample are calculated respectively, and lg (P_c) and lg (S_h) are linearly fitted, and the fractal dimension corresponding to each fractal interval is calculated through 3D capillary tube model. The CPpoints of Sample

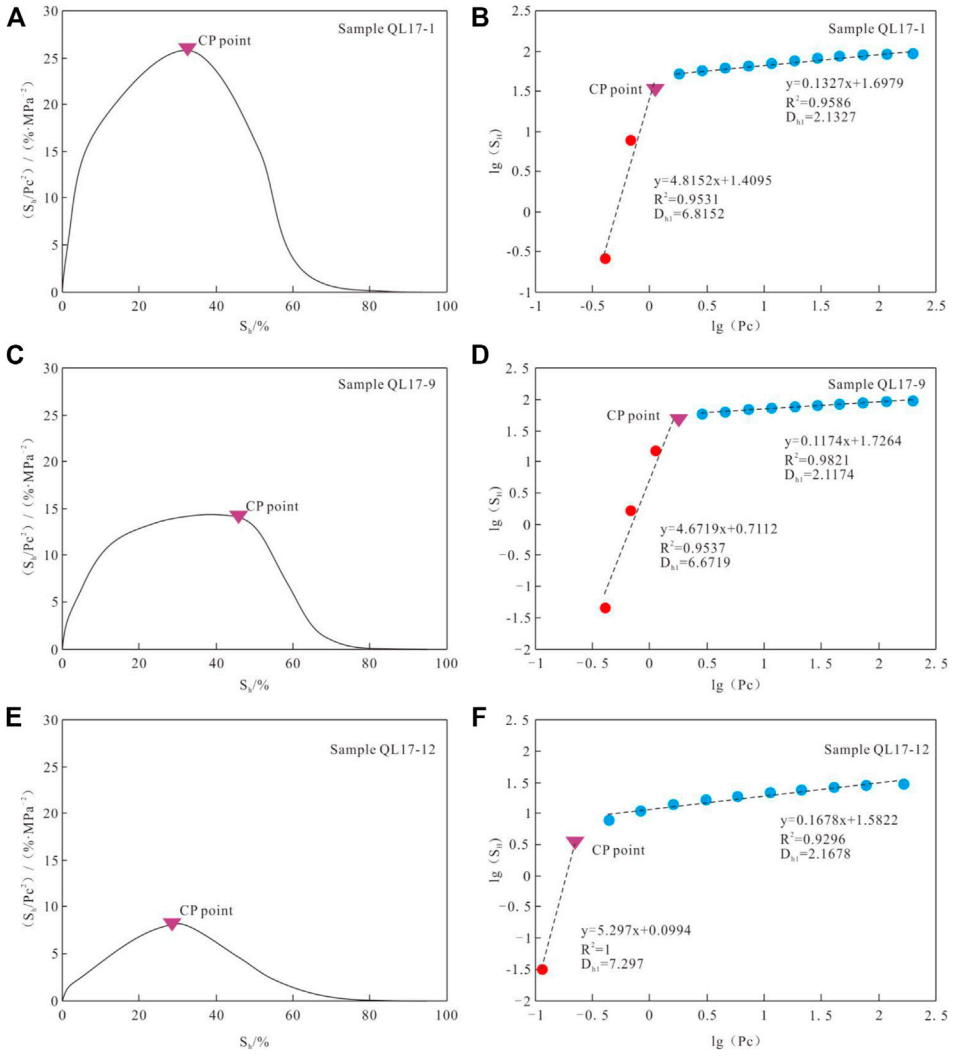

FIGURE 8
(A) The CP point of Sample QL17-1. **(B)** Cross-plot of Lg(P_c) vs. Lg(S_H) based on Sample QL17-1. **(C)** The CP point of Sample QL17-9. **(D)** Cross-plot of Lg(P_c) vs. Lg(S_H) based on Sample QL17-9. **(E)** The CP point of Sample QL17-12. **(F)** Cross-plot of Lg(P_c) vs. Lg(S_H) based on Sample QL17-12. The red and blue circles represent the large pores and small pores, respectively.

QL17-1, Sample QL17-9 and Sample QL17-12 and the corresponding segmentation points in the plot of lg (P_c) versus lg (S_h) are shown in Figure 8. The results show that the position of the segmentation point of the capillary pressure curve of different samples is different. The fractal dimension of the large pores (D_{h1}) can be calculated according to the slope of the left line segment of CPpoint, and the fractal dimension of the small pores (D_{h2}) can be calculated according to the slope of the right line segment.

The fractal dimension calculation results of each sample based on HPMI data and the corresponding pore radius of fractal interval segmentation points (SP_h) are shown in Table 2, where D_{h1} ranges 4.3505~7.1684, with an average of 6.055 and the determination coefficient ranges 0.9477~0.9982. D_{h2} ranges from 2.1004 to 2.3841, with an average of 2.1758 and the coefficient of determination ranges 0.9094~0.9902. According to the fractal theory, the fractal dimension of a three-dimensional object is 2~3, when the fractal dimension is greater than 3 or less than 2 indicates that the object has no fractal characteristics. In the calculation results of this study, small pores have ideal fractal characteristics, while the fractal dimension of large pores is greater than 3; Lai and Wang (2015); Song et al. (2018) also used 3D capillary model to calculate the fractal dimension of pores in tight sandstone, and the fractal dimension of large pores obtained is also greater than 3. In fact, at present, most scholars believe that this phenomenon is not caused by the pore itself, but the assumption that the pore is regarded as a cylindrical capillary in the model is too simplified. When the mercury injection pressure is high, the pore size is small and close to the throat radius, so the ideal fractal dimension can be obtained through the 3D capillary tube model. When the mercury injection pressure is low, the pore radius is significantly larger than the throat radius, and the shape of the pore throat is similar to bead-string model (Zhu et al., 2019), Therefore, 3D capillary model is not suitable for calculating the fractal dimension of large pores in rocks.

TABLE 2 Fractal dimensions of samples based on HPMI and NMR data.

Reservoir type	Sample ID	HPMI					NMR							
		Large pores		SP_h (μm)	Small pores		Large pores		SP_{n1} (μm)	Small pores		SP_{n2} (μm)	Micropores	
		D_{h1}	R^2		D_{h2}	R^2	D_{n1}	R^2		D_{n2}	R^2		D_{n3}	R^2
I	QL16-13	6.7917	0.9477	0.652	2.1076	0.9701	2.8714	0.9413	0.849	2.7957	0.9278	0.121	0.5949	0.8659
	QL17-1	6.8152	0.9531	0.655	2.1327	0.9586	2.8522	0.9723	0.752	2.8208	0.9601	0.105	0.685	0.877
II	QL17-9	6.6719	0.9537	0.407	2.1174	0.9821	2.908	0.9282	0.581	2.7602	0.9127	0.089	0.5	0.8715
	QL202-125	5.6993	0.9791	0.407	2.1433	0.9266	2.8967	0.9722	0.582	2.8004	0.8811	0.076	0.4767	0.8916
	QL16-11	5.7881	0.9781	0.253	2.1425	0.9757	2.9082	0.8197	0.396	2.8397	0.8709	0.128	0.6382	0.8615
	QL203-5	7.1684	0.9605	0.406	2.1251	0.9613	2.9298	0.9572	0.519	2.8342	0.9236	0.182	0.6402	0.8649
	QL205-1-41	6.5595	0.9543	0.406	2.1004	0.9712	2.906	0.9727	0.599	2.8265	0.988	0.099	0.7538	0.8568
	QL205-1-56	6.9297	0.9982	0.253	2.1417	0.9565	2.9085	0.9833	0.423	2.8779	0.9717	0.258	1.0562	0.8452
III	QL202-69	5.9661	0.9896	0.253	2.2073	0.9094	2.9483	0.9675	0.312	2.8176	0.8946	0.098	0.6872	0.8709
	QL202-63	4.9878	0.9904	0.161	2.2814	0.9479	2.9908	0.9807	0.411	2.9598	0.9913	0.042	1.8052	0.8258
	QL16-15	4.9291	0.9943	0.252	2.2257	0.9902	2.993	0.9945	0.587	2.9822	0.9097	0.270	0.813	0.834
	QL203-13	4.3505	0.9903	0.161	2.3841	0.9709	2.9918	0.9276	0.370	2.9592	0.9481	0.196	1.5851	0.733

10.3389/feart.2023.1183734

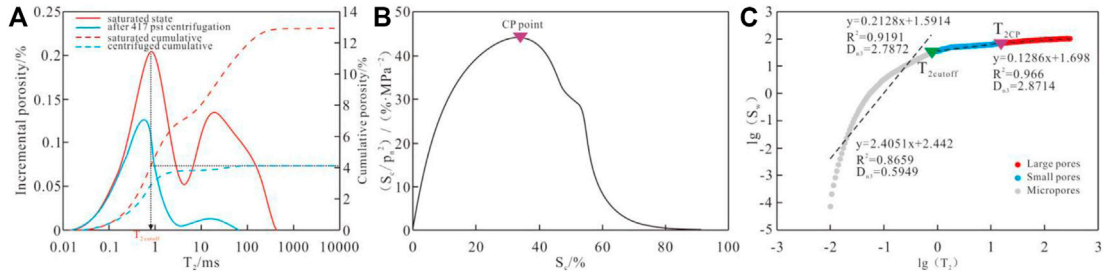

FIGURE 9
(A) The $T_{2cutoff}$ of Sample QL16-13. **(B)** The CP point of Sample QL16-13. **(C)** The plot of lg(T_2) vs. lg(S_w) based on NMR of Sample QL16-13. The grey, blue and red circles represent the large pores (T_2 greater than T_{2CP}), small pores (T_2 between $T_{2cutoff}$ and T_{2CP}) and micropores (T_2 less than $T_{2cutoff}$), respectively.

Fractal dimensions based on NMR

When calculating fractal dimension based on NMR data, it is also necessary to consider the difference of fractal dimension in different intervals, that is, the difference of fractal characteristics of pores with different sizes. Guo et al. (2019) and Wu et al. (2022a) divide the reservoir pores into two types, namely, large pore and small pore, with $T_{2cutoff}$ as the segmentation point. Wang and Wang. (2022) divided the pores into three types, namely, macropores, mesopores and micropores, with T2cutoff and 9T2cutoff as the segmentation point. By comparing the T_2 spectra of samples before and after centrifugation, Wang and Zeng. (2020) divided the pores into three types according to the content of movable fluid: fully movable macropores, partially movable mesopores and completely immovable micropores. Some researchers did not consider the mobility of the fluid when calculating the fractal dimension of pores with different sizes, but based on the full-size pore size distribution, taking the actual pore size as the dividing standard. Wu et al. (2022b) put 5 μm、1 μm, 0.1 μm as the segmentation point, the pores are divided into four types from large to small, namely, macropores, mesopores, micropores and ultra-micro pores. Zang et al. (2022a) takes 1 μm, 0.1 μm as the segmentation point, then the pores are divided into three types from large to small, namely, micron pores, submicron pores and nanopores. In fact, taking the pore size as the segmentation standard has only mathematical significance, and cannot accurately reflect the difference of pore seepage capacity. In addition, due to the existence of experimental error, the left peak of the T_2 spectrum of the same sample before and after centrifugation may cross each other, which will affect the pore classification results. Therefore, considering the mobility of fluid and the connectivity of pores, this paper proposes a new method of pore type classification based on the full size pore size distribution.

Firstly, pores with relaxation time less than $T_{2cutoff}$ are divided into micropores. Then, based on the full-size pore distribution, the pore radius is converted into the non-wetting phase fluid injection pressure (P_n) through the Washburn equation, and the cumulative frequency (S_c) is taken as the non-wetting phase fluid saturation according to the order of pore size from large to small, then the position of the maximum value in the plot of S_c/P_n^2-S_c is the CP point, representing the segmentation point between the pores with good connectivity and poor connectivity. The relaxation time corresponding to this point is expressed as T_{2CP}, the pores with relaxation time greater than T_{CP} are defined as large pores, and the pores with relaxation time between $T_{2cutoff}$ and T_{2CP} are defined as small pores.

The process of obtaining fractal dimensions of different types of pores based on NMR data of sample QL16-13 is shown in Figure 9. First, determine the $T_{2cutoff}$ and T_{2CP} values of each sample, and divide the pores into large pores, small pores and micropores, corresponding to three fractal intervals respectively. According to the order of relaxation time from small to large, the cumulative frequency value is taken as the wetting phase fluid saturation (Sw), and linear regression analysis is performed on the lg (T_2); lg (S_w) in different fractal intervals to obtain various pores fractal dimensions. The fractal dimension of each sample calculated based on NMR data and the corresponding pore radius of fractal interval segmentation points (SP_{n1}, SP_{n2}) are shown in Table 2. The fractal dimension (D_{n1}) of large pores ranges 2.8522~2.993, with an average of 2.9254, and the determination coefficient is 0.8197~0.9945, with an average of 0.9514; The fractal dimension (D_{n2}) of small pores ranges 2.7602~2.9822, with an average of 2.8562, and the determination coefficient is 0.8709~0.9913, with an average of 0.9316; The fractal dimension (D_{n3}) of micropores ranges 0.4767~1.8052, with an average of 0.8530, and the determination coefficient is 0.7330~0.8916, with an average of 0.8498. The results show that with the decrease of pore size, the fractal dimension also gradually decreases, indicating that the heterogeneity gradually weakens. In addition, in this study, the fractal dimension of micropores is less than 2. In the study of pore fractal characteristics of tight sandstone by Guo et al. (2019), Wang and Wang (2022) and Wu et al. (2022a) based on NMR data, the fractal dimension of micropores is also less than 2. Shao et al. (2017) and Li et al. (2018a) believe that the main reason for this result is that the effect of the surface roughness of micropores on the relaxation time is greater than the specific surface area. Therefore, the fractal dimension of micropores mainly reflects the surface structure characteristics, but cannot effectively characterize the spatial structure characteristics of micropores.

Discussion

According to the fractal theory, the fractal dimension D_{h1} of large pores based on HPMI and D_{n3} of micropores based on NMR

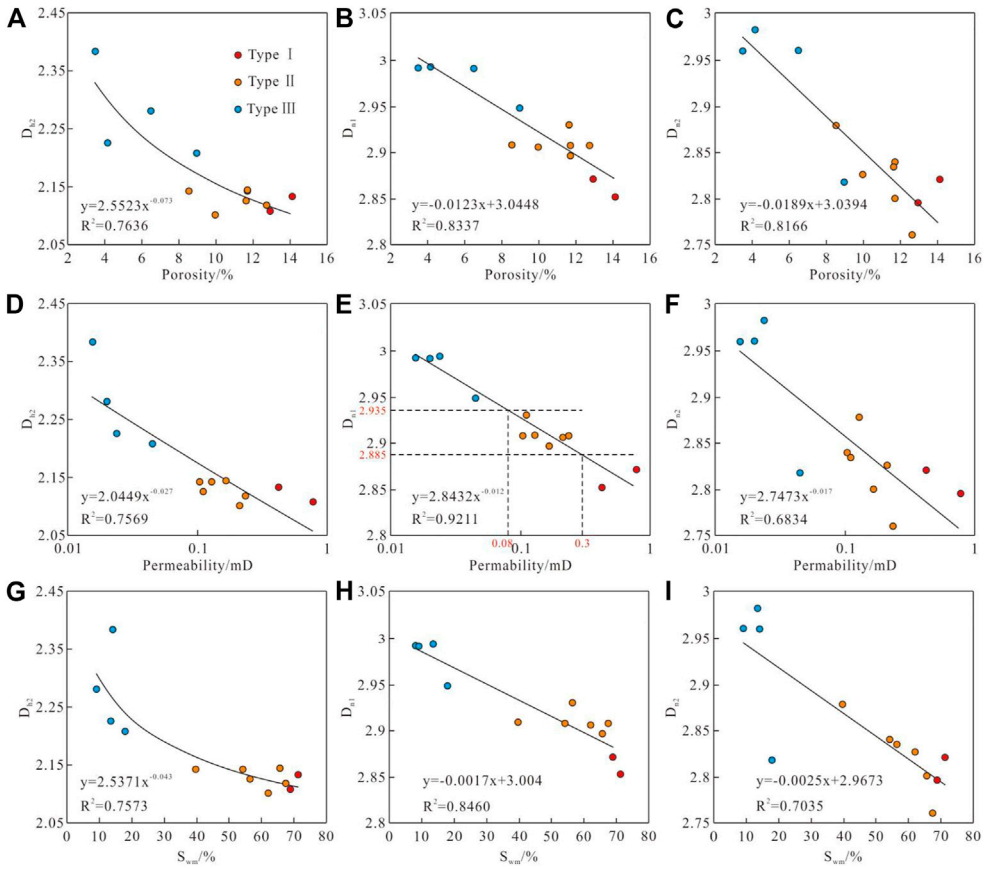

FIGURE 10
The relationship between fractal dimension, porosity, permeability and movable fluid saturation. The relationship between porosity and D_{h2}, D_{n1}, D_{n2} are shown in **(A–C)**, respectively. The relationship between permeability and D_{h2}, D_{n1}, D_{n2} are shown in **(D–F)**, respectively. The relationship between movable fluid saturation and D_{h2}, D_{n1}, D_{n2} are shown in **(G–I)**, respectively.

cannot truly reflect the fractal dimension of pores. Therefore, this study will take the fractal dimension D_{h2} of small pores based on HPMI, D_{n1} and D_{n2} of large pores and small pores based on NMR as the main discussion objects.

Relationship between fractal dimension and physical properties

The correlation between fractal dimensions D_{h2}, D_{n1} and D_{n2} and physical properties is shown in Figure 10. The porosity, permeability, mobile fluid saturationand and fractal dimension of the reservoir are negatively correlated, indicating that with the increase of heterogeneity of same kind of pores, the reservoir quality gradually becomes worse and the fluid mobility gradually weakens. The relationship between reservoir porosity and D_{h2} is a power function (Figure 10A), while the relationship with D_{n1} and D_{n2} is linear (Figure 10B,C). The correlation between D_{n1} and D_{n2} and porosity is strong, and their determination coefficients are 0.8337 and 0.8166, respectively, indicating that the reservoir capacity is jointly controlled by large pores and small pores. The relationship between permeability and fractal dimension is power function (Figure 10D,E,F) and the correlation between D_{n2} and permeability is the strongest, with a determination coefficient of 0.9211. The correlation between D_{h1} and D_{n2} and permeability is weak, and their determination coefficients are 0.7569 and 0.6834 respectively, indicating that large pores are the most important seepage channels of the reservoir and play a decisive role in the seepage capacity of the reservoir. The saturation of movable fluid has a power function relationship with D_{h2}, and a linear relationship with D_{n1} and D_{n2} (Figure 10G,H,I). Among them, the correlation between movable fluid saturation and D_{n1} is the highest, with the determination coefficient of 0.8460, and the correlation with D_{h1} and D_{n2} is weak, with the determination coefficient of 0.7573 and 0.7035 respectively, indicating that the large pore throat is the main occurrence space of movable fluid in the reservoir.

At the same time, the fractal dimension D_{n1} has a good correspondence with different types of reservoirs (Figure 10E). According to the regression equation between reservoir permeability and D_{n1}, the fractal dimension of large poreof type I reservoir is less than 2.880, the fractal dimension of large pore of type II reservoir is between 2.88 and 2.935, and the fractal dimension of large pore of type III reservoir is more than 2.935. Therefore, D_{n1} can be used as one of the parameters for reservoir quality evaluation.

10.3389/feart.2023.1183734

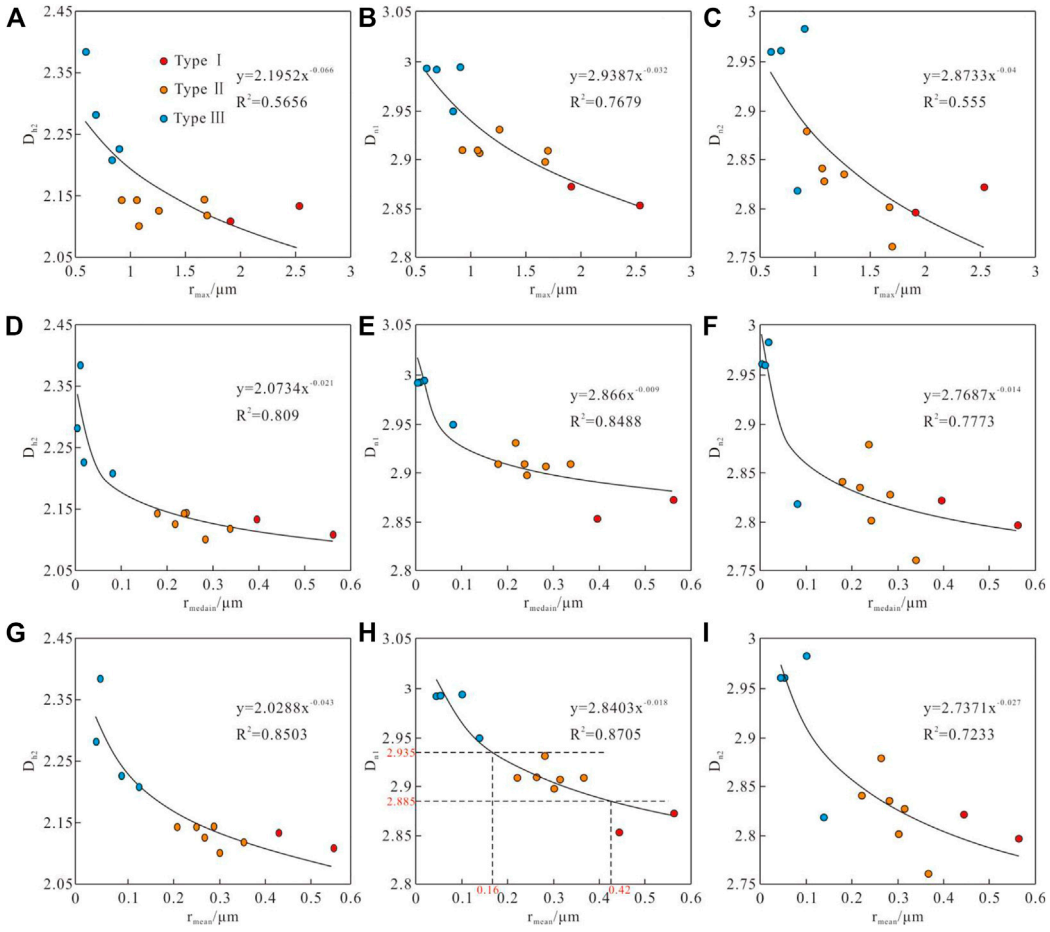

FIGURE 11
The relationship between fractal dimension and pore size. The relationship between maximum pore radius and D_{h2}, D_{n1}, D_{n2} are shown in **(A–C)**, respectively. The relationship between median pore radius and D_{h2}, D_{n1}, D_{n2} are shown in **(D–F)**, respectively. The relationship between weighted mean pore radius and D_{h2}, D_{n1}, D_{n2} are shown in **(G–I)**, respectively.

Relationship between fractal dimension and pore-throat structure

The maximum radius, median radius and weighted mean radius of pores can be obtained from the full-size pore distribution curve. The correlation between the above three parameters and D_{h2}, D_{n1} and D_{n2} is shown in Figure 11. The relationship between pore size and fractal dimension is power function and has negative correlation, indicating that the heterogeneity gradually increases with the decrease of pore size of the same kind. The maximum radius, median radius and weighted mean radius have the strongest correlation with D_{n1}(Figure 11B,E,H), with the determination coefficients of 0.7679, 0.8488 and 0.8705 respectively, followed by the correlation with Dh1(Figure 11A,D,G), with the determination coefficients of 0.5656, 0.8090 and 0.8503 respectively, and the correlation with D_{n2} is the worst (Figure 11C,F,I), with the determination coefficients not exceeding 0.8. The above analysis shows that the pore size distribution of the reservoir is mainly controlled by the size of large pores, and the median radius and weighted mean radius have the greatest impact on the reservoir quality. In addition, D_{n1} has a good correspondence with the weighted mean pore radius of different types of reservoirs. According to the regression equation between the weighted average pore radius and D_{n1}, the weighted mean radius of type I reservoirs is greater than 0.42 μm, the weighted mean radius of type II reservoir is between 0.16 μm and 0.42 μm, the weighted mean radius of type III reservoir is less than 0.16 μm (Figure 11H).

The correlation of sorting coefficient, skewness coefficient, tortuosity and movable fluid saturation with D_{h1}, D_{n1} and D_{n2} is shown in Figure 12. The correlation between sorting coefficient and skewness and fractal dimension is weak, and the determination coefficient between each parameter is only 0.1526~0.5593 (Figure 12A,F), indicating that PSD is not the main factor affecting pore heterogeneity and reservoir quality. Both tortuosity and movable fluid saturation are negatively correlated with fractal dimension, indicating that reservoir heterogeneity increases with the decrease of pore tortuosity and fluid mobility. The correlation between tortuosity and fractal dimension is relatively high, with a power function relationship with D_{h1} and D_{n2}, and a linear relationship with D_{n1} (Figure 12C,F,I). Among them, the porosity tortuosity has the strongest correlation with Dh1, with a determination coefficient of 0.8503, followed by D_{n2}, with a

10.3389/feart.2023.1183734

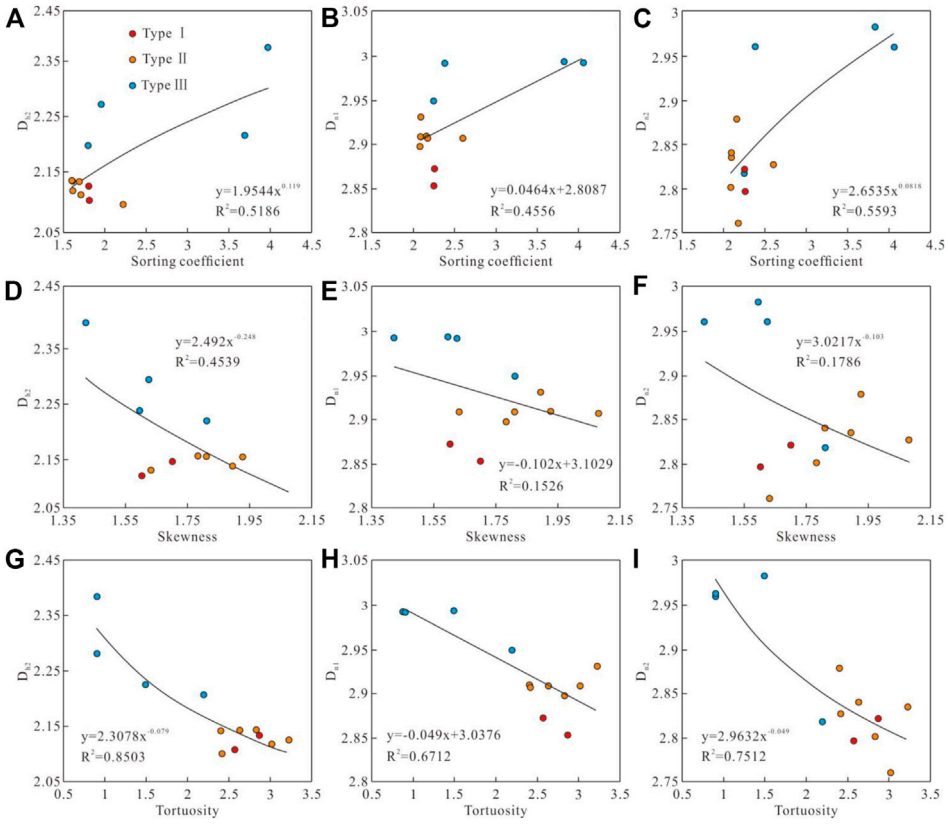

FIGURE 12
The relationship between fractal dimension, sorting coefficient, skewness and tortuosity. The relationship between sorting coefficient and D_{h2}, D_{n1}, D_{n2} are shown in **(A–C)**, respectively. The relationship between skewness and D_{h2}, D_{n1}, D_{n2} are shown in **(D–F)**, respectively. The relationship between tortuosity and D_{h2}, D_{n1}, D_{n2} are shown in **(G–I)**, respectively.

TABLE 3 Comprehensive evaluation indicators for meandering stream facies reservoirs in study area.

Reservoir type	Permeability (mD)	Rmean (μm)	D_{n1}
I	>0.3	>0.42	<2.88
II	0.08~0.3	0.16~0.42	2.88~2.935
III	<0.08	<0.16	>2.935

determination coefficient of 0.7512, and the worst correlation with D_{n1}, with a determination coefficient of only 0.6712. This phenomenon is due to the positive correlation between tortuosity and pore-throat coordination number, while the throat size is small, This phenomenon is due to the positive correlation between tortuosity and pore throat coordination number, while the throat size is small, so the fractal dimension of large pores can not accurately reflect the configuration of pore and throat, resulting in poor correlation between macropores and tortuosity.

Comprehensive evaluation indicators for reservoirs

Based on the above analysis, there is a good correlation between the permeability, mean pore radius, and Dn_1 of the reservoir, and the differentiation between different types of reservoirs is good. Therefore, comprehensive reservoir evaluation indicators can be established based on the above parameters. Among them, the permeability represents the macroscopic seepage ability of the reservoir, the mean pore radius represents the size of the reservoir space, and Dn_1 mainly characterizes the heterogeneity of the pore system.

As shown in Table 3, the permeability of Type I reservoir is less than 0.3 mD, and the mean pore radius is greater than 0.42 μm, the fractal dimension of large pores is less than 2.88; The permeability of type II reservoir ranges from 0.08 mD to 0.3 mD, and the mean pore radius ranges from 0.16 μm to 0.42 μm, the fractal dimension of large pores ranges from 2.88 to 2.935; The permeability of type III reservoir is less than 0.3 mD, and the mean pore radius is less than 0.16 μm, the fractal dimension of large pores is greater than 2.935.

Conclusion

This paper studies the pore structure and fractal characteristics of J_2S^2 tight sandstone in central Sichuan Basin, and the conclusions are as follows.

1)The tight sandstone reservoir of meandering stream facies is developed in J_2S^2 member of central Sichuan Basin, with an average porosity of 9.7% and an average permeability of 0.189 mD. Based on the difference of physical properties, the J_2S^2 reservoir in this area can be divided into three types. The permeability of type I reservoir is more than 0.3 mD, and the porosity is mainly more than 12%; The permeability of type II reservoir is 0.08~0.3 mD, and the porosity is mainly 8%~12%; The permeability of Class III reservoir is less than 0.08 mD, and the porosity is mainly less than 8%.

2)Based on the HPMI and NMR fitting methods and centrifugal experiments, the full-size pore distribution curve of the sample and the saturation of movable fluid can be obtained, so as to obtain relatively accurate pore geometry, topology parameters and seepage capacity parameters. Pore radius of type I reservoir is mainly distributed at 0.01 μm~2 μm. The tortuosity is between 2.571 and 2.869, the average movable fluid saturation is 70.12%, and the pore radius of type II reservoir is mainly 0.003 μm~1 μm. The tortuosity is between 2.401 and 3.224, the average movable fluid saturation is 57.59%, and the pore radius of type III reservoir is mainly 0.001 μm~0.4 μm. The tortuosity is between 0.905 and 2.195, and the average movable fluid saturation is 13.46%.

3)Taking Capillary-Paraachor point (CP point) as the segmentation point of capillary pressure curve, pores can be divided into two types: large pores and small pores. Taking the relaxation time T_{2CP} corresponding to CP point and $T_{2cutoff}$ as the segmentation points of T_2 spectrum, pores can be divided into three types: large pores, small pores and micropores. The fractal dimension D_{h2} of small pore based on HPMI and the fractal dimension D_{n1} and D_{n2} of large pores and small pores based on NMR are between 2 and 3, which can effectively characterize the heterogeneity of reservoir pores. The fractal dimension D_{h1} of large opores based on HPMI is greater than 3 due to the inapplicability of 3D capillary tube model, while the fractal dimension D_{n3} of small pores based on NMR is less than 2 due to the diffusion relaxation. Therefore, D_{h1} and D_{n3} cannot characterize the heterogeneity of reservoir pores.

4)D_{h2} ranges 2.1004~2.3841, with an average of 2.1758; D_{n1} ranges 2.8522~2.993, with an average of 2.9254; D_{n2} ranges 2.7602~2.9822, with an average of 2.8562. Among them, D_{n1} has a strong negative correlation with porosity, permeability, pore radius, and movable fluid saturation, indicating that the reservoir's Storage capacity, seepage capacity and pore size are mainly controlled by the large pores, and with the reservoir quality becoming worse, the pore size decreases, and the pore heterogeneity increases.

5)There is a good correspondence between D_{n1} and the permeability and average pore radius of different types of reservoirs, so D_{n1} can be used as one of the effective reservoir evaluation parameters. Meanwhile, effective comprehensive evaluation indicators for reservoirs can be established based on the above parameters

Data availability statement

The datasets presented in this study can be found in online repositories. The names of the repository/repositories and accession number(s) can be found in the article/supplementary material.

Author contributions

LF contributed as the major author of the article. LF and YJ conceived the project. GG, CY, XZ, and QZ collected the samples. GC and ZW analyzed the samples. All authors contributed to the article and approved the submitted version.

Funding

The study was funded by the scientific research project of Southwest Oil and Gas Field Company (Grant No. XNS20220-42) and the 973 Prophase Special Program of China (Grant No. 2011CB211701) is acknowledged.

The funder was not involved in the study design, collection, analysis, interpretation of data, the writing of this article or the decision to submit it for publication.

Conflict of interest

The authors LF, YJ, GC and ZW were employed by PetroChina Key Laboratory of Unconventional Oil and Gas.

The authors GG, CY and XZ were employed by PetroChina Southwest Oil and Gas Field Company. The author QZ was employed by Tight Oil and Gas Exploration and Development Project Department of PetroChina Southwest Oil and Gas Field Company.

Publisher's note

References

Amadu, M., and Pegg, M. J. (2018). Theoretical and experimental determination of the fractal dimension and pore size distribution index of a porous sample using spontaneous imbibition dynamics theory. *J. Petrol. Sci. Eng.* 167, 785–795. doi:10.1016/j.petrol.2018.04.037

Awan, R. S., Liu, C., Aadil, N., Yasin, Q., Salaam, A., Hussain, A., et al. (2021). Organic geochemical evaluation of Cretaceous Talhar shale for shale oil and gas potential from lower Indus basin, Pakistan. *J. Petrol. Sci. Eng.* 200, 108404. doi:10.1016/j.petrol.2021.108404

Clarkson, C. R., Freeman, M., He, L., Agamalian, M., Melnichenko, Y. B., Mastalerz, M., et al. (2012). Characterization of tight gas reservoir pore structure using USANS/SANS and gas adsorption analysis. *Fuel* 95, 371–385. doi:10.1016/j.fuel.2011.12.010

Cui, H., Zhu, S., Wang, J., Gao, Y., Wan, C., and Tong, H. (2022). Physical properties, pore-throat structure, fractal characteristics and their effects on the gas-bearing capacity of tight sandstone: A case study from the northern tianhuan depression, Ordos Basin, China. *Nat. Resour. Res.* 31, 1559–1584. doi:10.1007/s11053-022-10059-2

Dai, C., Cheng, R., Sun, X., Liu, Y., Zhou, H., Wu, Y., et al. (2019). Oil migration in nanometer to micrometer sized pores of tight oil sandstone during dynamic surfactant imbibition with online NMR. *Fuel* 245, 544–553. doi:10.1016/j.fuel.2019.01.021

Dong, X., Meng, X., and Pu, R. (2023). Impacts of mineralogy and pore throat structure on the movable fluid of tight sandstone gas reservoirs in coal measure strata: A case study of the shanxi formation along the southeastern margin of the Ordos Basin. *J. Petrol. Sci. Eng.* 220, 111257. doi:10.1016/j.petrol.2022.111257

Ge, X., Fan, Y., Zhu, X., Chen, Y., and Li, R. (2015). Determination of nuclear magnetic resonance T-2 cutoff value based on multifractal theory - an application in sandstone with complex pore structure. *Gwophysics* 80 (1), D11–D21. doi:10.1190/geo2014-0140.1

Guo, B., Ghalambor, A., and Duan, S. (2004). Correlation between sandstone permeability and capillary pressure curves. *J. Pet. Sci. Eng.* 43, 239–246. doi:10.1016/j.petrol.2004.02.016

Guo, R., Xie, Q., Qu, X., Chu, M., Li, S., Ma, D., et al. (2020). Fractal characteristics of pore-throat structure and permeability estimation of tight sandstone reservoirs: A case study of chang 7 of the upper triassic Yanchang Formation in longdong area, Ordos Basin, China. *J. Petrol. Sci. Eng.* 184, 106555. doi:10.1016/j.petrol.2019.106555

Guo, X., Huang, Z., Zhao, L., Han, W., Ding, C., Sun, X., et al. (2019). Pore structure and multi-fractal analysis of tight sandstone using mip, NMR and NMRC methods: A case study from the kuqa depression, China. *J. Petrol. Sci. Eng.* 178, 544–558. doi:10.1016/j.petrol.2019.03.069

Huang, H., Chen, L., Sun, W., Xiong, F., Ji, W., Jia, J., et al. (2018). Pore-throat structure and fractal characteristics of shihezi formation tight gas sandstone in the Ordos Basin, China. *Fractals* 26 (2), 1840005. doi:10.1142/S0218348X18400054

Huang, H., Li, R., Xiong, F., Hu, H., Sun, W., Jiang, Z., et al. (2020). A method to probe the pore-throat structure of tight reservoirs based on low-field NMR: Insights from a cylindrical pore model. *Mar. Petrol. Geol.* 117, 104344. doi:10.1016/j.marpetgeo.2020.104344

Huang, W., Lu, S., Hersi, O. S., Wang, M., Deng, S., and Lu, R. (2017). Reservoir spaces in tight sandstones: Classification, fractal characters, and heterogeneity. *J. Nat. Gas. Sci. Eng.* 46, 80–92. doi:10.1016/j.jngse.2017.07.006

Lai, J., and Wang, G. (2015). Fractal analysis of tight gas sandstones using high-pressure mercury intrusion techniques. *J. Nat. Gas. Sci. Eng.* 24, 185–196. doi:10.1016/j.jngse.2015.03.027

Li, K. (2010). Analytical derivation of brooks-corey type capillary pressure models using fractal geometry and evaluation of rock heterogeneity. *J. Petrol. Sci. Eng.* 73, 20–26. doi:10.1016/j.petrol.2010.05.002

Li, K., and Horne, R. N. (2006). Fractal modeling of capillary pressure curves for the Geysers rocks. *Geothermics* 35, 198–207. doi:10.1016/j.geothermics.2006.02.001

Li, L., Wang, Y., Kürschner, M. W., Ruhl, M., and Vajda, V. (2020). Palaeovegetation and palaeoclimate changes across the triassic-jurassic transition in the Sichuan Basin, China. *Palaeogeogr. Palaeocl.* 556, 109891. doi:10.1016/j.palaeo.2020.109891

Li, P., Zheng, M., Bi, H., Wu, S., and Wang, X. (2017). Pore throat structure and fractal characteristics of tight oil sandstone: A case study in the Ordos Basin, China. *J. Petrol. Sci. Eng.* 149, 665–674. doi:10.1016/j.petrol.2016.11.015

Li, Y., Wang, Z., Pan, Z., Niu, X., Yu, Y., and Meng, S. (2019). Pore structure and its fractal dimensions of transitional shale: A cross-section from east margin of the Ordos Basin, China. *Fuel* 241, 417–431. doi:10.1016/j.fuel.2018.12.066

Li, Z., Shen, X., Qi, Z., and Hu, R. (2018a). Study on the pore structure and fractal characteristics of marine and continental shale based on mercury porosimetry, N2 adsorption and NMR methods. *Energy. Fuels.* 53, 12–21. doi:10.1016/j.jngse.2018.02.027

Li, Z., Wu, S., Xia, D., He, S., and Zhang, X. (2018b). An investigation into pore structure and petrophysical property in tight sandstones: A case of the Yanchang Formation in the southern Ordos Basin, China. *Mar. Petrol. Geol.* 97, 390–406. doi:10.1016/j.marpetgeo.2018.07.014

Liu, D., Sun, W., and Ren, D. (2019). Experimental investigation of pore structure and movable fluid traits in tight sandstone. *Processes* 7 (3), 149. doi:10.3390/pr7030149

Liu, M., Xie, R., Li, C., Li, X., Jin, G., and Guo, J. (2018). Determining the segmentation point for calculating the fractal dimension from mercury injection capillary pressure curves in tight sandstone. *J. Geophys. Eng.* 15 (4), 1350–1362. doi:10.1088/1742-2140/aab1d8

Mandelbrot, B. B., Passoja, D. E., and Paullay, A. J. (1984). Fractal character of fracture surfaces of metals. *Nature* 308 (5961), 721–722. doi:10.1038/308721a0

Mandelbrot, B. B., and Wheeler, J. A. (1983). The fractal geometry of nature. *Q. Rev. Biol.* 147 (3), 286–287. doi:10.1119/1.13295

Nelson, P. H. (2009). Pore-throat sizes in sandstones, tight sandstones and shales. *AAPG Bull.* 93, 329–340. doi:10.1306/10240808059

Nie, R., Zhou, J., Chen, Z., Liu, J., and Pan, Y. (2021). Pore structure characterization of tight sandstones via a novel integrated method: A case study of the sulige gas field, Ordos Basin (northern China). *J. Asian. Earth. Sci.* 213, 104739. doi:10.1016/j.jseaes.2021.104739

Nooruddin, H. A., Hossain, M. E., Al-Yousef, H., and Okasha, T. (2014). Comparison of permeability models using mercury injection capillary pressure data on carbonate rock samples. *J. Petrol. Sci. Eng.* 121, 9–22. doi:10.1016/j.petrol.2014.06.032

Pfeifer, P. (1984). Fractal dimension as working tool for surface-roughness problems. *Appl. Surf. Sci.* 18 (1-2), 146–164. doi:10.1016/0378-5963(84)90042-4

Pfeiferper, P., and Avnir, D. (1983). Chemistry nonintegral dimensions between two and three. *J. Chem. Phys.* 79 (7), 3369–3358.

Qiao, J., Zeng, J., Jiang, S., and Wang, Y. (2020). Impacts of sedimentology and diagenesis on pore structure and reservoir quality in tight oil sandstone reservoirs: Implications for macroscopic and microscopic heterogeneities. *Mar. Pet. Geol.* 111, 279–300. doi:10.1016/j.marpetgeo.2019.08.008

Qu, Y., Sun, W., Tao, R., Luo, B., Chen, Lei., and Ren, D. (2020). Pore-throat structure and fractal characteristics of tight sandstones in Yanchang Formation, Ordos Basin. *Mar. Petrol. Geol.* 120, 104573. doi:10.1016/j.marpetgeo.2020.104573

Schmitt Rahner, M., Halisch, M., Peres Fernandes, C., Weller, A., and Sampaio Santiago dos Santos, V. (2018). Fractal dimensions of pore spaces in unconventional reservoir rocks using X-ray nano- and micro-computed tomography. *J. Nat. Gas. Sci. Eng.* 55, 298–311. doi:10.1016/j.jngse.2018.05.011

Shao, X., Pang, X., Li, H., and Zhang, X. (2017). Fractal analysis of pore network in tight gas sandstones using NMR method: A case study from the Ordos Basin, China. *China* 31 (10), 10358–10368. doi:10.1021/acs.energyfuels.7b01007

Song, Z., Liu, G., Yang, W., Zou, H., Sun, M., and Wang, X. (2018). Multi-fractal distribution analysis for pore structure characterization of tight sandstone—a case study of the upper paleozoic tight formations in the longdong district, Ordos Basin. *Mar. Petrol. Geol.* 92, 842–854. doi:10.1016/j.marpetgeo.2017.12.018

Sun, L., Zou, C., Jia, A., Wei, Y., Zhu, R., Wu, S., et al. (2019). Development characteristics and orientation of tight oil and gas in China. *Petrol. explor. Dev.* 46, 1073–1087. doi:10.1016/s1876-3804(19)60264-8

Wang, F., Jiao, L., Liu, Z., Tan, X., Wang, C., and Gao, J. (2018a). Fractal analysis of pore structures in low permeability sandstones using mercury intrusion porosimetry. *J. POROUS. MEDIA.* 21 (11), 1097–1119. doi:10.1615/JPorMedia.2018021393

Wang, F., and Wang, L. (2022). Pore structure analysis and permeability prediction of shale oil reservoirs with HPMI and NMR: A case study of the permian lucaogou Formation in the jimsar sag, junggar basin, NW China. *J. Petrol. Sci. Eng.* 214, 110503. doi:10.1016/j.petrol.2022.110503

Wang, F., Yang, k., and Cai, J. (2018b). Fractal characterization of tight oil reservoir pore structure using nnclear mahnetic resonance and mercury intrusion porosimetry. *Fractals* 26 (2), 1840017. doi:10.1142/S0218348X18400170

Wang, F., Yang, K., You, J., and Lei, X. (2019). Analysis of pore size distribution and fractal dimension in tight sandstone with mercury intrusion porosimetry. *Physics* 13, 102283. doi:10.1016/j.rinp.2019.102283

Wang, F., and Zeng, F. (2020). Novel insights into the movable fluid distribution in tight sandstones using nuclear magnetic resonance and rate-controlled porosimetry. *Nat. Resour. Res.* 29, 3351–3361. doi:10.1007/s11053-020-09635-1

Wang, Q., Chen, D., Wang, F., Gao, X., Zou, Yi., Tian, Z., et al. (2021a). Origin and distribution of an under-pressured tight sandstone reservoir: The Shaximiao Formation, central Sichuan Basin. *Mar. Petrol. Geol.* 132, 105208. doi:10.1016/j.marpetgeo.2021.105208

Wang, Q., Zeng, F., Wang, L., Hou, X., Cheng, H., and Gao, J. (2021b). Fractal analysis of tight sandstone petrophysical properties in unconventional oil reservoirs with NMR and rate-controlled porosimetry. *Energy. Fuels.* 35, 3753–3765. doi:10.1021/acs.energyfuels.0c03394

Washburn, E. W. (1921). The dynamics of capillary flow. *Phys. Rev.* 17, 273–283. doi:10.1103/physrev.17.273

Wu, K., Chen, D., Zhang, W., Yang, H., Wu, H., Cheng, X., et al. (2022a). Movable fluid distribution characteristics and microscopic mechanism of tight reservoir in Yanchang Formation, Ordos Basin. *Front. Earth. Sc-switz.* 10, 840875. doi:10.3389/feart.2022.840875

Wu, K., Liu, C., Ouyang, S., Luo, B., Zhao, D., Sun, W., et al. (2022b). Investigation of pore-throat structure and fractal characteristics of tight sandstones using HPMI, CRMI, and NMR methods: A case study of the lower

shihezi Formation in the sulige area, Ordos Basin. *J. Petrol. Sci. Eng.* 210, 110053. doi:10.1016/j.petrol.2021.110053

Xiao, D., Jiang, S., Thul, D., HuangLu, W. Z., and Lu, S. (2017). Combining rate-controlled porosimetry and NMR to probe full-range pore throat structures and their evolution features in tight sands: A case study in the songliao basin, China. *Mar. Petrol. Geol.* 83, 111–123. doi:10.1016/j.marpetgeo.2017.03.003

Zang, Q., Liu, C., Awan, R. S., Yang, X., Li, G., Wu, Y., et al. (2022a). Occurrence characteristics of the movable fluid in heterogeneous sandstone reservoir based on fractal analysis of NMR data: A case study of the chang 7 member of ansai block, Ordos Basin, China. *J. Petrol. Sci. Eng.* 214, 110499. doi:10.1016/j.petrol.2022.110499

Zang, Q., Liu, C., Awan, R. S., Yang, X., Lu, Z., Li, G., et al. (2022b). Comparison of pore size distribution, heterogeneity and occurrence characteristics of movable fluids of tight oil reservoirs formed in different sedimentary environments: A case study of the chang 7 member of Ordos Basin, China. *Nat. Resour.* 31 (1), 415–442. doi:10.1007/s11053-021-09986-3

Zhang, X., Wu, C., and Li, T. (2017). Comparison analysis of fractal characteristics for tight sandstones using different calculation methods. *J. Geophys. Eng.* 14 (1), 120–131. doi:10.1088/1742-2140/14/1/120

Zhang, Z., and Weller, A. (2014). Fractal dimension of pore-space geometry of an Eocene sandstone formation. *Geophysics* 79, 377–387. doi:10.1190/geo2014-0143.1

Zhu, H., Zhang, T., Zhong, D., Li, Y., Zhang, J., and Chen, X. (2019). Binary pore structure characteristics of tight sandstone reservoirs. *Petrol. explor. Dev.* 46 (6), 1297–1306. doi:10.1016/S1876-3804(19)60283-1

Zou, C., Yang, Z., Tao, S., Li, W., Wu, S., Hou, L., et al. (2012a). Nano-hydrocarbon and the accumulation in coexisting source and reservoir. *Petrol. explor. Dev.* 39, 15–32. doi:10.1016/s1876-3804(12)60011-1

Zou, C., Zhu, R., Liu, K., Su, L., Bai, B., Zhang, X., et al. (2012b). Tight gas sandstone reservoirs in China: Characteristics and recognition criteria. *J. Petrol. Sci. Eng.* 88-89, 82–91. doi:10.1016/j.petrol.2012.02.001

frontiers | Frontiers in Earth Science

TYPE Original Research
PUBLISHED 02 June 2023
DOI 10.3389/feart.2023.1185213

OPEN ACCESS

EDITED BY
Shuai Yin,
Xi'an Shiyou University, China

REVIEWED BY
Saipeng Huang,
University of Barcelona, Spain
Jianhua He,
Chengdu University of Technology, China

*CORRESPONDENCE
Junyong Zhu,
zhujy22@mails.jlu.edu.cn

RECEIVED 13 March 2023
ACCEPTED 15 May 2023
PUBLISHED 02 June 2023

CITATION
Yiming A, Bian B, Liu H, Wang J, Wang X, Zhu J, Zhu Y, Liu L and Su D (2023), Development characteristics and main controlling factors of Carboniferous volcanic reservoirs in the Shixi area, Junggar Basin.
Front. Earth Sci. 11:1185213.
doi: 10.3389/feart.2023.1185213

Development characteristics and main controlling factors of Carboniferous volcanic reservoirs in the Shixi area, Junggar Basin

Abulimiti Yiming[1], Baoli Bian[1], Hailei Liu[1], Jiangtao Wang[1], Xueyong Wang[1], Junyong Zhu[2]*, Yongcai Zhu[1], Longsong Liu[1] and Dongxu Su[1]

[1]Research Institute of Exploration and Development, Xinjiang Oilfield Company, PetroChina, Karamay, China, [2]College of Earth Sciences, Jilin University, Changchun, China

The Carboniferous volcanic reservoirs in the Shixi area of the Junggar Basin are complex and diverse. Identifying the characteristics and main factors controlling high-quality volcanic reservoirs is the key to increasing oil and gas reserves and production in this area. Through core observations, thin section identification, physical property and pore structure analyses, combined with production data, the main controlling factors and development modes of high-quality reservoirs were analysed. The results show that the Carboniferous strata in the Shixi area mainly contain andesite and dacite of overflow facies, followed by volcanic breccia and tuff of explosive facies. Volcanic reservoirs in the study area are high-porosity–low-permeability and medium-porosity–low-permeability reservoirs. Volcanic breccia of explosive facies has the best physical properties, showing the characteristics of high porosity and medium permeability. The reservoir space is mainly composed of gas cavities, corrosion pores and fractures, among which the corrosion pores are the most important reservoir spaces of the Carboniferous volcanic rocks. Lithology and lithofacies, weathering and corrosion, and fractures are the main factors controlling the development of high-quality volcanic reservoirs. Volcanic rocks that had experienced weathering and denudation for a long time developed a large number of secondary corrosion pores due to the corrosion of soluble minerals or volcanic ash. Fractures further improved the physical properties, causing volcanic rocks to eventually develop into weathering crust reservoirs. The physical properties of the volcanic rocks far away from the weathering crust were improved through primary gas cavities and structural fractures, and these volcanic rocks eventually developed into the inner reservoir.

KEYWORDS

Junggar Basin, Carboniferous, volcanic reservoirs, main controlling factors, development modes

1 Introduction

As a special type of oil and gas reservoir, volcanic reservoirs have become an important new field for global oil and gas exploration (Zhang et al., 2016). At present, more than 300 volcanic oil and gas reservoirs have been discovered in more than 100 countries worldwide, and the potential of oil and gas resources is massive (Wang et al., 2012). At

present, onshore volcanic oil and gas exploration has entered the stage of rapid development, and proven geological reserves have increased greatly. Industrial oil and gas flow has been found in Carboniferous and Permian volcanic rocks in the Songliao Basin, Bohai Bay Basin, Junggar Basin and Santanghu Basin (Wang et al., 2021). Since 1998, great breakthroughs have been made in the exploration of Carboniferous volcanic reservoirs in the eastern Junggar Basin. In 2008, the Kelameili gas field was discovered in the Carboniferous volcanic rocks in the eastern Junggar Basin, and this discovery opened a new opportunity for the exploration and development of volcanic oil and gas in the Junggar Basin (Chen et al., 2020). In recent years, large oil reservoirs, such as C210, JL10, and C471, have been discovered in the northwest margin of the basin, and the proven geological petroleum reserves have reached 250 million tons. With the continuous breakthrough in the exploration of Carboniferous volcanic rocks in the eastern and western Junggar Basin, the exploration of Carboniferous rocks in the hinterland of the basin has received attention again. The discovery of Carboniferous oil and gas in the hinterland of the basin began in 1992. Well SX1, which was drilled in the Carboniferous buried hill of the Shixi uplift, yielded high industrial oil flow, which opened the door for the exploration of the Shixi oilfield, with proven geological reserves of 38.94 million tons (Li H et al., 2021). After decades of exploration and research, major breakthroughs have been made in SX16, SX161H, SX101, SX102, and other wells, indicating that the Shixi area has large prospects for oil and gas resources.

The reservoir characteristics and physical properties of volcanic rocks play an important role in the accumulation and distribution of oil and gas in volcanic strata. Volcanic reservoir spaces are of various types. According to their morphological characteristics, volcanic reservoir spaces can be divided into primary pores, secondary pores and fractures. The reservoir spaces of the Carboniferous volcanic rocks in the Shixi area are mainly primary pores, corrosion pores and fractures, which are found in typical pore–fracture reservoirs (Li S B et al., 2021; Wang and Wang, 2021). The types of reservoir spaces in volcanic rocks with different lithologies are different. Some lava has primary gas cavities, while some volcanic breccia and tuff have secondary corrosion pores. Diagenesis controls the preservation of primary pores and the development of secondary pores during the evolution of volcanic rocks (Feng et al., 2015; Lan et al., 2021). Wang et al. (2021) divided the diagenetic stage of deep volcanic rocks in the Songliao Basin into the cooling diagenesis stage, postmagmatic hydrothermal stage, weathering denudation and leaching stage and burial diagenesis stage according to the diagenetic evolutionary sequence and spatiotemporal pore evolutionary process. Qu et al. (2014) divided the diagenesis of the Kelameili gas field in the Junggar Basin into a syngenetic stage, epigenetic stage and burial diagenesis stage. The burial evolution of volcanic rocks determines the diagenetic evolutionary sequence of a region. Previous studies have suggested that volatilization, corrosion, shrinkage, devitrification, and recrystallization play an important role in improving volcanic reservoirs, while hydrothermal precipitation and crystallization, compaction, cementation and filling in the penecontemporaneous period are not conducive to the development of volcanic reservoirs (Guo H et al., 2021). At present, volcanic activity, tectonic movement, lithology, lithofacies, corrosion and weathering are considered to be important factors controlling the development of high-quality volcanic reservoirs. Qin et al. (2012) believed that volcanic reservoirs in the Junggar Basin were mainly distributed in tectonic belts with strong tectonic action and relatively developed fractures. Lithology and lithofacies are the basic influencers of reservoir properties. Weathering and leaching are very important for influencing reservoir properties. Volcanic rocks can become effective reservoirs only after weathering and leaching occur. A large number of primary gas cavities formed by volcanic eruptions are not connected, while weathering and leaching can connect the reservoir pores near the weathering crust to form effective reservoirs.

The lithology and lithofacies of the Carboniferous volcanic rocks in the Shixi area are complicated, and the long-term weathering and multistage tectonic transformation cause the volcanic rocks to have strong heterogeneity. Explorations show that there are great differences in the gas content and productivity of wells in the Shixi area. Therefore, it is urgent to identify the types and characteristics of high-quality Carboniferous volcanic reservoirs in the study area and determine the main factors controlling the development of high-quality volcanic reservoirs. Based on a summary of previous research results, combined with the production data and experimental analysis, this paper carried out research on the characteristics of volcanic reservoirs, the main controlling factors and the development model of high-quality reservoirs. The research results are expected to provide a geological basis for predicting the distribution of high-quality volcanic reservoirs and guiding future exploration and development in the Shixi area.

2 Geological setting

The Shixi area is located in the subunits of the Shixi uplift and Mobei uplift in the southern part of the Luliang uplift in the centre of the Junggar Basin and is adjacent to the West sag of the Pen 1 well and the Shinan sag in the north and south, respectively, with superior oil and gas conditions (Sun et al., 2019). The strata in the Shixi area are well developed, ranging from Carboniferous to Neogene. From bottom to top, the strata are as follows: Carboniferous strata, the Permian Wuerhe Formation (P2w); Triassic Baikouquan Formation (T1b), Karamay Formation (T2k) and Baijiantan Formation (T3b); Jurassic Badaowan Formation (J1b), Sangonghe Formation (J1s), Xishanyao Formation (J2x), and Toutunhe Formation (J2t); and Cretaceous strata. The Permian is missing in the main part of the Shixi uplift, forming an angular unconformity. The top of the Jurassic is unconformable with the Cretaceous. In the early Carboniferous period, the Luliang island arc was affected by the subduction of oceanic crust, which resulted in large-scale volcanic eruptions and the development of extremely thick volcanic rocks. The drilling results show that the upper Carboniferous series in the Shixi area mainly contains alternating overflow facies and explosive facies, but mainly overflow facies. The rock types of overflow facies mainly include basalt, andesite, dacite and rhyolite. Volcanic breccia and tuff are the main explosive facies. The upper Carboniferous volcanic rocks can form large-scale oil and gas reservoirs by connecting with the oil- and gas-generating depression through the large convex fault (Figure 1).

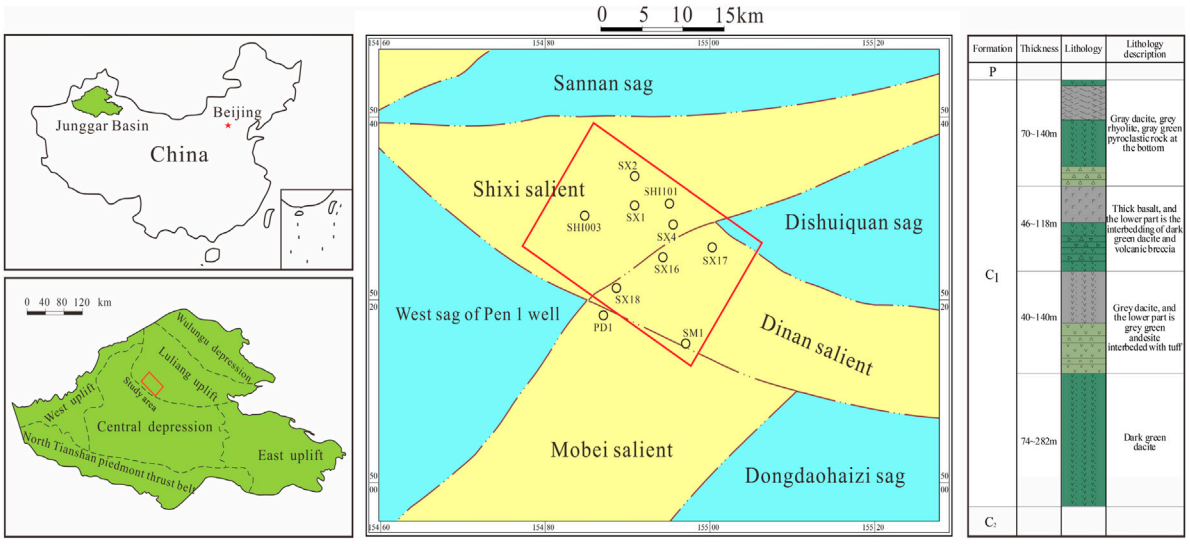

FIGURE 1
Location of the study area and lithological histogram of the Carboniferous strata.

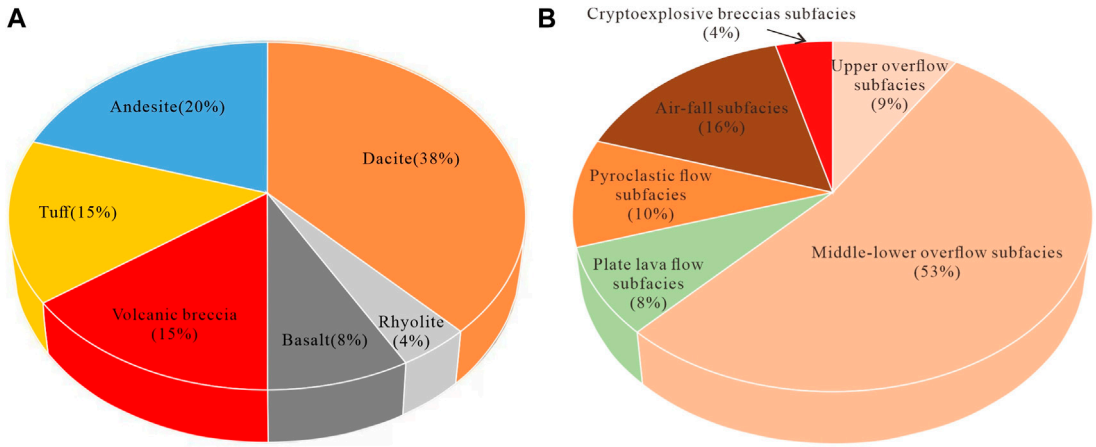

FIGURE 2
Lithologies **(A)** and lithofacies **(B)** statistics of Carboniferous volcanic rocks in the Shixi area.

3 Samples and experiments

3.1 Samples

In this study, Carboniferous volcanic rock cores from 9 wells in the Shixi area were observed and described, and volcanic rock core samples from 6 wells were collected for experimental analyses of the lithology and reservoir.

3.2 Experiments

An Olympus microscope was used to observe rock thin sections. The minerals, pores, lithologies and other characteristics of volcanic rock samples were analysed. Samples of different lithologies were selected for the subsequent experimental analysis of reservoir physical properties and pore structures.

An Axios-max wavelength dispersive X-ray fluorescence spectrometer was used to analyse the major elements of volcanic rocks. Based on GB/T14506-2010, the test was conducted at 24°C, and the relative humidity was 24%. The instrument used for trace element analysis was a NexION300D plasma mass spectrometer. Based on GB/T14506.30-2010, the test was conducted at 20°C, and the relative humidity was 22%.

Petrophysical properties (porosity and permeability) were completed at Northeast Petroleum University. The experimental equipment was a PoroPDP-200 overburden pressure porosimeter from American Core Company, and the experimental test was

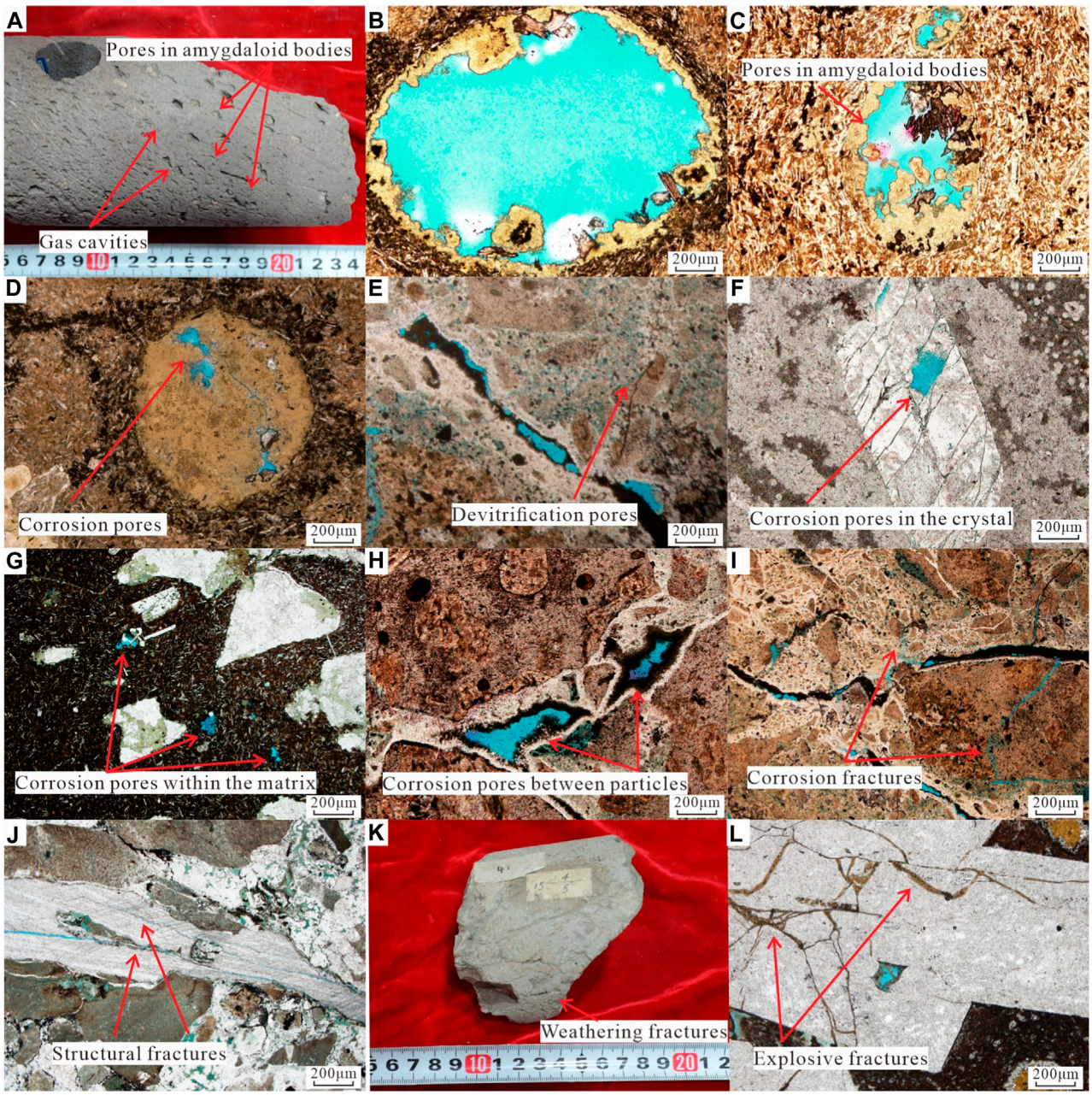

FIGURE 3
Characteristics of the volcanic reservoir space in the Shixi area. [**(A)**. Pores in amygdaloid bodies, SX4, 4,720 m; **(B)** Gas cavities, SX16, 4,805 m; **(C)** Apricot kernel inner pores, SX16, 4,806 m; **(D)** Corrosion pores in amygdaloid bodies, SX16, 4,805 m; **(E)** Devitrification pores, SX3, 4,867.5 m; **(F)** Corrosion pores in the crystals, SX4, 4,606 m; **(G)** Corrosion pores in the matrix, SX16, 4,812 m; **(H)** Corrosion pores between particles, SX3, 4,867 m; **(I)** Corrosion fractures, SX3, 4,867.5 m; **(J)** Structural fractures, SX3, 4,721 m; **(K)** Weathering fractures, SX1, 4,295.2 m; **(L)** Explosive fractures, SX4, 4,822.68 m).

carried out according to the SY/T5336-1996 national standard. After the samples were washed and dried, 25 massive rock samples were used under the condition of 25°C. The porosity of each sample was measured and calculated according to Boyle's law, and the permeability was measured by the unsteady state method.

Nitrogen adsorption experiments were completed at Northeast Petroleum University. The experiment was carried out by the fully automatic gas adsorption instrument ASAP2460 specific surface area and pore analyser of Mack Instruments, which followed the national standards GB/T19587-2004 and GB/T21651.2-2008 of the People's Republic of China. Nitrogen was used as the adsorbent, and the corresponding time points and different nitrogen adsorption amounts were recorded at −195.8°C for adsorption experiments (Lollar et al., 2014; Hirschmann and Cottrell, 2017).

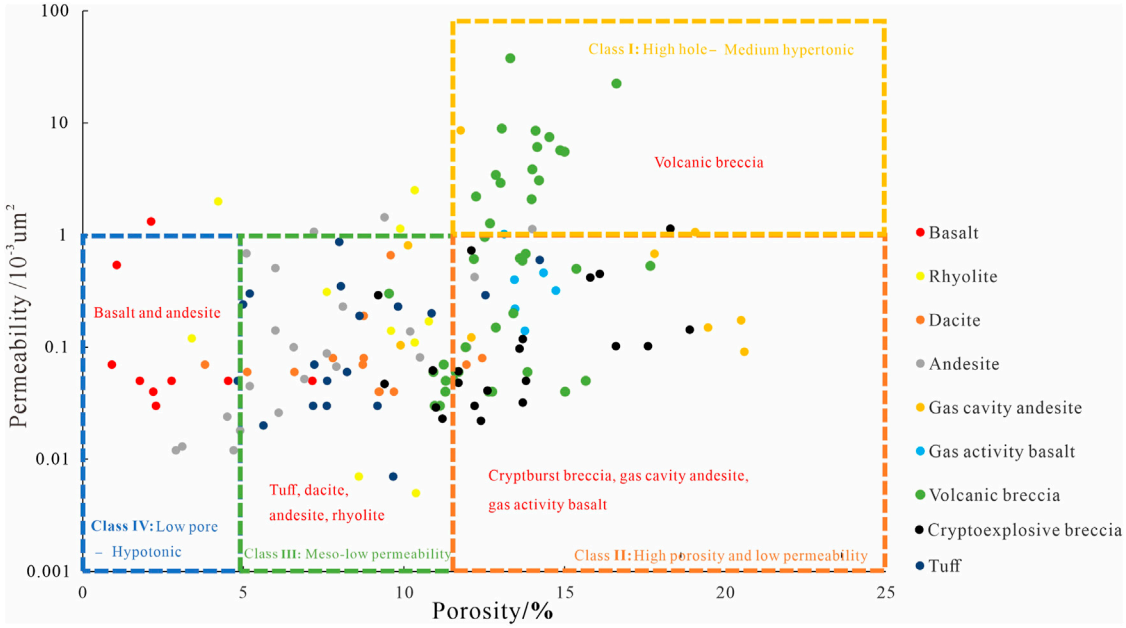

FIGURE 4
Physical properties of Carboniferous volcanic rocks in the Shixi area.

4 Results

4.1 Volcanic lithology

The division of the lithology and lithofacies of volcanic rocks is the basic work that is conducted to study volcanic reservoirs. According to the logging data of wells in the study area, combined with core observations and descriptions and thin section identification, the lithology of Carboniferous volcanic rocks in the Shixi area was identified based on the classification scheme of volcanic rock lithology (Wang et al., 2003; Zhang J et al., 2010; Xue et al., 2021). The Carboniferous volcanic rocks in the study area can be divided into volcanic lava and pyroclastic rock. Volcanic lava can be divided into basic basalt, intermediate andesite, intermediate–acidic dacite and acidic rhyolite. Pyroclastic rocks include tuff and volcanic breccia. The intermediate-acidic dacite and intermediate andesite in the study area are the most developed, accounting for 38% and 20% of the total lithology. The second most common rocks are volcanic breccia and tuff, which account for an equal proportion (15%). Basic basalt (8%) and acidic rhyolite (4%) are only minorly present in the study area (Figure 2A).

According to the lithology–fabric–genetic volcanic lithofacies classification scheme (Qin et al., 2016), the volcanic lithofacies types in the study area include explosive facies, overflow facies and volcanic vent facies. The intermediate–acidic overflow facies include the upper subfacies and middle–lower subfacies. The explosive facies are mainly air-fall and pyroclastic flow subfacies. The volcanic vent facies includes only the cryptoexplosive breccia subfacies, and the basic overflow facies is plate lava flow subfacies. The study area mainly contains the middle–lower subfacies of the intermediate–acidic overflow facies (53%), followed by the air-fall subfacies of the explosive facies (16%). Volcanic vent facies are not developed (Figure 2B).

4.2 Reservoir space types

Core and thin section observations and descriptions show that the reservoir space types of the Carboniferous volcanic reservoirs in the Shixi area are divided into primary pores, secondary pores and fractures. The primary pores of the volcanic reservoirs in the study area are mainly gas cavities and apricot kernel inner pores. The gas cavities are mainly present in the upper subfacies of the intermediate and intermediate–acidic overflow facies. The gas cavities are characterized by directional elongation because they were formed when the lava gradually cooled. Microscopically, pores of different sizes and densities appear in isolation or in groups (Figures 3A, B). Most of the gas cavities were not effectively preserved, but secondary mineral filling with the participation of fluid occurred in the burial stage. Due to the influence of differential filling, some gas cavities did not completely fill the minerals and retained apricot kernel inner pores (Figure 3C). The apricot kernel inner pores are polygonal or angular. Such pores have no obvious traces of corrosion, and their contours are mostly affected by filling minerals. The apricot kernel inner pores are mostly associated with gas cavities; that is, where the primary gas cavities are present, the apricot kernel inner pores are also present.

The secondary pores are mainly corrosion pores formed by corrosion and devitrification pores formed by devitrification. Corrosion pores are the most developed pore type in the Carboniferous volcanic reservoir in the study area and are present in all kinds of volcanic rocks. They formed by a series of corrosion events in the phenocrysts, grains and matrix during diagenetic evolution. According to the different development sites, the corrosion pores can be further divided into intergranular corrosion pores, intragranular corrosion pores, matrix corrosion pores and apricot kernel corrosion pores

TABLE 1 Reservoir physical properties of Carboniferous volcanic rocks in the Shixi area.

Lithology	Porosity ($\frac{\text{Min} \sim \text{Max}}{\text{Average}}$)/%	Permeability ($\frac{\text{Min} \sim \text{Max}}{\text{Average}}$)/$10^{-3}$ μm^2
Basalt	$\frac{0.91 \sim 7.15}{2.757}$	$\frac{0.03 \sim 1.32}{0.244}$
Andesite	$\frac{2.9 \sim 14}{7.32}$	$\frac{0.012 \sim 1.44}{0.291}$
Gas Cavity Andesite	$\frac{9.6 \sim 20.6}{15.704}$	$\frac{0.091 \sim 8.57}{1.307}$
Gas Cavity Basalt	$\frac{13.12 \sim 14.73}{13.812}$	$\frac{0.14 \sim 1.02}{0.427}$
Volcanic Breccia	$\frac{9.54 \sim 17.67}{13.17}$	$\frac{0.03 \sim 37.72}{3.178}$
Cryptoexplosive Breccia	$\frac{9.2 \sim 18.9}{13.452}$	$\frac{0.022 \sim 4.035}{0.192}$
Tuff	$\frac{4.83 \sim 14.23}{8.301}$	$\frac{0.005 \sim 0.87}{0.201}$

(Figures 3D–H). The shape of the corrosion pores is irregular, and their connectivity is related to the mineral properties and corrosion strength. Corrosion pores are present in volcanic reservoirs with high soluble mineral contents and strong fluid activity in the formation. In addition, corrosion pores around gas cavities and fractures are present, indicating that gas cavities and fractures, as channels of fluid migration, promote the development of corrosion pores (Figure 3I). Devitrification pores are microscopic pores formed by devitrification of glass in volcanic rocks, resulting in volume reduction. Devitrification widely exists in tuff in the study area, so devitrification pores are the main pore type in dense tuff (Figure 3E).

The fractures in the study area are mainly structural fractures and corrosion fractures, followed by weathering fractures, blasting fractures, shrinkage fractures, *etc.* The fractures in the study area are relatively developed, and the pores of different scales are connected to form the main oil and gas flow channels, which greatly improves the permeability of volcanic reservoirs. The structural fractures are mostly high-angle fractures and oblique fractures, which are mostly filled with minerals. They have the characteristics of straight, long extensions and deep cutting. The phenomenon of structural fractures cutting through minerals can be observed under the microscope (Figure 3J). Affected by corrosion, corrosion fractures are also present in Carboniferous volcanic reservoirs. Most of them are secondary fractures formed on the basis of the corrosion of tectonic fractures and intergranular fractures filled with soluble minerals, which are often found in volcanic breccia. Carboniferous volcanic rocks are subjected to long-term weathering and denudation, and a large number of weathering fractures are present in the top weathering crust, and these fractures cut each other and break the rocks (Figure 3K). In addition, explosive fractures are also present in some volcanic rocks, especially in cryptoexplosive breccia, which breaks phenocrysts (Figure 3L). Diagenetic shrinkage fractures are not present in the study area, which has little effect on the physical properties of the reservoir.

4.3 Reservoir physical properties

The lithologies of the Carboniferous volcanic rocks in the Shixi area are complex and diverse, and the reservoir properties of volcanic reservoirs with different rock types are obviously different. The reservoir capacity of volcanic reservoirs determines whether oil and gas can accumulate. Therefore, it is very important to identify the reservoir properties of different types of volcanic reservoirs and clarify the types of high-quality volcanic reservoirs for the exploration of volcanic reservoirs in the study areas (Rimmer, 2004; Zhang Y. et al., 2010).

The Carboniferous volcanic reservoirs in the Shixi area are divided into four types according to the characteristics of porosity and permeability (Figure 4): Class I is a high porosity-medium permeability reservoir ($\varphi \geq 12\%$, $K \geq 1\times10^{-3}$ um^2). Class II is a high porosity-low permeability reservoir ($\varphi \geq 12\%$, $K \leq 1\times10^{-3}$ um^2). Class III is a medium porosity-low permeability reservoir ($5\% \leq \varphi < 12\%$, $K \leq 1\times10^{-3}$ um^2). Class IV is a low porosity-low permeability reservoir ($\varphi < 5\%$, $K \leq 1\times10^{-3}$ um^2). The reservoir physical property data show that the heterogeneity of the Carboniferous volcanic reservoir is strong, and the porosity values are mainly between 0.91% and 20.6%, with an average of 12.98%. The permeability values range from 0.005×10^{-3} um^2 to 37.72×10^{-3} um^2, with an average of 1.113×10^{-3} um^2 (Table 1). The Carboniferous volcanic reservoir is a Class II reservoir with high porosity and low permeability and a Class III reservoir with medium porosity and low permeability. The volcanic breccia reservoir of the explosive facies is a Class I high-quality volcanic reservoir, showing high porosity–medium permeability characteristics. The cryptoexplosive breccia reservoir of the volcanic vent facies and the gas-cavity lava reservoir of the upper subfacies of the overflow facies are Class II high-quality volcanic reservoirs, showing high-porosity and low-permeability characteristics.

4.4 Reservoir pore structure

Nitrogen adsorption experiments were carried out to qualitatively and quantitatively characterize the pore structure types and characteristics of volcanic reservoirs. According to the International Union of Pure and Applied Chemistry (IUPAC), hysteresis loops can be roughly divided into four types. Different hysteresis loop morphologies can reflect the characteristics of the pore structure (Wrihgt et al., 1987; Wignall and Twitchett, 1996). In the process of nitrogen injection and adsorption, capillary condensation occurs first in the micropores. With increasing relative pressure, capillary condensation occurs in the mesopores and macropores until all spaces are filled with adsorbed substances

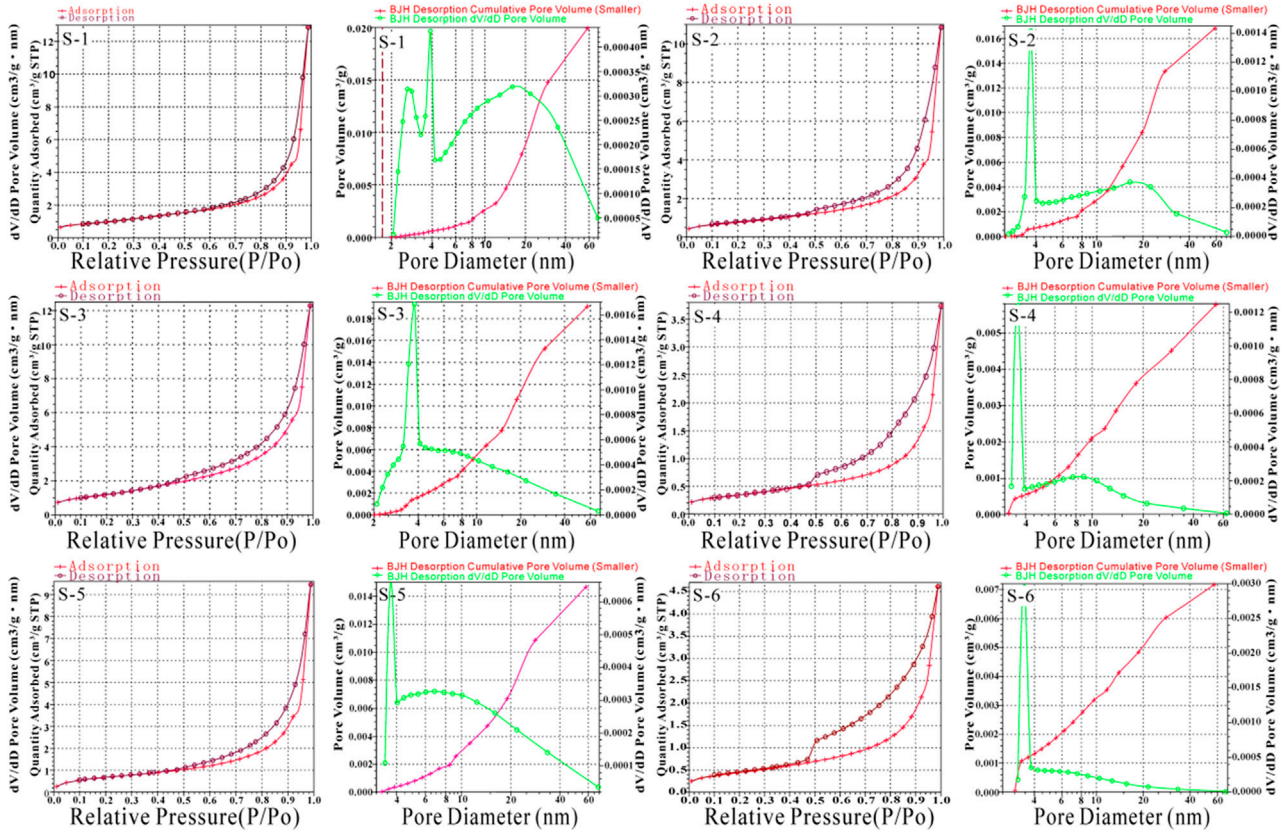

FIGURE 5
Nitrogen adsorption curves and pore size distributions of Carboniferous volcanic rocks. (S-1: Volcanic breccia, SX3, 4,720.81 m; S-2: basalt, SX4, 4,720.8 m; S-3: gas cavity andesite, SX4, 4,590 m; S-4: tuff, SX3, 4,786.59 m; S-5: cryptoexplosive breccia, SX16, 4,805.5 m; S-6: dense basalt, SX4, 4,720.2 m).

(Melnik et al., 2005). However, the removal of capillary condensation occurs first in the macropores in the process of desorption, followed by mesopores and micropores, which leads to the phenomenon that the adsorption curve does not coincide with the desorption curve, namely, the hysteresis phenomenon. The stronger the hysteresis phenomenon is, the more obvious the hysteresis loop is, and the more inhomogeneous the pore size is (Pearce et al., 1984; Quanei and Russell, 2003; Patricia and Nora, 2007).

There are two types of pores in the Carboniferous volcanic reservoirs in the study area: plate-shaped pores and inkpot-shaped pores. Small hysteresis loops are visible in the adsorption–desorption curves of volcanic breccia, gas-cavity lava and cryptoexplosive breccia, which are manifested as H3-type hysteresis loops. This indicates that plate-shaped pores are developed in these three types of volcanic rocks. The connectivity of these volcanic rocks is good. The desorption curves of dense lava and tuff show a sudden drop near P/Po=0.5, and the hysteresis loops do not show adsorption restriction at high relative pressure, indicating H2-type hysteresis loops. This indicates that there are inkpot-shaped pores in these two types of volcanic rocks, with large numbers of small pores and narrow throats (Figure 5).

The specific surface, pore volume, and average pore size of the samples are shown in Table 2. Mesopores and macropores in volcanic breccia, gas-cavity lava and cryptoexplosive breccia are developed, which contribute greatly to the pore volume. However, dense lava and tuff mainly contain micropores and a certain number of mesopores, resulting in small pore volumes, which is consistent with the results of the porosity and permeability of volcanic rocks. The specific surface areas of lava and tuff are larger than those of volcanic breccia, gas-cavity lava and cryptoexplosive breccia because the micropores developed in lava and tuff increase the specific surface area. Therefore, the reservoir properties of volcanic breccia, gas-cavity lava and cryptoexplosive breccia are better than those of lava and tuff in terms of both the pore type and pore structure.

5 Discussion

5.1 Factors controlling high-quality reservoirs

Whether volcanic rocks can become effective reservoirs depends on many factors (Su et al., 2011; Nazari and Riahi, 2020; Chen et al., 2021; Meng et al., 2021). The above analysis shows that the development of Carboniferous high-quality volcanic reservoirs in the Shixi area is mainly controlled by three factors: the lithology and

TABLE 2 Pore structure parameters of Carboniferous volcanic rocks.

Samples	Specific surface/(m^2/g)	Pore volume/(cm^3/g)	Average pore diameter/nm
S-1	3.5815	0.008403	19.9971
S-2	2.8048	0.007396	17.2649
S-3	4.3700	0.010300	13.0399
S-4	7.4481	0.003874	5.8592
S-5	2.2583	0.006504	10.7936
S-6	5.6073	0.004091	6.1035

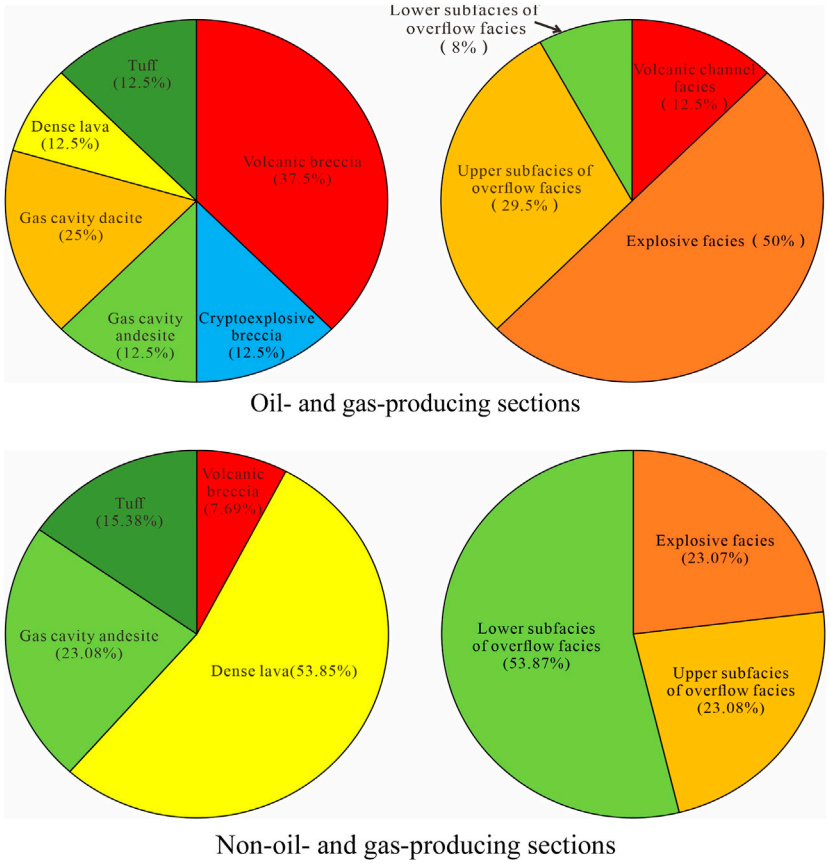

FIGURE 6
Lithologies and lithofacies of the Carboniferous tested oil-containing section in the Shixi area.

lithofacies, weathering and corrosion, and fractures. Favourable lithology and lithofacies are the basis for high-quality reservoir development. Weathering and corrosion are the keys to high-quality reservoir development, and fractures further improve the physical properties of volcanic reservoirs.

5.1.1 Favourable lithology and lithofacies are the basis for high-quality reservoir development

Lithology and lithofacies not only determine the type and development of primary pores but also affect the corrosion and the number of fractures, thus determining the effectiveness of reservoirs (Li et al., 2010; Shan et al., 2011; Wang et al., 2020). According to the statistics of the lithology and lithofacies of the tested oil-containing sections in the Shixi area, it is found that the oil- and gas-producing sections are mainly the volcanic breccia of the pyroclastic flow subfacies and the gas-cavity lava of the upper subfacies, followed by some cryptoexplosive breccia of volcanic vent facies. The non-oil- and gas-producing sections are dominated by dense lava of the lower subfacies (Figure 6).

The volcanic breccia is reformed by weathering and corrosion, and some minerals and volcanic ash in the volcanic breccia have dissolved and form secondary pores (Figure 7A). In addition, the compaction resistance of breccia plays an important role in the preservation of pores, which is beneficial to the formation of high-quality reservoirs (Sruoga and Rubinstein, 2007; Yuan et al., 2015; Guo L et al., 2021).

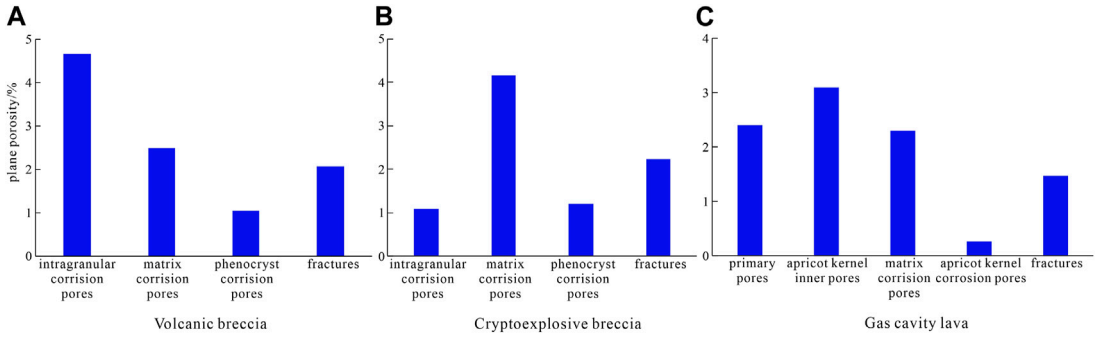

FIGURE 7
Plane porosity analysis of volcanic rocks of different lithologies.

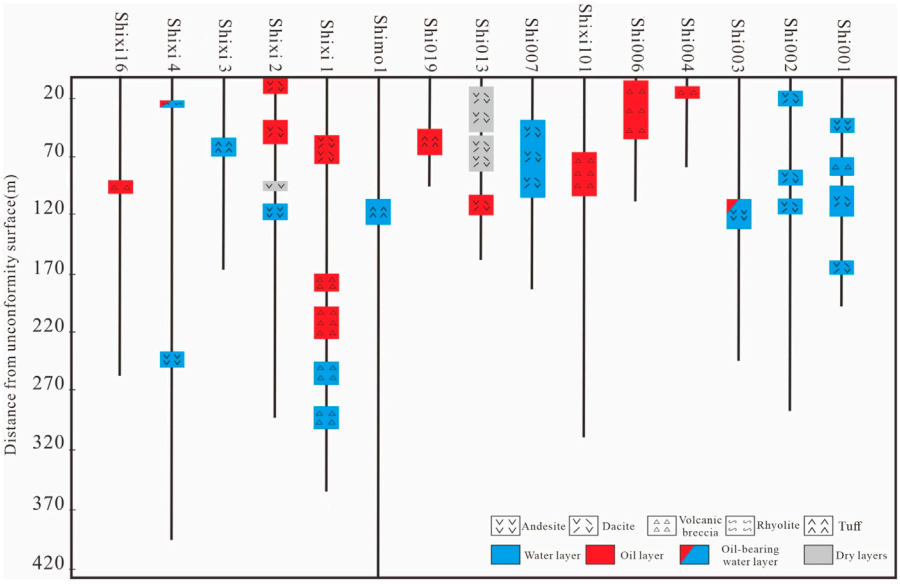

FIGURE 8
Oil test results of the Carboniferous volcanic reservoirs in the Shixi area.

Cryptoexplosive breccia not only contains corrosion pores but also explosive fractures, which also show good physical properties (Figure 7B). The primary gas cavities of gas-cavity lava, which are important reservoir spaces of this kind of reservoir, are quite developed. Additionally, corrosion pores in the gas-cavity lava are also developed (Figure 7C). The concomitant formation of gas cavities and corrosion pores indicates that the primary pores increase the contacts between fluids and minerals. Therefore, volcanic breccia, gas-cavity lava and cryptoexplosive breccia are the lithologic bases for the development of high-quality volcanic reservoirs in the study area.

5.1.2 Weathering and corrosion are the key to the development of high-quality reservoirs

Favourable lithology and lithofacies can provide the basis for high-quality reservoir development, but high-quality reservoirs cannot form due to the lack of late corrosion. The pores and fractures formed by corrosion not only increase the reservoir space but also connect some isolated pores (He et al., 2007; Mao et al., 2015; Ma et al., 2019).

Under the influence of the late Hercynian movement, the closure of the West Junggar Ocean and Kalamari Ocean resulted in an intracontinental tectonic environment in the study area. The Carboniferous volcanic rocks were uplifted and denuded from the end of the Carboniferous to the middle of the Permian. Denudation resulted in the absence of upper Carboniferous strata and lower Permian strata, which provided a prerequisite for the development of volcanic weathering crust reservoirs on top of the Carboniferous strata (Li, 2019a; Fan et al., 2020). Vertically, the tops of volcanic rocks are strongly corroded and contain fractures. As weathering and corrosion weaken, the integrity of deep rocks improves. The

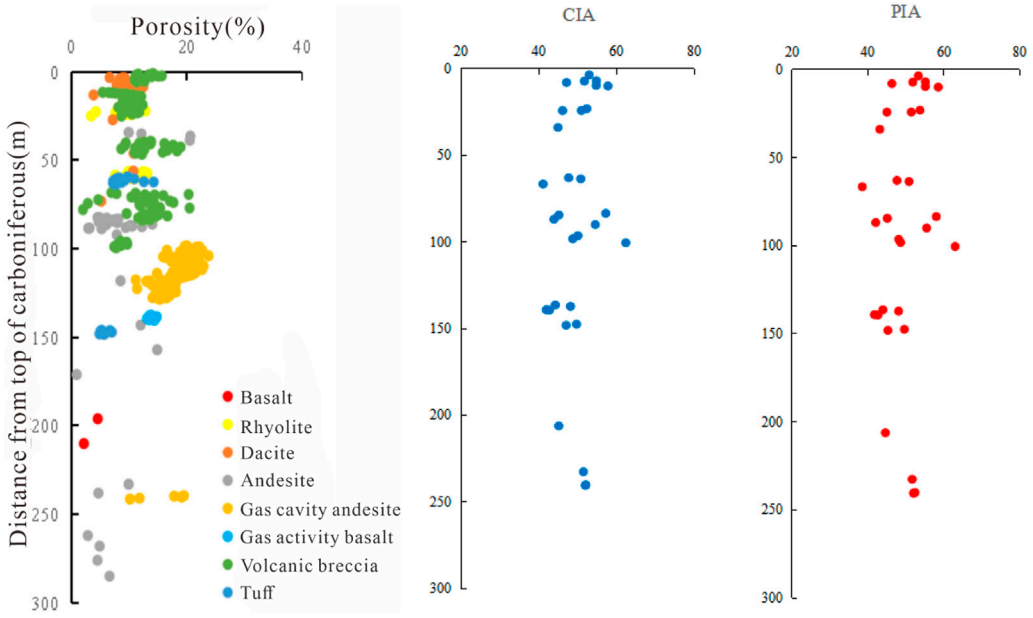

FIGURE 9
Relationships between the porosity, CIA and PIA and the distance from the top of the Carboniferous strata.

development of corrosion pores and fractures is weakened significantly until no development occurs. The oil test results of Carboniferous volcanic reservoirs show that the closer to the top of the Carboniferous, the better the test production of the drilling is, indicating that weathering and corrosion control the distribution of oil and gas in the study area (Figure 8).

The weathering crust underwent hydrolysis, hydration, oxidation and other chemical processes during its formation, which both increased and decreased the contents of elements in volcanic rocks (Liu et al., 2020; Li et al., 2022). The depth of the weathering crust is dictated by the porosity, chemical index of alteration (CIA) and plagioclase index of alteration (PIA) (Figure 9). The porosity, CIA and PIA change regularly based on the distance from the top of the Carboniferous strata. The porosity, CIA and PIA decrease at approximately 200 m from the top of the Carboniferous strata, indicating that 200 m is approximately the bottom of the weathering crust.

5.1.3 Fractures further improve the reservoir physical properties of volcanic reservoirs

Fractures are very important for hydrocarbon accumulation in tight volcanic reservoirs. Fractures not only improve the physical properties of volcanic reservoirs but also serve as the main migration channels for formation fluid, which promotes the development of corrosion pores and fractures. The fractures in the study area are mainly structural fractures and corrosion fractures, of which structural fractures have a great impact on the physical properties of the reservoir (Li et al., 2017; Gao et al., 2021).

Three stages of fractures are present in the study area: the near SN- and NE-trending shear fractures that formed in the middle and late Hercynian, the NW-trending shear fractures that formed in the Indosinian, and the NE- and EW-trending fractures that formed in the Yanshan–Himalayan (Li, 2019b). The closer to the fault zone, the more fractures that develop. Surface water or formation fluid migrates along the faults and fractures, increasing the contact with minerals and effectively improving the corrosion efficiency. Moreover, the faults cause the strata to be uplifted and weathered, which controls the thickness and distribution of the weathering crust reservoir. Figure 10 shows that the unfilled and half-filled fractures in the study area account for approximately 28% and 46% of the total number of fractures, respectively. These unfilled and half-filled fractures play an important role in the enrichment of oil and gas. The porosity and permeability of volcanic reservoirs in the study area are negatively correlated with the distance from the faults, indicating that the closer the volcanic rock is to the fault zone, the higher the porosity and permeability of the reservoir are, and the more favourable the area is for the development of high-quality reservoirs.

5.2 Modes of high-quality volcanic reservoir development

On the basis of identifying the main factors controlling high-quality volcanic reservoirs in the study area, a model for the development of high-quality volcanic reservoirs in the Carboniferous strata in the Shixi area is established (Figure 11). According to the different formation mechanisms, the reservoirs can be divided into weathering crust reservoirs and inner reservoirs. The reservoir space in the weathering crust reservoir is mainly composed of the secondary pores formed by weathering and corrosion. Due to the distance from the top of the Carboniferous strata, the weathering of the inner reservoirs is weak, and the reservoir space is composed of primary gas cavities and fractures.

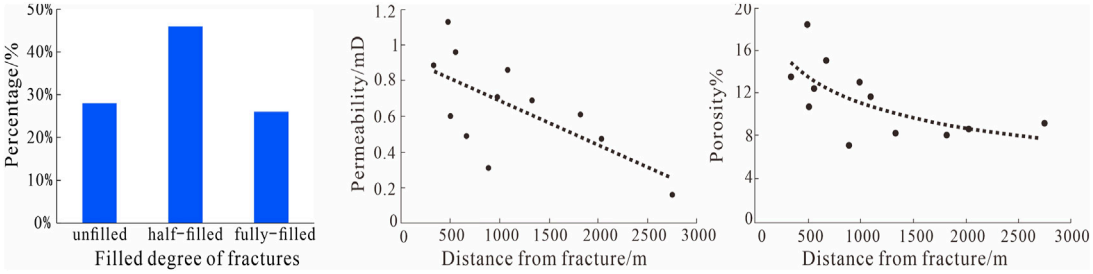

FIGURE 10
Fracture-filling characteristics and relationships between the porosity, permeability and distance from faults.

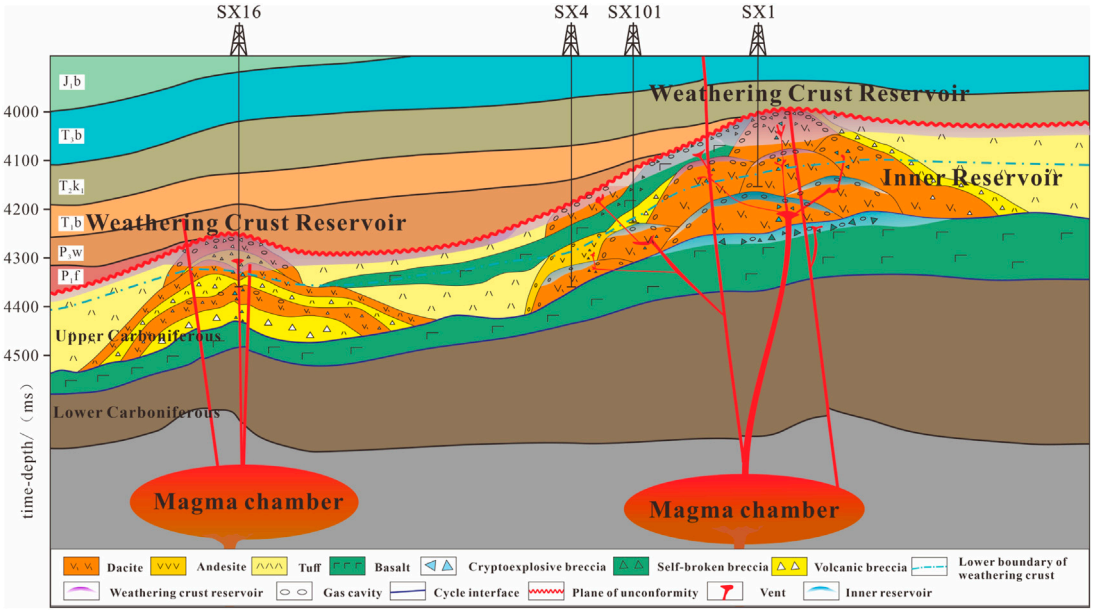

FIGURE 11
Model for the development of Carboniferous high-quality volcanic reservoirs in the study area.

Vertically, the weathering crust reservoir at the top of the Carboniferous strata underwent long-term weathering and corrosion, resulting in a large number of secondary corrosion pores. The weathering crust reservoir also developed a large number of structural fractures and weathering fractures, which not only improved the reservoir properties but also further promoted the corrosion of minerals. The inner reservoir is far from the top of the Carboniferous strata. The corrosion in the inner reservoir was relatively weak, and secondary corrosion pores were not developed, which improved the physical properties through gas cavities and structural fractures. Horizontally, favourable lithology and lithofacies, ancient landforms, and fractures are the most important controlling factors. The volcanic breccia of the pyroclastic flow subfacies of the explosive facies, the gas-cavity lava of the upper subfacies of the overflow facies and the cryptoexplosive breccia of the volcanic vent facies are more likely to contain high-quality reservoirs. Volcanic rocks located in uplifts and slopes are more likely to form high-quality weathering crust reservoirs. Volcanic rocks located in sags can also form high-quality inner reservoirs via primary gas cavities and fractures.

6 Conclusion

The Carboniferous strata in the Shixi area of the Junggar Basin mainly contains intermediate–acidic dacite, andesite and some volcanic breccia and tuff. The volcanic lithofacies are mainly the middle–lower subfacies of the intermediate–acidic overflow facies, followed by the air-fall subfacies and pyroclastic flow subfacies of the

explosive facies. In terms of reservoir characteristics, the secondary corrosion pores in the volcanic rocks are the most developed, followed by the primary gas cavities in the upper subfacies of the overflow facies. In addition, a certain number of fractures are also present in volcanic rocks. Primary pores and fractures promote corrosion, and the association of corrosion pores with primary pores and fractures is common. Volcanic breccia, gas-cavity lava, and cryptoexplosive breccia are three types of high-quality volcanic reservoirs with good physical properties and pore structures in the Shixi area. Favourable lithology and lithofacies, weathering and corrosion, and fractures are the three main factors controlling the development of high-quality volcanic reservoirs. Volcanic breccia, gas-cavity lava, cryptoexplosive breccia and other favourable lithologies underwent weathering, corrosion and fracture transformation to form weathering crust reservoirs, and gas-cavity lava can contain inner reservoirs in the deep Carboniferous strata via primary gas cavities.

Data availability statement

The original contributions presented in the study are included in the article/Supplementary Material, further inquiries can be directed to the corresponding author.

Author contributions

AY and JZ is responsible for the idea, writing and revision of this paper. BB, HL, JW, and XW are responsible for the data analysis and drawing. YZ is responsible for provided research materials. LL and DS is responsible for reviewing and editing. All authors contributed to the article and approved the submitted version.

Funding

This paper is supported by the 14th Five-year Major Project of CNPC "Continental Deep and Ultra-Deep Oil and Gas Enrichment Law and Exploration Evaluation Research" (2021DJ0206) and China Petroleum Prospective Basic Technology Research Project "Marine Devonian-Carboniferous Oil and Gas Geology Research in Northern Xinjiang" (2022DJ0507).

Acknowledgments

The authors would like to thank the staff of the laboratories that performed the tests and analyses. We are also grateful to the editors and reviewers, whose comments improved the quality of this manuscript.

Conflict of interest

Authors AY, BB, HL, JW, XW, YZ, LL, and DS were employed by Xinjiang Oilfield Company.

The remaining authors declare that the research was conducted in the absence of any commercial or financial relationships that could be construed as a potential conflict of interest.

Publisher's note

References

Chen, L., Yang, Y., Wang, F., Lu, H., Zhang, Y., Wang, X., et al. (2020). Exploration history and enlightenment of Junggar Basin. *Xinjiang Pet. Geol.* 41, 505–518. doi:10.7657/XJPG20200501

Chen, G., Li, T., Yang, L., Zhang, G., Li, J., and Dong, H. (2021). Mechanical properties and failure mechanism of combined bodies with different coal-rock ratios and combinations. *J. Min. Strata Control Eng.* 3 (2), 023522. doi:10.13532/j.jmsce.cn10-1638/td.20210108.001

Fan, C., Li, H., Qin, Q., Shang, L., Yuan, Y., and Li, Z. (2020). formation mechanisms and distribution of weathered volcanic reservoirs: A case study of the carboniferous volcanic rocks in northwest Junggar Basin, China. *Energy Sci. Eng.* 8 (8), 2841–2858. doi:10.1002/ese3.702

Feng, Z., Huo, Q., Wang, X., Zeng, H., and Fu, L. (2015). Organic geochemical characteristics and paleosedimentary environment of source rocks in the first member of Qingshankou Formation. *Petroleum Geol. Oilfield Dev. Daqing* 34, 1–7. doi:10.3969/J.ISSN.1000-3754.2015.04.001

Gao, Y., Li, S., Ba, Z., Mirenisha, T., Zhou, H., Xu, C., et al. (2021). Oral administration of *Bacillus subtilis* subunit vaccine significantly enhances the immune protection of grass carp against GCRV-II infection. *Petroleum Geol. Oilfield Dev. Daqing* 40, 30–41. doi:10.3390/v14010030

Guo, H., Ji, M., Sun, Z., and Zhou, Z. (2021). Energy evolution characteristics of red sandstone under cyclic load. *J. Min. Strata Control Eng.* 3 (4), 043019. doi:10.13532/j.jmsce.cn10-1638/td.20211008.001

Guo, L., Zhou, D., Zhang, D., and Zhou, B. (2021). Deformation and failure of surrounding rock of a roadway subjected to mining-induced stresses. *J. Min. Strata Control Eng.* 3 (2), 023038. doi:10.13532/j.jmsce.cn10-1638/td.20200727.001

He, X., Liu, Y., Xu, X., Liu, B., and Zhang, S. (2007). Controlling factors of Carboniferous volcanic reservoirs and favorable reservoir prediction in Xi Quan area, Junggar Basin. *Lithol. Reserv.* 29, 42–51. doi:10.3969/j.issn.1673-8926.2017.03.006

Hirschmann, M. M., and Cottrell, E. (2017). Effect of pressure on Fe3+/Sigma Fe ratio in a mafic magma and consequences for magma ocean redox gradients. *Geochimica Cosmochimica Acta J. Geochem. Soc. Meteorit. Soc.* 204, 83–103. doi:10.1016/j.gca.2017.01.023

Lan, S., Song, D., Li, Z., and Liu, Y. (2021). Experimental study on acoustic emission characteristics of fault slip process based on damage factor. *J. Min. Strata Control Eng.* 3 (3), 033024. doi:10.13532/j.jmsce.cn10-1638/td.20210510.002

Li, W., He, S., Tan, K., Zhang, F., and Zhao, Y. (2010). New perspective for phage display as an efficient and versatile technology of functional proteomics. *Nat. Gas. Geosci.* 21, 909–919. doi:10.1007/s00253-009-2277-0

Li, H., Qin, Q., Li, Z., Fan, C., Zhong, K., Li, Z., et al. (2017). Characteristics and distribution of cracks in Carboniferous buried volcanic reservoirs of the Shixi oilfield. *Geol. Explor.* 53 (6), 1219–1228. doi:10.13712/j.cnki.dzykt.2017.06.018

Li, A., Su, S., Li, X., Zhang, J., Jing, C., and Zhao, Z. (2022). Effects of organic matter graphitization on shale gas accumulation in the lower paleozoic longmaxi formation from the changning area, southern sichuan basin. *Lithosphere* 12, 7102509. doi:10.2113/2022/7102509

Li, H., Li, J., Xu, X. Y., Yang, G. X., Wang, Z. P., Xu, Q., et al. (2021). Petrogenesis and tectonic implications of alkali basalts in kalamaili area, east junggar, Xinjiang (NW China): Constraints from petrology, geochronology and geochemistry. *Acta Geol. Sin.* 95 (11), 3282–3300. doi:10.19762/j.cnki.dizhixuebao.2020281

Li, S. B., Guo, X. G., Zheng, M. L., Wang, Z. S., and Liu, X. L. (2021). Lithology identification of Carboniferous volcanic rocks in Xiquan area, eastern Junggar Basin. *Lithol. Reserv.* 33 (1), 258–266. doi:10.12108/yxyqc.20210124

Li, Z. (2019a). *Study on reservoir characteristics of Carboniferous volcanic weathered crust reservoir in Shixi oilfield, Junggar abdomen*. Chengdu: Southwest Petroleum University. doi:10.27420/d.cnki.gxsyc.2019.000185

Li, Y. X. (2019b). *Fracture characteristics and prediction of carboniferous volcanic rocks in Shixi Oilfield, Junggar Basin*. Chengdu: Southwest Petroleum University. doi:10.27420/d.cnki.gxsyc.2019.000738

Liu, X., Wang, Q., Dai, L., Liu, S., and Hao, Y. (2020). Reservoir characteristics and formation mechanisms of lacustrine Carbonate and volcanics mixing sediments, Laizhouwan Sag. *Earth Sci.* 45, 3579–3588. doi:10.3799/dqkx.2020.119

Lollar, B. S., Onstott, T. C., Lamcrampe-Couloume, G., and Ballentine, C. J. (2014). The contribution of the Precambrian continental lithosphere to global H_2 production. *Nature* 516 (7531), 379–382. doi:10.1038/nature14017

Ma, S., Chen, C., Luo, J., Wei, L., Liu, Y., Dai, J., et al. (2019). Research of major controlling factors on favorable reservoir of the Carboniferous volcanic rocks in Xi Quan area, Junggar Basin. *Geol. J. China Univ.* 25, 197–205. doi:10.16108/j.issn1006-7493.2018087

Mao, Z., Zhu, R., Luo, J., Wang, J., Du, Z., Su, L., et al. (2015). Reservoir characteristics, formation mechanisms and petroleum exploration potential of volcanic rocks in China. *Petroleum Sci.* 12, 54–66. doi:10.1007/S12182-014-0013-6

Melnik, O. E., Barmin, A. A., and Sparks, R. S. J. (2005). Dynamics of magma flow inside volcanic conduits with bubble overpressure buildup and gas loss through permeable magma. *J. Volcanol. Geotherm. Res.* 143, 53–68. doi:10.1016/j.jvolgeores.2004.09.010

Meng, Q., Jin, Z., Sun, D., Liu, Q., Zhu, D., Liu, J., et al. (2021). Geological background and exploration prospects for the occurrence of high-content hydrogen. *Pet. Geol. Exp.* 43 (02), 208–216. doi:10.11781/sysydz202102208

Nazari, S. M., and Riahi, M. A. (2020). Geomechanical unit modeling using seismic and well log data in one of the southwestern Iranian oilfields. *Pet. Explor. Prod. Technol.* 10 (7), 2805–2813. doi:10.1007/s13202-020-00962-w

Patricia, S., and Nora, R. (2007). Processes controlling porosity and permeability in volcanic reservoirs from the Austral and Neuquen basins, Argentina. *AAPG Bull.* 9, 115–129. doi:10.1306/08290605173

Pearce, J. A., Harris, N. B. W., and Tindle, A. G. (1984). Trace element discrimination diagrams for the tectonic interpretation of granitic rocks. *Petro* 25, 956–983. doi:10.1093/petrology/25.4.956

Qin, X., Shi, Y., Wu, W., Kou, Y., Wang, L., Li, X., et al. (2012). Controlling factors of carboniferous volcanic reservoirs in Junggar Basin. *Acta Sci. Nat. Univ. Pekin.* 48, 54–60. doi:10.13209/j.0479-8023.2012.009

Qin, Z., Wei, P., and Zhang, S. (2016). The lithofacies of Carboniferous volcanic rocks in Dixi-Wucaiwan area. *J. Southwest Petroleum Univ. Sci. Technol. Ed.* 38, 9–21. doi:10.11885/j.issn.16745086.2014.12.07.04

Qu, J., Gao, C., Cha, M., and Zhang, Y. (2014). Eye and vision (E & V): The critical link between eye and vision. *J. China Univ. Petroleum Ed. Nat. Sci.* 38, 1–8. doi:10.1186/s40662-014-0001-3

Quanei, S. L., and Russell, K. (2003). Rock strength as a metric of welding intensity in pyroclastic deposits. *Eur. J. Mineralogy* 15, 855–864. doi:10.1127/0935-1221/2003/0015-0855

Rimmer, S. M. (2004). Geochemical paleoredox indicators in devonian-mississippian black shales, central appalachian basin (USA). *Chem. Geol.* 206, 373–391. doi:10.1016/j.chemgeo.2003.12.029

Shan, X. L., Chen, Y. P., Tang, L. M., and Yi, J. (2011). Comprehensive evaluation method for volcanic rock reservoirs and its application: Taking songnan gas field for example. *J. Shandong Univ. Sci. Technol.* 30 (3), 1–6. doi:10.16452/j.cnki.sdkjzk.2011.03.001

Sruoga, P., and Rubinstein, N. (2007). Processes controlling porosity and permeability in volcanic reservoirs from the Austral and Neuquen basins, Argentina. *AAPG Bull.* 91, 115–129. doi:10.1306/08290605173

Su, P., Qin, Q., Yuan, Y., and Jiang, F. (2011). Characteristics of volcanic reservoir fractures in upper wall of Hong Che fault belt. *Xinjiang Pet. Geol.* 32, 457–460. CNKI: SUN:XJSD.0.2011-05-005.

Sun, J., Xue, J., Hou, G., Wu, A., Song, M., and Zhu, F. (2019). Sedimentary characteristics and models of sandy clastic flow in lacustrine depression: A case study of jurassic Sangonghe Formation in bun-1 jing Xi depression, Junggar Basin. *J. China Univ. Min.* 13, 858–869. doi:10.13247/j.cnki.jcumt.000973

Wang, J., and Wang, X. (2021). Seepage characteristic and fracture development of protected seam caused by mining protecting strata. *J. Min. Strata Control Eng.* 3 (3), 033511. doi:10.13532/j.jmsce.cn10-1638/td.20201215.001

Wang, P., Chi, Y., and Liu, W. (2003). Volcanic facies in Songliao Basin: Class type, characteristics and reservoir significance. *J. Jilin Univ. (Earth Sci. Ed.* 33, 449–456. doi:10.13278/j.cnki.jjuese.2003.04.011

Wang, W., Gao, B., Wei, P., Pan, J., Li, F., and Yi, Z. (2012). Research on volcanic reservoirs characteristics and oil and gas accumulation model. *Prog. Geophys.* 27, 2478–2491. doi:10.6038/j.issn.1004-2903.2012.06.023

Wang, L., Xu, Y., Zhang, Y., Liu, Z., and Shang, F. (2020). Predominant factors and development mode of carboniferous reservoirs in chepaizi uplift, Junggar Basin. *J. Northeast Petroleum Univ.* 44, 79–90. doi:10.3969/j.issn.2095-4107.2020.02.008

Wang, H., Lin, C., Jiang, F., Wang, J., Zhao, Y. H., and Xing, B. (2021). Risk factors for early dislocation of the hip after periacetabular tumour resection and endoprosthetic reconstruction of the hemipelvis, Songliao Basin. *Glob. Geol.* 40 (2), 382–390. doi:10.3969/j.issn.1004-5589.2021.02.015

Wignall, P. B., and Twitchett, R. J. (1996). Oceanic anoxia and the end Permian mass extinction. *Science* 272, 1155–1158. doi:10.1126/science.272.5265.1155

Wrihgt, J., Schrader, H., and Holser, W. T. (1987). Paleoredox variations in ancient oceans recorded by rare Earth elements in fossil apatite. *Geochimica Cosmochimica Acta* 51, 631–644. doi:10.1016/0016-7037(87)90075-5

Xue, F., Liu, X., and Wang, T. (2021). Research on anchoring effect of jointed rock mass based on 3D printing and digital speckle technology. *J. Min. Strata Control Eng.* 3 (2), 023013. doi:10.13532/j.jmsce.cn10-1638/td.20201020.001

Yuan, X., Li, W., Dong, H., Wang, T., Zhang, B., and Li, S. (2015). Characteristics and controlling factors of Permian volcanic reservoirs in Kebai area. *Fault-Block Oil Gas Field* 22, 445–449. doi:10.6056/dkyqt201504008

Zhang, F., Hou, Y., Zhu, M., Cui, W., Hu, T., Chen, G., et al. (2016). Current status and development trend of volcanic reservoir logging evaluation technology. *Prog. Geophys.* 31, 1732–1751. doi:10.6038/pg20160443

Zhang, J., Wang, Z., and Zhao, J. (2010). Study on igneous reservoir characteristics and oil and gas accumulation law in Shixi oilfield, Junggar Basin. *Gas Explor. Dev.* 33, 1–6. doi:10.12017/dzkx.2022.041

Zhang, Y., Zhu, X., Li, Y., Wu, J., and Ge, X. (2010). Log evaluation of tight clastic reservoirs in the deep of Western Sichuan Basin. *Nat. Gas. Ind.* 30 (01), 31–35. doi:10.3787/j.issn.1000-0976.2010.01.008

frontiers | Frontiers in Earth Science

TYPE Original Research
PUBLISHED 20 June 2023
DOI 10.3389/feart.2023.1171050

OPEN ACCESS

EDITED BY
Shuai Yin,
Xi'an Shiyou University, China

REVIEWED BY
Zhenwei Guo,
Central South University, China
Jianwei Feng,
China University of Petroleum (East China), China
Jingshou Liu,
China University of Geosciences Wuhan, China
Jiawei Li,
Texas A&M University, United States

*CORRESPONDENCE
Zhaolong Liu,
liuzhaol69@petrochina.com.cn

RECEIVED 21 February 2023
ACCEPTED 06 June 2023
PUBLISHED 20 June 2023

CITATION
Liu Z, Chen D, Gao Z, Wu Y, Zhang Y, Fan K, Chang B, Zhou P, Huang W and Hu C (2023), 3D geological modeling of deep fractured low porosity sandstone gas reservoir in the Kuqa Depression, Tarim Basin.
Front. Earth Sci. 11:1171050.
doi: 10.3389/feart.2023.1171050

3D geological modeling of deep fractured low porosity sandstone gas reservoir in the Kuqa Depression, Tarim Basin

Zhaolong Liu[1]*, Dong Chen[2], Zhiyong Gao[1], Yongping Wu[2], Yongzhong Zhang[1], Kunyu Fan[2], Baohua Chang[1], Peng Zhou[2], Weigang Huang[1] and Chunlei Hu[2]

[1]PetroChina Research Institute of Petroleum Exploration and Development, Beijing, China, [2]Tarim Oilfield Company, Korla, China

The fractured reservoir is one of the significant petroleum reservoir types in China, representing over one-third of total reserves. The Kuqa Depression in the Tarim Basin is dominated by fractured low-porosity sandstone gas reservoirs with characteristic tight matrix, developed fractures, and edge and bottom water. However, the continued development of these reservoirs has led to various problems, including strong reservoir heterogeneity, low well control, complex gas-water relationships, and early water invasion. Addressing these issues requires a detailed understanding of the reservoir's geological characteristics. One method for achieving a fine reservoir description is through the use of 3D geological modeling. This high-level, comprehensive characterization technique is widely used throughout the entire life cycle of oil and gas field development. A 3D geological model can accurately predict the actual underground reservoir characteristics and provide a geological basis for later numerical simulation work. Based on a study of the geological characteristics of the Kuqa Depression in the Tarim Basin, a 3D geological modeling technique was developed, which includes structural modeling, facies modeling, petrophysical modeling, and fracture modeling. This technology has been successfully applied to many deep gas reservoirs in the Kuqa Depression of the Tarim Basin, leading to enhanced gas recovery.

KEYWORDS

fractured gas reservoir, 3D geological modeling, fracture modeling, Tarim Basin, Kuqa Depression

1 Introduction

The concept of 3D geological modeling was proposed in the late 1980s. After 4 decades of development, significant progress has been made in modeling methods, algorithms, and software. Nowadays, it is moving toward big data analysis, deep learning, and artificial intelligence (Høyer et al., 2015; Li et al., 2016; Varga and Wellmann, 2016; Snyder et al., 2018; Liu et al., 2021a; Zhou et al., 2021; Shi and Wang, 2022). 3D geological modeling is an interdisciplinary field that integrates geology, mathematics, and computer science. This method comprehensively utilizes seismic, geology, well logging, well testing, and reservoir engineering data to establish a 3D digital quantitative geological model by quantitatively characterizing the structure, sedimentation, reservoir properties, and fluid properties (Jia

et al., 2007; Wu and Li, 2007; Calcagno et al., 2012; Jørgensen, 2015; Schneeberger et al., 2017; Ursegov et al., 2018a; Grose et al., 2019; Chen et al., 2021; Yuan et al., 2022; Zhan et al., 2022). Numerous studies have been conducted on 3D geological modeling in recent years. For example, Qiu and Jia (2000) summarized the technology development of geological modeling in the past decade in China and accurately proposed the development direction of the fine outcrop study, stochastic modeling method, high-resolution sequence stratigraphy, and well-to-seismic ties. By using the modeling method of "multi-phase constraint, hierarchical facies control, and multi-step modeling", Guo et al. (2015) solved the problem of poor application of traditional modeling methods in braided fluvial tight sandstone gas reservoir of the Sulige gas field, and it improved the accuracy and reliability of the prediction model. Hu et al. (2014) built an accurate model highly consistent with the oilfield production performance by applying the "multi-stage, multi-condition" constraint modeling method of seismic inversion. Ursegov et al. (2018b) proposed a new adaptive approach to create full-field geological and hydrodynamic models of unconventional carbonate reservoirs with heavy oil, and the adaptive hydrodynamic models were history-matched. Irakarama et al. (2021) proposed a new method for implicit structural modeling that extended the inherent properties of the classic one-dimensional discrete second derivative operator to higher dimensions, and the results were robust and numerically efficient.

The Kuqa Depression development of the Tarim Oilfield currently faces the challenge of maintaining stable production and expediting production initiation. One crucial issue that needs to be addressed is the determination of an optimal well count and gas production rate within the Kuqa Depression. However, due to the limited availability of data, it becomes imperative to establish a refined 3D geological model that accurately represents the subsurface characteristics during this development period. 3D geological modeling is an essential technique for the characterization of reservoirs and is widely used in all stages of oil and gas field development. The geological model provides the basis for the reservoir development plan, such as the prediction of the development index, the deployment of well locations, and the design of well trajectories. However, due to the unique reservoir characteristics of deep burial (6000–8000 m), strong heterogeneity (sand ratio of 15%–90%), low matrix porosity (4%–12%), and fracture development (0.1–0.8 numbers per meter) in the Kuqa Depression of the Tarim Basin, there are several challenges in 3D geological modeling. Firstly, due to the buried depth of the Kuqa reservoir being generally more than 7,000 m, the poor seismic data limits the accuracy of the underground structure characterization. Secondly, the "small number of wells and fast production construction" development plan only allows for 1–3 wells at the early development stage, making it difficult to predict reservoir properties at the edge accurately. Thirdly, with a low well pattern density of 8–12 wells per square kilometer and a large well spacing of 2–5 km, it is challenging to predict inter-well characteristics accurately. Finally, the widespread development of fractures in the Kuqa reservoir presents difficulties in describing fracture parameters such as shape, length, and aperture and predicting fracture distribution through 3D geological modeling.

2 Geological setting

The Kuqa Depression of the Tarim Basin is mainly a fractured gas reservoir with abundant resources. The proven reserves of the Kuqa reservoir are 1476.7 billion cubic meters, which accounts for 68% of the proven gas reserves and 72% of the gas production in the Tarim Oilfield. It is the main block responsible for increasing reserves and production in the Tarim Oilfield (Figure 1). Keshen 8, Keshen 24, Dabei 102, Dabei 201, Bozi 1, Bozi 3, and other gas fields are the primary reservoirs, and they generally have characteristics of ultra-deep, high temperature, high pressure, low porosity, low permeability, and developed fractures. The reservoir depth ranges between 6,000 and 8,000 m, while the reservoir pressure and temperature range between 100 and 130 MPa and 140°C–190°C, respectively. Additionally, the reservoir thickness ranges between 260 and 350 m, while the effective matrix porosity and permeability are 4%–12% and 0.05–0.15×10 $^{-3}$μm^2, respectively. Currently, the total number of gas wells in this area is 232, with 182 wells in production (78.4% of the total). The average well production is 374,000 m^3/day, and the gas recovery rate ranges between 2% and 3%.

3 Materials and methods

The Kuqa Depression in the Tarim Basin is a sedimentary system that includes alluvial fan, fan delta or braided river delta, and shore-shallow lake (Gu et al., 2001; Zhang et al., 2008; Pan et al., 2013; Lai et al., 2018; Liu et al., 2019; Liu et al., 2021b; Chen et al., 2021; Liu et al., 2022; Liu et al., 2022). The subfacies are mainly subaqueous distributary channels and mouth bars of the fan delta or braided river delta. The provenance is mainly from the South Tianshan debris, and the paleocurrent flow direction is from north to south. The sandbody is relatively stable, and the lithofacies are mainly sandstone and mudstone. The main sandbody of the Kuqa reservoir is formed by multi-stage channels that overlay and connect with each other. Outcrop studies show that the thickness of the mud interlayer is less than 4 m, the length of the mud interlayer is 10–600 m, and the density of the mud interlayer is 0.1–0.4 m per meter. Logging analysis shows that the mud interlayer thickness is 1–5 m, the mud interlayer frequency is 0.1–0.3 numbers per meter, and the mud interlayer density is 0.1–0.8 m per meter (Figure 2). The interlayer is primarily distributed among sandbodies, while its continuity is deficient, leading to a lack of sealing effect on the reservoir. This study indicates that the reservoir exhibits robust connectivity.

Under the multi-stage tectonic movement during Yanshanian and Himalayan periods, the fault system demonstrates substantial development. Within the designated study area, a comprehensive analysis reveals the existence of 41 secondary and tertiary faults, exhibiting varying lengths ranging from 440 to 29,054 m. These faults primarily exhibit a predominant trend oriented in the NEE direction. Fractures are generally developed in the Kuqa reservoir. The fractures are typically high-angle or vertical structural fractures, with a density ranging from 1 to 5 fractures per meter (Figure 3). These fractures are primarily semi-filled or unfilled, and the fillings are predominantly composed of calcite and gypsum. The aperture of the fractures ranges from 0.1 to 0.6 mm, and the fracture effectiveness is generally good (Figure 4). Fractures can be classified into three types based on their genetic mechanisms,

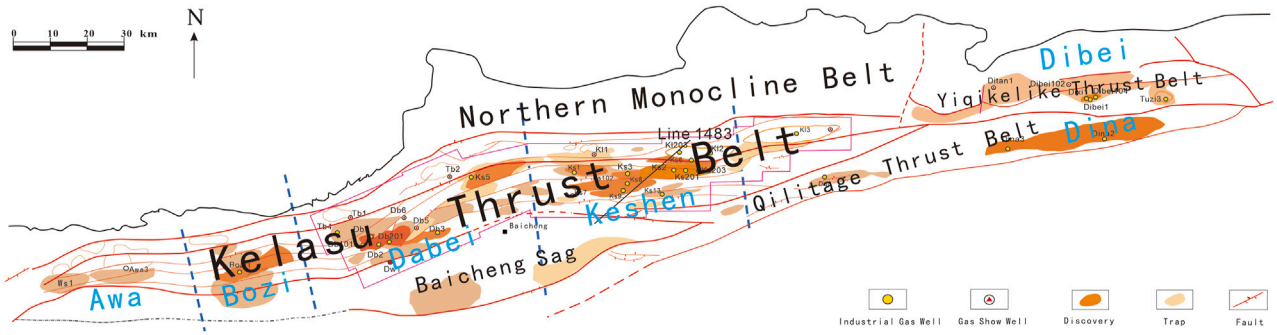

FIGURE 1
Gas reservoir distribution of the Kuqa Depression in the Tarim Basin (modified from the Tarim Oil Field Company report).

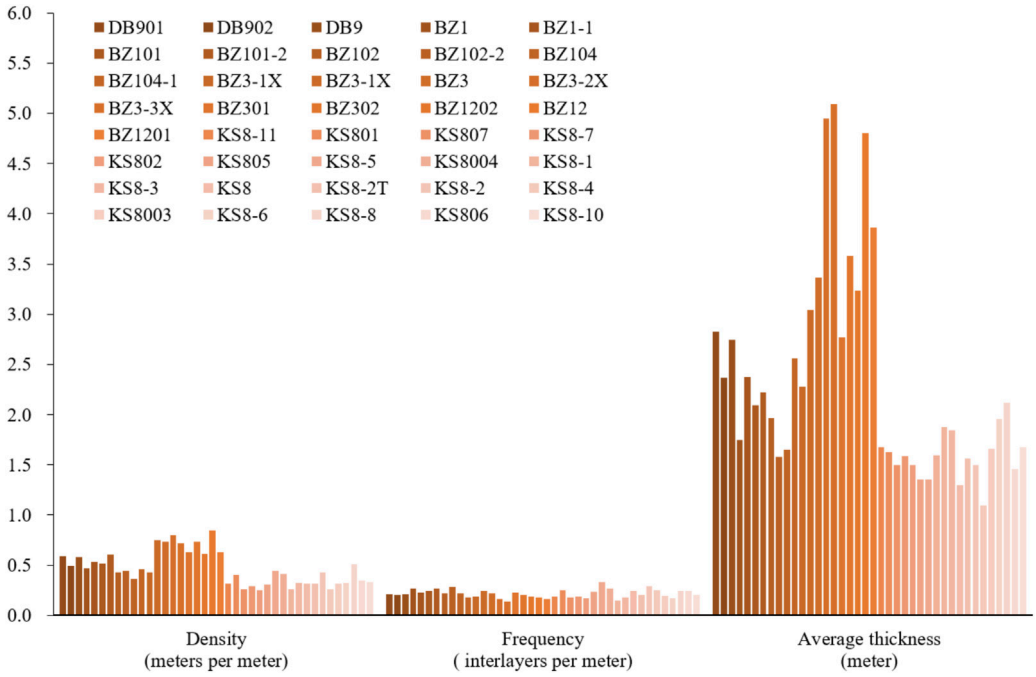

FIGURE 2
Mud interlayer statics of typical gas wells in the Kuqa Depression.

geometric scales, and penetrability: large-scale, medium-scale, and small-scale. Large-scale fractures possess the ability to penetrate multiple sets of compound sandbodies, with lengths that can extend up to hundreds of meters, heights reaching tens of meters, and apertures measuring several millimeters. They primarily control inter-well and inter-layer seepage flow. Medium-scale and small-scale fractures, on the other hand, tend to be relatively limited in scale, predominantly developing within the sandbody and exhibiting lengths generally less than 100 m. These types of fractures mainly exert influence over inner-layer seepage flow (Table 1).

Aiming to address the primary challenges of 3D geological modeling of deep fractured low porosity sandstone gas reservoirs, a 3D geological modeling technique has been developed for the Kuqa Depression of the Tarim Basin, building upon existing 3D geological modeling methods and geological data. This technique includes structural modeling using well top and seismic data, facies modeling using lithology data, petrophysical modeling using matrix property data, and fracture modeling using imaging logging data. During the modeling process, performance data such as initial production and well-testing data are fully utilized, resulting in building a multi-scale fracture-matrix-performance 3D geological model (Figure 5). The 3D geological modeling technique comprises four key techniques: 1) Structural modeling under well-to-seismic ties, 2) facies modeling under the stochastic object, 3) reservoir petrophysical modeling under facies

FIGURE 3
Fracture characterization of the Kuqa River outcrop.

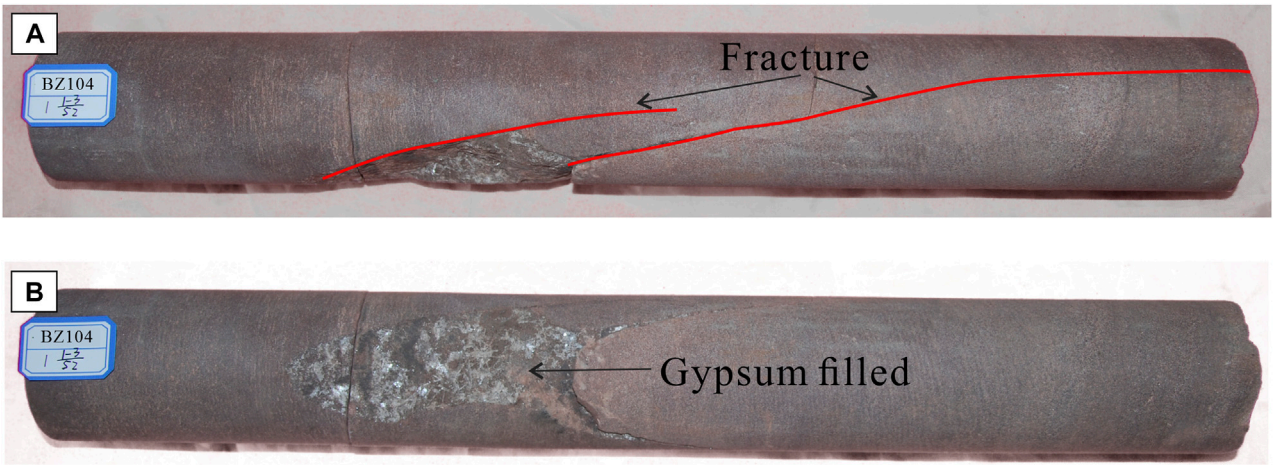

FIGURE 4
Fracture and filling characterization of well BZ104 coring. **(A)** High-angle structural fracture developed; **(B)** Gypsum is filled in the fracture.

TABLE 1 Fracture classification standard in the study area.

Fracture scale	Main distribution characteristics	Length	Height	Aperture	Geostress	Seepage flow
Large-scale	Penetrate through multiple sets of compound sandbodies and cut across the mudstone interlayers	>100 m	10–100 m	1–10 mm	Local geostress field	Control inter-well and inter-layer flow
Medium-scale	Develop within the compound sandbodies and cut across the bedding, with distribution controlled by the mudstone interlayers	10–100 m	1–10 m	0.1–1 mm	Derivative geostress field	Control inner-layer flow
Small-scale	Develop within the sandbody and is controlled by bedding	<10 m	0.01–1 m	0.01–0.1 mm	Derivative geostress field	Control inner-layer flow

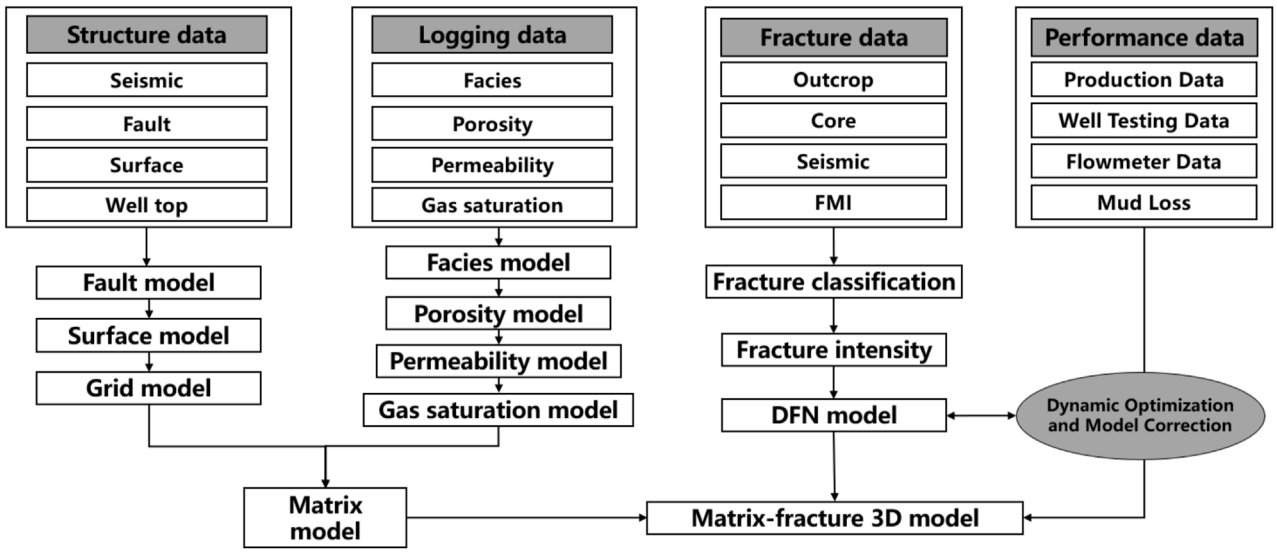

FIGURE 5
Flow chart of multi-scale fracture-matrix-performance 3D geological modeling.

constraint, and 4) fracture modeling under multi-condition constraint and static-performance data combined.

The research area encompasses two geological components, namely, matrix and fractures. Initially, a comprehensive grid model is constructed by integrating seismic, fault, surface, and well topographical data, employing the "structural modeling under well-to-seismic ties" within structural modeling. This grid model incorporates fault and surface models, providing a solid foundation for subsequent modeling stages. Subsequently, leveraging the grid model, the lithofacies model is established through the application of "facies modeling under stochastic object," taking into consideration logging data related to lithofacies, porosity, permeability, and gas saturation. Furthermore, the "reservoir petrophysical modeling under facies constraint" is employed to build models for porosity, permeability, and gas saturation. Lastly, employing field outcrop, core, seismic, and imaging logging data, an innovative approach "fracture modeling under multi-condition constraint and static-performance data combined" is employed in fracture modeling. By incorporating dynamic data such as production data, well-test data, flow meter data, and mud loss data, the fracture modeling process is effectively constrained, leading to the establishment of a 3D geological model that accurately reflects the actual geological conditions.

4 Results

4.1 Structural modeling under well-to-seismic ties

Aiming to address the poor quality of seismic data in the Kuqa Depression, the wide-azimuth seismic technique has been utilized to enhance the signal-to-noise ratio and resolution of the seismic data. Wide-azimuth seismic is employed to enhance the azimuth angle of seismic sampling, consequently augmenting the aspect ratio of the azimuth observation acquisition system from 0.22 to 0.45. In comparison to conventional 3D seismic data, the seismic data obtained through this high-density wide-azimuth seismic technology encompasses a more comprehensive seismic wave field, facilitating richer amplitude imaging and azimuthal anisotropy information. This expanded dataset serves as a foundation for subsequent seismic data processing and interpretation, offering a more precise and detailed basis for the accuracy demands of 3D structural modeling. The method of well-to-seismic ties has been applied to interpret the target structure, resulting in a significant reduction in the error of target depth to within 25 m. Additionally, over the past 5 years, the well drilling success rate has been 100%.

Structural modeling is the first and most critical step in 3D geological modeling, providing the framework for facies and petrophysical modeling. The accuracy of the structural model is essential for ensuring high-quality modeling results (Wu et al., 2005; Marquer et al., 2006; Calcagno et al., 2008; Pakyuz-Charrier et al., 2018b; Zhong, 2019; Almedallah et al., 2021; Hillier et al., 2021; Lan et al., 2021). Structural modeling involves the development of both fault and surface models, with the well-to-seismic ties method employed to create the structural framework based on fine structural interpretation.

Based on the contour map derived from seismic interpretation, the faults are imported into the modeling software. Then, the faults from different surfaces are classified, which are used to analyze the vertical extension length and dip angle. After building the initial fault model, the model is repeatedly modified according to the fault relationships using a 3D visual interactive window. This is done to ensure that the fault model is consistent with the seismic surface and that the distribution of faults in three-dimensional space is reasonable.

The first step in building the surface model is pillar gridding, which divides the structure into thousands of grids to reflect the

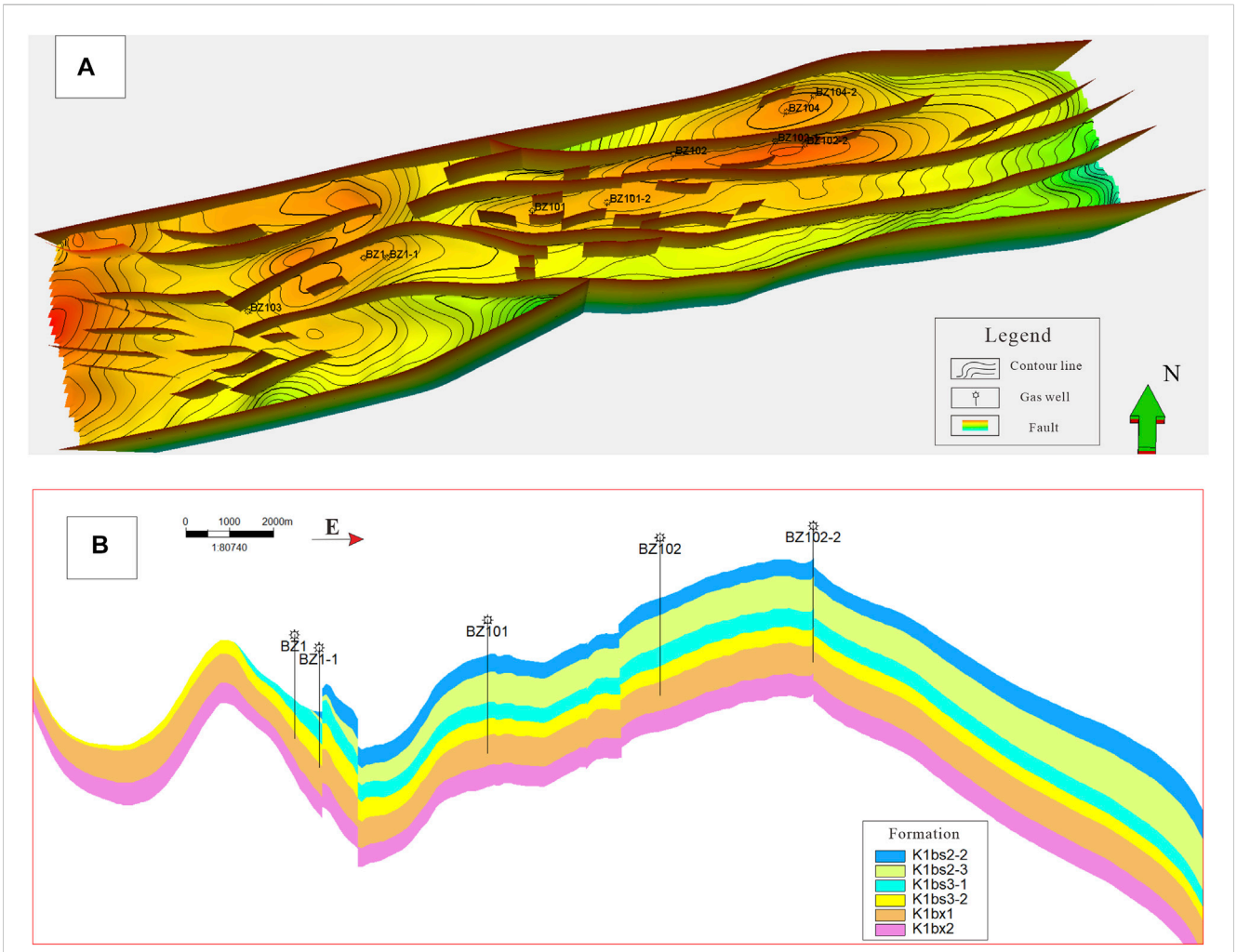

FIGURE 6
3D structural model of the study area. **(A)** Surface and faults model; **(B)** Intersection of the 3D structural model.

structure's elevation. Considering the complex anticline structural reservoir and computing speed, a plane grid size of 50 m × 50 m is adopted. Typically, well tops and structural maps are used to constrain surface modeling. However, some Kuqa reservoirs modeled by this traditional method have issues such as formation pinch-out and formation crossing, which differ from the actual underground formation. Due to the stable sedimentary environment, the Kuqa reservoir has relatively uniform formation thickness, and the poor seismic data makes it difficult to match the well tops exactly with the structure. Therefore, a comprehensive dataset of top structure, bottom structure, and well tops is used to build the surface model. The structural model created using this method is more consistent with the actual structural characteristics (Figure 6).

4.2 Facies modeling under the stochastic object

Facies modeling involves two main methods: deterministic modeling and stochastic modeling. Common methods used in facies modeling include object modeling, truncated Gaussian simulation, sequential indicator simulation, multipoint simulation, and indicator Kriging simulation. Each of these methods has its own advantages and applicable conditions, and the optimal method should be selected based on the geological conditions of the gas reservoir being studied (Falivene et al., 2006; Correia et al., 2014; Wellmann et al., 2014; 2018; Pakyuz-Charrier et al., 2018a; 2019; Wellmann and Caumon, 2018; Ferrer et al., 2021; Laudadio et al., 2022).

Because of the challenges posed by the strong heterogeneity, low well control degree, and limited wells in the Kuqa reservoir, the stochastic object modeling method is adopted to build a facies model based on the geological characteristics of the study area. This method involves stochastically simulating the facies model using object parameters such as shape, length, width, thickness, and direction to reflect the statistical probability and trend distribution of the geological object. Based on the lithology and sedimentation analysis, sandstone is used as the background and mudstone as the object during the stochastic simulation. The mudstone content is derived from well logging analysis, and geological parameters, such as direction, length, length-width

FIGURE 7
3D facies model of the study area.

ratio, and thickness, are primarily based on outcrop and single-well statistical research. Furthermore, the mudstone distribution is used as a trend to constrain the facies modeling and accurately predict the facies distribution between wells. The Kuqa facies model obtained using this method accurately shows the sandbody distribution, and the geometric characteristics of the subaqueous distributary channel, mouth bar, and interdistributary bay are consistent with the previous geological research (Figure 7). Influenced by the provenance from the north, the formation of the braided river delta front sedimentary system occurs in a north-to-south direction. The model exhibits a sand ratio of 69.1%. Regarding the spatial distribution, the central and western regions display a greater thickness of sandstone in the horizontal plane. In the vertical direction, as depth increases, there is a gradual increase in the content of mudstone, accompanied by a gradual decrease in the sand ratio.

4.3 Reservoir petrophysical modeling under facies constraint

Similar to the facies modeling simulation methods, petrophysical modeling of the reservoir involves techniques such as sequential Gaussian simulation, Gaussian random function simulation, Kriging simulation, and moving average simulation (Linsel et al., 2020; Yong et al., 2020; Giraud et al., 2021; Ursegov et al., 2021). In line with the geological features of the study area, sequential Gaussian simulation is utilized to stochastically model the reservoir properties, including porosity, permeability, and gas saturation under facies constraints.

Due to the nappe-thrust tectonic movement in the study area, each block exhibits morphological features with a long axis in the east-west direction and a short axis in the north-south direction, where the long axis is perpendicular to the provenance direction. With a large well spacing, the variogram analysis of various petrophysical data must consider the structural and sedimentary characteristics to determine key parameters such as major range, minor range, and vertical range. Failure to consider these characteristics during variogram analysis can lead to the mistaken assumption that the main major range is in the east-west direction, which is inconsistent with the actual provenance direction of the north-south direction. This contradiction between the petrophysical model and actual reservoir characteristics can be avoided by considering the structural and sedimentary characteristics during variogram analysis.

Using facies constraints during sequential Gaussian simulation can help predict properties in different facies and reduce uncertainty between wells (Liu et al., 2022; Liu et al., 2023). The lithologies of the Kuqa reservoir are predominantly sandstone and mudstone. Range parameters from variogram analysis are used in sandstone petrophysical modeling, while a minimum value (porosity is 1%, permeability is 0.001×10^{-3} μm^2, gas saturation is 1%) is directly assigned for the mudstone petrophysical modeling. The model is set with a major range of 1480.3, a minor range of 876.9, and a vertical range of 4.3. By conducting statistical probability analysis on the acoustic impedance and lithofacies types (sandstone and mudstone) at the well locations, the relationship between different lithofacies and corresponding acoustic impedance is established. Additionally, the probability of porosity occurrence in mudstone for different acoustic impedance is determined through correlation analysis. The research findings indicate a positive correlation between permeability and porosity in the study area. To enhance the accuracy and reliability of the permeability model, we integrate porosity as a co-Kriging parameter. This integration allows us to control the permeability model based on the corresponding porosity, and we improve the accuracy and reliability of the permeability model in the study area. This study leverages single well logging interpretation to establish the gas saturation data, which serves as the foundational input for simulating the static distribution relationship between gas and water within the reservoir using a random simulation algorithm. The resulting porosity, permeability, and gas saturation models contain geological characteristics of sedimentation and petrophysical distribution, which are more consistent with the actual geological characteristics (Figure 8). The model exhibits a porosity range of 3.5%–8.2%, with an

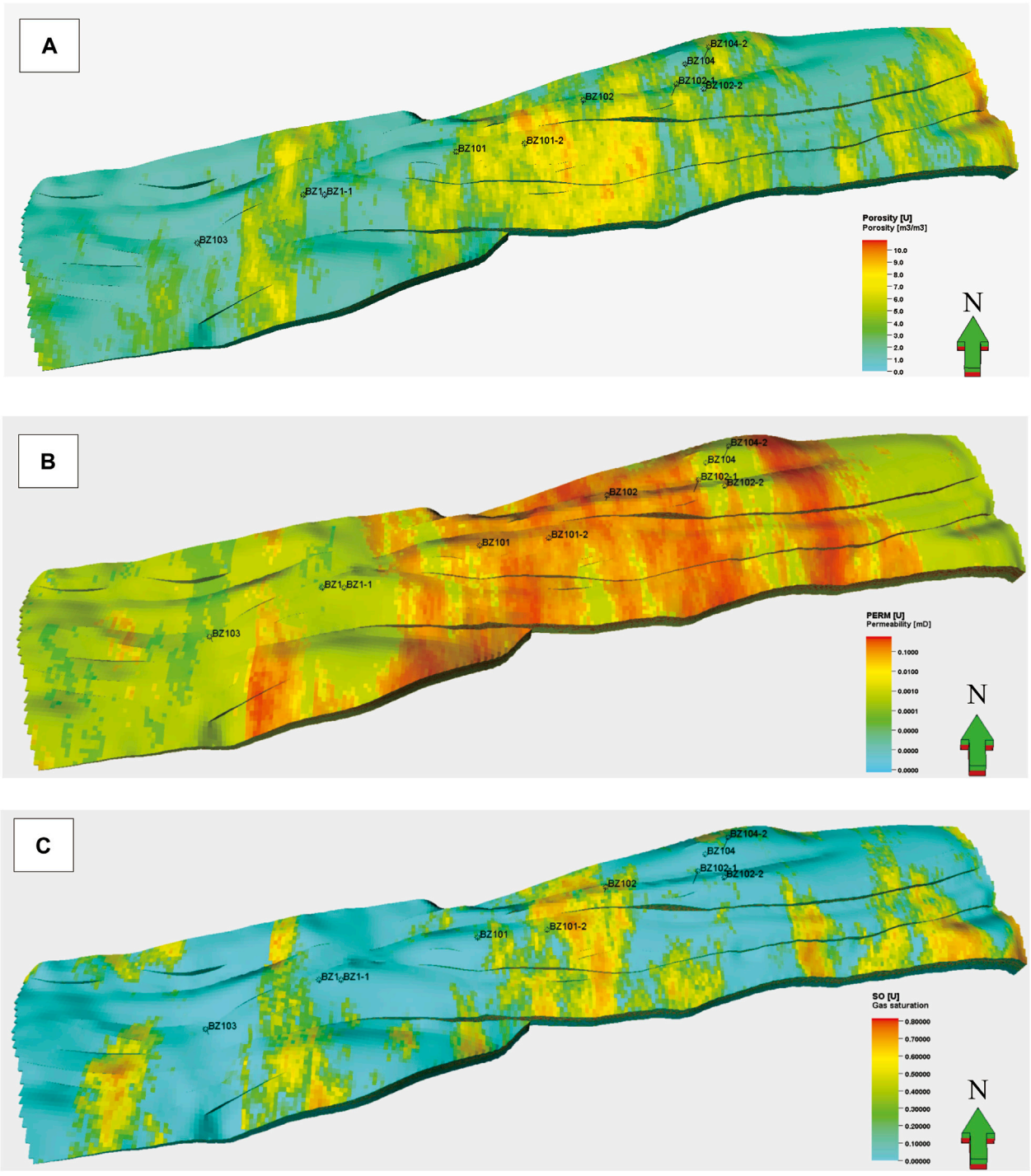

FIGURE 8
3D reservoir petrophysical model of the study area. **(A)** Porosity model; **(B)** Permeability model; **(C)** Gas saturation model.

average porosity of 4.5%. The permeability ranges from 0.06 to 4.7 × 10^{-3} μm^2, with an average permeability of 0.068 × 10^{-3} μm^2. The gas saturation ranges from 50% to 81%, with an average of 63%. In terms of spatial distribution, the middle reservoir demonstrates favorable properties overall on the horizontal plane. However, as the burial depth increases in the vertical direction, the reservoir properties gradually deteriorate.

4.4 Fracture modeling under multi-condition constraint and static-performance data combined

Fracture modeling using seismic attributes, such as the ant-tracking technique, cannot accurately identify fractures in the Kuqa Depression of the Tarim Basin due to poor seismic data quality.

Therefore, in fracture modeling, it is necessary to consider various influential factors such as geostress, faults, and structural position that affect the development of fractures. Through comprehensive analysis involving field outcrops, core observations, experimental analysis, and other methodologies, a comprehensive examination of various factors influencing the extent of fracture development has been conducted. Genesis analysis indicates that fractures are primarily controlled by factors such as faulting, folding, structural location, and lithology. These factors play significant roles in shaping the development and distribution of fractures. We assume that these fractures are further constrained by curvature, geostress, distance from the anticline axis, and distance from the fault. Fracture development is concentrated near faults and folds where geostress is concentrated, with the 200–300-m area around these structures being the primary fracture development zone. Different lithologies have different rock mechanics parameters, leading to varying numbers of fractures formed under the same geostress. The Kuqa reservoir has a tight matrix, and the fractures developed around the wells are the primary channels for fluid flow into the wellbore. Initial production data can effectively reflect the fracture development around the wells.

Based on the analysis of fracture azimuth, the fractures in the Kuqa Depression have been divided into two groups with nearly north-south and nearly east-west directions, respectively. By coupling the characteristics of the paleostress field, three main periods of fracture formation have been determined. It is considered that the Himalayan period is the primary formation period, during which the fractures have a low filling and good effectiveness under compressive geostress.

With the rapid development of fracture research and computer technology in recent years, fracture prediction has evolved from conventional interpolation methods to space subdivision methods, such as discrete fracture network modeling (Benedetto et al., 2014; Pellerin, 2014; Hyman et al., 2015; Azim, 2021; Ceccato et al., 2021; Wang et al., 2021; Berrone and Raeli, 2022; Lopes et al., 2022; Yan et al., 2022). Stress-intensity factors are relative to fracture pressure, fracture height, and layer stress (Li et al., 2022). Equilibrium fracture height can be calculated based on the relationships between the stress-intensity factors at the tips and the fracture toughness in the layers (Weng et al., 2011; Li and Wu, 2022).

$$K_I^u = \sqrt{\frac{1}{\pi h}}\int_{-h}^{h}(P(y)-\delta(y))\sqrt{\frac{h+y}{h-y}}dy \quad (1)$$

$$K_I^l = \sqrt{\frac{1}{\pi h}}\int_{-h}^{h}(P(y)-\delta(y))\sqrt{\frac{h+y}{h-y}}dy \quad (2)$$

Where K_I^u and K_I^l are the stress-intensity factors at the upper and lower tips, respectively; h is the fracture height, $P(y)$ is the fracture pressure, and $\delta(y)$ is the *in-situ* stress.

In accordance with the fracture characteristics of the study area, fractures of different groups and periods are simulated during discrete fracture network modeling. Based on outcrop data, the deterministic modeling of the structural trace method under fault constraint is used to predict large-scale fractures. Using the constraints of curvature, geostress, distance from the anticline axis, and distance from the fault, medium and small-scale discrete fracture network models are built based on fracture development properties and large-scale fracture models. Performance constraint properties are established by integrating several performance data, including initial production, well test permeability, and drilling fluid loss. The modeling process utilizes the co-kriging method to effectively incorporate performance constraint properties into the fracture distribution prediction. By coupling fractures of different periods and scales, a multi-scale fracture model under multiple constraints is built (Figure 9). The fractures exhibit a distribution with two main sets of fractures oriented in EW and NS directions. These fractures display an inclination angle ranging from 52° to 89°, with an average angle of 72°. Fracture development is notably pronounced in the elevated regions of the structure and close proximity to the fault zone. These areas exhibit a higher fracture density, indicating a greater abundance of fractures, and demonstrate favorable effectiveness in terms of their connectivity and fluid flow properties.

Based on the 3D geological modeling technique, the DFN fracture model can be used to predict the early water invasion of the fractured reservoirs in the Kuqa Depression. Particular focus is given to the fracture zone that connects the edge water and the gas well, and the numerical simulation research based on the DFN model is conducted. This approach enables accurate anticipation of the distribution characteristics of the remaining gas and facilitates analysis of the dynamic interplay between the gas and water phases. By adopting this comprehensive methodology, a deeper understanding of the gas reservoir behavior is achieved, resulting in precise predictions of gas and water distribution. Ultimately, this enhanced reservoir management approach ensures effective decision-making and resource optimization.

4.5 Model quality control

Ensuring the accuracy of a geological model requires quality control measures at every step of the modeling process. For instance, in the grid model, geometrical properties such as grid height and volume are made to eliminate negative grids. The structural model must be checked repeatedly to confirm consistency in the distribution trend between surfaces, faults, and raw structural data. In property models (facies, porosity, permeability, and gas saturation), consistency is confirmed by comparing the distribution trends of logging data, upscaling data, and model data, as well as creating property distribution maps and reservoir profiles. Due to limited wells and rapid development, validation through wells decimation is generally not feasible. Instead, the model is primarily checked and corrected by drilling new development wells at later stages. The fracture model can be validated with performance data during the modeling process and tested with newly monitored performance data. Upon importing the 3D geological model into the numerical model, the model's accuracy is evaluated through the first history matching rate analysis. The first history matching rate refers to the coincidence rate obtained from the history matching of well pressure, gas production, and other parameters without adjusting any performance and model parameters. If the first history matching rate reaches 60% or more, the geological model is typically considered accurate.

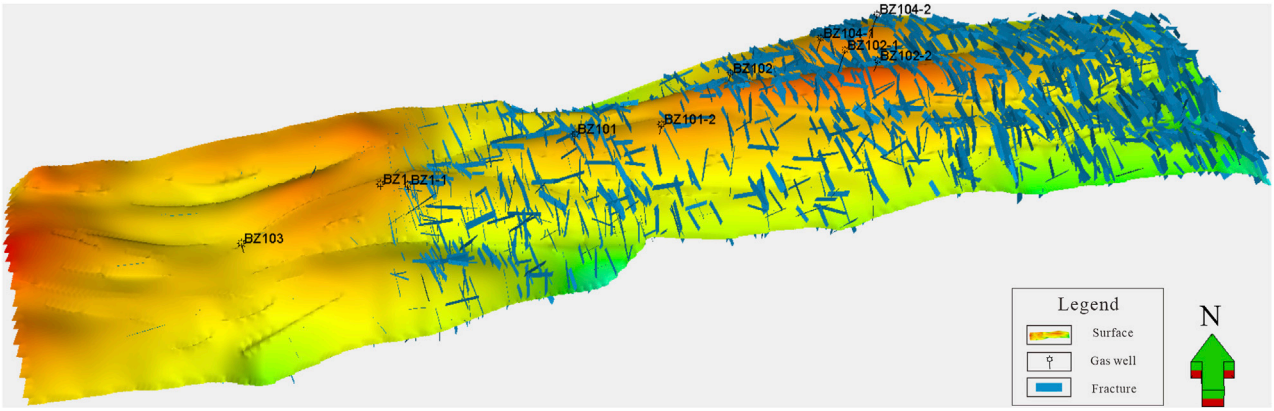

FIGURE 9
Discrete fracture network model of the study area.

The 3D geological model built in this study includes no negative grids, and the distribution trends of logging data, upscaling data, and model data are consistent overall. The distribution characteristics of model properties also align with previous geological understanding. With a first-history matching rate of 75% for well pressure and 100% for gas production, the established 3D geological model is confirmed to be both accurate and credible.

5 Discussion

The application of the 3D geological modeling technique has been successful in many deep fractured low porosity sandstone gas reservoirs in the Kuqa Depression of Tarim Basin, including Keshen 2, Keshen 8, Dabei201, Dabei 9, Bozi 1, and Bozi 3. Four key techniques were used to address the challenges in modeling the structure, facies, reservoir petrophysics, and fractures. When considering the reservoir attributes surrounding a well, inter-well prediction necessitates the creation of numerous well-connected correlation profiles. However, this process is both time-consuming and labor-intensive, and inter-well reservoir attribute prediction is often considered subjective. Although seismic data can provide valuable insights into the distribution of sandbodies and gas-bearing characteristics in the study area, its resolution typically exceeds 50 m, making it insufficient for a detailed reservoir description. In contrast, 3D geological modeling integrates logging, seismic, and other data, offering significant advantages over traditional reservoir characterization methods. It allows for reservoir characterization accuracy at sub-meter levels, enabling precise reservoir description. Additionally, random mathematical methods can be employed to predict cross-well attributes, guided by geostatistical statistical outcomes and geological understanding. This approach offers distinct advantages, including high accuracy, reduced human influence factors, and efficient processing speed. 3D geological models are consistent with the actual structural characteristics, which provide the model basis for enhancing gas recovery.

By using the four key techniques, a favorable development area was predicted, and it supported the deployment of more than 60 wells. The favorable development formation was evaluated, and it supported the perforation and fracturing designs. Based on the structural model, facies model, reservoir petrophysical model, and fracture model, numerical simulation was used to predict and optimize the reasonable development index. Factors such as well production allocation, gas recovery rate, and well numbers directly affect gas recovery. According to the production performance, well-controlled dynamic reserves, and numerical simulation results, it is suggested that the reasonable gas recovery rate of the Kuqa reservoir should be controlled below 2%, and the reasonable well production allocation should be 10–50 $\times$ 10^4 cubic meters per day. The application of this technique has enhanced the gas recovery by 6%–15% over a 30-year development period, demonstrating the significant potential for wider implementation across other reservoirs.

6 Conclusion

Aiming to address the challenges posed by the tight matrix, developed fracture, and strong reservoir heterogeneity of the Kuqa reservoir, a 3D geological modeling approach for deep fractured low porosity sandstone gas reservoirs was developed, utilizing geological and performance data. Compared with the traditional geological modeling method, this method requires fewer data and provides better systematicness and strong pertinence. As a result, it is highly effective at addressing modeling challenges associated with limited well numbers and poor-quality seismic data. This method includes four key techniques: 1) Structural modeling using well-to-seismic ties, 2) facies modeling utilizing stochastic objects, 3) reservoir petrophysical modeling under facies constraints, and 4) fracture modeling under multiple-condition constraints and static-performance data combination.

"Structural modeling under well-to-seismic ties" is used to address the issue of inaccurate structural models caused by deep burial and poor seismic data. "Facies modeling under stochastic objects" is used to address the challenge of strong reservoir heterogeneity, a small number of wells, and complex sedimentary geometry. "Reservoir petrophysical modeling under facies constraints" is employed to resolve the petrophysical problem arising from large well spacing and the need for accurate prediction between wells. Finally, "Fracture modeling

under multi-condition constraints and static-performance data combined" is applied to tackle the challenge of predicting fractures accurately despite poor seismic data.

The application of 3D geological modeling has proven to be effective in the Kuqa Depression of the Tarim Basin. The built models support the adjustment of the reservoir development index and are expected to enhance the gas recovery by 6%–15% at the end of the development period. This technique has a strong theoretical basis and systematic approach, which effectively addresses the challenge of modeling deep-fractured low-porosity sandstone gas reservoirs. Moreover, this technique is user-friendly and can provide guidance and support for modeling work. As such, it has the potential to be widely adopted in other gas reservoirs.

Data availability statement

The original contributions presented in the study are included in the article/supplementary material, further inquiries can be directed to the corresponding author.

Author contributions

All authors listed have made a substantial, direct, and intellectual contribution to the work and approved it for publication.

Funding

This research was funded by the Technology and Engineering Project of PetroChina Company Limited, "Research on Efficient Development Technology for Deep or Ultra-deep Gas Reservoir (2022KT0704)", and "Pilot Test for Safe and Efficient Development of Ultra-deep Fractured Sandstone Gas Reservoir (2022KT0702)". The funder was not involved in the study design, collection, analysis, interpretation of data, the writing of this article or the decision to submit it for publication.

Conflict of interest

The authors ZL, ZG, YZ, BC and WH were employed by PetroChina Research Institute of Petroleum Exploration and Development. Authors DC, YW, KF, PZ, and CH were employed by Tarim Oilfield Company.

Publisher's note

All claims expressed in this article are solely those of the authors and do not necessarily represent those of their affiliated organizations, or those of the publisher, the editors and the reviewers. Any product that may be evaluated in this article, or claim that may be made by its manufacturer, is not guaranteed or endorsed by the publisher.

References

Almedallah, M. K., Al Mudhafar, A. A., Clark, S., and Walsh, S. D. C. (2021). Vector-based three-dimensional (3D) well-path optimization assisted by geological modelling and borehole-log extraction. *Upstream Oil Gas Technol.* 7, 100053–100114. doi:10.1016/j.upstre.2021.100053

Azim, R. A. (2021). Estimation of fracture network properties from FMI and conventional well logs data using artificial neural network. *Upstream Oil Gas Technol.* 7, 100044–100116. doi:10.1016/j.upstre.2021.100044

Benedetto, M. F., Berrone, S., Pieraccini, S., and Scialò, S. (2014). The virtual element method for discrete fracture network simulations. *Comput. Methods Appl. Mech. Eng.* 280, 135–156. doi:10.1016/j.cma.2014.07.016

Berrone, S., and Raeli, A. (2022). Efficient partitioning of conforming virtual element discretizations for large scale discrete fracture network flow parallel solvers. *Eng. Geol.* 306, 106747–106816. doi:10.1016/j.enggeo.2022.106747

Calcagno, P., Bouchot, V., Thinon, I., and Bourgine, B. (2012). A new 3D fault model of the bouillante geothermal province combining onshore and offshore structural knowledge (French west indies). *Tectonophysics* 529, 185–195. doi:10.1016/j.tecto.2011.08.012

Calcagno, P., Chilès, J. P., Courrioux, G., and Guillen, A. (2008). Geological modelling from field data and geological knowledge. *Phys. Earth Planet. Interiors* 171, 147–157. doi:10.1016/j.pepi.2008.06.013

Ceccato, A., Viola, G., Antonellini, M., Tartaglia, G., and Ryan, E. J. (2021). Constraints upon fault zone properties by combined structural analysis of virtual outcrop models and discrete fracture network modelling. *J. Struct. Geol.* 152, 104444–104518. doi:10.1016/j.jsg.2021.104444

Chen, G. B., Li, T., Yang, L., Zhang, G. H., Li, J. W., and Dong, H. J. (2021). Mechanical properties and failure mechanism of combined bodies with different coal-rock ratios and combinations. *J. Min. Strata Control Eng.* 3, 023522. doi:10.13532/j.jmsce.cn10-1638/td.20210108.001

Chen, Z., Li, Q., Liu, M., Song, B., Cao, M., and Wang, M. (2021). Uranium mineralization formed through multi-stage superposition: Case of the Qianjiadian deposit in Songliao Basin, China. *Energy Geosci.* 2, 32–40. doi:10.1016/j.engeos.2020.07.004

Correia, M. G., Maschio, C., Schiozer, D. J., and Santosdos, M. S. (2014). Upscaling approach for meso-scale heterogeneities in naturally fractured carbonate reservoirs. *J. Petroleum Sci. Eng.* 115, 90–101. doi:10.1016/j.petrol.2014.01.008

Falivene, O., Arbués, P., Howell, J., Muñoz, J. A., Fernández, O., and Marzo, M. (2006). Hierarchical geocellular facies modelling of a turbidite reservoir analogue from the eocene of the ainsa basin, NE Spain. *Mar. Petroleum Geol.* 23, 679–701. doi:10.1016/j.marpetgeo.2006.05.004

Ferrer, R., Emery, X., Maleki, M., and Navarro, F. (2021). Modeling the uncertainty in the layout of geological units by implicit boundary simulation accounting for a preexisting interpretive geological model. *Nat. Resour. Res.* 30, 4123–4145. doi:10.1007/s11053-021-09964-9

Giraud, J., Ogarko, V., Martin, R., Jessell, M., and Lindsay, M. (2021). Structural, petrophysical, and geological constraints in potential field inversion using the tomofast-x v1.0 open-source code. *Geosci. Model Dev.* 14, 6681–6709. doi:10.5194/gmd-14-6681-2021

Grose, L., Ailleres, L., and Laurent, G. (2019). Integrating Fault kinematics into implicit 3D modelling of fault networks. *ASEG Ext. Abstr.* 2019, 1–3. doi:10.1080/22020586.2019.12072997

Gu, J., Fang, H., and Jia, J. (2001). Diagenesis and reservoir characteristics of cretaceous braided delta sandbody in Kuqa depression, Tarim Basin. *Acta Sedimentol. Sin.* 19, 517–523. doi:10.3969/j.issn.1000-0550.2001.04.007

Guo, Z., Sun, L., Jia, A., and Lu, T. (2015). 3-D geological modeling for tight sand gas reservoir of braided river facies. *Petroleum Explor. Dev.* 42, 83–91. doi:10.1016/s1876-3804(15)60009-x

Hillier, M., Wellmann, F., Brodaric, B., de Kemp, E., and Schetselaar, E. (2021). Three-dimensional structural geological modeling using graph neural networks. *Math. Geosci.* 53, 1725–1749. doi:10.1007/s11004-021-09945-x

Høyer, A.-S., Jørgensen, F., Foged, N., He, X., and Christiansen, A. V. (2015). Three-dimensional geological modelling of aem resistivity data - a comparison of three methods. *J. Appl. Geophys.* 115, 65–78. doi:10.1016/j.jappgeo.2015.02.005

Hu, Y., Yu, X., Li, S., Chen, G., Zhou, Y., and Gao, Z. (2014). Improving the accuracy of geological model by using seismic forward and inversion techniques. *Petroleum Explor. Dev.* 41, 190–197. doi:10.11698/PED.2014.02.08

Hyman, J. D., Karra, S., Makedonska, N., Gable, C. W., Painter, S. L., and Viswanathan, H. S. (2015). DFNWorks: A discrete fracture network framework for modeling subsurface flow and transport. *Comput. Geosciences* 84, 10–19. doi:10.1016/j.cageo.2015.08.001

Irakarama, M., Laurent, G., Renaudeau, J., and Caumon, G. (2021). Finite difference implicit structural modeling of geological structures. *Math. Geosci.* 53, 785–808. doi:10.1007/s11004-020-09887-w

Jia, A., Guo, J., and He, D. (2007). Perspective of development in detailed reservoir description. *Petroleum Explor. Dev.* 34, 691–695. doi:10.3321/j.issn:1000-0747.2007.06.010

Jørgensen, F., Høyer, A. S., Sandersen, P. B., He, X., and Foged, N. (2015). Combining 3D geological modelling techniques to address variations in geology, data type and

density - an example from southern Denmark. *Comput. Geosciences* 81, 53–63. doi:10.1016/j.cageo.2015.04.010

Lai, J., Han, N., Jia, Y., Ji, Y., Wanf, G., Pang, X., et al. (2018). Detailed description of the sedimentary reservoir of a braided delta based on well logs. *Geol. China* 45, 304–318. doi:10.12029/gc20180207

Lan, S. R., Song, D. Z., Li, Z. L., and Liu, Y. (2021). Experimental study on acoustic emission characteristics of fault slip process based on damage factor. *J. Min. Strata Control Eng.* 3, 033024. doi:10.13532/j.jmsce.cn10-1638/td.20210510.002

Laudadio, A. B., Schetselaar, E. M., Mungall, J. E., and Houlé, M. G. (2022). 3D modeling of the esker intrusive complex, ring of fire intrusive suite, mcfaulds lake greenstone belt, superior province: Implications for mineral exploration. *Ore Geol. Rev.* 145, 104886–104923. doi:10.1016/j.oregeorev.2022.104886

Li, J., Liu, Y., and Wu, K. (2022). A new higher order displacement discontinuity method based on the joint element for analysis of close-spacing planar fractures. *SPE J.* 27, 1123–1139. doi:10.2118/208614-PA

Li, J., and Wu, K. (2022). An efficient model for hydraulic fracture height growth considering the effect of bedding layers in unconventional shale formations. *SPE J.* 27, 3740–3756. doi:10.2118/210572-PA

Li, Q., Zhang, L., Cao, D., Dong, Q., Cui, Y., and Chen, C. (2016). Usage, status, problems, trends and suggestions of 3D geological modeling. *Geol. Prospect.* 52, 759–767. doi:10.13712/j.cnki.dzykt.2016.04.018

Linsel, A., Wiesler, S., Haas, J., Bär, K., and Hinderer, M. (2020). Accounting for local geological variability in sequential simulations-concept and application. *IJGI* 9, 409–423. doi:10.3390/ijgi9060409

Liu, J., Mei, L., Ding, W., Xu, K., Yang, H., and Liu, Y. (2023). Asymmetric propagation mechanism of hydraulic fracture networks in continental reservoirs. *GSA Bull.* 135, 678–688. doi:10.1130/B36358.1

Liu, J., Yang, H., Xu, K., Wang, Z., Liu, X., Cui, L., et al. (2022). Genetic mechanism of transfer zones in rift basins: Insights from geomechanical models. *GSA Bull.* 134, 2436–2452. doi:10.1130/B36151.1

Liu, Y., Xia, H., Sun, Q., Lin, C., Zhao, H., Li, H., et al. (2019). Sequence stratigraphy and depositional evolution of the bashijiqike formation in the western tabei uplift, Tarim Basin. *Nat. Gas. Geosci.* 30, 62–73. doi:10.11764/j.issn.1672-1926.2018.10.003

Liu, Y., Zhang, W., Duan, T., Lian, P., Li, M., and Zhao, H. (2021a). Progress of deep learning in oil and gas reservoir geological modeling. *Bull. Geol. Sci. Technol.* 40, 235–241. doi:10.19509/j.cnki.dzkq.2021.0417

Liu, Z., Zhang, Y., Liu, H., Lv, Z., and Huang, W. (2021b). Analysis of gas well classifications and productivity influencing factors in kela-2 gas field. *CT&F - Cienc. Tecnol. Futuro* 11, 63–70. doi:10.29047/01225383.382

Liu, Z., Zhang, Y., Zhang, Y., Zhao, L., Peng, P., Liu, H., et al. (2022). Influencing factor analysis on the fractured tight sandstone gas reservoir characteristics: A case study of Bozi 3 gas reservoir in the Tarim Basin. *Front. Earth Sci.* 10. doi:10.3389/feart.2022.881934

Lopes, J. A. G., Medeiros, W. E., La Bruna, V., de Lima, A., Bezerra, F. H. R., and Schiozer, D. J. (2022). Advancements towards DFKN modelling: Incorporating fracture enlargement resulting from karstic dissolution in discrete fracture networks. *J. Petroleum Sci. Eng.* 209, 109944–110018. doi:10.1016/j.petrol.2021.109944

Marquer, D., Calcagno, P., Barfety, J.-C., and Baudin, T. (2006). 3D modeling and kinematics of the external zone of the French western alps (belledonne and grand châtelard massifs, maurienne valley, savoie). *Eclogae Geol. Helv.* 99, 211–222. doi:10.1007/s00015-006-1183-z

Pakyuz-Charrier, E., Giraud, J., Lindsay, M., and Jessell, M. (2018a). Common uncertainty research explorer uncertainty estimation in geological 3D modelling. *ASEG Ext. Abstr.* 2018, 1–6. doi:10.1071/ASEG2018abW10_2D

Pakyuz-Charrier, E., Jessell, M., Giraud, J., Lindsay, M., and Ogarko, V. (2019). Topological analysis in Monte Carlo simulation for uncertainty estimation. *Solid earth.* 10, 1663–1684. doi:10.5194/se-2019-78

Pakyuz-Charrier, E., Lindsay, M., Ogarko, V., Giraud, J., and Jessell, M. (2018b). Monte Carlo simulation for uncertainty estimation on structural data in implicit 3-D geological modeling, a guide for disturbance distribution selection and parameterization. *Solid earth.* 9, 385–402. doi:10.5194/se-9-385-2018

Pan, R., Zhu, X., Liu, F., Li, Y., Ma, Y., Di, H., et al. (2013). Sedimentary characteristics of braided delta and relationship to reservoirs in the cretaceous of kelasu tectonic zone in Kuqa depression, xinjiang. *J. Palaeogeogr.* 15, 707–716. doi:10.7605/gdlxb.2013.05.058

Pellerin, J., Lévy, B., Caumon, G., and Botella, A. (2014). Automatic surface remeshing of 3D structural models at specified resolution: A method based on voronoi diagrams. *Comput. Geosciences* 62, 103–116. doi:10.1016/j.cageo.2013.09.008

Qiu, Y., and Jia, A. (2000). Development of geological reservoir modeling in past decade. *Acta Pet. Sin.* 21, 101–104. doi:10.3321/j.issn:0253-2697.2000.04.019

Schneeberger, R., de La Varga, M., Egli, D., Berger, A., Kober, F., Wellmann, F., et al. (2017). Methods and uncertainty estimations of 3-D structural modelling in crystalline rocks: A case study. *Solid earth.* 8, 987–1002. doi:10.5194/se-8-987-2017

Shi, C., and Wang, Y. (2022). Data-driven construction of three-dimensional subsurface geological models from limited site-specific boreholes and prior geological knowledge for underground digital twin. *Tunn. Undergr. Space Technol.* 126, 104493–104516. doi:10.1016/j.tust.2022.104493

Snyder, D. B., Schetselaar, E., Pilkington, M., and Schaeffer, A. J. (2018). Resolution and uncertainty in lithospheric 3-D geological models. *Min. Pet.* 112, 133–147. doi:10.1007/s00710-018-0619-2

Ursegov, S. O., Zakharian, A. Z., and Serkova, V. I. (2021). Adaptive geological modelling and its application for petroleum reservoir conditions. *Earth Sci.* 666, 022065–022067. doi:10.1088/1755-1315/666/2/022065

Ursegov, S., Zakharian, A., and Serkova, V. (2018a). *Geological modeling of reservoir systems-an adaptive concept*. Netherlands: European Association of Geoscientists and Engineers, 1–9. doi:10.3997/2214-4609.201802191

Ursegov, S., Zakharian, A., and Taraskin, E. (2018b). *Full field unconventional carbonate reservoir modelling using adaptive simulation technique*. Netherlands: European Association of Geoscientists and Engineers, 1–5. doi:10.3997/2214-4609.201800837

Varga, M. de la, and Wellmann, J. F. (2016). Structural geologic modeling as an inference problem: A bayesian perspective. *Interpretation* 4, SM1–SM16. SM1–SM16. doi:10.1190/INT-2015-0188.1

Wang, D., Hao, B., and Liang, X. (2021). Slurry diffusion of single fracture based on fluid-solid coupling. *J. Min. Strata Control Eng.* 3, 013038. doi:10.13532/j.jmsce.cn10-1638/td.20200429.001

Wellmann, F., and Caumon, G. (2018). "3-D structural geological models: Concepts, methods, and uncertainties," in *Advances in geophysics*. Editor C. Schmelzbach (Berlin, Germany: Elsevier), 1–121. doi:10.1016/bs.agph.2018.09.001

Wellmann, J. F., de la Varga, M., Murdie, R. E., Gessner, K., and Jessell, M. (2018). Uncertainty estimation for a geological model of the sandstone greenstone belt, western Australia - insights from integrated geological and geophysical inversion in a bayesian inference framework. *Geol. Soc. Lond. Spec. Publ.* 453, 41–56. doi:10.1144/SP453.12

Wellmann, J. F., Lindsay, M., Poh, J., and Jessell, M. (2014). Validating 3-D structural models with geological knowledge for improved uncertainty evaluations. *Energy Procedia* 59, 374–381. doi:10.1016/j.egypro.2014.10.391

Weng, X., Kresse, O., Cohen, C., Wu, R., and Gu, H. (2011). Modeling of hydraulic-fracture-network propagation in a naturally fractured formation. *SPE Prod. Operations* 26, 368–380. doi:10.2118/140253-PA

Wu, Q., Xu, H., and Zou, X. (2005). An effective method for 3D geological modeling with multi-source data integration. *Comput. Geosciences* 31, 35–43. doi:10.1016/j.cageo.2004.09.005

Wu, S., and Li, Y. (2007). Reservoir modeling: Current situation and development prospect. *Mar. Orig. Pet. Geol.* 12, 53–60. doi:10.3969/j.issn.1672-9854.2007.03.009

Yan, L., Liu, Q., and Liu, X. (2022). Research on 3D geological modeling of fractured-vuggy carbonate reservoirs. *Energy Rep.* 8, 491–500. doi:10.1016/j.egyr.2022.03.052

Yong, H., Wenxiang, H., and Bincheng, G. (2020). Combining sedimentary forward modeling with sequential gauss simulation for fine prediction of tight sandstone reservoir. *Mar. Petroleum Geol.* 112, 104044–104115. doi:10.1016/j.marpetgeo.2019.104044

Yuan, H., Yin, S., Dong, L., and Tan, C. (2022). Restoration of the pre-jurassic paleogeomorphology and its control on hydrocarbon distribution in western ordos basin. *Energy Geosci.* 3, 485–494. doi:10.1016/j.engeos.2021.06.007

Zhan, X., Lu, C., and Hu, G. (2022). A formal representation of the semantics of structural geological models. *Sci. Program.* 2022, 1–18. doi:10.1155/2022/5553774

Zhang, R., Zhang, H., Shou, J., Shen, Y., and Li, C. (2008). Geological analysis on reservoir mechanism of the lower cretaceous bashijiqike formation in Dabei area of the Kuqa depression. *Chin. J. Geol.* 43, 507–517. doi:10.3321/j.issn:0563-5020.2008.03.006

Zhong, D., Wang, L. g., Bi, L., and Jia, M. t. (2019). Implicit modeling of complex orebody with constraints of geological rules. *Trans. Nonferrous Mater. Soc. China* 29, 2392–2399. doi:10.1016/S1003-6326(19)65145-9

Zhou, Y., Zuo, R., Liu, G., Yuan, F., Mao, X., Guo, Y., et al. (2021). The great-leap-forward development of mathematical geoscience during 2010-2019: Big data and artificial intelligence algorithm are changing mathematical geoscience. *Bull. Mineralogy, Petrology Geochem.* 40, 556–573. doi:10.19658/j.issn.1007-2802.2021.40.038

frontiers | Frontiers in Earth Science

TYPE Original Research
PUBLISHED 23 June 2023
DOI 10.3389/feart.2023.1170791

OPEN ACCESS

EDITED BY
Hu Li,
Southwest Petroleum University, China

REVIEWED BY
Wenming Ji,
China University of Petroleum (East China), China
Lin Wei,
China University of Geosciences, China
Mianmo Meng,
China University of Geosciences Wuhan, China

*CORRESPONDENCE
Ze Deng,
dengze@petrochina.com.cn
Jinliang Gao,
jinliang0205@126.com

RECEIVED 21 February 2023
ACCEPTED 05 June 2023
PUBLISHED 23 June 2023

CITATION
Yu Y, Deng Z, Gao J, Li P and Zhang C (2023), Main controlling factors of natural fractures in tight reservoirs of the lucaogou formation in the jimsar sag, Xinjiang, China.
Front. Earth Sci. 11:1170791.
doi: 10.3389/feart.2023.1170791

Main controlling factors of natural fractures in tight reservoirs of the lucaogou formation in the jimsar sag, Xinjiang, China

Yixin Yu[1,2], Ze Deng[3]*, Jinliang Gao[3]*, Peng Li[4] and Chen Zhang[5,6]

[1]State Key Laboratory of Petroleum Resources and Prospecting, China University of Petroleum, Beijing, China, [2]College of Geosciences, China University of Petroleum, Beijing, China, [3]PetroChina Research Institute of Petroleum Exploration and Development, Beijing, China, [4]Bureau of Geophysics Prospecting Inc, CNPC, Research Center of Geology, Zhuozhou, China, [5]State Key Laboratory of Oil and Gas Reservoir Geology and Exploitation, Chengdu University of Technology, Chengdu, China, [6]Institute of Sedimentary Geology, Chengdu University of Technology, Chengdu, China

Natural fractures act as critical flow channels and reservoir space in the Lucaogou Formation tight reservoir of the Jimsar Sag. It is essential to identify the main controlling factors of natural fractures in order to achieve efficient development of tight oil in this area. There are mainly three types of natural fractures, including tectonic fractures, diagenetic fractures, and abnormal overpressure-induced fractures. Diagenetic fractures are predominantly bedding seams. The fracture development is affected by multiple factors including brittle minerals, lithology, tectonic stress, bed thickness, and total organic carbon (TOC). Large tectonic stress, smaller bed thickness, and higher total organic carbon are all favorable for the development of tectonic fractures and bedding seams. The controls of brittle minerals and lithology on fracture development are different for tectonic fractures and bedding seams. Specifically, carbonate minerals stimulate the tectonic fracture development, while brittle minerals have no control over the bedding seam development; tectonic fractures are most developed in the dolomitic rocks, while bedding seams are most developed in the argillaceous rocks. The calculated fracture density variation coefficients reveal that tectonic stress and brittle minerals are the main controlling factors of tectonic fracture development; total organic carbon and lithology are the main control factors of bedding seam development.

KEYWORDS

tectonic fracture, diagenetic fracture, main controlling factor, tight oil reservoir, jimsar sag

1 Introduction

Tight Reservoirs are typically composed of fine-grained sedimentary rocks with low matrix permeability (Nelson, 2009; Ghanizadeh et al., 2015; Zhang et al., 2021). Natural fractures play important roles in these tight reservoirs, because they act as flow channels for hydrocarbon migration and they can connect hydraulic fractures and matrix pores with the wellbore during production (Becker et al., 2010; Li et al., 2019; Zhao et al., 2021). Therefore, it is of great significance to investigate the controlling factors of natural fractures in order to evaluate the occurrence and distribution of oil and gas in tight reservoirs, thereby minimizing drilling and well-completion costs (Gale et al., 2007; Fall et al., 2012; Laubach et al., 2016).

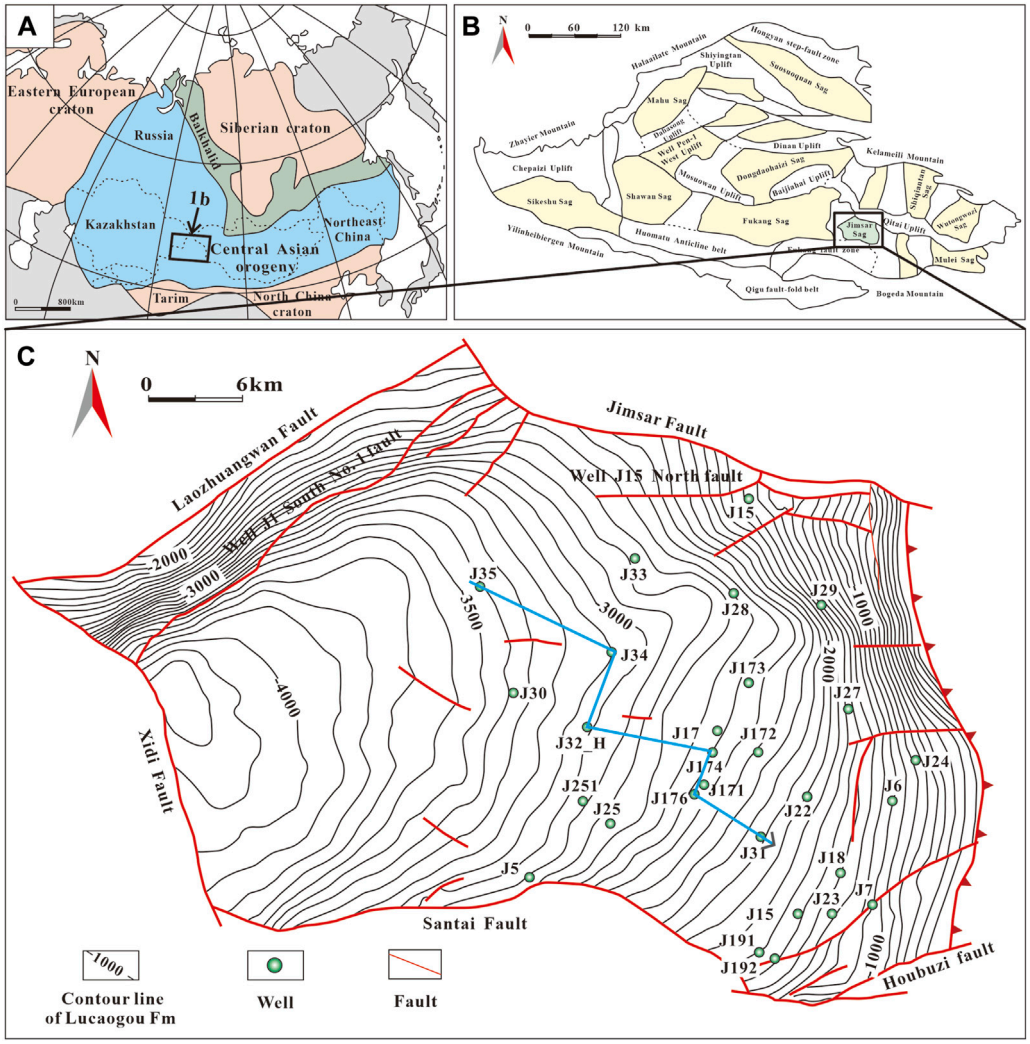

FIGURE 1
(A) Geological map of the Central Asian orogeny (Zhang et al., 2017). **(B)** Structural units of the Junggar Basin and the location of the Jimsar Sag (Zhang et al., 2017). **(C)** Structural map of the Jimsar Sag (Zhang et al., 2017).

The Permian Lucaogou Formation of the Junggar Basin is one of the main targets for tight oil exploration in China. Since 2010, breakthroughs have been made in the southeastern Junggar Basin, including industrial oil production in Wells J30, J174, and J251 (Du et al., 2014). This might be related to adjacent high-quality source rocks, which have a total organic carbon (TOC) content of >2%, a predominance of Type-II$_1$ organic matter, and a maturity (R_o) of 0.8%–1.0%. In general, the Permian Lucaogou Formation source rocks in the Junggar Basin are in the low-mature to mature stage, presenting high oil generation potential that is estimated to be 380 million tons (Kuang et al., 2012; Cao et al., 2016).

The Jimsar Sag experienced multiple stages of tectonic activities during Late Paleozoic, Mesozoic, and Cenozoic, which resulted in complex stratigraphic configurations and structural characteristics as well as abundant tectonic fractures (Wu et al., 2013; Zhang et al., 2017). Moreover, complex diagenesis and extensive hydrocarbon generation and expulsion have vital effects on the opening of bedding seams. These fractures greatly impact the oil content in the Lucaogou Formation tight reservoirs. Nonetheless, previous research mainly focuses on the tectonic setting (Zheng et al., 2018), reservoir rock lithology (Cao et al., 2019), pore structure (Liu et al., 2019; Tian et al., 2019), and sedimentary characteristics (Ma et al., 2019), with insufficient attention paid to illustrating the main controlling factors of natural fractures. This knowledge gap restrains the efficient exploration and development of tight oil in the study area.

In this study, core description, Total Organic Carbon (TOC) analysis, Xray diffraction (XRD) analysis, and Focused Ion Beam Scamming Electron Microscopy (FIB-SEM; Wang et al., 2016) were used to study the fracture development characteristics and genesis in the tight reservoirs of the Lucaogou Formation in the Jimsar Sag. The objectives are four-fold: 1) to identify fractures in the tight oil reservoirs via several approaches; 2) to clarify the types, formation mechanisms, and development characteristics of the fractures; 3) to build a comprehensive system for fracture parameter characterization and evaluation; and 4) to reveal main factors controlling the fracture development in tight oil reservoirs.

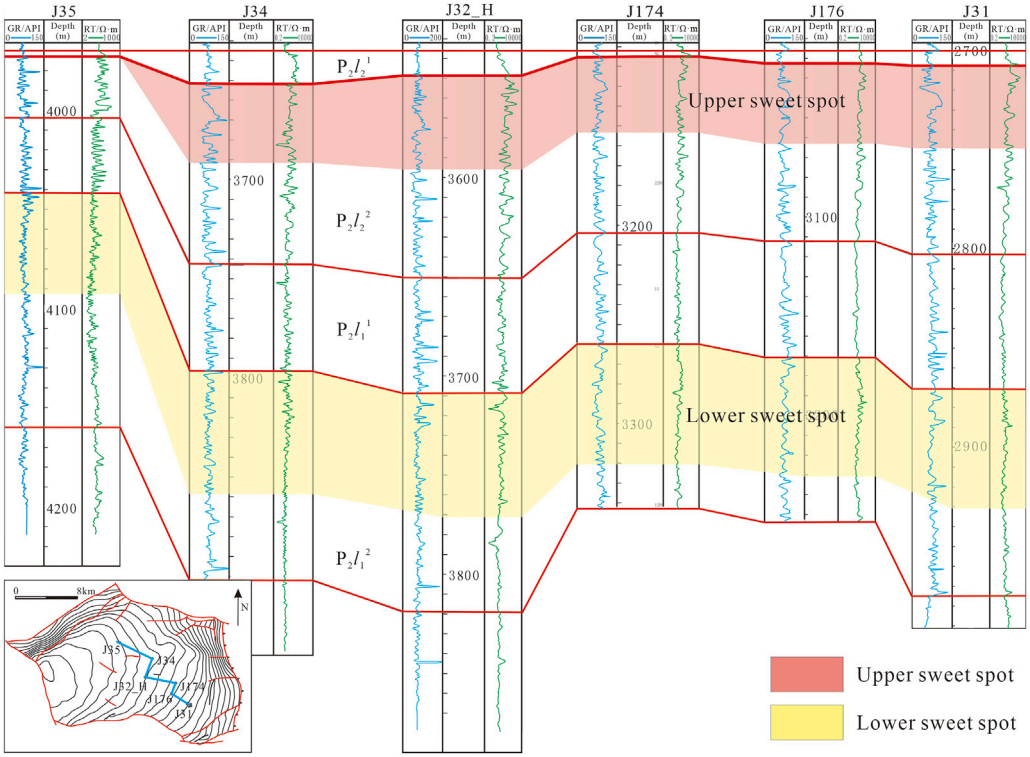

FIGURE 2
Stratigraphic correlation of the Lucaogou Formation in the Jimsar Sag, the Junggar Basin (modified from an internal report of the PetroChina Karamay Oilfield).

2 Geological setting

The Junggar Basin is located in the southern part of the Central Asian orogeny (Figure 1A), covering an area of about 1.3×10^5 km^2. It is a Mesozoic-Cenozoic sedimentary basin developing on the Paleozoic basement (Li et al., 2016; Zhang et al., 2017). The Jimsar Sag lies in the southeastern part of the basin (Figure 1B) and presents itself as a half-graben sag on a Middle Carboniferous fold basement. It is bounded by faults from all directions, including the Jimsar fault in the north, the Laozhuangwan Fault in the northwest, the Xidi fault in the southwest, the Santai fault in the south, and the Houbuzi fault in the southeast (Figure 1C).

The Jimsar Sag has experienced multi-stage tectonic movements since the Paleozoic (Zhang et al., 2017). The Jimsar fault was formed during the Late Carboniferous, when the Shaqi Uplift in the north of the Jimsar Sag was formed. The Jimsar Sag experienced intensive tectonic subsidence during the early Middle Permian, followed by the deposition of lacustrine sediments during the Late Permian to the Early Triassic (Wu et al., 2013; Zhang et al., 2017). The latest exploration demonstrates that oil reservoirs occur in the Permian Lucaogou and Wutonggou Formations.

The Lucaogou Formation is divided into the first (P_2l_1) and second (P_2l_2) members from bottom to top, referred to as the Lu-1 and Lu-2 Members, respectively. The Lu-1 Member is composed of the upper first sand group ($P_2l_1^1$) and the lower second sand group ($P_2l_1^2$), while the Lu-2 Member consists of the first ($P_2l_2^1$) and second ($P_2l_2^2$) sand groups from top to bottom (Figure 2). The Permian Lucaogou Formation is seen with long-interval hydrocarbon shows in high-permeability and high-porosity "sweet spots". There are broadly two sweet spots in the Lucaogou Formation, namely, the second sand group of the Lu-2 Member ($P_2l_2^2$) (the upper sweet spot) and the second sand group of the Lu-1 Member ($P_2l_1^2$) (the lower sweet spot). They are subdivided into 10 layers in accordance with their physical properties, including four layers of the upper sweet spot (STD 1–4) and six layers of the lower sweet spot (XTD 1–6).

3 Methods

To assess the main factors controlling fractures in tight oil reservoirs, we analyzed the mineral content and TOC content, and observed Focused Ion Beam Scamming Electron Microscopy of cores from seven wells (J30, J32, J174, J015, J5, J251, and J15). All experiments are performed in the State Key Laboratory of China University of Petroleum (Beijing).

3.1 X-ray diffffraction mineral analysis

A total of 130 samples from seven wells were selected for mineralogical composition analysis. Bulk minerology was

FIGURE 3
Photos of tectonic fractures, bedding seams, and abnormal overpressure-induced fractures. **(A)** Shear fractures in outcrops, Dalongkou reservoir profile. **(B)** Shear fractures in outcrops, Xiaolongkoucun profile. **(C)** Tensile fractures in outcrops, Dalongkoucun profile. **(D)** Bedding seams in outcrops, Dalongkou reservoir profile. **(E)** Tensile fractures in cores, 3590.60 m, Well J251. **(F)** Bedding seams in cores, 2311.80 m, Well J29. **(G)** Bedding seams in cores, 2363.42 m, Well J176. **(H)** Abnormal overpressure-induced fractures in cores, 4044.72 m, Well J30. **(I)** Abnormal overpressure-induced fractures in cores, 3126.42 m, Well J174.

determined via Xray diffraction (XRD) analysis. Crushed samples were mixed with ethanol, ground by hand and then smear-mounted on glass slides to create randomly oriented powder preparations (48 μm). Measurements were conducted on a Bruker D8 DISCOVER diffractometer, using Co. Kα-radiation at 45 kV and 35 mA. The diffffracted beam was measured with a scintillation detector. Quantitative phase analysis was performed using Rietveld refifinement, with customized clay mineral structure models (Wang et al., 2020).

3.2 TOC analysis

A total of 36 samples from seven wells were selected for Total Organic Carbon (TOC) analysis. Powdered samples were weighed, then acidifified with hydrochloric acid to remove carbonates. After rinsing and drying, de-carbonated samples were reweighed and combusted at high temperature in a Leco C230 carbon analyzer. Total organic carbon content is expressed as a weight percentage. This analysis was conducted in accordance with the Chinese National Standard GB/T19145-2003 (Wang et al., 2020).

3.3 Focused Ion Beam Scamming Electron Microscopy observation

Focused Ion Beam Scamming Electron Microscopy (FIB-SEM) is a method to focus a beam of ions on and scanning over the samples (Wang et al., 2016). The atomic bombardment on the surfaces of the samples by the ion beam will sputter the atoms. It provides a neo technology for the research of the micro-nanopores. The instrument used was a FEI-HELIOS-NanoLab 650 manufactured by US FEI Company. As observed with the backscattering function, the appearance of the organic matter was black with lowest brightness, the appearance of the pyrite was white with the highest brightness, and the appearance of the matrix minerals such as quartz and calcite was light gray. The pores were black notably.

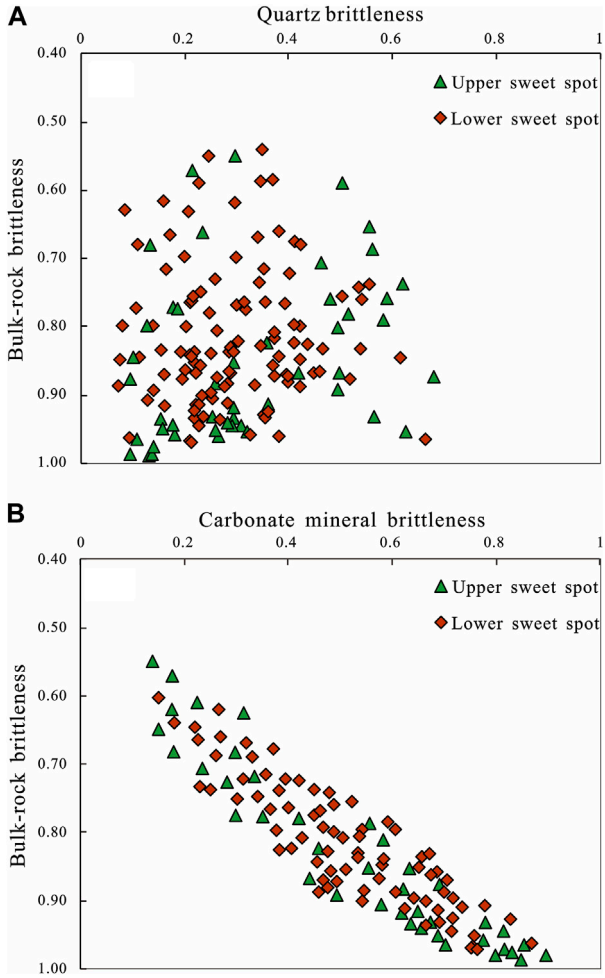

FIGURE 4
Correlations between different types of brittleness with 130 sample points from six typical wells (J5, J15, J30, J32, J174, and J251). **(A)** Quartz brittleness vs. bulk-rock brittleness. **(B)** Carbonate brittleness vs. bulk-rock brittleness.

4 Results and discussion

4.1 Fracture types

On an overall basis, the Permian Lucaogou Formation tight reservoir has well-developed natural fractures, as observed in outcrops, cores, and thin sections. These fractures are grouped into three types: tectonic fractures, diagenetic fractures, and abnormal overpressure-induced fractures.

4.1.1 Tectonic fractures

Tectonic fractures refer to fractures whose formation and distribution are controlled by local tectonic events or the tectonic stress field. Types, development degrees, and occurrences of tectonic fractures are dependent on the stress field distribution and tectonic position (Hou, 1994; Zeng et al., 2007; Yu et al., 2016). Tectonic fractures are widely developed in field outcrops and mainly include shear and tensile fractures. Some shear fractures present themselves in a conjugate arrangement (typically, X-shaped) in field outcrops (Figures 3A, B), with stable occurrence and long extension. The fracture surface is flat and smooth and is often found with striations. Field observation shows that shear fractures have a length range of 1–5 cm and an aperture range of 0.02–0.1 cm. Tensile fractures are scattered, with limited extensions and zigzag fracture surfaces. Their lengths are mainly 1–2 cm and the aperture is 0.02–0.3 cm (Figure 3C). In cores, some shear fractures only have one part of the expected X-shape (Figure 3E), which may be attributed to the anisotropic compressive strength associated with rock heterogeneity (Zeng et al., 2008). The core observation shows that fillings inside tectonic fractures are mostly quartz and calcite, with sporadic argillaceous fillings.

4.1.2 Diagenetic fractures

Diagenetic fractures are near-horizontal fractures generated via geological processes such as pressure solution, compaction, and pressure relief (He et al., 2011; Luo et al., 2017; Zeng et al., 2017). Diagenetic fractures in this study are predominantly bedding seams, with main occurrences at interfaces of bedding. They are parallel to each other and follow the directions of rock beds and micro-bedding. At the outcrop scale, these fractures have long extensions of 5–15 m and yet limited apertures of 0.05–0.1 cm (Figure 3D). At the core scale, they can penetrate the whole core (Figures 3F, G) with apertures of 0.02–0.1 cm. Field outcrops and drilling cores both show that diagenetic fractures are mostly filled with calcite, quartz, argillaceous minerals, and hydrocarbons.

4.1.3 Abnormal overpressure-induced fractures

Abnormal overpressure-induced fractures are found in cores, which are mostly drainage fractures formed via hydraulic processes (Liu et al., 2017; Zhang et al., 2017; Zeng et al., 2017). They are mostly observed at the core scale (Figures 3H, I) and are less seen in the field outcrop. They present irregular distribution in the form of vein groups and curved extensions in cores. Their apertures are highly variable—ranging from 0.5 mm to 10 mm, with a maximum of 20 mm. Their lengths are generally several centimeters. Most of them are filled and have low oil content, as seen in cores.

4.2 Influential factors of fracture development

Reservoir fractures are controlled by numerous factors (Zeng et al., 2013; Bucknall and Polymer., 2016; Ju and Sun, 2016). Moreover, their distribution and development degree are highly heterogeneous, which plays an important role in the exploration and development of tight reservoirs. However, previous studies mostly target fractures in conventional reservoirs, with insufficient attention to fractures in tight reservoirs. In this study, five factors are found to control the development of tectonic fractures and diagenetic fractures, including brittle minerals, lithology, bed thickness, tectonic stress, and TOC.

4.2.1 Brittle minerals

Brittle minerals such as calcite and quartz can normally promote the development of fractures (Zeng and Li, 2010). However, this kind of promotion varies from mineral to mineral. There are three methods of mineral brittleness evaluation (Diao, 2013; Wang et al.,

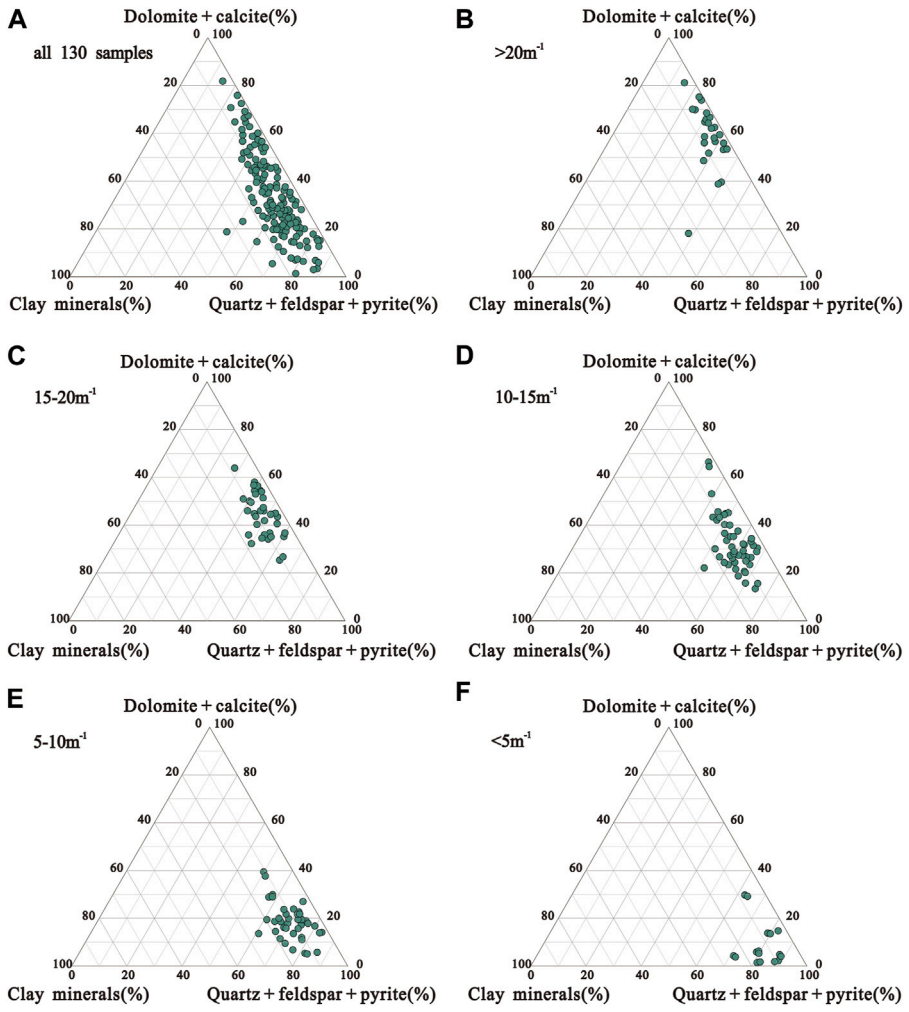

FIGURE 5
Ternary diagrams of mineral compositions for samples with tectonic fractures. **(A)** All samples (130 samples). **(B)** Samples with a tectonic fracture density greater than 20 m^{-1}. **(C)** Samples with a tectonic fracture density of 15–20 m^{-1}. **(D)** Samples with a tectonic fracture density of 10–15 m^{-1}. **(E)** Samples with a tectonic fracture density of 5–10 m^{-1}. **(F)** Samples with a tectonic fracture density below 5 m^{-1}.

2013; Wan et al., 2016), which are respectively based on i) Young's modulus and Poisson ratio (elastic parameters), ii) the relative content of brittle and clay minerals, and iii) mineral composition. Particularly, carbonate rocks are found to significantly contribute to the brittleness of reservoirs rich in carbonate minerals (Fridrun et al., 2015).

The studied Lucaogou Formation has a high content of carbonate rocks, with a wide range of 3.6%–87.3% and an average of 45.8%. Therefore, carbonate rocks should be one of the most influential factors of reservoir brittleness. In this study, the brittleness is characterized by the ratio of different minerals:

Quartz brittleness = quartz/(quartz + carbonate minerals + clay minerals).

Carbonate mineral brittleness = carbonate minerals/(quartz + carbonate minerals + clay minerals).

Bulk-rock brittleness = (quartz + carbonate minerals)/(quartz + carbonate minerals + clay minerals).

As shown in Figure 4, the studied reservoir has high brittleness, with bulk-rock brittleness above 0.5. The bulk-rock brittleness presents no notable correlation with quartz brittleness (Figure 4A), while it seems to linearly scale with the carbonate mineral brittleness (Figure 4B). Therefore, carbonate minerals are more important to the bulk-rock brittleness.

As illustrated in Figure 5, feldspar, quartz, pyrite, calcite, and dolomite have absolute controls on the development of tectonic fractures. In contrast, they have no notable control on the development of diagenetic fractures (Figure 6). Specifically, dolomite and calcite are the main controlling factors of tectonic fractures (Figure 5).

4.2.2 Lithology

In this study, samples are collected from intervals that are far away from faults, belong to the same tectonic belt, and have similar bed thicknesses. The linear densities of tectonic and diagenetic fractures are summarized and plotted for several lithologies, including dolomite, dolomitic sandstone, dolomitic mudstone, limestone, siltstone, fine-grained sandstone, medium-grained sandstone, coarse-grained sandstone, conglomerate, sandy

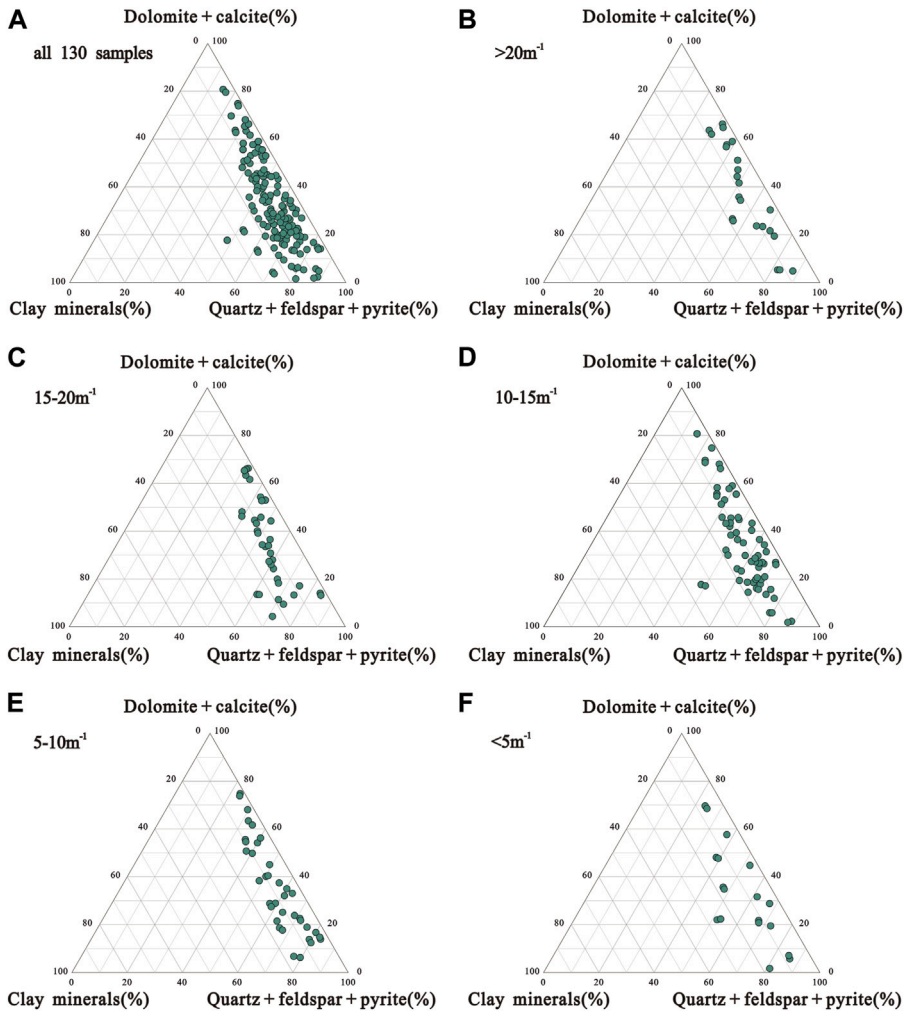

FIGURE 6
Ternary diagrams of mineral compositions for samples with diagenetic fractures. **(A)** All samples (130 samples). **(B)** Samples with a diagenetic fracture density greater than 20 m^{-1}. **(C)** Samples with a diagenetic fracture density of 15–20 m^{-1}. **(D)** Samples with a diagenetic fracture density of 10–15 m^{-1}. **(E)** Samples with a diagenetic fracture density of 5–10 m^{-1}. **(F)** Samples with a diagenetic fracture density below 5 m^{-1}.

mudstone, muddy sandstone, limy mudstone and mudstone of the upper and lower sweet spots respectively.

As illustrated in Figure 7, the same lithology has the same control on fracture development in the upper and lower sweet spots. Tectonic fractures are more developed in dolomitic rocks (Figure 7A), with linear densities of 2.80 m^{-1} in dolomite, 2.46 m^{-1} in dolomitic sandstone, and 1.97 m^{-1} in dolomitic mudstone for the upper sweet spot; those values for the lower sweet spot are 3.18, 2.25 and 2.29 m^{-1}, respectively. This is because dolomitic rocks are more brittle—under the same stress conditions, their bearable strains before cracking are smaller and they are more prone to generating tectonic fractures than soft/plastic rocks (Zeng et al., 2008). For both the upper and lower sweet spots, the linear density of tectonic fractures drops in the order of limestone, siltstone, fine-grained sandstone, medium-grained sandstone, and conglomerate, which indicates the control of rock particle sizes on the development of tectonic fractures. With smaller particles and lower pore volumes, rocks are associated with higher rigidity brittleness and are easier to crack under tectonic stress. Muddy rocks tend to absorb more stresses via plastic deformation, and the resultant development of tectonic fractures is relatively low.

The control of lithology on diagenetic fractures is considerably different from that on tectonic fractures. Diagenetic fractures are more developed in argillaceous rocks (i.e., mudstone, dolomitic mudstone, muddy sandstone, and limy mudstone) (Figure 7B), with the maximum linear density in mudstones, reaching 4.81 m^{-1}. Diagenetic fractures are also well-developed in carbonate rocks (dolomite and muddy dolomite). The plentiful diagenetic fractures in muddy rocks are attributed to the intensive hydrocarbon generation and expulsion of organic matter in such rocks, which can cause dissolution and pressurization.

To conclude, lithology has strong control effects on the development of tectonic and diagenetic fractures. Specifically, tectonic fractures are most developed in dolomite, with an

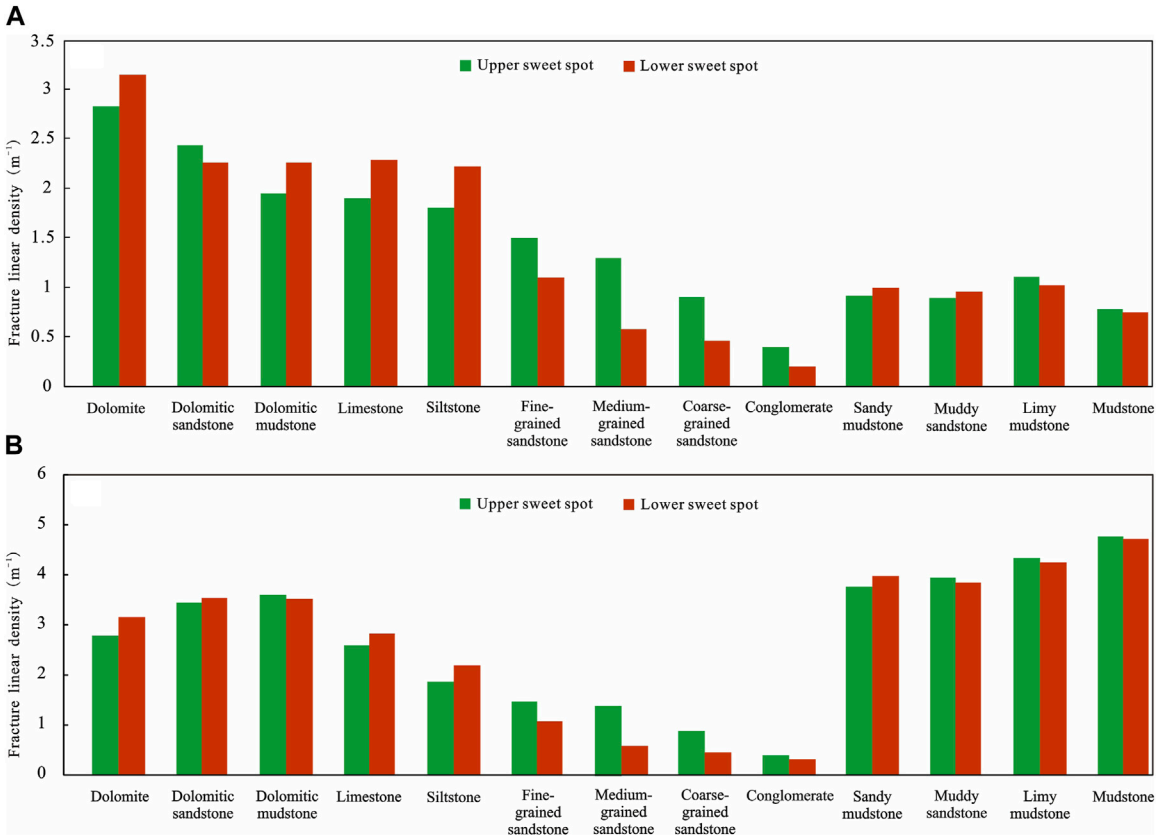

FIGURE 7
Lithology vs. fracture density for the upper and lower sweet spots. Green and red represent the upper sweet spot and the lower sweet spot, respectively. **(A)** tectonic fracture. **(B)** diagenetic fracture.

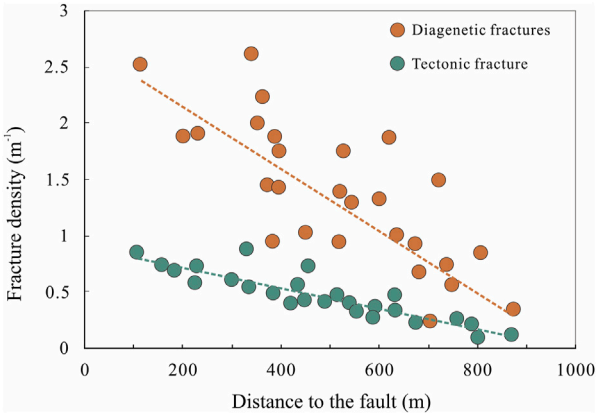

FIGURE 8
Correlation between fracture density and faulting intensity.

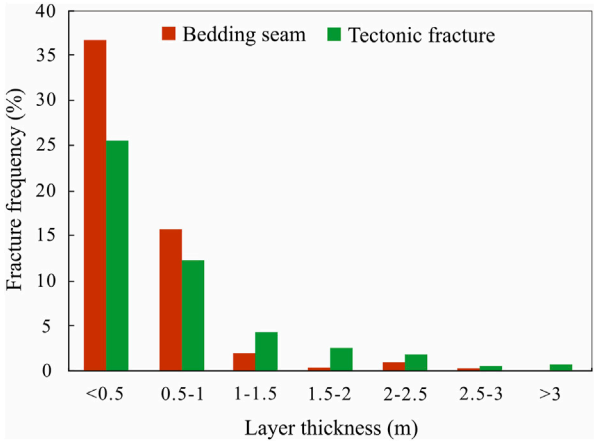

FIGURE 9
Correlation between fracture density and bed thickness. The frequency of bedding fractures and tectonic fractures decreases with the increase of layer thickness.

average density of 2.96 m^{-1}. Compared with siltstone and fine-grained sandstone, argillaceous rocks have lower development of tectonic fractures, as they have larger plastic deformation to absorb more stresses under the same tectonic condition. Meanwhile, medium-grained sandstone, coarse-grained sandstone, and conglomerate have the least developed tectonic fractures, because their larger particles and higher pore volumes lead to lower strengths that, in turn, promote resistance to cracking after elastic deformation. As for diagenetic fractures, they are most developed in mudstone, with an average density of 4.85 m^{-1}, which is attributed

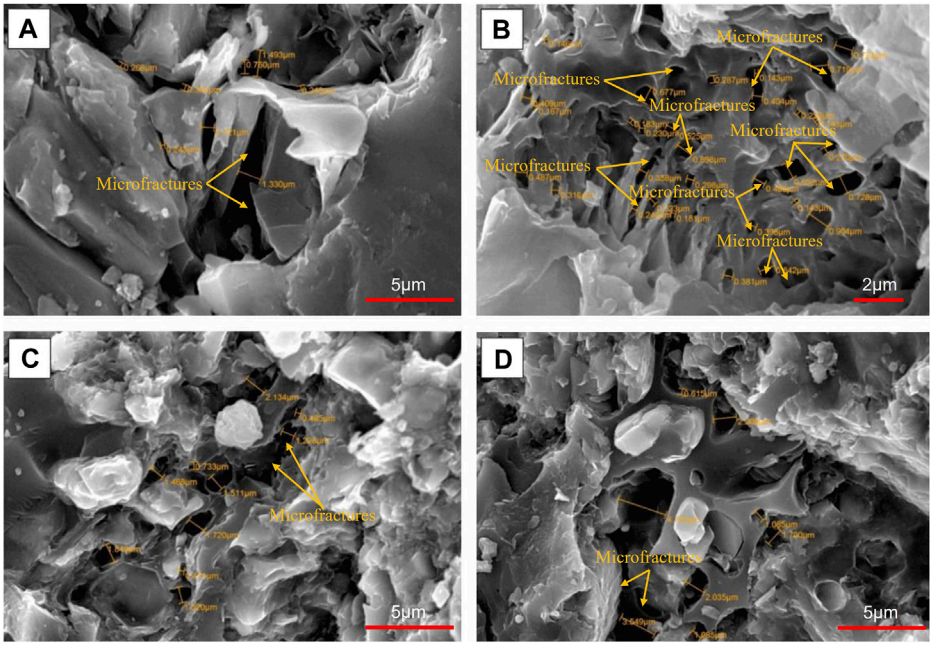

FIGURE 10
SEM images of fractures generated by hydrocarbon generation. **(A, B)** Microfractures occur inside of the organic matter. **(C, D)** Microfractures occur at the edge of the organic matter.

to the organic acid dissolution and pressurization during hydrocarbon generation and expulsion.

4.2.3 Tectonic stress

Tectonic stress represents a main control on the reservoir fracture development. It is easier to form fractures in more tectonically-active zones. Statistics of field outcrops show that tectonic stress has consistent controls on tectonic and diagenetic fractures. With the same lithology, the tectonic fracture density grows in zones nearer to faults, and the same pattern is also identified for diagenetic fractures (Figure 8), due to the opening of weak bedding planes driven by tectonic stress. It is also noted in field outcrops that the densities of tectonic and diagenetic fractures are higher around larger faults than those near smaller faults. In addition, field outcrops are often associated with conjugate shear fractures, while cores tend to present a single shear fracture. This may be attributed to the underground confining pressure, which in turn reflects the control of tectonic stress on fracture development.

4.2.4 Bed thickness

Observation of field outcrops and cores reveals that mudstone and sandstone alternate with each other in forms of interbedding, which leads to the higher development of bedding seams/diagenetic fractures. To eliminate the effects of dissolution, the following analysis involves only sandstone, since dolomite contains higher contents of carbonate minerals. Statistics suggest that tectonic fractures and bedding seams are both affected by bed thickness. Their density climbs up, as the bed becomes thinner. The bed thickness over 3 m is found with the least development of fractures; on the contrary, the highest development of fractures occurs in the case of the bed thickness below 0.5 m (Figure 9).

4.2.5 TOC

Under the same stress, organic matter abundance is one of the factors affecting fracture development in mudstones (Liu et al., 2017; Zhang et al., 2017). The control of TOC on fracture development depends on organic matter distribution, organic matter and water consumption by hydrocarbon generation, and hydrocarbon generation-induced pressurization. The existence of organic matter bands becomes more prominent and influential, with higher organic matter abundance, and micro-fractures tend to occur inside and at the edge of such organic matter bands (Zhang et al., 2017).

The Lucaogou Formation in the Jimsar Sag has extensive development of argillaceous source rocks (Kuang et al., 2014), with TOC mostly of 1.29%–13.82% and averaging 5.34%. Fractures are created via the pressurization and dissolution processes during hydrocarbon generation and expulsion.

Microfractures often occur inside and at the edge of the organic matter (Figure 10), which may be attributed to the consumption of water and organic matter by hydrocarbon generation or the pressurization also induced by hydrocarbon generation (Zhang et al., 2017). The organic matter adjacent to clay minerals (e.g., illite) is also seen with numerous internal pores and fractures. The reason behind this observation may be that a large volume of fluids is generated during the conversion from smectite to illite to form transitional smectite-illite mixed minerals; such minerals are highly catalytic and promote hydrocarbon generation to create more organic pores and fractures (Zhang et al., 2017).

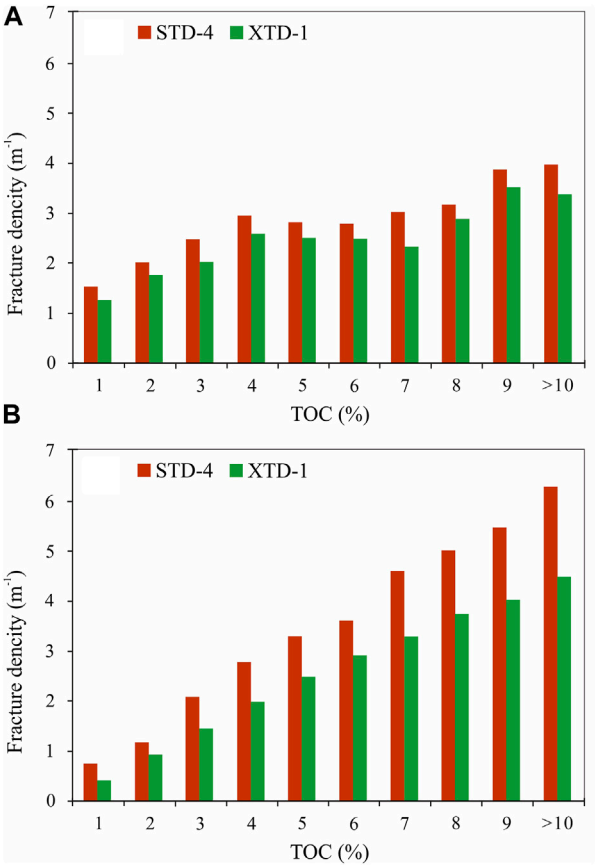

FIGURE 11
TOC vs. fracture density for the upper and lower sweet spots. Fracture density increase with the increase of TOC. **(A)** Tectonic fractures. **(B)** Bedding seams.

Here the STD-4 layer of the upper sweet spot and the XTD-1 layer of the lower sweet spot are taken as examples to investigate the correlation between TOC and fracture development. The STD-4 layer is mainly composed of dolomitic mudstone and dolomite, with a total content of calcite and dolomite up to 45.89%, while the XTD-1 layer is predominantly silty-fine sandstone and sandy mudstone, with the total calcite-dolomite content of 32.50%. As revealed in Figure 11, TOC has considerably decisive effects on the development of bedding seams. For both the STD-4 and XTD-1 layers, the bedding seam density grows with the rising TOC. Although the tectonic fracture density also climbs up with the increasing TOC, such a variation trend is weaker than that of bedding seams. To sum up, higher TOC results in the higher development of both tectonic fractures and bedding seams, and yet the control of TOC on bedding seams is stronger than that on tectonic fractures.

The incremental pressure induced by hydrocarbon generation can lead to the failure of rocks and the opening of weak bedding planes to form tectonic fractures and bedding seams respectively (Luo et al., 2017; Fall et al., 2015). In addition, hydrocarbons and acid fluids expelled during hydrocarbon generation may dissolve bedding planes to form bedding seams (Fall et al., 2015). Some fractures have prominent hydrocarbon shows, indicating that the hydrocarbon generation-expulsion is one of the important contributors to fracture formation.

4.3 Main controlling factors of fracture development

4.3.1 Tectonic fractures

As discussed in Section 4, the development of tectonic fractures varies with layer thicknesses. However, outcrops, cores, and imaging logging all reveal that the Lucaogou Formation reservoir is mostly transitional rocks, with interbedding of centimeter-scale beds of different lithologies. Statistics of bed thicknesses in cores show that beds thinner than 10 cm account for more than 80% of the total (Figure 12). Therefore, it is safe to say that the dependency of tectonic fracture development on bed thickness is rather small for

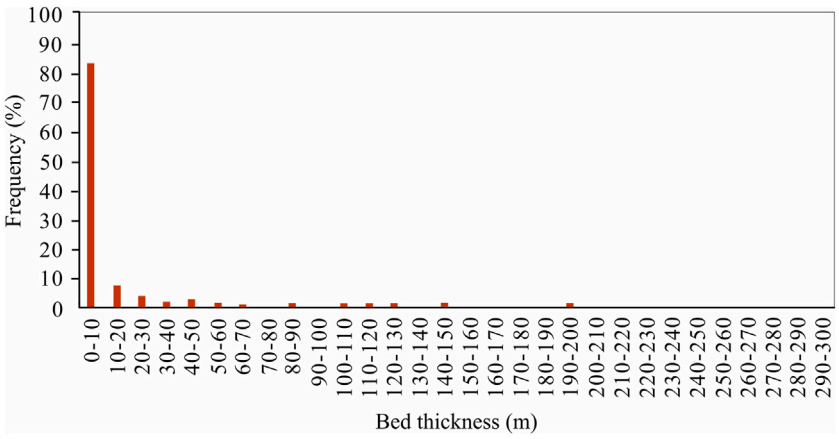

FIGURE 12
Histograms of bed thickness distribution.

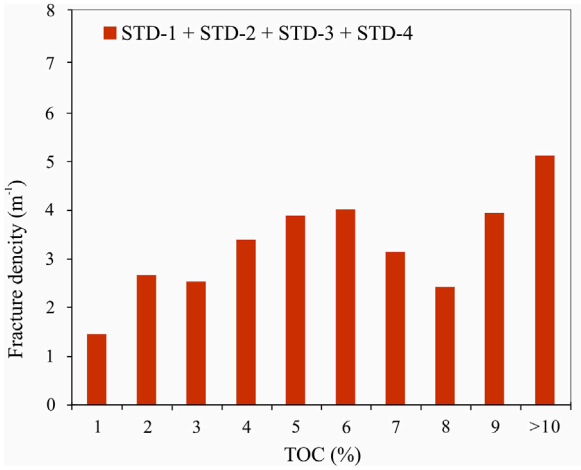

FIGURE 13
TOC vs. tectonic fracture density for the upper sweet spot.

the Lucaogou Formation characterized by the "relatively homogeneous" bed thickness, despite that the bed thickness to some extent restrains the development of tectonic fractures.

Linear positive correlations are found between TOC and tectonic fracture density for both the STD-4 and XTD-1 layers of the upper and lower sweet spots respectively. However, no notable correlation is found in the statistics of the samples of the four layers in the upper sweet spot (Figure 13). It is noted that samples from STD-4 and XTD-1 layers (Figure 11A) have similar brittleness indexes, whereas those from the four layers of the upper sweet spot in Figure 13 have varied brittle mineral contents. Moreover, the overall brittleness index of the upper sweet spot is lower than those of STD-4 and XTD-1 layers. In other words, with varied contents of quartz and carbonate minerals, no notable correlation is found between TOC and tectonic fracture density. This means that the development of tectonic fractures is affected jointly by mineral brittleness and TOC, and the effect of brittle minerals is stronger than that of TOC.

The above analysis indicates that brittle minerals, lithology, and tectonic stress may be the main control factors for fracture development in the Lucaogou Formation tight reservoir among all influential factors. To quantitatively characterize the main control factors for fracture development, the fracture density variation coefficient is introduced in this research (Yang, 2011).

$$V = \frac{\delta_j}{F_a} \tag{1.1}$$

$$\delta_f = \sqrt{\sum_{i=1}^{n} (F_i - F_a)^2 / n} \tag{1.2}$$

$$F_a = \frac{1}{n} \sum_{i=1}^{n} F_i \tag{1.3}$$

where V is the fracture density variation coefficient, dimensionless; δ_f is the standard deviation of a variable; f_a is the mean fracture density of all samples; F^i is the fracture density of the ith sample; n is the sample quantity.

The coefficient of variation of fracture density can be used to evaluate the impact of a single factor, with a larger value indicating a stronger impact. Tectonic stress and brittle minerals are found to result in the largest coefficient of variation, followed by lithology, TOC, and bed thickness successively (Table 1).

4.3.2 Bedding seams

As discussed in Section 4, brittle minerals have no considerable control over the development of bedding seams—bedding seams can be well developed in rocks with high and low calcite-dolomite contents. Similar to the case of tectonic fractures, the "relatively homogenous" bed thickness results in low dependency of the bedding seam development on layer thickness. It is often observed in field outcrops that the bedding seam density grows as it approaches the fault in the case of the same lithology; nevertheless, the bedding seam density of mudstone far away from the fault is higher than that of sandstone nearer to the fault. These demonstrate the higher effects of lithology than tectonic stress on the development of bedding seams.

The above analysis shows lithology and TOC may be the main control factors of the bedding seam development. This is verified by the calculated coefficients of variation of the bedding seam density. In addition, as suggested in Table 2, the effects of tectonic

TABLE 1 The coefficients of variation of tectonic fracture density corresponding to various control factors.

	Brittle minerals	Lithology	Tectonic stress	Bed thickness	TOC
Coefficient of variation	0.96	0.86	1.21	0.28	0.31
Ranked effect	4	5	6	1	2

TABLE 2 The variation coefficients of bedding seam density corresponding to various control factors.

	Brittle minerals	Lithology	Tectonic stress	Bed thickness	TOC
Coefficient of variation	0.78	0.48	0.29	0.99	0.78
Ranked effects	3	2	1	4	3

stress and bed thickness on the bedding seam development are rather small.

5 Conclusion

1) Natural fractures in the Lucaogou Formation tight reservoir, Jimsar Sag are mainly three types, including tectonic fractures, diagenetic fractures, and abnormal overpressure-induced fractures. Tectonic fractures include shear and tensile fractures; diagenetic fractures are predominantly bedding seams; abnormal overpressure-induced fractures are mainly drainage fractures.
2) The development of natural fractures is affected by brittle minerals, lithology, tectonic stress, bed thickness, and TOC. Specifically, dolomite and calcite (carbonate minerals) make the greatest contributions to the formation of tectonic fractures; in contrast, brittle minerals have no notable control over the development of bedding seams. The dolomitic rock has the highest development of tectonic fractures, while the most-developed bedding seams are found in the argillaceous rocks. The development of both tectonic fractures and bedding seams grows with the increasing tectonic stress. Higher bed thickness leads to suppressed development of both tectonic fractures and bedding seams. At last, the densities of both tectonic fractures and bedding seams are inversely proportional to TOC.
3) Tectonic stress and brittle minerals are the main control factors of the development of tectonic fractures. For bedding seams, the main control factors are TOC and lithology.

Data availability statement

The datasets presented in this study can be found in online repositories. The names of the repository/repositories and accession number(s) can be found in the article/supplementary material.

Author contributions

YY, ZD, and JG contributed to conception and design of the study. CZ organized the database. YY, ZD, and CZ performed the statistical analysis. YY wrote the first draft of the manuscript. ZD, JG, and CZ wrote sections of the manuscript. All authors contributed to the article and approved the submitted version.

Funding

This work is financially supported by the grants from PetroChina Research Institute of Petroleum Exploration and Development (No. 2022KT1401, 2021DJ2302). Key Laboratory of Tectonics and Petroleum Resources (China University of Geosciences, Ministry of Education, Wuhan 430074, China) (No. TPR-2021-01).

Conflict of interest

The authors ZD and JG were employed by PetroChina Research Institute of Petroleum Exploration and Development. The author PL was employed by Bureau of Geophysics Prospecting Inc.

The authors declare that this study received funding from China University of Petroleum, Beijing. The funder had the following involvement in the study: design, collection, and writing of this article. The authors declare that this study received funding from PetroChina Research Institute of Petroleum Exploration and Development. The funder had the following involvement in the study: the decision to submit it for publication and interpretation of data. The authors declare that this study received funding from Bureau of Geophysics Prospecting Inc, CNPC, Research Center of Geology. The funder had the following involvement in the study: design, data collection and analysis. The authors declare that this study received funding from Chengdu University of Technology, Chengdu. The funder had the following involvement in the study: design, preparation of the manuscript.

Publisher's note

References

Becker, S. P., Eichhubl, P., Laubach, S. E., Reed, R. M., Lander, R. H., and Bodnar, R. J. (2010). A 48 m.y. history of fracture opening, temperature, and fluid pressure: Cretaceous Travis Peak Formation, East Texas basin. *Bone* 38 (5), 1081–1093. doi:10.1130/b30067.1

Bucknall, C. B., and Polymer, G. (2016). Fracture of: Factors controlling toughness. Reference module in materials science and materials engineering. *Encyclopedia of Materials: Science and Technology*, 7322–7326.

Cao, Y. C., Zhu, N., Zhang, S. M., Xi, K. L., and Xue, X. J. (2019). Diagenesis and reserving space characteristics of tight oil reservoirs of permian Lucaogou Formation jimusar sag of jungar basin, China. *J. Earth Sci. Environ.* 41 (3), 253–266.

Cao, Z., Liu, G. D., Kong, Y. H., Wang, C. Y., Niu, Z. C., Zhang, J. Y., et al. (2016). Lacustrine tight oil accumulation characteristics: Permian Lucaogou Formation in jimusaer sag, Junggar Basin. *Int. J. Coal Geol.* 153, 37–51. doi:10.1016/j.coal.2015.11.004

Diao, H. Y. (2013). Rock mechanical properties and brittleness evaluation of shale reservoir. *Acta Petrol. Sin.* 29 (9), 3300–3306.

Du, J. H., He, H. Q., Li, J. Z., Yang, T., Haung, F. X., Guo, B. C., et al. (2014). Progress in China's tight oil exploration and challenges. *China Pet. Explor.* 19 (1), 1–8.

Fall, A., Eichhubl, P., Bodnar, R. J., Laubach, S. E., and Davis, J. S. (2015). Natural hydraulic fracturing of tight-gas sandstone reservoirs, Piceance Basin, Colorado. *Geol. Soc. Am. Bull.* 127 (1-2), 61–75. doi:10.1130/b31021.1

Fall, A., Eichhubl, P., Cumella, S. P., Bodnar, R. J., Laubach, S. E., and Becker, S. P. (2012). Testing the basin-centered gas accumulation model using fluid inclusion observations: Southern Piceance Basin, Colorado. *AAPG Bull.* 96 (12), 2297–2318. doi:10.1306/05171211149

Fridrun, P., Newton, J. M., and Paul, F. (2015). The bending strength of tablets with a breaking line-Comparison of the results of an elastic and a "brittle cracking" finite

element model with experimental findings. *Int. J. Pharm.* 495 (1), 485–499. doi:10.1016/j.ijpharm.2015.09.004

Gale, J. F. W., Robert, M. R., and Holder, J. (2007). Natural fractures in the Barnett Shale and their importance for hydraulic fracture treatments. *AAPG Bull.* 91 (4), 603–622. doi:10.1306/11010606061

Ghanizadeh, A., Clarkson, C. R., Aquino, S., Ardakani, O. H., and Sanei, H. (2015). Petrophysical and geomechanical characteristics of Canadian tight oil and liquid-rich gas reservoirs: I. Pore network and permeability characterization. *Fuel* 153 (1), 664–681. doi:10.1016/j.fuel.2015.03.020

He, Z. J., Liu, B. J., and Wang, P. (2011). Genesis of bedding fractures and its influences on reservoirs in Jurassic, Yongjin area, Junggar Basin. *Petroleum Geol. Recovery Effic.* 18 (1), 15–17. doi:10.13673/j.cnki.cn37-1359/te.2011.01.004

Hou, G. T. (1994). Fractal analysis of fractures. *J. Basic Sci. Eng.* 2 (4), 299–305. doi:10.16058/j.issn.1005-0930.1994.04.005

Ju, W., and Sun, W. F. (2016). Tectonic fractures in the lower cretaceous xiagou Formation of qingxi Oilfield, jiuxi basin, NW China. Part two: Numerical simulation of tectonic stress field and prediction of tectonic fractures. *J. Petroleum Sci. Eng.* 146, 626–636. doi:10.1016/j.petrol.2016.05.002

Kuang, L. C., Gao, G., Xiang, B. L., Wang, X. L., Wang, C. Y., and Liu, G. D. (2014). Lowest limit of organic carbon content in effective source rocks from Lucaogou Formation in Jimusar Sag. *Petroleum Geol. Exp.* 36 (2), 224–229. doi:10.11781/sysydz201402224

Kuang, L. C., Tang, Y., Lei, D. W., Chang, Q. S., Ou, Y. M., Hou, L. H., et al. (2012). Formation conditions and exploration potential of tight oil in the Permian saline lacustrine dolomitic rock, Junggar Basin, NW China. *Petroleum Explor. Dev.* 39 (6), 700–711. doi:10.1016/s1876-3804(12)60095-0

Laubach, S. E., Fall, A., Copley, L. K., Marrett, R., and Wilkins, S. J. (2016). Fracture porosity creation and persistence in a basement-involved laramide fold, upper cretaceous frontier formation, green river basin, USA. *Geol. Mag.* 153 (5-6), 887–910. doi:10.1017/s0016756816000157

Li, D., He, D. F., and Tang, Y. (2016). Reconstructing multiple arc-basin systems in the altai–junggar area (NW China): Implications for the architecture and evolution of the Western central asian orogenic belt. *J. Asian Earth Sci.* 121, 84–107. doi:10.1016/j.jseaes.2016.02.010

Li, H., Tang, H. M., Qin, Q. R., Zhou, J. L., Qin, Z. J., Fan, C. H., et al. (2019). Characteristics, formation periods and genetic mechanisms of tectonic fractures in the tight gas sandstones reservoir: Acase study of Xujiahe Formation in YB area, Sichuan Basin, China. *Journal Petroleum 5cience Eneineering* 178, 723–735. doi:10.1016/j.petrol.2019.04.007

Liu, D. D., Zhang, C., Luo, Q., Zhang, Y. D., Gao, Y., Zhang, Y. C., et al. (2017). Development characteristics and controlling factors of natural fractures in Permian Lucaogou Formation tight reservoir in Jimsar sag, Junggar Basin. *China Pet. Explor.* 22 (4), 36–47. doi:10.3969/j.issn.1672-7703.2017.04.004

Liu, Y. S., Dong, X. H., Yan, L., Chen, F. L., Gao, Y. L., and Chen, Z. X. (2019). Quantitative characterization of pore structure of Lucaogou Formation in jimsar sag. *Xinjiang Pet. Geol.* 40 (3), 284–289. doi:10.7657/XJPG20190305

Luo, Q., Wei, H. Y., Liu, D. D., Zhang, C., Zu, D. Y., Zhang, Y. C., et al. (2017). Geofluids in deep sedimentary basins and their significance for Petroleum accumulation. *Petroleum Geol. Exp.* 39 (1), 1–4. doi:10.1155/2017/3571359

Ma, K., Liu, Y. M., Hou, J. G., Huang, S., Yan, L., Chen, F. L., et al. (2019). Densification mechanism of tight reservoirs from mixed sedimentation in saline lacustrine environment: A case study of permian Lucaogou Formation, jimsar sag. *Xinjiang Pet. Geol.* 40 (3), 253–261.

Nelson, P. H. (2009). Pore-throat sizes in sandstones, tight sandstones, and shales. *AAPG Bull.* 93 (3), 329–340. doi:10.1306/10240808059

Tian, W., Liu, H. Q., He, S. L., Wang, J., and Xie, l. (2019). Characterization of microscopic pore structure of tight oil reservoirs in Lucaogou Formation,Jimusaer Sag. *Petroleum Geol. Recovery Effic.* 26 (4), 24–32. doi:10.13673/j.cnki.cn37-1359/te.2019.04.004

Wan, X. Q., Peng, C., Pan, J. N., Wang, X. Y., and Dong, Y. Z. (2016). Coal measures argillutite mineral composition and brittleness analysis in yuzhou coalfield. *Coal Geol. China* 28 (10), 24–28. doi:10.3969/j.issn.1674-1803.2016.10.06

Wang, P. F., Jiang, Z. X., Ji, W. M., Zhang, C., Yuan, Y., Chen, L., et al. (2016). Heterogeneity of intergranular, intraparticle and organic pores in longmaxi shale in sichuan basin, south China: Evidence from SEM digital images and fractal and multifractal geometries. *Mar. Petroleum Geol.* 72, 122–138. doi:10.1016/j.marpetgeo.2016.01.020

Wang, P., Ji, Y. L., Pan, R. F., Wang, Z. Z., and Wu, Y. (2013). A comprehensive evaluation method of shale brittleness: A case study from the lower silurian longmaxi Fm in block W, sichuan basin. *Nat. Gas. Ind.* 33 (12), 48–53. doi:10.3787/j.issn.1000-0976.2013.12.006

Wang, X., Jiang, Z. X., Zhang, K., Wen, M., Xue, Z. X., Wu, W., et al. (2020). Analysis of gas composition and nitrogen sources of shale gas reservoir under strong tectonic events: Evidence from the complex tectonic area in the yangtze plate. *Energies* 13 (1), 281. doi:10.3390/en13010281

Wu, J. J., You, L. P., and Yang, H. S. (2013). Structural evolution and hydrocarbon accumulation of Fukang fault zone in Junggar Basin. *Xinjiang Pet. Geol.* 34 (1), 36–40.

Yang, X. J. (2011). *Characteristics and origin of fractures in tight sandstone reservoirs with low permeability, Dabei Gas Field*. China: China University of Petroleum. (East China).

Yu, X., Hou, G. T., Neng, Y., Li, J., and Wei, H. X. (2016). Development and distribution characteristics of tectonic fractures in kuqa depression. *Geol. J. China Univ.* 22 (4), 644–656. doi:10.16108/j.issn1006-7493.2015255

Zeng, L. B., Kang, Y. S., and Xiao, S. R. (2008). Development characteristics and geneses of the fractures in low-permeability sandstone reservoir in the northern depression of Tuha Basin. *J. Xi'an Shiyou Univ. Nat. Sci. Ed.* 23 (1), 22–25.

Zeng, L. B., and Li, Y. G. (2010). Tectonic fractures in tight gas sandstones of the upper triassic xujiahe Formation in the western sichuan basin, China. *Acta Geol. Sin. Engl. Ed.* 84 (5), 1229–1238. doi:10.1111/j.1755-6724.2010.00293.x

Zeng, L. B., Qi, J. F., and Wang, Y. X. (2007). Origin type of tectonic fractures and geological conditions in low-permeability reservoirs. *Acta Pet. Sin.* 28 (4), 52–56.

Zeng, L. B., Su, H., Tang, X. M., Peng, Y. M., and Gong, L. (2013). Fractured tight sandstone oil and gas reservoirs: A new play type in the dongpu depression, bohai bay basin, China. *AAPG Bull.* 97 (3), 363–377. doi:10.1306/09121212057

Zeng, L. B., Zhao, X. Y., Zhu, S. J., and Zhao, J. Y. (2017). Waterflood-induced fractures and its signifcance for development of lowpermeability sandstone oil reservoirs. *Petroleum Sci. Bulletion* 2 (3), 336–343. doi:10.3969/j.issn.2096-1693.2017.03.031

Zhang, C., Zhu, D. Y., Luo, Q., Liu, L. F., Liu, D. D., Yan, L., et al. (2017). Major factors controlling fracture development in the Middle Permian Lucaogou Formation tight oil reservoir, Junggar Basin, NW China. *J. Asian Earth Sci.* 146, 279–295. doi:10.1016/j.jseaes.2017.04.032

Zhang, F., Jiang, Z. X., Xiao, H. M., Hu, B., Chen, P., Tang, X. L., et al. (2021). Testing origin of reservoir quality difference of tight sandstones in the Yanchang Formation, Ordos Basin, China. *Mar. Petroleum Geol.* 2021, 105507. doi:10.1016/j.marpetgeo.2021.105507

Zhao, W., Jia, C. Z., Jiang, L., Zhang, T., He, M. X., Zhang, F., et al. (2021). Fluid charging and hydrocarbon accumulation in the sweet spot, Ordos Basin, China. *J. Petroleum Sci. Eng.* 200, 108391. doi:10.1016/j.petrol.2021.108391

Zheng, M. L., Tian, A. J., Yang, T. Y., He, W. Jun., C, L., Wu, H. S., et al. (2018). Structural evolution and hydrocarbon accumulation in the eastern Junggar Basin. *Oil Gas Geol.* 39 (5), 907–917. doi:10.1743/ogg20180506

Frontiers in Earth Science

Investigates the processes operating within the major spheres of our planet

Advances our understanding across the earth sciences, providing a theoretical background for better use of our planet's resources and equipping us to face major environmental challenges.

Discover the latest Research Topics

See more →

Frontiers

Avenue du Tribunal-Fédéral 34
1005 Lausanne, Switzerland
frontiersin.org

Contact us

+41 (0)21 510 17 00
frontiersin.org/about/contact